WL-TR-95-4089

DAMAGE TOLERANCE CONCEPTS
FOR TITANIUM-ALUMINIDE COMPOSITES

J.A. HALL, A. PERALTA, R. L. HOLLARS, ALLIEDSIGNAL ENGINES
D. HARMON, M.A. FINEFIELD, MCDONNELL DOUGLAS AIRCRAFT
M.R. JAMES, D.B. MARSHALL, ROCKWELL INTERNATIONAL SCIENCE
CENTER

AUGUST 1995

FINAL REPORT FOR 13 SEPTEMBER 1989 - 13 DECEMBER 1994

MATERIALS DIRECTORATE
WRIGHT LABORATORY
AIR FORCE MATERIEL COMMAND
WRIGHT-PATTERSON AIR FORCE BASE, OHIO 45433-7734
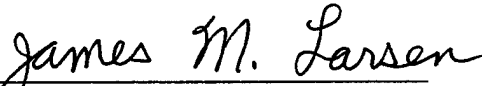
NOTICE

WHEN GOVERNMENT DRAWINGS, SPECIFICATIONS, OR OTHER DATA ARE USED FOR ANY PURPOSE OTHER THAN IN CONNECTION WITH A DEFINITELY GOVERNMENT-RELATED PROCUREMENT, THE UNITED STATES GOVERNMENT INCURS NO RESPONSIBILITY OR ANY OBLIGATION WHATSOEVER. THE FACT THAT THE GOVERNMENT MAY HAVE FORMULATED OR IN ANY WAY SUPPLIED THE SAID DRAWINGS, SPECIFICATIONS, OR OTHER DATA, IS NOT TO BE REGARDED BY IMPLICATION OR OTHERWISE IN ANY MANNER CONSTRUED, AS LICENSING THE HOLDER OR ANY OTHER PERSON OR CORPORATION, OR AS CONVEYING ANY RIGHTS OR PERMISSION TO MANUFACTURE, USE, OR SELL ANY PATENTED INVENTION THAT MAY IN ANY WAY BE RELATED THERETO.

THIS REPORT IS RELEASABLE TO THE NATIONAL TECHNICAL INFORMATION SERVICE (NTIS). AT NTIS, IT WILL BE AVAILABLE TO THE GENERAL PUBLIC, INCLUDING FOREIGN NATIONS.

THIS TECHNICAL REPORT HAS BEEN REVIEWED AND IS APPROVED FOR PUBLICATION.

JAMES M. LARSEN, Project Engineer
Materials Behavior Branch
Metals and Ceramics Division

ALLAN W. GUNDERSON, Chief
Materials Behavior Branch
Metals and Ceramics Division

WALTER M. GRIFFITH, Asst. Chief
Metals and Ceramics Division
Materials Directorate

IF YOUR ADDRESS HAS CHANGED, IF YOU WISH TO BE REMOVED FROM OUR MAILING LIST, OR IF THE ADDRESSEE IS NO LONGER EMPLOYED BY YOUR ORGANIZATION, PLEASE NOTIFY, WL/MLLN, WRIGHT-PATTERSON AFB OH 45433-7817 TO HELP US MAINTAIN A CURRENT MAILING LIST.

COPIES OF THIS REPORT SHOUL.D NOT BE RETURNED UNLESS RETURN IS REQUIRED BY SECURITY CONSIDERATIONS, CONTRACTUAL OBLIGATIONS, OR NOTICE ON A SPECIFIC DOCUMENT.

REPORT DOCUMENTATION PAGE

1. AGENCY USE ONLY (Leave blank)	2. REPORT DATE	3. REPORT TYPE AND DATES COVERED
	31 Aug 1995	Final 13 Sep 1989 - 13 Dec 1994

4. TITLE AND SUBTITLE

Damage Tolerance Concepts for Titanium-Aluminide Composites

5. FUNDING NUMBERS

F33615-89-C-5621
PE: 62102F
PR: 2420
TA: 01
WU: AC

6. AUTHOR(S)

J.A. Hall, A. Peralta, R.L. Hollars,
D. Harmon, M.A. Finefield, M.R. James, D.B. Marshall

7. PERFORMING ORGANIZATION NAMES(S) AND ADDRESS(ES)

AlliedSignal Engines
PO Box 52181
Phoenix, AZ 85072-2181

8. PERFORMING ORGANIZATION REPORT NUMBER

21-8755

9. SPONSORING/MONITORING AGENCY NAMES(ES) AND ADDRESS(ES)

Materials Directorate
Wright Laboratory
Air Force Materiel Command
Wright Patterson AFB OH 45433-7734

10. SPONSORING/MONITORING AGENCY REPORT NUMBER

WL-TR-95-4089

11. SUPPLEMENTARY NOTES

12a. DISTRIBUTION/AVAILABILITY STATEMENT

Approved for public release, distribution is unlimited.

12b. DISTRIBUTION CODE

13. ABSTRACT (Maximum 200 words)

Titanium-Aluminide metal matrix composites (MMCs) provide one of the enabling technologies needed in achieving the objectives of the Integrated High Performance Turbine Engine Technology (IHPTET) Initiative. These materials are targeted for applications that require high-temperature strength and stiffness, high creep and oxidation resistance, and acceptable ductility and fatigue resistance.

The damage Tolerance Concepts for Titanium-Aluminide Composites Program addresses life management and reliability issues. Specific objectives of this program were to develop and establish design tools, behavior models, inspection methods, and Engine Structural Integrity Program (ENSIP) strategies required for alpha-two MMC fracture-critical components.

14. SUBJECT TERMS

Propulsion, Metal-Matrix-Composite, High Temperature, Titanium-Aluminide, Compresor, MMC, ENSIP, IHPTET

15. NUMBER OF PAGES

330

16. PRICE CODE

17. SECURITY CLASSIFICATION OF REPORT	18. SECURITY CLASSIFICATION OF THIS PAGE	19. SECURITY CLASSIFICATION OF ABSTRACT	20. LIMITATION OF ABSTRACT
Unclassified	Unclassified	Unclassified	SAR

Table of Contents

viii

List of Figures

List of Tables

Foreword

SECTION 1.0
INTRODUCTION

Titanium-Aluminide metal matrix composites (MMCs) provide one of the enabling technologies needed in achieving the objectives of the Integrated High Performance Turbine Engine Technology (IHPTET) Initiative. These materials are targeted for applications that require high-temperature strength and stiffness, high creep and oxidation resistance, and acceptable ductility and fatigue resistance.

Successful use of Ti_3Al MMCs requires the technology to predict their behavior under various thermomechanical loading conditions. The Damage Tolerance Concepts for Titanium-Aluminide Composites Program addresses life management and reliability issues.

This program developed and established design tools, behavior models, and Engine Structural Integrity Program (ENSIP) strategies required for alpha–two MMC fracture-critical components. These elements developed the needed technology, including methods to predict both the mode and rate of damage cumulation of relevant loading conditions and composite architectures.

To accomplish the program, AlliedSignal Engines (AE) teamed with McDonnell Douglas Aerospace (MDA) and Rockwell International Science Center (RISC). This teaming approach is shown in Figure 1.

As an IHPTET engine contractor, AE defined the required damage tolerance technologies and the relevant MMC materials architectures and loading conditions. MDA provided a strong base in MMC materials technology and associated design tool development, while RISC provided support technology in micromechanical modeling of MMC systems.

1.1   Industry Survey of MMC Operating Requirements

The IHPTET contractors were surveyed and asked to summarize their projected material requirements for high strength and long life of Titanium-Aluminide composites. A total of four engine companies responded to the survey. The operating requirements among the surveyed were very diverse; they address fatigue, creep and temperature capabilities. Table 1 shows the summary of the requirements.

1

• Alpha-Two MMC Material Fabrication/Processing
• Alpha-Two MMC Behavior

• Micromechanics Modeling
• Nondestructive Evaluation
• Constituent & Composite Testing

AlliedSignal Engines

Phase I | Phase II | Phase III | Phase IV | Phase V | Phase VI

McDonnell Douglas Aircraft

Rockwell International Science Center

• Alpha-Two MMC Material Procurement
• Alpha-Two MMC Behavior
• MMC Design Tools/Codes
• Micromechanics Modeling

• Alpha-Two MMC Behavior
• Micromechanics Modeling
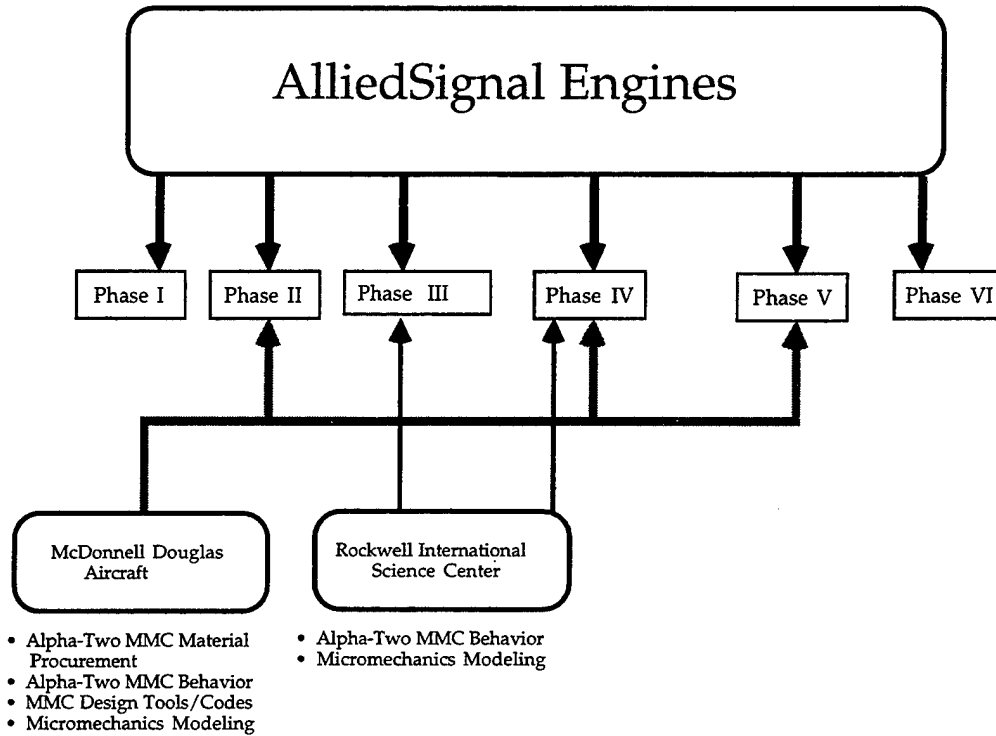
Figure 1. **The AE/MDA/RISC team.**
The AE/MDA/RISC team will develop life-prediction methodology and assess feasibility of ENSIP concepts for SCS6/Ti-Al composites.

Table 1. **Projected IHPTET Titanium-Aluminide composite applications.**

Component	Low Cycle Fatigue	Creep	Strength	Maximum Metal Temperature
Impeller	896–1,035 MPa @ 482°C, 15,000 cycles	414 MPa @ 704°C	-	760°C
Combustor Case	-	-	896–1,035 MPa @ 482°C	-
Core Mounted Fan	965 MPa @ 316°C 15,000 cycles	-	-	-
Axial Compressor	827 MPa @ 316°C 15,000 cycles	-	-	-

Table 1 cont.   Projected IHPTET Titanium-Aluminide composite applications.

Contractor A

Component	Stress Requirement	Temperature Requirement	Stress + Temperature Requirement (Creep)
Link	240 MPa	200°C	(0.2%)
Shroud	965 MPa	480°C	(0.2%) 100 hr, 830 MPa
AFT Compressor Stages (Ti$_3$Al MMC)	σ oper (L) 620–690 MPa σ oper (T) 70–140 MPa σ oper (T-T) MPa	540°C–675°C	σ_{max} < 0.2% creep strength (min) for total service life (6000 hrs) Hold time = 10 hrs min at any descrete pt. in engine operating envelope
AFT Compressor Stages (Ti$_3$Al MMC)	σ oper (L) 620–690 MPa σ oper (T) 70–140 MPa σ oper (T-T) MPa	675°C–815°C	σ_{max} < 0.2% creep strength (min) for total service life (6000 hrs) Hold time = 10 hrs min at any descrete pt. in engine operating envelope
Exhause Frame	0 MPa–450 MPa cycle Primarily bending 10^5 cycles required	540°C peak + thermal shock (apply 390°C–550°C in 2 seconds)	480°C, 450 MPa

Contractor B

Component	Stress Requirement	Temperature Requirement	Stress + Temperature Requirement (Creep)
- LPC, HPC , Blades, Rotors, Vanes Case - Intermediate Case - Diffuser Case - Turbine Exhause Case - Nozzle, Augmentor Structure	1550 MPa Modulus 210 GPa Kmax 27.5 MPa(m)$^{0.5}$ LCF 135 MPa, 8000 Type 1 Cycles (Long.) 170 MPa, 8000 Type 1 Cycles (Trans.) HCF 310 MPa Endurance Limit da/dN C = 3.5 X 10E-10, M = 3.1 (55°C Below Max Temperature) Non Burning	815°C	100 hr, 0.1% creep 345 MPa (Transverse) 1035 MPa (Longitudinal)

Contractor C

Applied Stress (MPa)	Temperature (°C)
770	315
785	370
910	385
785	510
840	510
785	720
815	720

The companies involved in the IHPTET program foresee application of Titanium-Aluminide (Ti-Al) composites for a wide variety of components that extend from the compressor section to selected parts in the turbine section. In the compressor section the companies are considering application of Ti-Al composites for impeller wheels, compressor disks, cases and vanes to name a few. For the hot section, the companies are considering uses in the turbine case, exhaust frame, links, and augmentor nozzles, among others.

The advantage of the composite material over the monolithic material is its superior longitudinal strength, but with a decrease in its transverse strength. This anisotropy in the strength must be considered in the design. For this reason, some IHPTET contractors have specified strength requirements in both directions. Design requirements and operating conditions for the above components are very distinct and requirements must be specified on a component by component basis. The overall design goals for components address fatigue, creep and strength requirements; fatigue requirements range from 8,000 to 100,000 cycles; creep requirements are limited to a maximum of 0.2% creep for a service life of 6,000 hours; and, strength requirements in excess of 965 MPa (140 ksi) for the longitudinal direction and 170 MPa (25 ksi) in the transverse direction. Operating temperature requirements are in the 480°C to 815°C (900°F to 1500°F) range.

1.2   JTAGG II Impeller Requirements

Presented are the design conditions for the JTAGG impeller. This impeller design consists of a SCS6/Ti6242 composite system and of IMI834 blades and cladding. The composite system has been designed to obtain the highest possible strength. The high hoop stress areas consist of a 40 percent fiber volume fraction with a reduction to 20 percent in the moderately high radial stress areas. In the web area where the radial stress is greatest, a monolithic system is used because it provides much higher strength than a composite system would provide. The strength design criteria used in this impeller consisted of a minimum Low Cycle Fatigue (LCF) life of 15,000 Type I cycles, 600 hrs to 0.2 percent creep, no material yielding during normal operating conditions and a capability of 122 percent burst speed.

The architecture of the 40 percent volume fraction composite consists of a hexagonal type array with triangular cell that, instead of being equilateral, forms an isosceles triangle. The architecture of the 20 percent volume fraction is such that a layer of fibers, of the 40 percent arrangement, in the thickness direction is removed every other fiber row. This architecture arrangement provides the best compromise for strength and manufacturability.

4

The design conditions are as shown in Table 2. As shown in the table, the controlling failure mode for the 40 percent fiber volume arrangement is LCF, while the controlling failure mode for the 20 percent fiber volume fraction is the yield strength. Creep strength is controlled by the global deformation of the structure; an evaluation of the creep strength has not been performed at this point.

Table 2.   Design point stress summary for the JTAGG impeller design.

Metal Temp (°C)	Room Temp Stress (MPa)	Design Point Stres (MPa)	Allowable Stress (MPa)
MMC Longitudinal 40% Zone, LCF Failure Mode			
595	51	1186	1200
538	-17.2	1186	1200
482	-86.2	1150	1200
427	-124.1	1170	1200
MMC Transverse 40% Zone, Yield Failure Mode			
595	27.6	103	83
538	0	110	90
482	-34.5	117	96.5
427	-48.3	124	103
MMC Transverse 20% Zone, Yield Failure Mode			
595	27.6	160	152
538	-48.3	180	165.5
482	-48.3	214	186.2
427	-48.3	234	193

SECTION 2.0
MANAGEMENT SUMMARY

2.1   Model Development and Integration

The McDonnell Douglas Aircraft MMCLIFE code was modified to extend its design capabilities to include engine design considerations and crack configurations observed in engine components. These include typical engine load and temperature spectra, crack bridging and material testing specimen configurations.

The capabilities of the MMCLIFE code include a combination of micro and macro mechanical analyses. The micromechanical analyses are used to determine elastic/plastic matrix behavior, laminate properties and initial failure modes. The macro mechanical analyses are used to determine laminate stresses, strains and overall failure modes. These analyses capabilities are included in four MMCLIFE code modules: 1) strength module, 2) unnotched fatigue module, 3) crack initiation module and 4) crack growth module. The theoretical enhancements are described in Section 3 of this volume; the User's Manual is included in an appendix volume to this report.

The enhancement of the MMCLIFE code established a design tool for preliminary sizing of metal matrix components. This computer code is available for use in a UNIX operating system.

2.2   Testing

Tensile, LCF, creep and crack growth test results at temperatures up to 650°C (1200°F) are reported herein, along with results and analyses of micromechanical examinations.

2.2.1   Residual Stress Stability

Stability of the residual longitudinal stresses after various room and elevated temperature fatigue cycles was investigated. X-Ray and Neutron Diffraction techniques indicate that the average matrix residual stress very quickly deteriorates to values less than half of the original level. This behavior can be rationalized from a cursory examination of the stress strain curves presented in the testing section. In addition, a micromechanical analysis described in Section 4.10 revealed that the residual stress deterioration was due to loading of the specimen to levels above the matrix yield point and not to any material system instability. The micromechanical analysis revealed also that matrix relaxes during the first cycle due to high loading levels above the matrix yield point.

2.2.2   Interface Strength Measurements

Interfacial shear strength measurements indicate values of near 50 MPa (7.4 ksi), deterioration to near 20 MPa (2.9 ksi) with interface sliding at room temperature. Values near zero are indicated at 650°C (1200°F) due to Coefficient of Thermal Expansion (CTE) differences. Recent RISC IR&D work has found that SCS6/Ti alloy MMCs exhibit virtually no interfacial normal strength. Because of this, measurements were conducted only for interfacial shear strength.

2.2.3   Mechanical Property Testing

2.2.3.1   Tensile Testing

The MMC system used for this program displays near rule of mixtures strength and stiffness properties. The matrix is unique in that it is nondirectional in the plane of the consolidated foil but it is much stronger in the thickness direction. The in-plane isotropy is accompanied by an unusually low modulus. Transverse tensile properties are low but show little effect of prior cyclic thermal exposure.

2.2.3.2   Shear Strength Testing of MMC

Duplicate, longitudinal, Iosipescu shear test specimens, tested at room temperature, gave nearly identical results with a shear modulus near 130 GPa (18.8 Mpsi) and an elastic strength of about 160 MPa (23 ksi). Matrix plasticity appears to occur without fiber fracture even after large shear micro strains were achieved.

2.2.3.3   Fatigue Testing

2.2.3.3.1   Low Cycle Fatigue of Matrix Only Specimens

A few matrix specimens were tested at room temperature giving an apparent fatigue limit after less than about 50,000 cycles of 190 MPa (28 ksi). Shortage of material precluded a detailed definition of the LCF curve.

2.2.3.3.2   Low Cycle Fatigue of Longitudinal MMC Specimens

Longitudinal low cycle fatigue (LCF) properties of the MMC appear to be dominated by the flaw initiation event when tested at stresses approaching those useful for gas turbine disk applications. After a short period of initial crack growth, failure is catastrophic. At lower test stresses, flaw growth seems to be very slow, encouraging the notion of a change in flaw growth mechanism as stress is increased, perhaps leaving the crack bridging mode to become unbridged cracks.

Room Temperature LCF of the longitudinal MMC used in this program reveals a strong maximum stress effect on life with an apparent threshold, for run-out about 689.5 MPa (100 ksi) when the R is 0.1.

Room temperature tests on previously thermally exposed longitudinal samples shows a strengthening effect in the long life region and a reduction in strength in the short life region.

Elevated temperature LCF testing indicates some reduction in LCF life when tests are conducted in air and there is some evidence that, when the tests are conducted in an inert environment, LCF life may be somewhat better. The evidence for this, however, is slight but consistent with added ductility in the matrix and with an additional reduction in residual tensile stress in the matrix, all associated with the higher temperature.

2.2.3.3.3 Low Cycle Fatigue of Transverse Specimens

Low cycle fatigue tests of transverse specimens reveal extremely low strength for this property. It was observed that the strength for the transverse specimens is about half of the strength of the monolithic material. This can be justified by the fact that the encircling of the fibers by the matrix creates a notch-type stress concentration on the matrix; such notch would degrade the fatigue capabilities of the matrix and the composite.

The effect of handling and operational damage on the composite was evaluated through an impact foreign object damage test. Testing of the composite in the transverse direction after damage revealed that LCF life in the transverse orientation is heavily discounted.

2.2.3.4 Crack Growth Testing

2.2.3.4.1 Crack Growth of Longitudinal Specimens

Longitudinal crack growth tests were difficult to run because of problems in getting singular cracks to nucleate and grow from the Single Edge Notched (SEN) specimens employed. In order to alleviate this problem, three point bend precracking was applied to selected SEN specimens at relatively light loads. The results were that a singular crack was initiated in most of the specimens but it soon branched. It was assumed that the notch tip stress field discontinuity, being large compared to the plastic zone radius of the matrix material, would contribute to the bifurcated cracking.

Therefore, it was decided that once the singular cracks were noticed, the three point bend fatigue crack initiation was ceased and the notch was machined away, leaving a fatigue crack at the edge of the specimen, absent the notch effect and with completely

bridged starting cracks. Singular cracks did continue to grow for an extended growth period when axial testing was resumed. With this success, all future longitudinal crack growth testing was done in the manner described above.

Selected serial sections made of crack growth specimens indicate extensive crack bridging occurs from the SEN notches, at maximum stresses of at least 689.5 MPa (100 ksi), and supports the need to include this phenomenon in the models adopted. Additionally, LCF samples with maximum stresses as high as 1034.2 MPa (150 ksi) exhibit numerous prefailure cracks with extensive bridging.

There was observed a crack acceleration associated with hold time at maximum load in room temperature tests, implying the existence of some sort of time dependent damage mechanism. Tests designed to highlight the effects of hold time at maximum load indicate a significant influence of time dependent damage mechanisms which are operative even at room temperature. This effect appears to be transitory, with growth rate returning to prehold levels after a number of cycles. Furthermore, room temperature crack growth is accelerated immediately following a short time exposure of the bridged crack at 650°C (1200°F) but the crack remained bridged. Hold time, test frequency and consolidation thermal cycle have a negative impact in the fatigue crack growth behavior at room temperature of the longitudinal MMC.

Comparisons of crack growth data from this program with that obtained in other programs with similar materials indicate they belong to separate population groups. The outside data were gathered at rather high frequencies (>3 Hz) whereas the current program focused on 20 cpm with dwell effects imposed on top of this. This may explain the differences, in that environment and other time dependent effects are much more likely to influence the results at high frequencies than at low frequencies. These effects deserve further investigation.

Elevated temperature crack growth testing of the longitudinal MMC and Matrix only specimens is reported herein. Essentially, the crack growth rate is rather independent of the crack length, much as seen with the room temperature tests. There is a clear acceleration of fatigue crack growth during dwell at maximum load.

Termination of the tests, by failure at rather small crack lengths, imply low apparent fracture toughness of the program material and presents significant challenges to utilizing these materials in an ENSIP environment.

Elevated temperature crack growth on the matrix material indicate the alloy to have a much less steep growth rate curve and with higher toughness and probably a higher threshold than the same material at room temperature. The crack growth characteristics appear to be well described by conventions based on linear elastic fracture mechan-

9

ics. However, there is an apparent degrading influence of a short hold time on the crack growth resistance at elevated temperature.

2.2.3.4.2   Crack Growth of Transverse Specimens

Room temperature and elevated temperature testing of transverse specimens revealed that crack growth resistance is very low. And as observed in the longitudinal specimens, the crack growth resistance is further degraded with hold time at maximum load at both room and elevated temperature. This can be explained by the fact that there are no fibers bridging the crack, and the composite system actually acts as a monolithic system with a row of holes.

2.2.3.4.3   Transverse Crack Growth

Crack growth testing on 90° specimens presents additional difficulties in that, below a certain nominal stress threshold, crack initiation in the notch is extremely difficult. Resolution of this problem was to gradually increase the nominal stress in very small increments and monitor the crack growth via Potential Drop techniques (ASTM E647) with sensitivities very tightly set to stop the test on first indication.

The room temperature and elevated temperature crack growth resistance is low for all transverse tests and there is an additional acceleration associated with dwell at maximum load, even at room temperature. The apparent ΔK_{th} and ΔK failure are quite close, indicating a low damage tolerance in the case of cracks growing along the fiber direction.

2.2.3.4.4   Crack Path Analysis

One room temperature SEN crack growth specimen, with notch intact, was sectioned after bifurcated cracks had proceeded extensively. Layer-by-layer microstructural examination revealed, generally, two major cracks in the matrix but no fiber cracking. The cracks, at the surface, had arrested. This is clear evidence of crack bridging as a crack retardation mechanism. The nominal stress for this specimen was 593 MPa (86 ksi) with an initial notch length of 0.6 mm (0.025 inch).

Contrary to the results of the 593 MPa (86 ksi) far field stress specimen results, cracks grown at the more interesting stress levels of 689.5 MPa (100 ksi) and above did not arrest themselves despite having fully bridged cracks. Examination of specimens tested at nominal stresses as high as 965 MPa (140 ksi) indicate that there is significant matrix crack growth where crack bridging by the fibers is dominant. LCF testing at room temperature resulted in multiple cracks at maximum stresses in the 1000 MPa (145 ksi) range, all of which were bridged until just prior to failure.

2.2.3.4.5 Influence of Thermal Cycle on Fatigue Crack Growth

Thermal exposure at high or moderate temperature produces at least a transient increase in growth rate. It is also clear that once cracks have penetrated the surrounding structure in this alloy/fiber system, thermal exposure provides significant degradation of the crack growth resistance despite the maintenance of the fiber bridging.

Fiber bridging, while introducing some scatter in the growth rates, is not seen to produce crack deceleration at stresses of interest to engine component designers. Growth rates are slower than in monolithic materials, and they appear to be linear with crack length rather than follow classical Linear Elastic Fracture Mechanics when the crack is permitted to grow extensively under constant far field stress conditions.

2.2.3.4.6 Stress Effect on Room Temperature Fatigue Crack Growth

The linear nature of the crack length vs. numbers of cycles plots at a constant far field stress, after initial transients are exceeded, suggests that ΔK is not a very good indicator of crack driving force. This situation leads to a speculation that the driving force for crack growth is primarily the far field stress. This is consistent with the bridging model, once a well developed crack is present. At this point da/dn is relatively insensitive to crack length. With weaker matrix alloys, this will occur earlier.

2.2.3.5 Creep Testing

Transverse MMC creep testing reveals a very low creep strength for the material. This is not surprising as the matrix alone exhibited very low creep strength and the transverse creep strain is a matrix dominated property.

2.2.3.6 Matrix Poisson Ratio

Poisson ratio testing was performed on the matrix only Ti-24-11 specimens. Results show a high degree of texture in this material property with the Poisson ratio in both the in-plane direction showing extremely high values on the order of 0.63, and in the thickness direction extremely low values on the order of 0.13.

2.2.3.7 Fiber Strength Testing

SCS6 fiber strength tests were performed for pristine fibers from beginning of production coils, fibers uncomposited but woven, fibers composited, and composited and fatigued fibers. The results show an extremely high variability from group to group of the pristine fibers and indication of two concurrent failure modes. Also, there is no indication of fiber degradation with consolidation nor cyclic loading. The difference

in strength observed between these groups is minor and it falls within the range observed in the variation from group to group.

2.2.3.8 Coefficient of Thermal Expansion

The coefficient of thermal expansion (CTE) was measured for a matrix-only, a pristine composite and a fatigue composite specimens. The matrix CTE shows again a textured behavior in this property. The longitudinal and in-plane CTE are very much the same with a marked CTE difference in the thickness direction. The CTE in the composite specimens agree reasonably well when compared to rule of mixture predictions.

2.2.4 Micromechanical Observations

2.2.4.1 Longitudinal Fatigue Crack Growth

Fatigue crack growth tests in longitudinal specimens at temperatures at least up to 650°C (1200°F) indicate that the initially bridged precracks remain virtually bridged throughout the test until failure of the specimen; however, at far field test stress levels of interest to gas turbine engine disk reinforcement, there is no sustained crack deceleration of a growing crack. The crack growth rates appear to be a rather linear function of stress after transitioning from an initially higher, but unpredictable, growth rate.

Fractographic observations on longitudinal fatigue crack growth specimens indicate that, on a very local scale, cracks grow more rapidly between fibers intersecting the crack plane and tend to slow down as they encounter the fibers. The net result is a lower macro growth rate, for a given ΔK than would be indicated by either the matrix material tests or by the striation spacing measurements, on the fracture surface, in the field between the fibers.

Longitudinally polished, tested, samples, provide evidence of matrix fiber separation along the fiber length for a distance from the crack plane of several fiber diameters near the origin, tapering down to just a few fiber diameters at the crack tip. This delamination does not extend beyond the crack tip in the direction of the crack growth.

Longitudinal loading presents significant resistance to fatigue crack growth with fiber bridging but at high stress this bridging does not cause crack deceleration in a uniform stress field. The fibers tend to inhibit crack growth by a mechanism that simply reduces the effective stress intensity on the matrix by virtue of load distribution. While the growth rate is low, the effective fracture toughness is not exceptionally high. At the high stresses involved, it will be necessary to deal with a statistical distribution of fiber strengths as a small fraction of broken fibers strongly influences the MMC's resistance to crack growth.

2.2.4.2   Transverse Crack Growth

Transverse crack growth, at all temperatures, is strongly influenced by the fiber/matrix interface which offers no resistance. The fiber volume fraction will severely influence the area of this weak plane. Furthermore, the matrix material's intrinsic resistance to crack propagation is the only clearly available variable to influence this property aside from the reduced fiber volume fraction.

Transverse loading of the program MMC offers very low effective fracture toughness and a relatively low threshold ΔK with the result being a very short critical crack size. Estimates of critical stress at a reasonable detectable crack length of 0.7 mm indicate catastrophic failure at less than 108 MPa (16 ksi) transverse stress.

2.3   Model Verification

2.3.1   MMCLIFE Code Verification

Model verification consisted of evaluation of the MMCLIFE code and evaluation of the damage mechanics model for composite stress-strain behavior and strength. The MMCLIFE code verification consisted of performing a prediction of a simplified isothermal mission cycle for a crack growth specimen starting with a small, fully bridged, precrack. These predictions were then used to specify confirmatory test conditions, specimens were tested and then the predicted life were compared to the observed lives. The results show that the MMCLIFE code does a poor job in predicting the life of the longitudinal specimens. But it does a reasonable job in predicting transverse specimen lives.

It was observed that the interfacial shear stress plays a big role in the crack growth variability of the longitudinal specimens. From data summarized in Section 3, a large variability was observed from specimen to specimen, and from matching of the crack growth from the confirmatory specimens, it was observed that variability in interfacial shear even exist during the same test. At the beginning of the test very low shear is present and it increases as the crack increases. The variability on the transverse specimens is attributed to the variability of the transverse stiffness ratio parameter. As shown in data summarized in Section 3, this parameter changes from specimen to specimen and with crack size.

In general the predictive capabilities of the MMCLIFE code are considered acceptable as a preliminary tool since it has been able to match observed lives of specimens tested under a major and minor cycle spectrum with a hold time. To match the prediction, change in only one of the parameters was required for each specimen type. This is particularly important since variability of such parameter is observed from specimen

13

to specimen and even during the test itself. In order to enhance the predictive capabilities of the MMCLIFE code, it is important that the interfacial shear stress behavior be properly understood for the longitudinal specimens and that the transverse stiffness ratio definition be properly understood for the transverse specimens.

2.3.2   Modified Rule of Mixture Model Verification

The rule of mixture models used for stress-strain predictions was modified using damage mechanics principles and verified by matching the stress-strain curves of the longitudinally tested specimens. The modified model satisfactorily predicts the full stress strain behavior of the composite, three regions on this curve are observed analytically: the linear portion up to the point where the fibers go from compression to tension; a second portion where the matrix is below its yield point and the fibers are in tension and are susceptible to failing; and a third portion where the matrix is above its yield point and the fibers are failing to a larger extent. For this material system, the second portion is very short and almost invisible in the stress-strain curves. The proof of the validity of this model is noticed when the model successfully predicted the full stress-strain curve for a cyclic test.

2.4   Guidelines for Improved Material Processing and Durability

The matrix alloy selected for this program lacks sufficient strength for the Metal Matrix (MM) conditions appropriate for most gas turbine disk applications. This strength debit results in inadequate transverse properties and in low damage tolerance. Furthermore, crystallographic texture in the matrix presents problems in life prediction which require matrix properties as input parameters and the matrix properties are now assumed to be isotropic. Hence, without severe modification of the model, matrix material must be stronger at all temperatures of use as well as virtually free of anisotropy, in all orthogonal directions.

Alloy modifications can improve strength but processing must incorporate controls to permit installation of creep resistant microstructures. This is not a trivial task because foil manufacturing and MM debulking require microstructures that result in just the opposite characteristics. Post consolidation thermal treatments are an obvious approach.

Residual stresses due to consolidation add to the applied stresses and have an effect of degrading certain properties but are a necessity for load transfer from the matrix to the fiber in the absence of true chemical bonding between the MM constituents.

Transverse strength and crack growth resistance of MM systems remain their weak point and, short of increasing the interfacial strength and reducing fiber volume frac-

tion, no solution is clear. The former is a subject of a concurrent development program, F33615-91-C-6547. The latter will require the availability of a higher strength fiber system.

2.5   ENSIP Guidelines

It is apparent that without major breakthroughs in both materials and NDE technology, ENSIP concepts are impractical for highly stressed MMC reinforced components used at elevated temperatures. At ambient temperatures, where attractive strength limiting MMC applications make sense and where large transverse stresses are avoided, results of this program imply feasibility of ENSIP. The same sort of conclusion would be drawn for other titanium alloy because of the lack of interfacial strength and the thermal expansion mismatch between the fiber and the matrix.

At elevated temperatures or conditions imposing reasonable off-axis stresses, the program MMC has virtually no damage tolerance. A higher creep strength matrix may help retain the gripping action of the matrix on the fiber and, thereby, increase the use temperature of a Titanium Metal Matrix Composite.

SECTION 3.0
MODEL DEVELOPMENT AND INTEGRATION

3.1 MDA MMCLIFE Code

This section summarizes the development of the MDA MMCLIFE code. MMCLIFE is a multistage analysis routine for prediction of strength and life of fiber reinforced metal matrix composite when subjected to spectrum loads and thermal profiles. The MMCLIFE routine is based on a combination of micro-mechanics and macro-mechanics analyses: micro-mechanics analyses are used to determine elastic/plastic matrix behavior, lamina properties, and initial failure modes; macro-mechanics analyses are used to determine laminate stresses, strains, and overall failure modes. This routine can be used to predict lamina and laminate stiffnesses, stresses about a notch and through the net section, laminate strength (notched or unnotched), crack initiation lives, and crack growth. The analyses are based on simple analytical methods and were programmed in FORTRAN for a Digital VAX computer with a VMS operating system and an IRIS workstation with a UNIX operating system.

All of the analyses are available in a computer program called MMCLIFE V3.0. These analyses include 1) lamina or laminate stiffness, 2) lamina or laminate stresses, 3) lamina or laminate unnotched and notched strengths, 4) lamina or smeared laminate notched crack initiation, and 5) ply-by-ply or smeared laminate notched crack growth.

The approach in developing the MMC strength and fatigue analyses was to create a design tool to be used by engineers to obtain initial sizing requirements for specific MMC applications. This requires the use of simplified analytical procedures along with a limited amount of test data to provide a tool that does not require a lot of CPU time, yet still provides accurate results.

Detailed studies of micromechanical models were required to understand MMC material behavior when subjected to various loading conditions. Once the material response was understood, simpler expressions were derived to describe the phenomenon. In some cases, such as failure mode initiation and location, simplified models were developed based on observation and interpretation of test data.

The combined micromechanical and macro-mechanical analyses within MMCLIFE allow the code to be used to predict a wide range of MMC properties and behaviors. Trade studies can be performed to compare the predicted response of various fiber and matrix combinations. This requires input data describing the constituent material properties (i.e. fiber and matrix stiffness and strength, matrix fatigue life and

16

crack growth data). In this case, the analysis uses a modified Rule of Mixtures (ROM) analysis to build lamina mechanical properties and classical lamination theory to build laminate mechanical properties. In addition, matrix crack growth stress intensity data are modified by the ratio of the composite modulus to matrix modulus to approximate lamina data. This analysis provides a consistent means of evaluating and comparing the performance of new MMC material systems, although the accuracy of the simplified approximations would be in question until test data could provide verification. More accurate strength and fatigue life results can be obtained by supplying lamina data in addition to constituent data. Lamina data should be available for more mature systems.

MMCLIFE was developed as an engineering design tool and is, therefore, user-friendly and incorporates rapid analysis techniques which allow the program to be run interactively. The purpose of this routine is to provide quick and accurate strength and life predictions for metal matrix composites based on limited amounts of test data.

3.2 History of Development of MMCLIFE Code

The analyses developed are an extension of those developed under two previous Air Force Contracts; F33615-87-C-3219, "Thermomechanical Load History Effects in Metal Matrix Composites (Reference 1) and F33615-83-C-3219, "Durability of Continuous Fiber Reinforced Metal Matrix Composites" (Reference 2)." The analysis program developed under the first contract was based solely on test data for continuously reinforced Boron/Al 6061. In addition, those analyses were limited to isothermal conditions and constant amplitude loads for fatigue. Under the second contract the material database for analysis development was expanded to include a continuously reinforced titanium matrix composite: SCS6/Ti-15V-3Cr-3Sn-3Al. The analyses were also extended to account for material property temperature dependence and are, therefore, capable of predicting lamina and laminate response under thermomechanical conditions.

3.3 Development of MMCLIFE V3.0

3.3.1 Objectives of "Damage Tolerance Concepts" Contract

The contract objective is to broaden the range of applicability of the MMCLIFE analysis tool by 1) including the SCS6/Ti-24-11 database developed under this contract and as much as is pertinent of the data developed under other Titanium Aluminide MMC programs and 2) to extend the analysis capabilities to include engine design concerns. The MMCLIFE tool was originally developed to focus on airframe specimen configurations and spectrum load and temperature applications. Under this contract the tool was extended to include engine typical load and temperature spectra and specimen configurations.

3.3.2 Extending the Capabilities of MMCLIFE V3.0

Although Version 3.0 of the MMCLIFE code has been updated and improved in every section, primary emphasis was spent on the crack growth section. The crack growth analyses are now capable of predicting cracks growing from edge flaws. In addition, crack bridging was included to differentiate between cracks which grow in the matrix around fibers and cracks which grow through fibers. The bridging analysis was developed by Cox, Marshall, Evans, and McMeeking as discussed in Section 3.6.3.3

3.4 Discussion of Analyses in MMCLIFE V3.0

In the sections that follow, the theory behind the analysis within the code is presented. For completeness, the entire MMCLIFE code is presented including sections developed under earlier Air Force contracts (Reference 1 and Reference 2).

3.4.1 Lamina Mechanical Behavior

3.4.1.1 Constituent Properties (Stiffness and Strength)

ROM expressions are used to predict lamina stiffness at room and elevated temperatures. This requires knowledge of how the constituent materials behave at temperature. A hyperbolic tangent function is used to fit the data points using a least squares curve fitting procedure. The form of the function is:

$$P_j = \sum_{k}^{\substack{\text{\# of data} \\ \text{points}}} A_k \, \tanh\!\left(\frac{T_k - T_{ref}}{T_k} \right) \qquad [1]$$

where P_j is the jth material property (i.e. matrix modulus, matrix strength, fiber modulus, fiber strength, etc.), T_k is the kth temperature, T_{ref} is the reference temperature, and A_k are the curve fit constants.

The hyperbolic tangent function has a shape which can easily be fit to degrading properties, such as material stiffness and strength.

3.4.1.2 Lamina Properties (Stiffness and Strength)

Lamina material properties, such as stiffness and strength, are predicted based on the properties of the constituents using Rule of Mixtures (ROM) equations. Fiber and matrix properties, along with fiber volume percentages, are required. The basic equations which describe longitudinal and transverse stiffness of a continuously reinforced lamina are analogous to those expressions used in electrical field theory which describe the

18

effective capacitance required of a single capacitor which could replace a series or parallel combination of capacitors and store the same amount of charge for a given potential difference. The ROM stiffness equations are

$$E_1 = E_m(1 - V_f) + E_f V_f \qquad [2]$$

$$E_2 = \left[\frac{V_f}{E_f} + \frac{1 - V_f}{E_m}\right]^{-1} = \frac{E_f E_m}{E_f(1 - V_f) + E_m V_f} \qquad [3]$$

where E_1 and E_2 are the longitudinal and transverse lamina stiffness, E_m and E_f are the fiber and matrix stiffness, and V_f is the fiber volume fraction. Similar expressions are used to describe lamina Poisson's ratio and the shear stiffness.

$$v_{12} = v_f V_f + v_m(1 - V_f) \qquad [4]$$

$$G_{12} = \left[\frac{V_f}{G_f} + \frac{1 - V_f}{G_m}\right]^{-1} = \frac{G_f G_m}{G_f(1 - V_f) + G_m V_f} \qquad [5]$$

where v_{12} and G_{12} are the lamina Poisson's Ratio and shear stiffness, and

$$G_f = \frac{E_f}{2(1 + v_f)} \qquad [6]$$

$$G_m = \frac{E_m}{2(1 + v_m)} \qquad [7]$$

v_f and v_m are the Poisson's Ratio for the fiber and matrix, respectively.

A modified set of ROM equations were used to predict lamina longitudinal and transverse strengths, F_{tu}^L and F_{tu}^T respectively. The corresponding equations for lamina strength prediction are:

$$F_{tu}^L = F_{tu}^f V_f + E_m \varepsilon_f (1 - V_f) \qquad [8]$$

$$F_{tu}^T = F_{tu}^m (1 - V_f) \qquad [9]$$

where ε_f is the fiber failure strain and F_{tu}^f and F_{tu}^m are the fiber and matrix ultimate strengths.

Depending on the maturity level of the material system to be analyzed, some lamina mechanical property data may be available. If so, this data are used in the analysis to provide a better fit of the ROM predictions. The ROM predictions are still generated because it is necessary to calculate lamina properties at various temperatures. While an interpolation of the lamina data are possible, it is more accurate to use the temperature dependent relationships derived for the constituents to predict lamina behavior and then shift the predicted lamina relationships to match any available lamina data. In addition, lamina data may be sparse, while for most matrix materials, properties at several temperatures are known.

A least squares curve fit is used to fit the ROM predictions to lamina data, when available. This method was used to fit lamina longitudinal and transverse stiffness and strength data for SCS6/Ti-24-11. Lamina data were available for 3 temperatures: 27°C (80°F), 550°C (1022°F), and 650°C (1200°F). Simply by providing one data point, it was found that the lamina predictions were substantially improved as compared to the rest of the lamina data (Figure 2 through Figure 5). This implies that without knowing any lamina properties, the constituent hyperbolic tangent curve fit combined with the ROM equations provides a good description of lamina property behaviors with increasing temperature.

SCS6/Ti-24-11
Least Squares Curve Fit
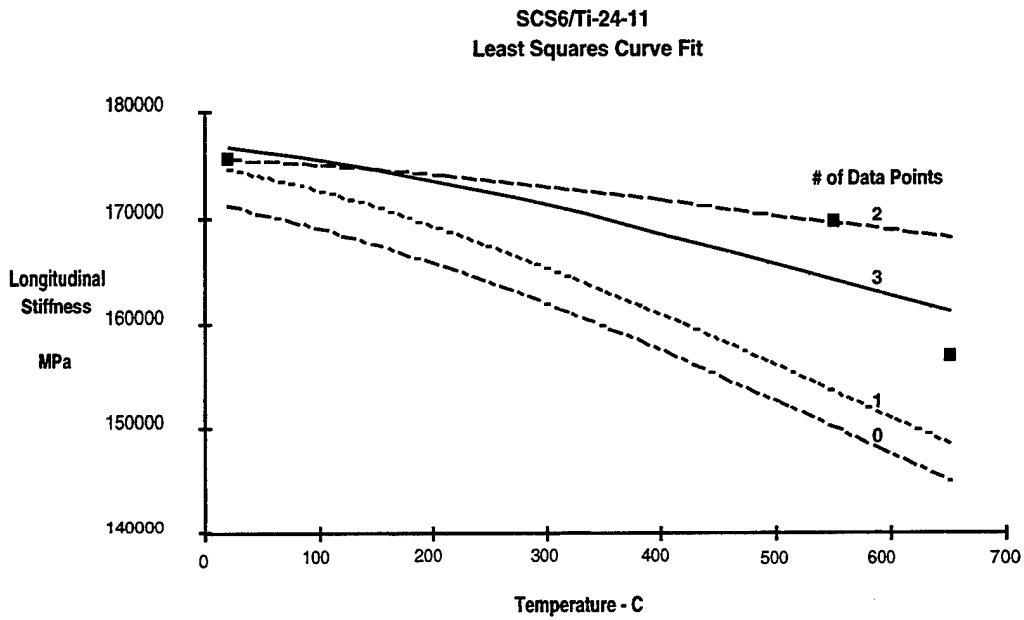
Figure 2.   Least square curve fit of lamina longitudinal stiffness.

SCS6/Ti-24-11
Least Squares Curve Fit
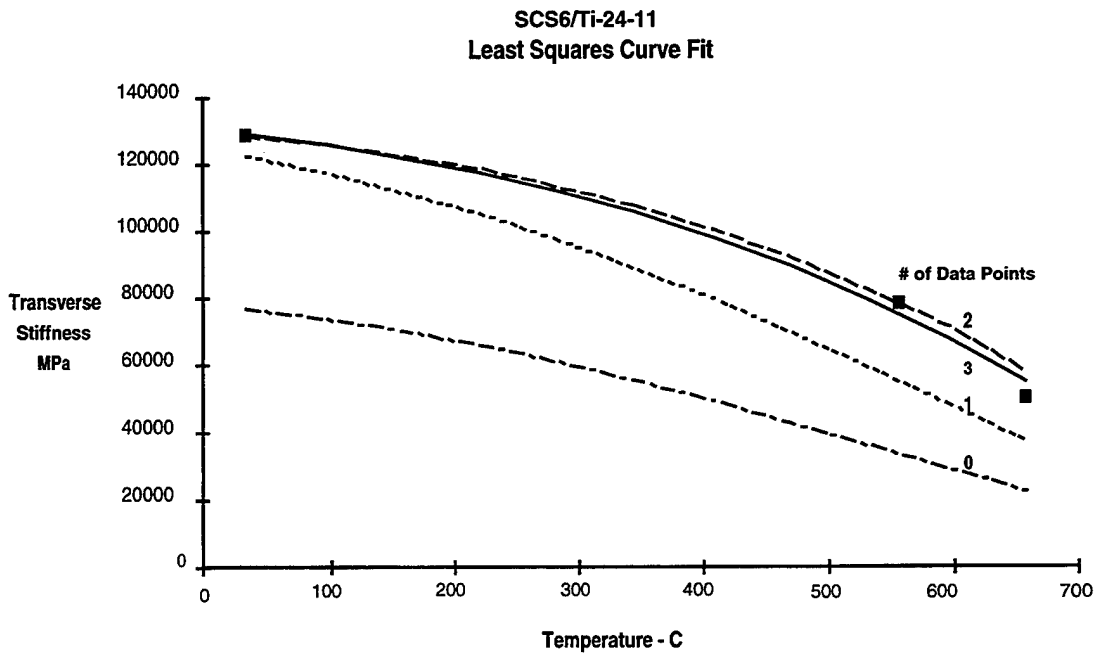
Figure 3.   Least square curve fit of lamina transverse stiffness.

SCS6/Ti-24-11
Least Squares Curve Fit
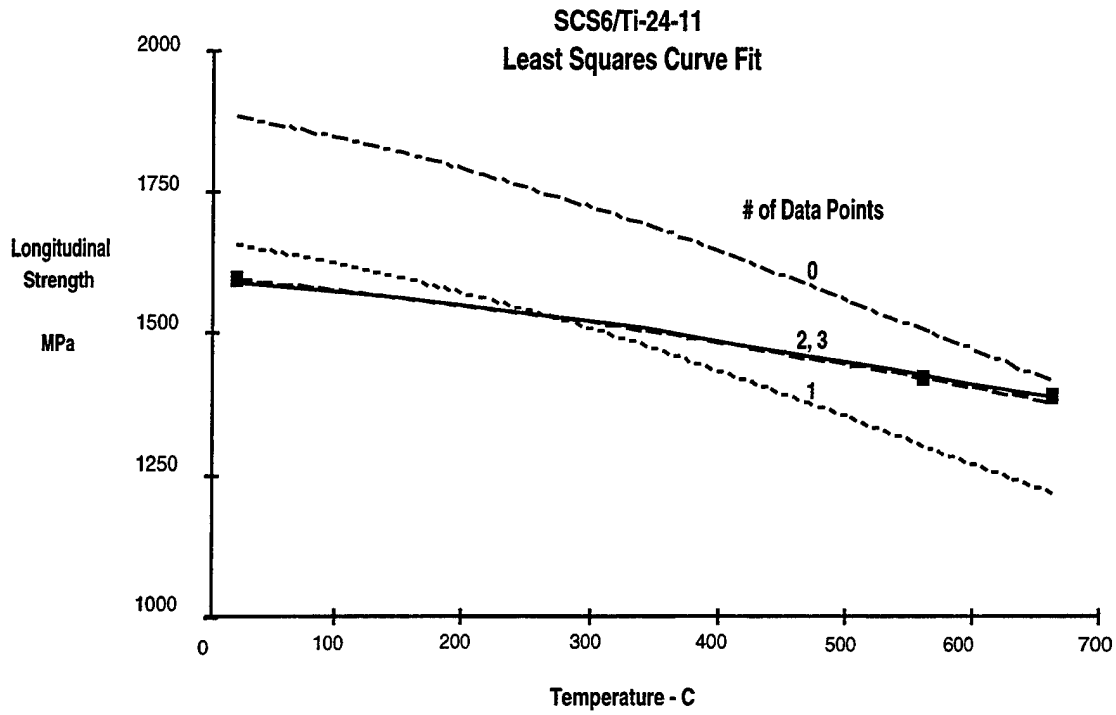
Figure 4. Least square curve fit of lamina longitudinal strength.

SCS6/Ti-24-11
Least Squares Curve Fit
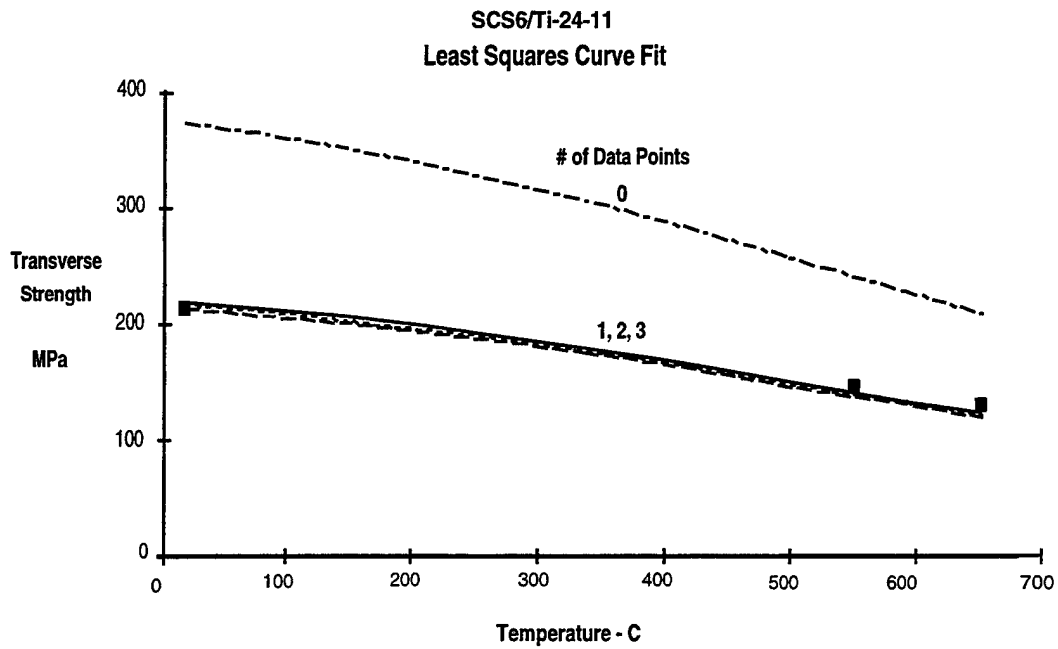
Figure 5. Least square curve fit of lamina transverse strength.

22

3.4.1.3   Notched Stress Analysis

3.4.1.3.1   Stresses Around Notch Perimeter

Accurate notched strength prediction is dependent on an accurate representation of the stress state around the notch. In this section, the method used to develop the stress concentrations due to an open notch is discussed. Strength prediction is discussed in Section 3.5.

The notched stress analysis is developed for in-plane biaxially loaded laminates with center notches of any elliptical shape. Closed form equations were derived by Lekhnitskii (Reference 3) to describe the local stress at any point on the notch perimeter. This expression was defined for an infinitely wide anisotropic ply (Figure 6).

$$\sigma_\theta = \sigma_x F_x(\phi,\theta) + \sigma_y F_y(\phi,\theta) + \tau_{xy} F_{xy}(\phi,\theta) \qquad [10]$$

The tangential stress, σ_θ, at an angle, θ, around the notch is defined in terms of the gross stresses in the loading directions (σ_x, σ_y, and τ_{xy}), the Lekhnitskii variables (F_x, F_y, and F_{xy}), and the fiber orientation angle, ϕ.

$$F_x(\phi,\theta) = \frac{E_\theta}{E_1}\{[\cos^2\phi + (\mu_1\mu_2 - \eta)\sin^2\phi]\mu_1\mu_2\cos^2\theta \qquad [11]$$

$$+[(1+\eta)\cos^2\phi + \mu_1\mu_2\sin^2\phi]\sin^2\theta$$

$$-\eta(1+\eta - \mu_1\mu_2)\sin\theta\cos\theta\sin\phi\cos\phi\}$$

$$F_y(\phi,\theta) = \frac{E_\theta}{E_1}\{[\sin^2\phi + (\mu_1\mu_2 - \eta)\cos^2\phi]\mu_1\mu_2\cos^2\theta \qquad [12]$$

$$+[(1+\eta)\sin^2\phi + \mu_1\mu_2\cos^2\phi]\sin^2\theta$$

$$-\eta(1+\eta - \mu_1\mu_2)\sin\theta\cos\theta\sin\phi\cos\phi\}$$

$$F_{xy}(\phi,\theta) = \frac{E_\theta}{2E_1}(1+\eta - \mu_1\mu_2)\{-\eta\cos2\phi\sin2\theta \qquad [13]$$

$$+[(1-\mu_1\mu_2)\cos2\theta - \mu_1\mu_2 - 1]\sin2\phi\}$$

where

$$E_\theta = \left[\frac{\sin^4\theta}{E_1} + \sin^2\theta\cos^2\theta\left(\frac{1}{G_{12}} + \frac{2\nu_{12}}{E_1}\right) + \frac{\cos^4\theta}{E_2}\right]^{-1} \qquad [14]$$
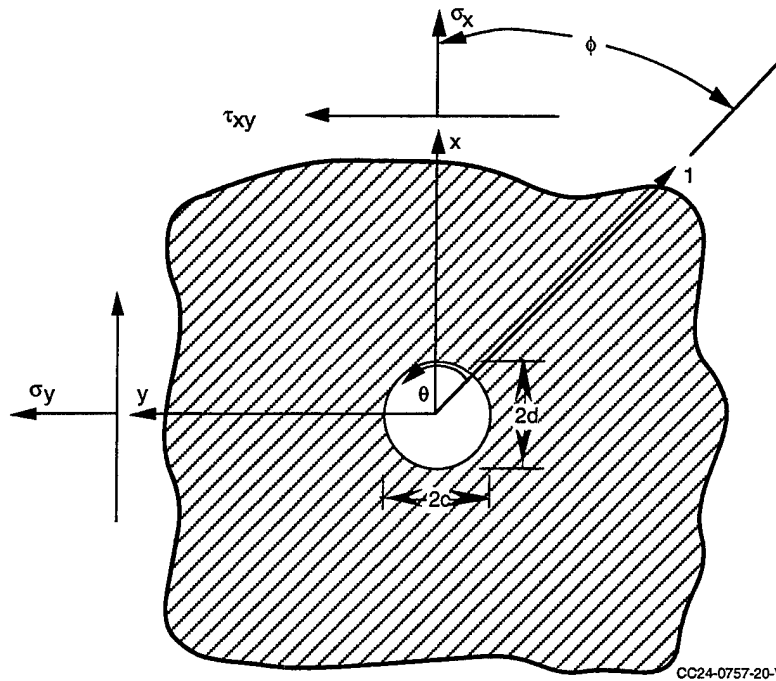
Figure 6. Notched specimen geometry used for stress analysis.

$$\eta = \sqrt{\frac{E_1}{G_{12}} - 2\nu_{12} + 2\sqrt{\frac{E_1}{E_2}}} \qquad [15]$$

$$\mu_1\mu_2 = -\sqrt{\frac{E_1}{E_2}} \qquad [16]$$

The angle, θ, is measured from the fiber axis (1 direction). The angle, ϕ, is measured from the x loading axis. These expressions are greatly simplified when analyzing a zero degree ply, $\phi=0$.

$$F_x(0,\theta) = \frac{E_\theta}{E_1}\{\mu_1\mu_2\cos^2\theta + (1+\eta)\sin^2\theta\} \qquad [17]$$

$$F_y(0,\theta) = \frac{E_\theta}{E_1}\{(\mu_1\mu_2 - \eta)\mu_1\mu_2\cos^2\theta + \mu_1\mu_2\sin^2\theta\} \qquad [18]$$

$$F_{xy}(0,\theta) = \frac{E_\theta}{2E_1}(1+\eta-\mu_1\mu_2)(-\eta\sin 2\theta) \qquad [19]$$

24

After rearranging terms, these equations can be written in the following form:

$$F_x(0,\theta) = \frac{E_\theta}{2E_1}\left[\left(K_{90}^x + K_0^x\frac{E_1}{E_2}\right) - \left(K_{90}^x - K_0^x\frac{E_1}{E_2}\right)\cos 2\theta\right] \qquad [20]$$

$$F_y(0,\theta) = \frac{E_\theta}{2E_1}\left[\left(K_0^y + K_{90}^y\frac{E_2}{E_1}\right) + \left(K_0^y - K_{90}^y\frac{E_2}{E_1}\right)\cos 2\theta\right] \qquad [21]$$

$$F_{xy}(0,\theta) = \frac{-E_\theta}{2E_1}\left[\left(K_{90}^x - K_0^x\frac{E_1}{E_2}\right)\eta\sin 2\theta\right] \qquad [22]$$

The terms K_{90}^x and K_0^x represent the stress concentrations at the edge ($\theta=90°$) and at the top ($\theta=0°$) of the notch in an infinitely wide 0° ply subject to loading in the x direction (which for a 0° ply is the same as the 1 direction). Similarly, K_{90}^x and K_0^x are the stress concentration factors in a 0° ply subject to loading in the y direction (or 2 direction).

$$K_{90}^x = 1 + \eta \qquad [23a]$$

$$K_0^x = \mu_1\mu_2\frac{E_2}{E_1} \qquad [23b]$$

$$K_0^y = 1 + \eta\sqrt{\frac{E_2}{E_1}} \qquad [24a]$$

$$K_{90}^y = \mu_1\mu_2 \qquad [24b]$$

Analyzing the tangential stress around a notch in an off-axis ply is performed by rotating and analyzing the ply as a 0° ply with applied loads determined through a Mohr's circle analysis. In this way, we can still use the simplified expressions derived above.

All of the expressions derived above are valid for infinite width panels. Our analysis must also be applicable to finite width panels. Finite width effects are accounted for by substituting finite width expressions for K_{90}^x, K_0^x, K_{90}^y, and K_0^y. These expressions have been derived for panels with different width/diameter ratios and different orthotropic panels. Although previously reported in the final report for the Air Force contract "Durability of Continuous Fiber Reinforced Metal Matrix Composites" (Reference 2), the analysis is repeated here for convenience. In the following discussion, K_t and $K_{t\,net}$ represent the net section and gross section stress concentration factors at the point 90° along the notch from the primary loading axis. Similarly, the stress concentration at the top of the notch, 0° from the loading axis, is represented by K_{t0}.

The general expression for a stress concentration at the edge of a notch was obtained by curve fitting data published in Peterson's Handbook (Reference 4). The gross section stress concentration factor is then determined as:

$$Kt = \frac{Kt\text{-}net}{(1 - 2c/W)}$$ [25]

where W is the width of the laminate and "c" and "d" are the notch radii perpendicular and parallel to the loading, respectively. The curve fit for $K_{t\text{-}net}$ was generalized to include orthotropic panels. The expression is written below for a 0° ply with longitudinal stiffness, E_1, transverse stiffness, E_2, shear stiffness, G_{12}, and Poisson's Ratio, v_{12}.

$$K_{t\text{-}net} = 2 + f_1 f_2^2 + f_1 f_2^4 + 0.643 f_3 (1 - f_2^4) + 0.167 f_3 (1 - f_4^4) + 0.109 f_3 f_5 (2c/W)$$ [26]

where

$$f_1 = \frac{(c/d_{eff} - 1)}{2}, f_2 = 1 - 2c/W, f_3 = \frac{c}{d_{eff}} - 1, f_4 = 4\frac{c}{W} - 1, f_5 = 1 - (2c/W)^{100}$$ [27]

and

$$d_{eff} = (2d/\eta)[1 - (2c/W]^{0.125(\eta/2-1)}$$ [28]

$$\eta = \sqrt{\frac{E_1}{G_{12}} - 2v_{12} + 2\sqrt{\frac{E_1}{E_2}}}$$ [29]

which is the exact solution derived by Lekhnitskii (Reference 3) for orthotropic plates of infinite width and degenerates to the well known K_t of 3 for infinite, isotropic plates.

In composites, the fibers typically have a higher stiffness than the matrix material. The higher stiffness fibers in a 0° lamina will increase the stress concentration at the edge of the hole. Similarly, the stress concentration in an isotropic material can be increased by changing the circular hole into an ellipse with its major axis perpendicular to the loading. In order to calculate the stress concentrations in notched metal matrix composites, an effective notch dimension, c_{eff}, is defined which accounts for the material orthotropy.

An extensive check of this curve fit was performed using boundary collocation analysis for a wide range of orthotropic materials.

Based upon results from finite element and boundary collocation analyses for notched laminates with varying stiffness properties and width to diameter ratios, an expression for the stress concentration at the top of the hole, K_{t0}, in a 0° ply has also been generated. This expression is

$$K_{t0} = \frac{\sqrt{\frac{E_2}{E_1}} + 2.8\left(\frac{2c}{W}\right)^2}{1 + \frac{0.00865}{\left(\frac{W}{2c} - 1\right)^{2.76}}} \tag{30}$$

and has been compared to finite element results.

The corresponding finite width stress concentration factors to be used in the Lekhnitskii based, tangential stress equations, described earlier, are given by:

$$K_{90}^x = K_t \qquad K_0^x = K_{t0} \tag{31}$$

The expressions for K^y_{90} and K^y_0 are found by realizing that a 0° ply loaded transversely (y direction) is the same as a 90° ply loaded longitudinally (x direction). Since the angle, θ, around the notch is measured from the fiber axis, K^y_0 is calculated by switching the values of E_1 and E_2 and by substituting ν_{21} for ν_{12} into the expression for K_t.

$$\nu_{21} = \nu_{12} \frac{E_2}{E_1} \tag{32}$$

Similarly, K^y_{90} is calculated by making the same switches and substitutions into the expression for K_{t0}.

The expressions derived above provide a completely general expression for the tangential stress at any point around a notch. These expressions account for finite width effects and plate orthotropy. The shear stress concentration factor in the loading direction is easily computed from the tangential stress through the application of Mohr's circle.

3.4.1.3.2   Net Section Stress Distribution

Notched strength prediction is also dependent on the stress distribution in the net section. A simple procedure has been developed to evaluate this expression. It is assumed that the stress gradient from the notch is in the form of an exponential decay. Therefore, the stress distribution is written as:

$$\frac{\sigma}{\sigma_g} = A + B\left[1 + \frac{y-c}{\rho}\right]^{-C} \qquad [33]$$

In this expression, the notch radius is given by $\rho = d^2/c$ where "c" and "d" are the radius of the notch perpendicular and parallel to the loading, respectively. The exact form of this equation is determined through the application of three boundary conditions. These conditions state the following:

1) The stress concentration at the edge of the hole must equal K_t,

$$\frac{\sigma}{\sigma_g} @(y = c) = K_t = A + B \qquad [34]$$

2) The stress gradient at the edge of the hole must equal $C_1\frac{K_t}{\rho}$ (Reference 5),

$$\frac{d\sigma}{dy}(y = c) = -C_1\frac{K_t}{\rho} \therefore C = -C_1\frac{K_t}{B} \qquad [35]$$

3) The load across the net section must equal the applied load

$$P = wt\sigma_g = 2t \int_c^{W/2} \sigma(y)dy \qquad [36]$$

Solving for A, B, and C is a nonlinear problem so, an iterative procedure is used.

This analysis is extremely simple and has been proven to be very accurate when compared to classical problems (Reference 6).

3.5 Laminate Strength Prediction

Strength prediction analyses were based on both aluminum and titanium matrix composites. Predictions can be made for any laminate subject to any in-plane load condition. The user simply needs to supply relative load ratios of longitudinal to transverse to shear. In addition, strength predictions are provided for a range of temperatures consistent with those required for the specific application of interest.

The strength analysis models the matrix behavior as elastic-perfectly plastic. It was assumed that most design applications would require a majority of 0° plies in a laminate. If so, then these plies would dominate material behavior and the elastic-per-

fectly plastic matrix behavior assumption would be sufficient. This assumption simplifies the analysis.

3.5.1 Unnotched Analysis

A laminate strength analysis was developed which accounts for a biaxial in-plane load state. The biaxial load condition capability was felt to be important since most applications will experience biaxial loads. A ply-by-ply failure analysis is performed. An elastic-perfectly plastic stress versus stain behavior has been assumed for every ply; unless the ply is loaded parallel to the fibers in which case a perfectly linear behavior is assumed. The analysis uses a Tsai-Hill failure criteria to determine when a ply has reached its linear elastic limit.

The biaxial analysis requires a description of the applied in-plane running loads to the laminate. The parameters N_x, N_y, and N_{xy}, were defined to represent the ratio of these applied running loads. For example, if interested in an equal state of biaxial loads then $N_x = N_y = N_{xy} = 1$. Similarly, if the laminate load ratios were $N_x = 1$, $N_y = 0.5$, and $N_{xy} = 0$, then the composite would be loaded one-half as much transversely as longitudinally, and there would be no shear loading.

Standard laminated plate theory as described by Jones (Reference 7) is used to calculate laminate stiffnesses. The full stiffness matrix is calculated including the extension, bending, and coupled terms. This allows for the analysis of nonsymmetric laminates and of laminates subjected to thermal loads. The load ratios are multiplied by the stiffness matrix of the laminate to obtain the strains in each ply. Since nonsymmetric laminates are allowed, the strains in each ply may differ due to curvature. From the individual ply strains, the corresponding stresses are obtained and converted to their principal components parallel and perpendicular to the fibers. A modified form of the Tsai-Hill failure criterion is then applied to determine which ply reaches its linear elastic limit. The form of this criterion is:

$$\frac{\left(\sigma_1 R + \sigma_1^T\right)^2}{X^2} - \frac{\left(\sigma_1 R + \sigma_1^T\right)\left(\sigma_2 R + \sigma_2^T\right)}{X^2} + \frac{\left(\sigma_2 R + \sigma_2^T\right)^2}{Y^2} + \frac{\left(\tau_{12} R + \tau_{12}^T\right)^2}{S^2} = 1 \qquad [37]$$

where σ_1^T, σ_2^T and τ_{12}^T are the initial longitudinal, transverse, and shear stress state in the ply, R is a scale factor, $R\sigma_1$, $R\sigma_2$, and $R\tau_{12}$ are the stress increments for the ply to reach its elastic limit, X, Y and S are the failure strengths of the ply, and σ_1, σ_2, and τ_{12} are the longitudinal, transverse, and shear stresses calculated from the user-supplied load ratios, N_x, N_y, and N_{xy}, σ_1, σ_2, and τ_{12} are different for each ply in the laminate.

29

X, Y, and S are the lamina longitudinal, transverse, and shear strength, respectively. Since an elastic perfectly-plastic behavior is assumed for each lamina, these values are assumed to be the stress at the ply's linear elastic limit. Determination of X and Y was discussed in the previous section. Lamina shear strength is calculated indirectly, using X, Y, and an off-axis strength, σ_ϕ. Typically, a value for the 15 degree off-axis lamina is used. The expression used to find the shear strength, S is:

$$\sigma_\phi = \sqrt{\dfrac{1}{\dfrac{\cos^4\phi}{X^2} + \left(\dfrac{1}{S^2} - \dfrac{1}{X^2}\right)\cos^2\phi\sin^2\phi + \dfrac{\sin^4\phi}{Y^2}}} \qquad [38]$$

where σ_ϕ is the off-axis strength and ϕ is the ply orientation. This equation is solved for S.

$$S = \sqrt{\dfrac{1}{\dfrac{1}{\sigma_\phi\cos^2\phi\sin^2\phi} - \dfrac{\tan^2\phi}{Y^2} + \dfrac{1-\cot^2\phi}{X^2}}} \qquad [39]$$

Once a ply is predicted to reach its elastic limit, the mode of failure for the ply is determined and the stiffness of the ply is reduced. The mode of failure is determined from the three principal ratios within the Tsai-Hill failure criteria as written above. The ratio which is maximum is defined to be the dominant mode of failure for the ply. This mode of failure dictates how the stiffness reduction is to be performed. If the stress ratio corresponding to the longitudinal strength, X, is maximum then the fibers are critical and represent the dominant failure mode. In this case, the fiber stiffness for this ply is reduced by a factor of 1000. If, on the other hand, the stress ratio corresponding to the transverse strength, Y, or the shear strength, S, is maximum, then matrix yielding is considered the dominant mode. Therefore, the matrix stiffness would be reduced by a factor of 1000. This factor was chosen to avoid any computational singularities that may occur if a value of 0 was used instead.

After reduction of the appropriate stiffness term (fiber stiffness for fiber failures or matrix stiffness for matrix yielding) for the specific ply only, then the overall laminate stiffnesses are recomputed. By reducing the stiffness contribution of the ply, little additional load will be picked up by it. The load carried in the ply up till the ply reached its elastic limit has already been saved in the total ply stress terms, σ^T.

Criteria for determination of final laminate failure are dependent on the applied load conditions. In a laminate with at least one ply which has applied loads directly parallel

to its fibers, final failure is fiber dominated and is defined to occur when those fibers are predicted to fail. However, in a laminate which has no plies loaded in a direction parallel to its fibers, final laminate failure will be matrix dominated and is defined to occur when the matrix is predicted to have yielded in each ply.

Comparisons of uniaxial SCS6/Ti-15-3 unnotched test data with predictions obtained from the analysis discussed above are provided in Figure 7. Material properties were supplied for room temperature, 650°C (1200°F), and 815°C (1500°F). The data included both 40% and 32% fiber volume fractions. Elevated temperature material properties were provided based on actual data, when available, and based on estimates, when actual data were not available. The strength predictions agreed well with the test data (about 4-10% error). This is considered good, since a portion of the error was probably introduced by estimating elevated temperature material properties.

CC24-0757-32-V/bcb
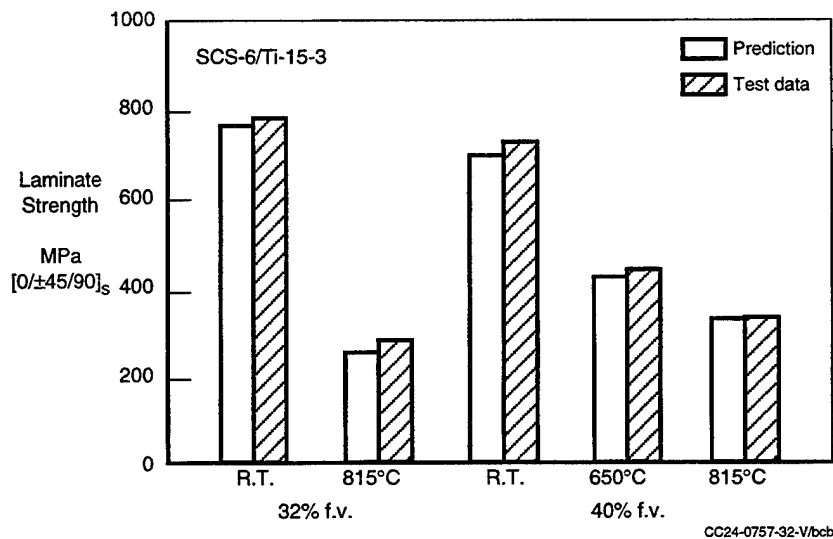
Figure 7.   Uni-axial strength predictions are accurate.

3.5.2 Notched Analysis

3.5.2.1 General Notched Analysis

The notched strength analysis combines the unnotched strength prediction procedure discussed in Section 3.5.1 with the notched stress analyses in Section 3.4.1.3 and adds separate procedures to specifically account weak versus strong matrix effects on how failure initiates in plies with applied loading parallel to its fibers. Weak and strong matrix material systems refer to the type of failure experienced by a notched lamina loaded parallel to the fibers. A weak matrix lamina is predicted to fail when the first fiber breaks at the notch edge. This system is not capable of picking up the load originally carried by the fiber. Conversely, a strong matrix system is capable of carrying load carried by a finite number of fibers. Typically, an aluminum or resin matrix composite is considered a weak matrix system and a titanium matrix composite is considered a strong matrix system.

The notched strength analysis using the first fiber failure criterion works very well for resin and aluminum matrix composites. However, for titanium matrix composites, the strength predictions using this method are highly conservative. Therefore, a second analysis has been developed. Both methods are discussed in more detail below (Sections 3.5.2.2 and 3.5.2.3).

The general procedure for predicting notched strength is very similar to that for unnotched strength. The difference in the notched analysis is that the stress state at each point along the notch perimeter must be determined and analyzed using the Tsai-Hill failure criterion.

Specifically, given the applied load ratios, N_x, N_y, and N_{xy}, the gross (far-field) ply strains and principal stresses are calculated identically as they were in the unnotched analysis. The local stress state at the notch perimeter is calculated in the form of the tangential stress, σ_θ. The method of determining the tangential stress was defined in detail in Section 3.4.1.3.1. Mohr's circle is used to calculate the components of stress parallel and perpendicular to the fibers (σ_1^T, σ_2^T and τ_{12}^T) at each point around the notch (between $\theta=0°$ and $\theta=180°$). The Tsai-Hill failure criterion is then applied (as described in Section 3.5.1) to determine the gross applied stress required to cause each point to reach its elastic limit. Failure will initiate at the angle that requires the minimum gross applied stress.

At this point in the analysis, care must be taken to determine which lamina strength allowables, X, Y, and S, are used in the Tsai-Hill failure equation. When analyzing unnotched tension strengths, the stress state is always positive, such that the tension allowables are used. However, for the complex case of a notched laminate, some loca-

tions around the notch perimeter will be in a state of compression and, therefore, compression allowables must be used.

If failure initiates at a point around the perimeter in a ply with no applied loading parallel to the fibers, then the lamina stiffnesses are reduced just as they were in the unnotched analysis. If the mode of failure is fiber, the fiber modulus for this ply is reduced by a factor of 1000. On the other hand, if the mode of failure is matrix yielding, then the matrix modulus is reduced by the same factor.

If failure initiates in a ply with applied loading parallel to its fibers (i.e., a 0° ply loaded longitudinally or a 90° ply loaded transversely), then the procedure for determining the stress level for this ply becomes more involved. At this point, it is necessary to determine the relative strength of the matrix material compared to the lamina. Depending on whether the matrix is characterized as weak or strong will determine how the remaining analysis for this ply is performed.

In this analysis, weak and strong matrix material systems are determined by a comparison of the matrix yield strain with the lamina failure strain. If the matrix yield strain is less than 75% of the zero degree lamina ultimate strain, then the weak matrix strength analysis is used. The 75% is an arbitrary number and is adjustable. For this program material, the matrix was determined to be weak.

Once the proper analysis is performed, the stiffnesses for the failed ply are reduced and the notched strength analysis continues. Final laminate failure is defined in the same way as for the unnotched analysis.

A verification of the two strength analyses was achieved by comparing predictions with notched test data for Boron/Aluminum, $(B_4C)B/Ti-15-3$, and SCS6/Ti-15-3 (Figure 8). These data include unidirectional and crossplied laminates with different width to diameter ratios. These tests were all uniaxial. The biaxial portion of the analysis has not yet been verified.

In these predictions, the only difference in how the analysis proceeds is in how the 0° plies are treated in the aluminum (weak) versus titanium (strong) matrix composite. Also, since only the 0° plies are loaded parallel to its fibers, final laminate failure was predicted to occur when the 0° fibers had failed.
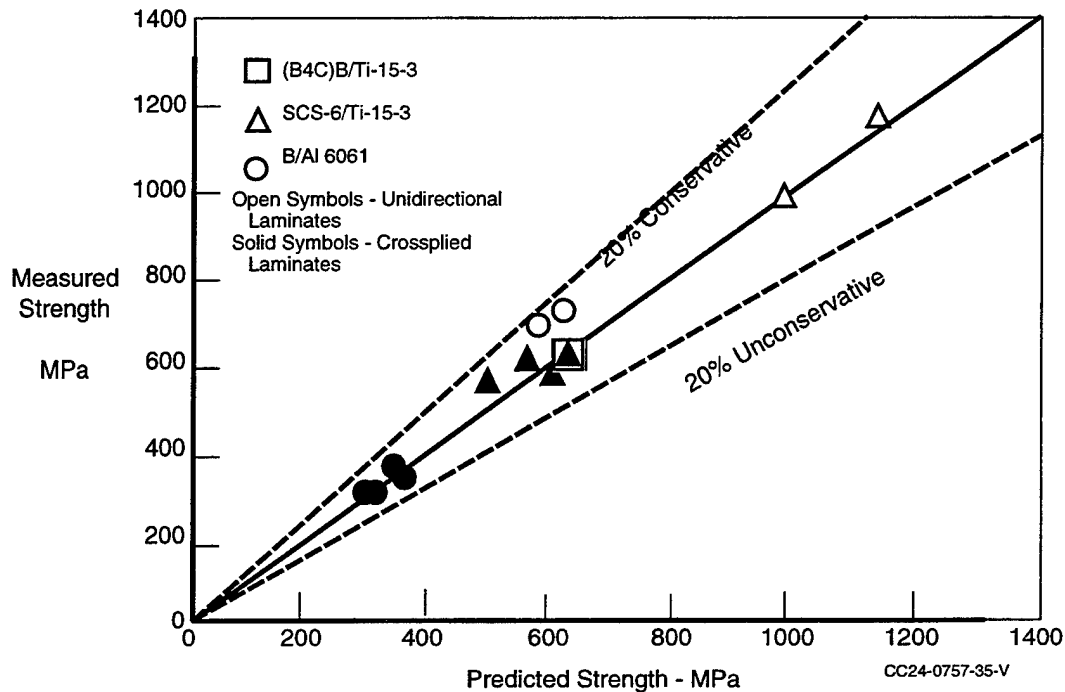
Figure 8. Un-iaxial strength predictions are conservative.

3.5.2.2   Weak Matrix Composite Notched Strength Analysis

For notched analysis, the local stress state around the hole must be analyzed to determine the failure mode and where the failure will occur. This analysis is done on a ply-by-ply basis. If the matrix material is weak in shear, such as aluminum, a yield zone is likely to form near the hole before fibers at the notch edge fail. The effect of this yield zone on the stress state around the hole must be accounted for in order to predict the true failure load. In a weak matrix material laminate failure is predicted to occur when the fibers at the notch edge fail. The matrix material is not strong enough to carry the additional load previously carried by the fiber.

A stress analysis around the notch perimeter indicates that the matrix is critical in shear for a weak matrix material. The stress concentration analysis described in Section 3.4.1.3.1 was used to predict the tangential, longitudinal, and shear stress concentration around a finite width Boron/Aluminum 0° laminate with a center hole subject to uniaxial tension loads. The critical shear stress occurs at an angle of 67° from the load axis. If the matrix has exceeded its shear yield strength at this point, a yield zone forms which will continue to grow with additional loading.

A notched laminate strength analysis for weak matrix materials is not complete unless it accounts for matrix yielding along the fibers. Accurate notched strength prediction

is dependent on modeling the additional load carried in the laminate once matrix yielding starts to occur.

For a uniaxially loaded 0° laminate, the net effect of matrix yielding is to reduce the stress concentration at the edge of the notch, K_t, and to therefore, allow the laminate to carry more load. This behavior is modeled using a simplified shear lag theory.

Yielding will occur at the point around the hole where the shear stress exceeds the shear strength of the material. As the load in the laminate increases the matrix material will continue to yield along the fibers. The effect of this yielding is to reduce the amount of load carried by the material directly in line with the notch. Therefore, less load is transferred through the laminate at the notch and the stress concentration at the edge of the hole is reduced. The matrix will continue to yield until the applied stress multiplied by the current stress concentration at the edge of the hole exceeds the material longitudinal tension strength. Theoretically, the matrix could continue to yield all the way to the top of the specimen. If this occurs then the failing net section stress should equal the ultimate longitudinal strength of the material.

Matrix yielding along the fibers is modeled by transforming the notch in the laminate to an elliptical notch whose major diameter is parallel to the fibers. The equation for the major diameter was empirically determined to be:

$$R_x^{1.5} = L^{1.5} + R_x^{1.5} \qquad [40]$$

By adjusting the geometry of the notch, K_t is decreased at the notch edge. The "L" term in the above equation refers to the length of the yield zone and is determined using the following relationship:

$$L = \frac{(\sigma - \sigma_0)2c}{F_{su}} \qquad [41]$$

where σ_0 is the applied stress at which yielding first occurs, σ is the applied stress in the laminate, 2c is the notch minor diameter, and F_{su} is the allowable shear stress.

The length of the yield zone from the notch is determined by the amount of load carried around the hole in shear. This load divided by the yield zone length and the specimen thickness is equated to the ultimate matrix shear yield strength.

Although this method of accounting for yielding in 0° plies works very well in a uniaxial analysis, it does not lend itself easily to biaxial analysis. In a biaxial analysis, yielding can occur in any ply regardless of its orientation.

Modeling yielding in every ply is a complicated task. This involves tracking the amount of matrix yielding in every ply separately. Following the modeling scheme described above, each ply would eventually have different notch configurations to account for the matrix yielding in the ply.

In the metal matrix systems tested under this contract, the transverse strength is far more critical than the shear strength. Using a uniaxial analysis, it is sufficient to consider matrix yielding effects for 0° plies only because the transverse strength will be critical in the off-axis plies. Similarly, in a biaxially loaded laminate, an off-axis ply is more likely to fail at a point around the notch where the transverse stress component exceeds the transverse strength. Yielding will be most important in 0° and 90° plies. Therefore, the model accounts for yielding in 0° plies when longitudinal loading is present and in 90° plies when transverse loading is present. This allows the use of the modified shear-lag theory described above.

3.5.2.3   Strong Matrix Composite Notched Strength Analysis

The notched strength method for strong matrix materials, such as titanium, is based on the fact that the fibers at the notch edge will fail before the matrix yields in shear or tension. The objective of this method is to determine how many fibers will fail before the matrix achieves its maximum load carrying capability. Two assumptions are made in this analysis: 1) the yielding load is the maximum load carried by the matrix and 2) the local stress at the location where the next fiber fails is equal to the lamina longitudinal strength. The load in the ply is obtained by summing the contributions from two areas: 1) in the damaged area where the fibers have failed and 2) where the fibers are still intact.

$$P = 2t\left(F_y l_d + \int_{l_d+b}^{W/2} \sigma_x(y)dy \right) \qquad\qquad [42]$$

In this expression, F_y is the matrix yield strength, "c" is the notch radius perpendicular to the fibers, W is the specimen width, and l_d is the length of the zone where the fibers have failed. The stress distribution through the net section is denoted by $\sigma_x(y)$.

The zero degree ply ultimate load is equal to the largest value of P as l_d is incremented through the net section. The exact value of l_d which corresponds to the ultimate load may be determined by differentiating the expression for P with respect to l_d and then solving for l_d.

The expression for the stress distribution is assumed to be an exponential decay of the stress gradient from the notch.

36

$$\sigma_x(y) = \sigma_g \left(A + B \left[1 + \frac{y-c}{\rho} \right]^{-C} \right) \qquad [43]$$

In this expression σ_g is the gross stress and $\rho = d^2/c$ where "c" and "d" are the radius of the notch perpendicular and parallel to the loading, respectively. A, B, and C are constants which are determined through the application of three boundary conditions. This method was discussed in detail in Section 3.4.1.3.2.

3.6   Fatigue Life Analyses

Use of MMC materials in any application requires a thorough understanding of the fundamental mechanisms which control damage initiation and growth. Metal matrix composites are very complex material systems which combine metal alloys, which can have large amounts of plasticity and complex fatigue failure mechanisms, with stiff, brittle ceramic fibers at extremely high temperatures. Depending on the operating temperature for the material, the composite can have a significant residual stress state due to the differences in thermal expansion between the fiber and matrix which can not be ignored during analysis. Additionally, in a multidirectional composite there may be significant residual stresses between plies. To further appreciate the complexity of this material system, now consider that there is an interface layer between the fiber and matrix which, to some extent, bonds the matrix to the fiber. The composition and properties of the interface are dependent on the constituents and the consolidation process and is, therefore, not well defined. Both the residual stress state and the interface properties affect fatigue behavior of the composite.

Due to the complex nature of the material and new damage modes which may be present, fatigue analyses for metal matrix composites must include damage initiation and growth models for several types of failure modes. This is a challenging task, considering that the application of fatigue analyses for metal structures alone is not always a straightforward task.

The analysis approach was to develop a design tool for engineering purposes rather than a more detailed scientific model. There are few, if any, design tools available for the engineer who is attempting to design a MMC structure for a given application. However, there are a number of researchers in government, industry, and academia working on specific, scientific models which describe many different portions of the problem. The design tool was developed by taking advantage of as much of this detailed work as possible to improve the accuracy. However, since not all aspects of the model are thoroughly understood at this point, the model does rely on lamina data where possible. At a minimum, the model requires matrix fatigue data and manipulates it for lamina life analysis.

The computer program which contains this design tool is written in modular format. Therefore, as better understanding is acquired, specific routines, within the code may be replaced by more advanced models. The code, therefore, serves as a foundation in which future enhancements may be added.

There are three areas to be considered when investigating fatigue in metal matrix composites: 1) when damage first appears, 2) the type of damage that will occur, and 3) how it will grow. The fatigue analyses and the philosophy behind them are discussed below.

3.6.1 Damage Initiation

3.6.1.1 Unnotched Damage Initiation Life Analysis

The unnotched fatigue life model is based on a damage accumulation scheme which tracks damage in both the fiber and the matrix. Given a generic load and temperature profile, constituent stresses are determined including residual stresses in the fiber and matrix and for creep in the matrix. The model assumes that the fibers are insensitive to creep.

The material properties required for each constituent include stiffness and strength versus temperature, thermal expansion coefficient, and normalized stress versus life curves. If performing a creep analysis, strain versus time data for several stress levels and temperatures is required. The stress versus life curve for the fibers is obtained from unnotched zero degree laminate fatigue tests. For the SCS6/Ti-24-11 material tested under this contract, the curve shown in Figure 9 is sufficient. Modified Rule of Mixture equations are used to calculate lamina stiffnesses and strengths. The accuracy of the predictions are then improved through the use of lamina data as described in Section 3.4.1.2.

The temperature and load profiles are divided into segments. In each segment the load and temperature are defined as constant, ramping or cyclic. Depending on the segment definition for load and temperature, a finite number of points throughout the segment are defined at which the constituent stresses are determined.

The constituent stress analysis performed at each point begins with a temperature dependent stiffness calculation. The ROM procedure defined in Section 3.4.1.2 is used to calculate lamina stiffnesses and laminated plate theory is used to calculate laminate stiffnesses. Interpolation schemes are used to find properties for temperatures not included in the data provided for the analysis. Extrapolation of data are not performed. In the event that a temperature exceeds the range of data provided, then the closest boundary temperature is used in the analysis.

38
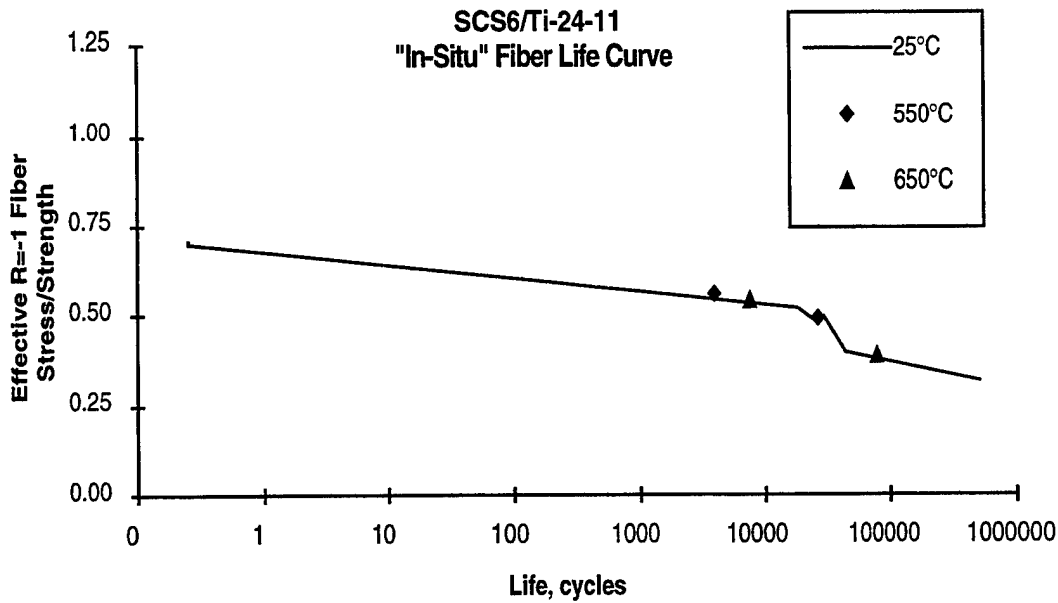
Figure 9.   0° fiber stress controls fatigue life.

Total laminate strains, {e}, are a function of the mid-plane strains, $\{\varepsilon_o\}$, the laminate curvatures, $\{\kappa\}$, and the distance from the center plane through the thickness, z.

$$\{\varepsilon\} = \{\varepsilon_o\} + \{\kappa\}z \qquad\qquad [44]$$

The mid-plane strains and the laminate curvature are determined by multiplying the laminate inverse stiffness matrix by the load and moment profile.

$$\begin{Bmatrix} \varepsilon_o \\ \kappa \end{Bmatrix} = \begin{bmatrix} A & B \\ B & D \end{bmatrix}^{-1} \begin{Bmatrix} N \\ M \end{Bmatrix} \qquad\qquad [45]$$

The load, {N}, and moment, {M}, vectors include thermal loads and moments due to thermal expansion mismatch between plies of different fiber orientation. Unsymmetrical laminates can be analyzed since the full stiffness matrix is calculated and used in determining the laminate strains.

Next, the stresses in each ply are calculated by multiplying the laminate mechanical strains by the corresponding ply stiffness matrix, $[\overline{Q}]$.

$$\{\sigma\}_{ply} = [\overline{Q}]\{\varepsilon - \varepsilon_{thermal}\} \qquad\qquad [46]$$

39

The matrices, $[A]$, $[B]$, $[D]$, and $[\overline{Q}]$, are defined in Reference 7. A transformation matrix is used to convert these stresses into the principal stresses, $\{\sigma'\}_{ply}$.

$$\{\sigma'\}_{ply} = [T]\{\sigma\}_{ply} \tag{47}$$

where

$$[T] = \begin{bmatrix} \cos^2\phi & \sin^2\phi & 2\sin\phi\cos\phi \\ \sin^2\phi & \cos^2\phi & -2\sin\phi\cos\phi \\ -\sin\phi\cos\phi & \sin\phi\cos\phi & \cos^2\phi - \sin^2\phi \end{bmatrix} \tag{48}$$

and ϕ is the ply orientation.

The fiber longitudinal mechanical stress, $\sigma_{mech}^{1,f}$, is based on the laminate strain level and is calculated by multiplying the longitudinal lamina stress due to the applied loads by the ratio of fiber to longitudinal lamina moduli:

$$\sigma_{mech}^{1,f} = \sigma_{11}\frac{E_f}{E_1} \tag{49}$$

The longitudinal stress in the matrix , $\sigma_{mech}^{1,m}$, is found using Rule of Mixtures as:

$$\sigma_{mech}^{1,m} = \frac{\sigma_{11} - \sigma_{mech}^{1,f}V_f}{(1-V_f)} = \sigma_{11}\frac{E_m}{E_fV_f + E_m(1-V_f)} \tag{50}$$

where s_{11} is the lamina longitudinal stress. The transverse fiber and matrix stresses due to mechanical loads are defined as:

$$\sigma_{mech}^{2,f} = 0 \qquad \sigma_{mech}^{2,m} = \sigma_{22}/(1-V_f) \tag{51}$$

where σ_{22} is the transverse lamina stress. Further, it is assumed that the matrix material carries all shear load:

$$\tau_{mech}^{12,f} = 0 \qquad \tau_{mech}^{12,m} = \tau_{12} \tag{52}$$

To calculate fiber and matrix residual stresses, it is assumed that a bond has formed between the matrix and fiber at the consolidation temperature, T_c, and that the bond is

still intact at temperature, T_i. The residual longitudinal fiber and matrix stresses, $\sigma_{res}^{1,f}$ and $\sigma_{res}^{1,m}$, in a lamina are calculated as:

$$\sigma_{res}^{1,f} = E_f \varepsilon_{res}^f = E_f (\alpha_f - \alpha_{11})(T_c - T_i) \tag{53}$$

$$\sigma_{res}^{1,m} = E_m \varepsilon_{res}^m = E_m (\alpha_m - \alpha_{11})(T_c - T_i) \tag{54}$$

where α_f, α_m, and α_{11} are the thermal expansion coefficients for the fiber, matrix, and lamina. The lamina longitudinal thermal expansion coefficient is calculated simply by summing all forces parallel to the fibers and equating them to zero.

$$\sum F = \left[\sigma_{res}^{1,f} V_f + \sigma_{res}^{1,f}(1 - V_f) \right] A_x = 0 \tag{55}$$

where A_x is the cross-sectional area of laminate. Substituting the expressions for the fiber and matrix residual stresses and solving for α_{11}, the following expression is obtained:

$$\alpha_{11} = \frac{\alpha_f E_f V_f + \alpha_m E_m (1 - V_f)}{E_f V_f + E_m (1 - V_f)} \tag{56}$$

Significant transverse stresses can also exist due to thermal expansion mismatch. Maximum values of matrix residual stress (at the fiber/matrix interface) can be approximated by an analysis based on a concentric cylinder elastic model (Reference 8). The final expression for the transverse matrix residual stress, $\sigma_{res}^{2,m}$, is:

$$\sigma_{res}^{2,m} = \frac{(\alpha_f - \alpha_m)(T_c - T_i)(1 - V_f)E_m E_f (1 + V_f)/(1 - V_f)}{E_f V_f + E_m (1 - V_f) + E_f/(1 + \upsilon_m(1 - V_f)) - \upsilon_f E_m} \tag{57}$$

The residual stresses in the fiber and matrix act upon the same area. Therefore, the transverse fiber residual stress, $\sigma_{res}^{2,f}$, is equal in magnitude to the transverse matrix residual stress.

$$\sigma_{res}^{2,f} = \sigma_{res}^{2,m} \tag{58}$$

The residual shear stress component is assumed to be zero such that:

$$\tau_{res}^{12,f} = 0 \qquad \tau_{res}^{12,m} = 0 \tag{59}$$

The total stress in the fiber and matrix neglecting creep is the sum of the mechanical and residual stresses.

$$\sigma_{m-r}^{1,f} = \sigma_{mech}^{1,f} + \sigma_{res}^{1,f} \qquad \sigma_{m-r}^{1,m} = \sigma_{mech}^{1,m} + \sigma_{res}^{1,m} \qquad [60]$$

$$\sigma_{m-r}^{2,f} = \sigma_{mech}^{2,f} + \sigma_{res}^{2,f} \qquad \sigma_{m-r}^{2,m} = \sigma_{mech}^{2,m} + \sigma_{res}^{2,m} \qquad [61]$$

$$\tau_{m-r}^{12,f} = \tau_{mech}^{12,f} \qquad \tau_{m-r}^{12,m} = \tau_{mech}^{12,m} \qquad [62]$$

Modification of the matrix and fiber stresses to account for matrix creep relaxation is performed only if the segment temperature, T_i, is greater than the matrix material creep threshold temperature. The objective of this step is to determine how much the matrix stress will relax during this time segment, t_i. A generic creep power law is used to account for instantaneous deformation (load dependent), primary creep (strain hardening), and steady-state creep (time dependent). The creep strain at temperature, T_i, is defined as:

$$\varepsilon = A_1 \sigma^{A_2} + A_5(1 - e^{-A_6 t})\sigma^{A_7} + A_3 \sigma^{A_4} t \qquad [63]$$

In this expression A_1, A_2, A_3, A_4, A_5, A_6, and A_7 are unknowns determined empirically from creep data (strain vs. time) for various stress levels. Initially (t=0), the strain is equal to $A_1 \sigma_i^{A_2}$. Assuming that strain remains constant, the relaxation stress, σ_r, after time, $t=t_i$, can be computed by equating the initial strain to the final strain.

$$A_1 \sigma_i^{A_2} = A_1 \sigma_r^{A_2} + A_5(1 - e^{-A_6 t_i})\sigma_r^{A_7} + A_3 \sigma_r^{A_4} t_i \qquad [64]$$

This equation can then be solved for the relaxation stress through a nonlinear solution procedure such as Newton-Raphson. A simpler solution is possible if it can be assumed that $A_2 = A_4 = A_7$:

$$\sigma_r = \sqrt[A_2]{\frac{A_1 \sigma_i^{A_2}}{A_1 + A_5(1 - e^{-A_6 t_i}) + A_3 t_i}} \qquad [65]$$

The final longitudinal and transverse matrix stresses after creep relaxation, $\sigma^{1,m}$ and $\sigma^{2,m}$, are found by substituting $\sigma_i = \sigma_{m-r}^{1,m}$ and $\sigma_i = \sigma_{m-r}^{2,m}$ in either of these equations. It is assumed that the matrix does not creep relax in shear.

When the matrix relaxes, the residual stresses are reduced. The new residual matrix stresses are:

42

$$\sigma_{res}^{1,m} = \sigma^{1,m} - \sigma_{mech}^{1,m} \qquad \sigma_{res}^{2,m} = \sigma^{2,m} - \sigma_{mech}^{2,m} \qquad [66]$$

The new residual fiber stresses are found by summing the residual forces and equating to zero. The resulting expressions are:

$$\sigma_{res}^{1,f} = -\sigma_{res}^{1,m} \frac{(1-V_f)}{V_f} \qquad \sigma_{res}^{2,f} = \sigma_{res}^{2,m} \qquad [67]$$

The total fiber stresses after matrix creep relaxation are found by adding the mechanical and new residual stresses.

$$\sigma^{1,f} = \sigma_{mech}^{1,f} + \sigma_{res}^{1,f} \qquad \sigma^{2,f} = \sigma_{mech}^{2,f} + \sigma_{res}^{2,f} \qquad [68]$$

The von Mises equation is used to calculate the fiber and matrix equivalent stresses, σ^f and σ^m.

$$\sigma^m = \sqrt{\frac{1}{2}[(\sigma^{1,m} - \sigma^{2,m})^2 + \sigma^{1,m^2} + \sigma^{2,m^2} + 6\tau^{12,m^2}]} \qquad [69]$$

Since the fiber shear stress is zero, the von Mises equation for the fiber simplifies to:

$$\sigma^f = \sqrt{\sigma^{1,f^2} + \sigma^{2,f^2} - \sigma^{1,f}\sigma^{2,f}} \qquad [70]$$

Matrix and fiber stresses are calculated at every point in the segment and for each segment of the spectrum. In fact, two new stress profiles have been created. However, these profiles already include the effects of temperature, residual stresses, and creep relaxation. Due to these effects, new peak and valley stresses exist for both the fiber and matrix. A rainflow counting routine is used to combine the new constituent level stress spectra into peak and valley pairs. Note, however, that these spectra are only valid until the first failure is predicted to occur. When this happens, new fiber and matrix stress profiles must be created using the same procedure described above, but with reduced stiffness properties to account for the failed constituent.

Miner's Rule is used to calculate the amount of damage in both the fiber and matrix. After combining the peak and valley pairs using a rainflow counting technique, a stress ratio, R, is calculated for each by dividing the valley stress by the peak stress. A

simplified stress ratio correction factor based on the expression developed by Smith, Watson, and Topper (Reference 9) is applied to obtain effective R = -1 stresses.

$$\sigma_{eff}^{f} = \sigma_{peak}^{f} \sqrt{\frac{1-R_f}{2}} \qquad \sigma_{eff}^{m} = \sigma_{peak}^{m} \sqrt{\frac{1-R_m}{2}} \qquad [71]$$

where

$$R_f = \frac{\sigma_{valley}^{f}}{\sigma_{peak}^{f}} \qquad R_m = \frac{\sigma_{valley}^{m}}{\sigma_{peak}^{m}} \qquad [72]$$

The effective fiber and matrix stresses are normalized by dividing by the corresponding fiber and matrix strengths at temperature, T_i. Then the life to failure is determined from the normalized stress and the input stress versus life curves. The damage in the fiber and matrix is calculated as:

$$D_{ply}^{f} = \frac{\# \text{ of cycles @ } \sigma_{eff}^{f}}{\text{Life @ } \sigma_{eff}^{f}} \qquad D_{ply}^{m} = \frac{\# \text{ of cycles @ } \sigma_{eff}^{m}}{\text{Life @ } \sigma_{eff}^{m}} \qquad [73]$$

Damage is tracked in each ply for both the fiber and matrix. The damage is cumulative. When the total damage exceeds 1, failure is predicted to occur.

Lamina and laminate stiffnesses are recalculated whenever a fiber or matrix failure occurs. If the matrix fails in a ply, the transverse and shear lamina stiffness, E_2 and G_{12}, are reduced by a factor of 1000. Conversely, if the fibers fail in a ply, the longitudinal stiffness, E_1, is reduced by a factor of 1000. This is the same procedure used in the strength analysis (See Section 3.5.1).

Definition of ultimate laminate failure is dependent on the type of applied loading. If the applied loading is not parallel to any of the fibers in any of the plies in the laminate then the laminate is predicted to fail when the matrix has failed in each ply. However, if the applied loading is parallel to the fibers in at least one ply, then it is assumed that these fibers will control the life of the specimen. In this case, failure will not occur until those fibers have failed. For example, a $[\pm 45]_s$ loaded longitudinally is predicted to fail when the damage for the matrix in each ply accumulates to one. However, when a $[0/\pm 45/90]_s$ is loaded transversely, failure will not occur until the fibers in the 90° ply fail.

The complete unnotched fatigue analysis described above was used to predict the response of both unidirectional and $[0/\pm 45]_s$ SCS6/Ti-15-3 when subject to isothermal constant amplitude loading (Figure 10). The R = 0.02 unidirectional data shown in Fig-

ure 10 were used to create the insitu fiber life curve for this analysis; therefore, it is not surprising that the analysis correlates with these data. However, based on this insitu fiber life curve, the analysis was also able to predict the R = 0.50 unidirectional response and the [0/±45]$_s$ response.

The analysis was also used to predict the life of unidirectional SCS6/Ti-24-11 at room and elevated temperatures (Figure 11) using the fiber life curve in Figure 9.

3.6.1.2 Notched Damage Initiation Life Analysis

The fatigue crack initiation routine for notched laminates combines the unnotched fatigue analysis described above with the notched stress analysis (Section 3.4.1.3.1). Essentially, the unnotched analysis is performed at multiple points around the notch. The same material property data required for the unnotched analysis is used here.
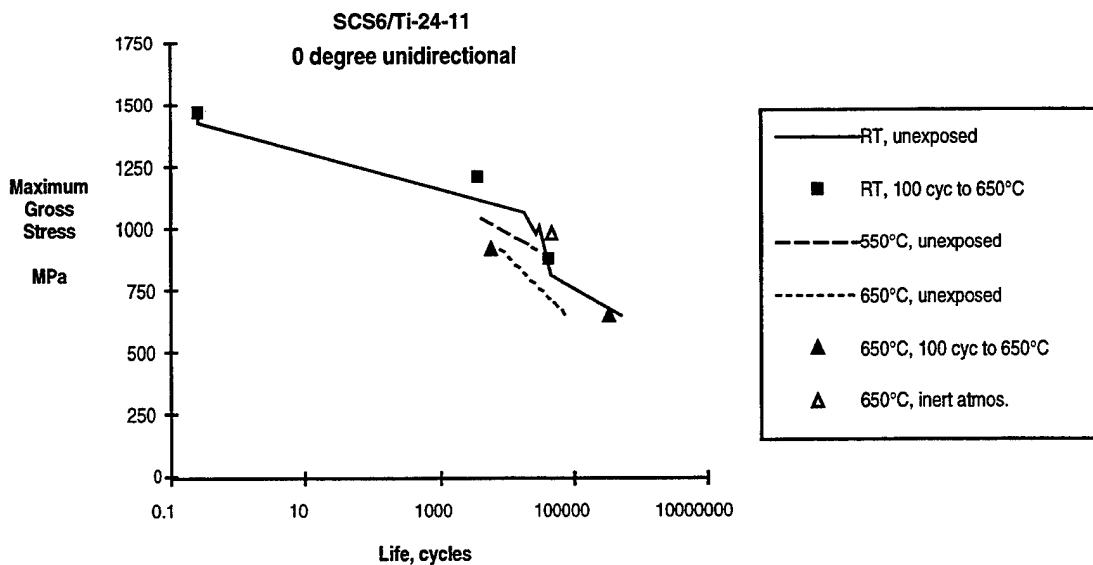
Figure 10. Unnotched fatigue life data (SCS6/Ti-24-11).
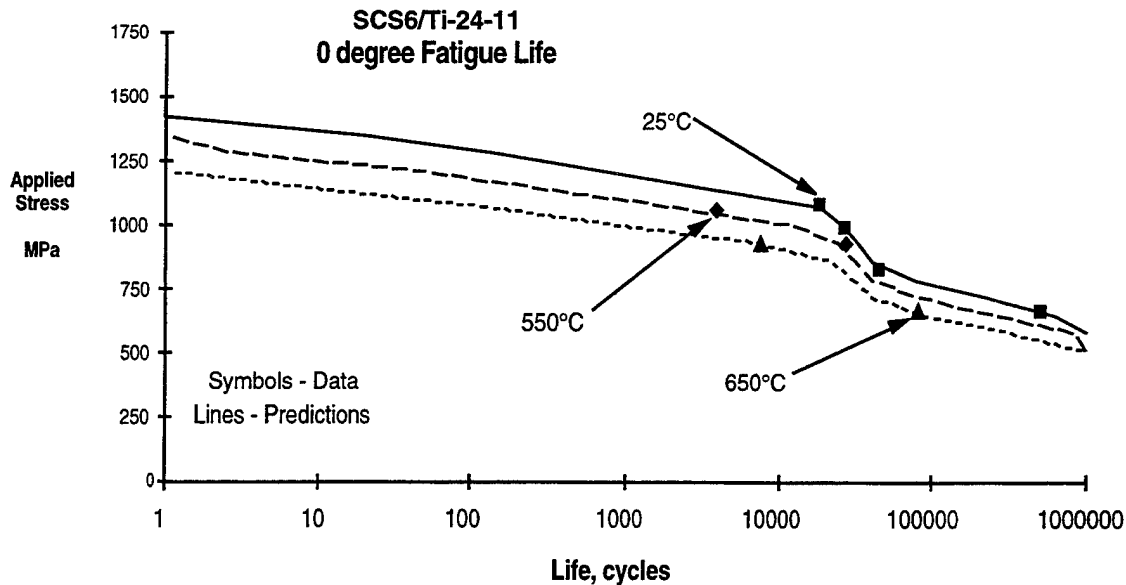
Figure 11. Fatigue analysis predicts temperature effects on life.

The laminate strain analysis considers the multiply, notched laminate as a single orthotropic lamina with a center notch. The properties used for the lamina are the ones calculated for the multiply laminate. The decision to represent the laminate as a single ply was made for two reasons. First, in the vicinity of the notch in an undamaged laminate, the strain field is a global response. Typically, when crack initiation is observed at the surface of the specimen, it tends to be through the thickness. Second, performing the damage analysis at every point around the notch, for every ply in a laminate, is a tedious, time consuming task, unwarranted for the type of design tool being created. The number of calculations are significantly reduced when performing the analysis on a single lamina with smeared laminate properties.

Laminate properties are calculated as described for the unnotched analysis except that a laminate coefficient of thermal expansion is also calculated. This term is calculated using the thermal loads, N_T, induced by the ply by ply thermal expansion terms and the inverse of the laminate stiffness matrix, $[\overline{Q}]^{-1}$, for the smeared lamina. $[\overline{Q}]^{-1}$ is determined by taking the laminate stiffness terms (E_x, E_y, G_{xy}, and n_{xy}) and utilizing them as "lamina" properties to calculate a "lamina" stiffness matrix that represents the laminate.

46

$$[\alpha]_{laminate} = \frac{1}{t\,\Delta T}[\overline{Q}]^{-1}\{N_T\} \qquad [74]$$

where t is the laminate thickness and ΔT is the temperature change.

The stress state around the hole is analyzed as in the notched strength routine (See Section 3.4.1.3.1). Using a closed form analysis developed by Lekhnitskii, the tangential stress is found at 5 degree increments around half of the notch. Once the tangential stress is determined it is broken down into longitudinal, transverse, and shear stresses. using Mohr's circle. These terms are then converted to fiber and matrix stresses at each point. The analysis then follows in the same manner as the unnotched routine.

The result of this analysis is not a prediction of laminate failure but the initiation of a crack at some point around the notch. The analysis can track crack initiation in the matrix, fiber, or both. It assumes the matrix to be elastic-perfectly plastic. As a result the code will provide similar matrix predictions regardless of whether the matrix is brittle or ductile and, therefore, the analysis predictions for matrix crack initiation tend to be conservative.

3.6.1.3   Fiber Life Curve Generation

An insitu fiber life curve can be created using unnotched 0° unidirectional fatigue test coupons. The stress in the zero degree fibers is calculated as:

$$\sigma_{0° \; fiber} = \sigma_{applied} \frac{1}{V_f} \qquad [75]$$

This expression assumes that the matrix begins to crack very early and therefore, carries no load. This assumption is based on high residual stresses due to the coefficient of thermal expansion (CTE) mismatch between fiber and matrix.

However, if this assumption is not valid, then the procedure to define the fiber life curve is more involved. Essentially, using the 0° unidirectional fatigue test data as a baseline, the life associated with the matrix must first be determined, then the fiber stress must be recalculated accounting for the failure of the matrix and the difference between the lamina life and the matrix life is the fiber life. The fiber stress calculation, in this case, can be more complicated than the above expression. The analysis in MMCLIFE V3.0 uses the lamina data and performs a preliminary fatigue analysis simply to calculate the fiber stress and fiber life using the methods discussed in Section 3.6.1.1. Once the fiber life curve is calculated it is saved for future use.

3.6.2   Damage Modes in Notched Laminates

Several damage modes have been observed in center notched MMC's. Specifically, two modes have been identified: 1) cracks growing through the net section, breaking or bridged by fibers and 2) matrix cracks growing parallel to fibers, in both 0 and off-axis laminates. The type of mode is controlled by many variables, including applied stress level, temperature, lamina stiffness, and interface properties. In this section, methods are described which predict the damage mode for a lamina given the load and temperature profiles and the material properties.

The basis for determining where cracks will initiate from a notch is a simple stress analysis of the notch perimeter. If a zero degree lamina loaded parallel to the fibers is analyzed, it is a simple task to determine the stress distribution along the entire notch perimeter, (Section 3.4.1.3.1). Fatigue cracks are most likely to initiate at those locations around the notch perimeter at which stresses are highest with respect to the strengths of the matrix or fiber, or the fiber-matrix interface. In weak matrix composites, such as polymers, aluminum alloys, or elevated temperature titanium, cracks initiate in shear parallel to the fibers. In stronger matrix materials cracks initiate at the notch edge. As described is Section 3.4.1.3.1, the local stress state at each point around the notch can be calculated in terms of longitudinal, transverse and shear stress components. When divided by the appropriate strength parameter (i.e. longitudinal stress/longitudinal lamina strength or shear stress/shear strength) it is obvious where these critical locations are located. The analysis provided in Section 3.4.1.3.1 is equally valid for more complicated (i.e. biaxial) loadings as well.

Using the stress analysis described in Section 3.4.1.3.1, a plot was developed for a longitudinally loaded, zero degree laminate with a center open hole which determines the transition from net section cracks which break or bridge fibers to cracks which grow parallel to fibers. The ratio of lamina longitudinal strength, $F_{tu}{}^{L}$, to shear strength, F_{su}, is plotted against the lamina stiffnesses (Figure 12). The transition line is found by determining the gross stress required to initiate a crack at the maximum shear stress location and compared to that required to start a crack at the notch edge. If the gross stress required to initiate failure at the notch edge is less than the gross stress required to fail the lamina in shear, then the crack will propagate through the net section. If the alternative is true, then the crack will propagate parallel to the fibers. When these stresses are written in terms of stress concentration factors, the following equation is derived:

$$\frac{F_{tu}^{L}}{F_{su}} = \frac{K_t}{K_s} \qquad\qquad [76]$$

The ratio of K_t/K_s is a function of material stiffness and can be calculated using the methods of Section 3.4.1.3.1.

In aluminum matrix composites, the shear strength is low, driving the strength ratio up and, therefore, results in cracks which initiate away from the notch edge parallel to the fibers. This correlates well with the prediction shown in Figure 12. The $(B_4C)B/Ti$ material system was subjected to a secondary heat treatment which degraded the fiber strength and resulted in cracks which grew through the net section. The SCS6/Ti material system tends to straddle the line depending on the lamina shear strength. An earlier panel had evidence of poor fiber spacing, which resulted in a low shear strength. Later material had better fiber spacing and raised the lamina shear strength enough to lower the point on the plot and, in many cases, caused initial shear cracks with multiple matrix cracks.

Anything which affects the strength and/or stiffness of a lamina can therefore affect the mode of damage. Temperature is an obvious example. At high temperatures the shear strength degrades faster than the longitudinal strength. The effect of this property degradation is to drive the damage mode to one in which cracks initiate away from the edge of the notch and up parallel along the fibers. This is demonstrated using the elevated temperature properties for SCS6/Ti in Figure 13.

$$\text{Plate Orthotropy, } \frac{\eta}{2} = \frac{\sqrt{\frac{E_1}{G_{12}} - 2v_{12} + 2}\sqrt{\frac{E_1}{E_2}}}{2}$$

CC24-0757-44-V/jam
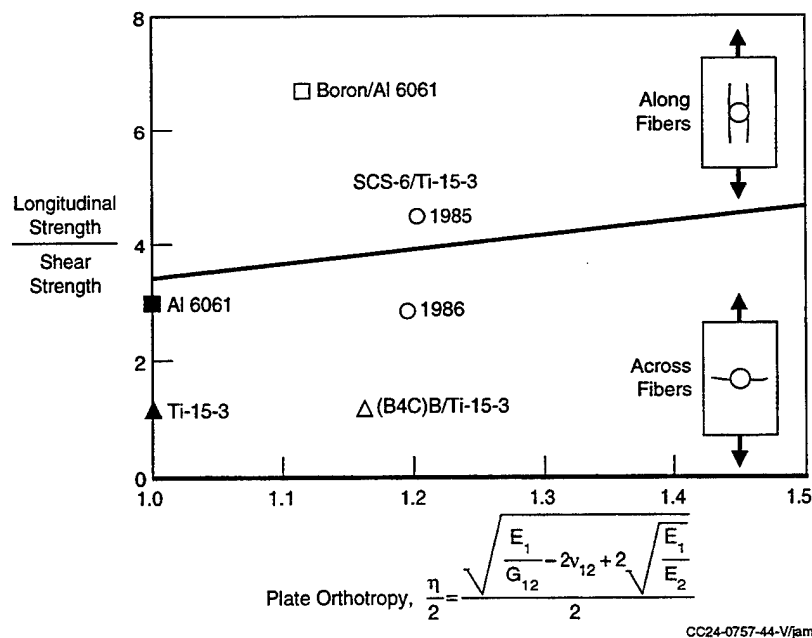
Figure 12. **Damage modes in notched coupons are a function of lamina strength.**

49
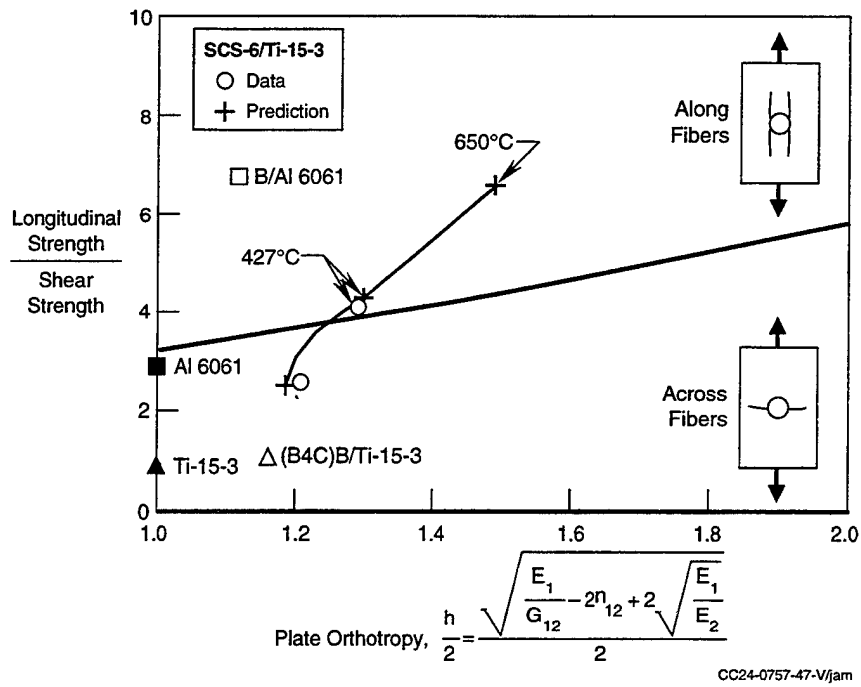
Figure 13. Damage modes change with temperature.

3.6.3 Damage Growth

3.6.3.1 Analysis Options

The analyses discussed in this section were developed to provide an estimate of the damage growth rate under thermomechanical loads based on a limited amount of data. Since this is meant to be a design tool, the analyses were designed to accept a variety of different data and to perform two different types of damage analyses. The goal here was to attempt to be flexible enough to handle newer material systems in which little or no damage growth data are available, in addition to older material systems having a larger amount of damage growth data.

The analysis will be performed either on a ply-by-ply basis or on a laminate basis. The ply-by-ply analysis consists of tracking crack growth in each ply individually without any influence of the surrounding plies. In this case, 0° plies can have any one of the types of cracks shown in Figure 14. However, off-axis plies are limited to cracks which grow along the fibers. The laminate analysis treats the laminate as a single orthotropic 0° ply with "effective" fiber and matrix properties to match laminate strengths and stiffnesses. In this case, laminate crack growth data may be provided only if the laminate being analyzed is identical in lay-up to the one for which data are provided.

MMC Fatigue Crack Growth
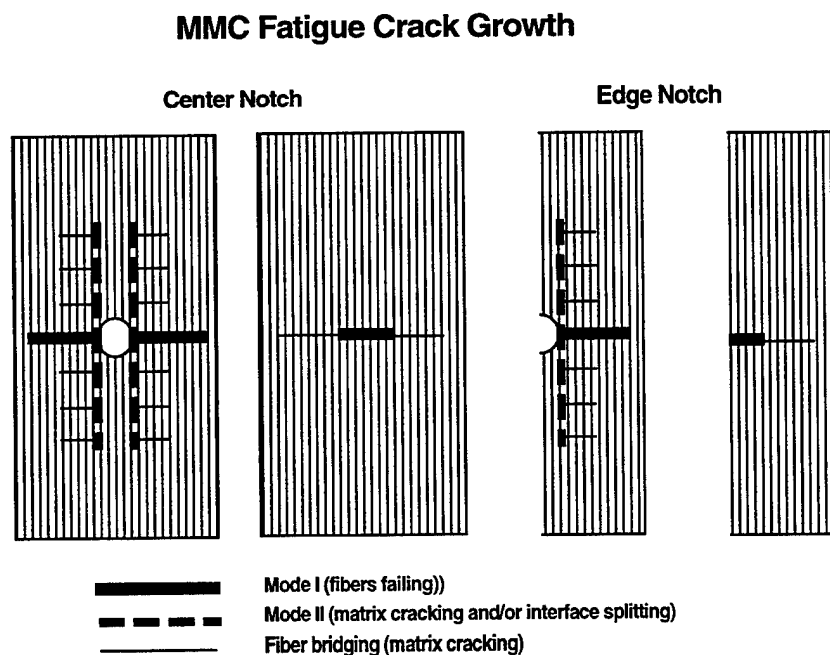
Figure 14. Crack growth analyses are capable of predicting several modes of damage.

A laminate analysis is simpler and probably more reliable since the laminate data provided will describe damage behavior specifically for that laminate. On the other hand, a ply-by-ply analysis will probably be more conservative since shielding effects due to adjacent plies are not accounted for in the analysis.

The analyses require matrix crack growth data at a minimum. If available, lamina or laminate data are used to refine the analysis for older material systems which have a more defined damage growth behavior.

Multiple sets of data may be supplied which define the isothermal, constant amplitude fatigue damage growth behavior for different temperatures, specimen geometries, stress levels, and stress ratios. The matrix data consists of crack growth rate, da/dN, versus stress intensity, ΔK. The lamina or laminate data consists of crack length versus cycles, N. The reason for the different data requirements for lamina or laminate data are that there are different types of damage that can occur and each mode of damage has a different stress intensity formulation. The lamina or laminate data provided for the analysis must identify the type of damage which occurred such that the proper stress intensity formulation may be used.

Damage growth analyses have been developed for two different modes of failure: 1) Mode I cracks which fail or bridge fibers and 2) Mode II cracks or mixed mode cracks which grow parallel to the fiber direction.

If an analysis is required using a new material system without any lamina or laminate damage growth data, then the matrix crack growth data along with the material properties of the lamina will be used to establish the type of damage mode to be experienced by the composite under the provided mechanical and temperature spectra. Fatigue damage growth modes in MMC's are dependent on several variables including lamina longitudinal strength, matrix shear strength, and lamina stiffness. It has been shown that as the matrix shear strength weakens in a unidirectional laminate, a transition occurs (Figure 13) between fatigue cracks which initiate and grow across the net section and those that initiate and grow parallel to the fibers (Section 3.6.2). Additionally, data developed under this contract and presented in Reference 1, indicates that the fiber/matrix interface also plays a significant role in failure modes. The weaker the interface the more likely multiple cracks will form and grow around fibers. Conversely, a stronger bond will cause cracks to grow through fibers.

Linear elastic fracture mechanics (LEFM) is used throughout the analysis. It was assumed that for most structural applications, laminates will be designed with a majority of 0° plies such that the overall laminate response will be linear elastic. More generally, the primary loading direction should be parallel to the fibers in the dominant ply in the laminate. Laminate deformation is significantly limited by the fibers whose be-

havior is elastic. Therefore, LEFM should be sufficient to supply a close model for the actual behavior.

LEFM is less desirable for a ply-by-ply analysis which includes off-axis plies. Off-axis plies may not behave elastically. Therefore, the crack growth analysis will be conservative since allowance for plasticity would tend to retard crack growth.

3.6.3.2   Stress Intensity Formulations

Mode I Cracks–This type of crack analysis is limited to net section cracks which propagate from center or edge notches and which eventually lead to catastrophic failure. This behavior has been seen in primarily titanium based alloy composites, such as (B_4C)Boron/Ti-15-3, SCS6/Ti-15-3, and SCS6/Ti-24-11 (Reference 1 and Reference 2).

Center Notches–The basic equation used to define the stress intensity for crack growth analysis is

$$\Delta K = \Delta \sigma \sqrt{\pi a} \beta \qquad [77]$$

where σ is the applied stress, "a" is the half crack length, and "β" is a geometry factor. The β factor is calculated for a net section crack growing from an elliptical opening. This allows for a generic model to predict stress intensity for specimens with circular holes as well as narrow holes approximating center cracks. The β factor for this analysis was originally derived (Reference 2) as

$$\beta = \left[1 + 0.12 \ (-4.4249s^2 + 3.4249s + 1.0) \ K_t \right] \qquad [78]$$

where $s = a/(a+c)$ and c is the radius of elliptical notch parallel to the crack. K_t is the stress concentration factor at the notch edge and is calculated using the stress analysis discussed in Section 3.4.1.3.1. For isotropic plates, this expression for β matches that for cracks growing from a circular notch in finite width plates (Reference 10). However, upon further evaluation it was found that this expression provides grossly large estimates of the stress intensity for noncircular notches.

An alternate method to determine the geometry factor, β, was developed by developing an expression to fit the geometry factor shown in Figure 15 (Reference 10) for a crack growing from an elliptical hole in a finite width plate. The form of this expression is:

$$\beta = F\left(\frac{d}{c}, \frac{c}{b}, \frac{a+c}{b}\right) = \frac{1}{\sqrt{1 - \frac{(a+c)}{b}}} \left(\frac{0.826}{\sqrt{1 - \frac{c}{b}}} - \frac{c}{2.5\,b} + \frac{c}{3\,b} \left(\frac{a}{b}\right)^{(-0.45 - \frac{1.1}{e^{\frac{d}{c}} + e^{-\frac{d}{c}}})} \right) \qquad [79]$$

The graph contains the following labels and equations:

$K_I = \sigma\sqrt{\pi a} \times F\left(\dfrac{d}{c}, \dfrac{c}{b}, \dfrac{L}{b}\right)$

Y-axis: $\sqrt{1-\dfrac{L}{b}} \times F\left(\dfrac{d}{c}, \dfrac{c}{b}, \dfrac{L}{b}\right)$

$\sqrt{1-\dfrac{L}{b}} \times F\left(\dfrac{d}{c}, \dfrac{c}{b}, \dfrac{L}{b}\right)$

d/c = 0, 1/4, 1/3, 1/2, d/c = 1, 2, ∞

c/b = 0.1, 0.2, 0.25, 0.4, 0.5, c/b = 0.6

1.122

(No Hole)

X-axis: $\rightarrow \dfrac{L}{b} = \dfrac{a+c}{b}$

Method: Estimated by Interpolation
Accuracy: Better Than 5% for Any d/c, c/b and L/b
Reference: Tada 1973
Note: For c/b<<1, See Page 19.8

CC34-0134-2-V/des
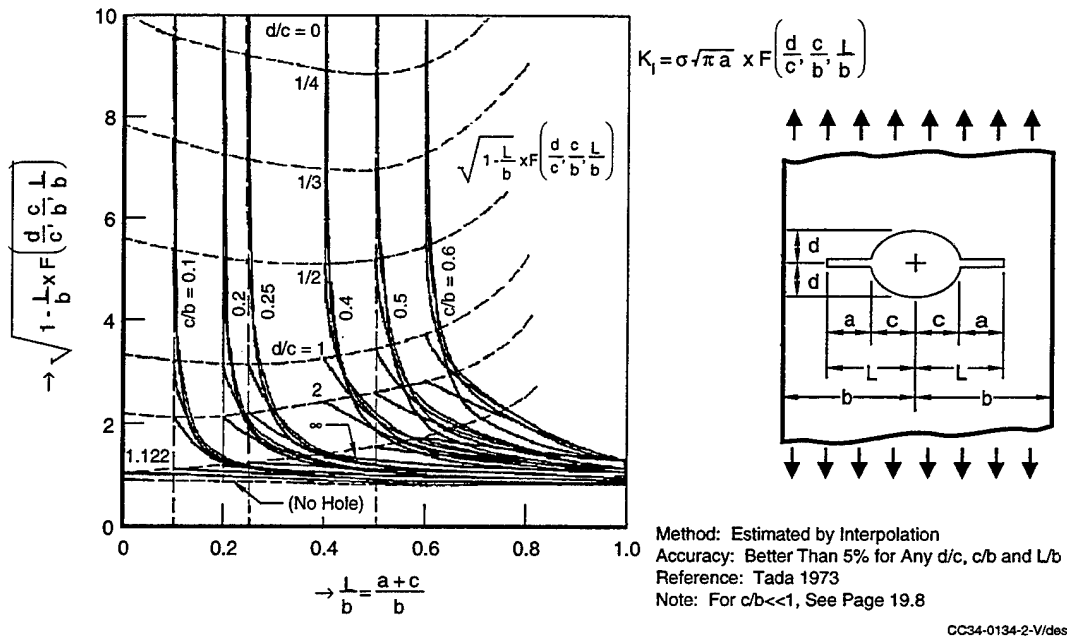
Figure 15. Geometry factors for a crack growing from an elliptical notch in a finite width panel.
(Tada, Paris, Irwin, 1985).

In this expression, a is the crack length, β is the half width of the specimen, and c and d are the major and minor notch diameters. As shown in Figure 16, this expression provides a family of curves which are similar in form and magnitude to those in Figure 15. A more accurate estimate was developed using neural network software. A neural network is useful for linear and nonlinear data modeling and is especially adept at providing algorithms for pattern matching trends in multiple sets of data. The algorithms developed by the neural net software is programmed in the MMCLIFE V3.0 code.

In the limiting case of a crack growing from a center slot a more accurate expression for β (Reference 10) is used:

$$\beta = \sqrt{\sec\left(\pi a / b\right)} \qquad [80]$$

This expression is accurate for isotropic materials to within 0.3% for 2a/b less than or equal to 0.7.

Edge Notches–The crack growth analysis includes stress intensity solutions for cracks growing from edge notches and slots. These solutions are based on those in Reference 10

54

$$\sqrt{1-\frac{a+c}{b}}\,\beta = \frac{0.826}{\sqrt{1-c/b}} - \frac{c}{2.5b} + \frac{c}{3b}\left(\frac{a}{b}\right)^{-0.45-\frac{1.1}{e^{\frac{dc}{}}+e^{-\frac{dc}{}}}}$$
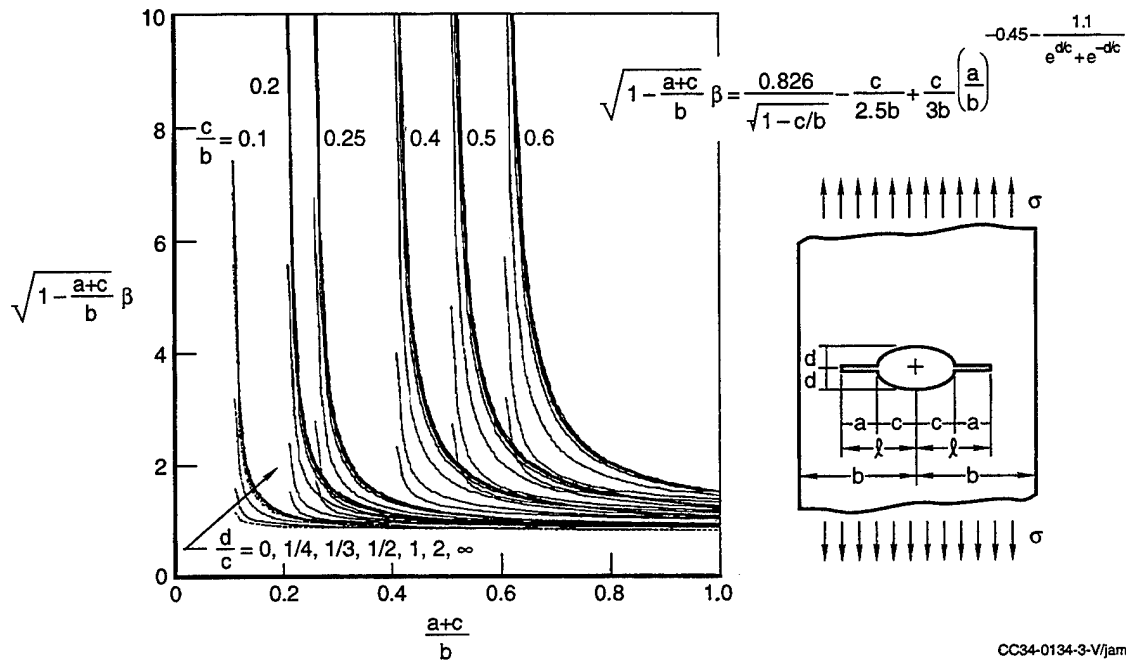
Figure 16. An expression was developed to approximate the form of the curves generated by Tada, Paris, Irwin, 1985.

for isotropic materials. The basic form of the stress intensity solution is the same as for the center notch:

$$\Delta K = \Delta\sigma\sqrt{\pi a}\,\beta \qquad\qquad [81]$$

As before, it is the geometry factor, β, which changes. The solution for the edge notch is shown in Figure 17. This solution is accurate within 2%. An expression was developed to approximate these curves. Using the same nomenclature as in Figure 17 this expression is:

$$\beta = F(s,\frac{d}{c}) = \frac{1.122}{s^{\left(\frac{-\log(1/K_t)}{2}\right)}} \qquad\qquad [82]$$

$$K_t = (1+2\frac{c}{d})(1+0.122\left(\frac{1}{1+d/c}\right)^{5/2}) \qquad\qquad [83]$$
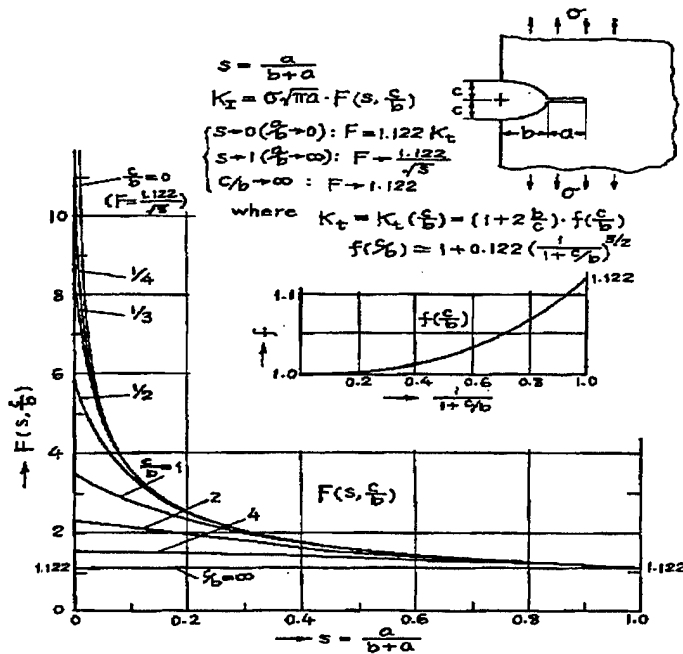
55

Figure 17. Geometry factors for a crack growing from an elliptical notch in an edge notched panel (Tada, Paris, Irwin, 1985).

In the limiting case of a crack growing from an edge slot a more accurate expression for β (Reference 10) is used:

$$\beta = \sqrt{\frac{2b}{\pi a}\tan\left(\frac{\pi a}{2b}\right)}\left(\frac{0.752 + 2.02(a/b) + 0.37\left(1-\sin\left(\frac{\pi a}{2b}\right)\right)^3}{\cos\left(\frac{\pi a}{2b}\right)}\right) \qquad [84]$$

This expression is accurate for isotropic materials to within 0.5% for any a/b.

Once ΔK is calculated for the lamina, the crack growth rate is determined using the crack growth data supplied for the lamina. This can be specifically either lamina data or matrix data. If only matrix data are available the lamina ΔK may be modified. This can be done by multiplying by the ratio of matrix stiffness to transverse lamina stiffness.

$$\Delta K_{matrix} = \Delta K \frac{E_m}{E_x}, f = \frac{E_m}{E_x} \qquad [85]$$

56

where E_m is the matrix modulus and E_x is the lamina transverse modulus. However, since there are many different opinions on how this conversion should be done, the analysis in MMCLIFE V3.0 includes a user supplied multiplication factor, f, which is used to modify ΔK.

Using the crack growth data from this contract, a correlation study was performed to determine the accuracy of the analysis. For this study, only matrix crack growth data were available to define crack growth rates. Therefore the lamina stress intensity factor was multiplied by a factor to obtain a matrix stress intensity value. The results of this study are summarized in Table 3, Figure 18 and Figure 19. In Table 3 each specimen is listed along with the stress level at which it was tested, the stress ratio, specimen width, initial crack length, and final steady-state crack length and life. Three sets of predictions were performed using the MMCLIFE V3.0 code. The first is a prediction of the life required to match the measured steady-state final crack length given a ΔK multiplication factor. Conversely, the second column is a prediction of the steady-state final crack length achieved after the measured number of cycles given a ΔK multiplication factor. These first two sets of predictions are plotted in Figure 18 and Figure 19. The final prediction is the ΔK multiplication factor required to match both of the measured final crack length and life.

The predicted crack growth shown in Figure 18 and Figure 19 are from the calculated average multiplication factor "f". Hence the good agreement of actual vs. predicted values in Figure 18 and Figure 19. The actual value for the multiplication factor is 0.45 for room temperature and 0.38 for 1200°C (650°F), as calculated using expression [85]. Much lower than the values needed to predict the crack growth behavior for the transverse specimens. As observed by the difference in these values, a relationship more in tune with composite behavior may have to be developed in future programs.

These plots indicate that a ΔK multiplication factor of approximately 1.18 provides good correlation for the room temperature data. This ignores specimen 2A/90B11 which fails after 2 cycles. At 1200°F, however, the required factor is approximately 1.5.

Mode II Cracks–Cracks which grow parallel to the fibers in longitudinally loaded 0° laminates are considered Mode II cracks. These cracks grow due to in-plane shear loads. These cracks have been observed in room temperature tests of Boron/Aluminum and in elevated temperature tests of SCS6/Ti-15-3. If the loading remains uniaxial, this mode of cracking is not catastrophic. Instead these cracks will continue to grow along the fiber and therefore, relieve the stress concentration at the notch edge. If biaxial loads are introduced then a Mode I crack driving mechanism will result in specimen failure.

Table 3.   Isothermal crack growth data and predictions for 90° specimens.

SCS6/Ti-24-11 90°C Crack Growth Data								MMCLIFE V3.0 f = 1.1809(27°C) f = 0.3384(550°C) f = 1.4757 (649°C)		
Spec ID	Temp °C	σ MPa	R	width cm	a0 cm	Nf-1 cycles	af-1 cm	Nf-1 cycles	af-1 cm	f
2A/90A11	27	138	0.10	1.2708	0.1265	359	0.1364	537	0.1323	1.289
2A/90A12	27	138	0.10	1.2713	0.1270	1166	0.1372	580	0.1506	1.035
2A/90B11	27	103	0.10	1.2692	0.2497	2	0.3614	1264	0.2499	3.5156
2A/90B12	27	103	0.50	1.2700	0.2522	219	0.2606	541	0.2555	1.3973
2A/90D21	27	83	0.10	1.2692	0.1356	17536	0.1671	17536	0.1671	1.1809
		69	0.10		0.1671	57865	0.1819	30436	0.2441	0.9521
		55	0.10		0.1819	496313	0.1905	77265	1.2692	0.6927
		90	0.10		0.1905	496836	0.1986	497501	0.1938	1.3781
		97	0.10		0.1986	497069	0.2703	500484	0.2012	4.1650
2A/90E21	550	34	0.10	1.2700	0.2286	166840	0.7239	166720	0.7244	0.3384
2A/90E11	649	34	0.10	1.2700	0.2629	3830	0.8674	3828	0.8674	1.4757
2A/90E12	649	34	0.10	1.2700	0.1552	1426	0.1996	2496	0.1783	1.8778
					0.1996	1460	0.2250	2478	0.2004	6.2734
					0.2250	8692	0.2758	3030	1.2700	0.7649
					0.2758	8803	0.3330	9878	0.2804	4.0586
					0.3330	35325	0.8791	11099	1.2700	0.5144

A weight function approach was used to compute the stress intensity factors for the Mode II cracks in a 0° ply. According to the weight function approach, the stress intensity factor for any given stress distribution acting in the plane of a crack can be determined from the following equation:

$$K = \int_0^a f(x)\, g(x,a)\, dx \tag{86}$$

where $f(x)$ is the shear stress along the crack plane without the presence of the crack and $g(x,a)$ is the weight function.

The shear stress distribution along the unnotched fibers adjacent to the notch was determined from a boundary collocation analysis (Figure 20). There was very little difference in this distribution for aluminum matrix composite versus titanium matrix composite. The weight function was taken from a point load stress intensity solution for a crack subjected to in-plane shear (Reference 11). This function is given by

$$g(x,a) = \frac{2}{\sqrt{\pi a [1 - \left(\dfrac{x}{a}\right)^2]}} \tag{87}$$
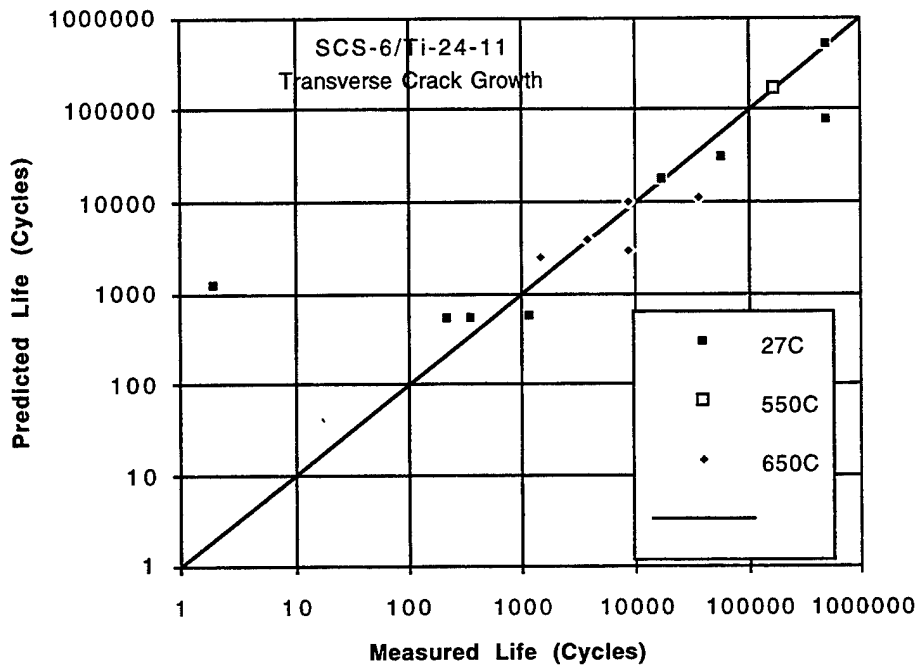
Figure 18. Crack growth analysis provided conservative results for 90° specimens (life).
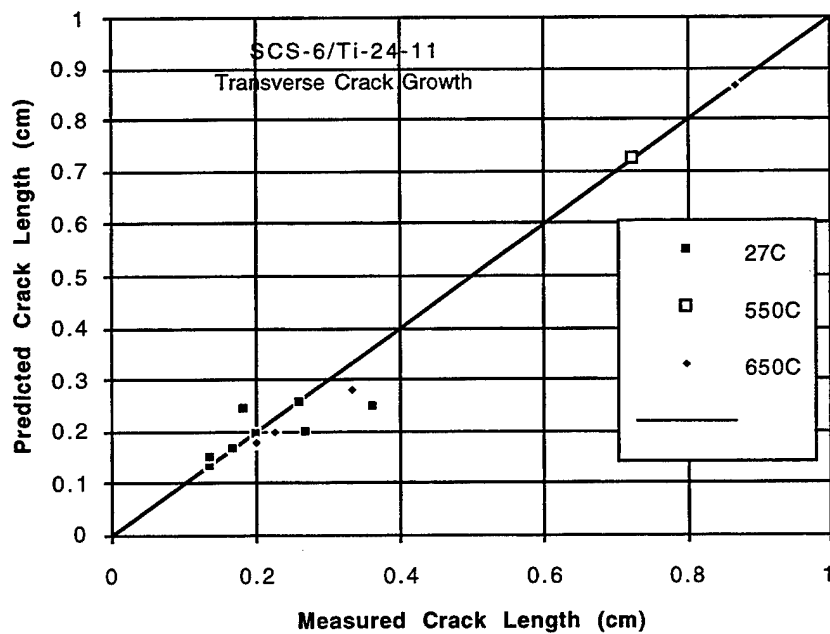
Figure 19. Crack growth analysis for 90° SCS6/Ti-24-11 specimens (crack length).

59
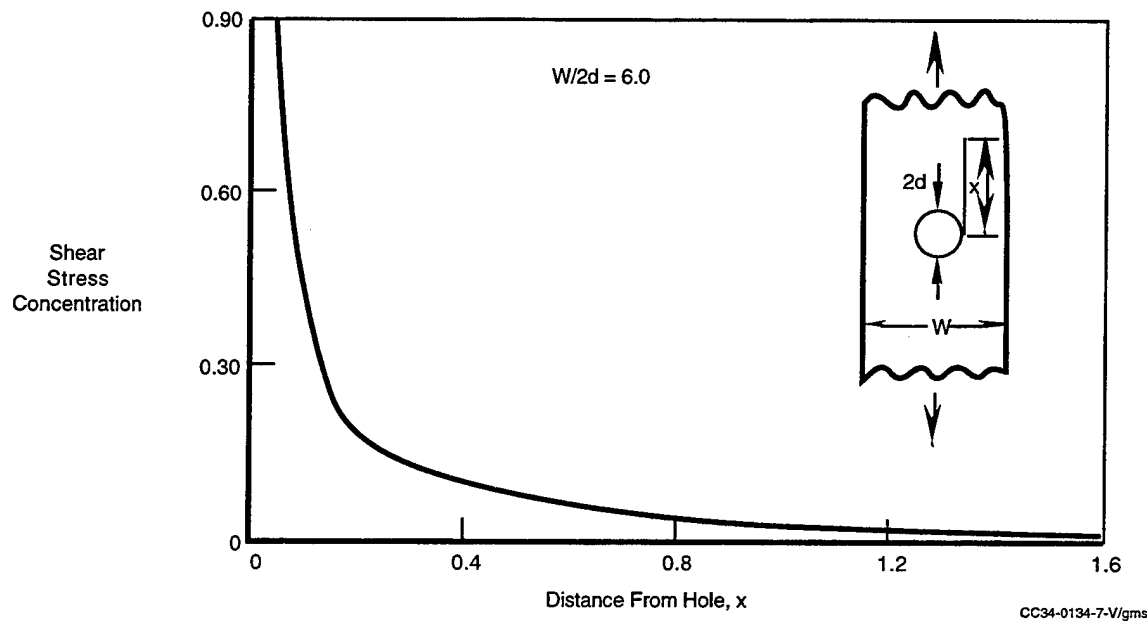
Figure 20. Shear stress distribution along fiber is nearly identical for both B/Al and SCS6/Ti Unidirectional composites.

The β factor for use in the standard stress intensity formulation can be calculated as follows:

$$\beta = \frac{\int_0^a f(x)\ g(x,a)\ dx}{\sigma\sqrt{\pi a}} \tag{88}$$

This expression was evaluated for a center hole coupon (W/2d=6.0). The curve fit for this expression is

$$\beta = \frac{1.0}{(1.2175 + 11.159\ a)} \tag{89}$$

The stress intensity factor for a flaw growing in the matrix between fibers, driven primarily by shear is almost constant with crack length (Reference 11), rather than increasing as the square root of crack length as normally occurs in tension cracking cases. This constant stress intensity factor results in nearly constant crack growth rates in boron/aluminum in which the flaw grows along the unnotched fibers (Figure 21). The crack growth rate decreases as the crack approaches the grip area, where the shear stress falls off. Similar behavior was observed in SCS6/Ti-15-3 at 538°C (1000°F) (Figure 22).

60
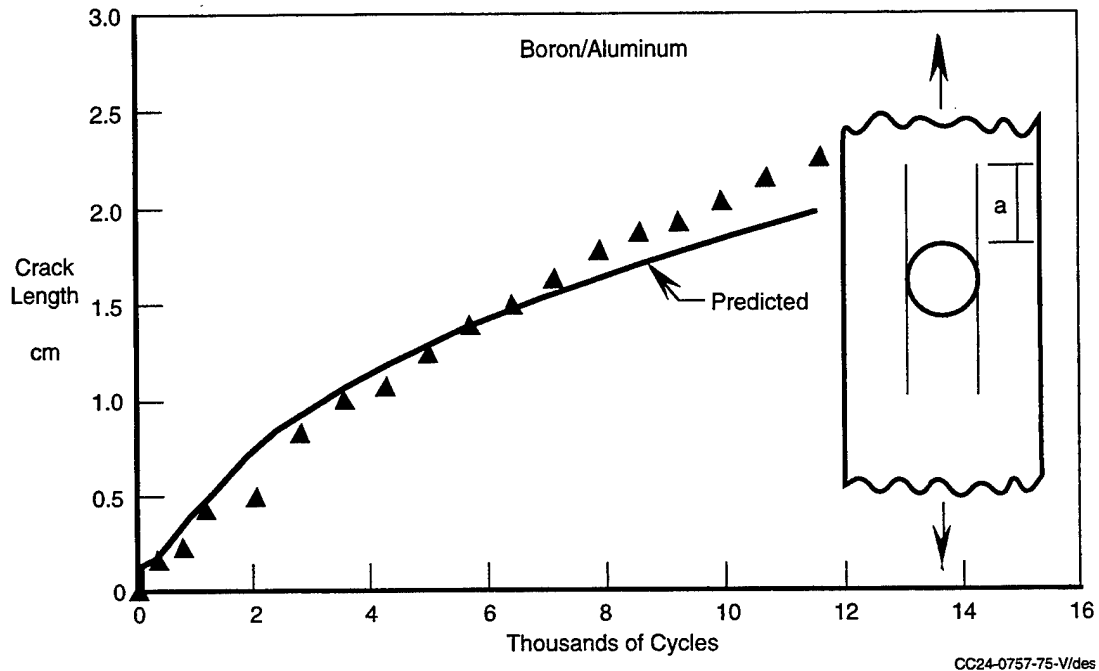
Figure 21. A crack growing parallel to load and fiber direction is predicted in a unidirectional B/Al coupon.
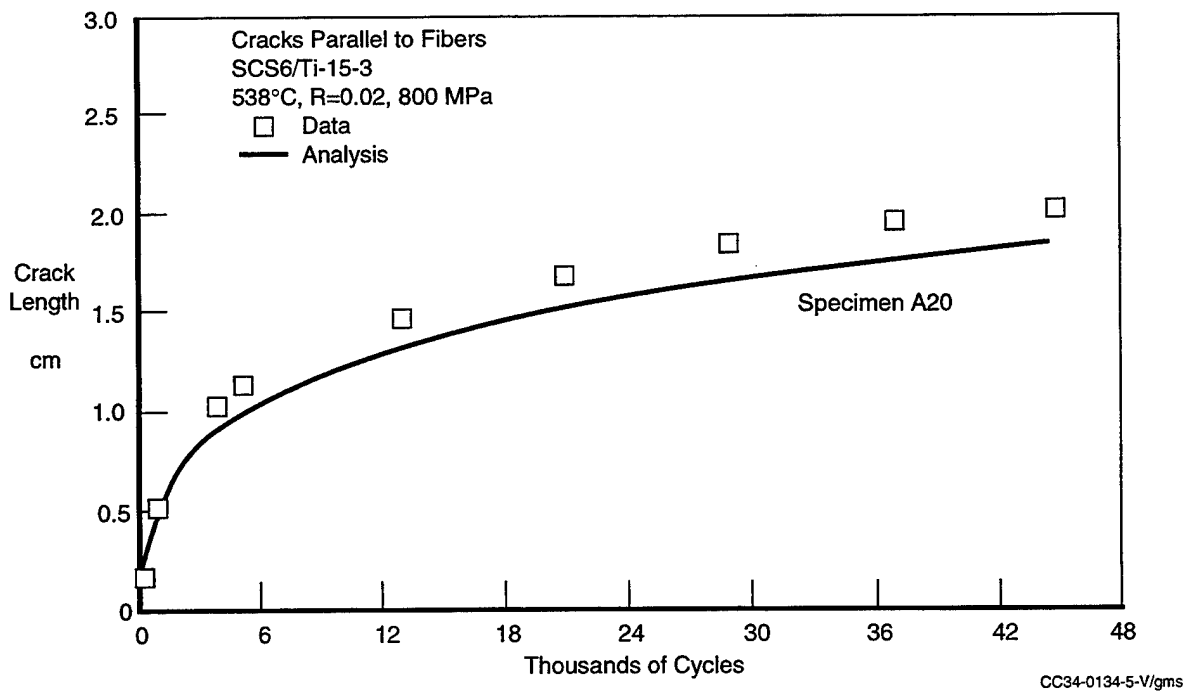
Figure 22. Crack growth parallel to load in SCS6/Ti at 538°C (1000°F).

Mixed Mode Cracks–Cracks which grow parallel to the fibers in off-axis plies are considered mixed-mode cracks. In this case, the stress state in the vicinity of the crack is broken down into normal and shear components using a Mohr's circle analysis. The normal and shear stresses are used to calculate Mode I and Mode II stress intensities.

$$K_I = \sigma\sqrt{\pi a}\beta \qquad K_{II} = \tau\sqrt{\pi a}\beta \tag{90}$$

The β factor for both of these equations is identical to that discussed for the Mode I cracks.

An effective stress intensity expression, K_{eff} is found by combining the Mode I and Mode II stress intensities in a way, so as to collapse the crack growth rates from different off-axis plies in to one curve. A strain energy density approach developed in Reference 12 resulted in the following expression:

$$\Delta K_{eff} = \sqrt{a_{11}\Delta K_I^2 + a_{12}\Delta K_I \Delta K_{II} + a_{22}\Delta K_{II}^2} \tag{91}$$

The terms a_{11}, a_{12}, and a_{22}, are constants determined empirically. The center term is used to describe non-self-similar crack growth. In the case of unidirectional MMC's, crack growth is assumed to be along the same path throughout the life of the laminate (i.e. self-similar) and, therefore a_{12} is zero. This assumption has proven valid for isothermal testing.

Assuming $a_{11}=a_{22}=1$, then the effective ΔK for the analysis is expressed as

$$\Delta K_{eff} = \sqrt{\Delta K_I^2 + \Delta K_{II}^2} \tag{92}$$

This expression has worked very well in collapsing 15 degree and 90° lamina crack growth versus stress intensity data for SCS6/Ti-15-3 (Figure 23).
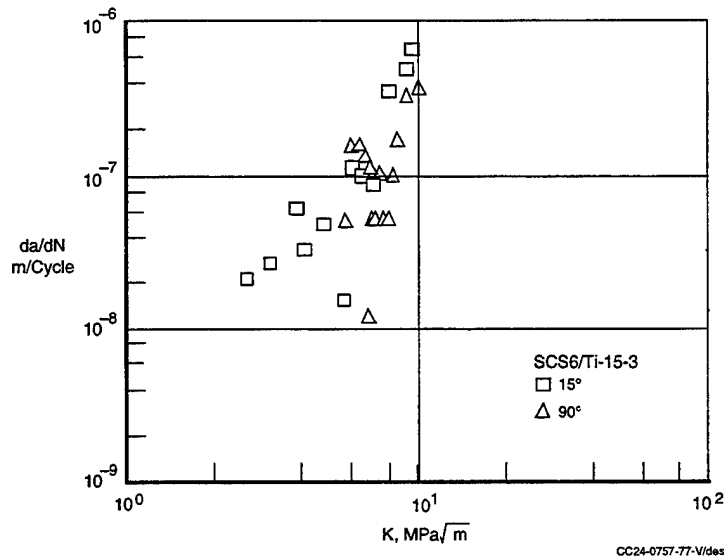
Figure 23. Effective stress intensity formulation was created to collapse crack growth rate data from off-axis specimens.

3.6.3.3   Effect of Fiber Bridging on Stress Intensity

Crack bridging is a mode of crack growth in which cracks propagate through the matrix material without failing fibers. The fibers bridge the crack and help reduce the crack tip stress intensity. As the cracks grow more load is shed from the matrix into the bridging fibers. When subject to constant amplitude cyclic mechanical loading this results in a decelerating crack tip. As load is shed to the fibers, the fiber stress increases. Once the stress approaches the fiber ultimate strength, fibers begin to fail. At this point, the load carried by these fibers is transferred to surrounding fibers and they also begin to fail. Therefore, once fiber failure begins to occur the remaining life of the specimen is relatively short. SCS6/Ti-24-11 was found to exhibit this type of bridging crack growth behavior.

Researchers at RISC and the University of California-Santa Barbara (UCSB) have developed detailed methods of predicting the crack tip stress intensity for cracks bridged by fibers. These methods model the fibers that bridge the cracks as closure tractions which act on the crack surfaces. The crack tip stress intensity is computed by subtracting the stress intensity due to the closure forces from that due to the applied loading. The key to this analysis is determining the stress in the bridging fibers as a function of position in the wake of the crack tip, $\sigma_s(x)$. This is done by equating the total crack open-

ing displacement to that due to the applied loading plus that due to the bridging fibers (Reference 2). This results in the following integral expression:

$$\frac{D(1-V_f)E_m(\sigma_s(x))^2}{4EE_f\tau V_f^2} = \frac{4(1-\nu^2)}{E}\left[\sigma\sqrt{a^2-x^2} - \int_0^a \sigma_s(\hat{x})H(\hat{x},x,a)d\hat{x}\right]$$ [93]

where

$$H(\hat{x},x,a) = \frac{1}{\pi}\log\left|\frac{\sqrt{a^2-x^2}+\sqrt{a^2-\hat{x}^2}}{\sqrt{a^2-x^2}-\sqrt{a^2-\hat{x}^2}}\right|$$ [94]

and where D is the fiber diameter, V_f is the fiber volume fraction, a is the crack length, ν is Poisson's Ratio, σ is the applied stress, E_m is the matrix modulus, E_f is the fiber modulus, E is the composite modulus, and E_t is a modulus that can be either E_m or E depending on the area of the matrix crack compared with the fiber spacing.

The solution to the integral equation is complicated and too cumbersome to be used in a design tool such as that being developed under this contract. However, by appropriately nondimensionalizing the expression, researchers at UCSB and RISC have produced series of plots which define the fiber bridging stress and the crack tip stress intensity (Reference 13 through Reference 17). Relationships which curve fit these plots also have been developed. These allow for easy translation into a design tool. This stress intensity can be used with appropriate crack growth rate data to predict crack growth.

Bridged matrix cracks were included into the MMCLIFE V3.0 code by incorporating the canonical functions for the crack tip stress intensity derived by Cox and Lo (Reference 13). These expressions are functions of the constituent moduli, fiber volume fraction, fiber radius, and the fiber/matrix interface shear stress.

Using the crack growth data from this contract, a correlation study was performed to determine the accuracy of the bridging analysis. The results of this study are summarized in Table 4 and Figure 24 through Figure 25. In Table 4 each specimen is listed along with the stress level at which it was tested, the stress ratio, specimen width, initial crack length, and final steady-state crack length and life. Three sets of predictions were performed using the MMCLIFE V3.0 code. The first is a prediction of the life required to match the measured steady-state final crack length given an interface shear stress. Conversely, the second column is a prediction of the steady-state final crack

Table 4. Isothermal crack growth data and predictions for 0° specimens.

							MMCLIFE V3.0 Predictions						
							w/o residual stresses			with residual stresses			
SCS6/Ti-14-21 0° Crack Growth Data (R=0.1)							τ = 7.585 MPa (27°C) τ = 3.448 MPa (550°C) τ = 3.448 MPa (649°C)			τ = 10.274 MPa (27°C) τ = 3.654 MPa (550°C) τ = 3.448 MPa (649°C)			
Spec ID	Temp °C	σ MPa	width cm	a0 cm	Nf-1 cycles	af-1 cm	Nf-1 cycles	af-1 cm	τ MPa	Nf-1 cycles	af-1 cm	τ MPa	Comments
2A/0C11	27	690	1.1339	0.0262	765780	0.1397	668500	0.1473	7.929	756800	0.1397	10.274	
2A/0D21	27	690	1.1323	0.0175	480544	0.1069	381100	0.1194	8.205	416800	0.1143	10.756	hold times
2A/0G11	27	690	1.1372	0.0277	865144	0.6495	20497000	0.1549	3.034	infinite	0.1473	3.861	
2B/0B11	27	690	1.1285	0.0183	1155361	0.3010	4430000	0.1727	5.102	5680000	0.1651	6.619	
2A/0F12	27	690	1.1344	0.0231	357597	0.2700	3388000	0.1067	3.861	4008000	0.1016	5.033	pre-exposed
2A/0F11	27	827	1.1478	0.0140	104394	0.0752	44200	0.1194	9.998	51100	0.1067	12.963	
2A/0B22	27	690	1.0188	0.0269	50850	0.0716	153200	0.0457	5.171	162800	0.0457	6.964	
		827		0.0716	57817	0.0831	63950	0.0787	5.171	67300	0.0762	7.791	
		965		0.0831	100313	0.2484	206517	0.1600	5.171	277817	0.1422	6.274	
2B/0A12	27	690	1.1303	0.0165	465485	0.2789	3691500	0.1168	4.068	4504000	0.1118	5.309	pre-exposed
		965		0.2789	495094	0.2954	28800	0.4978	17.238	43400	0.2896	9.170	pre-exposed
2A/0B13	27	1172	1.0109	0.0434	693	0.0607	800	0.0584	7.585	1088	0.0533	8.757	
2A/0B21	27	1172	1.0112	0.0480	7743	0.0960	2850	0.1422	10.687	4192	0.1194	12.480	
S/0A14	550	827	1.1433	0.0203	13110	0.0572	2903	0.1397	11.239	2870	0.1422	12.066	
2A/0D12	550	1034	1.1476	0.0229	1995	0.0724	2020	0.0721	3.448	1990	0.0724	3.654	
2A/0A22	649	690	1.1478	0.0330	34698	0.1130	35000	0.1118	3.448	35000	0.1118	3.448	
2A/0D22	649	690	1.1478	0.0356	34302	0.1016	27700	0.1118	3.999	27700	0.1118	3.999	
2A/0F13	649	690	1.1486	0.0292	26566	0.1397	53440	0.0965	2.137	53440	0.0965	2.137	hold times
S/0A13	649	690	1.2057	0.1651	160	0.1842	15600	0.1651	0.159	15600	0.1651	0.159	
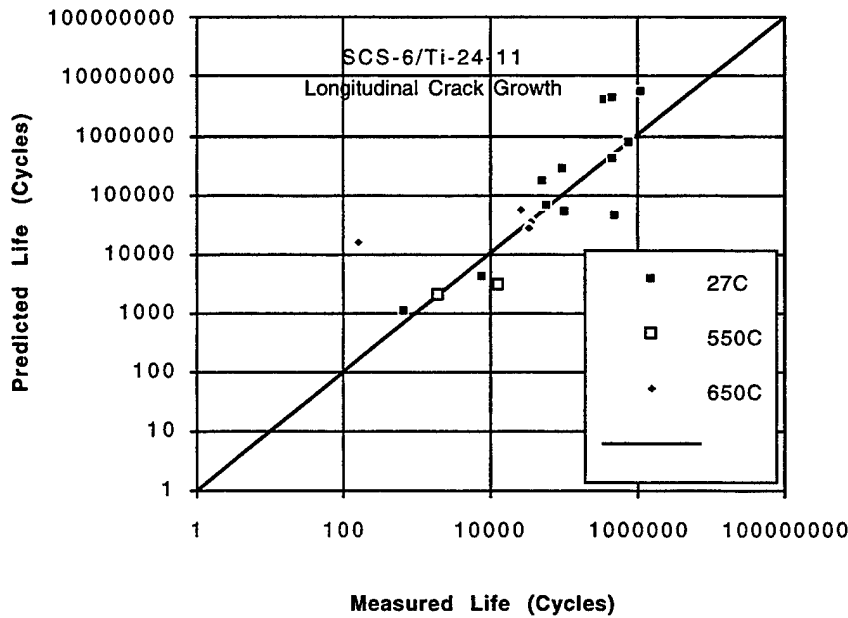
Figure 24. Crack growth analysis results for 0° specimens (life).
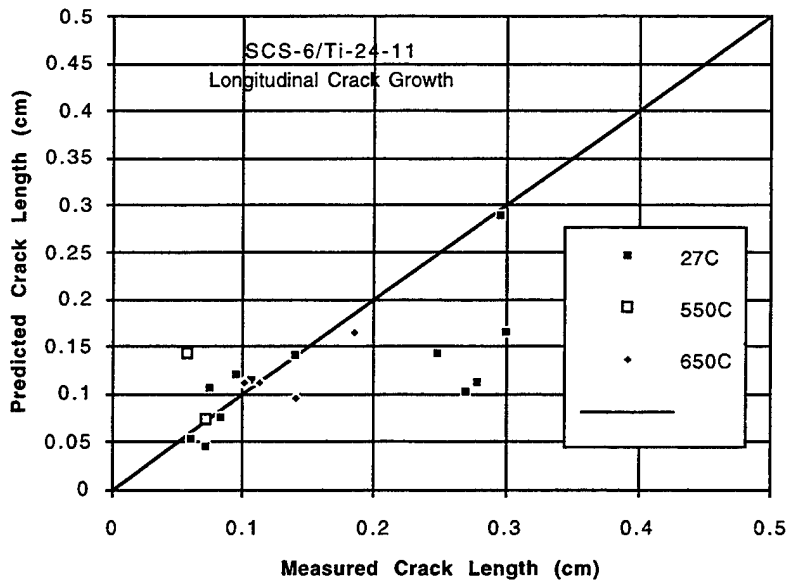
Figure 25. Crack growth analysis results for 0° specimens (crack length).

length achieved after the measured number of cycles given an interface shear stress. These first two sets of predictions are plotted in Figure 24 and Figure 25. The final prediction is the interface shear stress required to match both of the measured final crack length and life. The analysis was conducted with and without the effects of residual stresses for comparison.

Examination Table 4 reveals a large variation in the value of τ that must be input in order to predict the total life of the crack growth specimens. Also, with a fixed value of τ, the growth rate curves predicted vs. actual, Figure 25, produced a great deal of scatter. The reason for this is not well understood but likely include a variation in τ associated with interface damage incurred during cyclic loading and some errors in the assumptions surrounding the initial crack or notch geometry.

There is an inherent uncertainty associated with the assumption of a fully bridged initial crack in the specimens as prepared. After precracking, the initial notch was removed by machining the specimen edge until only the fatigue precrack remained. It was assumed in the analysis that this precrack behaved as one that was fully bridged. However, the machining operation did, in fact, cause damage to some of the fibers exposed at the edge of the specimen. The extent of the damage is not quantified but, since the fatigue precrack is short, a few fibers in the 8 layers are very likely to have been damaged, the effective notch conditions may not be those of a fully bridged crack. The uncertainty and variability of this situation may have contributed to an

apparent variation in the curve fitting parameter, τ, assigned to the interfacial shear or sliding friction strength term in Table 4.

These plots indicate that a shear interface stress of approximately 10.3 MPa (1.5 ksi) provides good correlation for the room temperature data. At elevated temperatures, however, the required interface stress is approximately 65% less. Figure 26 through Figure 33 plot the crack growth data against predictions made at different interface shear stresses for specific specimens.

The work discussed above does include effects due to residual stresses in the lamina due to thermal expansion mismatch between the fiber and matrix. The bridged crack tip stress intensity can be modified to account for this behavior by relating the lamina stress intensity to a matrix stress intensity. The integral equation discussed previously was solved for the bridging stress $\sigma_s(x)$ using an iterative procedure. The bridging stress acts like traction stresses applied to the crack surface. The associated stress intensity (ΔK_f) is found using a standard solution for traction stresses:

$$\Delta K_f = -2\sqrt{\frac{a}{\pi}} \int_{a_0}^{a} \frac{\Delta\sigma_s(x)}{\sqrt{a^2 - x^2}} dx \qquad [95]$$

The laminar effective stress intensity $\left(\Delta K_{lam\,eff}\right)$ is simply the sum of the applied stress intensity $\left(\Delta K_a\right)$ and the bridged stress intensity.

$$\Delta K_{lam\,eff} = \Delta K_a + \Delta K_f \qquad [96]$$

where:

$$\Delta K_a = \Delta\sigma_{app}\sqrt{\pi a} \qquad [97]$$

Where $\Delta\sigma_{app}$ is the change in lamina applied stress, and a is the crack length.

The effective matrix stress intensity can be calculated from the effective laminar stress intensity. The state of stress in the matrix due to consolidation and loading can be

67
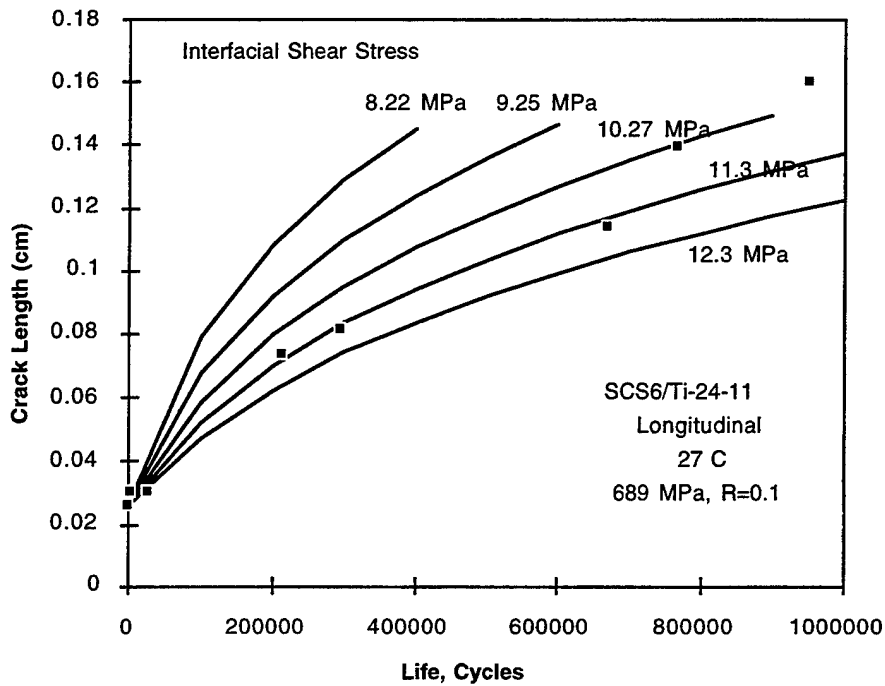
Figure 26. Crack growth data vs. predictions for specimen 2A/0C11. Max stress, R
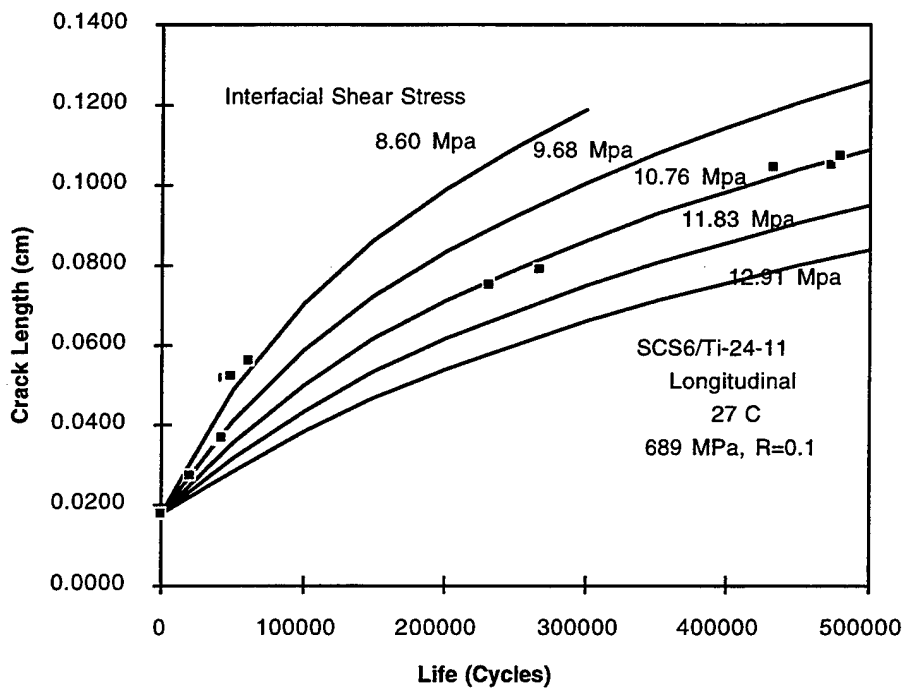
Figure 27. Crack growth data vs. predictions for specimen 2A/0D21. Max stress, R
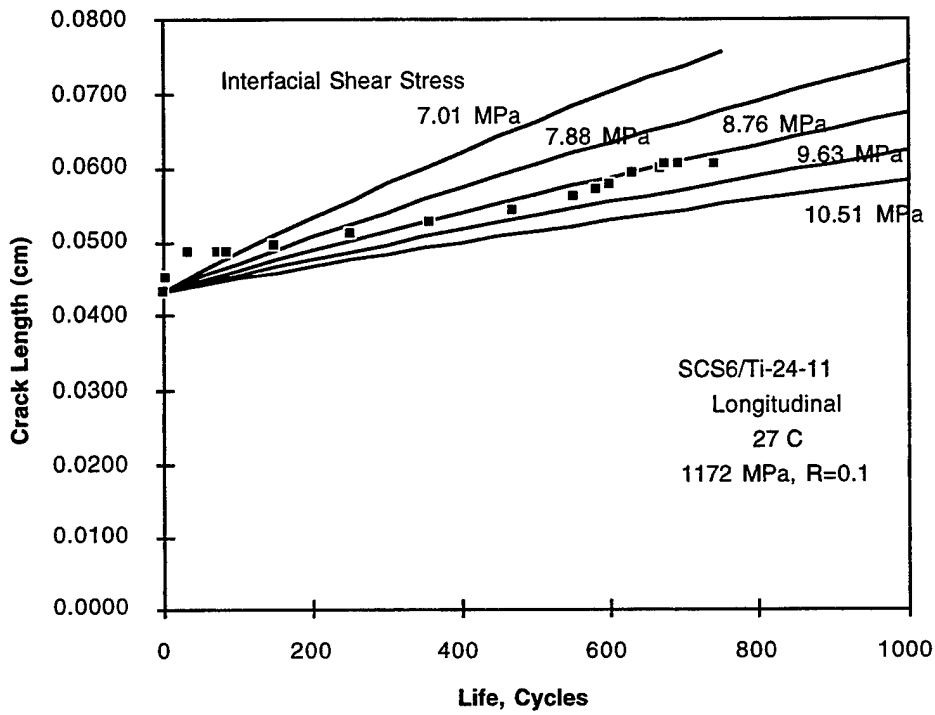
Figure 28. Crack growth data vs. predictions for specimen 2A/0B13.
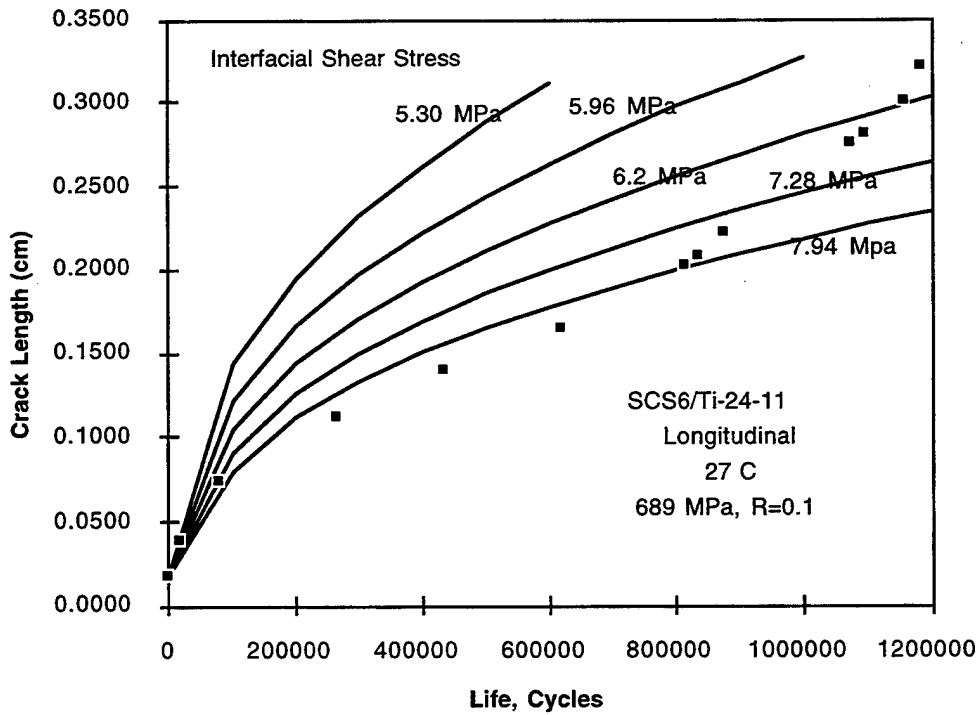
Figure 29. Crack growth data vs. predictions for specimen 2B/0B11.
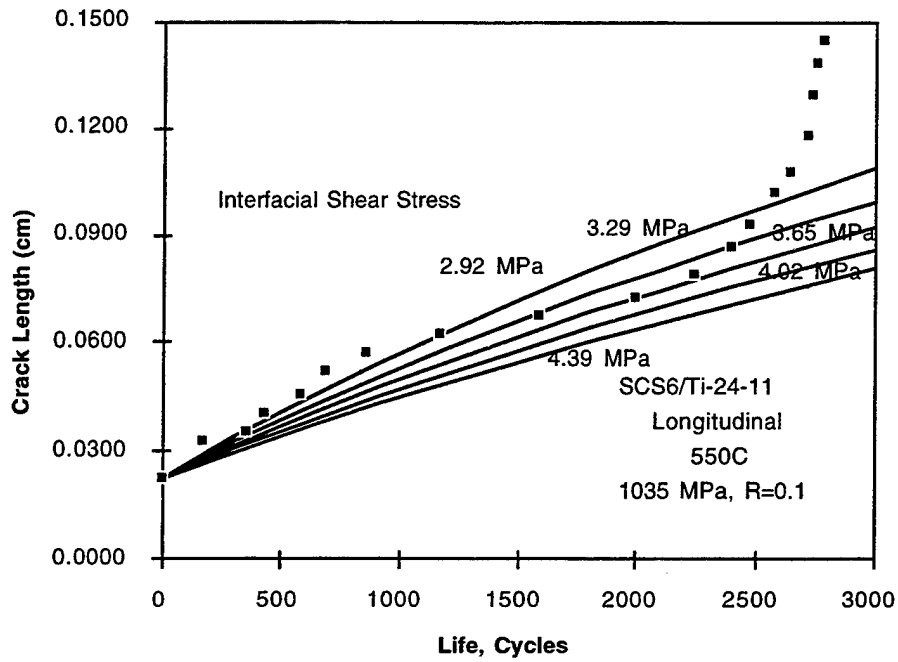
Figure 30. Crack growth data vs. predictions for specimen 2A/0B12.
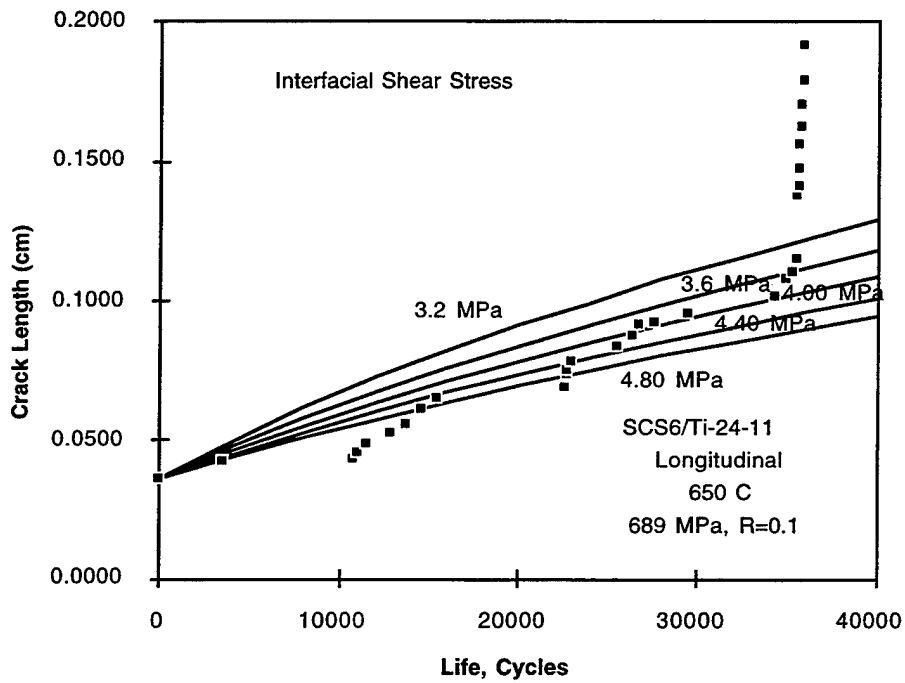
Figure 31. Crack growth data vs. predictions for specimen 2A/0D22.

70
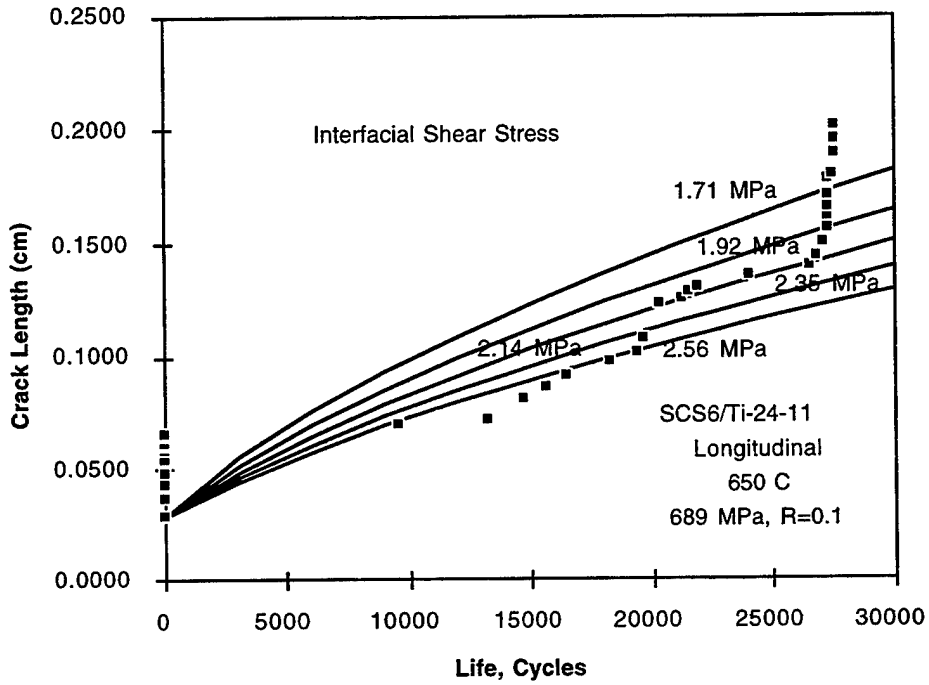
Figure 32. Crack growth data vs. predictions for specimen 2A/0F13.
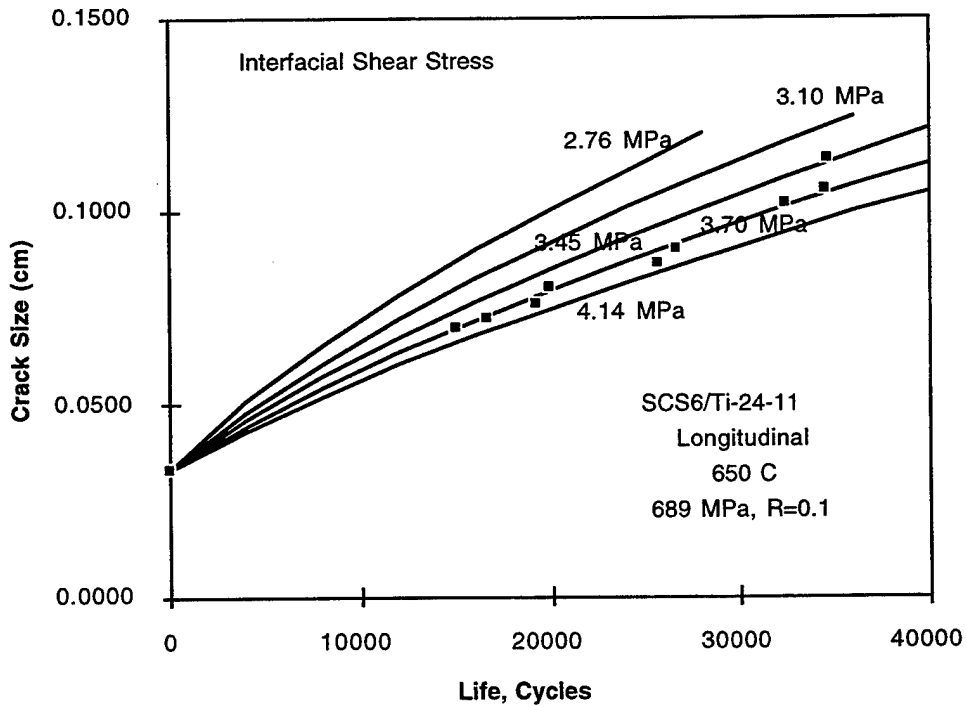
Figure 33. Crack growth data vs. predicitons for specimen 2A/0A22.

71

determined. The longitudinal thermal expansion mismatch stress in the matrix $\left(\sigma_{11\,res}\right)$ is:

$$\sigma_{11\,res} = \left(\alpha_m - \alpha_1\right)\Delta T_c E_m \qquad [98]$$

where

$$\alpha_1 = \frac{\alpha_f E_f V_f + \alpha_m E_m \left(1 - V_f\right)}{E_m \left(1 - V_f\right) + E_f V_f} \qquad [99]$$

and ΔT_c is the change in temperature from the consolidation temperature, E_f is fiber modulus, E_m is matrix modulus, α_1, α_f and α_m are the laminar longitudinal, fiber, and matrix coefficient of thermal expansion, respectively, and V_f is the fiber volume fraction.

The applied stress, $\left(\Delta\sigma_{app}\right)$, increases the state of stress in the matrix $\left(\Delta\sigma_m\right)$:

$$\Delta\sigma_m = \Delta\sigma_{app}\frac{\left(1 - V_f\right)E_m}{E_f} \qquad [100]$$

where E_1 is the lamina longitudinal modulus. The applied laminar stress cycle causes a gross stress cycle in the matrix:

$$\sigma_{m\,max} = \sigma_{11\,res} + \Delta\sigma_{m\,app\,max} \qquad [101]$$

$$\sigma_{m\,min} = \sigma_{11\,res} + \Delta\sigma_{m\,app\,min} \qquad [102]$$

where $\sigma_{m\,max}$ and $\sigma_{m\,min}$ are the maximum and minimum total stresses (assumed elastic) in the matrix during the applied cycle, and $\Delta\sigma_{m\,app\,max}$ and $\Delta\sigma_{m\,app\,min}$ are the maximum and minimum mechanical contributions to the total stress. The stress ratio (R) is affected by including residual stresses:

$$R = \frac{\sigma_{m\,min}}{\sigma_{m\,max}} \qquad [103]$$

72

and , hence, the total change in stress intensity in the matrix (ΔK_m) is unchanged:

$$\Delta K_m = \Delta K_{lam} \frac{\sigma_{m\,max} - \sigma_{m\,min}}{\sigma_{max\,app} - \sigma_{min\,app}} = \Delta K_{lam\,eff} \qquad [104]$$

where $\sigma_{max\,app}$ and $\sigma_{min\,app}$ are the maximum and minimum laminar applied stresses.

3.6.3.4   Environmental Influence on Damage Growth

The Wei-Landes approach for environmental acceleration of crack growth was incorporated into the damage growth analysis. This method is used to account for the effect of time at load upon crack growth. This approach uses the crack growth rate data for R = 0 tests at high and low frequencies to determine time dependent crack growth rate, da/dt, for a given temperature.

The Wei-Landes method, outlined in equation 105 through equation 107, as applied to elevated temperature crack growth, separates the crack growth due to mechanical load cycling from that due to sustained loads. It is assumed that the total crack growth is the sum of these two terms. Mechanical load crack growth is measured in terms of crack length per cycle, da/dN. Sustained load crack growth is measured in terms of crack length per time, da/dt.

To use the Wei-Landes method, two crack growth curves must be supplied: one obtained from a high frequency test and one from a low frequency test. An optimum curve for the low frequency data would be one which had the same loading speed as the high frequency data, but had a hold time at peak load.

Figure 34 demonstrates how the Wei-Landes model is used to determine da/dt from the differences between high and low frequency crack growth rate data. In this figure, 10 Hz is the high frequency and 0.10 Hz is the low frequency. First, it is assumed that hold time has little or no effect on crack growth rate at the 10 Hz frequency. Thus the difference between crack growth rates for cycles having the 10 second hold times (0.10 Hz) and those having no hold times (10 Hz) is used to determine da/dt for each test temperature. The da/dt versus Kmax curves for each temperature are integrated as a function of stress intensity factor to determine the cracking due to sustained loads during (1) loading, (2) hold at maximum load, and (3) unloading.

$$\frac{da}{dN_s} = \int_{T_s}^{T_f} \frac{da}{dt}(K)\ dt = \int_{T_s}^{T_1} \frac{da}{dt}(K)\ dt + \frac{da}{dt}(K_{max})\ (T_2 - T_1) + \int_{T_2}^{T_f} \frac{da}{dt}(K)\ dt \qquad [105]$$
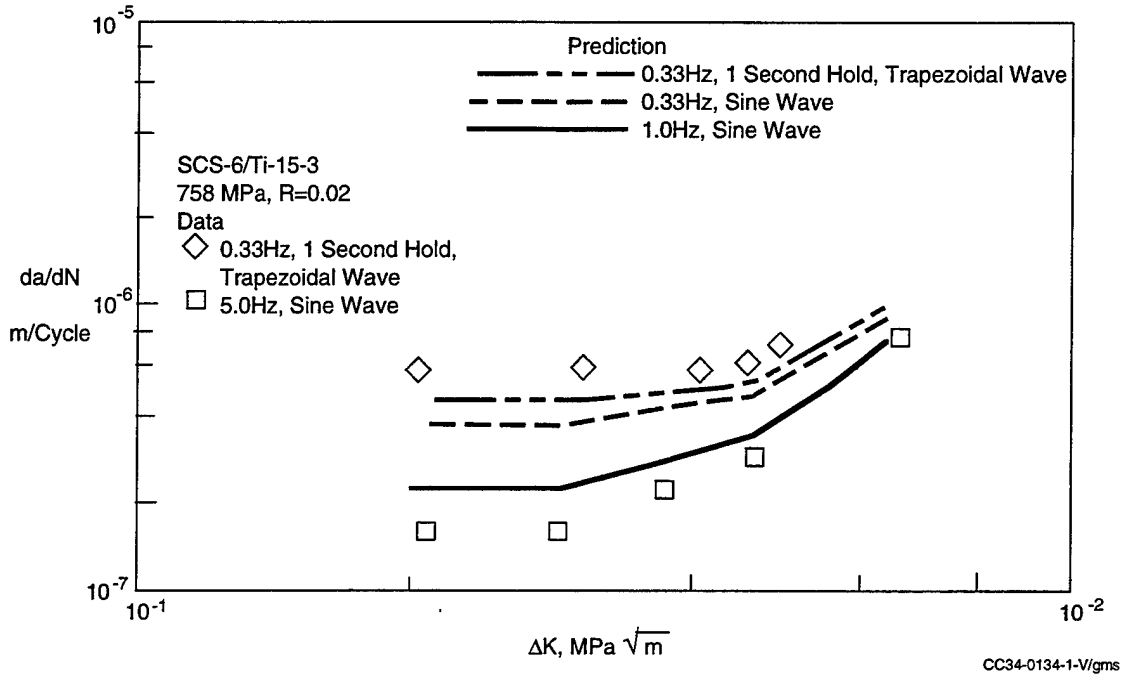
Figure 34. Crack growth acceleration in SCS/Ti due to time dependent effects is predicted using the Wei-Landes method.

The stress intensity, K, is a function of time, t, and T_s and T_f are the cycle start and finish times. The loading and unloading portions of the applied load curve are assumed to be in the form of a sine wave:

$$K(t) = K_{min} + (K_{max} - K_{min})\sin(\pi t) = K_{max}[R + (1.0 - R)\sin(\pi t)] \qquad [106]$$

where R is the stress ratio.

The total crack growth rate is found by summing the cyclic crack growth rate, da/dN_c, and the sustained crack growth rate, da/dN_s.

$$\frac{da}{dN} = \frac{da}{dN_c} + \frac{da}{dN_s} \qquad [107]$$

The cyclic crack growth rate is determined using the methods described in Section 3.6.3.2 for Mode I net section cracks.

3.6.3.5 Failure Criteria

A fracture mechanics approach is used to determine failure in composites which are subject to net section Mode I cracks which fail fibers. A laminate fracture toughness,

K_c, is calculated based on the crack growth data supplied to the analysis. If only matrix data are available, then the laminate stress intensity is converted to a representative matrix value by multiplying by the ratio of matrix to laminate stiffness and compared to the matrix fracture toughness.

If Mode I cracks are bridging the reinforcing fibers, then an alternate failure criteria should be used. Bridged cracks typically have decreasing growth rates due to the increasing bridging effect of the fibers as the matrix crack grows. Therefore, a maximum fracture toughness value may never be obtained. In this case, it is more reasonable to examine the stress in the bridged fibers. As the matrix crack grows the stress in the bridged fibers increases. Once the stress in the fibers near the notch root reaches a critical value, typically determined from strength data, then the fibers will begin to fail. Once fibers begin to fail the remaining life will be short. Recent work by Begley and McMeeking (Reference 18) has defined the stress distribution in the bridged fibers as a function of constituent properties, specimen geometry, and crack length. This work was provided in a FORTRAN subroutine which was then included into the MMCLIFE V3.0 code.

In the event, neither of these criteria provide adequate results the crack growth analysis may also be terminated by specifying a maximum crack length and/or a maximum number of cycles.

3.6.4 Thermomechanical Fatigue Analyses

Thermomechanical fatigue predictions were made using an earlier version of MMCLIFE for the system SCS6/Ti-15-3 under Air Force Contract F33615-87-C-3219 and reported in WL-TR-94-3015 (Reference 1). Moderate success was achieved and it is believed that the degree of success is dependent upon the rigor with which the TMF profile is input into the analysis. Simplified profiles can be devised to provide an upper and lower bounds to the expected test or service results.

Although the present program did not directly address the issue of TMF, it is likely that the fatigue analyses developed under this contract are capable of providing upper and lower bounds estimates of the material behavior for metal matrix composites when subjected to thermomechanical loads. These include crack initiation life, damage mode, damage growth, and specimen life.

Damage is tracked in the composite as a function of temperature. At any point in the applied profile, material properties and damage rates are determined for the specific temperature. These properties are used to determine the type of cracks that will grow during that specific loading increment using the procedures outlined in

75

Section 3.6.2. The analysis will track all three modes of damage as they occur throughout the life of the specimen using the methods discussed in Section 3.6.3.

3.7 Overview of MMCLIFE V3.0

The computer program MMCLIFE V3.0 is an updated release of MDC's metal matrix composite analysis routines. MMCLIFE V3.0 is very similar to version 2.0. The additions to the code occurred under a subcontract MDC to Allied Signal Engine Division on F33615-89-C-5621. This Air Force contract entitled "Damage Tolerance Concepts for Titanium Aluminide Composites" focused on utilization of MMCs in turbine engine components. The MMCLIFE analysis was modified to handle new geometric configurations (edge flaws), and many of the subroutines were updated to reflect lessons learned since V2.0. The analysis in MMCLIFE can still be used to predict the strength and stiffness of aluminum and titanium matrix composites at multiple temperatures. In addition, the analyses can predict life to fatigue crack initiation, and crack growth under fatigue and thermomechanical loading.

The MMCLIFE routine is based on a combination of micromechanic lamina and macromechanic laminate analyses. Micromechanic analyses are used to determine elastic/plastic matrix behavior, ply properties, and initial failure modes. Macromechanical analyses are used to determine laminate stresses, strains, and overall failure modes. The code incorporates a creep analysis to predict the behavior of the matrix material under sustained loads or thermal stresses at high temperatures. The code can also be used to predict the time dependent crack growth behavior of a laminate due to loading rate utilizing a Wei-Landes analysis. The code will accept lamina data in addition to constituent data and will utilize this data to improve the stiffness and strength predictions for the lamina. Improvements were made in the notched analysis in the new program. In addition to circular notches and center cracks the program now handles edge flaws (notches and bridged cracks). In order to accurately predict laminate behavior due to thermally induced bending stresses and strains, stacking sequence is a required input.

The user's manual for MMCLIFE V3.0, published in Volume 2 of this contract report, describes procedures involved with running the computer code. Examples of how data are entered as well as what the code produces are described. Examples of all interactive screens are shown along with examples of the data files required to run the program. All of the assumptions and constants are discussed to give the user a feel for the analyses the program is capable of performing. As with any engineering tool a little common sense is important. Good data will give good results and the more data provided the better the results will be.

SECTION 4.0

TEST RESULTS AND DISCUSSIONS

4.1 Basic Materials Characterization

4.1.1 Materials Used

At the beginning of this contract, the matrix alloy had not yet been selected from a choice of two, Ti-25Al-10Nb-3V-1Mo (Super alpha-2) and Ti-24Al-11Nb (Alpha-2) (both in atomic %). The former had shown higher strength properties (N62269-86-0248) while the latter had been selected for a larger Airframe related MMC program at McDonnell Douglas (F33615-67-C-3209). Also, it was thought that the Super Alpha-2 had tendencies for metallurgical instability with unknown effects on properties. Because McDonnell Douglas was a subcontractor in this program and the origin for the baseline MMC life prediction code, MMCLIFE, it was decided that an addition to the purchase order for a much larger lot of the McDonnell Douglas Aircraft material would leverage the delivery and cost benefit of a larger order. Additionally, it was thought that a sharing of the database would be feasible. As it turned out, production problems at the supplier, Textron Specialty Materials (TSM), prevented capitalizing on these projected benefits and special lots of MMC panels were finally delivered to AlliedSignal Engines for use in this program. The total area of MMC panel was substantially less, necessitating a modification to the test plan.

4.1.2 Foil Characteristics

Cold rolled , 0.11 mm (0.0045") foil, produced by Texas Instruments (TI) starting with 0.04 cm (0.016") gage hot rolled sheet made by TIMET from their heat G0694, was purchased for use in this program. The foil delivered was of uniform gage and basically flat with a few small irregularities that were determined not to have a significant effect on the potential quality of MMC panels to be made with woven fiber mat reinforcement. It is noted that if the etched groove approach to loading fibers had been selected, these irregularities may have been very important, possibly making the foil unusable.

Impurity analysis of the foils from this batch was performed by TI; the results are seen in Table 5.

Table 5. **Impurity Analysis of Foil**

Element	wt %
oxygen	0.085
carbon	0.017
hydrogen	0.0023
nitrogen	0.006
iron	0.066

Tensile properties of the foil in the as-received condition are shown in Table 6. Tests were conducted in both the rolling direction and transverse directions on Ti-24Al-11Nb foil, (Heat G-0694). It is worthy of note that the properties are essentially isotropic in the plane of the foil.

Table 6. Tensile properties of foil as cold rolled and annealed

Tensile Properties (Room Temperature)

Batch Number	Number of Sampes Tested, Average is Reported	Orientation	UTS		YS		Total Elong.	Young's Modulus	
			MPa	ksi	MPa	ksi	%	GPa	Mpsi
4959	7	Longitudinal	621	90.1	361	52.3	11.8	60.0	8.7
	6	Transverse	629	91.3	365	53.0	11.5	59.3	8.6

4.1.3 Fiber Characteristics

Woven mat of SCS6 fibers with a cross weave of TiNb were produced by TSM with a cross weave pitch of about 4.8 mm (0.19"). Fiber was selected from lots where tensile tests on the coiled fiber exceeded 3800 MPa (550 ksi) fracture strength.

4.1.4 Panel Manufacture

4.1.4.1 Matrix Only (NEAT) Test Panels

NEAT Foil panels were fabricated by HIP consolidation of an MMC panel in which a large section of the panel was free of fibers. Nine layers of foil of Ti-24Al-11Nb (atomic percent) were utilized. Panel numbers K914051 through K914054 were produced by Textron Specialty Materials (TSM) by HIP on hard tools, utilizing 103 MPa (15 ksi) pressure at 996°C (1825°F). Standard TSM methods of assuring complete evacuation

78

and leak tight HIP packages were utilized. The MMC portion of the same panel was of inferior quality due to incomplete bonding and was judged inadequate for the program, however the unreinforced section or NEAT panels were sound and free of defects so they were released for use in this program.

4.1.4.2　　MMC Panels

In a similar manner, additional MMC panels with 8 fiber layers were produced using the same lot of foil and SCS6 woven fiber mat having TiNb cross weave at a pitch of 4.8 mm (0.19"). The fiber mat concentration, 129 fibers per inch, was designed to yield 35% fiber loading. Panels F914008 through F9140010 were judged, by virtue of x-Radiography and "C" scan, followed by selected cross section metallography, to be of sufficient quality for this program and were accepted. They were each cut roughly into four equal pieces, about 165 mm (6.5") in the fiber direction by 114 mm (4.5") in the transverse direction. The four subpanels were designated A, B ,C and D.

In these, as well as in the two previous unsuccessful panels, "C" scan techniques were disappointingly unsuccessful in detecting anything other than major delaminations. Clearly, more effective NDE methods must be developed to detect minor flaws.

All specimen blanks were laid out on the panels to make maximum use of the material. At this point, it was determined that there was not enough material to accomplish all of the planned testing so priorities were established in order to minimize the effect of the shortfall of material availability. The specimen blanks were removed from the panels by wire electric discharge machining (wire EDM). Final machining to the drawing requirements, Figure 14 and Figure 28, was done utilizing a diamond abrasive wheel.

The number of specimens of each type are illustrated in Table 7. There were a total of just 160 specimens available from the panel material provided. It is clear that the small number of available specimens of each category severely limited the amount of testing possible. As a result, it was decided to try and capture some data collected by other investigators on nominally the same MMC system. The results of these attempts are discussed elsewhere in this report and show that there is not sufficient similarity in properties to justify inclusion of these data in the database for the present program.

Table 7. Yield of specimen blanks from NEAT and MMC Panels

	[0]$_8$	[90]$_8$	NEAT
dog bone	25	25	22
SEN	41	25	20
Iosiopescu	2	0	0

4.1.5 Residual Stress Characterization

X–ray diffraction measurements have been carried out on four untested tensile samples and one coupon extracted from the as-processed MMC panel. Residual stresses in the coupon sample were also measured by neutron diffraction at Los Alamos National Laboratory's LANSCE facility under a collaborative agreement with the RISC. The x–ray technique measures the matrix lattice strain at the surface in a direction parallel to the fibers (longitudinal direction). Neutron diffraction measures the average lattice strain of each phase through the full thickness of the sample. Comparison of the x–ray and neutron measurement provides a good indication of the validity of surface x–ray measurements for assessing the residual stress state in the fiber/matrix core region of the composite. A paper comparing x–ray and neutron diffraction results on three different titanium matrix composites is attached as Appendix A.

4.1.5.1 The X–ray and Neutron Diffraction Residual Stress Measurements

The Results, given in Table 8, show a uniform surface longitudinal residual stress in the Ti–24Al–11Nb matrix between all samples, the average longitudinal residual stress on all samples being 407.1 MPa (59 ksi). The standard deviation among the four samples is ±27.6 MPa (±4 ksi), and all the individual measurements were within one standard deviation of the average. The excellent agreement between the neutron and x–ray results confirms that the surface x–ray measurement is a good indicator of the bulk residual stress.

Table 8. Longitudinal matrix residual stress (MPa).

	Side 1	Side 2	Average	Neutron
1B/0A11	404.0 ± 34	406.8 ± 28	406.8	-
1B/0A12	454.4 ± 28	405.4 ± 28	427.5	-
1B/0A21	411.6 ± 28	380.6 ± 28	393.0	-
1B/0A22	359.9 ± 34	392.3 ± 28	379.2	-
Coupon	418.5 ± 34	394.4 ±.34	406.8	351.6

4.1.6 Interfacial Property Measurements.

4.1.6.1 Stability of Interfacial Properties and Residual Stresses

Using the four fatigue samples, measurements of surface residual stress and interfacial properties during low cycle fatigue at both ambient conditions and at 650°C (1200°F) cycled in an inert atmosphere were made at the RISC. Nondestructive residual stress measurements were conducted by interrupting the Low Cycle Fatigue (LCF) tests, but the interfacial property measurements are destructive. Therefore, at each temperature one sample was cycled to failure and a second cycled to half the failure life. The second sample was then used for the interfacial property measurements.

4.1.6.2 Measurement Techniques

The interfacial properties were measured using a technique that involves pulling a single fiber from the composite, while measuring the applied force and relative displacements of the fiber and matrix. The displacements result from changes in strain distribution in the fiber as a debond crack grows stably along the fiber/matrix interface, with sliding occurring over the debonded region of interface. The test thus constitutes a miniature fracture mechanics test on the individual fiber, and is capable of providing quantitative measurement of the interfacial debond energy, the interfacial sliding resistance, and the residual stresses. However, special high resolution displacement mapping methods are needed to obtain the data because the displacements are very small.

The single fiber pulling experiment is shown schematically in Figure 35. The ends of the specimen in Figure 35a are glued to a loading fixture on the stage of an optical microscope. As the ends of the specimen are pulled apart, with the force being measured continuously by a load cell, high magnification micrographs are obtained from the region where the fiber enters the matrix, as in Figure 35b. Accurate measurements of the distance that the fiber pulls out of the matrix are obtained by measuring changes in separation of corresponding image features (from the matrix and the fiber) in pairs of micrographs, one obtained before load was applied to the specimen and the other during loading. For the data reported here, this differential measurement was obtained by stereo viewing of pairs of micrographs, although the measurement can also be done by computerized digital image correlation. Both methods yield relative displacement resolution of ~10 nm from optical micrographs (substantially smaller than the point-to-point resolution of the individual micrographs), provided the imaging conditions for both micrographs are identical (illumination and collection optics, focus, specimen orientation and position).

The specimens were prepared from beams (~ 40 mm x 3 mm x 0.7 mm) of the composite samples in Table 8 (specimen P1 from the virgin coupon, N1 from 1B/0A12, and O1 from 1B/0A22). A saw cut through the top layer of fibers (Figure 35a) at a predeter-
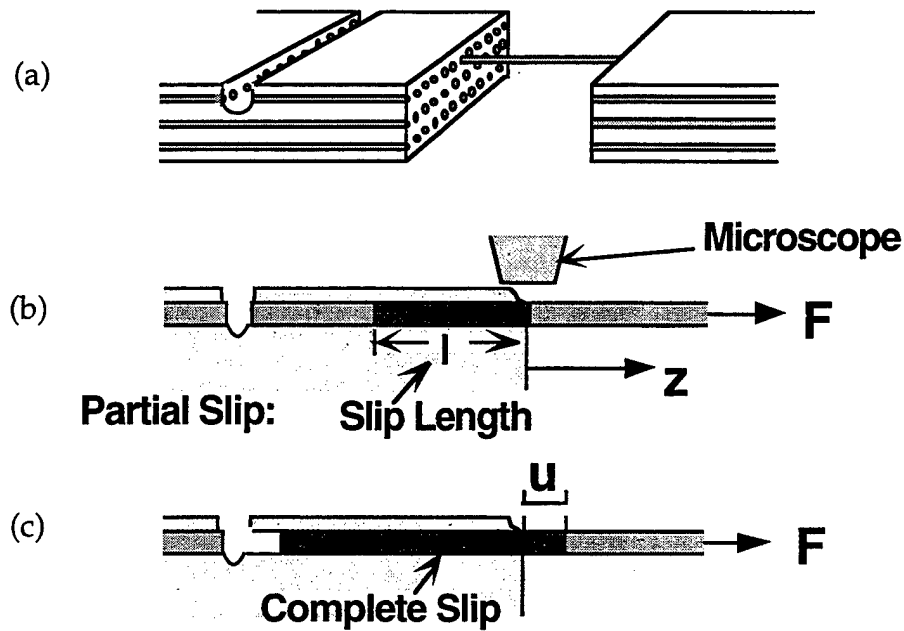
Figure 35. **Schematic diagram of fiber pulling experiments.**
(a) test specimen: (b) initial loading where sliding occurs partially along the
embedded length of fiber; and (c) pullout where entire embedded length of fiber
slides.

mined distance from the central section (typically ~ 2 mm) allowed data to be collected
during complete sliding of the fiber (Figure 35c), as well as from the initial loading region
where partial sliding occurs (Figure 35b).

The residual axial stresses in the fibers were obtained by measurement of the relax-
ation of the fibers when the matrix was removed. This was done by etching the matrix
away from the central region of a beam of composite, with the ends being masked, and
measuring the increased separation of the ends of the beam from optical micrographs
taken against a fixed reference gauge before and after etching. By using the differential
strain mapping techniques mentioned above to measure this relaxation, very high sen-
sitivity is possible (less than 1 MPa from specimens ~ 5 cm in length).

4.1.6.3 Analysis of Interfacial Property Measurements

The residual axial stresses in the fibers were calculated from the measured relaxation
strains using a concentric cylinder analysis, with the radius of the outer cylinder cho-
sen to accord with the measured fiber volume fraction. The analysis accounts for
Poisson's effect when the fiber relaxes during dissolution of the matrix. It also accounts

82

for differing elastic properties of the fiber and matrix as well as anisotropy in both the elastic properties and the elastic mismatch strain that is responsible for the residual stresses.

Calculation of interfacial properties and residual stresses from the fiber pulling measurements requires comparison of the experimental data with micromechanics modeling of the debonding and sliding process. For the types of composites of interest here, with weakly bonded (or unbonded) interfaces and sufficiently low sliding resistance, shear-lag models are appropriate. A recent analysis which accounts for effects of thermal and elastic mismatch of the fibers and matrix as well as interfacial debonding, with sliding over the debonded surfaces governed either by a Coulomb friction law or by a constant sliding stress, is attached as Appendix B.

The expressions relating the applied forces, p, and the sliding displacements, u, involve four parameters which are functions of (1) the debond energy, (2) a friction stress (or friction coefficient), (3) the residual stress and (4) a combination of the elastic properties and the anisotropy of thermal mismatch strain. However, the curve fitting required to evaluate these parameters is highly constrained. The debond energy parameter translates the curve $p(u)$ along the u axis and is therefore reflected in the intercept, or the load needed for initiation of sliding. The friction parameter appears only as a linear scaling factor for the displacements. If the residual axial strain in the fibers is measured separately as described above, and the elastic properties are known independently, then there is only one remaining parameter (the anisotropy in mismatch strain) to be determined by curve fitting to the *shape* of the function $p(u)$.

This anisotropy factor is defined by the ratio, λ, of the radial and axial mismatch strains. After fitting the parameters in this way, two predictions are available for checking their validity; one is to calculate the debond length at the peak load and compare with the known length (which is usually predetermined by cutting the fiber at a known embedded length), and the other is to compare predicted and measured displacements during unload/reload cycles prior to reaching the peak load.

In all of our previous measurements on intermetallic matrix composites, very good fits were obtained with the data for the constant friction model with $\lambda = 1$, whereas similar curve fitting with the Coulomb friction model (assuming a smooth interface) required unreasonably large values of λ ($\lambda = 10$). (For such large values of λ, the two models are almost the same. This response was attributed to the effect of interfacial roughness; the relative sliding of a rough interface in the constrained geometry of the fiber pullout test causes an increase in the normal interfacial stress, which tends to cancel the radial Poisson's contraction of the fiber. Therefore, the roughness effect is equivalent to an increase in λ over the region of sliding.

In most experiments with intermetallic matrix composites the relative sliding displacements are smaller than the average period of the roughness. Therefore the increase in λ would be expected to vary along the debonded region. A more detailed analysis of this effect has yielded a very simple result; the p(u) relation obtained is *equivalent* to that obtained from a friction law of the type $\tau = \tau_o + \mu\sigma_r$ where τ_o and μ are constants and σ_r is the radial interfacial stress. Moreover, p(u) is given by the *same* equations as described above for the Coulomb Friction model with $\lambda = 1$ and with two of the parameters ((3) and (4) above) multiplied by functions of $\chi \equiv \tau_o/\mu\sigma_r$. Therefore, the curve fitting follows the same procedure as described above, but with x rather than λ as the parameter obtained from the shape of the initial loading curve.

4.1.6.4 Results from Untested Composite

Specimen P1 was cut from the coupon sample in Table 8. The measured pullout forces and displacements are compared with the two analyses described above in Figure 36, and the parameters deduced from the fitted curves are summarized in Table 9 The data are consistent with the Coulomb friction law with $\lambda = 1$ (isotropic misfit strain) although a slightly better fit to the initial load data were obtained for $\lambda = 0.7$.

The parameters evaluated from these curve fits to the initial loading data are consistent with several independent measurements. The predicted response during the unload/reload cycles agrees closely with the measurements. The magnitude of the interfacial sliding resistance varied at the peak load between 68.9 MPa (10 ksi) at the surface and 103.4 MPa (15 ksi) at the end of the debond. These values are consistent with previous measurements in similar composites. The calculated debond length at peak load (915 µm) is consistent with the known embedded length (940 µm). Finally, from the measured residual axial stress in the fibers of -758 MPa (-110 ksi), the residual axial stress in the matrix, calculated from the force balance requirement, is 385 MPa (56 ksi), consistent with the x–ray measurement of 407 MPa (59 ksi) is shown in Table 9.

Beyond the peak load in Figure 36, the entire embedded length of fiber was pulled out of the matrix as depicted in Figure 35c. The average sliding stress along the remaining embedded length decreased by about a factor of 2 during the first 200 µm of sliding and remained relatively constant thereafter (Figure 37).

Subsequent observation, by SEM, of the fiber and the hole from which it was extracted indicated that debonding and sliding occurred at the interface between the outer SCS6 layer on the fiber and the layer of reaction products that formed in the matrix adjacent to the fiber during fabrication of the composite.
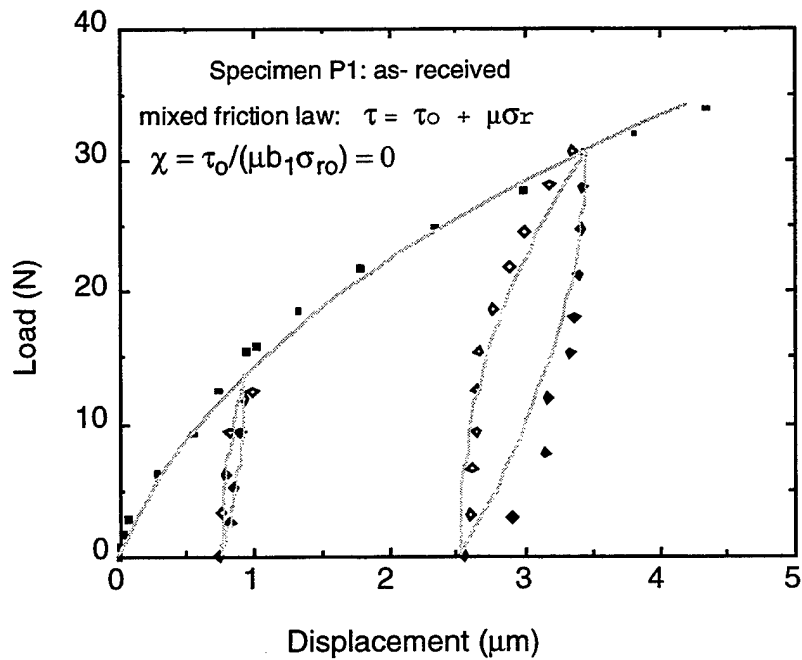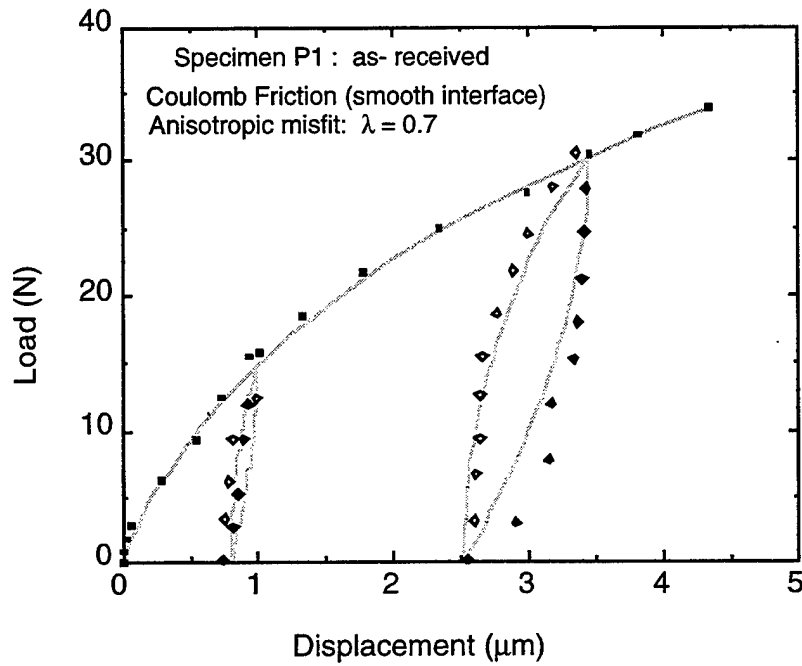
Figure 36. Comparison of fiber pullout data for as-received composite with theoretical analyses:
(a) Coulomb friction model with smooth interface; (b) rough interface model with isotropic misfit strain (the curve fit in this case gives $\tau_o = 0$, corresponding to Coulomb friction with a smooth interface).

Table 9. Properties evaluated from fiber pulling and matrix dissolution experiments.

	Specimen		
	P1 (as-received)	N1 (cycled 21°C)	O1 (cycled 650°C)
Volume fraction of fibers	0.34	0.39	0.35
Coulomb Friction Law			
Radial: axial misfit strain, λ	0.7	2.7	2.0
Residual axial fiber stress, MPa	-717	-248	-352
Residual axial matrix stress, MPa	365	159	186
Friction coefficient, μ	0.74	1.1	0.75
Maximum friction stress, MPa	117	152	117
Minimum friction stress, MPa	62	34	28
Debond energy J/m^2	< 21	< 3	< 5
Modified Friction Law (Roughness) $\tau = \tau_0 + \mu\sigma_r$ *(with $\lambda=1$)*			
$\chi \equiv \tau_0/\mu\sigma_{ro}$	0	1.5	1.0
Residual axial fiber stress, MPa	-758	-200	-310
Residual axial matrix stress, MPa	386	124	165
Friction coefficient, μ	0.51	1.0	0.65
Maximum friction stress, MPa	103	152	110
Minimum friction stress, MPa	69	34	34
Debond energy J/m^2	< 24	< 2	< 4
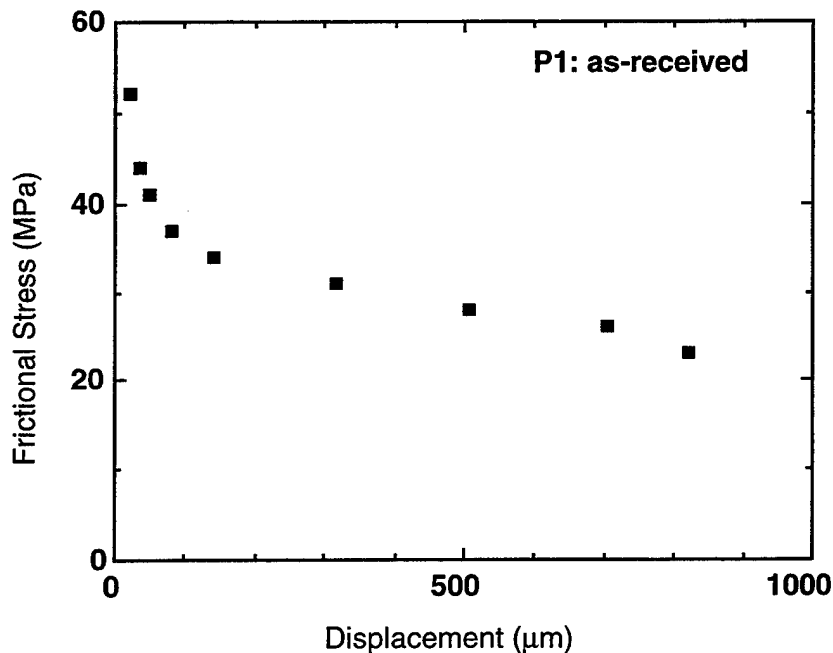
Figure 37. Average frictional stress over embedded length during pullout beyond the peak load of Figure 36.
(complete slip as depicted in Figure 35c.)

86

4.1.7   Stability of Residual Stresses and Interfacial Properties

In order to predict fatigue properties, it is necessary to understand the manner in which residual stresses in the MMC constituents and the interface properties are influenced by service conditions. To this end, samples were cycled at room and elevated temperatures and residual stresses measured. Similarly, the interface strengths were measured.

4.1.7.1   X–ray Measurements

X–ray diffraction measurements during and after cyclic fatigue have been carried out on four tensile samples. The x–ray technique measures the matrix lattice strain at the surface in a direction parallel to the fibers (longitudinal direction). The results given in Table 10 show that the longitudinal residual stress in the Ti–24Al–11Nb matrix relaxes very rapidly.

Table 10.   Longitudinal matrix residual stress (MPa).

	°C	N_f	Cycles				
			0	250	500	$N_f/2$	Nf
1B/0A11	21	26690	407	165	165		172
1B/0A12	21		427	179	165	159	
1B/0A21	650	46628	393				269
1B/0A22	650		379			131	

All samples were cycled in load control at 1034 MPa (150 ksi), R = 0.1 at a frequency of 0.33 Hz. The stress-strain curves were nonlinear on the first cycle but very linear thereafter (Figure 38). Some ratcheting of the sample to positive mean strain was evident in all samples. The 650°C (1200°F) isothermal testing was done in an argon atmosphere using induction heating. A very thin bluish-gray oxide formed on the sample surfaces at high temperature which was removed with a dilute HF etch prior to the x–ray measurements.

The longitudinal residual stresses relaxed very rapidly during the room temperature cyclic loading, with most of the relaxation taking place before 10% of the cycles to failure. At the high cyclic load used here, it is likely the residual stress reached a near equilibrium state on the first few cycles. After the first few cycles, the measured values were constant within the experimental error of ±4 ksi (±27.6 MPa). Analysis presented in Section 4.10.5 indicates that the relaxation occurs in the first cycle.

Measurements were only made before and after fatigue for the high temperature testing so as to not disturb the isothermal test. The samples were clamped with hydraulic wedge grips at room temperature and held in load control at zero load during heating.

87
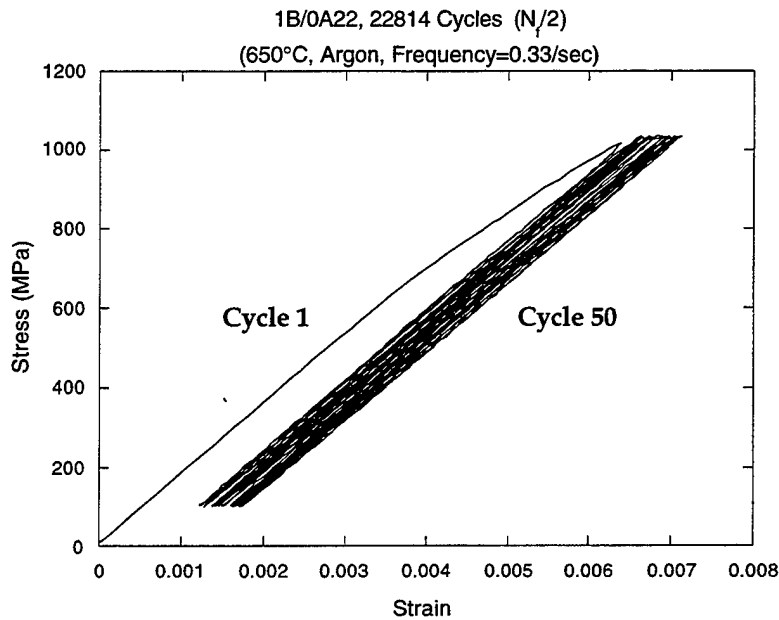
Figure 38. Composite stress-strain cycles showing cycles 1, 3, 5, 7, 10, 30, and 50.

The extensometer was zeroed just prior to cyclic loading. The measured longitudinal residual stress in the matrix is, surprisingly, quite different for the two samples (1B/0A21 and 1B/0A22) after fatigue. At a minimum, it might be conjectured that a new residual stress state would be induced in the matrix during cooling from the test temperature. Using the ratio of the test temperature to the consolidation temperature as 0.68, the expected residual stress would be about 262 MPa [0.68*386 MPa] (38 ksi [0.68*56 ksi]), that found for the fractured sample. However, the half life sample, 1B/0A22 exhibits a much lower residual stress, indicating additional relaxation. As seen in the next section, the measured value on the half-life sample, 1B/0A22 compares favorably with that obtained from the dissolution experiments on the same sample and, therefore, represents the true relaxed value. The residual stress is related to the amount of plastic deformation due to the applied load.

4.1.7.2 Interfacial Property Measurements

The measured pullout forces and displacements for composites that had been cycled at 21°C (71°F) (specimen N1) and 650°C (1200°F) (specimen O1) are compared with the analyses in Figure 39 and Figure 40. The parameters evaluated from the fitted curves are summarized in Table 9. The data from both specimens were consistent with the
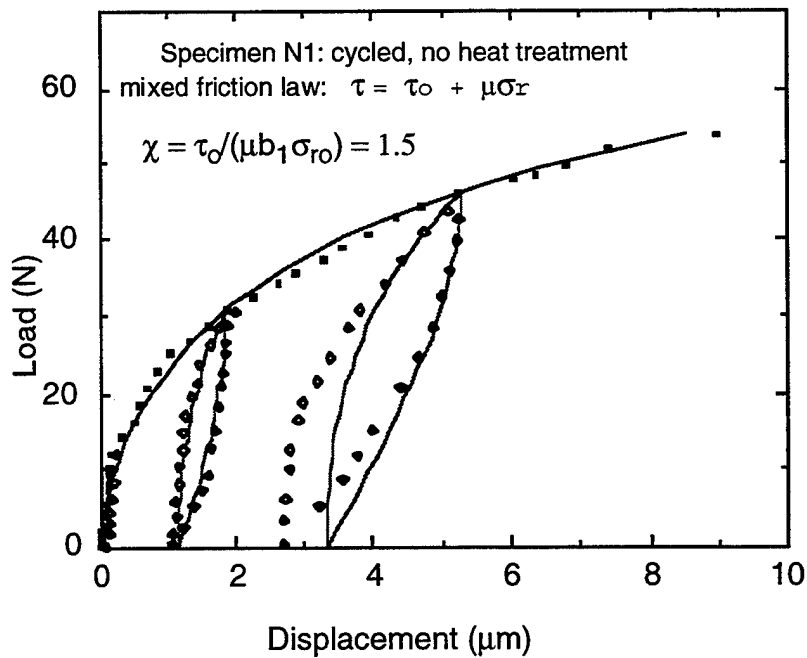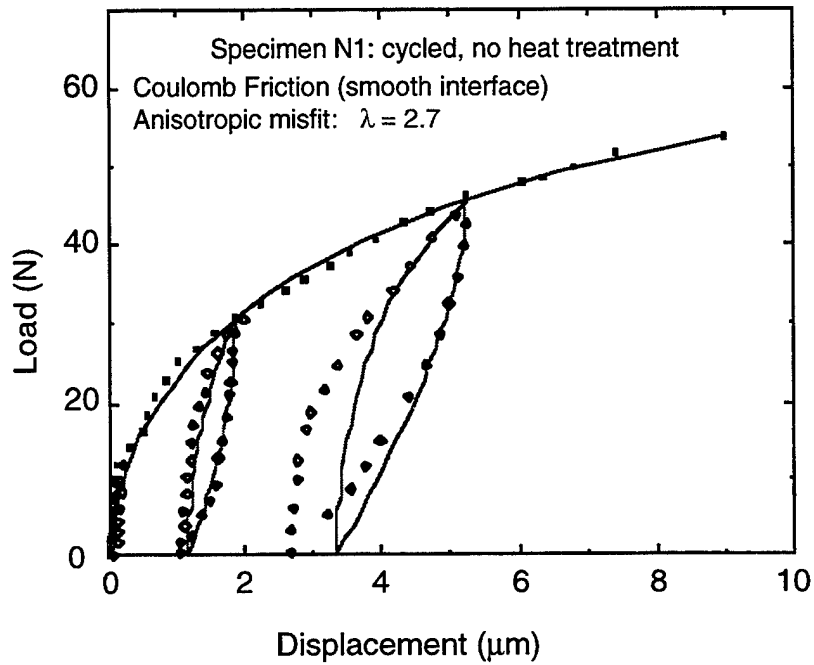
Figure 39. Comparison of fiber pullout data for composite that was exposed to cyclic loading at room temperature with theoretical analyses.
(a) Coulomb friction model with smooth interface; (b) rough interface with isotropic misfit strain.

89
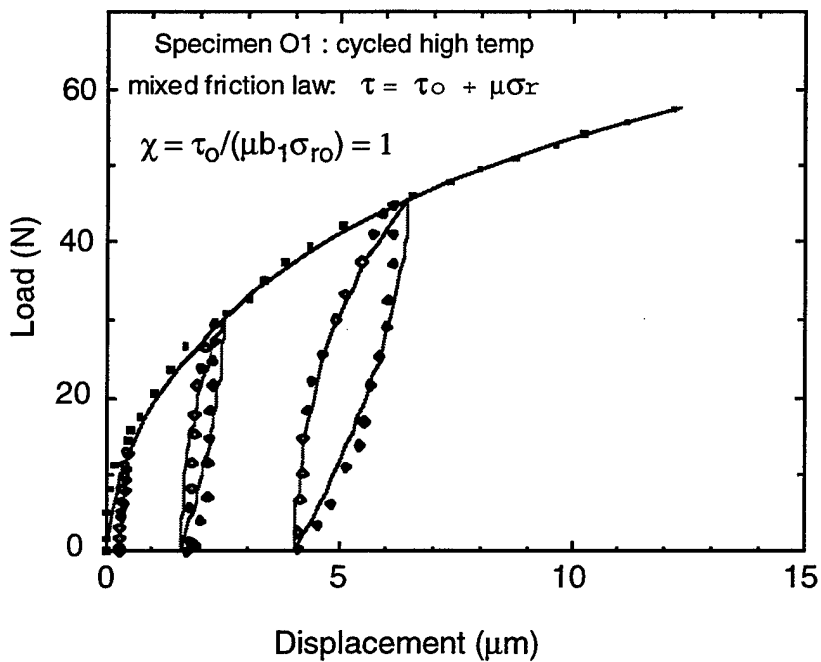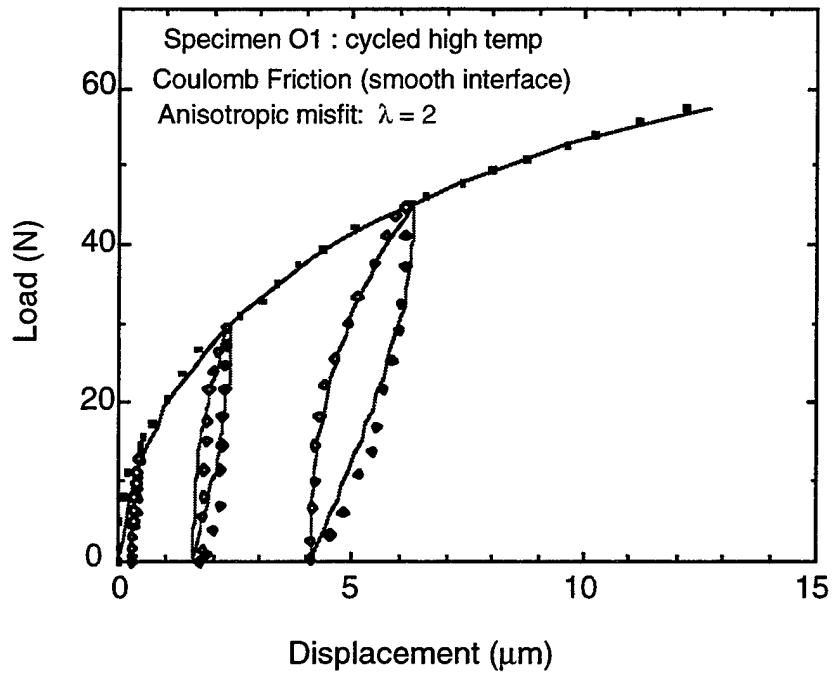
Figure 40. Comparison of fiber pullout data for composite that was exposed to cyclic loading at 650°C with theoretical analyses.

(a) Coulomb friction model with smooth interface; (b) rough interface with isotropic misfit strain.

90

Coulomb friction model, with radial misfit strain significantly larger than the axial misfit strain ($\lambda = 2.7$ for specimen N1 and $\lambda = 2.0$ for specimen O1). The significance of this anisotropy in mismatch strain is illustrated by comparing the measurements with the predicted response for an isotropic mismatch ($\lambda = 1$). In this case, the normal interfacial stress where the fiber enters the matrix would decrease to zero (owing to Poisson's contraction) at an applied load of 25 N. At this load, which is less than half of the measured peak loads, the fibers would pull completely out of the matrix (the debond length and the displacements asymptotically become infinite).

The load-displacement data for these two specimens can be fit equally well using the mixed friction law $\tau = \tau_0 + \mu\sigma_r$, with $\chi = 1.5$ for specimen N1 and $\chi = 1.0$ for specimen O1. For each specimen, the calculated values of the friction coefficient (μ), the maximum and minimum sliding resistance, and the maximum debond length are almost the same for the two models (Table 9). This confirms intuition; the influence of roughness on fiber sliding, leading to the mixed friction law, is similar to that of increasing λ. However, the calculated values of residual axial stress in the fibers from the two models differ slightly because the roughness does not influence stresses beyond the debonded region, whereas the anisotropy factor, λ, does affect these stresses.

The predicted unload/reload curves agree very closely with the data for specimen O1 and with one of the two cycles for specimen N1. The degree of recovery is underestimated by ~20% for the other unload/reload cycle of specimen N1. The reason for this discrepancy is not known.

SEM observation of the extracted fibers and the remaining holes indicated that debonding and sliding occurred at the same location as in the as-received specimen; between the outer SCS6 layer on the fiber and the reaction product layer. However, the carbon rich SCS6 coatings on these fibers contained fine circumferential cracks, spaced by ~10 μm. Apparently, these were caused by the cyclic loading, since such cracks were not observed in the as-received specimen.

Comparison of the results summarized in Table 9 for the as-received and cycled specimens indicates that significant changes were evident after cycling at both ambient and elevated temperatures. The residual *axial* stresses in the fibers and matrix were decreased by a factor of ~2 after high temperature cycling and ~3 after room temperature cycling. This relaxation of axial stress was accompanied by one of two phenomena, both of which affect the fiber pullout response similarly. One possibility is that the radial residual stresses were not altered by the fatigue loading, so that the relaxation of the axial stresses led to an anisotropic misfit strain. The other possibility is that the radial and axial stresses relaxed together (maintaining $\lambda = 1$), with damage in the interface causing interfacial roughness effects to increase.

4.1.7.2.1 Effects of Interfacial Roughness and Residual Stress

To distinguish the effects of roughness and radial residual stress, we determined the radial stresses separately by pulling fibers out of the composite and measuring the radial relaxation of the matrix around the hole in which the fiber had sat. These measurements were done with specimens in the as-received condition, after cyclic loading at room temperature, and after cyclic loading at 650°C (1200°F). Experimentally, the relaxation measurement involved preparing a specimen with a polished surface normal to the fibers, pulling one fiber out of the composite from beneath the polished surface, and comparing high resolution optical micrographs of the polished surface recorded before and after removal of the fiber using stereology to measure relative displacements.

This measurement and the previous axial relaxation measurement provides sufficient information to determine both the axial and radial misfit strains of the fibers and matrix. The expressions required to calculate these parameters and the corresponding residual stresses was obtained by extending the analysis of Hutchinson and Jensen (Reference 19). Details on the analysis and further explanation of the results are given in Appendix C.

For each of the three specimen conditions, the ratio of the radial to axial misfit strain (defined by the parameter λ) evaluated from the relaxation measurement was consistent with the values calculated previously from the fiber sliding measurements with the assumption that roughness effects were negligible. The values of λ and e^T (the axial misfit strain) obtained from these measurements are listed in Table 11. Also shown are the parameters determined previously from the fiber sliding experiments assuming no roughness effects, as given in Table 9. The results indicate that cyclic loading relaxes the axial misfit strain (by a factor of 3.8 at room temperature and a factor of 2.4 at 650°C (1200°F), but does not relax the radial misfit strain. (There is a small decrease in the residual radial stress after cyclic loading, but this is a Poisson's effect due to the decrease in the axial strains.)

Table 11. Parameters inferred from fiber relaxation and sliding measurements.

Measurement	Parameter	Composite		
		P1 As-received	N1 Cyclically Loaded RT	O1 Cyclically Loaded 650°C
Axial relaxation	e^T	0.0065	0.0017	0.0027
Radial relaxation	λ	0.7±0.1	2.9±0.2	2.2±0.2
Fiber sliding (from Table 9)	λ	0.7	2.7	2

92

4.1.8   Residual Stress and Interface Property Conclusions

The residual axial stresses in the matrix calculated from the fiber stresses measured by the dissolution technique are consistent with the x–ray measurements (Table 12). However, the differences between the two calculated stresses are not sufficiently large, given the measurement errors in the pullout data and in the x–ray measurements, to eliminate one of the fiber pull-out models. It is noteworthy that the residual stresses are relaxed to about 40% of their initial value for both the composite that was cycled at room temperature and that cycled at 650°C (1200°F). This is probably the result of the very high load amplitude dominating the relaxation process.

Table 12. Comparison of residual stress calculations.

Sample	Condition	Residual Stress (MPa)		
		X-ray	Fiber Pull-out (Coulomb Law)	Fiber Pull-out (Friction Law)
Coupon	as-received	407	365	386
1B/0A12	21°C cycled	159	159	124
1B/0A22	650°C cycled	138	186	165

The x–ray results on the samples cycled at room temperature showed that the residual stresses relax very quickly, possibly even on the first loading cycle. Analysis of the dissolution measurements showed that cycling did not have much effect on either the friction coefficient or the maximum friction stress. The debond energy was minimal after cycling, and smaller than the initial magnitude, although even the initial value was of negligible significance. Thus, it seems that low cycle fatigue, both at room and elevated temperature, most significantly relaxes the matrix residual stress (and thus the fiber residual stress) without affecting the interfacial properties too greatly.

In the analysis of interfacial properties, there is some difficulty in determining which model is best (the effects of roughness and anisotropy being similar). Fortunately, the distribution of shear stresses along the debond interface are insensitive to the model and the stresses are determined quite accurately from the experiment. A value of τ_{min}=29 ± 3 MPa would cover most possibilities for sliding. Also, wear causes additional decrease in the shear stress as seen in Figure 37 which shows a drop to 22 MPa. Similar values have been found by others indicating a useful value for the interfacial shear stress in crack bridging problems is probably about 20 MPa (2.9 ksi).

The Rockwell Science Center also conducted a sensitivity analysis to determine if volume fraction changes affected the interpretation of the parameter values. Volume frac-

tions of 0.38 instead of 0.34 for sample P1 (Table 9) had insignificant change on the calculated friction stress (i.e., less than the ±3 MPa error bar).

4.2 Tensile Test Results

4.2.1 Experimental Procedure

4.2.1.1 Description of Specimen, Grips, and Extensometry

All tensile tests were run on an MTS, closed loop servo-hydraulic test machine with the ram motion at 0.051 mm/min (0.002 in/min). The specimens were of a dog bone configuration with a reduced section of 29.2 mm (1.15"), described by Figure 41. Gripping of the specimen was accomplished with hydraulic grips, initially aligned with instrumented test specimens of construction similar to the program specimens. Strain was recorded from the output of a contact extensometer of 9.52 mm (0.375") gage length mounted at the center of the reduced section. The extensometer was left on the specimen to failure.

Notched tensile properties of the matrix at room temperature and 650° (1200°F) were determined using a flat specimen with a single edge notch. In this case, two separate notch lengths were used, 1.27 mm (0.050") and 2.54 mm (0.100"). The specimen dimensions are shown in Figure 42. Identical test specimen configurations are used for crack growth testing of both monolithic and MMC materials as described in Section 4.5.

4.2.1.2 Specimen Heating

4.2.1.2.1 Tensile Tests

Heating of the specimen gage section was accomplished using induction. Previous calibration of the uniformity of the temperature in the gage section was accomplished with welded thermocouples throughout the gage section of a dummy specimen of the same type. To avoid weld initiated failures, the program specimens were thermocoupled outside the gage section and temperature monitored at the gage center with infrared pyrometry, calibrated periodically to the thermocouples outside of the gage section.

4.2.1.3 Acoustic Emission

In addition to the load strain plots, Acoustic Emission was recorded throughout much of the testing for early indications of incipient failure. The Acoustic Emission transmitter was mounted on the grip, as close to the specimen as the induction heater would allow. Although the induction heater introduced some interference, the room temperature and some elevated temperature tests produced significant signals. Interpretation of these results is incomplete but the objective is to provide a tool for early detection of

2.92 cm
(1.15")

(0.50")

1.27 cm

0.762 cm
(0.300")

Profiles: 6.1 cm (2.4")
radius or greater

15.2 cm *
(6.0")

0.076-0.203 cm (As Received)
(0.03-0.080")

* If blank is less than 14.6 cm (5.75") in length,
maintain the gage section dimensions and center
specimen on length of the blank
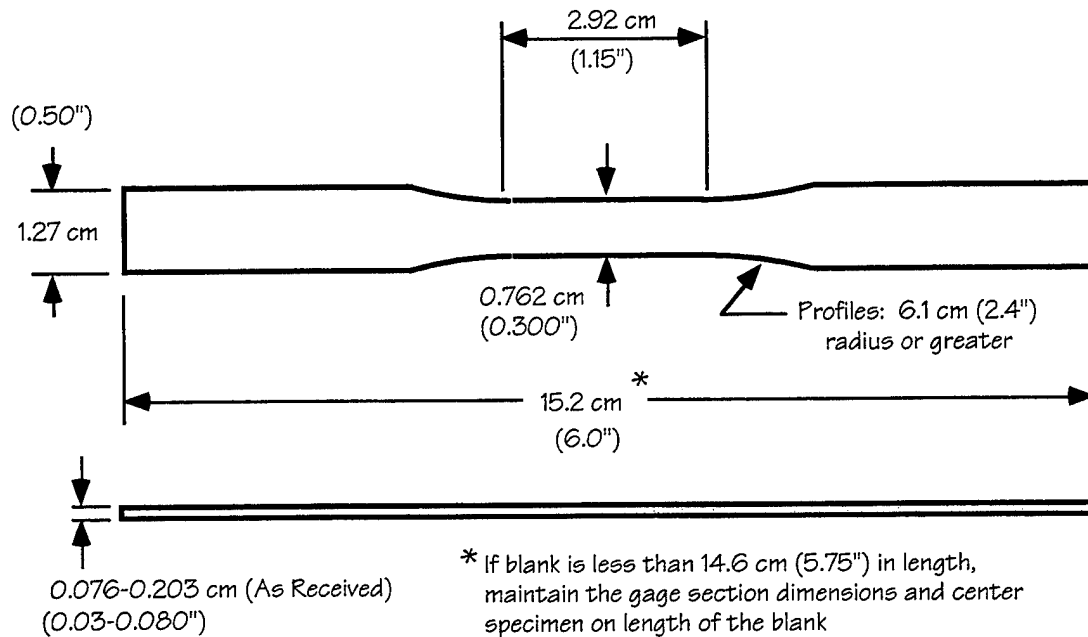
Figure 41.   **Dogbone specimen used for tensile and LCF testing.**

(5.0")
12.7 cm

1.27 cm
(0.50")

Notches must be diamond saw cut.
Notch configuration: 0.0254 cm
(0.010) inches wide
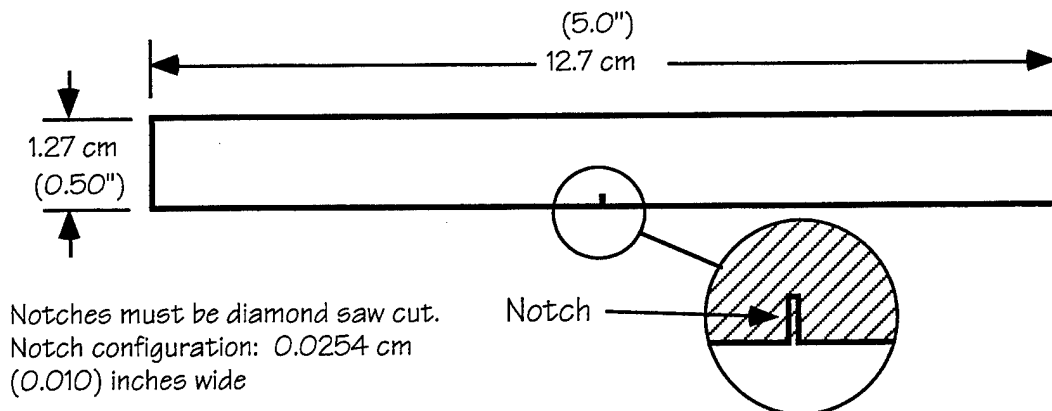
Notch

Bottom of notch may be round or square with
a root or corner radius less than 0.0127 cm
(0.005").

Figure 42.   **Single edge notched specimen.**
Used for notch tensile and crack growth testing. The notch depth was used at
nominally 0.636 mm, 1.27 mm and 2.5 mm (0.025, 0.050, and 0.100 inch), depending on
the test and intended nominal stress.

fatigue damage. Unfortunately, with the level of analysis available within the scope of this program, little of value was gained, and the effort was dropped.

4.2.2 Tensile Test Results

The tensile data gathered to date, on the Monolithic matrix and MMC materials is contained in Table 13 and Table 14 respectively.

4.2.2.1 Matrix Alloy Results

4.2.2.1.1 Tensile Results

The Ti–24–11 test material, made by HIP consolidation of foil materials, when tested at room temperature, gave very surprising results. Figure 43 is a replot of one of the two test results. Both were nearly identical yet they were taken 90° from one another. Notice that there appears to be an upper yield point and an extended strain without work hardening, followed by a classical work hardening portion. The true strain to failure for the two samples exceeds 0.13, which is much higher than expected based on results from other wrought forms of this alloy. The yield strength was exceedingly low, at less than 414 MPa (60 ksi), despite a grain size of 10 to 15 μm. Another feature of note is that there is no maxima on the plastic stress-strain curve, implying that there is no necking and that the extensive elongation is a result of adequate work hardening up to the stress where fracture processes dominated. Upon post test examination, the specimens showed no evidence of necking. Similar stress-strain curves were obtained at 550°C (1022°F) and 650°C (1200°F). The stress-strain curve for the 550°C (1022°F) test is seen in Figure 44.

The notched tensile results are seen in Table 13, along with the smooth tensile data. Comparing the Ultimate Tensile Strength (UTS) with the notch strength, it becomes clear that the matrix, although exhibiting high tensile elongation, is notch sensitive at both room temperature and at 650° (1200°F).

4.2.2.1.2 Work Hardening of The Matrix Alloy

By reconstructing the engineering stress-strain information into true stress and true strain, it was possible to determine the work hardening exponent for the matrix material. Figure 45 shows three linear portions of the log-log plot for M2B12. The form of this room temperature data are typical. At elevated temperature, only the latter stages presents a linear plot. The work hardening exponent reported in Table 13 is that determined near the end of the test.
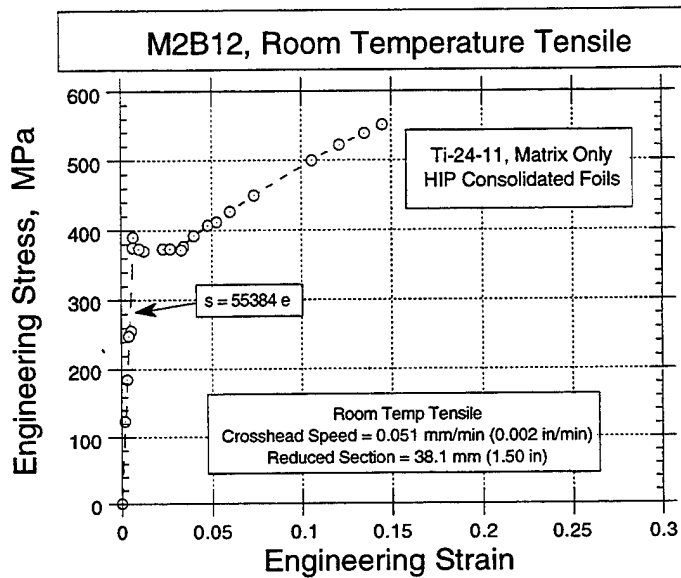
Figure 43. Room temperature tensile curve for HIP consolidated TI-24-11 foil (eight layers thick).
Note the modulus =55.3 GPa.
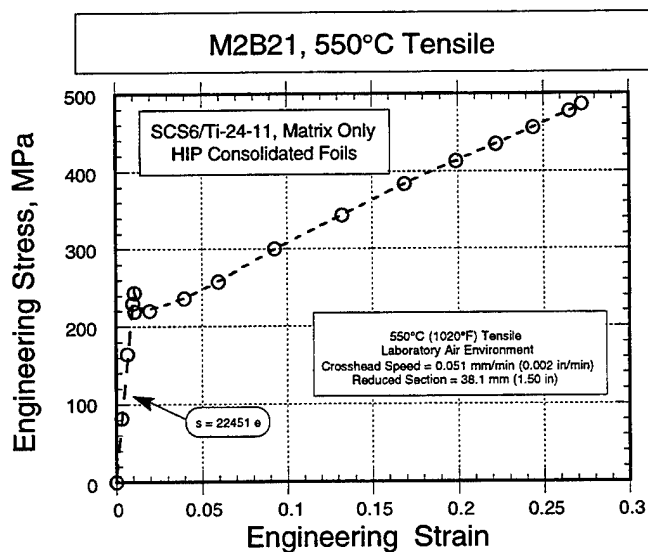
Figure 44. 550°C tensile curve for HIP consolidated TI-24-11 foil (eight layers thick).
Note the modulus = 22.45 GPa.

Table 13.   Matrix tensile test results.

Spec	Temp °C	Yield, MPa		UTS MPa	Engr Strain @ fail	Young's modulus GPa	True strain @ fail	Orig. width x thick, mm	Final Width x thick, mm	Work Hard Exp
M2B11	24	396		576	0.148	58.6	0.139	7.67 x 1.04	6.78 x 1.02	0.43
M2B12	24	391		550	0.145	55.8	0.124	7.65 x 1.02	6.86 x 1.02	0.41
M2B21	550	243		382	0.272	22.8	0.240	7.67X 1.07	6.15X 1.04	0.57
M2B22	650	217		308	0.302	nd	nd	7.67 x 1.07	6.05x 1.04	nd
		Elast Limit MPa	Notch, mm	Net Sect. Stress MPa						
M2A11	24	272	1.27	372						
M2A12	24	304	2.54	361						
M2A21	650	127	1.27	190						
M2A22	650	94.5	2.54	188						
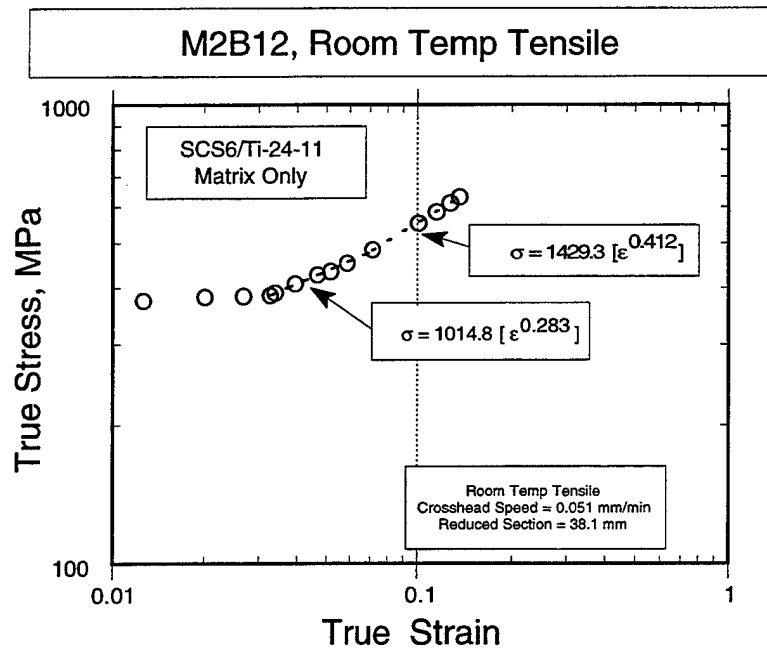
Figure 45.   Log-log plot of true stress and true strain, revealing work hardening exponent, n. In this case, n = 0.412 at the end of the test.

98

4.2.2.1.3 Temperature Effects on Matrix Strength

Figure 46 plots the effect of test temperature on yield strength and UTS for the matrix material alone.

4.2.2.1.4 Characterization of Matrix Material

A microhardness survey of the material failed to show directionality when taken on a plane parallel to the sheet surface. A hardness of 268 KHN using a 500 gram load was obtained in directions parallel and normal to the sheet edges. However, in the cross section, impressions taken parallel to the plane of the sheet gave hardness of about 256 KHN and normal to the surface a reading of about 150 KHN was obtained, (Figure 47). This leads to the conclusion that while there may be very little in-plane texture, the through thickness texture is significant. The presence of this texture may lead directly to the very low strength observed during the in-plane tests, and the absence of necking.

4.2.2.2 MMC Results

Table 14 presents the tensile test results on all MMC specimens.
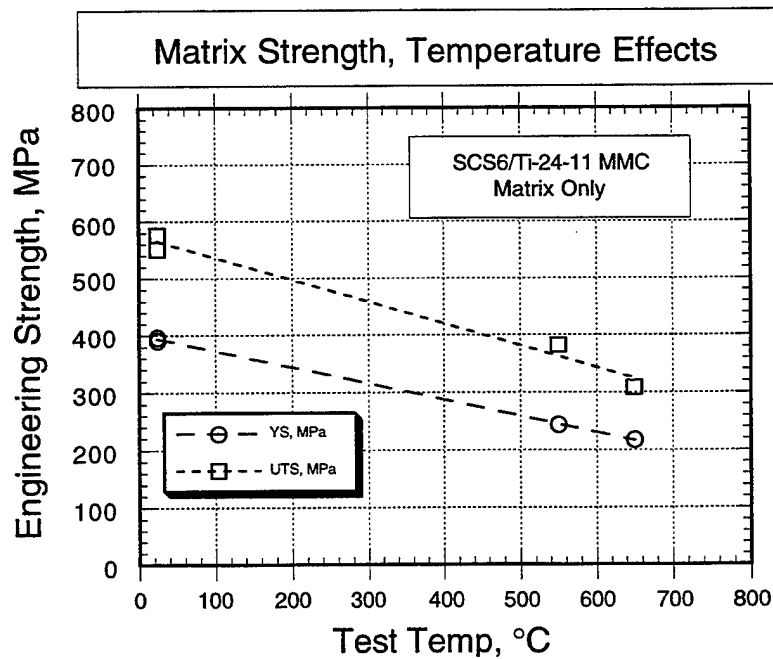
Figure 46. Effect of test temperature on matrix strength (Ti-24-11).

99
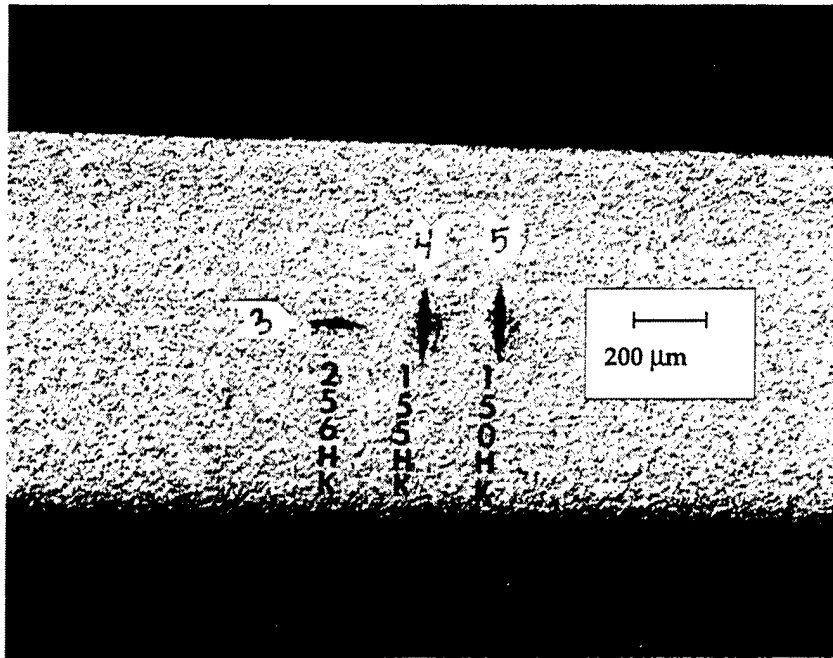
Figure 47.   500 g Knoop hardness impressions on the HIP consolidated foil matrix showing much higher hardness in the thickness direction than in the directions lying in the plane of the sheet.

Table 14.   Tensile test results for MMC specimens.

Specimen Number	Test Temp °C	Stress @ 1st Break MPa	Strain @ 1st Break	UTS. MPa	Modulus GPa	Failure Strain
LONGITUDINAL ORIENTATION						
1B/0A13	24	567	0.00320	1544	174	0.0110
1B/0A24	550	653	0.00390	1358	168	0.0098
1B/0A23	650	587	0.00380	1324	155	0.0095
1B/0B12 **	24	600	0.00320	1552	186	0.0110
1B/0B13 *	24	587	0.00320	1507	181	0.0110
1B/0B14 *	24	569	0.00320	1460	179	0.0110
1B/0B11 ***	24	629	0.00390		186	
1B/0B11		1066	0.00680	1576	186	0.0110
TRANSVERSE ORIENTATION						
1B/90A12	24	19.6	0.00099	30.6	136	0.0016
1B/90A22	550	11.4	0.00094	20.8	82.7	0.0037
1B/90A21	650	6.8	0.00050	18.6	93.8	0.0120
1B/90B11 *	24	15.0	0.00080	29.1	129	0.0017
1B/90B12 *	24	16.8	0.00100	29.4	113	0.0019

*   Specimens were thermally cycled in air, 50 times between 38°C and 650°C prior to RT test
**   Like above for 100 cycles
*** 1B/0B11 initially loaded to 1066 MPa, then unloaded and tested to failure

100

4.2.2.2.1 Longitudinal Tensile Properties

Tensile properties of MMCs, were determined from specimens machined parallel to the fiber reinforcement at room temperature, 550°C (1022°F) and at 650°C (1200°F). Typical tensile curves are represented by Figure 48 through Figure 50 and include samples which had seen a number of thermal cycles in air between 650°C (1200°F) and 38°C (100°F), after a very thorough surface cleaning.

Similar sets of unexposed and exposed samples were prepared and tested with a 90° orientation between the tensile axial and the reinforcing fibers.

The room temperature test of unexposed longitudinal sample showed a bilinear curve (Figure 48) as did the 650°C° (1200°F) test (Figure 49). The expected slight drop in initial modulus at the higher temperature is seen; however, the second part of the bilinear plot exhibited nearly the same slope at the two temperatures. Total strain to failure is somewhat reduced at the elevated temperature.

4.2.2.2.1.1 Effects of Thermal Cycling

After 100 thermal cycles in air, to 650°C (1200°F), the room temperature tensile curve is virtually identical to that obtained from the unexposed sample (Figure 48 and Figure 49). This implies no measurable degradation with this exposure, in contrast to results reported by Revelos and Smith at Wright Labs (Reference 20). The referenced work reported cyclic excursions to 815°C (1500°F) whereas the excursions in this project did not exceed 650°C (1200°F) which is a very realistic temperature maximum for this class of MMCs in gas turbine engine applications. This can be explained by the difference in the fiber residual stress at these two temperatures. Since fiber stress and related strain govern ultimate failure as discussed in Section 4.10.

4.2.2.2.1.2 Interrupted Tensile Test

Noting the bilinear nature of the tensile curves, the test was interrupted on one of the thermally exposed samples at a stress of about 1089 MPa (158 ksi) and unloaded. Upon reloading, the initial linear portion extended to a much higher stress than seen initially, finally breaking into the lower slope at the same stress and strain at which the specimen was initially unloaded. The total stress-strain history less the initial unloading curve is seen in Figure 51. This dependence of the bilinear "break" on the early strain history may add an additional degree of complexity to the incorporation of tensile data in the behavior or life prediction models for this program. Section 4.10.5 presents an explanation for this behavior and presents an approach that may be used to incorporate tensile data to the life prediction models.
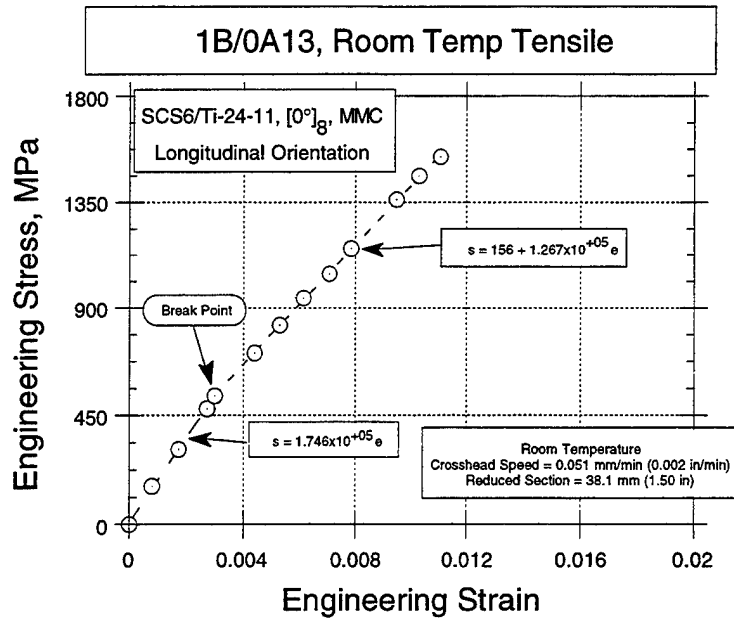
Figure 48. Room Temperature tensile test, at 0° orientation, of 8-ply MMC (SCS6/Ti-24-11). Note that the initial modulus = 174.6 GPa.
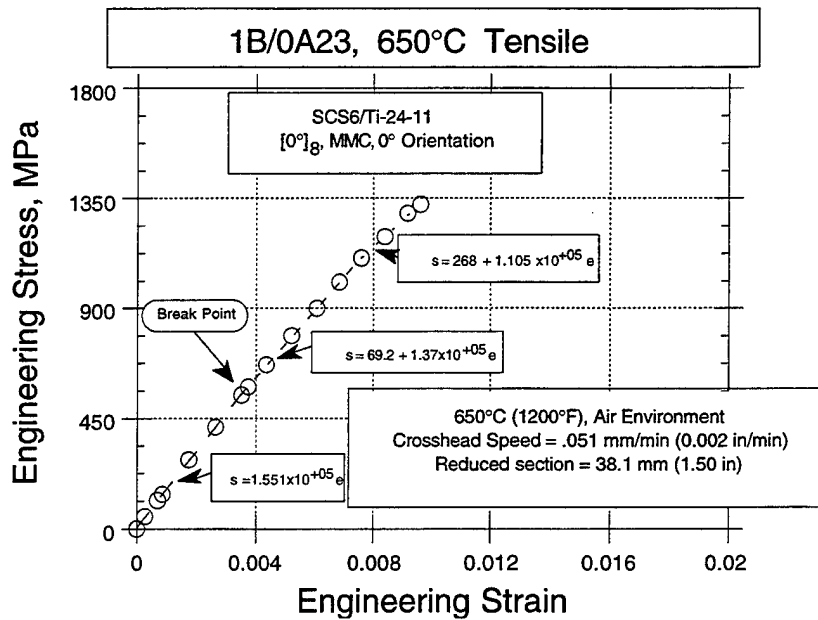
Figure 49. 650°C tensile test, at 0° orientation, of 8-ply MMC (SCS6/Ti-24-11). Note that the initial modulus = 155.1 GPa.
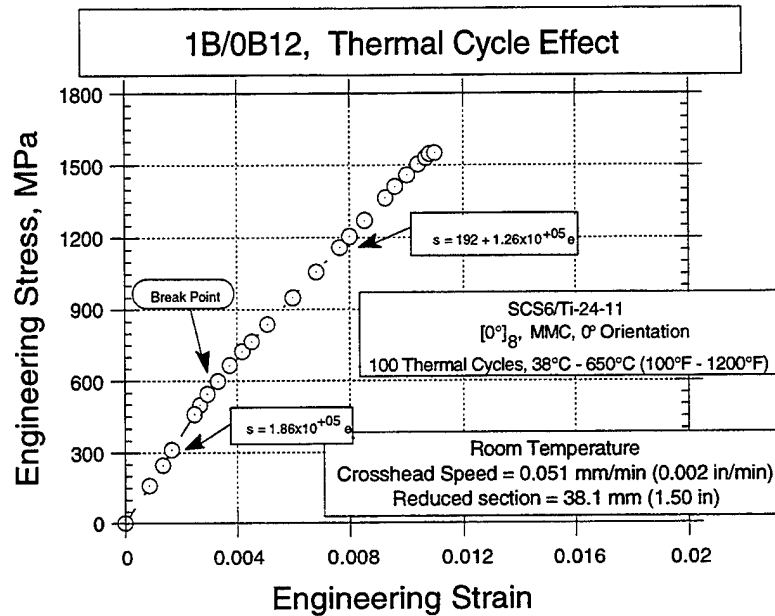
Figure 50. Room Temperature on thermally cycled (in air) MMC tested at 0° orientation (SCS6/Ti-24-11).
Note that the initial modulus = 186 GPa.
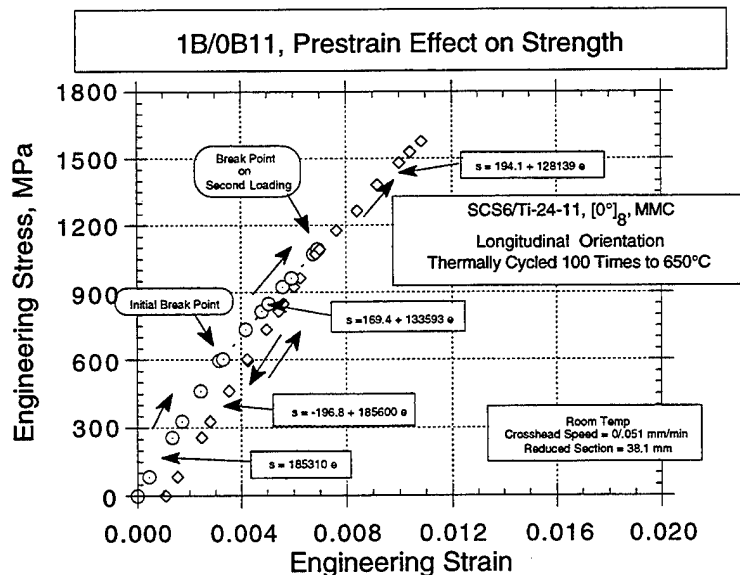
Figure 51. Room Temperature tensile test with intermediate unloading from a point beyond the initial change in slope.
Thermally cycled (in air). Tested at 0° orientation, of 8-ply MMC (SCS6/Ti-24-11). Note that the initial modulus = 183.5 GPa.

4.2.2.2.2 Transverse Tensile Properties

Transverse tensile tests at room temperature, for unexposed and thermally exposed samples are compared in Figure 52 and Figure 53 respectively.

4.2.2.2.2.1 Effects of Thermal Exposure

Close examination reveals very similar curves, indicating little effect of the exposure on the tensile properties, Figure 53.

4.2.2.2.2.2 Bilinear Behavior

Interpretation of the observed bilinear tensile curves for both the unexposed and thermally cycled cases being that the curve "break" is the stress at which the matrix pulls away from the fiber. It is also noted that the strength is about 207 MPa (30 ksi) in either case and the strain to failure less than 0.2 percent; both of which are far lower than obtained in the longitudinal tests. The strength correlates well with the matrix strength, discounted by its volume fraction and a K_t effect of the fibers (fiber cavity) of about 1.8. It is important to note that the matrix is very close to the yield point in the longitudinal direction and this must have an effect on the stress strain behavior in the transverse direction.

4.2.2.2.2.3 Elevated Temperature Tensile Test Results

The bilinear stress-strain curve is not seen when the 90° samples are tested at 650°C (1200°F) (Figure 54). Here the strength to the "break" is significantly reduced to about 48 MPa (7 ksi) and ultimate strength of less than 138 MPa (20 ksi). This is quite unlike the longitudinal samples which showed no noticeable effect of temperature.

4.2.2.2.2.4 Effects of Temperature on Strength of 90° MMC Samples

Figure 55 shows the decrease in both the stress at first break in linearity and the tensile strength as a function of temperature.

104
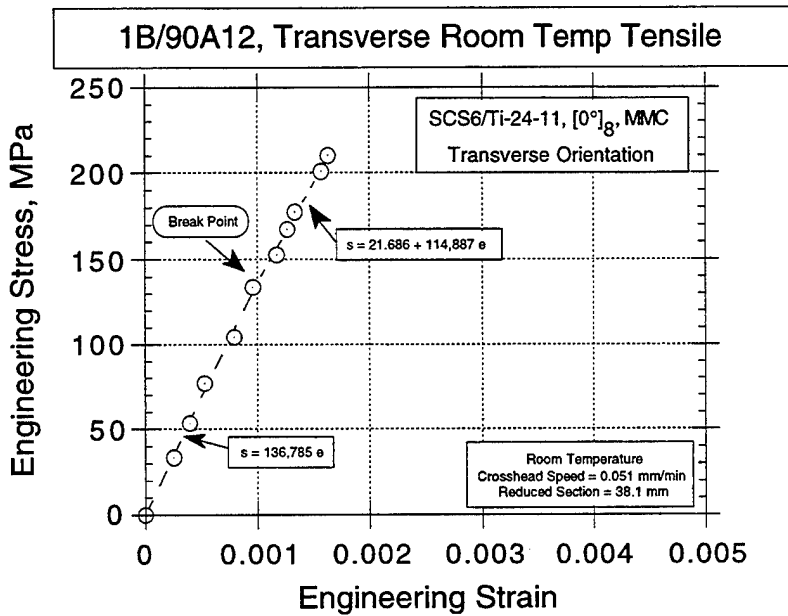
Figure 52. Room Temperature tensile test on unexposed sample, tested at 90° orientation (SCS6/Ti-24-11).
Note that the initial modulus = 136.8 GPa.
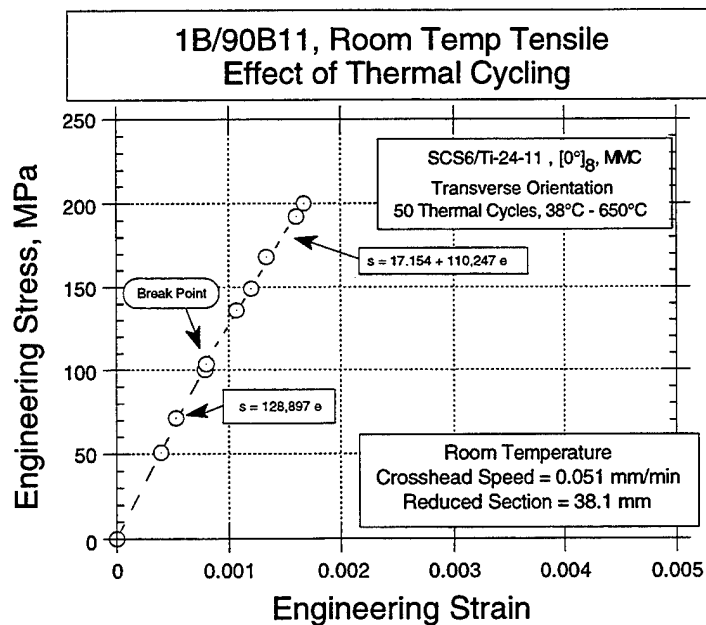
Figure 53. Room Temperature tensile test on thermally exposed (in air) sample, tested at 90° orientation (SCS6/Ti-24-11).
Note that the initial modulus = 128.9 GPa.
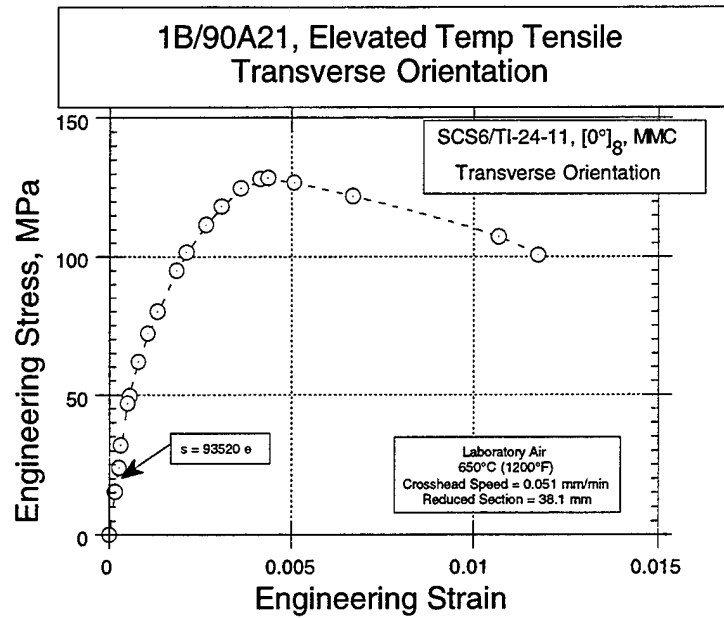
Figure 54. 650°C tensile test on unexposed sample, tested at 90° orientation (SCS6/Ti-24-11). Note: Initial modulus = 93.5 GPa.
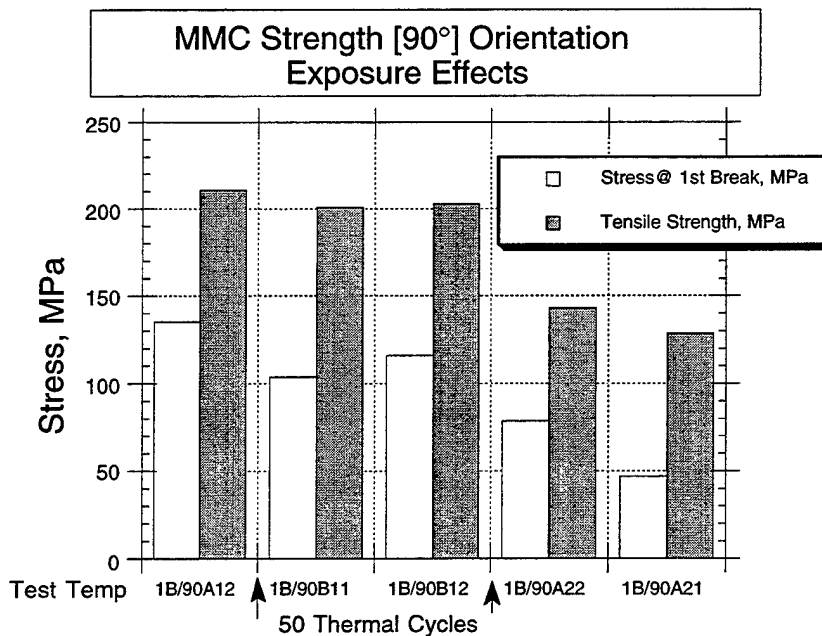
Figure 55. Exposure effects and test temperature on strength of [0°]$_8$ MMC tested normal to reinforcement fiber (SCS6/Ti-24-11).

4.2.3 Room Temperature Shear Test Results, Normal to Fiber Orientation

4.2.3.1 Experimental Procedure

Specimens machined according to Figure 56 having the reinforcing fibers oriented parallel to the long direction of the specimen were outfitted with strain gates at ±45° on both sides of the specimen at the point of highest shear stress. The readings were taken individually and after data reduction they were integrated to produce a shear stress vs. shear strain plot for the plane of highest shear.

The test fixture and test procedures used were those detailed in Reference 21 and all tests in this program were run at room temperature.

4.2.3.2 Shear Test Results

The final results of the two room temperature shear tests are plotted in Figure 57 and Figure 58. A shear modulus of 127 to 130 GPa and a shear yield strength of near 208 MPa are evident. Encouragingly, the two specimens gave nearly identical results.
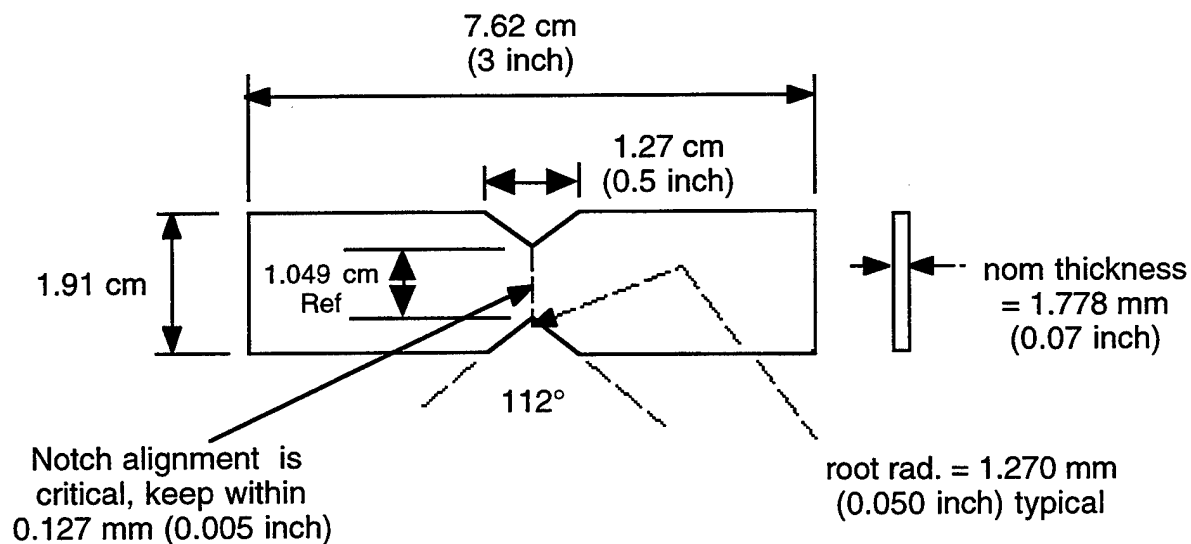
Figure 56. Iosipescu shear test specimen.

IOS-1, Room Temperature Shear Strength

0.2% YS = 206 MPa

SCS6/Ti-24-11 [0]₈ MMC
Shear Normal To Fibers

Room Temp
Iosipescu Shear Strength Test
Four Strain Gages, Two Per Side
Notch Angle = 110°, W= 19.1 mm (0.75 in)
Shear Width = 10.2 mm (0.40 in)

Shear Modulus = 130 GPa (18.85 Mpsi)

Shear Stress, MPa

Micro Strain
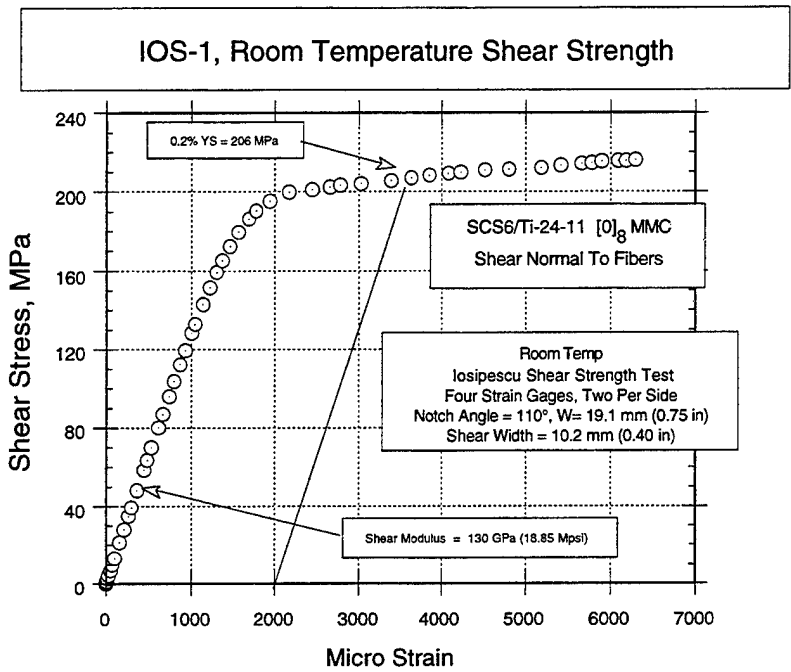
Figure 57. Room temperature shear strength results for Ios-1.

IOS-2, Room Temperature Shear Strength

0.2% YS = 210 MPa

SCS6/Ti-24-11 [0]₈ MMC
Shear Normal To Fibers

Room Temp
Iosipescu Shear Strength Test
Four Strain Gages, Two Per Side
Notch Angle = 110°, W= 19.1 mm (0.75 in)
Shear Width = 10.2 mm (0.40 in)

Shear Modulus = 127 GPa (18.45 Mpsi)

Shear Stress, MPa

Micro Strain
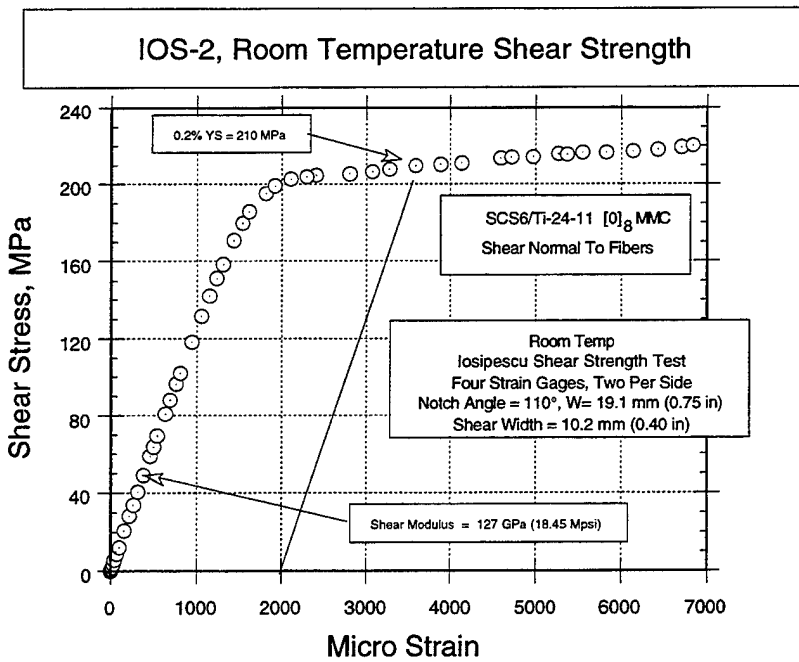
Figure 58. Room temperature shear strength results for Ios-2

108

4.2.4 Room Temperature Poisson Ratio, Matrix Material

4.2.4.1 Experimental Procedure

A standard tensile test coupon, described by Figure 42, was instrumented with longitudinal and long transverse strain gages, a longitudinal extensometer and an extensometer rigged to measure short transverse strains. The specimen was pulled at a constant strain rate of 0.002 using strain control mode in an MTS servo-hydraulic test machine fitted with hydraulically actuated grips. Electronic digitized data were collected during the test and the extensometer outputs were also concurrently plotted on an X-Y recorder as a backup and as a real-time indicator of the system's output. The slopes of the longitudinal, long transverse and short transverse stress strain curves were used to compute the Poisson's ratio. Two tests were run; one on a specimen which had previously been strained beyond yielding and one on an unstrained specimen.

4.2.4.2 Experimental Results

Examination of the data in Table 15 reveals a very highly directional value of Poisson ratio with the thickness direction being very much stiffer than the in-plane direction. This correlates well with the tensile strain measurement results shown in Table 13 wherein it is seen that although the tensile plastic strain to failure of NEAT foil is rather high (>.12) the thickness strain is nil. An overwhelming portion of the plastic Poisson strain being taken up in the long transverse direction. This highly textured nature of this material is also verified by hardness a study discussed in Section 4.2.2.1.4.

The low value of Young's modulus obtained in this test confirms the earlier measurements reported in Table 13. Furthermore, the Young's modulus and the Poisson ratio is not significantly affected by prior plastic strain.

Table 15.   Poisson Ratio on NEAT Foil

Material	Young's Modulus	Poisson Ratio, LT	Poisson Ratio, ST
Ti-6Al-4V sheet	111.7 GPa (16.2 Kpsi)	0.30	0.29
Ti-24-11 Prestrained	59.0, 57.4 GPa (8.56, 8.32 Mpsi)	0.67, 0.63	0.14, 0.06*
Ti-24-11 Unstrained	58.2, 57.9 GPa (8.44, 8.40 Mpsi)	0.62, 0.63	0.12, 0.15

Duplicate test were run as indicated
*   Extensometer alignment problem, data point is unreliable

4.3   Results of Impact Damage Assessment

4.3.1   Objective

As part of the job of assigning residual life to damaged MMC samples, it was necessary to devise a simple method to induce this damage. Because impact damage is always possible in any structure due to handling and operations and it is not likely to be obvious from the surface, a FOD related test was envisioned. Simple impact by a defined projectile with known kinetic energy was the route pursued in this program and the following is a discussion of the test procedures and the results.

4.3.2   Experimental Procedure

For tests 1, 2, and 3, a longitudinal specimen was cut from panel F914008D (panel dimensions where 15.24 cm (6 inches) in length with a 1.27 cm (0.5 inch) width. This beam was suspended between two parallel cylindrical rods of 0.635 cm (0.25 inch) diameter spaced 5.08 cm (2.0 inches) apart. The specimen was taped in place. For tests 4, 5, 6, and 7, machined, transverse LCF specimens were mounted flush to a flat steel anvil with no suspended length.

Table 16.   Impact damage test parameters.

Trial	Ball Weight (g)	Ball Diameter (mm)	Height of Drop (m)	Potential Energy (Newton-Meter)
1	31.93	19.52	1.041	0.326
2	31.93	19.52	1.702	0.532
3	31.93	19.52	3.155	0.994
4	31.93	19.52	3.155	0.994 *
5	31.93	19.52	3.155	0.994 *
6	31.93	19.52	0.600	0.192 *
7	31.93	19.52	0.610	0.192 *
* Transverse specimens resting on flat, heavy, steel anvil				

A spherical steel ball bearing of 19.52 mm (0.756 inch) diameter, weighing 31.93 grams, was dropped from various heights, through a tubular guide, to the center of the suspended span. The height of each trial is indicated in Table 16 along with the applicable potential energy. No attempt was made to capture the rebound energy or to assign the absorbed energy in the specimen. Tests 4, 5, 6, and 7 were each done on individual LCF specimens with the impact occurring in the gage section. All these LCF specimens were with transversely oriented fibers.

110

4.3.3 Ultrasonic "C" Scan Examination

Ultrasonic "C" scan of the impact zones of tests 1, 2 and 3, using the best techniques developed under this program, showed no indications in the zones associated with any of the trials. UT indications mentioned in earlier reports actually detected an initial defect associated with the initial consolidation of the MMC and was not associated with the impact damage. However, transverse and longitudinal cross sections for microstructural damage assessment were made through the impact center of trial number 3.

The impacted LCF specimens from trials 4, 5, 6, and 7 were fatigue tested in order to assess the degree of degradation associated with the two levels of damage. Results are reported in Section 4.4.3.1.3.

4.3.4 Metallographic Examination

Figure 59 is a composite of micrographs taken transverse to the MMC at the impact center of trial 3, with the impacted surface towards the top of the micrograph. The bottom row of fibers is the row nearest the face opposite the impacted face. What is easily seen is a longitudinal crack propagating from the eighth row of the eight layer MMC up through the fifth row which is half way through and presumably completely through the tensile side of the two dimensional tensile stress field generated by the impact. It is also clear that the earliest cracks propagated around the fibers, separating the reaction zone or the carbon rich layer from the fiber. Because the fifth, or center, row apparently did not exhibit this separation, it is reasonable to conclude that cracks may first pass by the fibers without creating the separation damage to the interface until the higher crack opening displacement in the crack's wake acts upon this part of the system.

Another significant observation is the multiple cracking in the matrix and the apparent tendency of all the crack paths and their parts to be microstructurally sensitive. Figure 60 is an illustration, taken at the end of the crack, showing the crystallographic nature of the transgranular cracking path.

4.3.4.1 Transverse Cracking

A near-longitudinal section was made from impact test 3 to identify fibers cracked in longitudinal tension, as would be expected near the surface opposite the impact zone. Figure 61 shows one of the very few transversely cracked fibers under the impact point. Comparing this with Figure 59, it can be concluded that the MMC has a very weak transverse impact strength.

111

4th layer

100 µm
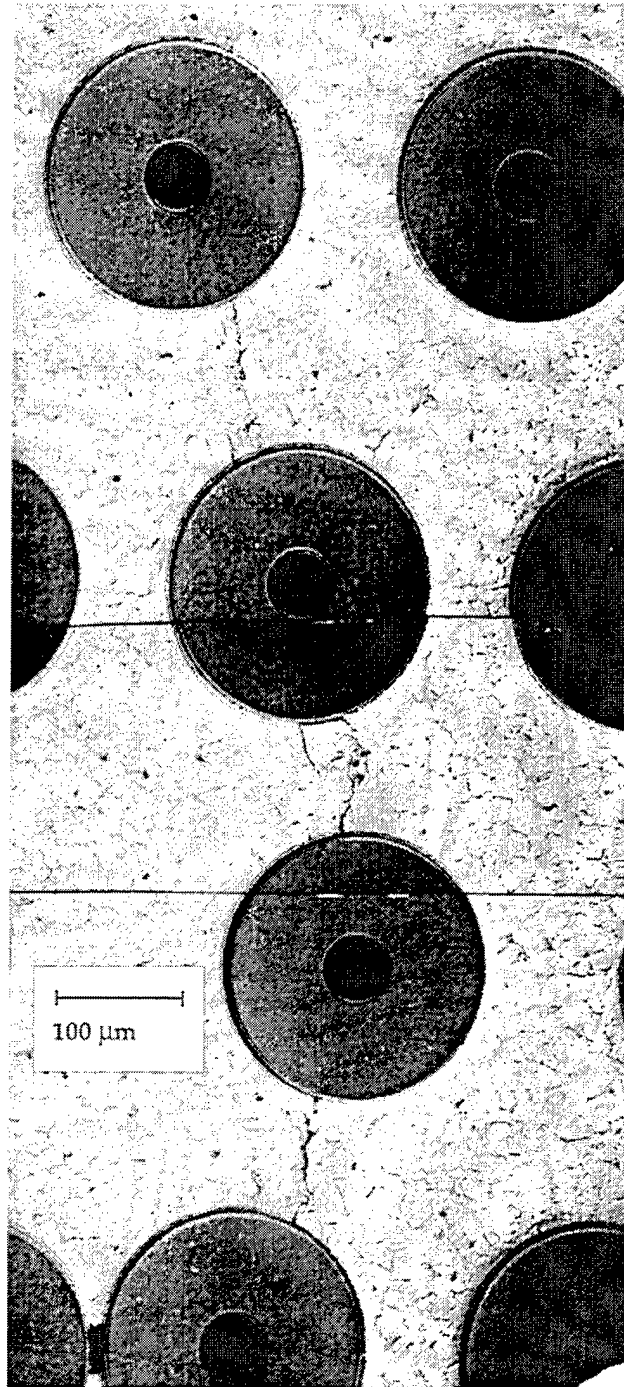
Figure 59. **Transverse section of longitudinal beam impacted from the left with 0.994 n-M energy from a 31.93 g projectile.**
The bottom portion of the photo shows the bottom of the 8-plys of fiber. Note the matrix cracking, interface separations, and the termination of the crack near the 4th layer. [SCS6/Ti-24-11]
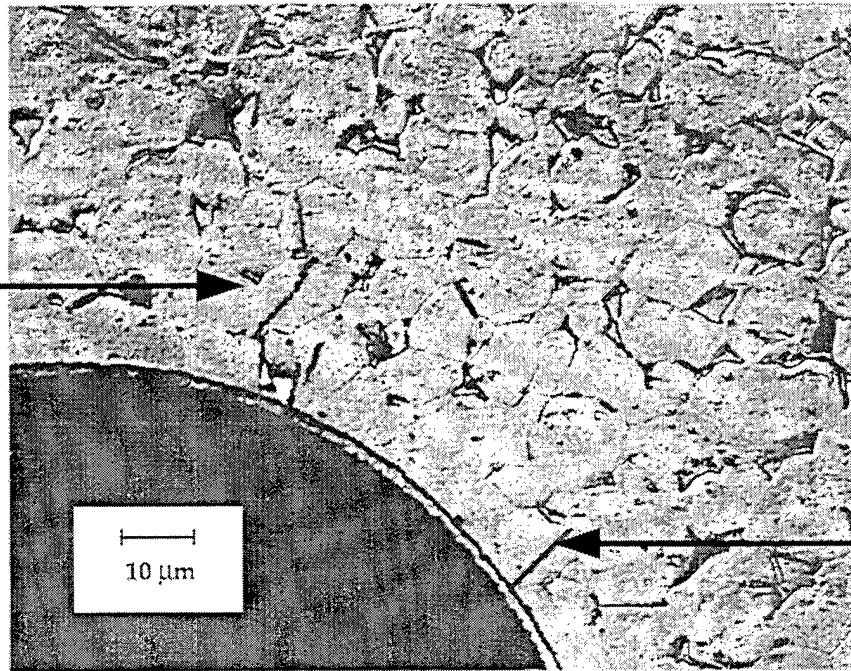
1000X

Figure 60. **Termination of the crack shown in Figure 59.**
Note the transgranular nature of the cracking and the multiple cracks. [SCS6/Ti-24-11]
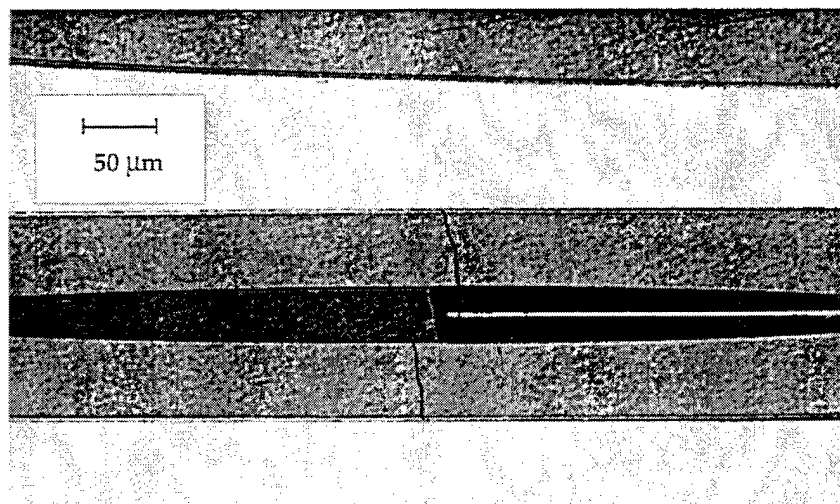
200X

Figure 61. **Cracked fiber in the tensile half of the same specimen described in Figure 59, with a near-longitudinal polish.**
Note: Very few cracks of this kind were found and none so large as the one shown in Figure 59 [SCS6/Ti-24-11].

113

4.3.4.2 Damage to LCF Specimens

A preliminary visual examination of the impacted specimens 4, 5, 6, and 7 indicate severe damage to have occurred with the higher energy level impact. Additional discussions regarding these LCF transverse specimens accompany analysis of the LCF data in Section 4.4.

4.4 Low Cycle Fatigue

4.4.1 LCF of Matrix

4.4.1.1 LCF of Matrix at Room Temperature

4.4.1.1.1 Experimental Procedure for Room and Elevated Temperature Testing

A dog-bone specimen configuration, described by Figure 41, was tested between hydraulically actuated grips in a servo-hydraulic, universal test machine. To avoid buckling, they were run in load control. The first few cycles (usually less than 100 cycles) were run very slowly, monitoring the system compliance until the hysteresis loops became small. The test was then completed at a frequency between 1 and 5 Hz. The total number of cycles to failure was determined and the influences of the stress range and the mean stress identified.

Induction heating was used for the elevated temperature tests, otherwise the same procedures were followed as used for room temperature tests.

4.4.1.1.2 Room Temperature, Matrix only, LCF Results

The LCF strength of the matrix parallels its relatively low tensile strength. Figure 62 shows the results on a linear plot of mean stress vs. cycles to failure. An apparent fatigue limit is seen near 186.2 MPa (27 ksi) mean stress, for a R value near 0.1. For lower R values a lower fatigue limit would be expected, as implied by the lower R value test result in this plot.

A semilog plot of the same data, maintaining the same curve fit equation, is seen in Figure 63 and shows a clear demarcation between LCF and HCF at lives about 10^4 cycles. The high stress end of the curve is anchored with ultimate tensile strength plotted at 0.5 cycles to failure.

Limited material availability precluded more complete development of matrix LCF properties in this program.
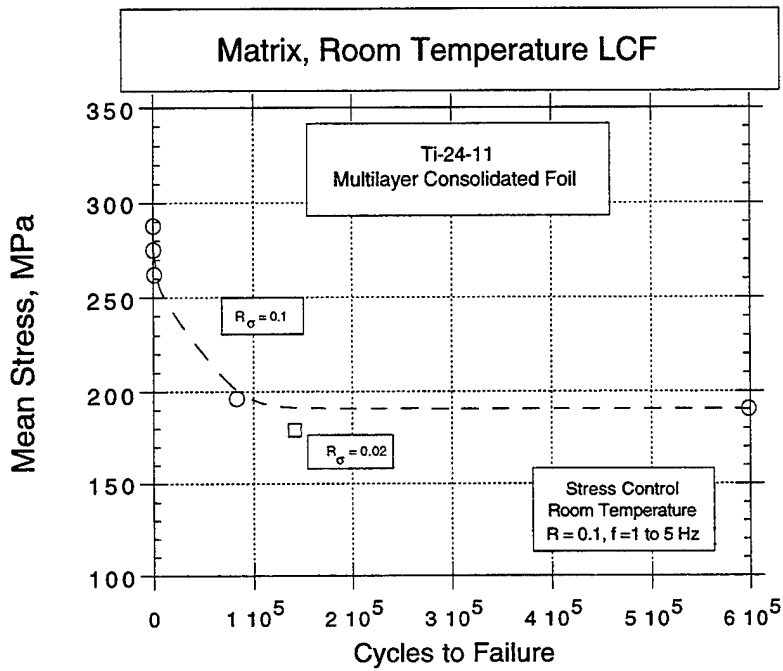
Figure 62. Linear low cycle fatigue plot for matrix only, Ti-24-11 eight layer consolidated foil.
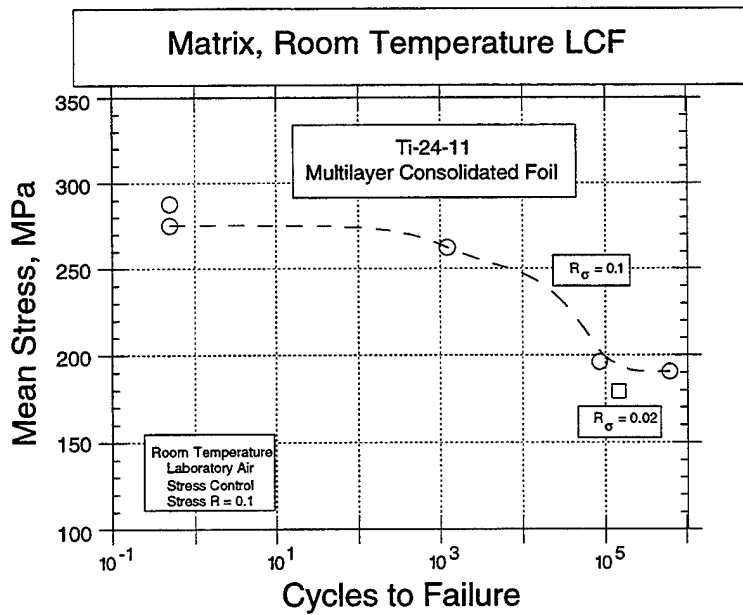
Figure 63. Semi-Log plot of room temperature LCF for matrix-only material (Ti-24-11, multilayer HIP consolidated foil).

4.4.1.2 LCF of Matrix at Elevated Temperature

No testing at elevated temperature was scheduled.

4.4.2 LCF of Longitudinal MMC Specimens

4.4.2.1 LCF of Longitudinal MMC Specimens at Room Temperature

4.4.2.1.1 Experimental Procedure

Dogbone specimens of the same configuration as used for the monolithic material were tested in a similar manner. Some tests were stopped as the system compliance was noticeably increased and replicas made of the specimen surface. In each of these cases, small cracks were detected and upon resumption of the testing, again in each case, failure occurred within a very few cycles (less than 100). In order to study the mechanisms involved, a few of the tests were terminated upon detection of the first crack. The LCF curve is made up of the results of a mix of these conditions but on the scale involved a 10 to 100 cycle additional life is insignificant.

One specimen was tested at the RISC as part of the characterization of residual stresses, and their result falls right among those tested at AE.

Due to limited material and test resources, a more detailed LCF characterization was not possible.

4.4.2.1.2 Room Temperature LCF Results for Longitudinal MMC

Figure 64 shows the combined results of the AE testing and the RISC testing. The form of the curve is similar to that seen with the monolithic tests at room temperature, although in this case, maximum stress is used, all at an R value of 0.1. The demarcation between LCF and HCF lies between 10^4 and 10^5 cycles to failure. As with the monolithic tests, the high stress part of the plot is anchored with tensile strength at 0.5 of one cycle. At the HCF end of the plot, a runout stress of about 689.5 MPa (100 ksi) is noted, and this is only about twice that experienced with the monolithic material.

The level of this apparent runout stress takes on special significance when examining fatigue crack growth results, summarized in Section 4.5.2.6. These define a maximum stress at which a crack will not grow.

4.4.2.1.3 Effect of Prior Cyclic Thermal Exposure on LCF

Selected [0°]$_8$ samples were cycled, in air, between 38°C (100°F) and 650°C (1200°F) for 100 cycles prior to room temperature testing. The LCF results are plotted on Figure 65,
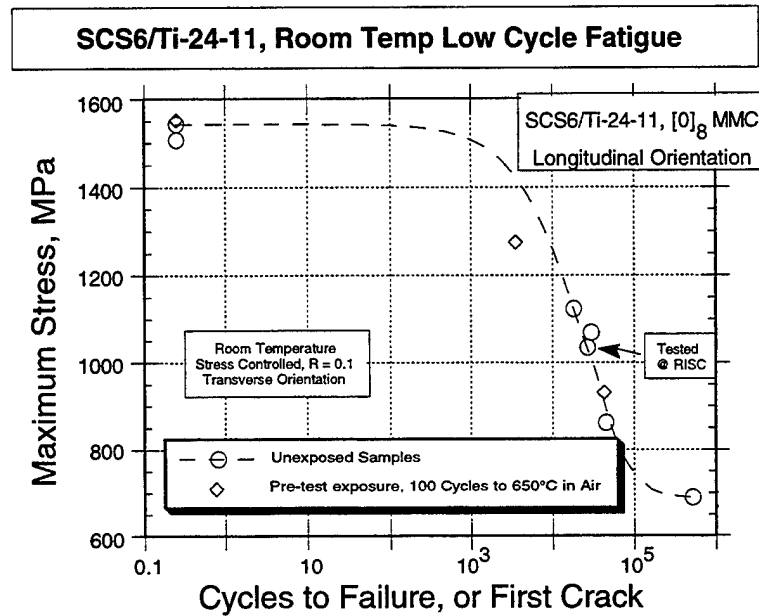
Figure 64. Room temperature low cycle fatigue for [0°]₈ MMC tested in 0° orientation (SCS6/Ti-24-11).

and indications are that the thermal exposure had little, if any, effect on subsequent LCF life.

4.4.2.1.4 Stability of Residual Stresses During Room and Elevated Temperature LCF Testing

As discussed in Section 4.1.7, in order to predict fatigue properties, it is necessary to understand the manner in which residual stresses in the MMC are affected by service conditions. To this end, a brief study of the residual stresses imposed during cooling from the MMC consolidation process, was carried out by RISC.

X-Ray diffraction measurements were carried out on four LCF samples. Two were tested at room temperature and two at elevated temperature. One of the specimens at each temperature was tested to failure and the second one was tested to half the life of the specimen that was tested to failure. The ones at room temperature had residual stress measurements several times before failure. The results of the residual stress measurements are shown in Table 17 and Figure 65. The conclusion from these tests is that the residual stresses relax quite rapidly into the testing. The reason for this behavior was understood through a micromechanical analysis performed after this testing. The analy-
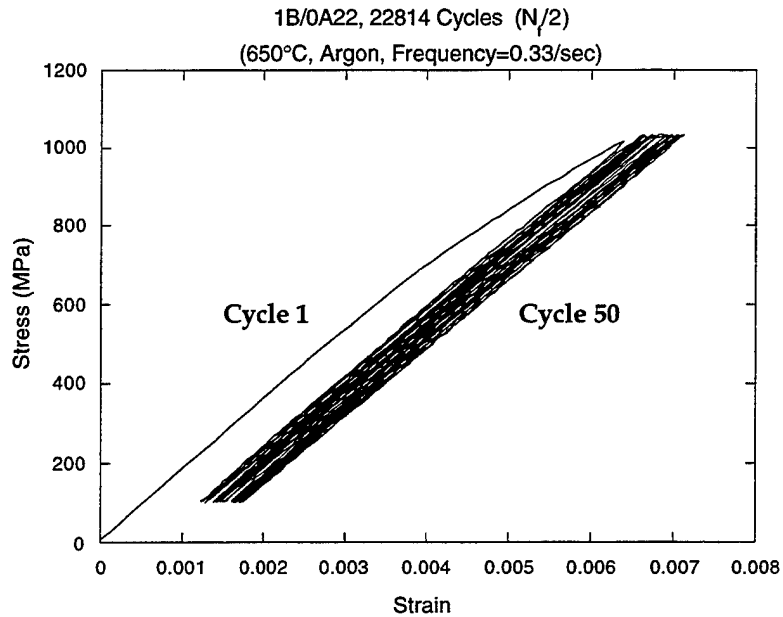
Figure 65. Composite stress-strain cycles showing cycle 1, 3, 5, 7, 10, 30, and 50.

sis is discussed in Section 4.10 and it indicates that the stress relaxation occurs during the first unloading.

Table 17. Longitudinal matrix residual stress (MPa)

Specimen	°C	N_f	Cycles
			0	250	500	$N_f/2$	Nf
1B/0A11	21	26690	407	165	165		172
1B/0A12	21		427	179	165	159	
1B/0A21	650	46628	393				269
1B/0A22	650		379			131	

118

4.4.2.2   LCF of Longitudinal MMC Specimens at Elevated Temperature

Results of elevated temperature LCF tests run in air under conditions otherwise similar to the room temperature tests, are plotted along with the room temperature results in Figure 66. This includes results from test specimens having had cyclic pre-exposures and includes one test run in an argon environment. Examination of the figure leads to a conclusion that at the higher stresses, elevated temperature results in lower life, while at 550° (1022°F), a longer life is projected. Perhaps this is due to environmental hardening of the specimen surface and the effect would be surface to volume ratio dependent. This strengthening is not so evident for the 650°C (1200°F) tests although there is some hint that cyclic exposure to 650°C (1200°F), prior to the 650°C (1200°F) LCF test, may provide a life increase in the lower fatigue stress range. When comparing the test run at 650°C (1200°F), in argon, with that run in air, there appears to be a decided advantage to the inert environment for maximum stresses on the order of 1000 MPa (145 ksi). The air environment does have an adverse effect on fatigue performance of this MMC system. Although prior exposure does not adversely affect tensile strength (Section 4.2.2.2.2.1), it does degrade low cycle fatigue.
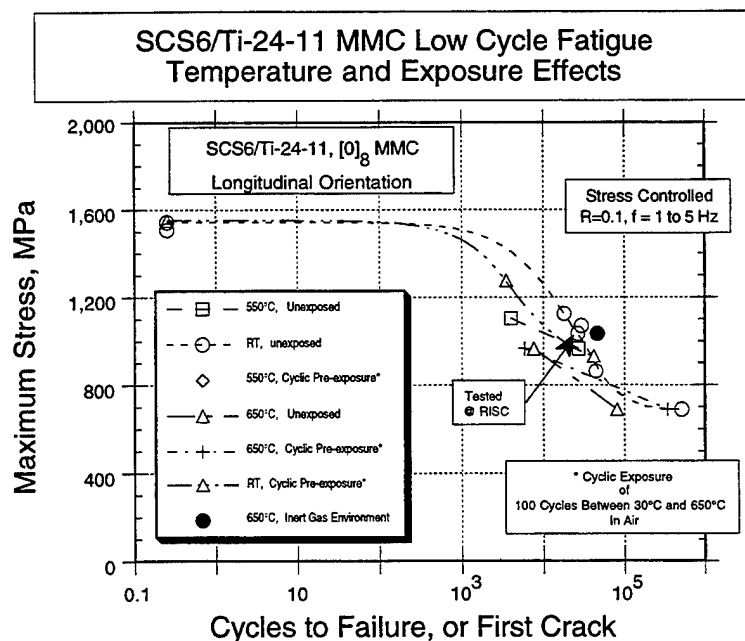
Figure 66.   LCF for longitudinal [0°]$_8$ MMCs showing effects of test temperature, prior exposure and inert environment on LCF life. (SCS6/Ti-24-11).

119

The time dependency of environmental degradation of MMCs is a complex issue and deserves specific attention beyond the scope of this program and is very likely to be MMC system dependent.

4.4.3 LCF of 90° MMC Specimens

4.4.3.1 LCF of 90° MMC Specimens at Room Temperature

4.4.3.1.1 Experimental Procedure

The [90°]$_8$ specimens were tested in a manner similar to the monolithic material, using the same specimen configuration.

4.4.3.1.2 LCF Test Results, MMC, Transverse Orientation

The room temperature LCF test results on transverse specimens are shown in Figure 67, where an apparent fatigue limit is seen near 179 MPa (26 ksi) maximum stress, at an R = 0.1. This is about half of that obtained with the matrix alone, as discussed in Section 4.4.1.1.2. This ratio is maintained, approximately, over the entire range of lives. Hence, it might be concluded that the [90°] MMC has about half of the fatigue strength as the matrix alone, at least at an R = 0.1.
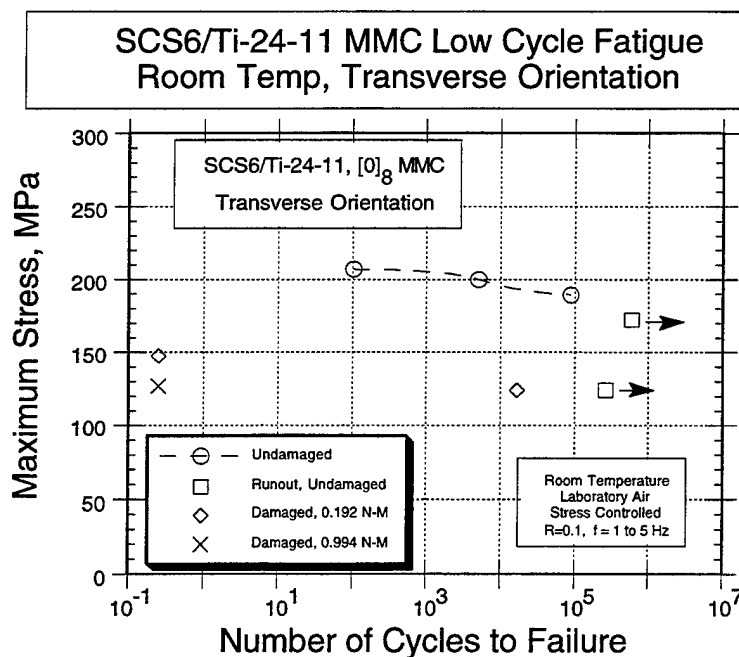
Figure 67.   Room Temperature LCF test results for 90° MMC.
Some specimens were damaged as described in Table 13.

120

4.4.3.1.3   Effect of Damage on LCF of MMC

In order to assess the effect of physical damage to the MMC, machined, [90°] MMC LCF specimens were damaged by dropping the same 31.93 gram ball bearing, discussed in Section 4.3.2, from heights of 61 cm (24 in) and 355 cm (132 in) on them. The specimens were taped flat on a steel plate to avoid bending. The damaged specimens were then tested in LCF at maximum stresses between 124 and 152 MPa (18 and 22 ksi).

Results of these tests are seen in Figure 67, along with the undamaged specimen results. It is clear that even the light amount of damage has resulted in significant reduction in fatigue life of these transverse specimens with a 55 to 68.9 MPa (8 to 10 ksi) reduction in fatigue strength. Somewhat greater debit is seen with the greater impact damage energy.

4.4.3.2   LCF of 90° Specimens at Elevated Temperature

No LCF testing at elevated temperature was planned for transverse MMCs.

4.4.4   Comparison of Room Temperature LCF Results With Previous Work Reported in WRDC-TR-89-4145.

In an attempt to augment program data with data taken in a previous program, which used similar constituent materials, room temperature LCF data from this program were compared with that reported by Gambone (Reference 22). Figure 68 shows the two groups of data plotted together. Some of the data in the present program having prior cyclic thermal exposures are also included without distinguishing them. As can be seen, the higher stress samples of this program exhibit considerably greater lives than those from Reference 22. At the lower stresses, near run out, the distinction among them is not clear. As will be discussed in Section 4.5, the run out stress for this class of MMCs may be associated with a threshold stress, below which cracks will not propagate, at least at room temperature.

It is clear from this plot, that the LCF data from Reference 22 cannot be merged with data from this program for the purposes of predicting LCF behavior.

4.5   Fatigue Crack Propagation

All FCP testing was accomplished on single edge notched (SEN) specimens described in Section 4.2.1.1. Various additional surface polishes were applied to selected test specimens to enhance analysis. Additional conditioning of the notch to reduce its radius soon was adopted in order to encourage the development of a single fatigue precrack.
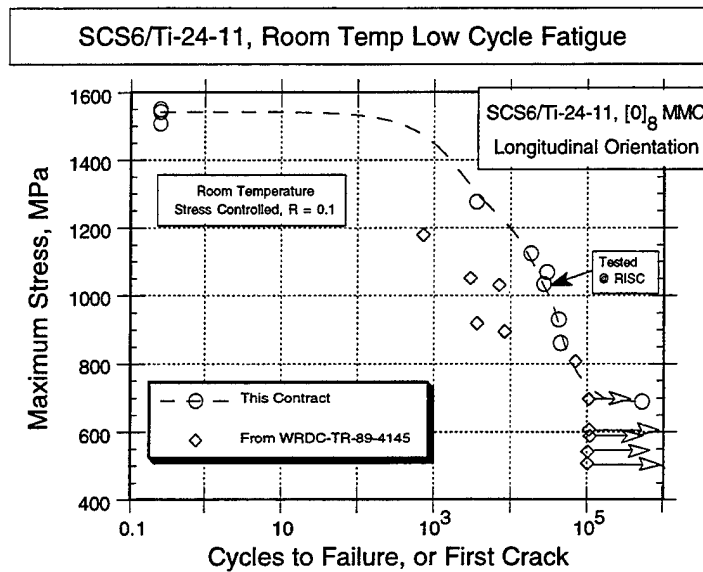
Figure 68. Room Temperature LCF comparison of results of this program with those of Reference 22.

Room temperature LCF behavior is sufficiently different to preclude merging of the LCF data.

4.5.1 Fatigue Crack Propagation in the Matrix

4.5.1.1 Experimental Procedure for Matrix FCP Testing

The specimen described above was instrumented for potential drop (PD) control as described by Johnson, et al. (Reference 23) of the stress intensity and a PC based control program, as described in ASTM E647. The system was used to preprogram the rate of change in ΔK, monitor the crack length and keep a record of the growth rate and the ΔK as a function of the number of cycles. The K solution used by the program is the one developed by D. Voron, C. Date, D. Wu and C. Desadier at AE with the assumption of rigidly gripped specimen ends and an elastically compliant unsupported length on the order of 76.2 mm (3.0 in).

This solution, based on a finite element analysis of the above described arrangement, is described below.

$$K = \sigma \sqrt{\pi a} \; f\left(\frac{a}{w}\right)$$ [108]

where

$$f\left(\frac{a}{w}\right) = 1.11 + 0.318 \left(\frac{a}{w}\right) + 2.673 \left(\frac{a}{w}\right)^2$$ [109]

122

4.5.1.2 FCP Results for Matrix Material at Room Temperature

4.5.1.2.1 Programmed ΔK test

Figure 69 displays the room temperature FCP results on the matrix material with a stress ratio R = 0.1. The curve was constructed of four components; a constant stress component 191.7 MPa (27.8 ksi) net section stress and an initial notch length of 1.27 mm (0.050") which was used to initiate the fatigue crack and grow it to a length where it was well beyond the initial plastic zone. This was followed by a programmed decreasing ΔK segment (K shedding) in an attempt to find a threshold. When the growth rate had decreased to about 1.52×10^{-9} m/cycle (6×10^{-8} in/cycle), the third segment was started and this involved an immediate adjustment in load to a ΔK of about 8.4 MPa$(m)^{0.5}$ (7.6 ksi $(in)^{0.5}$). This was the beginning of a programmed increasing ΔK (K Increase) which lasted until the crack growth rate approached 2.8×10^{-6} m/cycle (1.1×10^{-4} in/cycle) at which time the test was completed under constant load control starting at the last load to be recorded in the previous segment.

M1A81, Room Temp. Fatigue Crack Growth

Ti-24-11 Multilayer
Consolidated Foil Matrix
Room Temperature
R=0.1, SEN Specimen

Recovery From
Large, Sudden, Increase in ΔK

Effect of Initial
Plastic Zone in Notch

○ Initial Segment, Const. Nom. Stress
□ Secont Segment, Decreasing K
◇ Third Segment, Increasing K
✕ Fourth Segment, Const. Nom. Stress

da/dn, Meter/Cycle

Δ K, MPa $(m)^{1/2}$
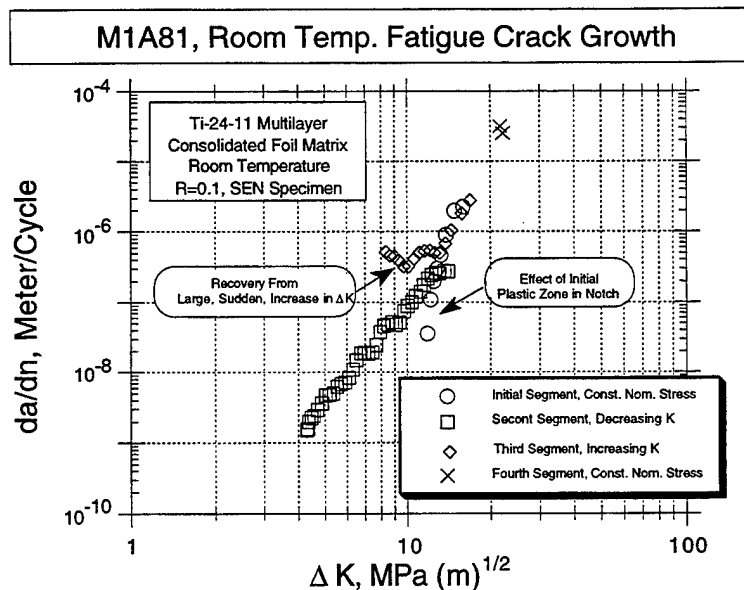
Figure 69. Room temperature crack growth for the matrix only material indicating "Near Paris Law" behavior over a wide range of ΔK.
Ti-24-11, multilayer consolidated foil)

123

4.5.1.2.2   Frequency Effects

Test frequency was periodically varied for one room temperature test between 3.333 and 0.333 Hz for a specimen tested with a load ratio, R = 0.1. Figure 70 is the a vs. N plot for this test with the various test frequency zones indicated and Figure 71 is the conventional plot of ΔK vs. da/dN, which compares quite well with the main part of the curve of Figure 69, indicating that not only is there little frequency effect at this stress ratio but also that, within the test parameters used, the rate or sense of the change of ΔK has little effect on crack growth. In both cases, however, the curve is quite steep with threshold K values not far different from those at failure an approximation of fracture toughness. Figure 72 plots the growth rate vs. crack length in order to pick up any potential transient effects. In this case there are none.

Testing at the higher stress ratio, R = 0.5, is a different matter. Figure 73 is the a vs. N plot for this test while Figure 74 presents the conventional plot of the results. The extreme outlyers indicate transients of over an order of magnitude higher growth rate. In order to help identify the cause, the data were plotted as growth rate vs. crack length in Figure 75. With a change in test frequency, the transients seem to occur. The implications of this are not clear. When changing the frequencies, as occurred at various times throughout all crack growth tests, replicas were made of both faces in the cracked region in order to precisely identify the crack length and anchor and recalibrate crack lengths determined by the Potential Drop (PD) method. While doing this, a minor load was maintained and concurrent plastic deformation may have occurred during the ensuing time period. This, in turn, may have influenced response to the next few fatigue cycles. Indeed it may also be a result of the change of test frequencies at this high R value.

The fact remains, however, that with the lower R, Figure 72, exhibited no such transients despite identical specimen handling and replication procedures.

124
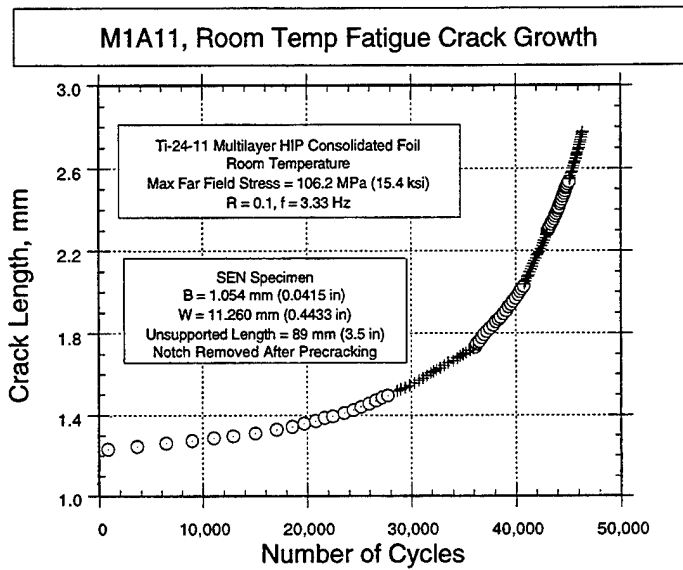
Figure 70. Matrix crack length vs. cycles for room temperature crack growth in matrix only material.

Test was under a constant far field stress of 106.2 MPa with a frequency of 3.33 Hz interrupted with 3 segments of 0.333 Hz.
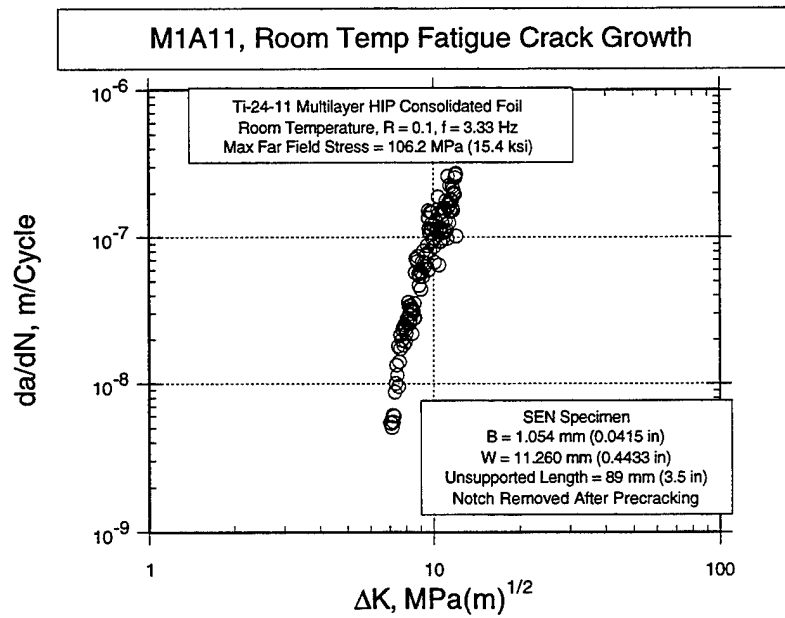
Figure 71. Matrix crack growth, in the form of da/dn vs. ΔK for the specimen of Figure 70.

125
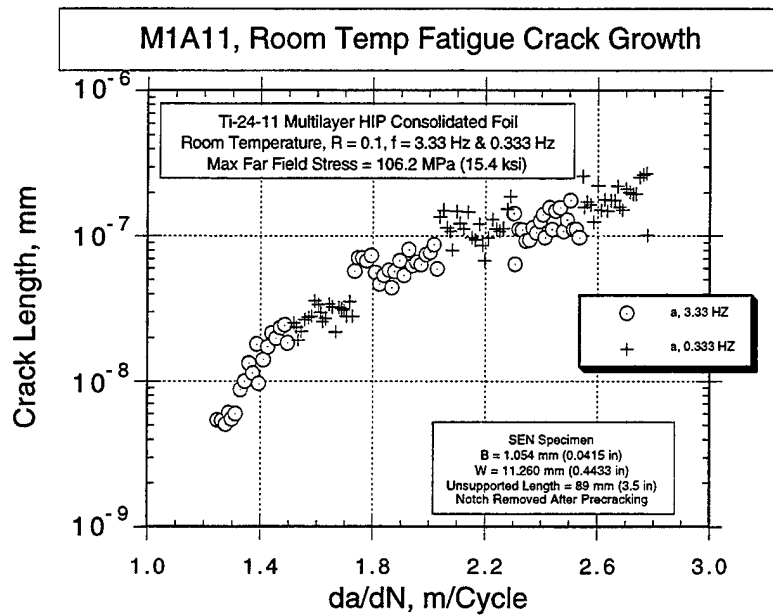
Figure 72. Matrix crack length vs. cycles for matrix material showing frequency effects when R = 0.1.
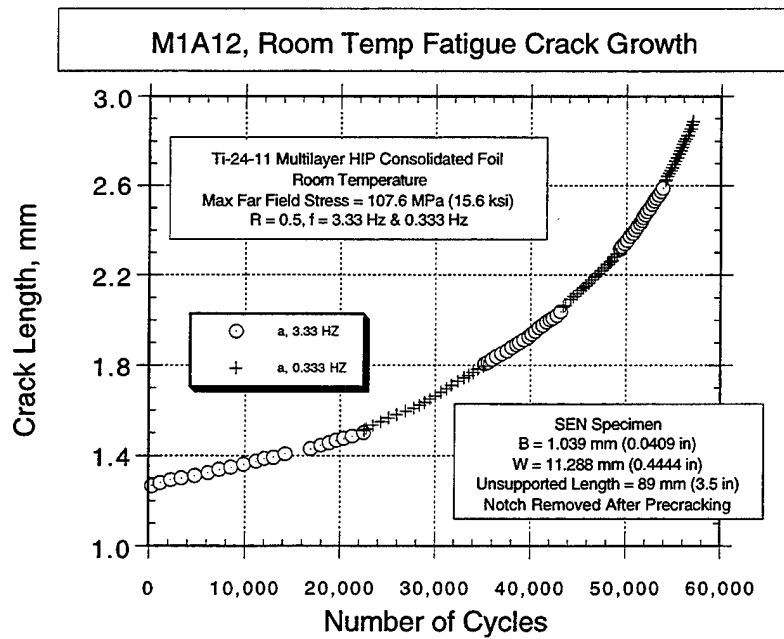
Figure 73. Matrix crack length vs. cycles for R = 0.5.
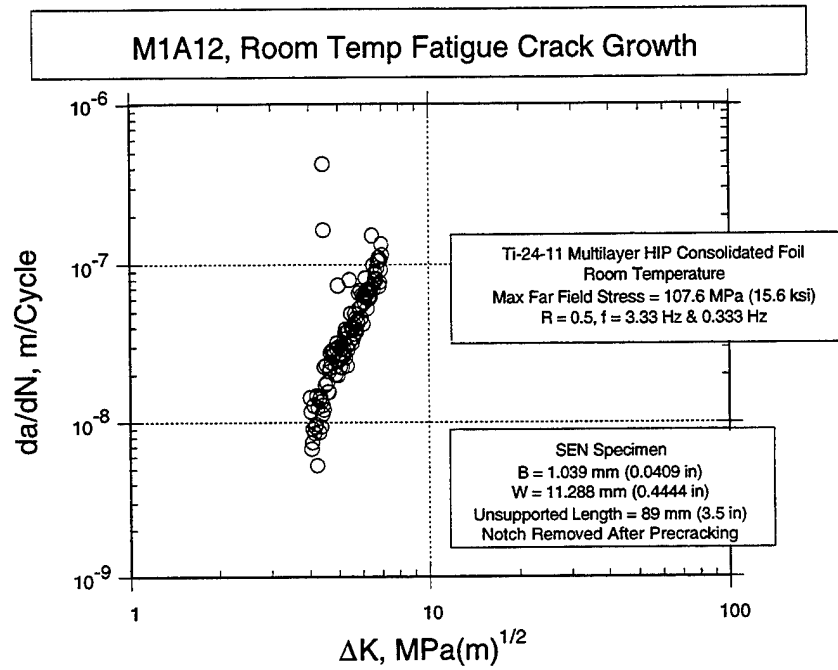
Figure 74. Material matrix, da/dn for the R = 0.5 case showing the accelerated growth rate.
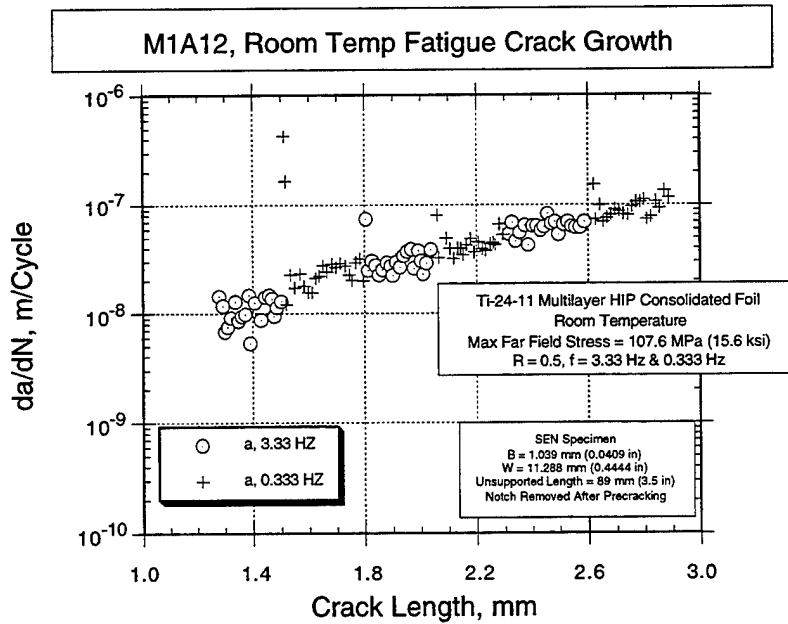
Figure 75. Illustration of the influence of changing test frequency on crack growth rate for matrix material.

4.5.1.3   FCP Results for Matrix Material at Elevated Temperature

4.5.1.3.1   450°C Fatigue Crack Growth in Matrix Material

A single crack growth specimen was tested at 450°C, using the same specimen and techniques described for the room temperature tests, Section 4.5.1.1. The maximum far field stress, in this case, was held constant at 137.9 MPa (20 ksi). The starting crack length, including notch was 1.433 mm (0.0564 in). The crack growth results for this specimen are seen in Figure 76 and Figure 77. At this temperature, the matrix is well behaved, exhibiting an apparent fracture toughness near 30 MPa(m)$^{0.5}$ and a threshold for crack growth at about 10 MPa(m)$^{0.5}$.

4.5.1.3.2   550°C (1022°F) Fatigue Crack Growth in Matrix Material

Two 550°C (1022°F) Fatigue Crack Growth tests were run with the same specimen geometry, including the initial crack length, with only the far field stress being the major variable. As expected, the test run with 103.4 MPa stress, Figure 78, had a longer life than did the higher (137.9 MPa) stress sample, Figure 79. The conventional da/dN vs. ΔK plots, Figure 80 and Figure 81, indicate a higher ΔK threshold, 6 or 7 MPa(m)$^{0.5}$ and for the lower far field stress of 103.4 MPa, compared to about 4 MPa(m)$^{0.5}$ for the 137.9 MPa test. In both cases, however, fracture toughness is near 35 MPa(m)$^{0.5}$.

The effect of a 90 second hold time at maximum load was investigated at this temperature with the a vs. N plot seen in Figure 82. The hold time data are highlighted. Converting this information to the conventional da/dN vs. ΔK plot, Figure 83, displays a few points lying far above the trend. Figure 84 is a da/dN vs. a curve with the hold time data highlighted. It clearly shows the hold time contributing not only to the wide scatter but to the extraordinarily high growth rates.
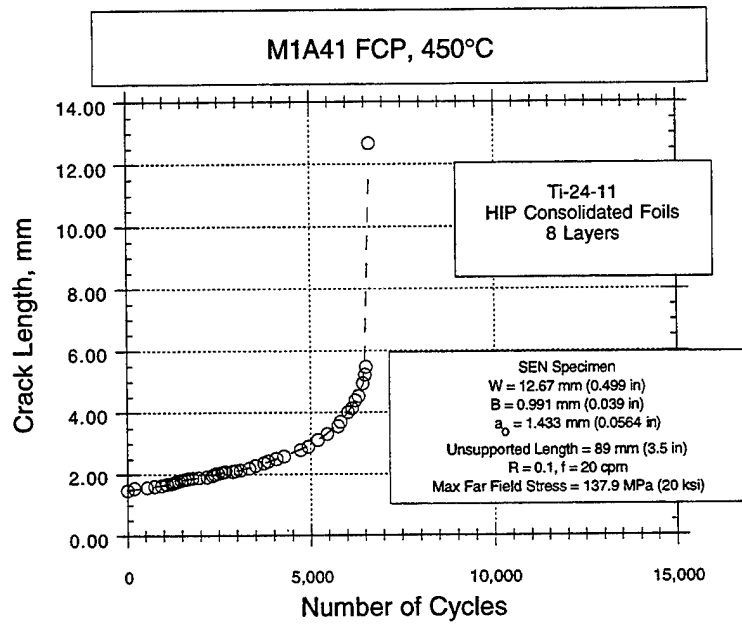
Figure 76. Matrix crack length vs. cycles, 450°C crack growth with maximum far field stress = 137.9 MPa.
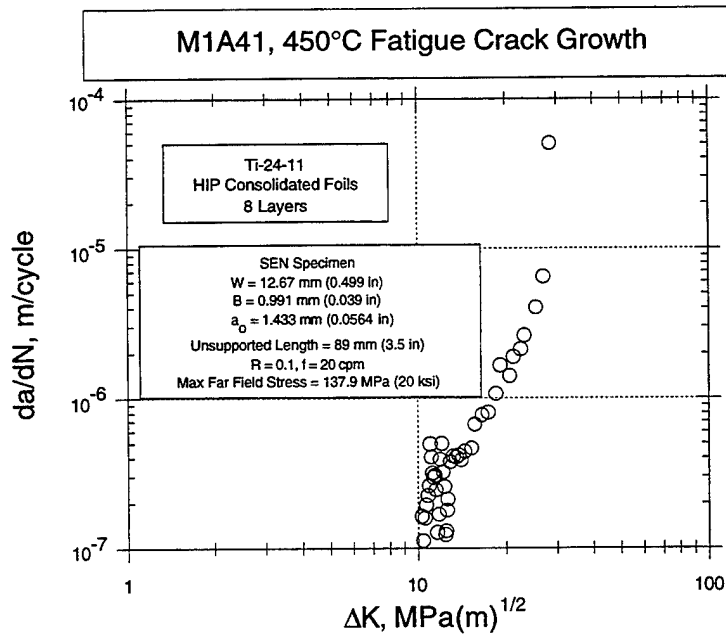
Figure 77. Matrix crack length rate vs. ΔK, 450°C, maximum far field stress = 137.9 MPa.

129
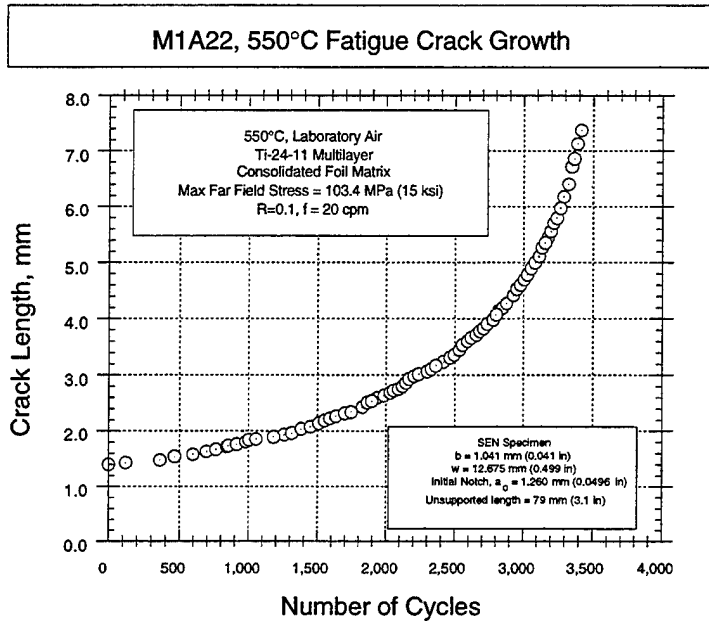
Figure 78. Matrix crack length vs. cycles, 550°C crack growth with maximum far field stress = 103.4 MPa.
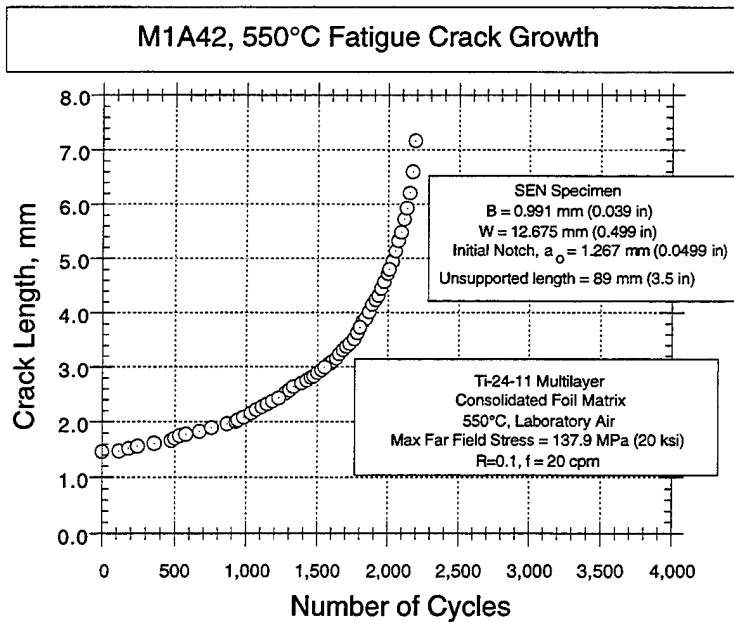
Figure 79. Matrix crack length vs. cycles, 550°C, crack growth with maximum far field stress = 137.9 MPa.

130
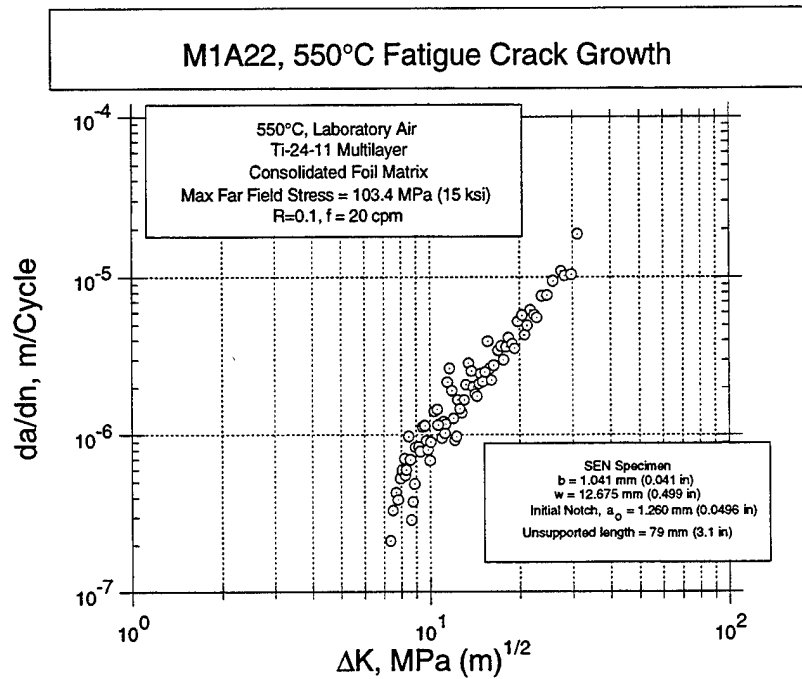
Figure 80. Matrix crack growth rate vs. ΔK, 550°C, maximum far field stress = 103.7 MPa.
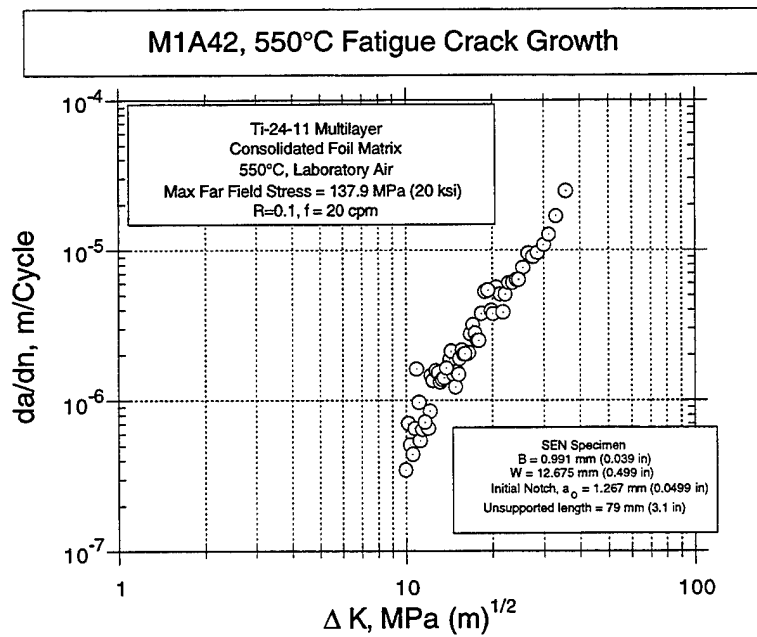
Figure 81. Matrix crack growth rate vs. ΔK, 550°C, maximum far field stress = 137.9 MPa.
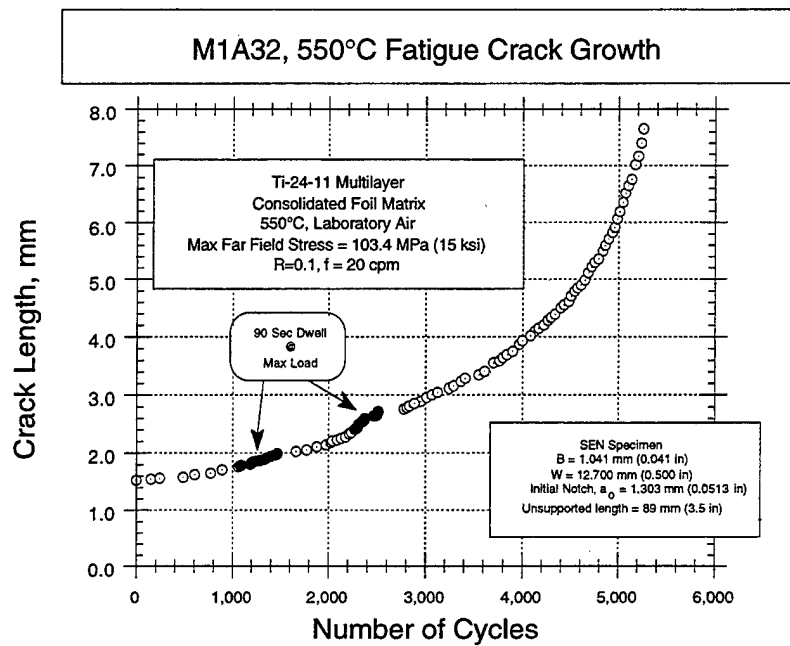
Figure 82. Matrix crack length vs. cycles, 550°C, crack growth, effect of 90 second dwell at maximum load.
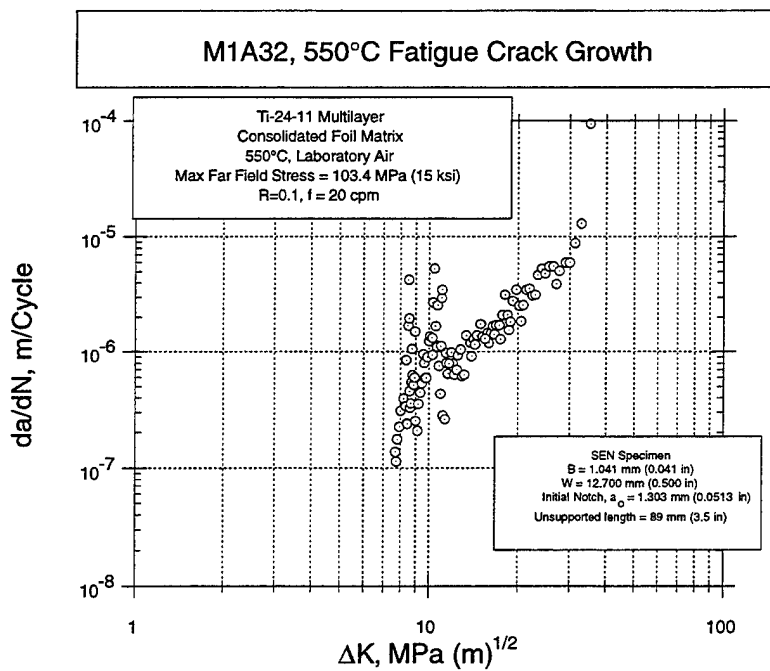
Figure 83. Matrix crack growth rate vs. ΔK, 550°C, with 90 second dwell segments.

M1A32, 550°C Fatigue Crack Growth

Ti-24-11 Multilayer
Consolidated Foil Matrix
550°C, Laboratory Air
Max Far Field Stress = 103.4 MPa (15 ksi)
R=0.1, f = 20 cpm

90 Sec Dwell
@
Max Load

SEN Specimen
b = 1.041 mm (0.041 in)
w = 12.700 mm (0.500 in)
Initial Notch, a$_o$ = 1.303 mm (0.0513 in)
Unsupported length = 89 mm (3.5 in)
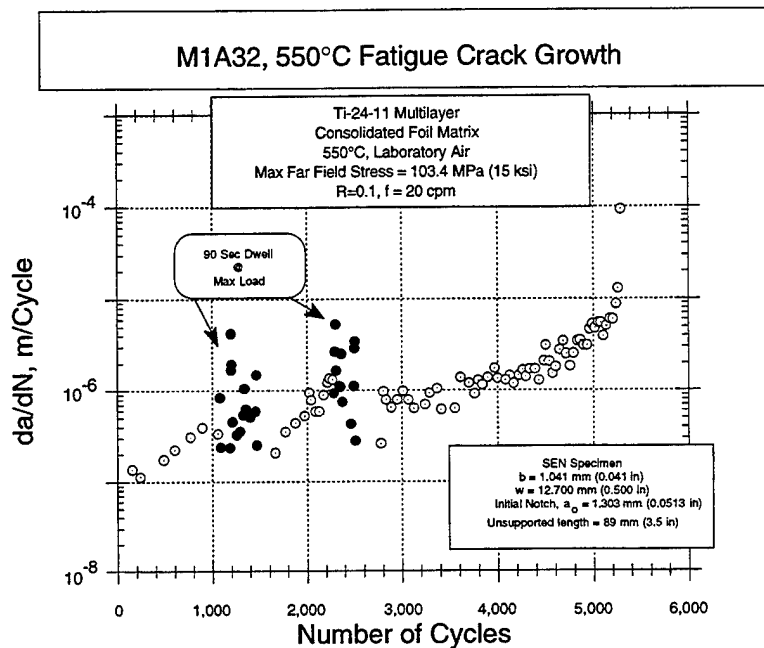
Figure 84. Matrix crack growth rate vs. number of cycles, 550°C, highlighting segments with dwell at maximum load.

4.5.1.3.2.1 R Value Effect on Crack Growth at 550°C

In order to determine the effect of stress ratio on fatigue crack growth in the matrix material at 550°C (1022°F), a test was run at an R of 0.5 to simulate the condition where the matrix is initially in tension due to the processing stress and the operational stresses are simply added. The former constitutes the minimum stress while the latter, added stresses, constitutes the maximum stress. Results of this test are seen in Figure 85 and Figure 86.

Combining the results of this R = 0.5 test with those of an R = 0.1 test we see that the higher R test specimen will last longer, Figure 87, but when examined in the form of a da/dn vs. ΔK plot, Figure 88, there is little to separate the two test conditions. There is a hint that the lower R test may result in a higher ΔK threshold, as would be expected.

4.5.1.3.3 650°C Fatigue Crack Growth in Matrix Material

At 650°C (1200°F), fatigue crack growth properties are similar to those at 550°C (1022°F). Figure 89 is the a vs. N plot for one such test while the conventional da/dN is seen in Figure 90. Comparing this figure with Figure 80, the conclusion is drawn that the crack growth resistance at 650°C (1200°F) is only slightly less than that at 550°C (1022°F).

133

M1A31, 550°C Fatigue Crack Growth

550°C, Laboratory Air
Ti-24-11 Multilayer
Consolidated Foil Matrix
Max Far Field Stress = 103.4 MPa (15ksi)
R=0.5, f = 20 cpm

SEN Specimen
B = 1.041 mm (0.041 in)
W = 12.751 mm (0.502 in)
Initial Notch, a_o = 1.422 mm (0.056 in)
Unsupported length = 79 mm (3.1 in)

Crack Length, mm

Number of Cycles
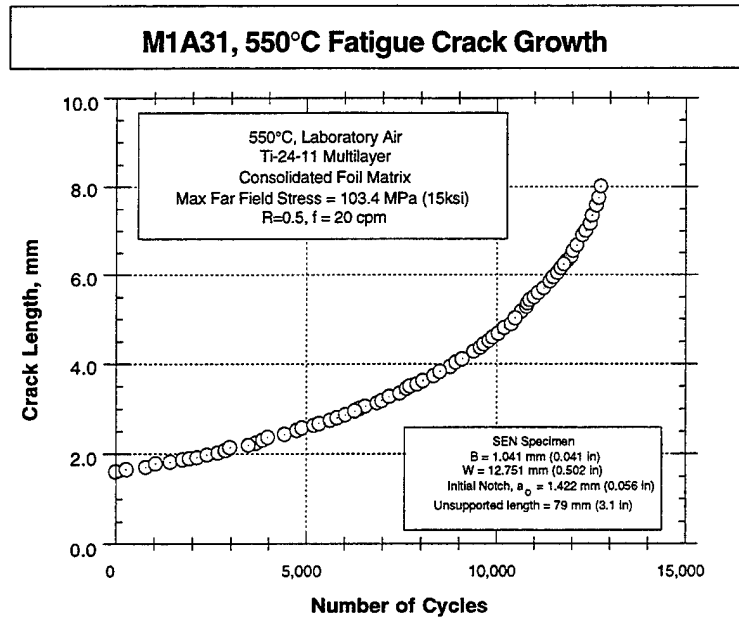
Figure 85. Fatigue crack growth, crack length vs. cycles, in matrix material at 550°C with an R of 0.5 and a constant maximum far field stress of 103.4 MPa.

M1A31, 550°C Fatigue Crack Growth

550°C, Laboratory Air
Ti-24-11 Multilayer
Consolidated Foil Matrix
Max Far Field Stress = 103.4 MPa (15 ksi)
R=0.5, f = 20 cpm

SEN Specimen
B = 1.041 mm (0.041 in)
W = 12.751 mm (0.502 in)
Initial Notch, a_o = 1.422 mm (0.056 in)
Unsupported length = 79 mm (3.1 in)

da/dN, m/cycle

ΔK, MPa(m)$^{1/2}$
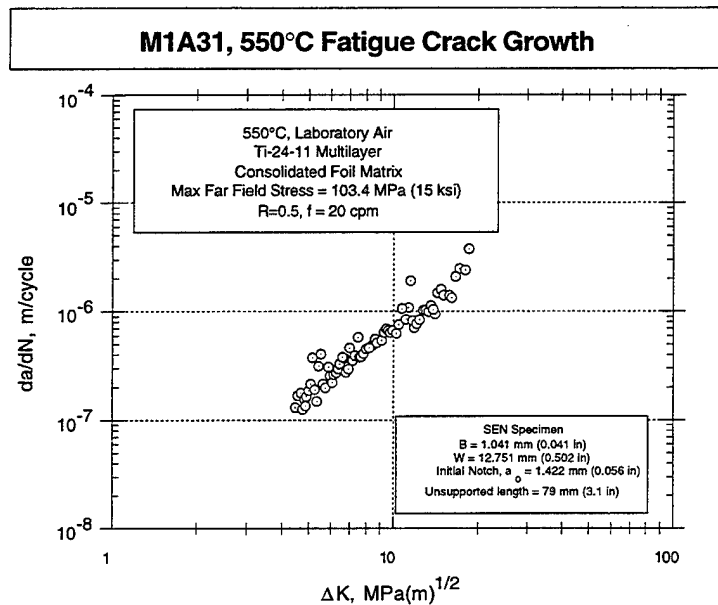
Figure 86. Fatigue crack growth, da/dN vs. ΔK, in matrix material at 550°C with an R of 0.5 and a constant maximum far field stress of 103.4 MPa.

134

M1A22 & M1A31, Fatigue Crack Growth
R Value Effect, 550°C

Ti-24-11 Multilayer
Consolidated Foil Matrix
Max Far Field Stress = 103.4 MPa (15 ksi)
f = 20 cpm

○ R=0.5, M1A31

□ R=0.1, M1A22

R = 0.1

R = 0.5

SEN Specimen
B = 1.041 mm (0.04 in)
W = 12.7 mm (0.5 in)
Unsupported length = 79 mm (3.1 in)
550°C, Laboratory Air
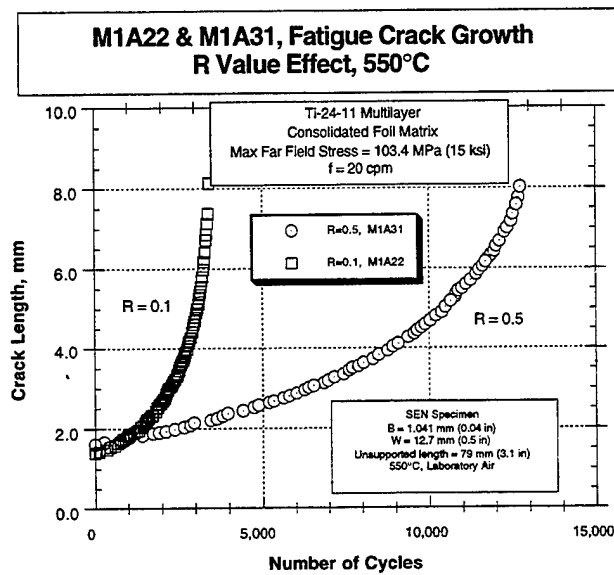
Figure 87. Fatigue crack growth, crack length vs. cycles, in matrix material at 550°C. Comparing results from test with a R of 0.5 with that at an R of 0.1. Both tests were conducted with a constant maximum far field stress of 103.4 MPa.

M1A22, 550°C Fatigue Crack Growth
R Value Effect

Ti-24-11 Multilayer
Consolidated Foil Matrix
Max Far Field Stress = 103.4 MPa (15 ksi)
f = 20 cpm

R = 0.1

R = 0.5

SEN Specimen
B = 1.041 mm (0.04 in)
W = 12.7 mm (0.5 in)
Unsupported length = 79 mm (3.1 in)
550°C, Laboratory Air
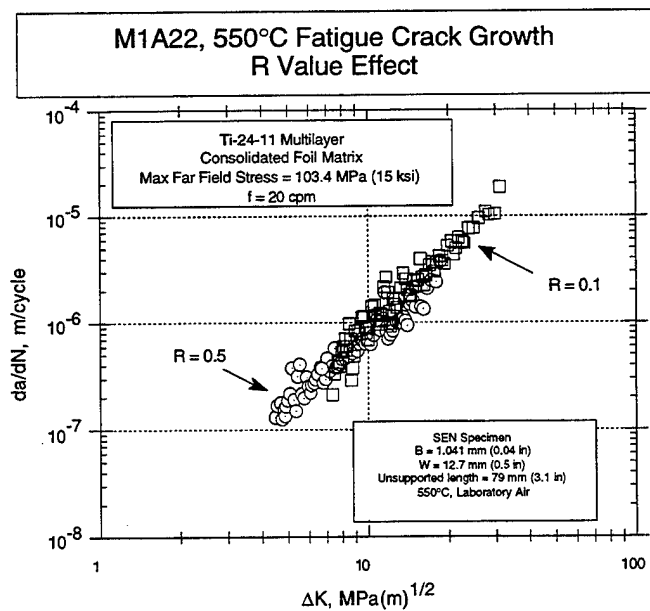
Figure 88. Fatigue crack growth, a vs. N, in matrix material at 550°C. Comparing results from test with a R of 0.5 with that at an R of 0.1. Both tests were conducted with a constant maximum far field stress of 103.4 MPa.

135
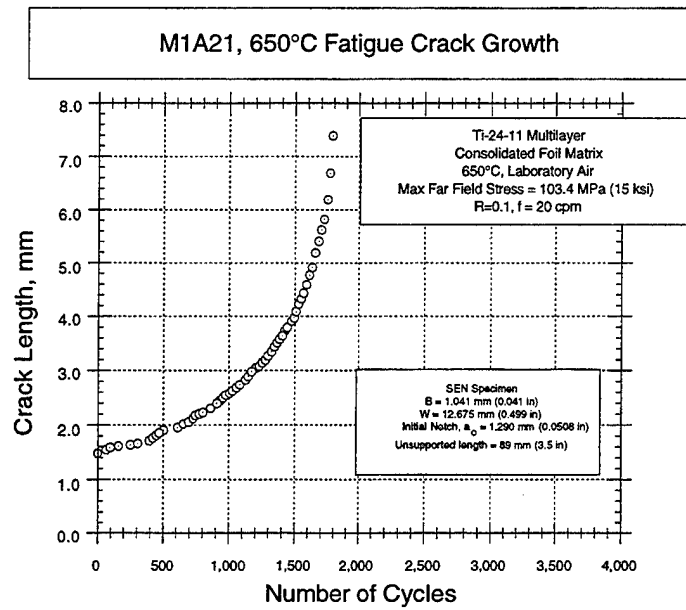
Figure 89. Matrix crack length vs. number of cycles, 650°C, maximum far field stress = 103.4 MPa.
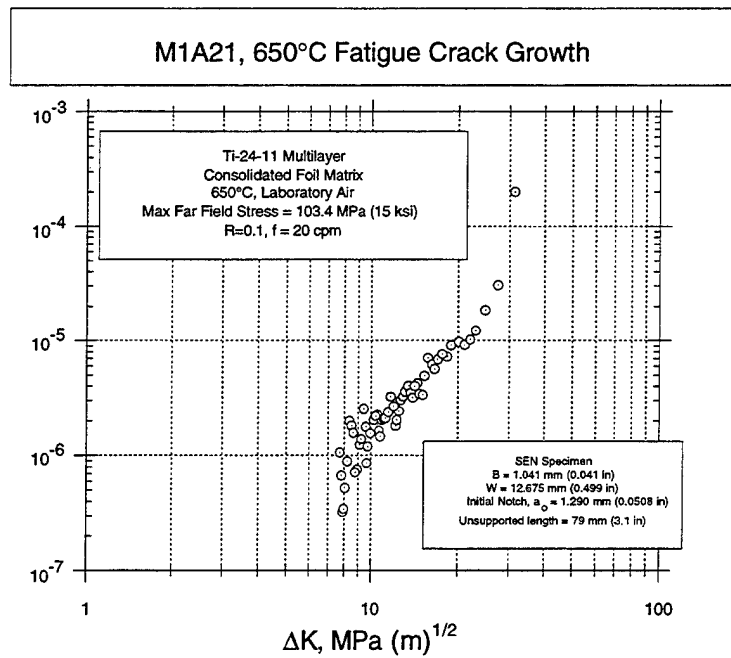
Figure 90. Matrix crack growth rate vs. ΔK, 650°C, maximum far field stress = 103.4 MPa.

Test results for a higher stress ratio, R = 0.5, on fatigue crack growth in the matrix material at this temperature are seen in Figure 91 and Figure 92. Comparing the latter figure with Figure 90, one can see that the threshold has decreased from about 7–8MPa(m)$^{0.5}$ to a level near 4 MPa(m)$^{0.5}$. The apparent fracture toughness remains in the 30 to 40 MPa(m)$^{0.5}$ range.

Dwell effects at maximum load, with durations of 90 seconds and 5-minutes, were investigated at this temperature and the results are plotted in Figure 96 through Figure 99. It is quite evident that crack growth is initially accelerated during the dwell periods, but resumed the nondwell rate after above 100 cycles. The results, aside from the dwell periods, compare favorably with the constant cycle growth rates displayed in Figure 90.

4.5.1.3.3.1 Hold Time Effect on Matrix Crack Growth at 650°C

In order to determine the effect of a dwell at maximum load on fatigue crack growth in the matrix material at 650°C (1200°F), a test was run with a 2 minute dwell at maximum load. The loading rate and unloading rate are the same as for the 20 cpm test in order to sort out the separate effects of loading rate and dwell when no transient loading is applied. Figure 93 and Figure 94 present the data from this test. In order to compare the results with a nondwell test, Figure 95 plots the da/dN vs. ΔK data of Figure 94 on top of the same sort of data from a 20 cpm test, Figure 90, with otherwise identical test conditions.

As can be seen, there is no effect of steady-state dwell at 650°C (1200°F) when comparing 20 cpm to a 2 minute dwell. The apparent dwell effects illustrated by interrupting 20 cpm tests with a few dwell cycles, as illustrated in Figure 96 through Figure 99 can be interpreted as being transitory in nature. A close look at these figures show that the da/dN decreases to the nondwell level after only a few cycles. It is not known why this occurs but should be an important factor when spectrum loading is applied. Considerably greater crack growth can occur in the first few dwell cycles than would be predicted from constant wave form data, such as that in Figure 94.

4.5.1.3.4 Summary of Elevated Temperature Crack Growth in Matrix Material

Elevated temperature crack growth tests in the matrix material indicate the alloy to have a much less steep growth curve, and with a higher toughness and probably about the same threshold, compared to the same material at room temperature. The crack growth characteristics appear to be well described by conventions based on linear elastic fracture mechanics. However, there is an apparent, transitory degrading influence of a short hold time on the crack growth resistance at all temperatures.
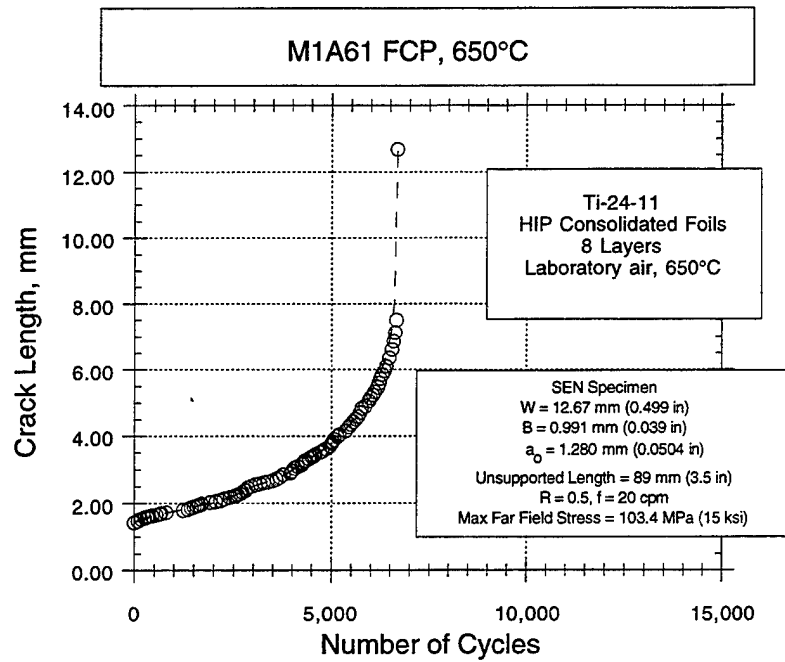
Figure 91. Crack length vs. number of cycles for Ti-24-11 matrix material at 650°C, with R = 0.1 and far field stress = 103.4 MPa.
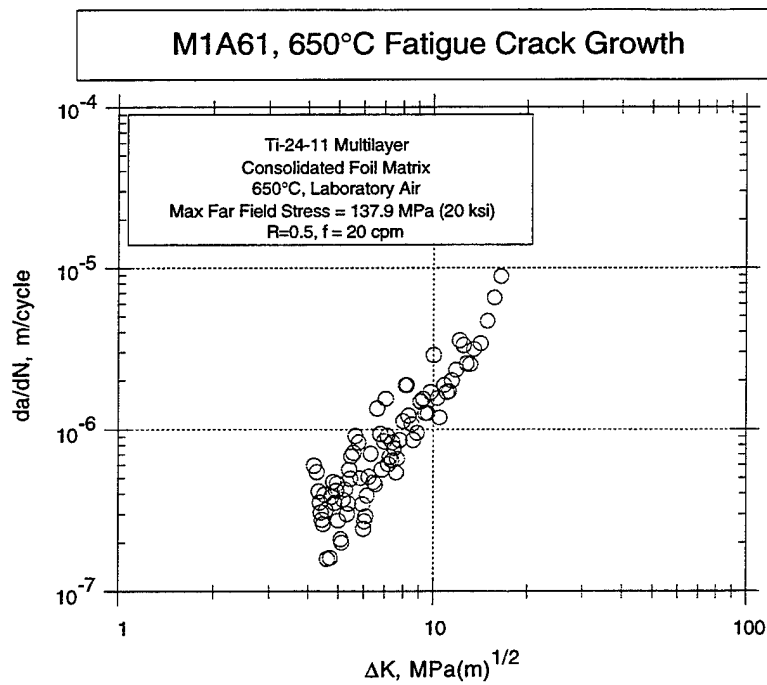
Figure 92. Matrix material, da/dn vs. ΔK at 650°C, for R = 0.1.
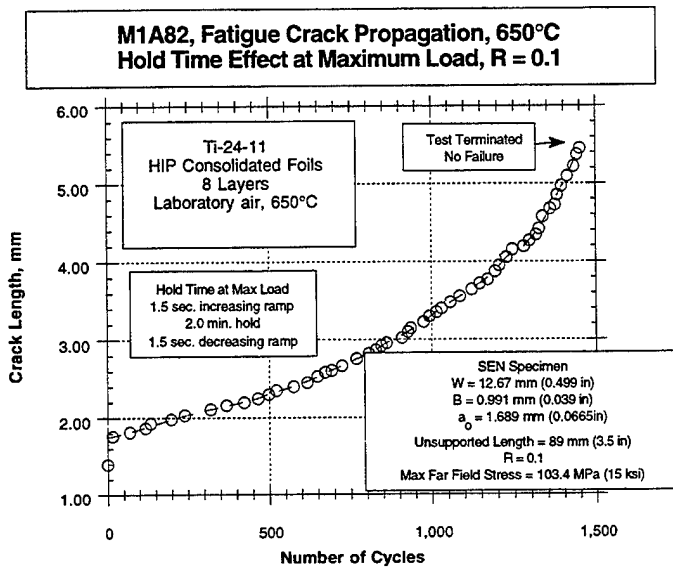
Figure 93. Dwell effects on fatigue crack growth. Shows a vs. N, in matrix material at 650°C, comparing results from test with an R of 0.1 and with a constant maximum far field stress of 103.4 MPa.
The same loading and unloading rate used for the 20 cpm tests were duplicated but punctuated with a dwell at maximum load for 2 minutes on each cycle.
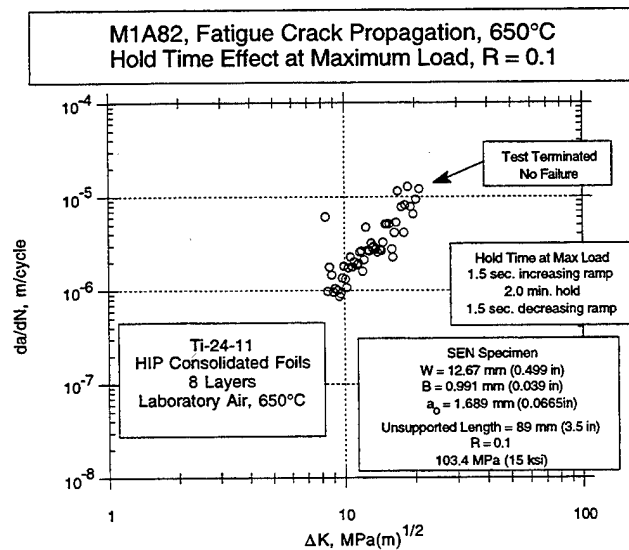
Figure 94. Dwell effects on fatigue crack growth. Shows da vs. ΔK, in matrix material at 650°C, comparing results from test with an R of 0.1 and with a constant maximum far field stress of 103.4 MPa.
The same loading and unloading rate used for the 20 cpm tests were duplicated but punctuated with a dwell at maximum load for 2 minutes on each cycle.

139
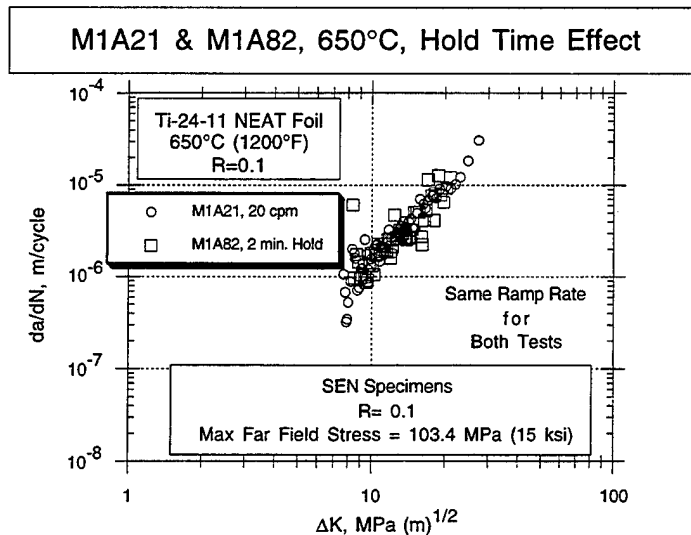
Figure 95. Dwell effects on fatigue crack growth. Shows da vs. ΔK, in matrix material at 650°C, comparing results from test with and without a dwell at maximum load.
Both tests were conducted with an R of 0.1 and with a constant maximum far field stress of 103.4 MPa. The same loading and unloading rate used for the 20 cpm tests were duplicated but punctuated with a dwell at maximum load for 2 minutes on each cycle.
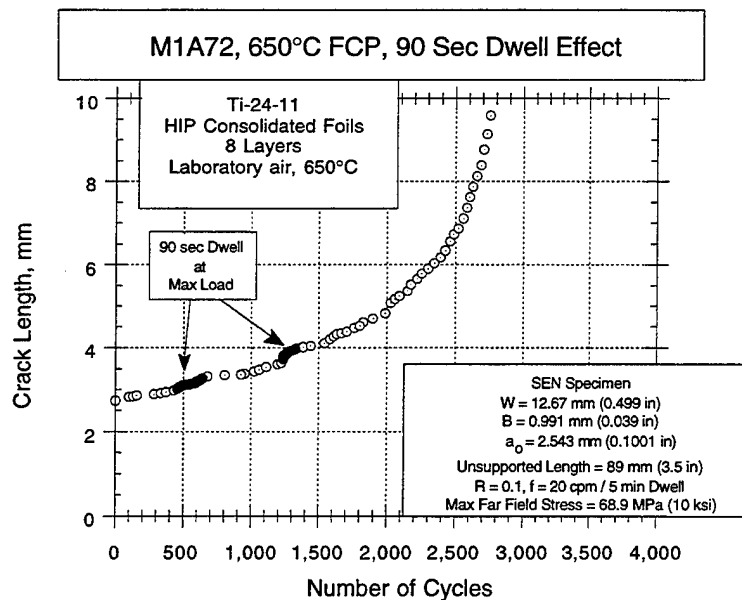
Figure 96. Matrix crack length vs. number of cycles at 650°C with two periods of 90 second dwell at maximum load.
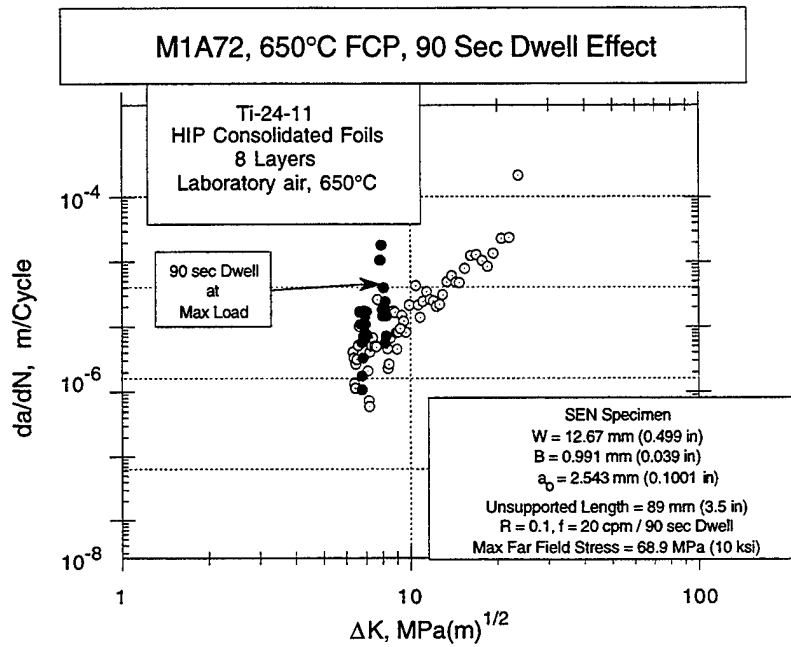
Figure 97.   Matrix da/dN vs. ΔK at 650°C, with 90 second dwell periods highlighted.
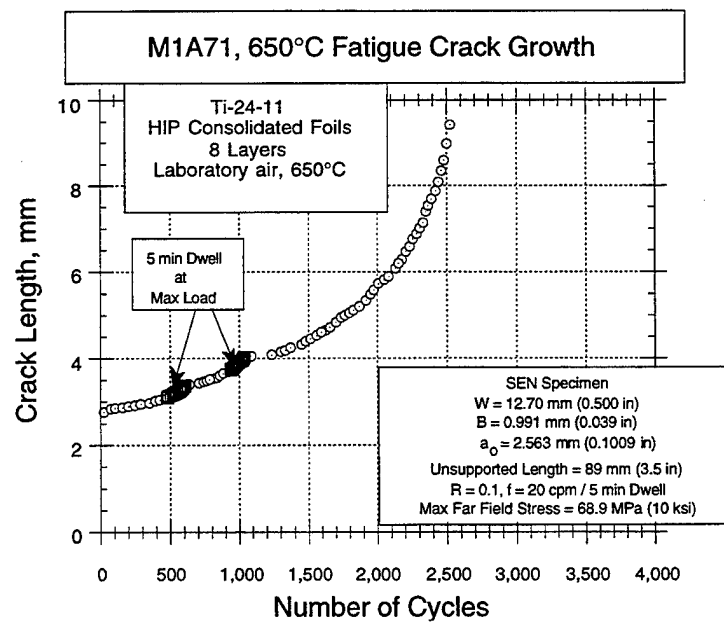
Figure 98.   Matrix crack length vs. number of cycles at 650°C, with 5 minute dwell at maximum load at points.

141

M1A71 FCP, 650°C, Hold Time Effect

Ti-24-11
HIP Consolidated Foils
8 Layers
Laboratory air, 650°C

5 min Dwell
at
Max Load

SEN Specimen
W = 12.70 mm (0.500 in)
B = 0.991 mm (0.039 in)
a_0 = 2.563 mm (0.1009 in)
Unsupported Length = 89 mm (3.5 in)
R = 0.1, f = 20 cpm / 5 min Dwell
Max Far Field Stress = 68.9 MPa (10 ksi)

(Y-axis: da/dN, m/Cycle, from 10^{-7} to 10^{-4}; X-axis: Crack Length, mm, from 0 to 10)
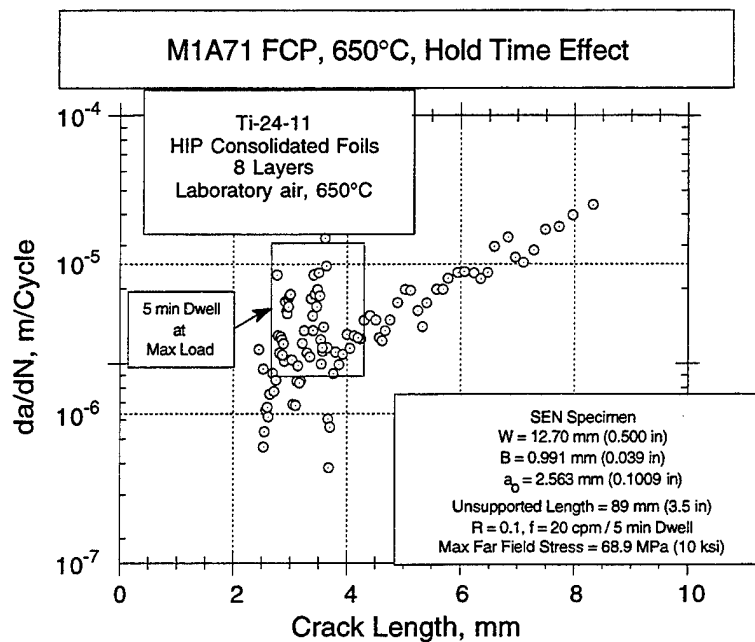
Figure 99. Matrix crack length vs. da/dN at 650°C, with 5 minute dwell points.

4.5.2 Fatigue Crack Propagation in Longitudinal MMC at Room Temperature

4.5.2.1 Experimental Procedure for Longitudinal MMC Fatigue Crack Growth Testing

Several of the initial crack growth tests were not analyzable in any simple manner as cracks tended to initiate from the machined notches in pairs and, with high far field stresses, they would very quickly turn 90° and propagate along the fibers, normal to the applied stress. This is thought to be a problem of crack propagation from an unbridged notch. The problem is especially important because it is anticipated that the service induced damage in MMC rotating structures is likely to involve initial cracks which are in the matrix only. Completely bridged initial crack growth is an important feature of damage tolerance concepts for such structures. Therefore, it became imperative that a method of running such tests be devised before consuming all of the MMC material.

AE developed a precracking method involving three point bending of notched SEN specimens. Singular cracks were nucleated on the machined notch, most of the time. For the successfully precracked specimens, the notch was machined away, leaving the completely bridged precrack in the SEN specimen. All subsequent longitudinal MMC speci-

142

mens, for both room and elevated temperature testing, were precracked, at room temperature, in this manner.

Crack growth at room temperature was established utilizing both potential drop techniques to indicate crack growth, in a dynamic sense, in order to determine points at which to interrupt the test to document the cracks directly in a high power microscope or by casting a replica. The latter two methods are the obvious points for precise analysis of the crack behavior and the PD technique used mostly for dynamic indications of crack growth.

4.5.2.2 Baseline Crack Growth of Longitudinal MMC at Room Temperature

Figure 100 presents the crack growth in an unexposed SEN sample at 689.5 MPa (100 ksi) far field stress. The initial fully bridged crack length was 0.262 mm (0.0103 in). As can be seen, the growth rate, as indicated by either the optical measurements or by PD indications, is virtually linear, when sufficiently long periods between measurements are taken. Noted, also, is the fact that the PD determined crack lengths are less than the directly observed values. This general feature was noted throughout the testing and is considered to be due, at least partially, to the conductivity of the bridging fibers. Note that the far field stress used is at the low end of the range for which the LCF curve (Figure 66) was generated. In this case, as in the LCF tests at room temperature, 689.5 MPa (100 ksi) stress was low enough to permit complete crack bridging. It is strange, though, that crack arrest was not observed as would be expected for the case of crack bridging, especially with matrix materials having ductility as high as 15% at the test temperature.

4.5.2.3.1 Frequency Effects on Fatigue Crack Propagation at Room Temperature

With otherwise the same test conditions used for the results seen in Figure 100, 20 cpm, as opposed to 5 Hz, was used to generate the crack growth curve seen in Figure 101. In this case, the rate appears to behave in a bilinear manner with an initial rate of about 1 $\times 10^{-5}$ mm/cycle, decreasing to about 3.8×10^{-6} mm/cycle at a crack length near 5 mm. The initial growth rate exceeds that obtained with the higher frequency test by a factor of 7.4 and with the longer crack, the decreased rate is only about 2.8 times faster. Clearly, there is an effect of frequency, implying a time dependent phenomenon in operation at room temperature. Whether this is a loading rate issue or a time-at-maximum-load issue cannot be concluded from this test alone. It does, however, present the behavior modeling task with additional challenges and is deserving of further investigation.

Fatigue Crack Growth, 2A/0C11

SCS6/Ti-24-11, $[0°]_8$ MMC
Tested in Longitudinal Orientation
Room Temperature
Notch Removed After Precrack
Singular Crack Maintained
Nominal Max Stress = 689 MPa
5 Hz, R = 0.1

Optical Meas

$a_{OM} = 0.262 + 1.360 \times 10^{-06} \times N$

PD Meas

$a_{PD} = 0.262 + 9.88 \times 10^{-07} \times N$

W = 11.338 mm (0.4464 in)
B = 1.699 mm (0.0669 in)
a_0 = 0.262 mm (0.0103 in) Fully Bridged
Distance Between Grips = 89 mm (3.5 in)
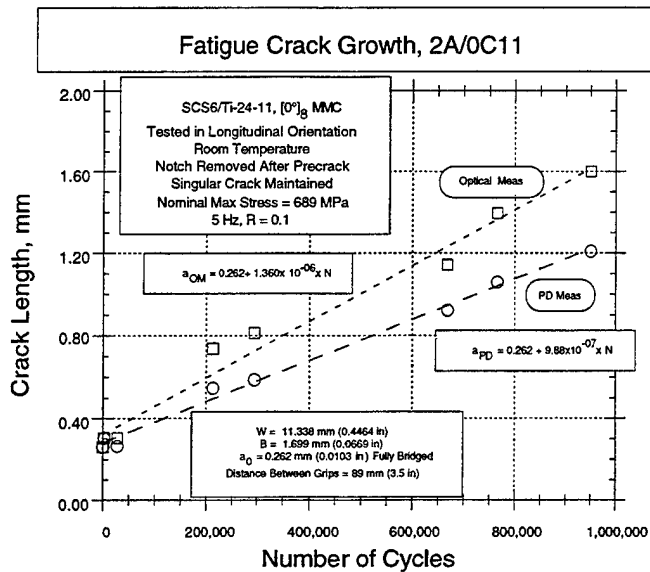
Figure 100. **Longitudinal MMC crack length vs. cycles for maximum far field stress = 689 MPa and R = 0.1.**
This plot illustrates the divergence of the potential drop computed crack length from the optically measured crack length.

2A/0G11 Fatigue Crack Growth

SCS6/Ti-24-11, $[0]_8$ MMC
Longitudinal Orientation
Room Temperature

$a = 3.16 + 3.84 \times 10^{-06} N$

$a = 0.190 + 1.01 \times 10^{-05} N$

Max Far Field Stress - 689 MPa (100 ksi)
R = 0.1, f = 20 cpm
B = 1.859 mm (0.0732"), W = 11.37 mm (0.4477")
a_0 = 0.277 mm (0.0109 in)
Unsupported length = 83 mm (3.25")
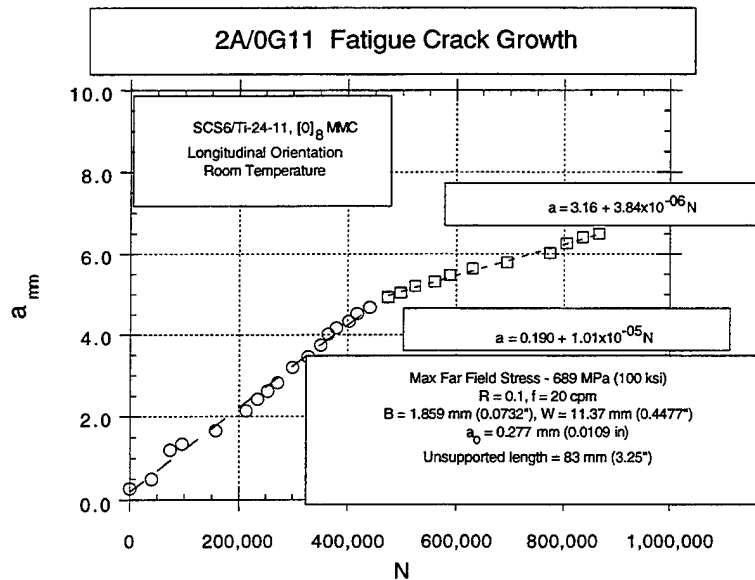
Figure 101. **Room temperature crack growth, a vs. N at 20 cpm and maximum far field stress = 689 MPa, R = 0.1.**
There is an apparent change in rate at about 5 mm crack length.

144

The 30 second hold and perhaps the 2 minute hold time influence appears to be small, as implied by Figure 102. This suggests that the time at maximum load is too short for time dependent factors such as creep to have a major influence. It must be cautioned that the duration of the above described hold time portion of the test was short and conclusions based on these observations are tenuous.

4.5.2.3.2 Hold Time Effects on Fatigue Crack Propagation at Room Temperature

Using the same stress used for the tests described by Figure 100 and Figure 101, the effect of hold time at the major load was examined. Reported in Figure 102 are the effects of 5 min, 2 min and 30 sec hold times at maximum load. As is obvious from the figure, there is an apparent influence of a 5-minute hold time on the crack propagation rate, when compared with the 20 cpm testing rate.

4.5.2.3.3 Summary of Frequency and Hold Time Effects on Fatigue Crack Propagation in Longitudinal Samples at Room Temperature

All crack growth testing was done using a triangular wave form and, therefore, frequency changes are accompanied with a proportional change in strain rate applied to the specimen.

Examining the results seen in Figure 100, Figure 101 and Figure 102, leads one to the conclusion that, at least with longer hold times, there may be a crack acceleration resulting from the hold time at maximum load. Speculation as to the mechanism may include creep relaxation of the matrix residual stresses which, in turn, tend to unload the compressive residual stress component in the fibers as well as matrix clamping stresses about the fiber circumference, affecting the load transfer capability.

The apparent frequency effect with effective times at maximum load less than the observed range where hold time effects are minimal, may imply involvement of a loading rate or strain rate mechanism. Titanium aluminide alloys are strain rate sensitive, and while the applied maximum stress on the matrix, in these cases, is low, it is compounded by a notch effect at the crack tip and by the presence of preset residual stresses. The average longitudinal residual stress in the matrix shown in Table 12, imply much higher stresses in the matrix at the fiber/matrix interface. Hence, because of the strain rate strengthening effect on the matrix, a high loading rate may not cause this local stress to exceed the local plastic limit but the lower rates may.

145
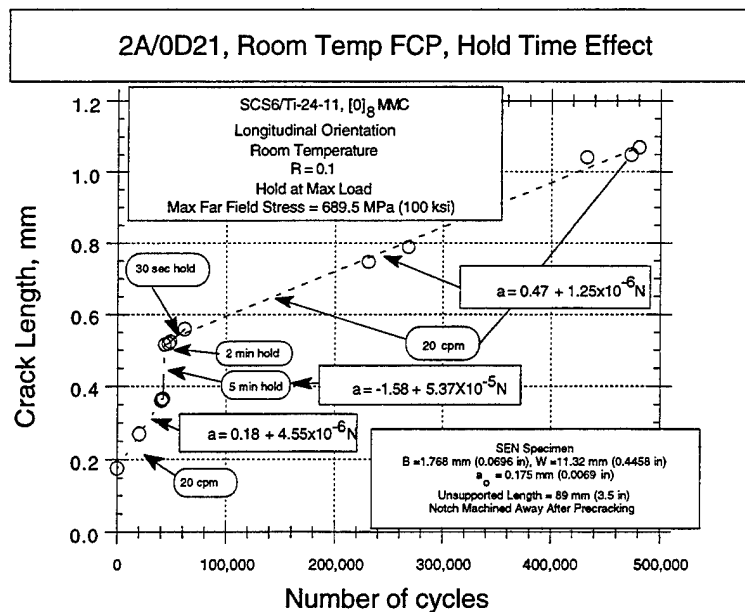
Figure 102. **Longitudinal MMC crack length vs. cycles with superimposed dwell at maximum load.**
Otherwise, the test conditions were similar to those described by Figure 100.

Therefore, at room temperature, there is an apparent loading rate effect, with the higher rates resulting in slower fatigue crack growth and this is compounded by a dwell effect at maximum load which also accelerates crack growth.

4.5.2.4   Influence of Thermal Cycle on Fatigue Crack Growth

4.5.2.4.1   Influence of Simulated Bonding Thermal Cycle on Fatigue Crack Growth

A 930°C (1706°F)/3 hour thermal cycle, in vacuum, was applied to a specimen and then tested identically to the specimen described in Figure 100. As seen in Figure 103, the initial growth rate is accelerated compared to the unexposed sample, but settled down to a growth rate only slightly higher, thereafter. Because the specimen was precracked after the exposure, an influence on the notch zone exposed fibers in not likely to be an important causative factor. The LCF testing done earlier (Section 4.4.2.1.4) exposed the fact that residual longitudinal tensile stresses in the matrix degrade after the first few cycles. The high temperature vacuum exposure may have changed the nature of the residual stresses and, therefore, the early part of the fatigue crack growth life. The remaining effect may be related to the difference in resultant residual stress levels be-

tween this exposure temperature and that of the MMC consolidation, which was about 80°C (145°F) higher.

The 930°C (1706°F) thermal exposure may have left the MMC in a higher zero stress state than it had originally been in. This is attributable to the relatively more rapid cooling from this heat treatment than the HIP consolidated panels had experienced. From the work reported in Table 10, it is concluded that cyclic stress exposure, even at room temperature, causes a reduction in longitudinal residual stresses in the matrix. But this is not instantaneous and likely to take more cycles when the applied stress is lower. In a qualitative way, this may relate to the initially much higher growth rate seen in this specimen.

When examining the data for this specimen by plotting da/dN vs. ΔK, it becomes clear that this approach is inadequate. Figure 104 displays a deceleration followed by an acceleration, as expected by the form of the a vs. N curve. Such a nonsingle valued function makes such data hard to use in this form, drawing one to the conclusion that the crack growth behavior of this MMC is not well characterized by linear fracture mechanics rules. The models being developed for predicting damage tolerance or crack growth behavior will address this. Recognizing that the cracks in these specimens are fully bridged, it is clearly inappropriate to engage the conventions of linear elastic fracture mechanics directly as many of the basic precepts are violated. For the purposes of establishing a database for use in the MMCLIFE derivatives, a vs. N data with all of the dimensions and constraints of the test will be utilized directly.

4.5.2.4.2 Effect of Simulated Service Temperature Exposure on Room Temperature Fatigue Crack Growth

By exposing a premachined, but not precracked, SEN specimen for 100 hours at 650°C (1200°F) and then testing as described above at 689.5 MPa (100 ksi) maximum far field stress, R = 0.1, f =20 cpm and a_0 = 0.165 mm, we find the growth rate to be nearly linear up to a crack length of 2.75 mm at which time the stress maximum was increased to 965 MPa (140 ksi). The growth rate increased from about 6.1×10^{-6} to 1.9×10^{-5}, a threefold increase. The region of the a vs. N plot near the stress transition is seen in Figure 105. When the slope at the lower stress conditions is compared with the baseline growth curve at the same frequency, Figure 101, the rate is about 60% slower. Whether this is an effect of the thermal exposure or merely part of the scatter, is not known. Any effect, though, is not major so long as the environment does not seriously degrade the fiber, the matrix/fiber interface or the matrix. As seen in the tensile test results where degradation was nil, the crack growth results show little effect.

The effect of increasing the far field stress by about 40%, to a level of interest in some disk designs, causes a rather rapid increase in growth rate. Figure 106 shows this ef-
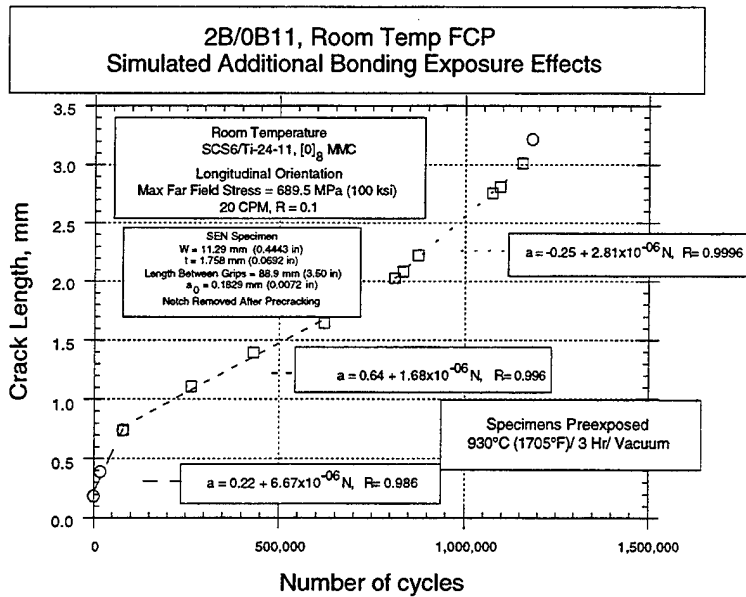
Figure 103. Room temperature longitudinal MMC crack length vs. cycles showing the effect of a pre-test exposure to simulate an additional diffusion bonding cycle. An initial high growth rate is evident.
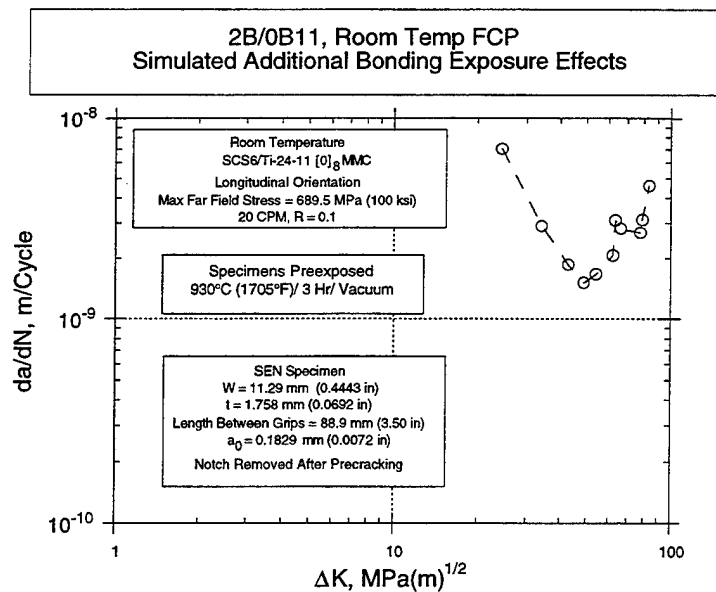
Figure 104. Test described by Figure 103, plotted as apparent da/dn vs. ΔK. This plot illustrates that crack arrest does not occur, despite maintenance of crack bridging.

148
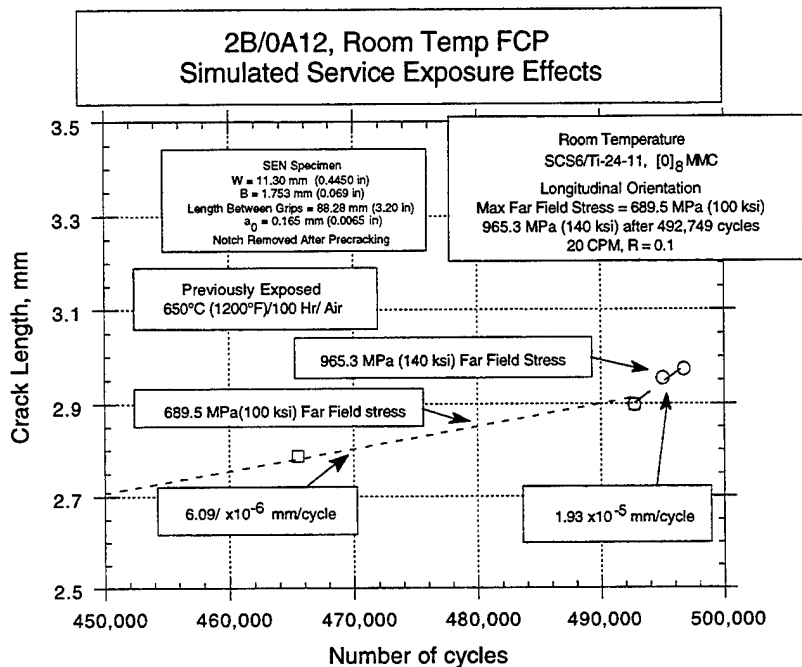
Figure 105. Room temperature MMC crack length vs. number of cycles. Prior exposure and far field stress effects.

fect on a standard da/dN vs. ΔK curve. It is clear that the acceleration is rapid. This nearly catastrophic growth occurs at a crack length equivalent to about 13 to 15 fiber spacings deep. The discussions on stress effects will follow in a later paragraph.

4.5.2.4.3 Effect of Short Time Thermal Exposure Interruption at 650°C on Room Temperature Fatigue Crack Growth Rate

In order to assess the effect of a short time exposure at engine operating temperatures on the growth rate of a growing crack, a room temperature test was interrupted with a thermal exposure of 650°C/30 min (1200°F/30 min) in an unloaded state. Subsequently, the test was resumed. The crack length vs. cycle count is plotted in Figure 107. A transient acceleration was seen after the exposure with the growth rate being about 83% higher.

After growth of about 1.1 mm, the rate decreased to a level near that of the initial part of the test. Growth during the transient was equivalent to about 5 inter-fiber spacings. Assuming that the distance, X, traveled by an assumed harmful species from the crack tip during the thermal exposure follows an expression $X = (Dt)^{0.5}$, and that
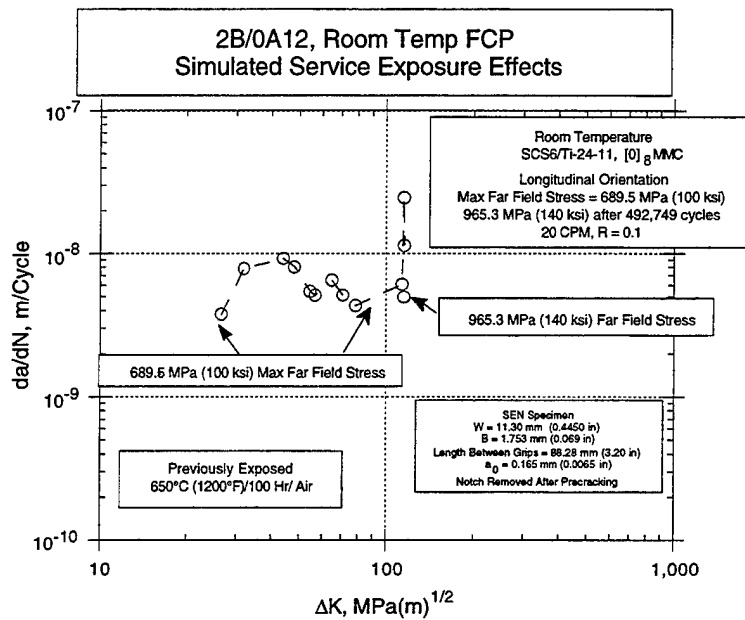
Figure 106. **Room temperature crack growth curves, uncorrected for bridging.**
This plot shows insensitivity growth rate to ΔK, but an apparent sensitivity to far field stress.
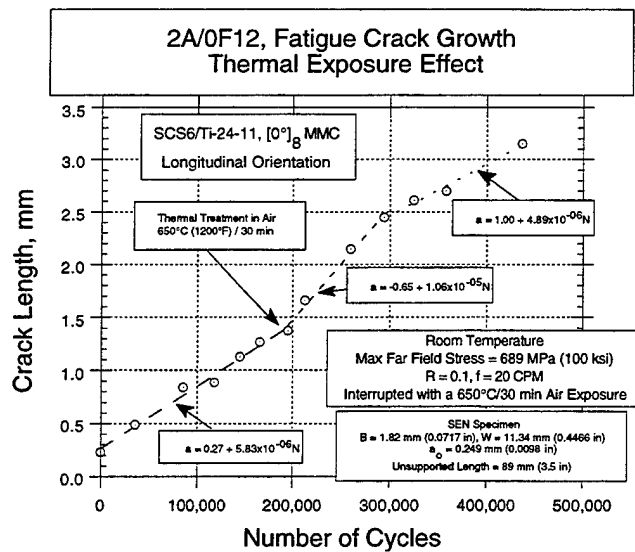
Figure 107. **Room temperature crack growth, interrupted by 650°C/30 minute thermal exposure in air.**
This test was run to simulate thermal exposure after cracks have propagated from a component surface into the MMC reinforcement. An 81.8% transient increase in growth rate results.

150

the degradation extends to a depth equal to the growth distance during the accelerated period, we can solve for an effective diffusivity.

$$0.11 \text{ cm } = (D * 1800 \text{ sec})^{0.5} \qquad [110]$$

$$D = 6.7 \times 10^{-6} \text{ cm}^2/\text{sec} \qquad [111]$$

This is extremely high for bulk diffusivity of oxygen at 650°C (1200°F), implying that, if oxygen is the bad actor, short circuit diffusion is more likely to be the mechanism that promotes post exposure crack acceleration and fiber/matrix interfaces may be the path. Because the clamping action of the matrix on the fibers is reduced at the elevated temperature of 650°C (1200°F), this is a likely candidate but verification is necessary. It remains clear, however, that once the MMC is breached in this system, temperatures as low as 650°C (1200°F) in an air environment, fatigue crack growth acceleration will occur. In this specimen, as in all the room temperature tests, nearly complete crack bridging by the SCS6 fibers was observed.

4.5.2.4.4 Summary of Thermal Exposure Effects on Subsequent Room Temperature Fatigue Crack Growth Rates.

In all of the tests, thermal exposure at high or moderate temperatures produces at least a transient increase in growth rate. It is also clear that once cracks have penetrated the surrounding structure in this alloy/fiber system, thermal exposure provides significant degradation of the crack growth resistance despite the maintenance of fiber bridging.

Fiber bridging, while introducing some scatter in the growth rates, is not seen to cause arrest at stresses of interest to engine component designers. Growth rates, though are slower than in monolithic materials. When plotted over extended crack length intervals, in a constant far field cyclic stress condition, the mean growth rate is not crack length dependent. This defies analysis by classical Linear Elastic Fracture Mechanics techniques, requiring treatment by a bridged-crack analysis.

4.5.2.5 Stress Effects on Room Temperature Fatigue Crack Growth Rate

It was noticed in Figure 105, on a 650°C (1200°F) thermally exposed sample, that the growth rate increased with stress. In order to scope the effect of stress on crack growth, an unexposed precracked SEN specimen was prepared with the machined notch removed to assure complete fiber bridging at the outset. Testing initiated with a far field stress level of 689.5 MPa and increased, to 827 MPa and the test was completed at 985 MPa. The results are plotted in Figure 108. It is evident that there is a discontinuity each

151

time the stress level is increased, as expected. The increase in growth rate is not a clear function of crack length, as seen with the linear a vs. N plots. It is apparent that stress effects must dominate, in the crack length and stress regions used in this program.

In Figure 109, is plotted the crack length vs. N for a test at a stress level of 837.4 MPa (120 ksi). The initial crack growth rate was very high at a frequency of 20 cpm and slowed down by a factor of about 6.2 when the frequency was increased to 1 Hz. It cannot be concluded, from this test alone, that the entire effect is due to frequency or loading rate. The crack length, at which time the frequency was changed, was about 0.27 mm which is on the order of one inter-fiber spacing. Hence, the crack size effect is likely to be a dominant feature which is accompanied by possible near-edge effects.

The effect of an even higher stress was investigated at 1173 MPa (170 ksi). Figure 110 plots the results of the first of a series of two tests run at this stress. The growth rate is very high, on the order of 2×10^{-4} mm/cycle. Failure in the grip region of the specimen precluded testing to greater crack lengths.

A second test was conducted at this stress level and reported in Figure 111. This test was concluded at a much longer crack length, also failing in the grip. Here, the initially high slope was repeated, at about the same rate as seen in Figure 110. This was followed by a linear growth rate to a total crack length of about 0.95 mm. Failure in the grip precluded analysis of the apparent fracture toughness of this specimen. However, it is clear that the growth rate, once the crack leaves the specimen edge, is decreased by a factor of about 5.9. This is nearly the same value noticed for the 837 MPa test when the frequency was increased on a very short, growing, crack. This tends to substantiate the short crack rationale for at least part of growth rate change test.
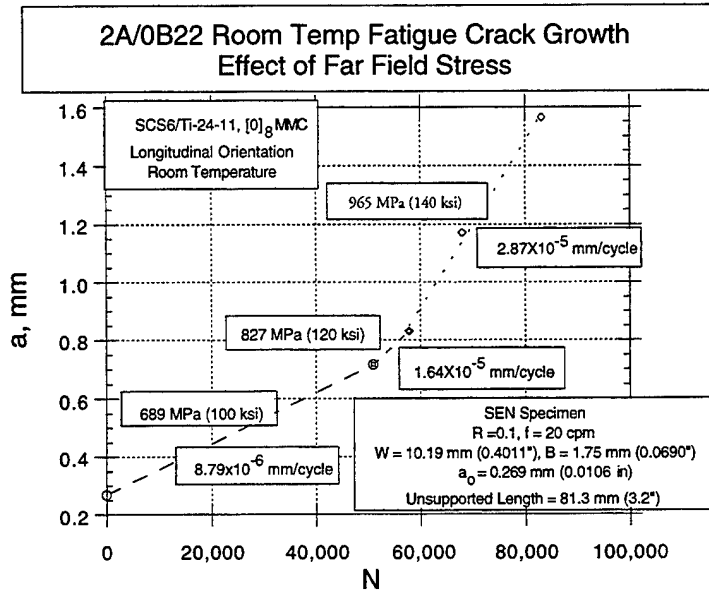
Figure 108. Room temperature fatigue crack growth, crack length vs. cycles, with progressively increased far field stress levels.
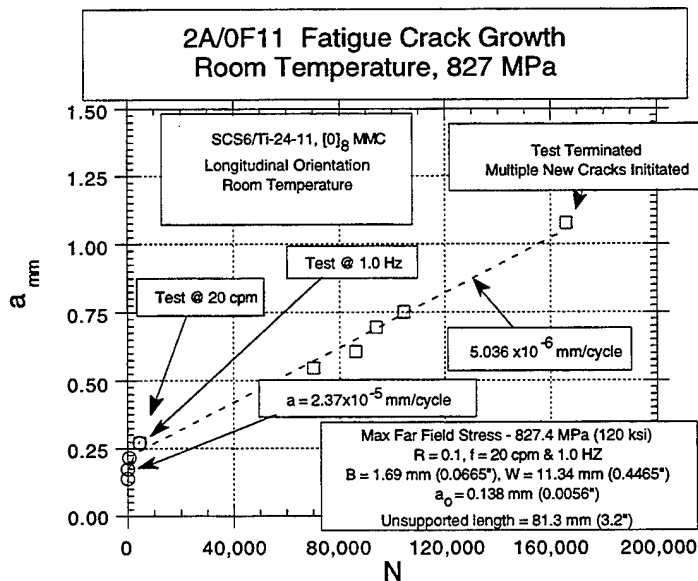
Figure 109. Room temperature fatigue crack growth, crack length vs. cycles, at maximum far field stress of 827.4 MPa.
Initial growth at lower frequency is more rapid, but relative effects of frequency and crack size are not clear.

153
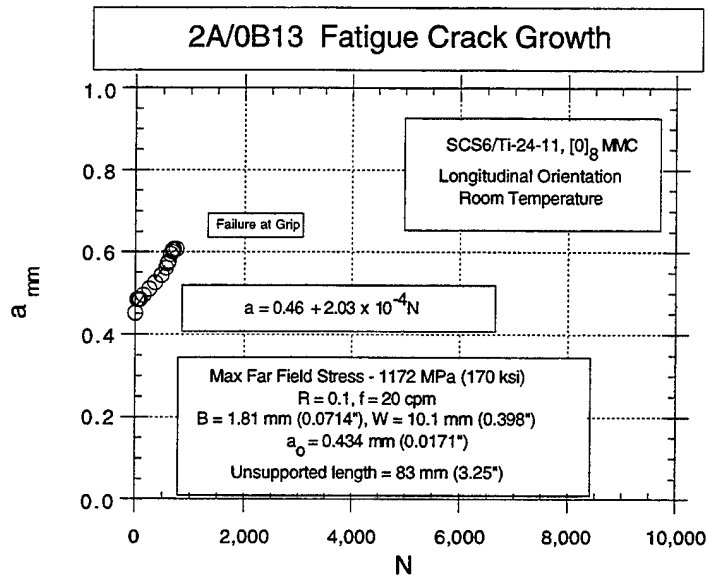
Figure 110. Room temperature fatigue crack growth, crack length vs. cycles, at maximum far field stress of 1172 MPa.

Very high initial growth rate is experienced until the crack reached 0.62 mm, at which time the specimen failed in the grip.
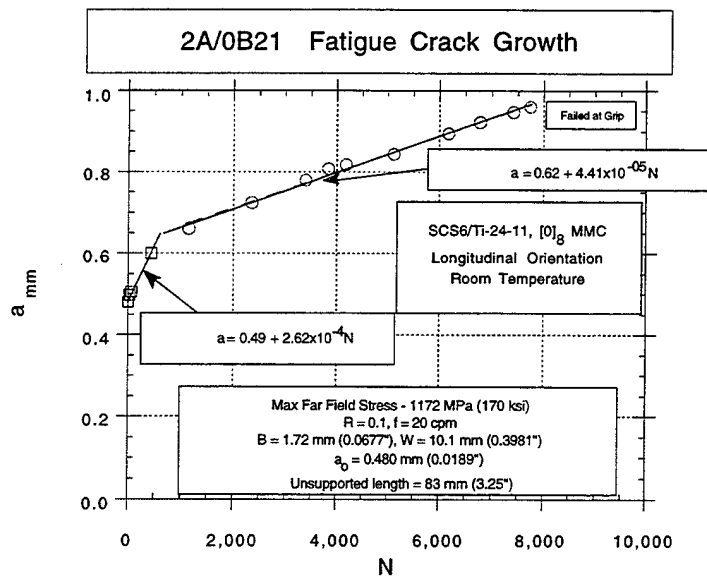
Figure 111. Room temperature fatigue crack growth, crack length vs. cycles, at maximum far field stress of 1172 MPa.

After an initial high growth rate, the slope settled down by a ratio of 0.168.

154

4.5.2.6 Stress Ratio Effects on Room Temperature Fatigue Crack Growth in Longitudinal Orientation

One room temperature fatigue crack grow test was conducted with a stress ratio, R = 0.5 in order to assess the effect on crack growth rate with a constant far field stress of 1207 MPa (175 ksi). The a vs. N data are plotted on Figure 112. During the test, at about 35,193 cycles, a second crack appeared on each surface of the SEN specimen on a plane contained in an extension of the original crack which, in turn, had been growing from the fully bridged precrack. At this point there was an acceleration of the initial crack. For reference, the secondary, coplanar, crack was tracked and the results plotted on the same figure. At some point, both cracks individually reduced their growth rates until fracture was eminent. When the two, coplanar, crack lengths are combined, the a vs. N plot takes on a form that indicates a rapid progression towards failure. Figure 113 shows this effect.

4.5.2.6.1 Comparison of Room Temperature Fatigue Crack Growth at Two R Values

Converted to the conventional da/dN vs. ΔK data with no attempt to correct for closure, data from the R = 0.5 test discussed above is plotted together with data from an R = 0.1 test run with a 1172 MPa (170 ksi) far field stress (Figure 111). The resulting plot is seen as Figure 114. It is not clear from this figure if the data belong in the same population as was the case for the matrix only test (Figure 88).

4.5.2.7 Summary of Room Temperature Crack Growth in Longitudinal Orientation

Because of the linear nature of the crack length vs. number of cycles plots at a constant far-field stress, after initial transients are transversed, it is apparent that applied ΔK is not a very good indicator of crack driving force. This situation, at least at room temperature where crack bridging is observed but crack arrest is not, leads to the speculation that the driving force for crack growth is primarily the far field stress.

In order to determine if crack growth is primarily stress and not crack length dependent in the stress ranges of interest for gas turbine engine design, the linear crack growth rates, highlighted throughout the room temperature crack growth test data presentations in Section 4.5.2.6 and earlier, were plotted as a function of maximum far field stress, all with a common cyclic frequency (20 cpm) and R value (0.1). The results in Figure 115 indicate a clear linear relationship of crack growth rate with stress. Superimposed on this plot are results of tests with hold time and with higher frequencies. It is also clear that hold times or lower test frequencies cause a higher crack growth rate. The data are not detailed enough to determine if there might be a frequency above which there is no longer an effect. The effect of R value was not investigated but is deserving of some
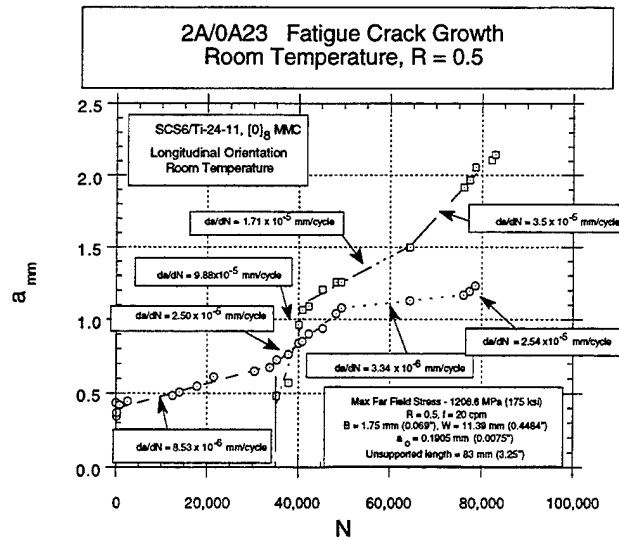
Figure 112. **Room temperature fatigue crack growth. Shows a vs. N, in longitudinally oriented MMC material with a maximum far field stress of 1206.6 MPa and a stress ratio of 0.5.**

A second crack initiated on the same plane as the original crack, on both sides at a position of a/W ~ 0.3. Both cracks were followed and the results plotted. Note the acceleration of the original crack once the second crack appeared.
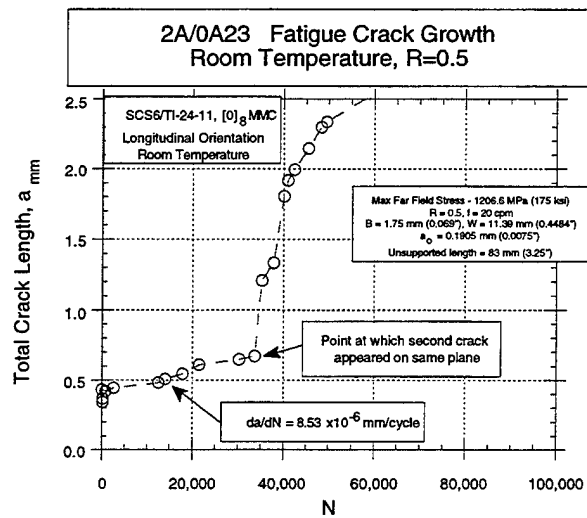
Figure 113. **Room temperature fatigue crack growth. Shows crack length vs cycles, in longitudinally oriented MMC material with a maximum far field stress of 1206.6 MPa and a stress ratio of 0.5.**

A second crack initiated on the same plane as the original crack, on both sides at a position of a/W ~ 0.3. The sum of the crack lengths is plotted here. Note the rapid acceleration of the original crack once the second crack appeared.

156
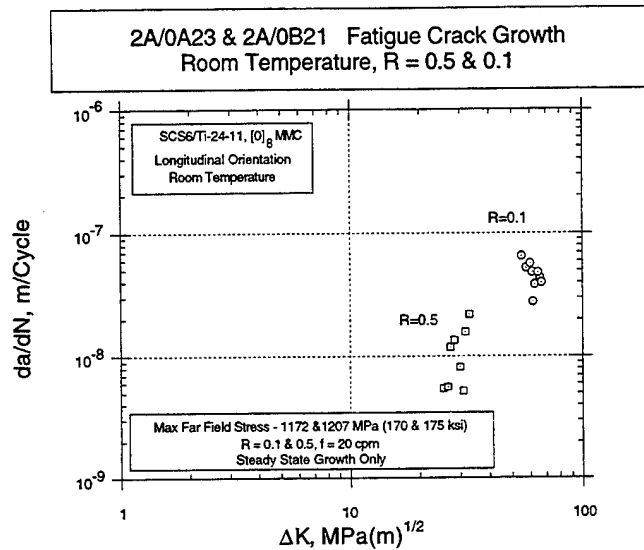
Figure 114. Room temperature fatigue crack growth. Shows da vs. ΔK, in longitudinally oriented MMC material for two tests with a maximum far field stress of 1172 and 1206.6 MPa and a stress of 0.1 and 0.5 respectively.
The higher stress ratio specimen is the same one described in Figure 112 and Figure 113 using only the crack growth data extracted prior to the formation of the secondary crack. In both cases, the extent of crack growth yielding acceptable data were too short to generate unambiguous comparisons.
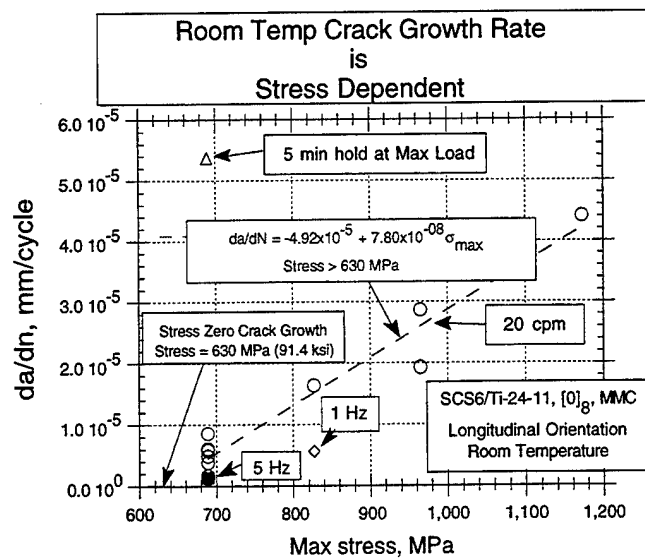
Figure 115. Stress dependency of room temperature fatigue crack growth rate, $[0°]_8$ MMC, SCS6/Ti–24–11.

attention as the superimposed effects of bonding of MMC reinforcements in a monolithic forging will superimpose a mean stress upon the applied stress and this mean stress may vary from location to location within the MMC insert.

Considering Figure 115, an extrapolation of the linear plot to a zero growth rate intersects the stress axis at about 630 MPa. This is amazingly similar to the apparent runout stress for room temperature fatigue discussed in Section 4.4.2.1.2.

A simple explanation of this observation deals with the crack opening displacement (COD) required for cyclic crack growth in the matrix. This COD is largely determined by the compliance of the specimen cross section and is limited by the compliance of the fibers in a fully bridged crack situation. If the stress on the cross section is low enough, the driving force, in terms of strain in the system, is below that required for crack propagation in the matrix. Fiber bridging in the initial cracks is an important ingredient in this mechanism and is what causes a no-growth situation. Consideration must be given to the total state of stress in the matrix. Residual stresses in the matrix, if high, may contribute to the initiation of a small crack but, once the crack is formed, residual stresses in the crack region are effectively relieved and have less contribution to the driving force for additional crack growth. Loading rate (frequency) will have an effect, also, in that the matrix will exhibit strain rate strengthening and, therefore, show an increase in the strain necessary to cause local fracture.

Of course, the stress associated with the threshold observed in Figure 115 is specimen geometry specific and may also be affected by stress gradients. Although identification of a threshold via the models applied to this project was not done, it is possible that the bridging models will, indeed, predict such a threshold and the models will accommodate the part or specimen geometry and stress gradient variables.

Transient periods of high growth rate seem to occur when the edge of the specimen has been exposed to damage of some sort, be it hot air or machining into the near-edge fibers. The latter will not be a problem with components wherein the MMC reinforcement will be buried but the former is an important aspect of life limitation once the propagating crack breeches the MMC reinforcement.

4.5.2.8   Comparison of Room Temperature Crack Growth in Longitudinal Orientation with Results from WRDC-TR-89-4145 (Reference 22)

In order to assess the suitability of data obtained in a previous program (Reference 22) for augmenting the data base for life prediction and damage tolerance in this program, a typical set of crack growth data from each test program was plotted in Figure 116. The data reported in the reference was taken under significantly different test conditions
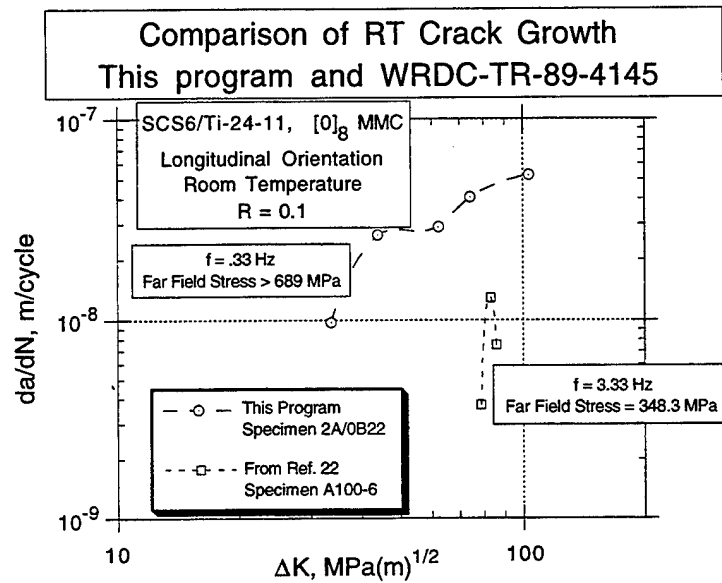
Figure 116. **Room temperature crack growth comparison with similar data reported elsewhere (Reference 22).**
The room temperature crack growth behavior is sufficiently different as to preclude merging of the two data sets.

of frequency, test specimen geometry and far field stress. The degree of bridging in the initial notch is unknown. However, an examination of Figure 116 clearly leaves one with the impression that either the materials fall into quite different populations or the conditions of the test have a major influence on the crack growth properties at room temperature. We have seen that, for the specimen configuration used, the crack growth rate is a linear function of far field stress in the program materials (see Section 4.5.2.6) and it is very strongly influenced by test frequency. The stress of 348.3 MPa, utilized by the investigators of Reference 22, would indicate a near zero growth rate, (see Figure 76). Because the initial length of cracks used in this investigation were short, the observation of zero crack growth may not extrapolate to the long crack situation of Reference 22, where ΔK is on the order of 70-90 $MPa(m)^{0.5}$.

In the absence of calibration tests from both programs tested in the same conditions, from the above analysis, it is prudent that room temperature fatigue crack growth data from Reference 22 not be merged with the data of this program to augment any sort of crack growth modeling. The complexing factor of the significant frequency effect noted in this program further exacerbate the problem of data merging. The program did not attempt to exercise the MMCLIFE models to attempt to collapse data, primarily due to the dissimilarity in test frequency and the observed, but not completely modeled, effect of test frequency.

It is entirely possible that, given an appropriate cross calibration of test specimens and techniques used in the two programs, the data may merge. This is most probable with fiber dominated properties such as fatigue and fatigue crack growth where loading is parallel to the reinforcing fibers.

4.5.3 Fatigue Crack Propagation in Longitudinal MMC at Elevated Temperatures

4.5.3.1 Testing Methods

Elevated temperature fatigue crack propagation testing was conducted using single edge notched (SEN) specimens described in Section 4.2.1.1. Induction heating methods were used, wherein the coils had been calibrated to give a uniform temperature zone of over 15 mm either side of the crack. All specimens had been precracked in three point bend as described in Section 4.5.2.1, and the original notch removed to provide an initially bridged singular crack with which to begin each test. Two long–focus, traveling, vernier–scale, microscopes were mounted to the test frame to optically monitor crack length on both sides of the SEN crack. All tests were run in load control with a maximum load adjusted to provide a predetermined far field stress on the SEN specimen. Crack length measurements were recorded for both sides of the specimen and averaged for analysis of the crack growth behavior.

4.5.3.2 Test Results at 550°C

4.5.3.2.1 Pre-Exposure at 550°C, 689.5 MPa Max Stress, 20,700 Cycles

Because an initial test attempt with 689.5 MPa (100 ksi) far field stress resulted in no growth from the initial bridged crack of 0.203 mm (0.008") after 20,700 cycles, the stress was boosted to 827.4 MPa (120 ksi) and the cycle counter reset to zero.

4.5.3.2.2 Test With Max Stress of 827.4 MPa, to Failure.

The results of this testing, with a rezeroed cycle counter after boosting the stress, are seen in Figure 117. There appear to be 5 distinct growth regions, including the last catastrophic portion.

Assuming a triangular lay-up of fibers with each layer at the material specification lay-up of 47 fibers per cm, we can see that a straight crack front would intersect a row of fibers every 0.106 mm. For the purpose of discussion, this spacing will be called the inter-fiber spacing (ifs). Starting with an initial crack length of 0.203 mm, the crack front would encounter a new row of fibers at 0.31 mm, 0.42 mm, 0.52 mm and 0.63 mm, etc. Note that the breaks in the plot of a vs. N occur at about 0.35 mm, 0.42 mm, 0.53

mm and 0.70 mm, at which point the crack failed in a catastrophic manner. Hence, the crack length at catastrophic failure was no longer than about $(0.70/0.106 =)$ 6.6 fiber rows. As each row was encountered by the advancing crack front, a change in crack growth rate was seen. The observation that the rate may either increase or decrease may attest to the variable effectiveness of the fiber bridging in this 8 layer composite. The crack length measurement increments are likely to be on a scale too fine for global analysis and the cracks too short to avoid edge effects (6 or 7 fiber rows), prior to specimen failure.

Excluding the first and last crack length measurements, a calculated da/dN vs. ΔK plot is presented as Figure 118. An average growth rate of between 10^{-8} to 10^{-6} m/cycle is observed, based on calculations from instantaneous crack length readings. No corrections for closure or bridging were attempted for this plot. Note that the failure occurred at a maximum K value of about 44.6 $MPa(m)^{0.5}$, an approximate fracture toughness for this material, crack geometry and specimen size at 550°C (1022°F) as it may have been modified by the thermal and thermomechanical exposures seen up to the point of failure.

4.5.3.2.3   Test at 550°C, 1034.2 MPa Max Stress

Crack growth behavior at a 1034.2 MPa (150 ksi) far field stress is presented in Figure 119 as a vs. N and as conventional da/dN vs. ΔK, without closure or bridging corrections, in Figure 120. From Figure 119, there can be identified at least four distinct, nearly linear, behaviors. The early crack growth appears to be rather rapid, 4.0×10^{-4} mm/cycle, from the initial precrack of 0.267 mm to a depth of about 0.52 mm which is close to an additional 2 average inter-fiber spacing (ifs). At this point, the crack appears to slow to a rate of about 1.6×10^{-4} mm/cycle and grow at that rate until a crack length of about 0.79 mm is reached. At this point, which corresponds to a total depth of about 5 average ifs beyond the precrack, the crack accelerates, in two stages, to failure at a crack length of 1.59 mm which is about 12 or 13 fiber distances beyond the precrack. The specimen failed at 2,386 total cycles.

Because K_b is strongly specimen configuration dependent and $K_Q = K_a - K_b$, it is not strictly appropriate to discuss K_a as though it were a material property but lacking direct information regarding K_b, and noting that the specimens used in this program are nearly identical, an apparent fracture toughness, K_a at the onset of catastrophic failure is considered an appropriate measure of toughness, for comparison purposes. Such is the case through out this report. Any error will be minimized if comparisons are restricted to the conditions at final fracture where bridging becomes strictly a strengthening rather than a cyclic crack growth inhibiting mechanism.
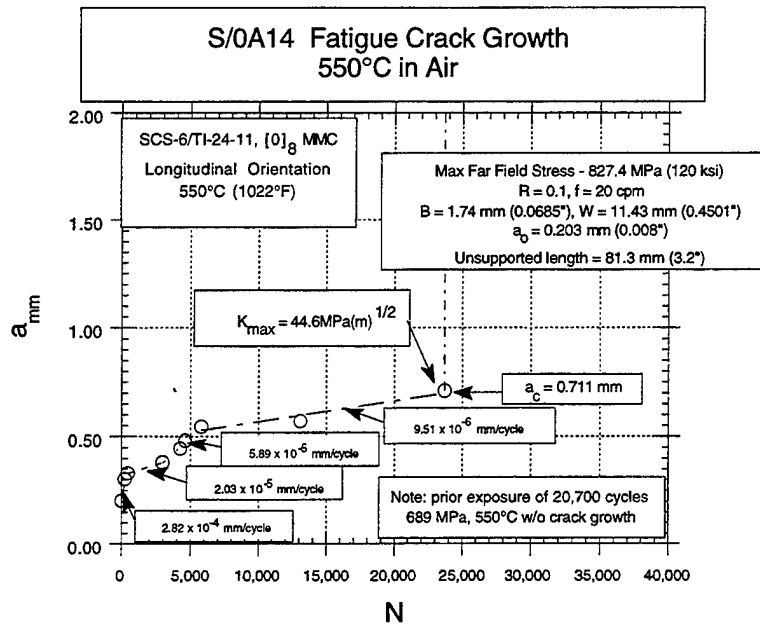
Figure 117. **Fatigue crack growth at 550°C.**
Initial far field stress = 689 MPa without crack growth at 20,700 cycles. Restarted test with far field stress at 827.4 MPa. Note: there are up to 5 distinct crack growth zones, including the catastrophic failure.
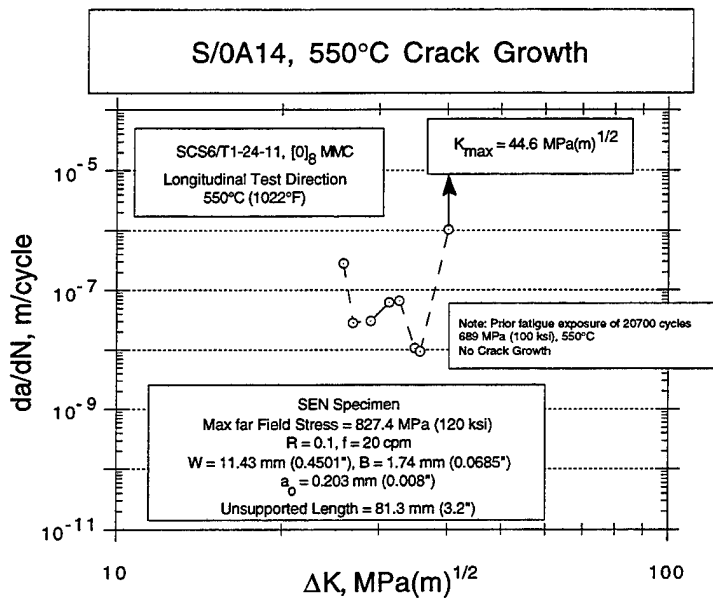
Figure 118. **Conventional fatigue crack growth vs. ΔK plot at 550°C.**
Initial far field stress = 689.5 MPa without growth to 20,700 cycles. Restarted test with stress increased to 827.4 MPa. Apparent fracture toughness = 44.6 MPa(m)$^{0.5}$.

162
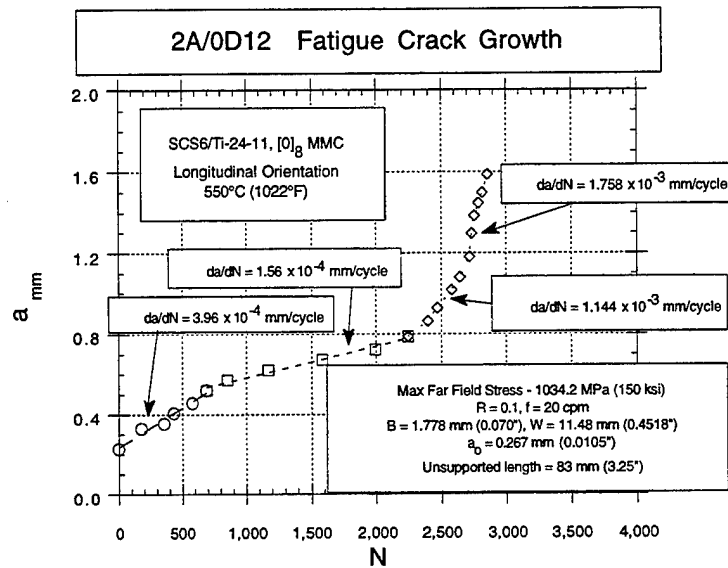
Figure 119. **Fatigue Crack growth at 550°C.**
Far field stress is 1034.2 MPa (150 ksi). There are four distinct growth behavior zones, each with nearly linear growth behavior. The entire life of this SEN specimen was consumed in the first 12 or 13 inter-fiber spacing distances from the precrack.
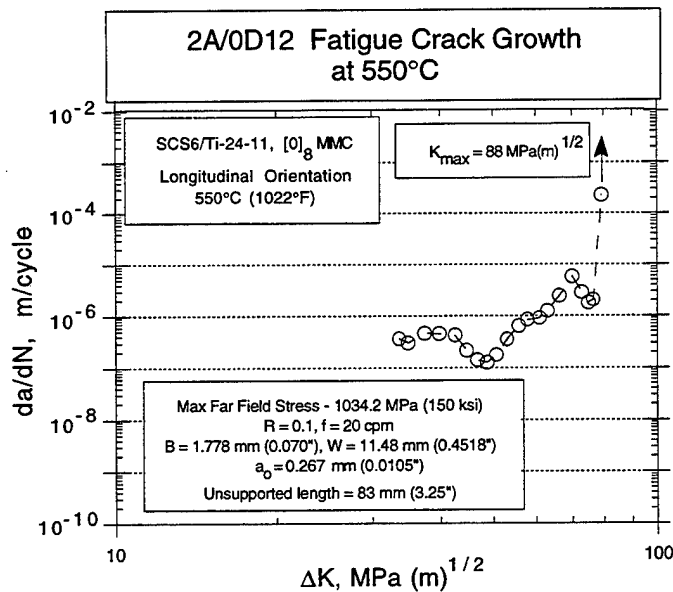
Figure 120. **Conventional fatigue crack growth vs. ΔK plot at 550°C.**
Far field stress = 1034.2 MPa. Note: apparent fracture toughness = 88 MPa(m)$^{0.5}$.

In Figure 120, the crack growth rate is seen to generally increase with increased ΔK until failure, at a K_{max} of about 88 MPa(m)$^{0.5}$. This latter value can be considered an indication of the material's fracture toughness at 550°C (1022°F) as it may have been modified by the thermal and thermomechanical history up to the time of the specimen failure. This is clearly higher than the K_{max} of 44.6 MPa(m)$^{0.5}$ calculated for a test at 827.4 MPa (120 ksi) far field stress (Para 4.5.3.2.2). The additional lower cyclic stress, long time, exposure of the latter may have induced some fiber damage.

4.5.3.2.4 Comparing Crack Growth with LCF Results

It is interesting to note that the LCF failure of a smooth specimen at the applied stress of 1034.2 MPa and temperature of 550°C (1022°F) occurred at a total of just over 10,000 cycles when tested at 1 to 5 Hz. The above discussed specimen failed with a propagation life of 2,850 cycles. If we assume that the total LCF life is partitioned simply into a propagation life and an initiation life, and furthermore, if we assume the frequency effect is small, we can then consider the difference in total lives of the two specimens to be the number of cycles necessary to generate an initial flaw equal to a_o in Figure 119 (0.267 mm). This difference, (10,000–2,850 =) 7,150 cycles, is taken to generate the initial flaw. This means that only 28.5% of the total life is consumed in crack propagation from the initial crack depth of 0.267 mm (0.010 in) = 2.5 ifs. A similar logic applied to the specimen in Figure 117 at a lower stress (827.4 MPa), shows that 30% of life is spent in propagation from an initial crack depth of 0.203 mm (0.008" = 2.0 ifs).

One conclusion, therefore, is that fatigue life of this MMC system at 550°C (1022°F) is dominated by the initiation events, much as with monolithic metals. This is not to discount the importance of an apparent threshold stress beyond which cracks will not propagate. This threshold is an unknown function of test variables and is worthy of additional study outside the bounds of this program. It is apparent that far field stress is one of the more important variables at room temperature.

Another factor, likely to be very important, is the effect of test frequency. As was discussed in Section 4.5.2.6 pertaining to room temperature tests, there is a great deal of evidence that a frequency effect exists in this material at room temperature, at least, which indicates a measurable increase in crack growth rate with decreased test frequency. It is logical to extend this observation to elevated temperature crack growth in the MMC of this study. In support of this hypothesis is the observed acceleration in crack growth in the matrix NEAT foil material with lower test frequencies and specifically with hold time at maximum load at both room and elevated temperatures. These results are discussed in Sections 4.5.1.2 and 4.5.1.3.

4.5.3.2.5 Comparison of Crack Growth with Two Different Far Field Stress Levels

Despite the observation that the apparent fracture toughness of the specimen with a far field stress of 1034.2 MPa (150 ksi), is much higher than the specimen tested at the lower far field stress of 827.4 MPa (120 ksi), the two results are plotted together in Figure 121. This figure appears to show the crack growth behavior of the two specimens to be quite similar. A merging of the growth data would be considered feasible, despite the differences in the far field stress for each specimen. However, the rather large differences in apparent fracture toughness, 88 compared to 44.6 MPa(m)$^{0.5}$, clearly indicates the materials' tolerance to crack-like defects is vastly different between the two specimens, the latter having seen prior cyclic exposure.

Considering a model of fracture toughness, or K_{max} at catastrophic failure, that simply involves the ability of the fibers to hold a portion of the applied load dictated by the volume fraction of the fibers in the remaining ligament, the bridged fibers and the strength of the fibers at the critical time in the specimen's history, a simple explanation for this behavior can be offered. The lower stress specimen experienced a previous large number of fatigue cycles at an even lower stress as well as a long exposure time. Also, due to the lower far field stress, a slower crack growth rate in this specimen provides
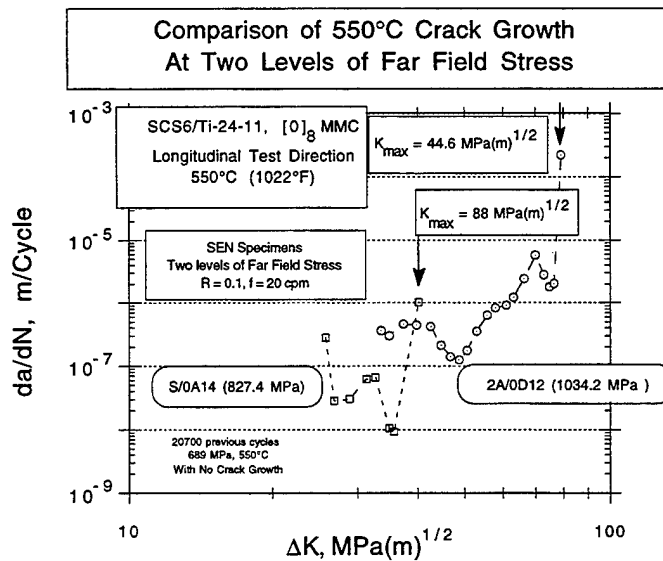
Figure 121. An overlay of the specimens tested at two far field stresses, 827.4 and 1034.2 MPa, both at 550°C.

The lower stress specimen had received a previous exposure of 20,700 cycles at 689.5 MPa maximum stress and the same temperature. Note the differences in apparent fracture toughness.

an even greater total time of exposure at the test temperature. If the fibers were to degrade to an extent related to the total thermal and fatigue exposures and cumulative time at the exposure temperature, the load carrying capacity of the remaining ligament of a crack growth specimen would also degrade. The apparent fracture toughness of the specimen, as indicated by the K_{max} of the cycle prior to failure, would also be degraded. The 550°C (1022°F) specimen with the greater cumulative time, temperature and cyclic fatigue exposure, exhibited the lower apparent toughness. This is in agreement with the qualitative model presented above.

The fact that the crack growth behavior seems to be in the same population for both the high stress and the previously exposed samples is an indication that the mechanisms of resistance to fatigue crack growth is not identical to that which provides resistance to catastrophic crack growth on monotonic loading.

Bridging of the crack by fibers will be an important feature in crack growth resistance so long as the fibers in the bridging zone are not stressed beyond their instantaneous strength. Therefore, so long as the cracks are short, even weakened fibers will serve the role of crack growth inhibitors or at least they will bear the loading increase by a factor associated with the matrix no longer able to carry a tensile load across the crack. Also, the matrix residual stresses are off loaded to the fiber. Under these circumstances, the crack growth rates will be largely controlled by the matrix properties which are not strongly affected by the 550°C (1022°F) exposure.

The simple effects of thermal exposure, specifically thermal cycling, on residual room temperature tensile properties was discussed in Section 4.2.2.2.1.1. It was clear that little effect on room temperature tensile properties was experienced by up to 100 thermal cycles to 650°C (1200°F). The time at temperature was on the order of 30 hours while that in the fatigue pre-exposure was on the order of 36 total hours. Similarly, as was the case for the elevated temperature LCF, fatigue crack growth resistance showed no clearly evident degradation from prior cyclic exposure in air. Hence, it may be logically concluded that it is not the unstained thermal cycles but it is the fatigue cycling component, along with the preexistence of a crack for the duration of the exposure, which are the major contributors to the reduction in apparent toughness. This, in turn, is attributable to a reduction in fiber strength in the first few fiber layers encountered by the moving crack. The influence of fibers on cyclic crack growth remains unchanged except to the extent that the terminal event, fracture, intervenes as a result of the reduced fracture toughness which, in turn, is due to degraded fiber strength. Research by J. Larsen, et al. (Reference 24) indicates that at 650°C (1200°F), SCS6 fibers exposed to the advancing crack, suffer from oxidation of the carbon rich coating. The resultant reduced interfacial friction stress, τ, significantly modifies the influence of bridging on

fatigue crack propagation resistance. Similar effects are possible at 550°C (1022°F) with extended exposure to air in the bridged crack.

4.5.3.3   Test Results at 650°C

4.5.3.3.1   Test with Maximum Far Field Stress of 689.5 MPa to Failure

As seen in Figure 122, the cyclic crack growth rate is nearly constant, at 2.1×10^{-5} mm/cycle, up to the point of catastrophic failure. The critical crack length was 1.13 mm, or about 7 to 8 fiber spacing from the end of the precrack. When the results are plotted as da/dN vs. ΔK in Figure 123, with no corrections attempted for crack closure or crack bridging, it is apparent that ΔK varied only slightly over the life of the test and the apparent fracture toughness was about 43 $MPa(m)^{0.5}$.

This is remarkably similar to the value obtained from the low stress test at 550°C (1022°F) (44.6 $MPa(m)^{0.5}$). In fact, the total thermal exposure time of this specimen was about 30 hours at 650°C (1200°F) while that of the low stress, 550°C (1022°F), test specimen was nearly the same, at 36 hours. The material did exhibit measurable crack growth at 650°C (1200°F), whereas at the same stress (689.5 MPa), the 550°C (1022°F) test failed to show crack growth, at least by the time 20,700 cycles had been run. One possible explanation for this may involve the ΔK at which the test was begun. In the lower temperature test, the initial ΔK was on the order of 25 $MPa(m)^{0.5}$ while at the higher temperature, the test was initiated at a ΔK of 33 $MPa(m)^{0.5}$. The rather linear behavior at the outset of the test in Figure 122 would imply a fatigue crack growth rate independence of ΔK, at least in the low growth rate region. This is not the obvious conclusion drawn from Figure 119, in which the initial growth rate was quite high. However, the influence of prior exposure history is unknown and no test was conducted wherein the far field stress was decreased to 689.5 MPa on a growing crack.

The conventional da/dN vs. ΔK plot of these data are shown in Figure 123. No attempt is made to correct for crack bridging or closure. As is evident from this plot, the crack growth rate is rather independent of ΔK up to the onset of catastrophic failure, where the instantaneous fracture toughness is exceeded.

A repeat of the above test was performed in order to verify the results and evaluate data scatter. The results are plotted in Figure 124, as a vs. N. Unfortunately, initial precrack length and early crack growth were not recorded. As seen in Figure 124, the growth rate can be concluded to be somewhat lower than, or on the order of, 7.29×10^{-5} mm/cycle. It is also rather constant, over the last millimeter prior to catastrophic failure, at 3.00×10^{-3} mm/cycle. Failure occurred at a crack length of 2.74 mm where the K_{max}, or apparent fracture toughness, was 84.5 $MPa(m)^{0.5}$ (Figure 125). This appar-
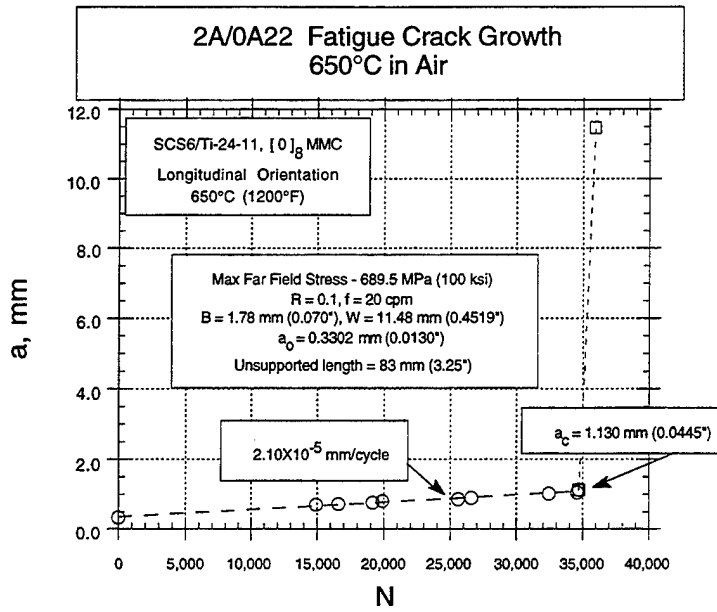
Figure 122. **Cyclic crack growth at 650°C in air with maximum far field stress of 689.5 MPa.** Critical crack length, a_c, at onset of catastrophic failure is 1.13 mm or about 7 to 8 inter-fiber spacings beyond the initial crack length, a_0.
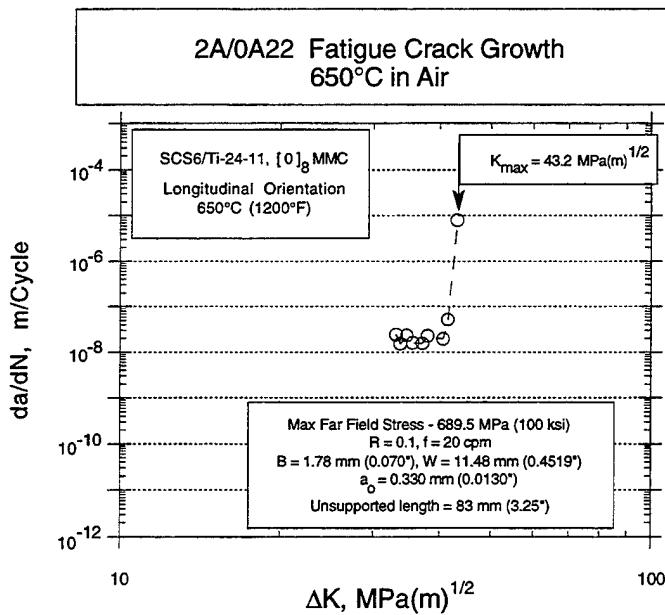
Figure 123. **Fatigue crack growth behavior at 650°C in air with a maximum far field stress = 689.5 MPa.**
An apparent fracture toughness of approximately 43.2 MPa(m)$^{0.5}$ is evident.

168
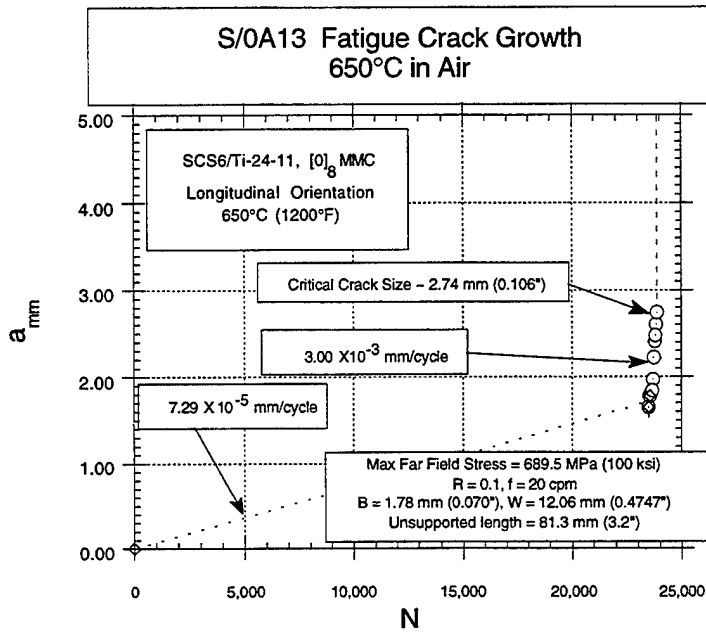
Figure 124. **Cyclic crack growth at 650°C in air with maximum far field stress of 689.5 MPa.** Critical crack length, a_c, at onset of catastrophic failure is 2.74 mm.
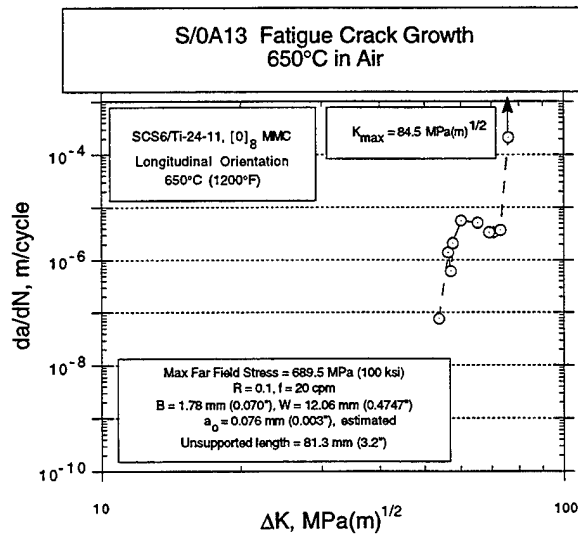
Figure 125. **Fatigue crack growth behavior at 650°C in air with a maximum far field stress = 689.5 MPa.**
An apparent fracture toughness of approximately 84.5 MPa(m)$^{0.5}$ is evident. The maxima in this plot is an artifact of the small crack grow increments at which readings were taken, relative to the fiber spacing.

169

ent fracture toughness is compared a the value of 43 MPa(m)$^{0.5}$ obtained from the previously discussed test. The only significant difference between the two tests is that the one with a higher apparent toughness started out with a smaller, but unquantified, precrack and it exhibited an acceleration prior to catastrophic failure from a crack length of about 1.7 mm.

4.5.3.3.2 Test with Maximum Far Field Stress of 827.4 MPa

One fatigue crack growth test was run at 827.5 MPa (120 ksi) far field stress and 650°C (1200°F) in order to determine the effect of the higher stress on growth rate. The results of the test are shown, as an a vs. N plot, in Figure 126. The rather linear form of the growth up to the point of eminent failure is evident. The growth rate is about 3.2×10^{-5} mm/cycle, compared to a rate of 2.1×10^{-5} mm/cycle exhibited by a similar test run at lower stress of 689.5 MPa (100 ksi). See Figure 122. In neither case was there a significant acceleration leading up to the failure event, a behavior characteristic in common with the room temperature tests.

Figure 127 displays the same information in the form of da/dN vs. ΔK, with no attempt at correcting for bridging or closure. From Figure 127, the apparent fracture toughness is about 60 MPa(m)$^{0.5}$ compared to a value of 43 MPa(m)$^{0.5}$ for a similarly conducted test at a lower far field stress of 689.5 MPa (100 ksi) described in Figure 123. The difference may lie in the inadequacy of ΔK as an independent variable or it may be a result of greater total exposure time at temperature associated with the lower stress test (35,000 cycles compared to 19,000). In this case, the growth rate is not as strongly affected by environmental degradation as is the apparent toughness.

Perhaps this latter may be a matter of the fiber strength being degraded but the crack retardation mechanism of bridging and fiber/matrix interface sliding being less affected.

4.5.3.3.3 Test with Maximum Far Field Stress of 689.5 MPa and a Single Overload Applied.

With test parameters otherwise similar to that described in Figure 122, a third test was conducted, with the plan to impose a single cycle, 19% overload during the test, and observe the post-overload behavior. Figure 128 shows the results. The crack growth rate is nearly linear, as in the previous test, up to a point of rapid acceleration where failure was eminent. This gives an average , linear, crack growth rate of about 2.25×10^{-5} mm/cycle. This is a remarkably similar value to that obtained in the previously discussed tests. Also, the crack length just prior to the catastrophic failure, $a_c = 2.76$ mm is close to the earlier value for a_c. The nearly identical results discussed above is sufficient to justify placing them in the same data population.

170
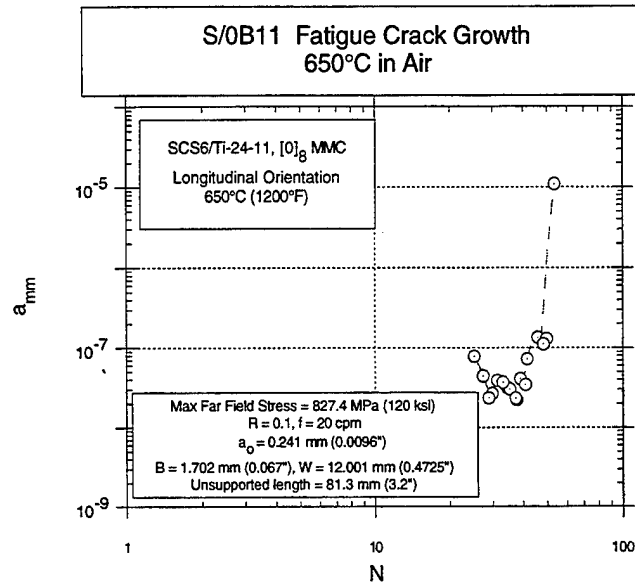
Figure 126. Fatigue crack growth in longitudinally oriented MMC sample at 650°C with a stress ratio of 0.1 and a maximum far field stress of 827.4 MPa.

The steady-state crack growth rate is 3.2×10^{-5} mm/cycles, compared to 2.1×10^{-5} mm/cycles for a similar test at 689.5 MPa as illustrated in Figure 123.
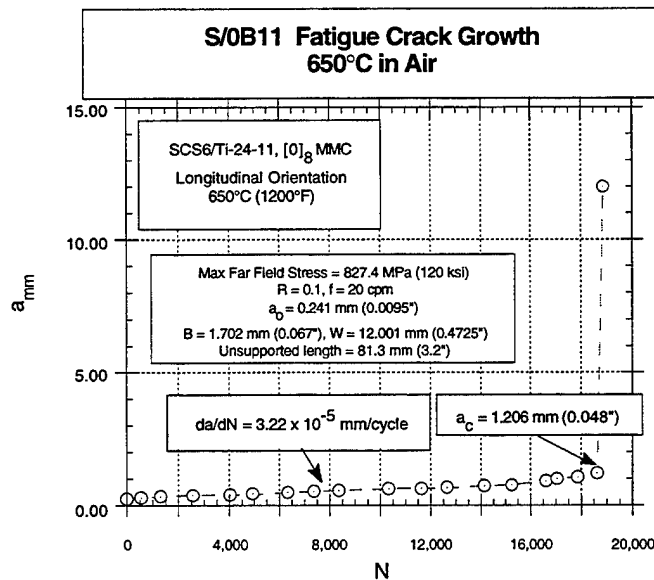
Figure 127. Fatigue crack growth in longitudinally oriented MMC sample at 650°C with a stress ratio of 0.1 and a maximum far field stress of 827.4 MPa.

The apparent fracture toughness is about 60 MPa(m)$^{0.5}$ compared to 43 MPa(m)$^{0.5}$ for the similar test run at 689.5 MPa seen in Figure 123.

171
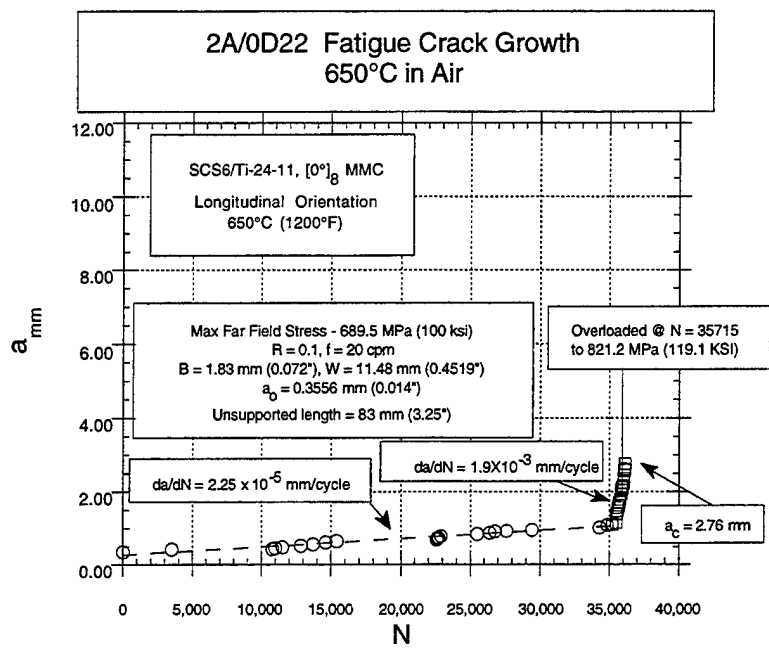
Figure 128. Cyclic crack growth behavior at 650°C, with a far field stress of 689.5 MPa. An overload of 19.1% was applied on one cycle at N = 35,715.

The overload was planned to occur at a specific crack length of 1.8 mm. As it turned out, this occurred as the crack was accelerating towards the end of the test so little useful information as to its effect on steady-state grow rates can be ascertained.

Figure 129 shows the same data plotted as da/dN vs. ΔK, with no attempt to correct for crack closure or crack bridging. There appears to be two distinct population groups. At the lower ΔK, a random pattern of results is noticed and at the higher ΔK, another ΔK independent growth rate is noticed until catastrophic failure occurs with an apparent fracture toughness of about 86 MPa(m)$^{0.5}$. The dividing line for the two groups is at 35,225 cycles of growth which equates to about 29 total hours of thermal exposure in cyclic crack growth testing. When analyzing the data together in Figure 129, one can draw a curve fit including the entire data group. Such a fit is represented on the plot.

The overload of 19% was applied at a ΔK of about 54 MPa(m)$^{0.5}$ and, as can be seen from Figure 129, there was no noticeable influence on the crack growth rate immediately following the overload. If the overload had served to break the fibers which would otherwise bridge the advancing crack, an acceleration would be expected. Either the overload was too low or the fibers were already broken, or otherwise incapable of carrying the local load at the crack tip. Judging from the fact that the crack was no longer

172
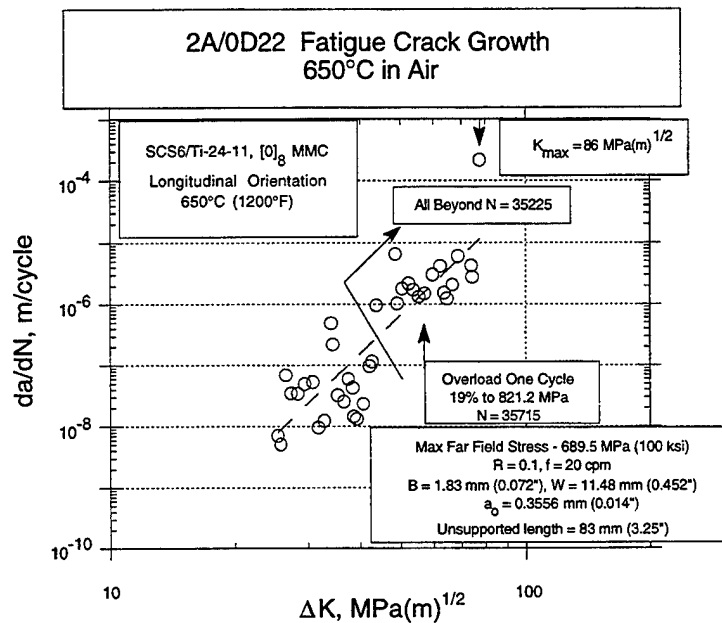
Figure 129. **Cyclic crack growth at 650°C with far field stress of 689.5 MPa.**
One cycle overload of 19.1% was applied at cycle 35,715 with no apparent effect on the subsequent growth rate. An apparent fracture toughness of 86 MPa(m)$^{0.5}$ is noted.

growing at a constant rate, but accelerating, as seen in Figure 128, the effectiveness of the reinforcing fibers had been lost prior to the overload. Hence the effect of overload on crack growth at 650°C (1200°F) was not possible to assess from this test.

4.5.3.3.4 Effect of Dwell at Maximum Load on Fatigue Crack Propagation at 650°C and Maximum Far Field Stress of 689.5 MPa

A 5-minute dwell at maximum load was imposed, on an otherwise 20 cpm test, during early stages of propagation and after 27,313 cycles. The overall crack length vs. number of cycles is plotted in Figure 130. An examination of the plot indicates a more rapid growth under conditions of dwell. Failure occurred at a total of 28,076 cycles with an accumulated time of about 135.5 hours cycling at 650°C (1200°F).

A more detailed examination of the data associated with the 5-minute dwell at the outset of the test is facilitated by examination of the plot of Figure 131. It is easily seen that an initially high growth rate of about 3.8×10^{-2} mm/cycle changes to a rate of 1.99×10^{-3} mm/cycle, or less than 1/20 of the initial rate. When this information is examined with respect to the number of inter-fiber spacing intersected by the crack front, it is clear
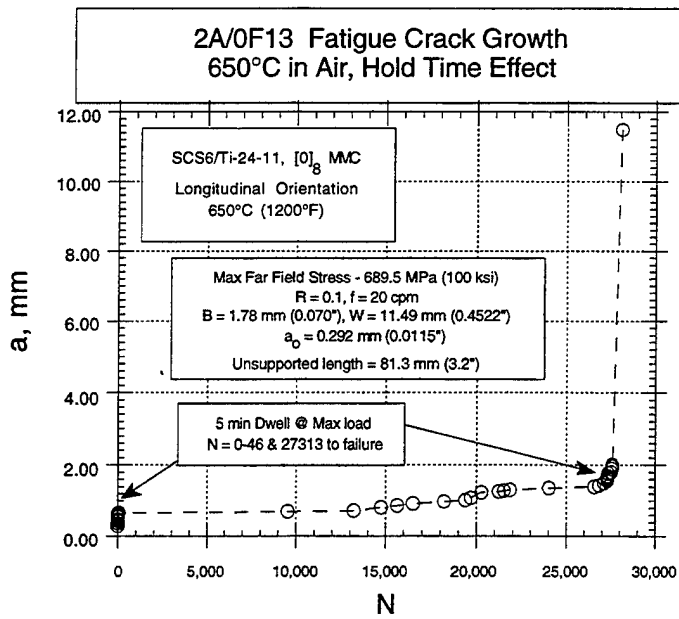
Figure 130. Crack length vs. number of fatigue cycles with a 5 minute dwell at maximum load for the first 46 cycles and after 23,713 cycles.
A generally more rapid growth rate is noted under dwell conditions.
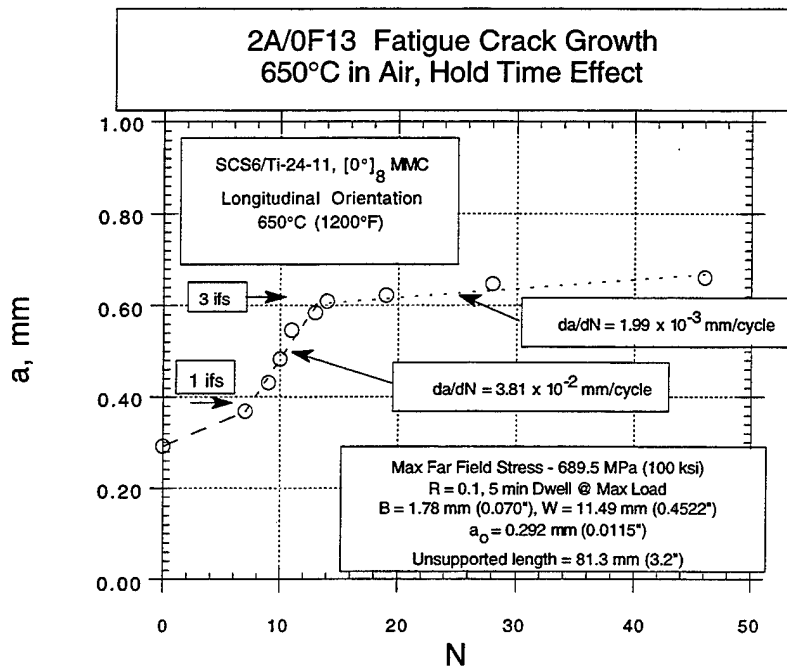
Figure 131. Details of early growth under conditions of 5 minute dwell at maximum load.

174

that: 1.) by the time the crack had propagated beyond the precrack a distance equivalent to about 4 inter-fiber spaces (ifs), the frequency had been increased to 20 cpm; 2.) the rapid growth period was evident only through the first 3 inter-fiber spacing. As to whether or not the rapid growth was due to the dwell or to the relative scatter in growth resistance, exacerbated by the edge effects of the specimen, is not certain from this information alone.

A closer look at the 20 cpm portion of the a vs. N data are seen in Figure 132. Here is seen that the average growth rate, initially is about 400 times less rapid than the growth rate of the preceding period with a 5-minute dwell. After the slow growth to about 4 inter-fiber spacing (ifs) beyond the initial precrack, (total time at temperature of about 20 hours), the growth rate did increase by a factor of over 10, but remains slower than during the initial 5-minute dwell period. On a finer scale than the inter-fiber spacing (ifs = 0.106 mm), there is considerable variation in growth rates. This is evident in Figure 132 beyond 15,000 cycles or so.

Upon returning to a 5-minute dwell at 27,313 cycles, there was an acceleration, as seen in Figure 133. Here is seen an immediate acceleration, followed by an apparent arrest followed again by another acceleration. For reference, the last few points of the 20 cpm period are included to illustrate the difference in crack growth rates for the two test conditions.

A summary of the da/dN vs. ΔK information, without any attempt to correct for crack closure of fiber bridging, is plotted in Figure 134. From this figure, one can determine that the apparent toughness of the material is on the order of 68.9 MPa(m)$^{0.5}$, and the initial, rapid crack growth under conditions of 5-minute dwell at maximum load does decay by over 4 orders of magnitude. The total crack growth, however, is less than about 4 inter-fiber spacing (ifs) during this period. The total time of exposure of over 135 hours at 650°C (1200°F) at the time of failure is an important factor and may have influenced the results. A degradation of the fiber coating (Reference 24) has been associated with a reduced bridging effect at 650°C (1200°F) under certain conditions and such a factor may be present in this test as well.

4.5.3.3.4.1 Discussion and Conclusions Regarding the Effect of Dwell on Fatigue Crack Growth at 650°C

The above discussions lead to a conclusion that there is a more rapid growth under dwell conditions. However, there may be a complex interaction with the environment that is not explained by the information gathered in this program. In general, more rapid growth behavior is associated with dwell. The total crack growth in this specimen was less than 2 mm (or 18 inter-fiber spacing) beyond the precrack. Crack termination, at a toughness of about 68.6 MPa(m)$^{0.5}$, limits this growth period. With a higher applied
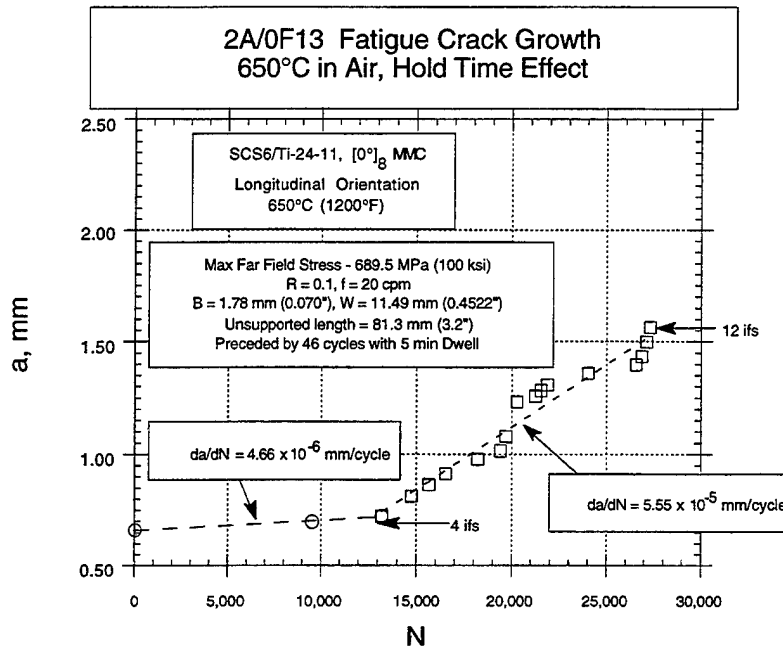
Figure 132. 650°C cyclic crack growth at 20 cpm following an initial block of 46 cycles with a 5 minute dwell at maximum load.
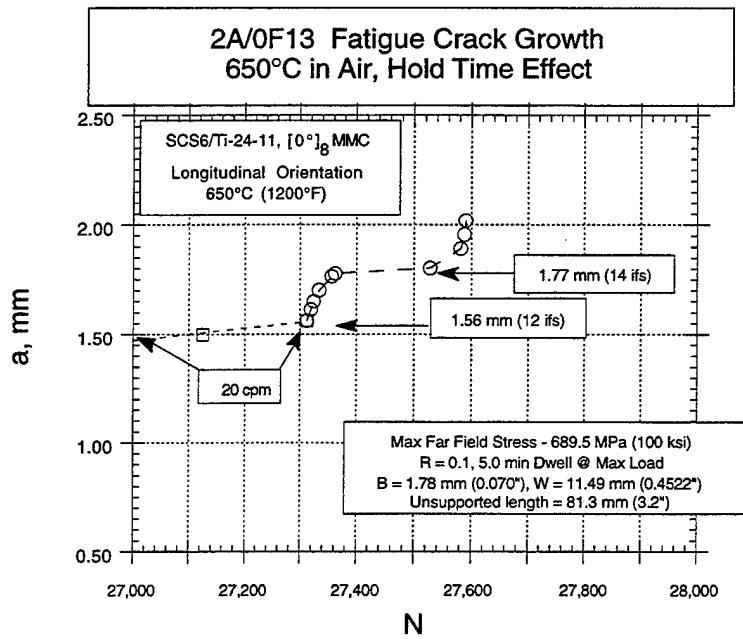
Figure 133. 650°C cyclic crack growth on the transition from 20 cpm test frequency to 5 minute dwell at maximum load.

176
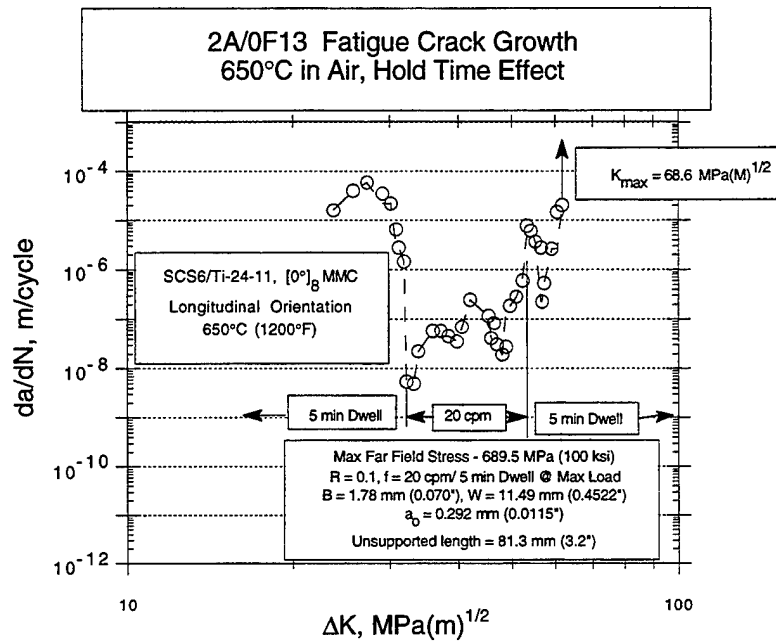
Figure 134. Conventional plot of da/dN vs. ΔK for 650° test with two blocks of 5 minute dwell at maximum load.

stress, a proportionately smaller total crack growth period would be experienced. This condition clearly implies that there is a very great significance to the near surface integrity of the MMC. The MMC's greatest portion of life is determined by flaw initiation and growth near the surface.

4.5.3.3.5 Comparison of Crack Growth Rates at 650°C with that Reported Elsewhere.

Test results from the two tests reported in Section 4.5.3.3.1 are compared with results from a similar test, on a longitudinal MMC Specimen with similar constituents, reported by Gambone, (Reference 22) in Figure 135. The tests in Reference 22 were conducted on larger SEN specimens and at a much higher test frequency (3.33 Hz compared to 0.33 Hz) than used in this program.

It is quite clear that the early stages of crack growth, below ΔK of about 50 MPa(m)$^{0.5}$, for all three specimens occurs at about the same rate. The higher frequency tests of Reference 22 continues to higher ΔK whereas the lower frequency tests terminate earlier. The reason for this behavior is likely to be a combination of cumulative time of thermal and cyclic exposure and the associated interface degradation as well as a possible different matrix baseline properties.

177
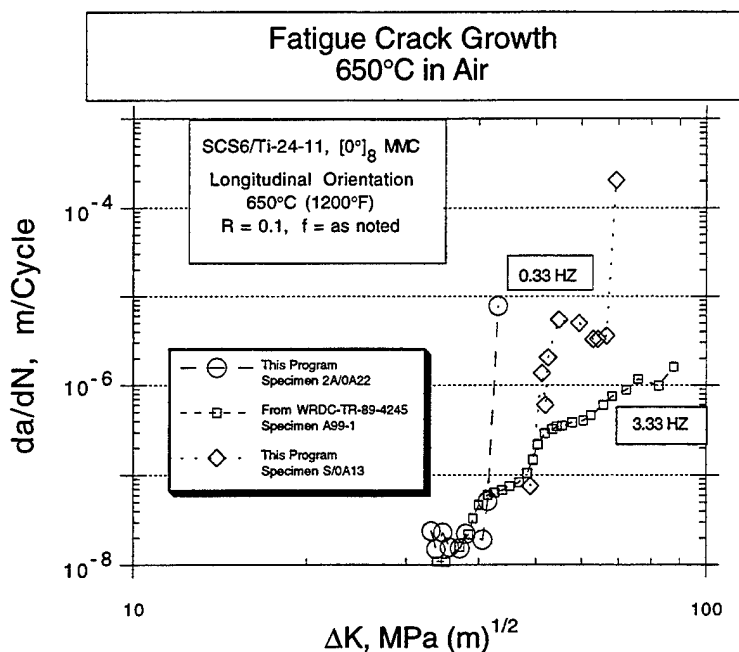
Figure 135. Comparison of Crack Growth behaviors of two specimens from this program with a similar test from Reference 22.

From the above analysis, it is clear that elevated temperature crack growth data from Reference 22 cannot be merged with the data of this program, for the purpose of life prediction or damage tolerance unless they can be used as an indication of a frequency effect. Unfortunately, 3.33 Hz is an unreasonably high frequency, relative to engine LCF cycles, and the associated data falls outside a reasonable engine cycle.

Clearly, materials characterization must be an integral part of any data package and, equally important, reproducible characteristics should be an important requirement in order to maximize the usefulness of such materials. Merely specifying a fiber and a matrix alloy and even the MMC consolidation parameters is not sufficient to guarantee reproducible properties.

4.5.3.4 Analysis of Crack Growth in Matrix Compared to Longitudinal MMC

The data for crack growth in longitudinal MMCs associated with bridging discussed by Larsen (Reference 24) where crack retardation was evident in MMC were presented in a format of da/dN vs. ΔK plots incorporating both matrix and MMC data. Crack closure corrections were not made for the matrix data as required by Larsen's analysis.

178

However, as discussed in Section 4.9, Section 6.6 and Section 6.7, there are other short-comings of a more serious nature.

4.5.3.4.1 Room Temperature Comparisons of Crack Growth in MMC and Matrix

Room temperature data from this program, for an R of 0.1, is plotted in Figure 136 in the same format. There is immediately noticed that the MMC exhibits the expected superior crack growth resistance. There is also evident a stress effect for the MMC plots. While the data for 689.5 MPa (100 ksi) and 827.4 MPa (120 ksi) background stress levels appear to belong to the same population, the behavior of the 1172 MPa (170 ksi) test was clearly of a different population, failing at a lower apparent fracture toughness. This stress effect, when all test data are considered, is collaborated by the plot of Figure 115 which implies that da/dN, when observed on larger scale is proportional to the stress alone and not strongly related to crack length.

Crack deceleration is seen in this plot but closer examination of the a vs. N plots of Figure 100 through Figure 103, Figure 105, Figure 107 and Figure 108 show that the variations in crack growth rate occur on crack length increments that are on the order of the inter-fiber spacing.
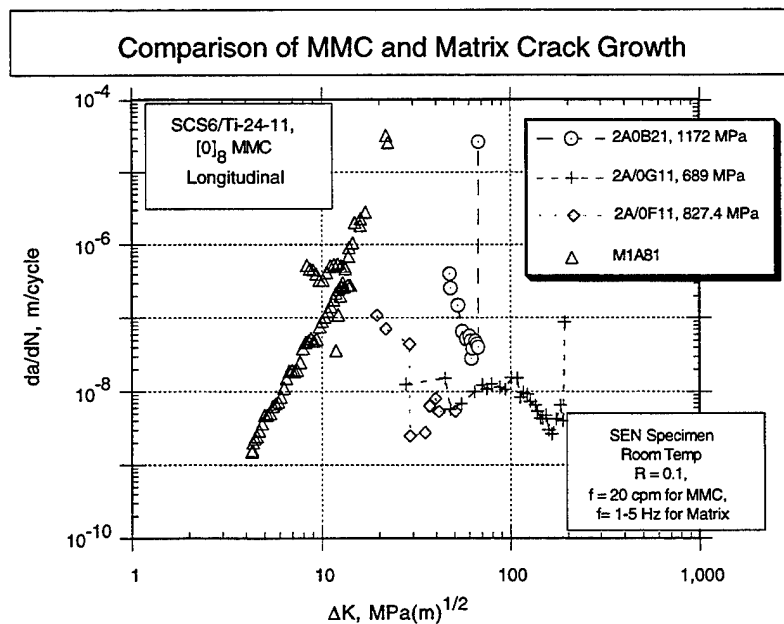
Figure 136. Room temperature fatigue crack growth comparing matrix with 0° MMC at maximum stress levels of 689, 827 and 1172 MPa and R = 0.1.

179

Unfortunately, when the stresses are high enough to be of interest to gas turbine engine disks, the critical crack length is too small to permit crack growth over enough inter-fiber space lengths to measure an "average" growth rate of a large crack.

Although not exercised, a bridging analysis much like that described by John, et al. (Reference 25), will predict the form of the data seen in Figure 136. The MMCLIFE code as modified during this contract deals with bridging internally and it was considered outside of the contract scope to analyze data by any other vehicle.

Metallographic analysis of fatigue crack growth specimens and LCF specimens in all stress ranges indicate that fibers bridge cracks and most of the bridging fibers remain intact until just prior to catastrophic failure. Evidence of this is presented in Section 4.9.3 for a specimen tested at room temperature and 689.5 MPa far field stress.

4.5.3.4.2 Comparisons of Crack Growth in MMC and Matrix at 550°C

Two 550°C (1022°F) specimens of longitudinal MMC tested at far field stresses of 827.4 MPa (120 ksi) and 1034.2 MPa (150 ksi) are compared to the matrix in Figure 137. Here, is also seen an initial deceleration followed by acceleration in the MMC. In both cases,
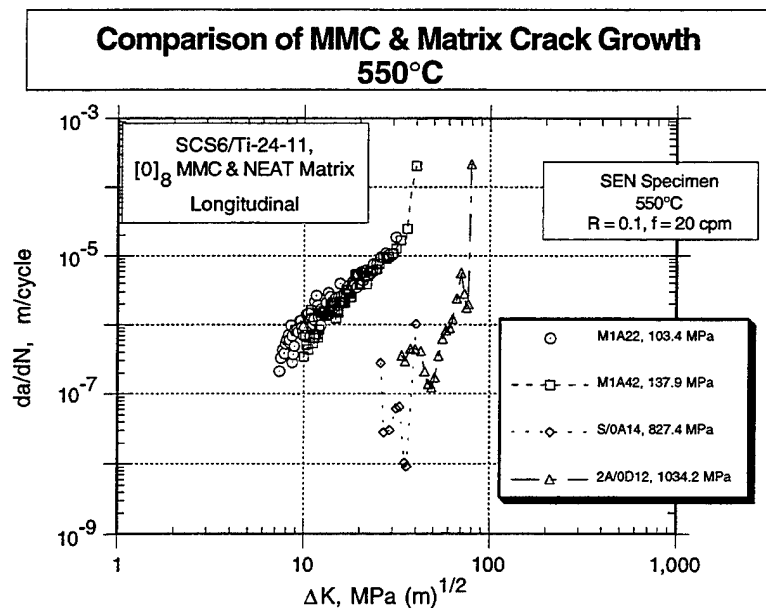
Figure 137. Fatigue crack growth at 550°C, comparing matrix and 0° MMC specimens. Max far field stress levels are 827.4 MPa (120 ksi) and 1034.3 MPa (150 ksi).

the deceleration occurred over a distance no greater than a few inter-fiber spacing (ifs) from the specimen edge. This was discussed in Section 4.5.3.2 and the question remains is this a short crack phenomenon, a phenomenon associated with edge effects, machining and so on, or is it merely an effect of small scale crack rate variations and the few specimens examined happened to have the faster growth zones near the edge of the SEN. In any case, the cracks are quite small as they transition to catastrophic growth, giving little warning before failure.

Compared to the room temperature behavior of the MMC, the 550°C (1022°F) crack growth is generally in the accelerating mode as the crack becomes longer. Although crack bridging is evident in these cases, it is ineffective in crack retardation to the extent of decelerating the crack. The proposed rationale for this effect was discussed in Section 4.5.3.2.4 wherein the effects of reduced hoop stress and the interfacial friction stress, τ, as a result of the elevated temperature, are highlighted.

4.5.3.4.3 Comparisons of Crack Growth in MMC and Matrix at 650°C

Comparisons similar to those at 550°C (1022°F) were done for tests at 650°C (1200°F). The results are seen in Figure 138 and, like the 550°C (1022°F) MMC results, an initial pe-
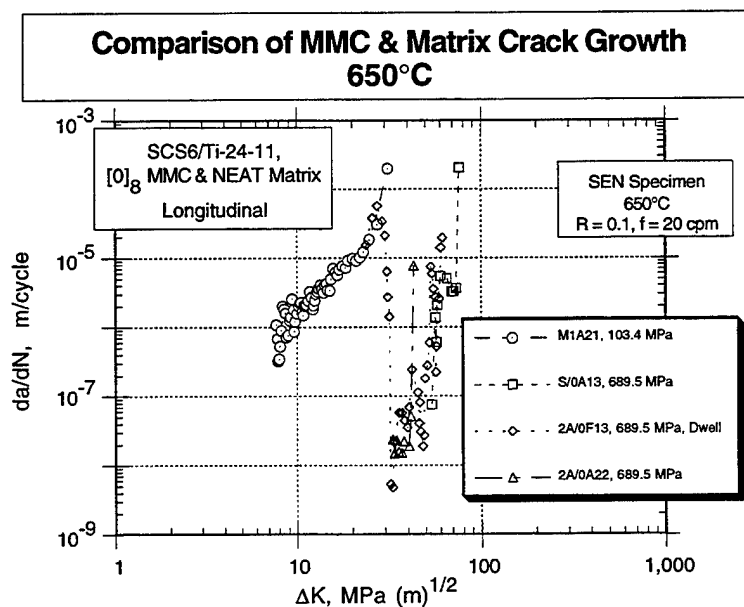
Figure 138.   Fatigue crack growth at 650°C comparing the matrix only behavior and 0° MMC specimens.
Max far field stress level used was 689.5 MPa (100 ksi).

181

riod of deceleration is followed by continuous acceleration to failure. The main difference between the results at the two temperatures is the shorter duration of deceleration at the higher temperature. The decelerating effect of crack bridging is rendered even less effective at 650°C (1200°F) than at 550°C (1022°F).

4.5.3.4.4 Summary of Elevated Temperature on Bridging Effects

A conclusion drawn from the above discussion is that, at elevated temperature, the effectiveness of crack bridging in creating damage tolerance by causing crack deceleration is greatly diminished. The reason for this is likely related to an effective reduction in friction stress, , due to the higher thermal expansion of the matrix, reducing the hoop clamping stress around the fiber circumference.

Use of MMC reinforcement in rotating components makes sense only when it is stressed to quite high levels and entering the da/dN vs. ΔK curve at high levels, once a crack is of detectable size, is the most likely case. Considering this, it may be further concluded that, because of the apparent small critical crack size and the limited spread between threshold and critical ΔK values in fatigue crack growth behavior, the MMC system used in this study is not a good candidate for applications at elevated temperature where damage tolerance is a necessary characteristic. Potential materials and manufacturing solutions to this are discussed in Section 6.

4.5.4 Fatigue Crack Propagation in Transverse MMC at Room Temperature

4.5.4.1 Experimental Issues

Baseline crack growth in the transverse orientation was difficult to obtain because early attempts to precrack specimens resulted in rapid failure as soon as the cracks were initiated from the machined notch. By running a large number of cycles at each of a series of increasing, but small, stresses it was possible to create small initial cracks. As with the longitudinal specimens, Potential Drop (PD) was used to give a dynamic indication of crack growth as was the long focal length microscope video recording system (Vision System). In the final analysis, optical microscopy, replicas and the Vision System recordings were all used to determine crack length throughout the test.

4.5.4.2 Baseline Test Results

Tests were conducted at a frequency of 20 cpm, a low far field stress of 137.9 MPa, an R of 0.1, and an initial crack length of 1.27 mm, the results of which are seen in Figure 139 and Figure 140. It is quite evident that catastrophic failure comes quickly as the difference between the threshold and the failure stress intensity factor range is less than

2.0 MPa(m)$^{0.5}$. There is little room for fatigue damage tolerance in this material when loaded in the transverse direction.

By increasing the test frequency by a factor of 3, little improvement is recognized. In fact, the total life is somewhat less but the da/dN vs. ΔK plot is nearly identical (Figure 140 and Figure 142). A direct comparison of frequency effects is seen in Figure 143.

Transverse creep may play a role in transverse crack growth behavior but with the severe hold time effect noticed, even at room temperature, it is likely that resistance to crack growth along the matrix/fiber interface, or lack of it, may have the dominate role in the mechanisms that lead to low crack growth resistance. This is particularly important when the crack tip stresses are high enough to cause local parting of the interface.

When stresses at a crack tip are below the point at which the matrix releases from the fiber (critical stress), then the time dependent properties of the matrix may increase their role in any hold time or frequency effects. Since Ti$_3$Al is strain rate sensitive, this critical stress is probably loading rate dependent. At elevated temperature the stress to cause the matrix to no longer clamp the fiber is diminished. The specific conditions for this situation are determined by the effective processing temperature, the differential thermal expansion, the cyclic stress history and the fiber volume fraction.
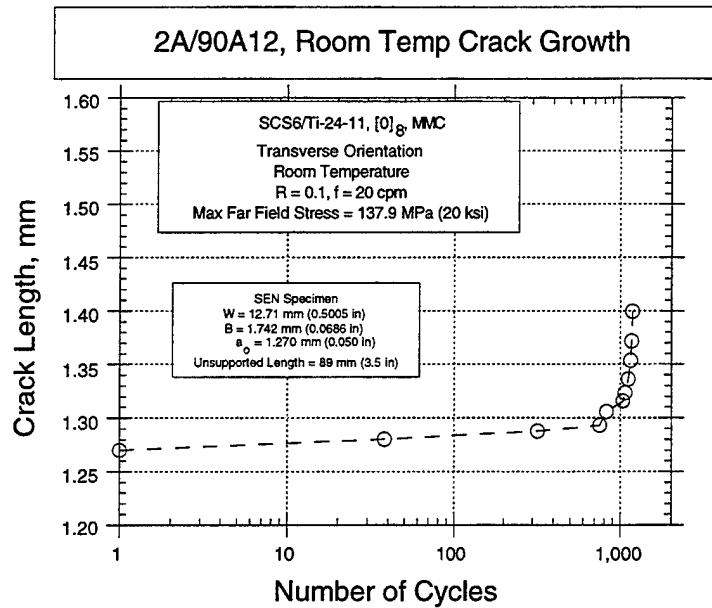
Figure 139. **Transverse MMC crack growth at room temperature.**
Crack length vs. cycles. Maximum far field stress = 137.9 MPa, cyclic frequency of 20 cpm and R = 0.1.
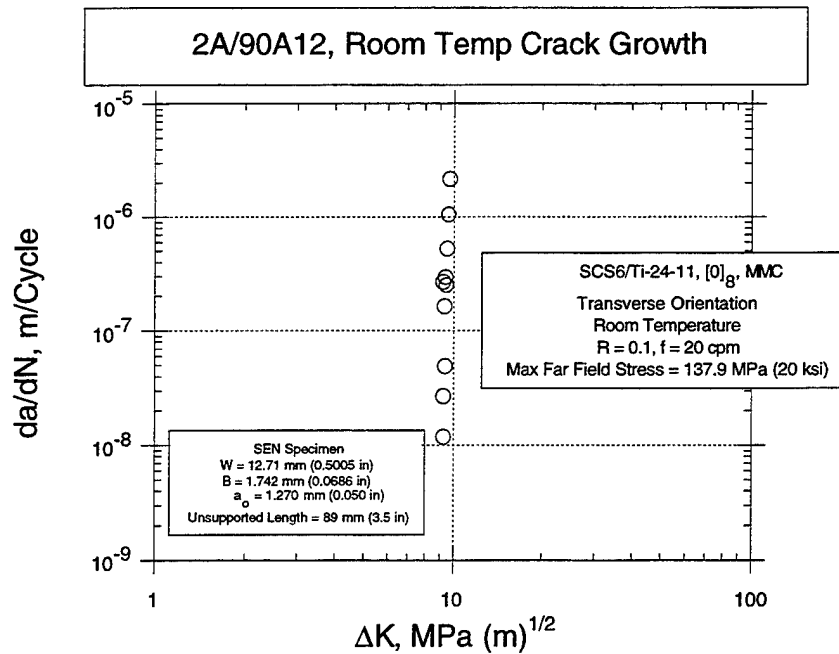
Figure 140. **Crack growth rate vs. apparent ΔK for the test described by Figure 139.**
Kmax is approximately 10.5 MPa(m)$^{0.5}$.

184
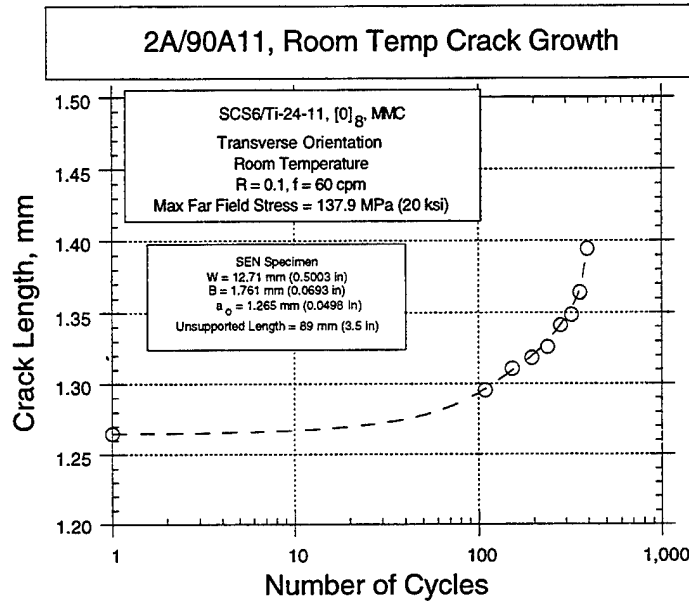
Figure 141. **Transverse MMC crack growth at room temperature.**
Crack length vs. cycles. Maximum far stress field stress = 137.9 MPa, cyclic frequency of 60 cpm and R = 0.1.
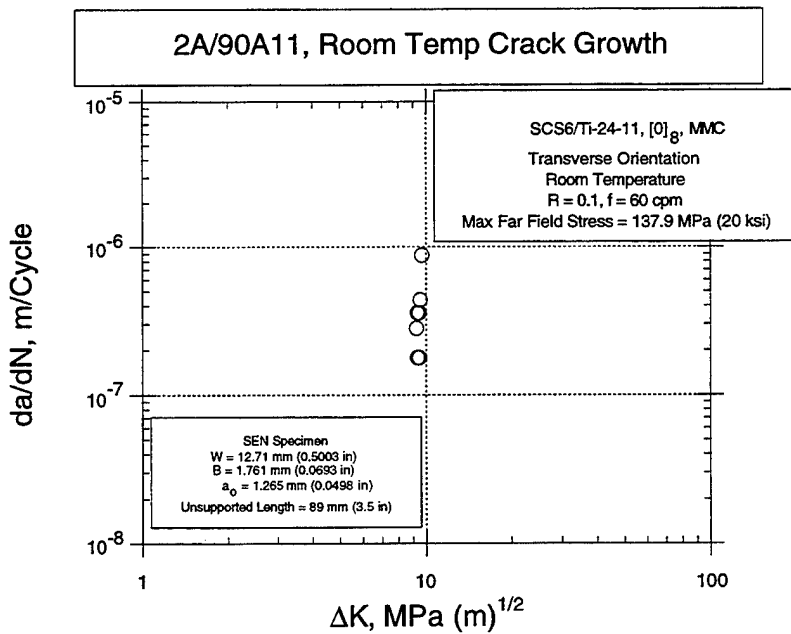
Figure 142. **Crack growth rate vs. apparent ΔK for the test described by Figure 141.**
Kmax is approximately 10.5 MPa(m)$^{0.5}$.

185
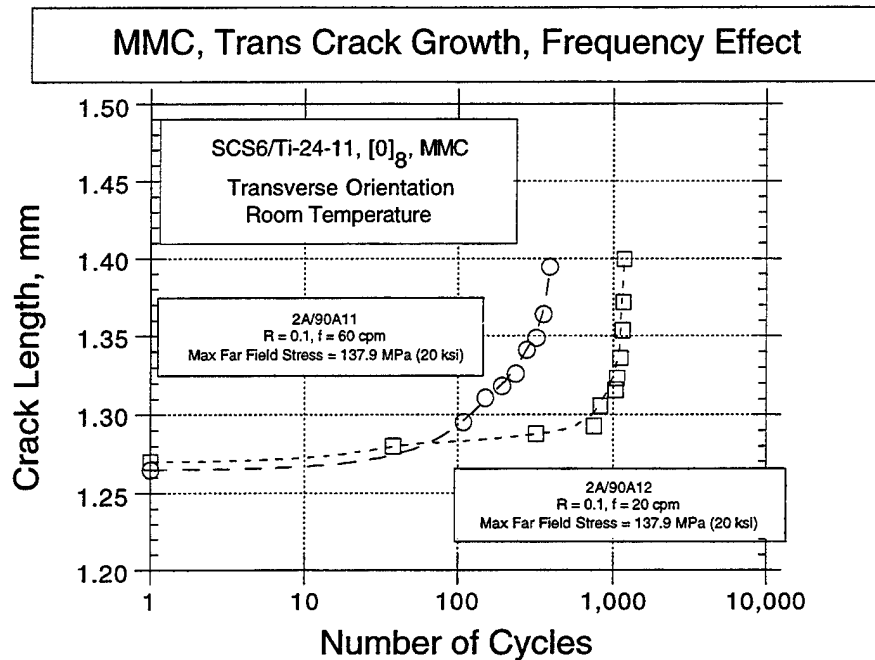
Figure 143. Transverse MMC, room temperature crack growth, frequency effects.

4.5.4.3 Stress Ratio Effects at Room Temperature

In order to determine the stress ratio effect on the crack growth behavior of SCS6/Ti-24-11, a specimen was tested at a stress ratio of 0.5. Figure 144 shows the crack size vs. the number of cycles and Figure 145 shows the crack growth rate as a function of ΔK. This specimen showed the same apparent toughness, 10-12 MPa(m)$^{0.5}$ showed by the specimens tested at a stress ratio of 0.1. It was also observed that the threshold ΔK was reduced to about 6.0 MPa(m)0.5.

In an attempt to capture the early crack growth missing from Figure 144, an additional room temperature test was run with the same stress ratio of 0.5. This time a lower far field stress of 68.9 MPa (10 ksi) was used, as was a longer initial crack length. The results are plotted as Figure 146. Examination of Figure 146 and Figure 147 reveal characteristics of room temperature fatigue crack growth in transverse loading to show no acceleration of growth rate prior to failure implying no warning of imminent failure.

Figure 147 presents a plot of 4 specimens, two each at stress ratio, R of 0.1 and 0.5. There is the expected clear distinction between the low and high stress ratio tests, with the higher R conditions resulting in higher growth rate. This separation is much more distinct in the mid range of ΔK than seen at higher temperatures (Section 4.5.6.5). Furthermore, in either case, the damage tolerance is nil as the spread between the threshold ΔK and that associated with catastrophic failure is very small at room temperature.

186
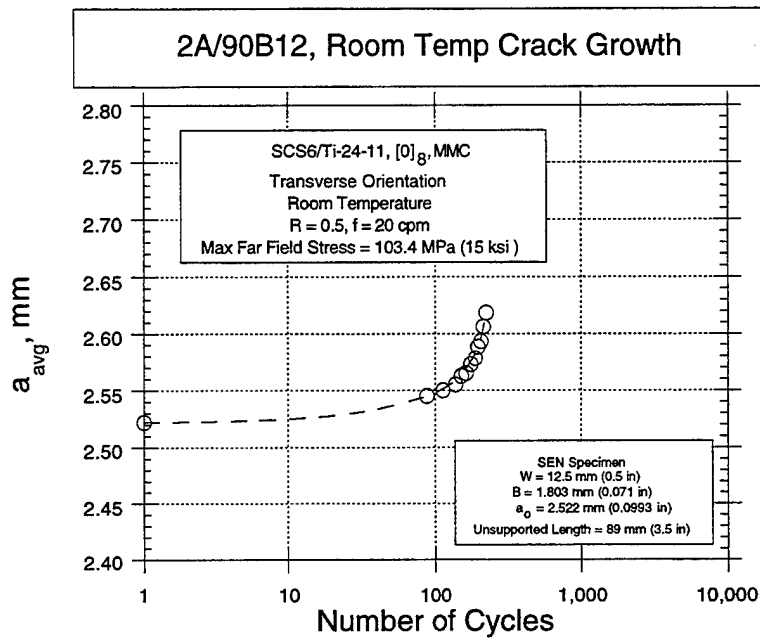
Figure 144. Transverse MMC room temperature crack growth as crack length vs. cycles. Maximum far field stress = 103.4 MPa, cyclic frequency = 20 cpm and R = 0.5.
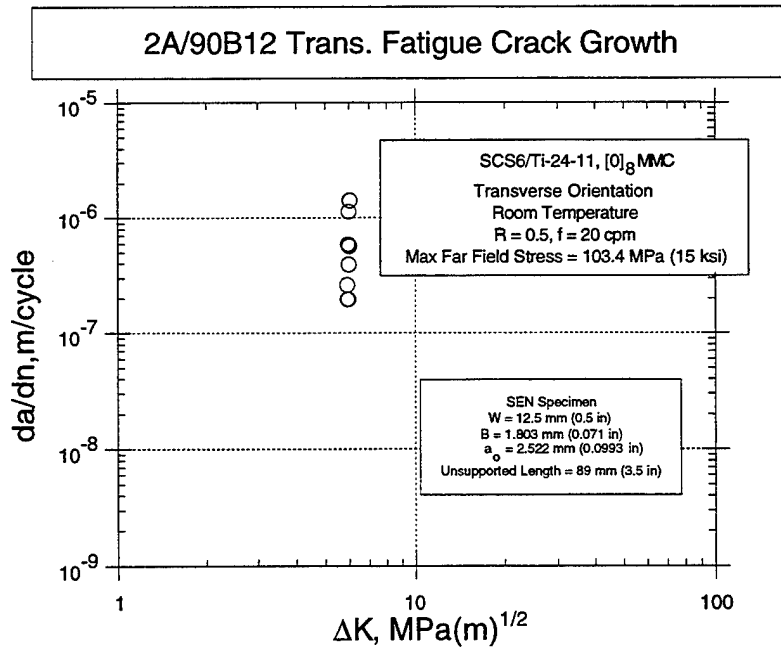
Figure 145. Crack growth rate vs. apparent ΔK for the test described by Figure 144. Kmax is approximately 12 MPa(m)$^{0.5}$.

2A/90B22 Transverse Crack Length vs. N

SCS6/Ti-24-11, $[0]_8$ MMC

Transverse Orientation
Room Temperature
R = 0.5, f = 20 cpm
Max Far Field Stress = 68.9 MPa (10 ksi)

da/dN = 6.56 x 10^{-3} mm/cycle

SEN Specimen
W = 12.78 mm (0.503 in)
B = 1.702 mm (0.067 in)
a_o = 4.001 mm (0.1575 in)
Unsupported Length = 89 mm (3.5 in)
Received 77,646 Precracking Cycles at Lower Stress
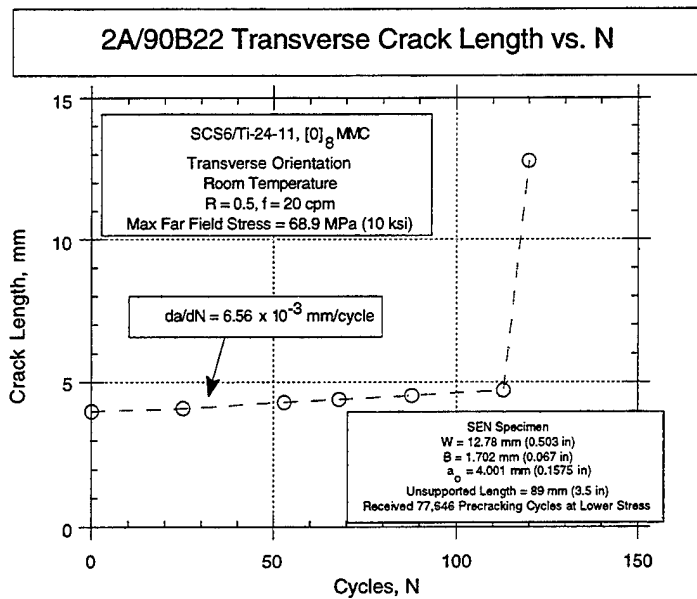
Figure 146. **Room temperature fatigue crack growth, a vs. N, in a transverse MMC specimen with an R = 0.1 and a maximum far field stress of 68.9 MPa.**
The initial growth is linear right up to the point of catastrophic failure.

**Transverse Fatigue Crack Growth
Stress Ratio Effect, Room Temperature**

SCS6/Ti-24-11, $[0]_8$ MMC

Transverse Orientation
Room Temperature
R = 0.1 and 0.5, f = 20 and 60 cpm
Far Field Stress = 69 - 138 MPa

R = 0.5

R = 0.1

□	2A/90A12, R = 0.1, 20cpm, 138 MPa
○	2A/90A11, R = 0.1, 60 cpm, 138 MPa
◇	2A/90B12, R=0.5, 20cpm, 103 MPa
△	2A/90B22, R=0.5, 20cpm, 68.9 MPa
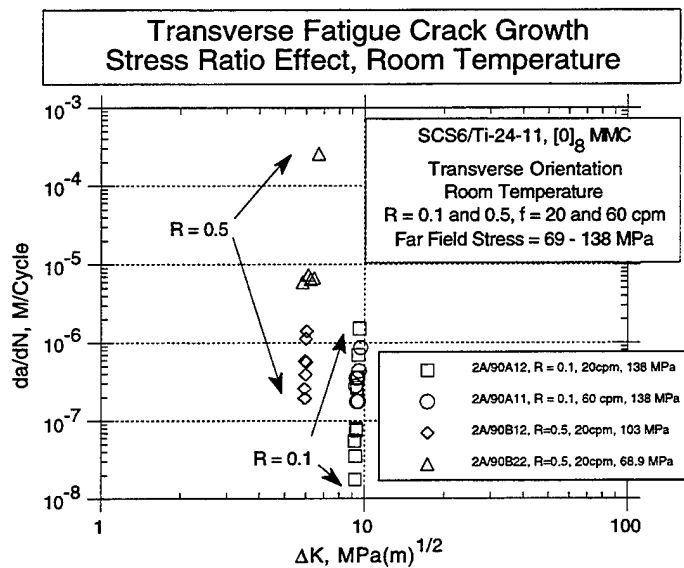
Figure 147. **Room temperature fatigue crack growth, da/dN vs. ΔN, in a transverse MMC specimen with an R = 0.1 and a maximum far field stress between 68.9 and 138 MPa.**
Separation by R is clearly illustrated. Also there is no obvious effect of test frequency in the 20 to 60 cpm range.

188

4.5.4.4   Hold–Time Effects on FCP at Room Temperature

Superimposing a hold time of 2 minutes at the maximum load causes a very rapid crack growth, with failure in less than 3 cycles under conditions, otherwise similar to the baseline. Figure 148 plots these results. Apparently, there is a large time dependent component to room temperature fatigue crack growth mechanism in the transverse orientation, even at very low stresses.

4.5.4.5   General Conclusions Regarding Transverse FCP at Room Temperature

The room temperature transverse crack growth resistance for this MMC is low and there is a superimposed time dependent mechanism of degradation. For this MMC system, damage tolerance for loading transverse to the reinforcing fibers is very low and fatigue loading in this direction must be minimized. Whether or not this is a universal feature of unidirectionally reinforced MMCs is unknown.

2A/90B11, Transverse FCP, Hold Time Effect

SCS6/Ti-24-11, $[0]_8$, MMC
Transverse Orientation
Room Temperature

R = 0.1, 2 min Hold
Max Far Field Stress = 103.4 MPa (15 ksi)

SEN Specimen
W = 12.69 mm (0.4997 in)
B = 1.74 mm (0.0685 in)
a_0 = 2.497 mm (0.0983 in)
Unsupported Length = 89 mm (3.5 in)
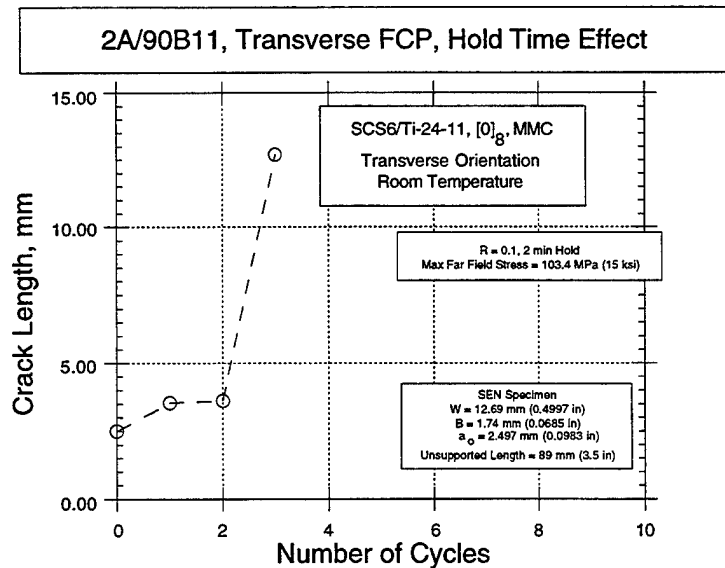
Figure 148.   Transverse MMC room temperature crack growth as crack length vs. cycles. Maximum far field stress = 103.4 MPa, cyclic, R = 0.1 with a 2 minute dwell at maximum load. Note that the failure occurred in less than 3 cycles, implying a large component of an operative time dependent damage mechanism.

189

4.5.5 Fatigue Crack Propagation in Transverse MMC at Elevated Temperatures

4.5.6.1 Test Procedures

Crack growth at elevated temperatures was measured by optical means on both faces of the specimen. Temperature was maintained using three thermocouples in the gage section, one of which was the control thermocouple for the induction heater. Induction coils were designed and proven with identical specimen blanks to maintain temperature uniformity over the entire gage section of the specimen. Crack length measurements were taken at frequent intervals to assure continuity in the data.

After a few initial failures, it was recognized that the far field stresses for the elevated temperature tests must be quite low to avoid early failure. It was decided to precrack the specimens at room temperature in an axial loading mode and then commence the crack growth test at elevated temperature.

4.5.6.2 Baseline FCP at 550°C

After an initial, short, rapid growth rate from the precrack, a near linear growth rate at 34.5 MPa far field stress and 20 cpm until a crack length of about 7 mm is reached and then catastrophic failure occurs (Figure 149). This is despite erratic growth rate on an instantaneous look (Figure 150). From the appearance of this figure, it is evident that ΔK does not describe the crack growth driving force very well.

4.5.6.3 Baseline FCP at 650°C

With test conditions like those for the 550°C (1022°F) test, at 650°C (1200°F) the total life to failure is less than 21% of the life at the lower temperature (Figure 151). The crack length, at the onset of instability, is similar, indicating the toughness not to be strongly sensitive to temperature under these test conditions. At 650°C (1200°F) the conventional plot of ΔK vs. da/dN appears more well behaved with some high points, probably associated with previously unseen subsurface cracks reaching the face of the specimen giving the appearance of nearly instantaneous crack growth (Figure 152).

4.5.6.4 Hold Time Effects on FCP at 650°C

By imposing a dwell for 5-minutes at crack lengths of about 2 mm and 3 mm, there appears to be an accelerate the growth rate (Figure 153) which returns to the trend when the cyclic rate is returned to 20 cpm. This acceleration is seen in the da/dN vs. ΔK plot of Figure 154. The dwell appears to accelerate the growth rate by an order of magnitude. The degree to which this effect is an environmentally induced phenom-
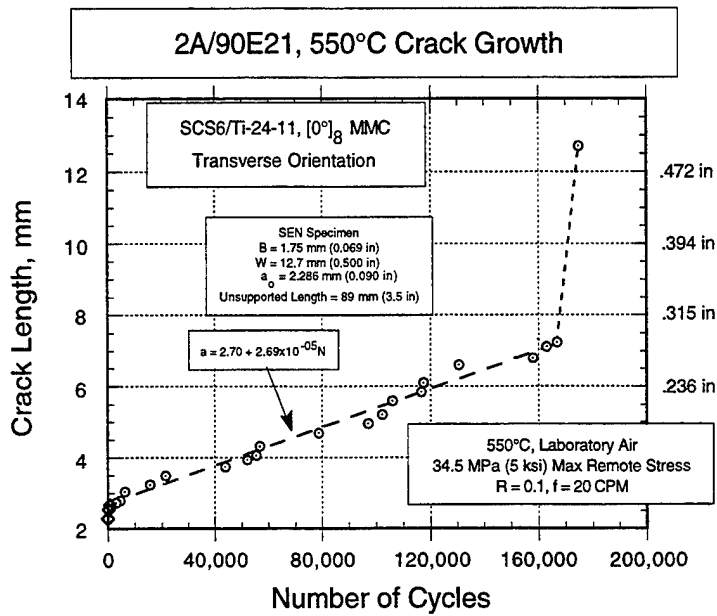
Figure 149. Transverse MMC, 550°C crack growth as crack length vs. cycles for a maximum far field stress = 34.5 MPa and a cyclic frequency of 20 cpm.
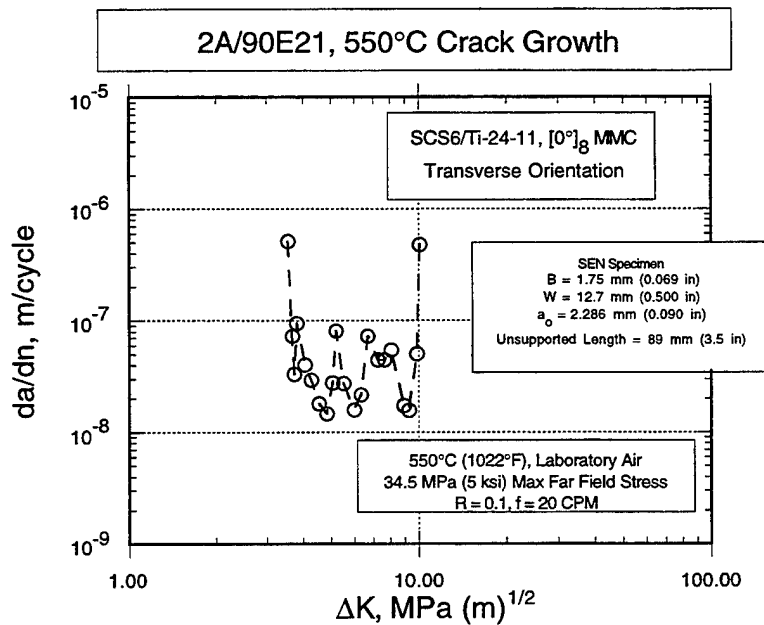
Figure 150. Crack growth rate vs. apparent ΔK, for the test described in Figure 149.
This plot indicates that the crack growth does not accelerate monotonically with increased ΔK.
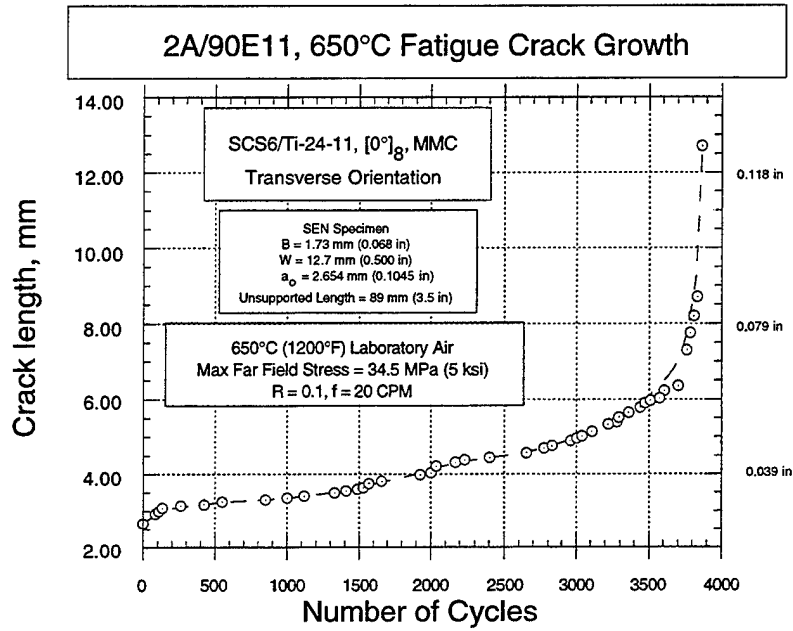
Figure 151. Transverse MMC, 650°C crack as crack length vs. cycles.
Maximum far field stress = 34.5 MPa and cyclic frequency = 20 cpm.
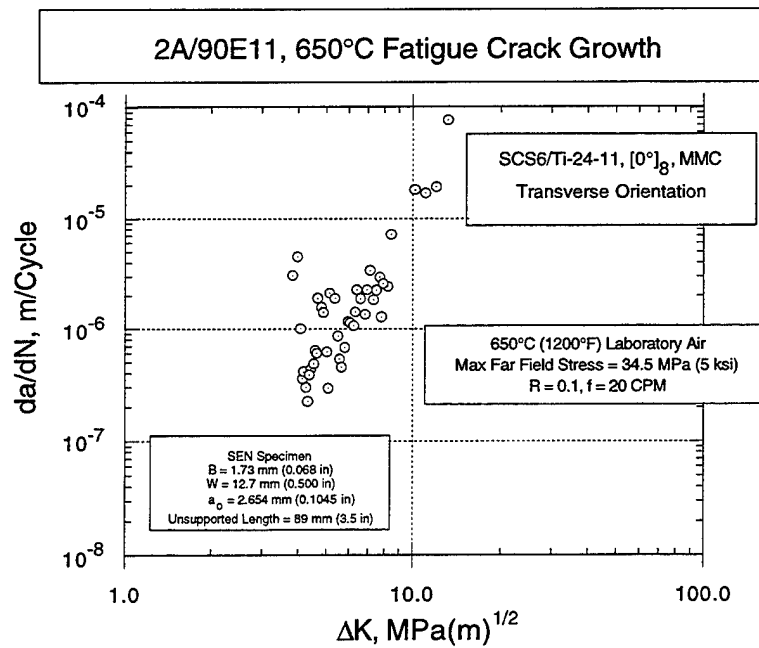
Figure 152. Crack growth rate vs. apparent ΔK, for the test described in Figure 151.
This plot indicates that the apparent crack growth rate is erratic.
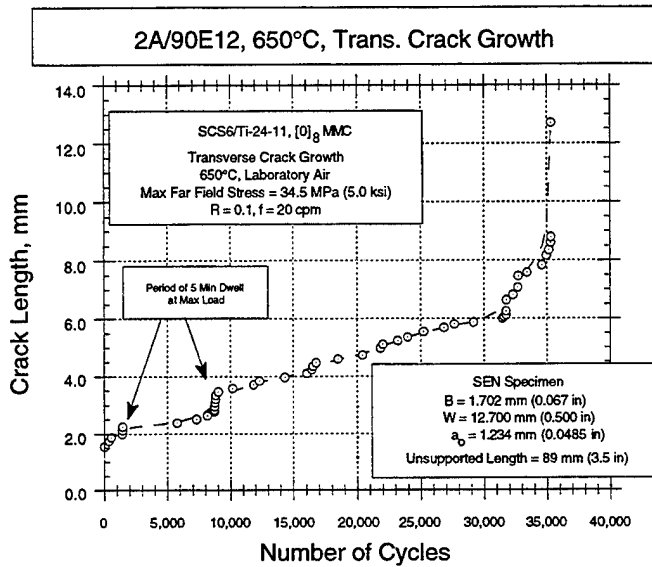
Figure 153. **Transverse MMC, 650°C crack growth as crack length vs. cycles.**
Maximum far field stress = 34.5 MPa and cyclic frequency = 20 cpm, interrupted with two segments of 5 minute dwell at maximum load. An apparent acceleration associated with the dwell cycles is noted.
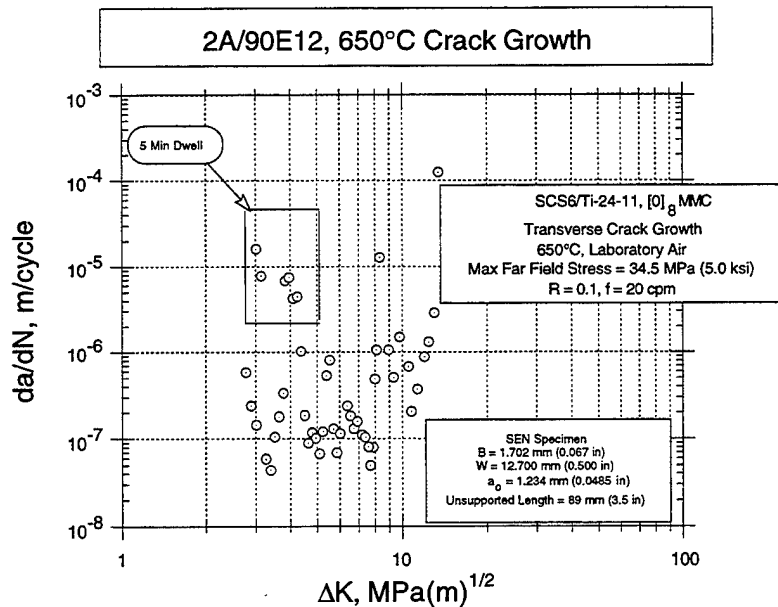
Figure 154. **Crack growth rate vs. apparent ΔK, for the test described in Figure 153.**
This plot indicates that the crack growth is erratic and at least some of the high growth rate is associated with the dwell period

enon is unknown, when viewed in the light of the hold time effects at room temperature (Section 4.5.4.4).

4.5.6.5 Stress Ratio Effects on FCP in Transverse Oriented MMC at 650°C

In order to assess the effects of stress ratio on the fatigue crack growth behavior of transverse MMCs at 650°C (1200°F), a single test was run with an R of 0.5. Figure 155 plots the results of this test in the conventional ΔK vs. da/dN format. As seen from the inserts, there is no obvious effect of far field stress in the range of 48 to 62 MPa (5 to 9 ksi). The form of the plot indicates a clearly higher failure stress intensity factor range than threshold stress intensity factor range. Also it is evident that the growth rate is high at quite low stress intensity factor range, implying low damage tolerance.

The effect of stress ratio is easily seen by superimposing similar plots of da/dN vs. ΔK for stress ratio tests at 0.1 and 0.5. Such a plot is seen in Figure 156 where we see that the failure ΔK and threshold ΔK are both higher for the lower R, much as seen with monolithic metals.
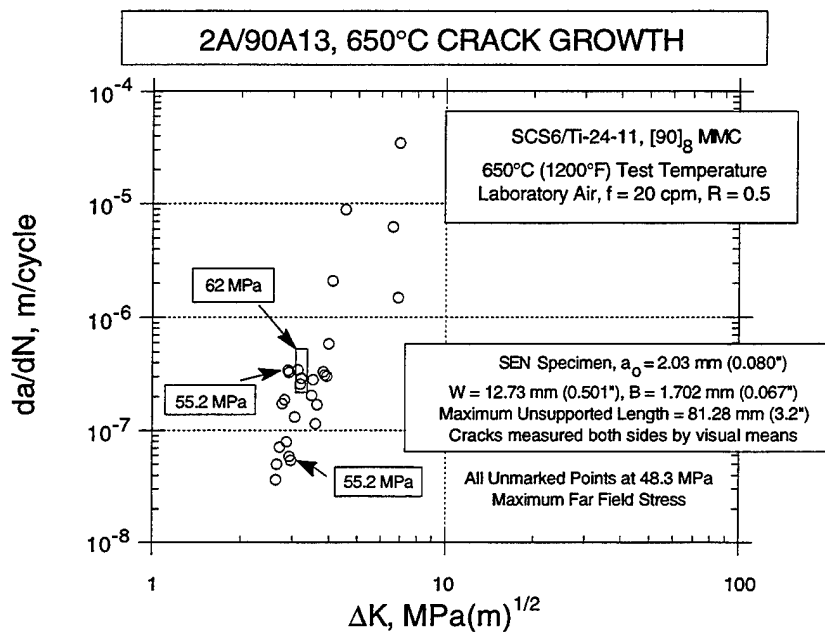
Figure 155. Fatigue rack growth at 650°C, da/dN vs. ΔK, in a transverse MMC specimen with an R = 0.5 and a maximum far field stress between 48 and 62 MPa.
There is no clear effect of far field stress on the plotted results.

194
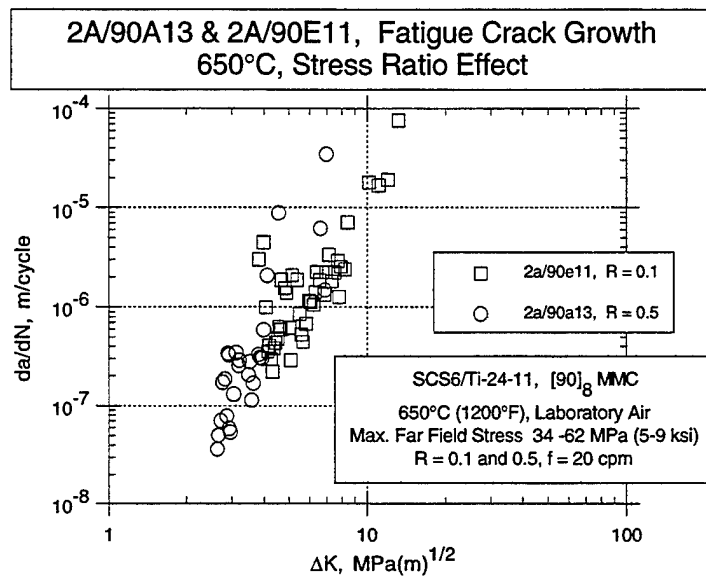
Figure 156. Fatigue rack growth at 650°C (1200°), da/dN vs. ΔK, in a transverse MMC specimen with R = 0.5 and 0.1.

Both tests were run with maximum far field stress between 34 and 62 MPa (5 and 9 ksi). The high R test appears to indicate a lower threshold ΔK, as anticipated.

Comparing Figure 71 and Figure 74 for room temperature tests at R = 0.1 and R = 0.5 on the matrix, one can easily conclude the same sort of trend. The circumstances surrounding the same sort of comparison at 550°C (1022°F) do not make such a clear distinction, primarily because of the lack of near threshold data in both cases. See Figure 88.

4.5.6.6 General Conclusions Regarding Transverse FCP at Elevated Temperature

Transverse fatigue crack growth resistance of the MMC at 550°C (1022°F) and 650°C (1200°F) is quite low and subject to additional time dependent degradation. The partitioning of this degradation between environmentally induced phenomenon and time dependent deformation phenomenon has not been done. Regardless, it is clear that the material under study is not damage tolerant in the case of loading transverse to the reinforcement fibers at elevated temperature, which is the same conclusion drawn for the room temperature case (Section 4.5.4).

4.6　Creep

All creep testing was performed in laboratory air using the smooth specimens described in Figure 41. Only 90° MMC and matrix only (NEAT consolidated foils) specimens were creep tested.

4.6.1　Experimental Procedures

The matrix only tests were run using a 25.4 mm (1.0 inch) extensometer with two parallel linear, differential capacitance transducers. The 90° MMC specimens were adversely affected by the use of the gage extensometer by causing premature failure at the point of contact with the gage clamp. Therefore, these tests were performed by continuously recording deflection of the bottom specimen grip. Data were recorded automatically on a personal computer at intervals of less than 1 second during the loading cycle and less frequently thereafter.

Temperature control and monitoring was accomplished using three thermocouples arranged to touch the gage section at the center and near each end. The furnace gradient was adjusted to maintain uniform temperature at all three positions.

Initial heat up was done while applying a minor load sufficient only to maintain a taut load train. Once temperature was stabilized, the transducers were zeroed and the test load applied. Immediately, the transducers were rezeroed, establishing the beginning of the test.

Tests were terminated, in most cases, prior to the onset of tertiary creep in order to analyze uniform strain behavior and permit conversion of the deflection readings to strain readings. To facilitate this calibration, prior to each test, microhardness marks were placed on each face of the gage section at regular intervals of 5.08 mm (0.20 in). Comparing the pre test and post test spacing of these marks, on specimens strained only into second stage creep, permitted verification of the recorded strain readings and also permitted calibration of the grip displacement readings and their conversion to strain readings.

4.6.2　Creep Results for Matrix Only Material

4.6.2.1　Strain–Time Data for Matrix Material

Figure 157 through Figure 165 depict the creep curves for 500°C (990°F), 550°C (1022°F), 660°C and 704°C tests, all run in laboratory air.

All tests were terminated prior to failure except the 550°C/241.3 MPa test (Figure 161) and the 650°C/103.4 MPa test (Figure 162). In both of these cases it is clear that the onset
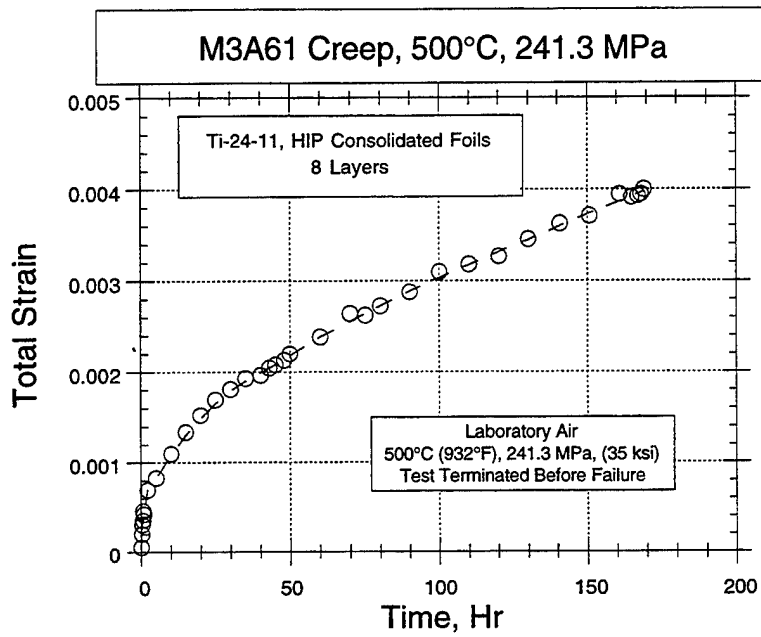
Figure 157. Matrix creep at 550°C and 241.3 MPa in laboratory air.
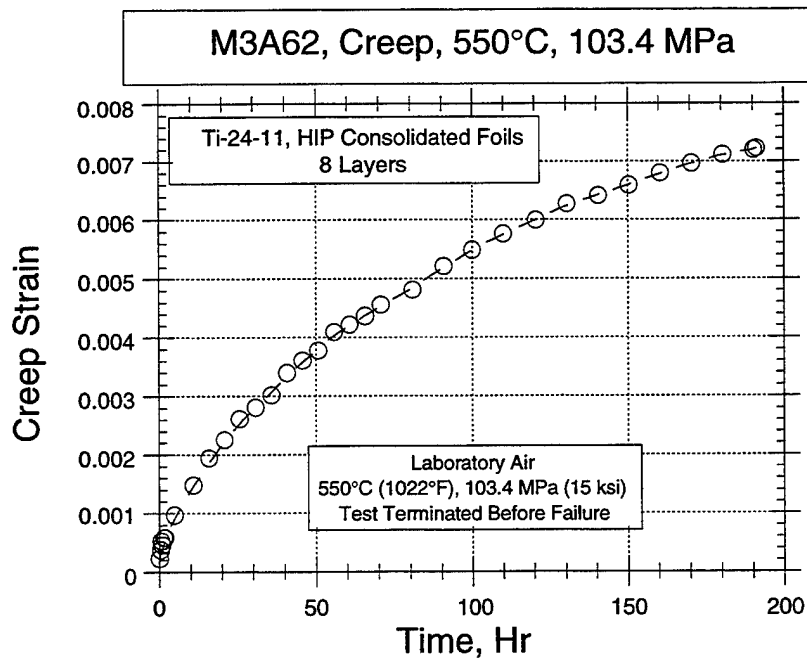
Figure 158. Matrix creep at 550°C and 103.4 MPa in laboratory air.

197
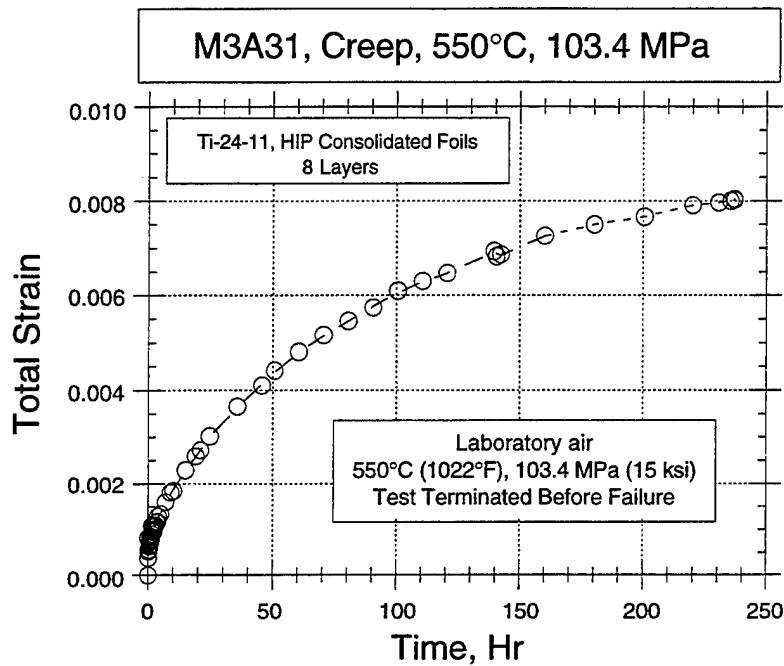
Figure 159.   Matrix creep at 550°C and 103.4 MPa in laboratory air.
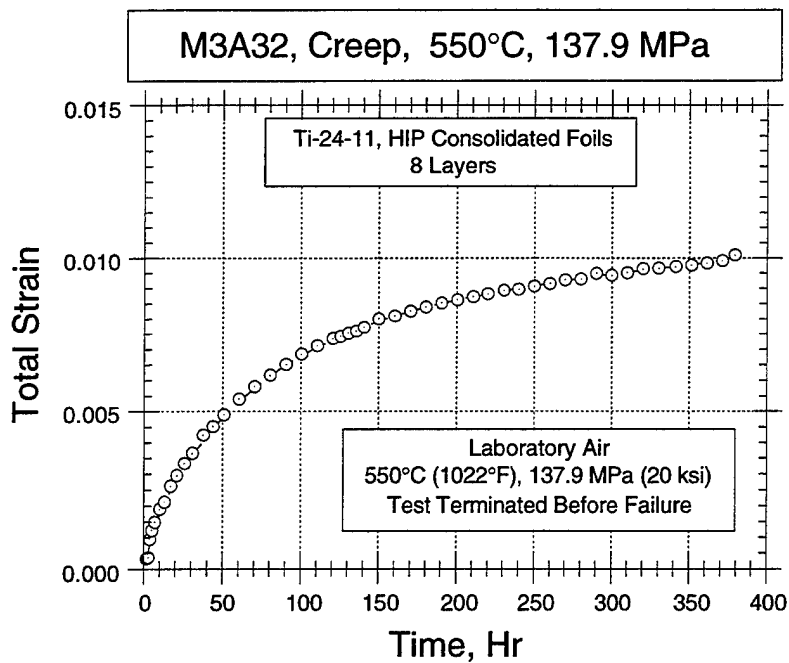
Figure 160.   Matrix creep at 550°C and 137.9 MPa in laboratory air.
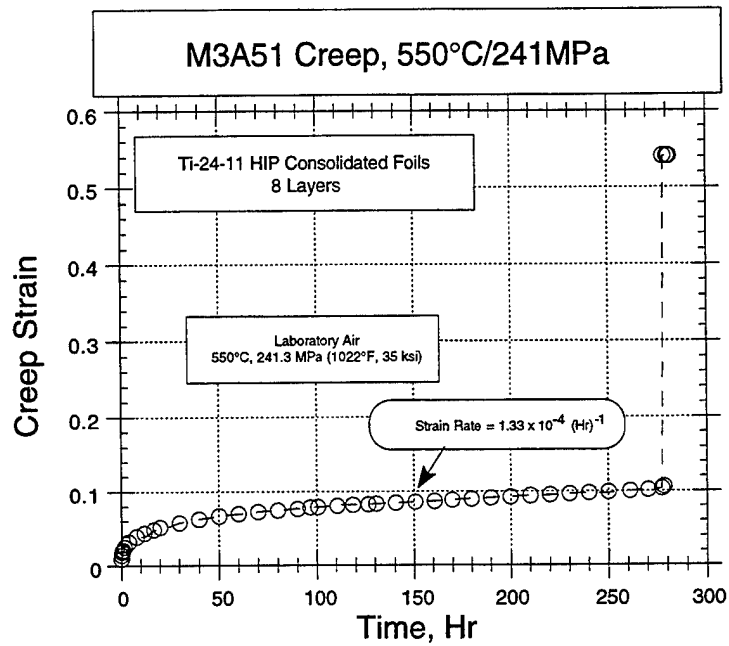
Figure 161. Matrix creep at 550°C and 241.3 MPa in laboratory air.
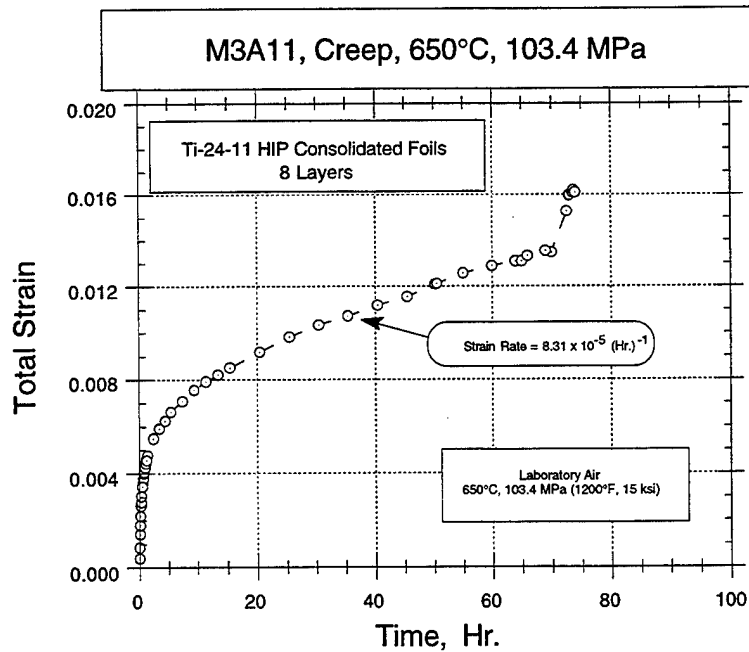
Figure 162. Matrix creep at 650°C and 103.4 MPa in laboratory air.

199
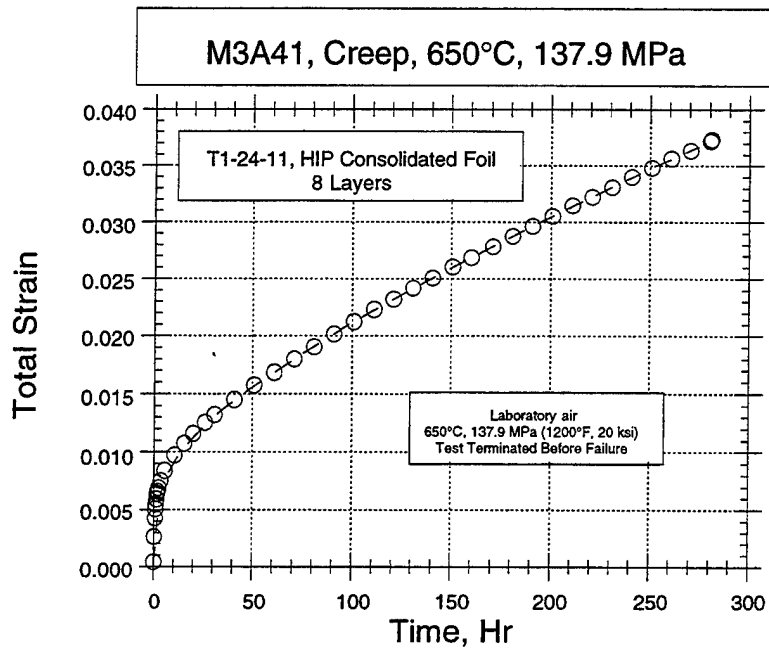
Figure 163. Matrix creep at 650°C and 137.9 MPa in laboratory air.
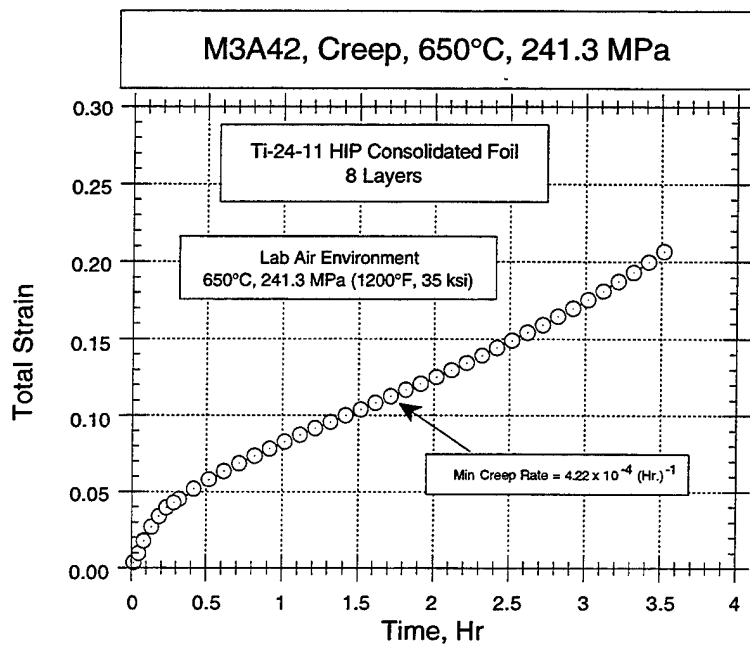
Figure 164. Matrix creep at 650°C and 241.3 MPa in laboratory air.
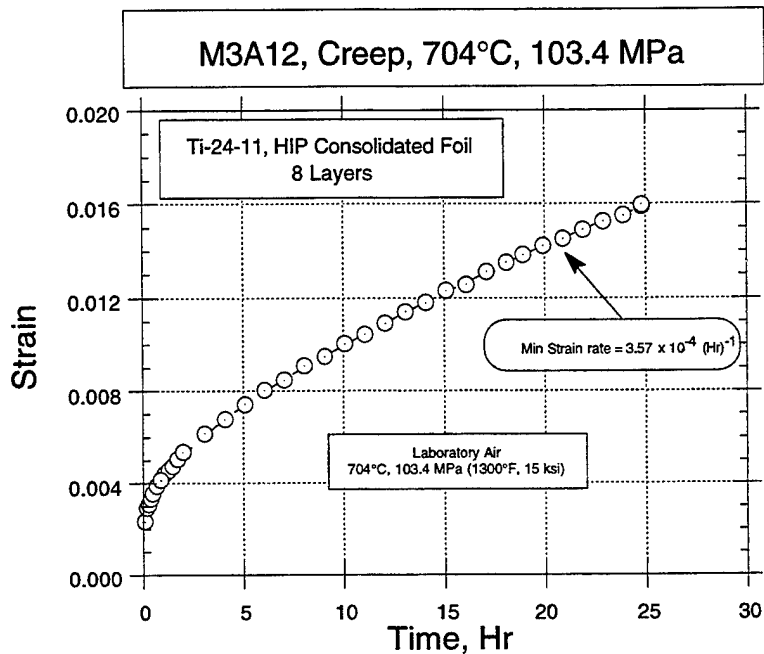
Figure 165. Matrix creep at 704°C and 103.4MPa in laboratory air.

of failure was rapid with very little tertiary creep evident. Close examination of the creep curves reveals extensive primary creep which, in most cases, amounts to the dominant strain even for those specimens taken to the onset of failure. It is also noted that extensive steady-state creep is absent in most tests; however, attempts were made to measure minimum creep rates in order to help identify creep rate controlling mechanisms.

It is clear that this material exhibits very low creep strength compared to published data from nominally the same composition. Ti-24-11 creep strength from forgings is considerably higher as seen in Table 18. A study of this table shows the matrix material for this program to exhibit considerably inferior creep resistance. A quick examination of the features of the material in this program (Section 4.2.2.1.4) reveals a logical reason for this effect. The foil material that, when consolidated into MMC or NEAT foils, retains a very fine equiaxed microstructure and such structures are known to have low creep strength. In addition, the texture of the foils, presents easy slip systems to in-plane strain, further reducing the strength. The low tensile strength discussed in Section 4.2.2.1, at both ambient and elevated temperatures, is clearly reflected in its creep strength.

Table 18. Creep properties of DTC program matrix vs. Ti–24–11 forgings from Reference 26.

Test Conditions	[Minimum Strain Rate, $(Hr)^{-1}$]	
	Forgings	Program Matrix
550°C/241.3 MPa		1.33×10^{-4}
593°C/344.7 MPa	0.9×10^{-4}	
650°C/241.3 MPa		4.22×10^{-4}
650°C/275.8 MPa	1.49×10^{-4}	
704°C/103.4 MPa		3.57×10^{-4}
704°C/241.3 MPa	3.8×10^{-4}	

4.6.2.2 Analysis of the Matrix Material Creep Curves

Because primary creep is such a large portion of the total creep strain to levels of interest in MMCs (<1%), it is of primary importance to characterize and enter into behavior models. Clearly, the matrix residual stresses associated with MMC consolidation will be affected by the low level of creep resistance exhibited by this material and may play a role in the degradation of residual stresses during elevated temperature LCF testing reported in Section 4.1.7.

The strain-time plots were dissected into time spent in primary creep, total primary creep strain, and minimum creep rate and the effects of stress and temperature on these.

Figure 166 through Figure 168 illustrate the effect of temperature on the total primary creep strain and the time spent in primary creep deformation for the three stresses of 103.4, 137.9 and 241.3 MPa (15, 20 and 35 ksi). For all three stresses, the time spent in primary creep decreased with temperature while, at the same time, the total primary creep strain increased. Similar trends were seen with increased stress at constant temperature as seen in Figure 169 and Figure 170.

4.6.2.3 Phenomenological Examination of Minimum Creep Rate

A phenomenological examination of the temperature effects on minimum creep rate is designed to help sort out the operative mechanisms of creep deformation. Figure 171 is an Arrhenius plot showing an apparent activation energy of the rate controlling mechanism for each of the three stresses employed in this investigation. The 103.4 and 137.9 MPa tests gave similar activation energies of about 138 to 164 KJ/mole °K while

202
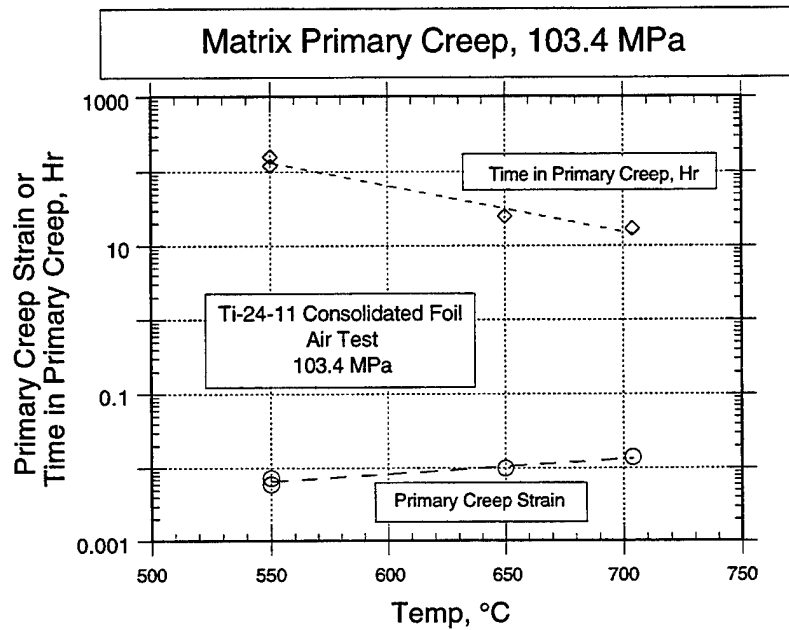
Figure 166. Matrix, primary creep summary of time and total strain in primary creep at 103.4 MPa, as a function of temperature.
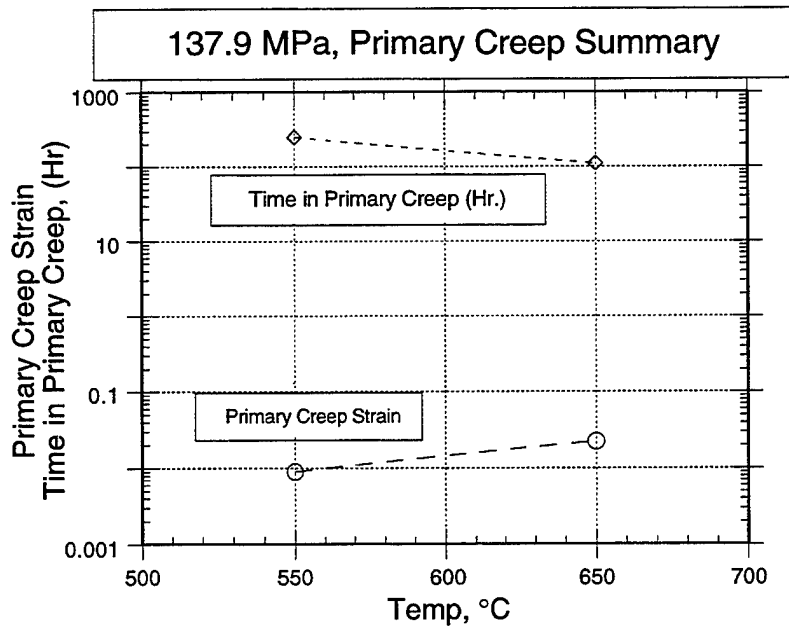
Figure 167. Matrix, primary creep summary of time and total strain in primary creep at 137.9 MPa, as a function of temperature.
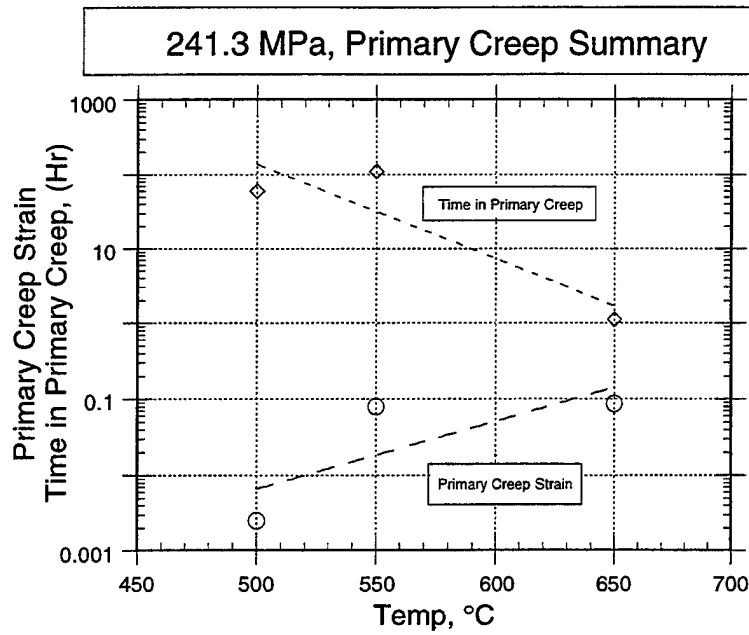
Figure 168. Matrix, primary creep summary of time and total strain in primary creep at 241.3 MPa, as a function of temperature.
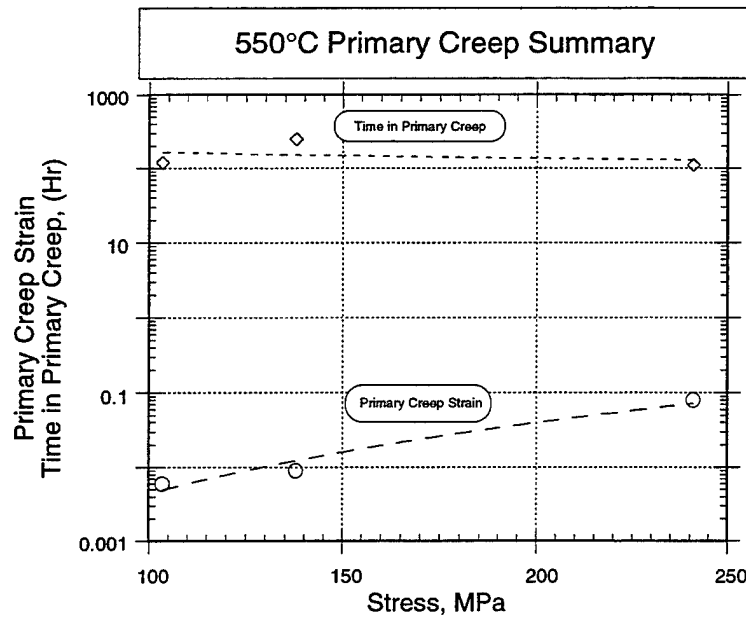
Figure 169. Matrix, primary creep summary of time and total strain in primary creep at 550°C, as a function of stress.
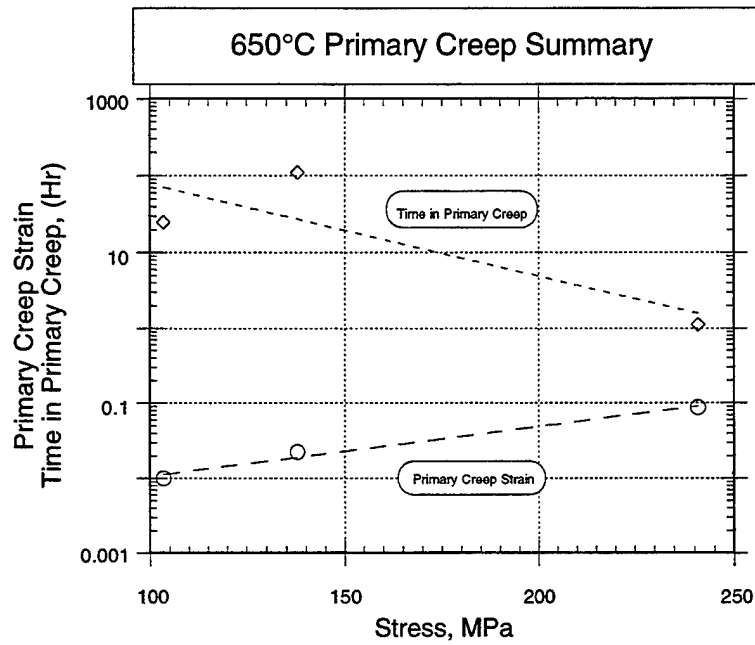
Figure 170. Matrix, primary creep summary of time and total strain in primary creep at 650°C, as a function of stress.
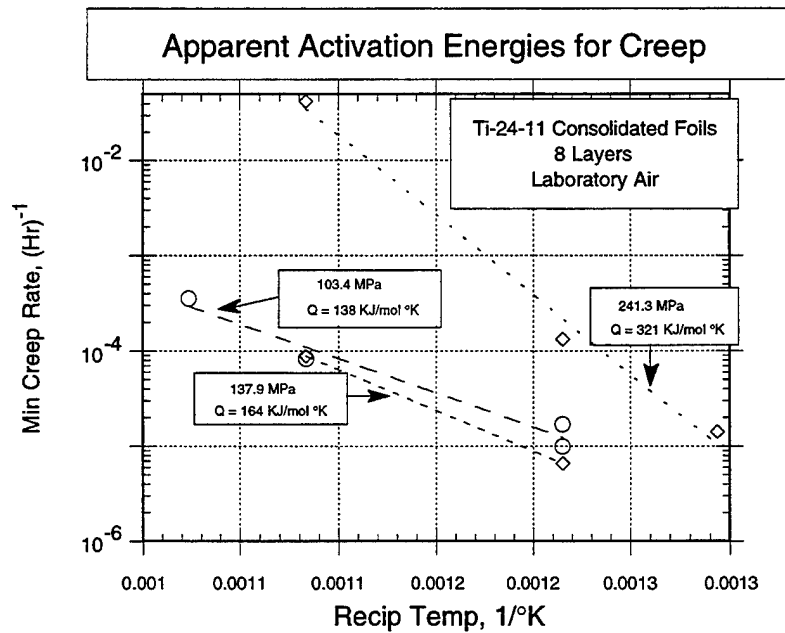
Figure 171. Arrhenius plot of minimum creep rate for matrix material, giving apparent activation energy for matrix creep at three stress levels.

the higher stress of 241.3 MPa resulted in an activation energy about twice as high. A possible explanation for this may be that, in the latter case, lattice diffusion is an important step in the deformation by enhancing dislocation climb or similar interactions. The lower stress tests, with lower strain rates may have been more strongly influenced by short circuit diffusion as along line or surface structural defects. The amount of data leading to this is not sufficient to warrant more definitive conclusions beyond saying that the stress (or strain rate) imposed does seem to affect the operative creep mechanism.

While the data are sparse, the strain rate for the 103.4 MPa test seems to be slightly higher than for the 137.9 MPa test. No explanation for this is offered unless a dynamic strain aging process is triggered by a higher primary creep strain associated with the latter, giving it greater resistance to creep in stage II.

Stress dependency of the minimum creep rate serves to indicate what sort of micromechanical mechanisms are operative or rate controlling. Figure 172 indicates that at 550° (1022°F), over the stress ranges tested, there is a significant contribution of interface sliding as indicated by the stress exponent lying between 2 and 3. On the other hand, at 650°C (1200°F), the exponent near 8 implies a dominance of dislocation motion in the creep deformation.
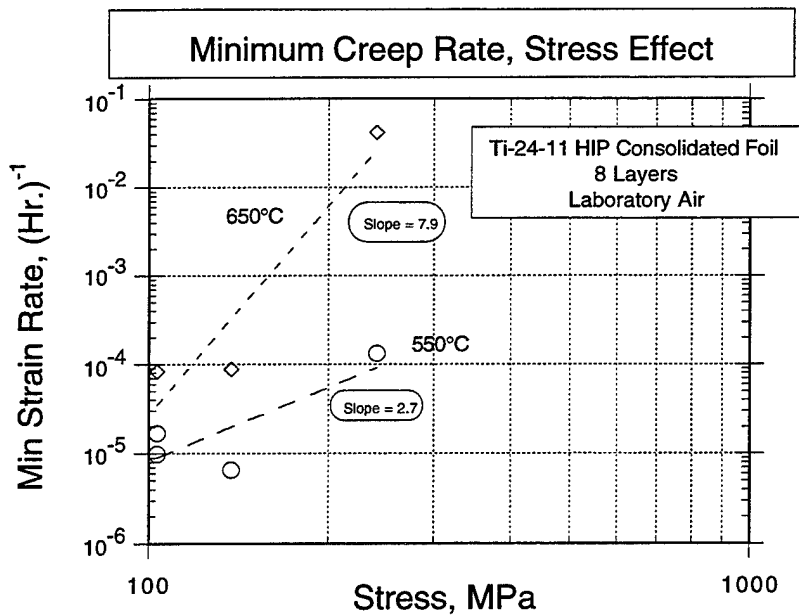
Figure 172. Stress sensitivity plot of minimum creep rate for matrix material at two temperatures to identify approximate stress exponents.

4.6.2.4 General Effects of Temperature and Stress on the Time to Various Total Plastic Strain Levels for Matrix

The low stress of 103.4 MPa, seen in Figure 173, gives a rather dramatic reduction in time to strains less than 1% as the temperature is increased from 550°C (1022°F) to 650°C (1200°F). This implies that the matrix dominated elevated temperature strength and creep properties in MMCs using this matrix are likely to exhibit a similar reduction over a similar temperature range. Figure 174 and Figure 175 at stresses of 137.9 and 241.3 MPa respectively exhibit similar trends, except at the higher stress, the creep strain rate appears to rapidly increase above 500°C (990°F). At constant temperatures of 550° (1022°F) and 650°C (1200°F), Figure 176 and Figure 177 illustrate the severe effect of stress above a level of about 137 MPa, further emphasizing potential deficiencies of any matrix dominated strength property.
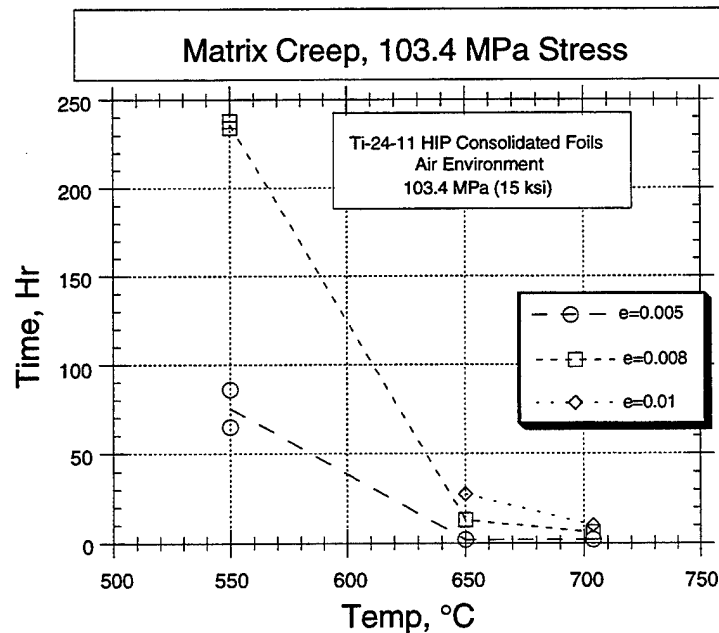
Figure 173.   Time to reach selected total creep strains as a function of temperature for 103.4 MPa creep stress.
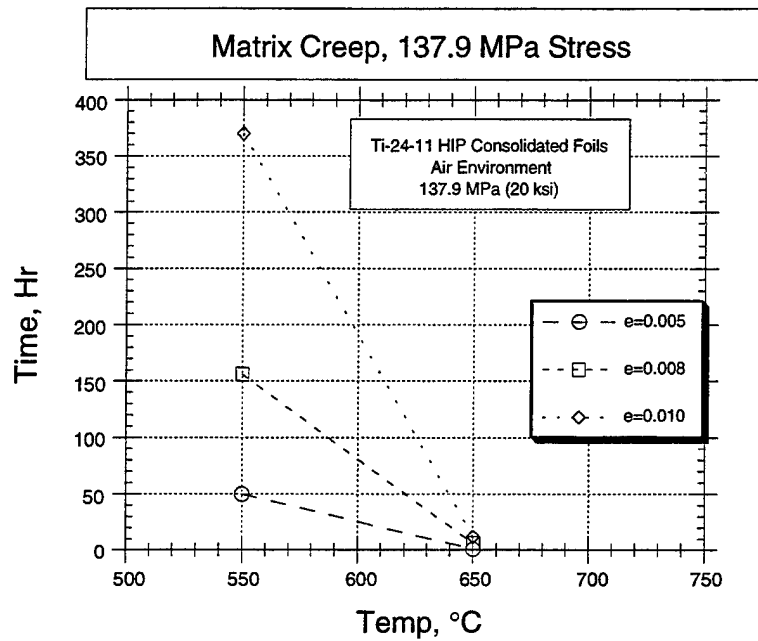
Figure 174. Time to reach selected total creep strains as a function of temperature for 137.9 MPa creep stress.
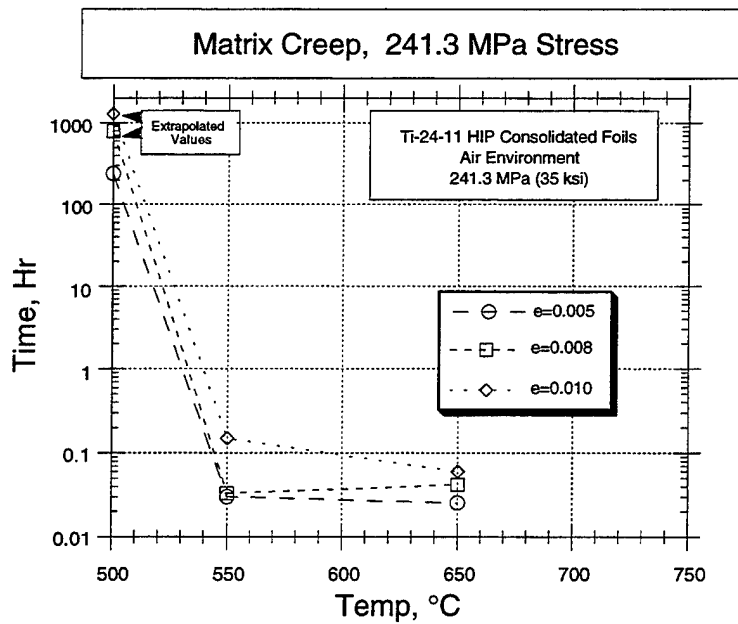
Figure 175. Time to reach selected total creep strains as a function of temperature for 241.3 MPa creep stress.

208
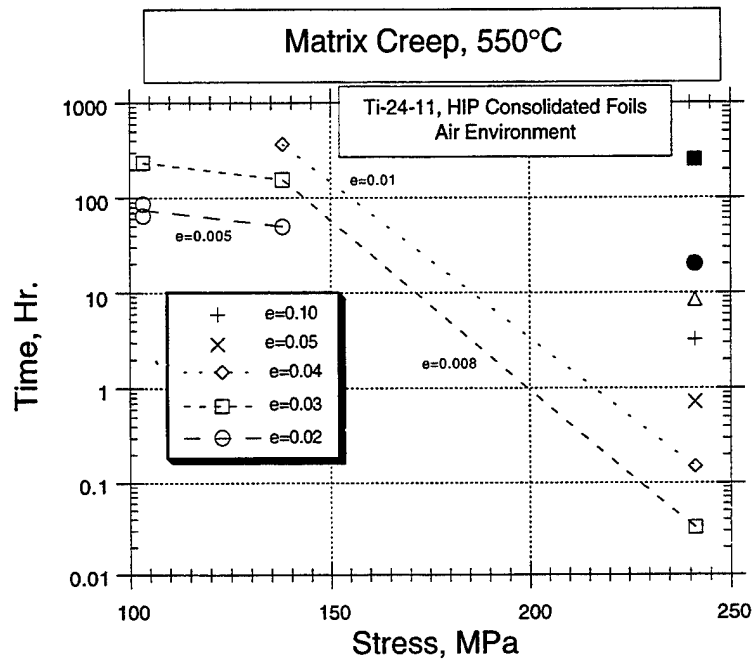
Figure 176. Time to reach selected total creep strains as a function of stress at 550°C.
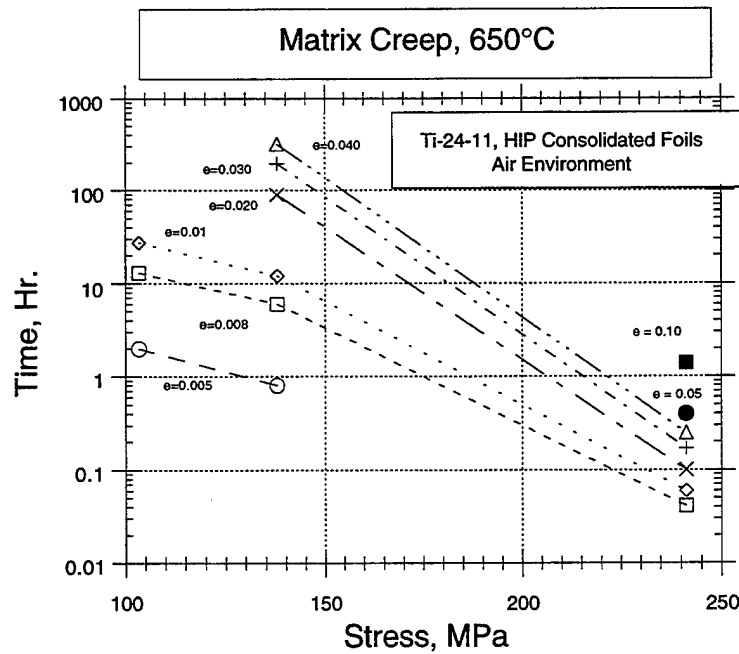
Figure 177. Time to reach selected total creep strains as a function of stress at 650°C.

4.6.3   Transverse Creep, MMC

4.6.3.1   Strain-Time Data for Transverse MMC Tests

The transverse creep strength of the program MMC material is presented as strain-time plots in Figure 178 through Figure 181 and summarized in Figure 182. As can be seen from these figures, very low stresses cause very high strains with the 41.4 MPa at 650°C (6 ksi at 1200°F) and lower stress at 704°C (1300°F) being the only conditions for which significant primary strain was detected. Early attempts at loading specimens to higher stresses resulted in very rapid failure.
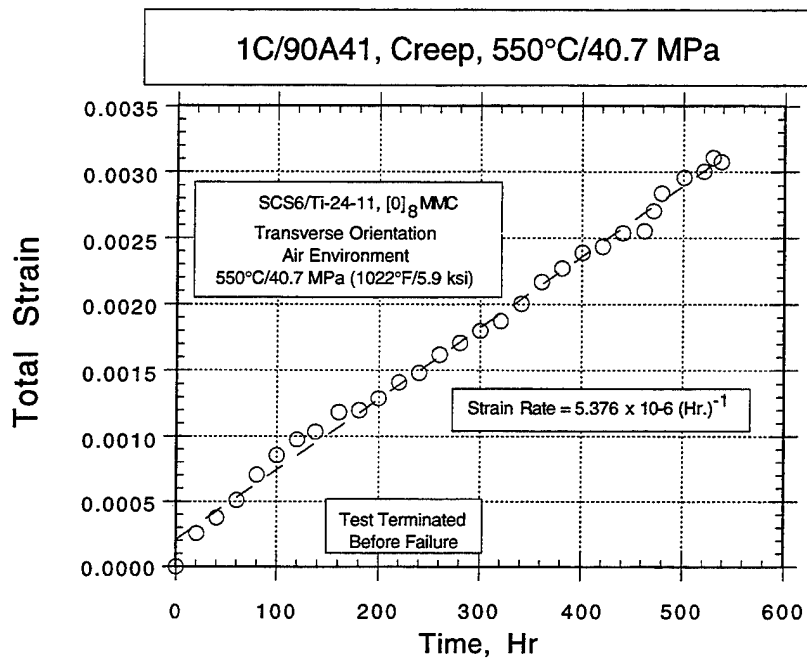
Figure 178.   Transverse MMC creep, 550°C, 40.7 MPa.
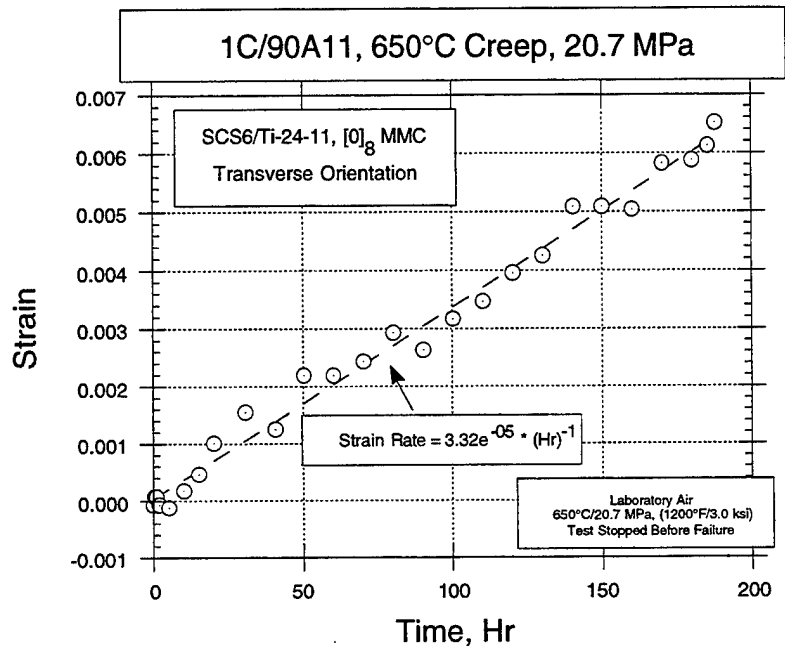
Figure 179.   Transverse MMC creep, 650°C, 20.7 MPa.
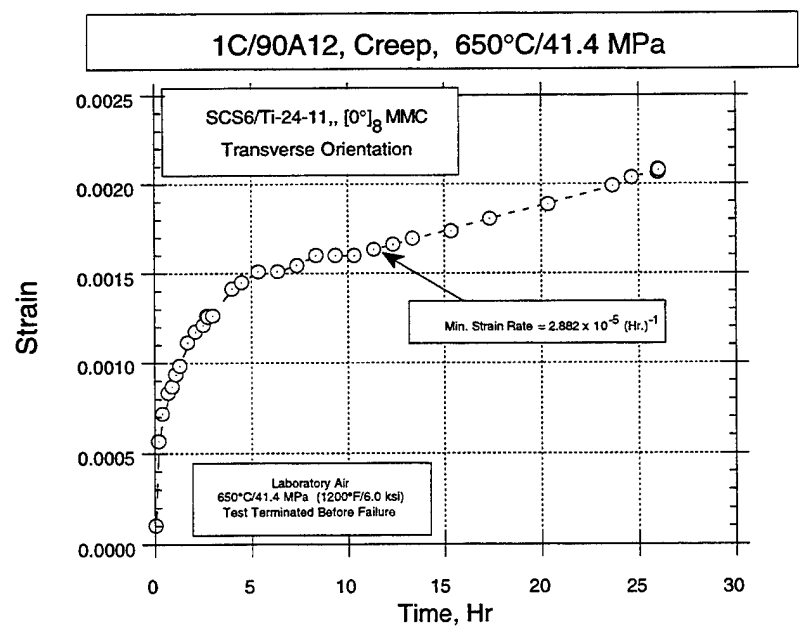
Figure 180.   Transverse MMC creep, 650°C, 41.4 MPa.

211
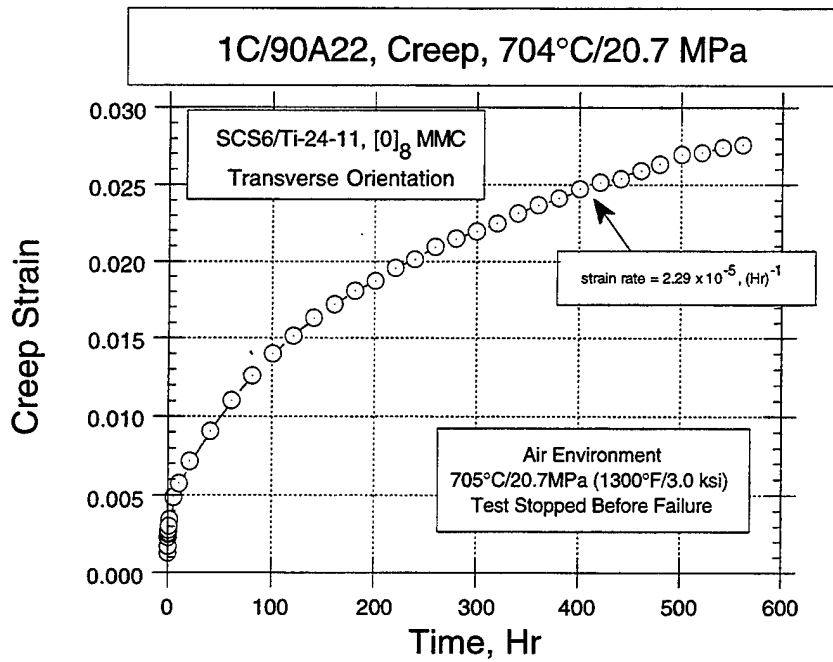
Figure 181. Transverse MMC creep, 704°C, 20.7 MPa.
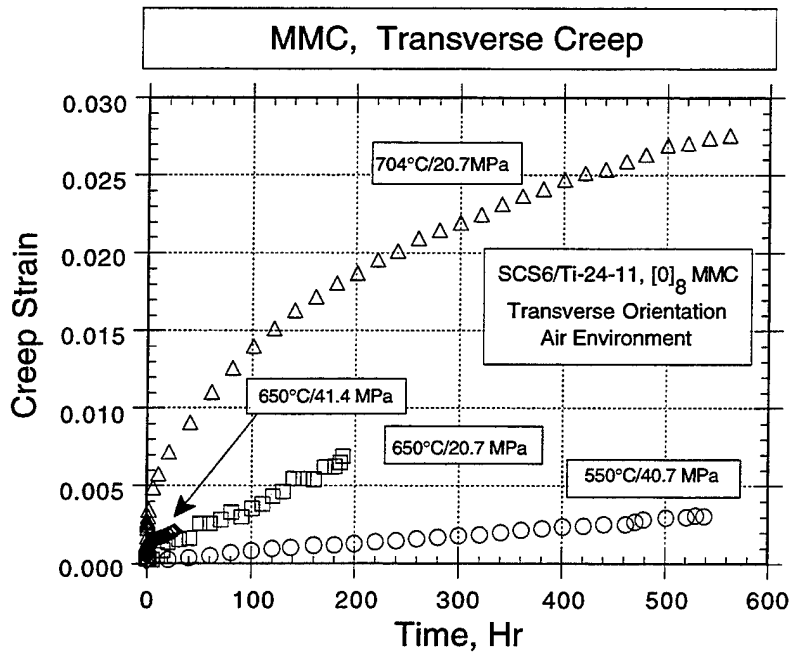
Figure 182. Transverse MMC, superimposed creep curves.

4.6.3.2   Comments Pertaining to the Transverse Creep Properties of the Program MMC Material

It is interesting to note that the stresses which give the rapid strain rates are on the order of those giving rapid fatigue crack growth in the transverse orientation at the same temperatures. The partitioning of environmental degradation and time dependent deformation is not clear from these tests but the result is clear that the program MMC is clearly incapable of sustaining a transverse stress of any significance at elevated temperatures whether it is static or cyclic (Section 4.5.5). In the former, deformation is high and probably unloads the clamping forces from the fibers and effectively reducing the longitudinal load carrying capacity. In the latter case, cyclic loading further exacerbates the transverse load carrying capability by permitting easy propagation of cracks parallel to the fiber reinforcements.

4.7   Statistical Analysis of Fiber Strength

A statistical analysis of the SCS6 Textron fiber was performed of the strength distribution of the fibers. The fibers were tested by Textron and then forwarded to AlliedSignal Engines; the data consisted of sets of fibers from the beginning of coil, end of coil and from fabric. Out of these data, only the sets from the beginning of coil were analyzed.

A second set of data tested at AlliedSignal Engines has also been analyzed. One group of data consists of fibers etched from a specimen that was fatigue tested and failed at the grips, this group is referred to as "fatigued." A second group of fibers was etched from a consolidated and untested specimen, referred to as "composited." And a third set of fibers that had not been composited, and they are referred to as "uncomposited." The following sections describe the results of the data.

The gauge length of all of these fiber tests was 1 inch. The fibers tested at AlliedSignal Engines were tested in a Sintech machine with a 50 lb load cell. All of these tests were performed at room temperature conditions.

4.7.1   Analysis of Fiber Strength from the Beginning of Coil

A total of 71 data sets from the beginning of coil were received from Textron. The number of point within each set range from 40 to 55 specimens. The data points from each set were ranked and plotted on Weibull paper, the sets were plotted on 7 different plots in groups of about 10 per plot, as shown in Figure 183 for one of the seven plots. This figure shows the strength variability from set to set as well as the scatter within each set. Of interest is the variability from set to set as well as the knee shown by the sets, indicative of more than one failure mode. A second observation that can be made is from a perusal of Figure 183 and Figure 184, Figure 183 shows a well marked behavior
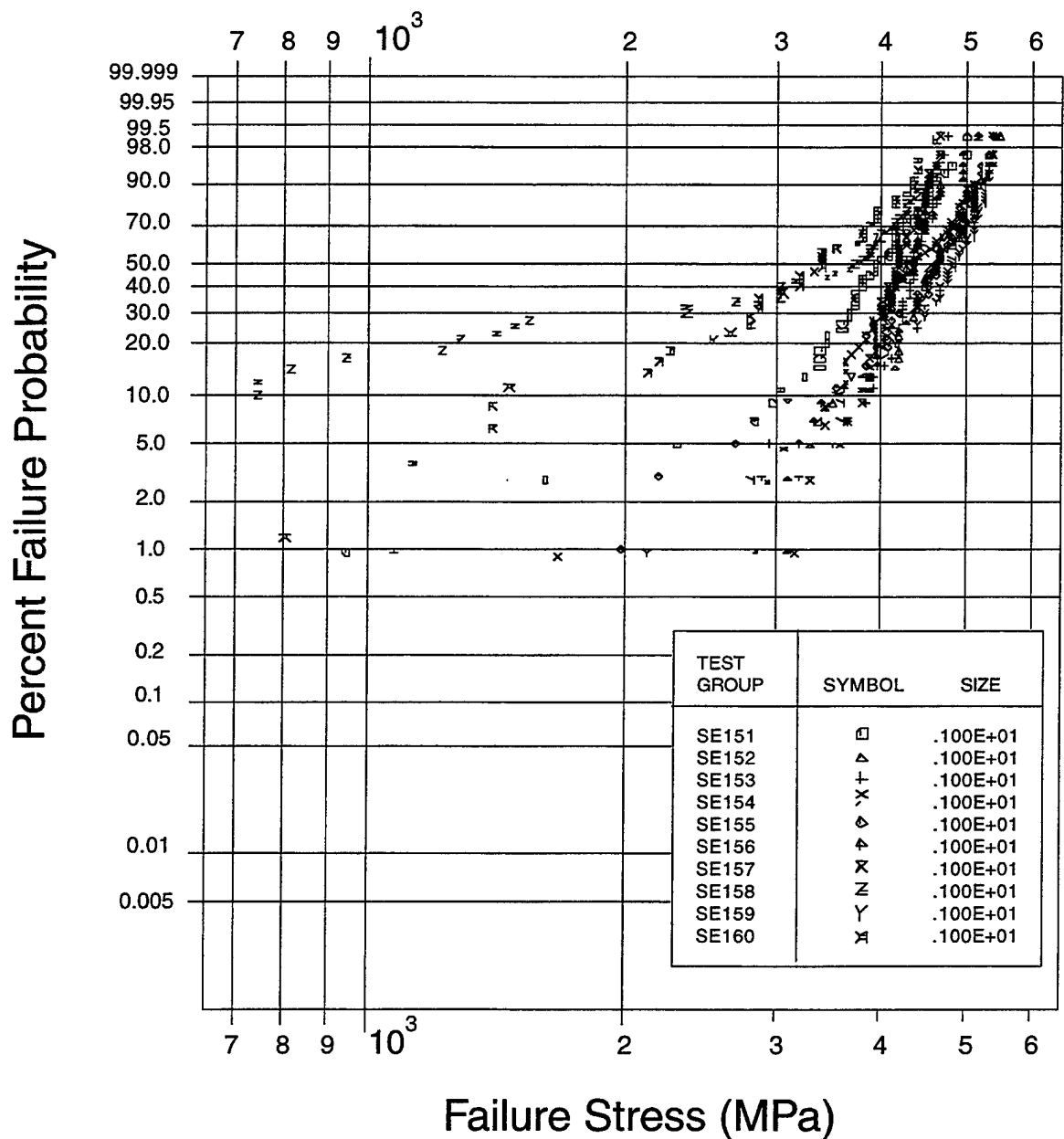
Figure 183. **Fiber strength variability for fibers from the beginning of coil.**
Shown is the strength variability from fiber to fiber, and set to set; shown also is the indication of concurrent failure modes.

of competing failure modes in the data sets, while the Figure 184 show a data more indicative of a single failure mode.

The variability of strength within a set is a well known behavior of ceramic materials; the knee in the curve can be interpreted as a result of two competing failure modes present in the fibers. Two classical competing failure modes for ceramic material are surface initiated failures and volume (core-SiC interface, Figure 192a) initiated failures. The resulting variability in each set can be understood and treated using Weibull Theory (Reference 27). The variability between sets can not be explained at this time.

4.7.2   Analysis of Uncomposited, Composited, and Fatigued Fiber Strength

4.7.2.1   Strength of Uncomposited Fibers, from Woven Mat

The uncomposited fibers were obtained from woven mats using Nb wire cross weave. Thirty fibers were tested and analyzed, a Weibull plot is shown in Figure 185. A summary of the Weibull parameters and average strength are shown in Table 19. These data appear to have a single failure mode; although, the lower tail has the tendency of curving to the left which may be hinting a second, competing, distribution. There may also be an inadvertent bias in the data by the process of weaving which will screen the weak fibers out of the resultant woven mat by virtue of the stains induced by the handling and manipulating steps.
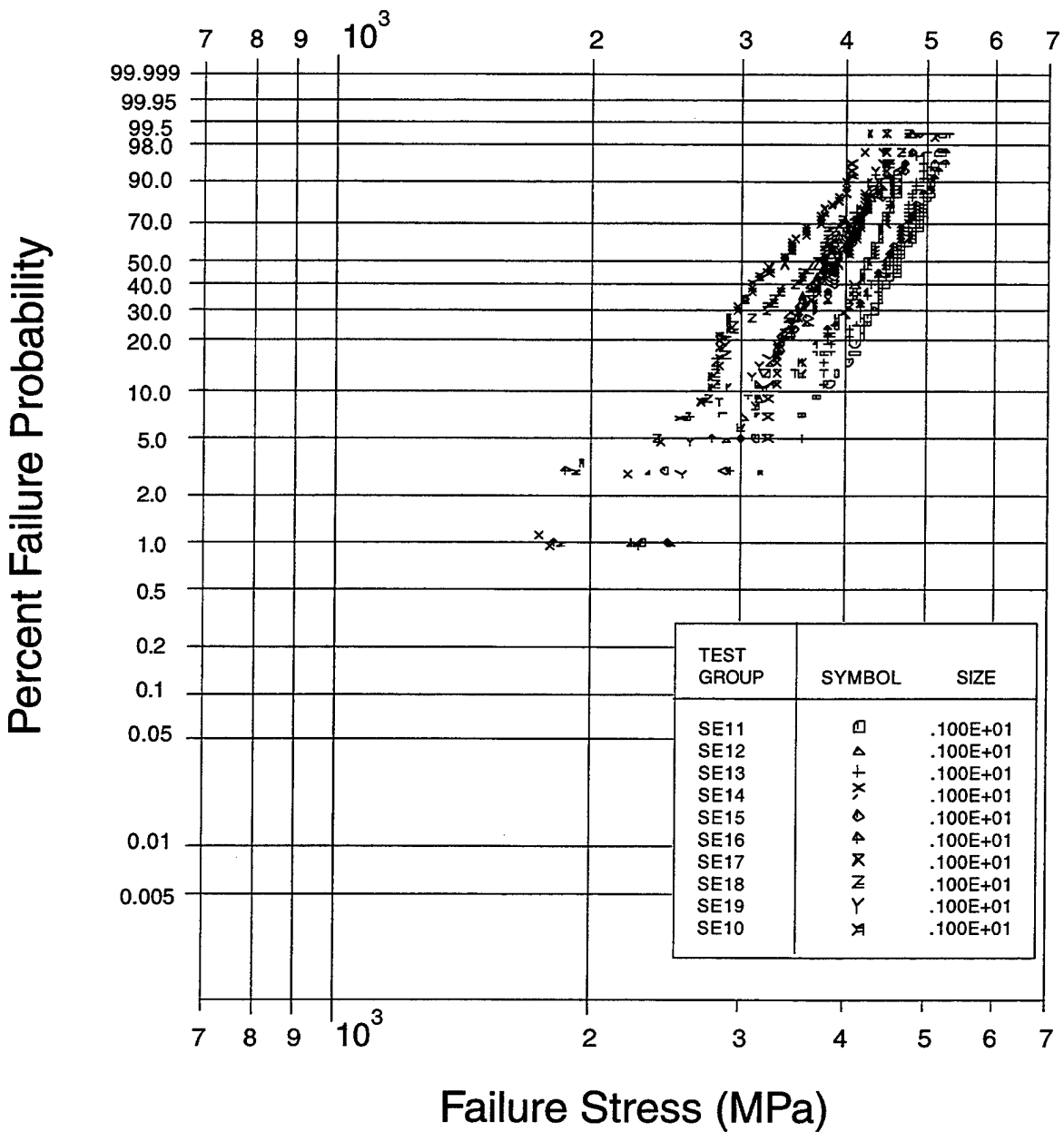
Figure 184. Fiber strength variability is shown for fibers from the beginning of coil. The concurrent failure modes are not very pronounced on the sets.

216
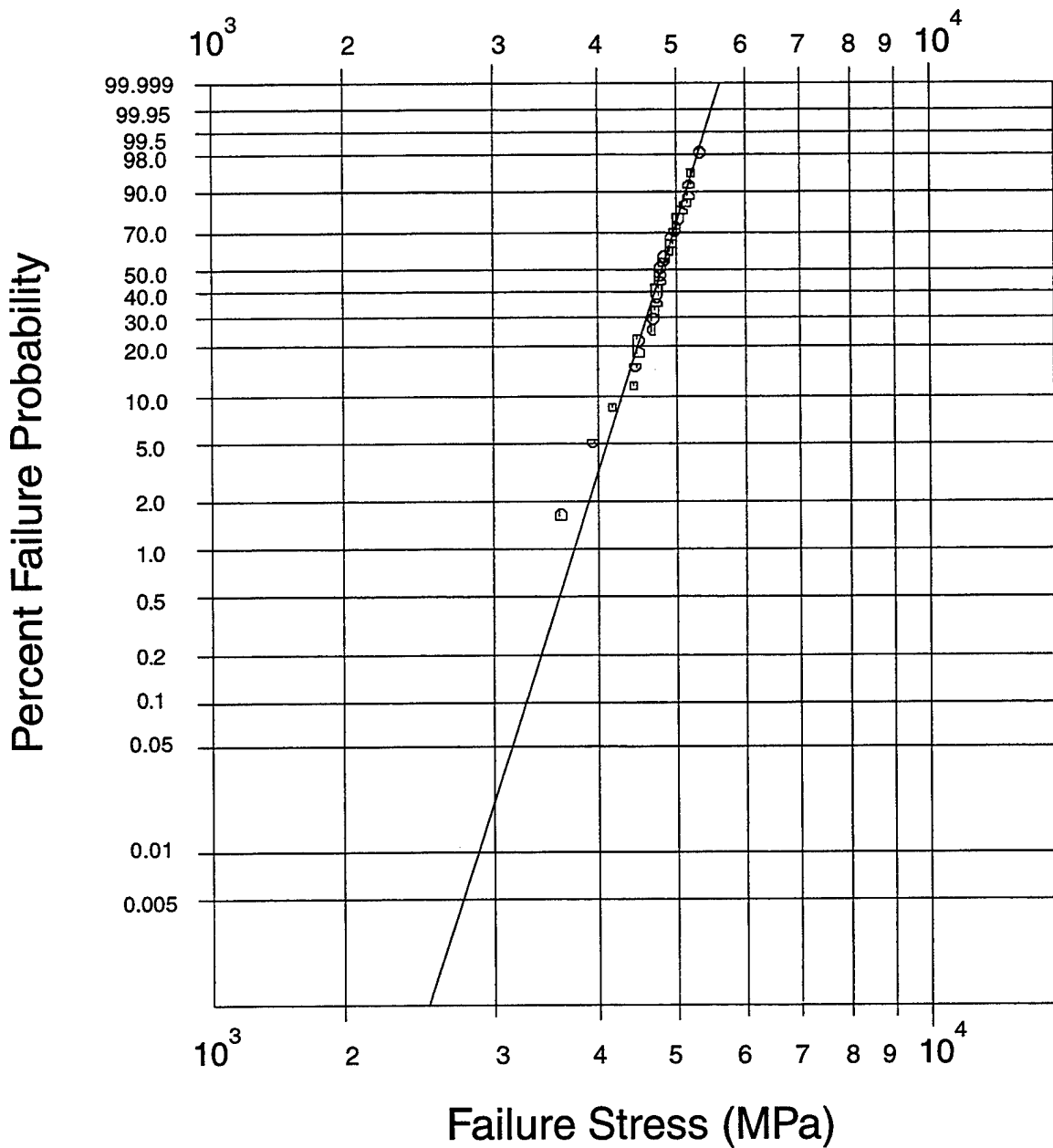
Figure 185. **Fiber strength variability for "uncomposited" fibers.**
This set of data fall in the high strength data when compared to the beginning of coil fiber strength.

217

Table 19. Statistical summary of fiber fracture data.

Name	Slope	Characteristic (MPa)	Average (MPa)
Uncomposited (Woven Mat) (Fig. 185)	17.3	4890	4730
Composited (Fig. 186)	10.3	3995	3800
Left Censored (Fig. 187)	12.8	4050	3888
Right Censored(Fig.188)	1.8	17350	15435
Fatigued (Fig. 190)	10.1	4240	4035

4.7.2.2 Strength of Composited Fibers

A set of fibers was removed from leftover panel sections by etching away the matrix. The fibers were then tested to failure. Etching of the matrix to release the SCS6 fibers was accomplished at room temperature with a fresh solution of 67v/o of 20w/o NH_4HF_2 in water and 33v/o concentrated HNO_3 (70%). Sixty fibers were tested and analyzed; a Weibull plot of the data are shown in Figure 186. This set of data shows clearly the existence of two concurrent failure modes, as had been observed in the analysis of the fibers from the beginning of coil, Figure 183. A second analysis was performed on this set assuming that there were two concurrent failure modes; the analysis had to assume that the lowest four strength fibers failed from a second failure mode, this was done for lack of fractographic information on the fibers. The intent of this second analysis is to match the Weibull parameters of the composited data to the uncomposited data which could possibly prove some type of damage on the fibers as a result of the consolidation. But the analysis was not successful in proving this hypothesis. The results of the analysis are plotted in Figure 187 through Figure 189. Figure 187 shows the data for the higher strength fibers, Figure 188 shows the data for the low strength fibers and Figure 189 shows the data for the combined data analysis. In order to do the proper analysis to prove the hypothesis we would need to know the failure origin of each fiber. To accomplish this, a series of tests would have to be run that would make sure that the failure origin is saved. Such analysis cannot be accomplished within the scope of this contract.
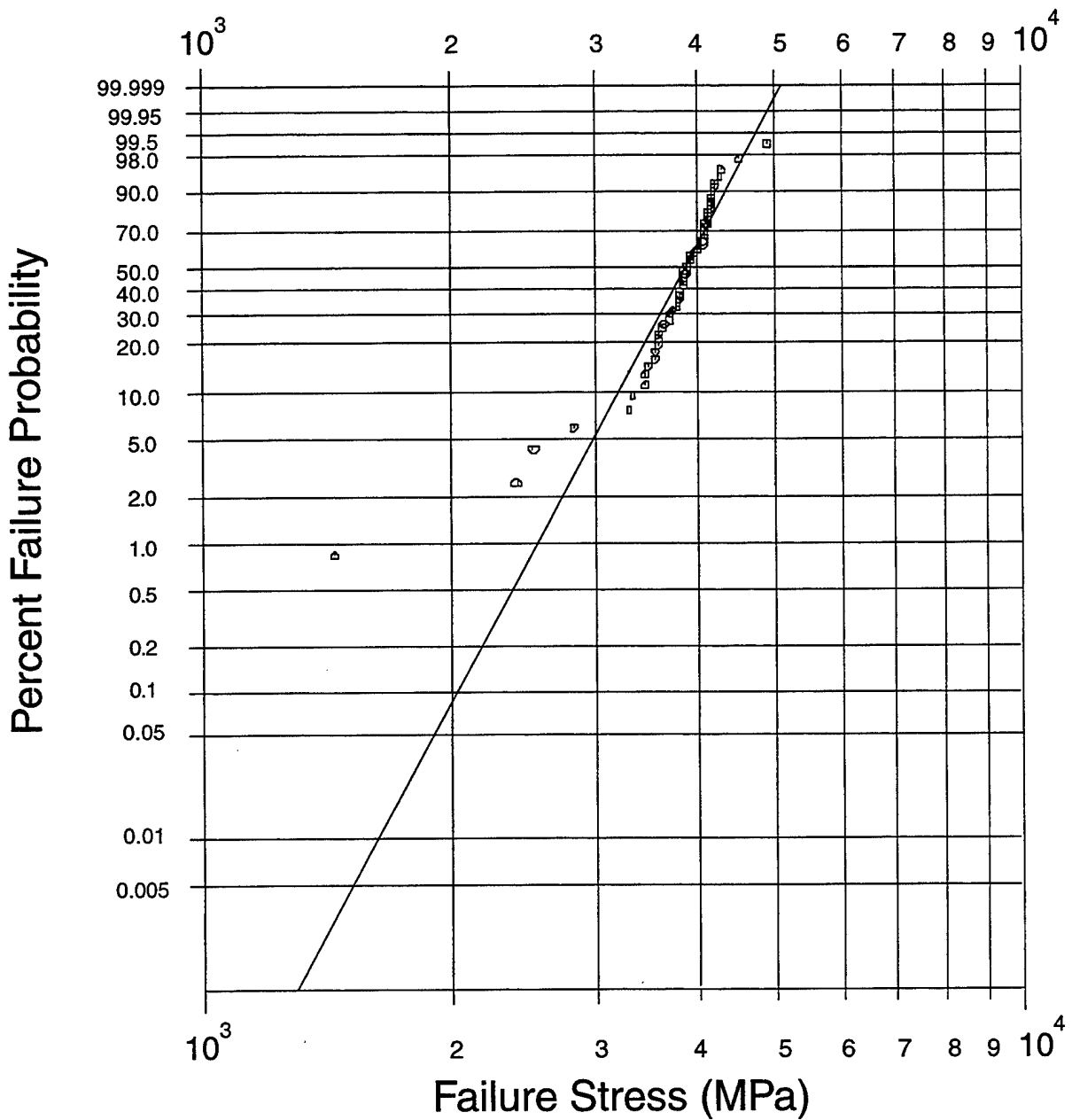
Figure 186. Fiber strength variability for "composited" fibers.
This set of data shows similar strength to the beginning of coil data. Two concurrent failure modes are clearly observed.
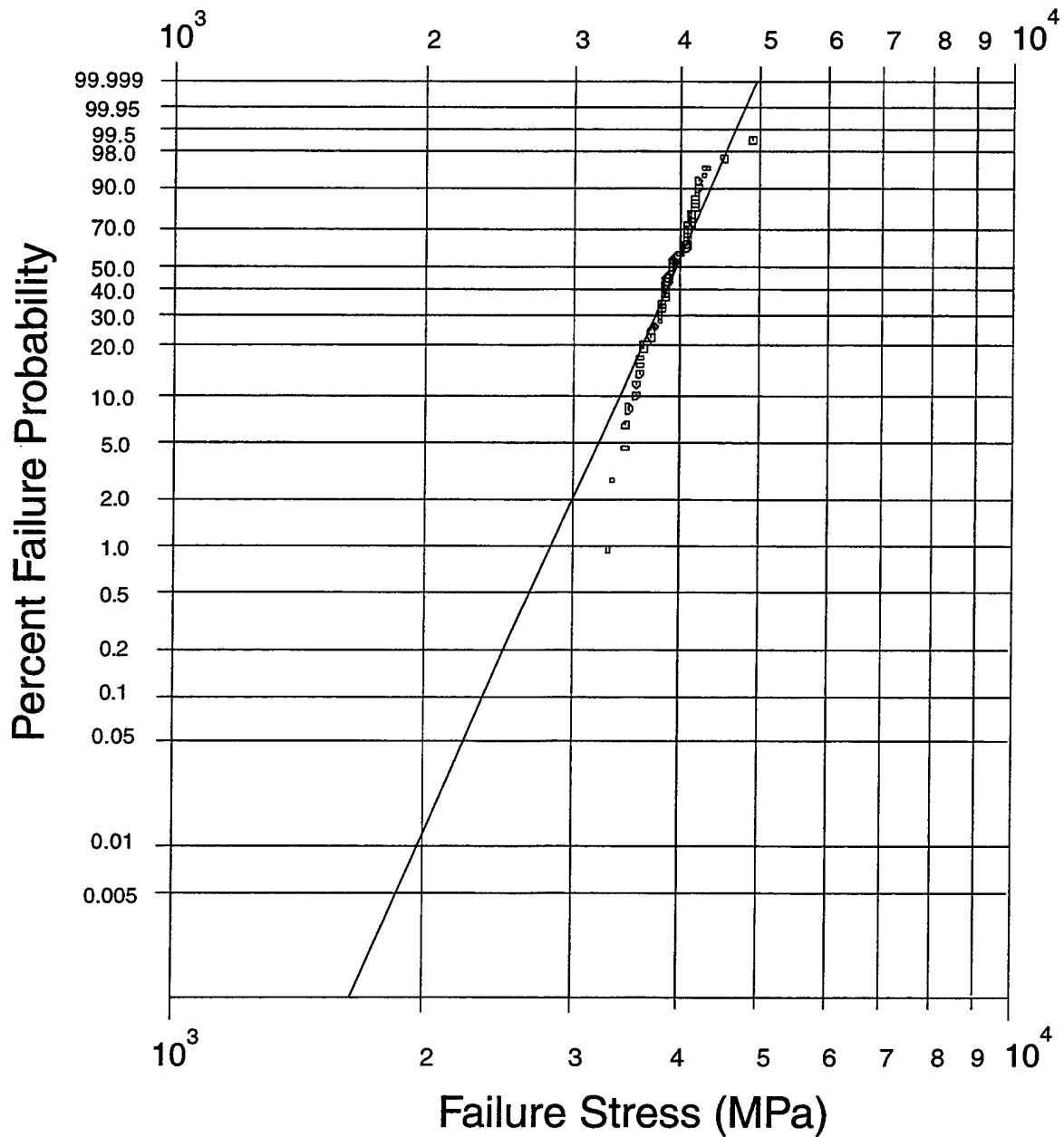
Figure 187. **Censored data analysis for the high strength "composited" fibers.**
The data censoring did not have a significant effect on the Weibull parameters. The
censoring performed on the data produced an artificial proof testing type of behavior
on the remaining data.
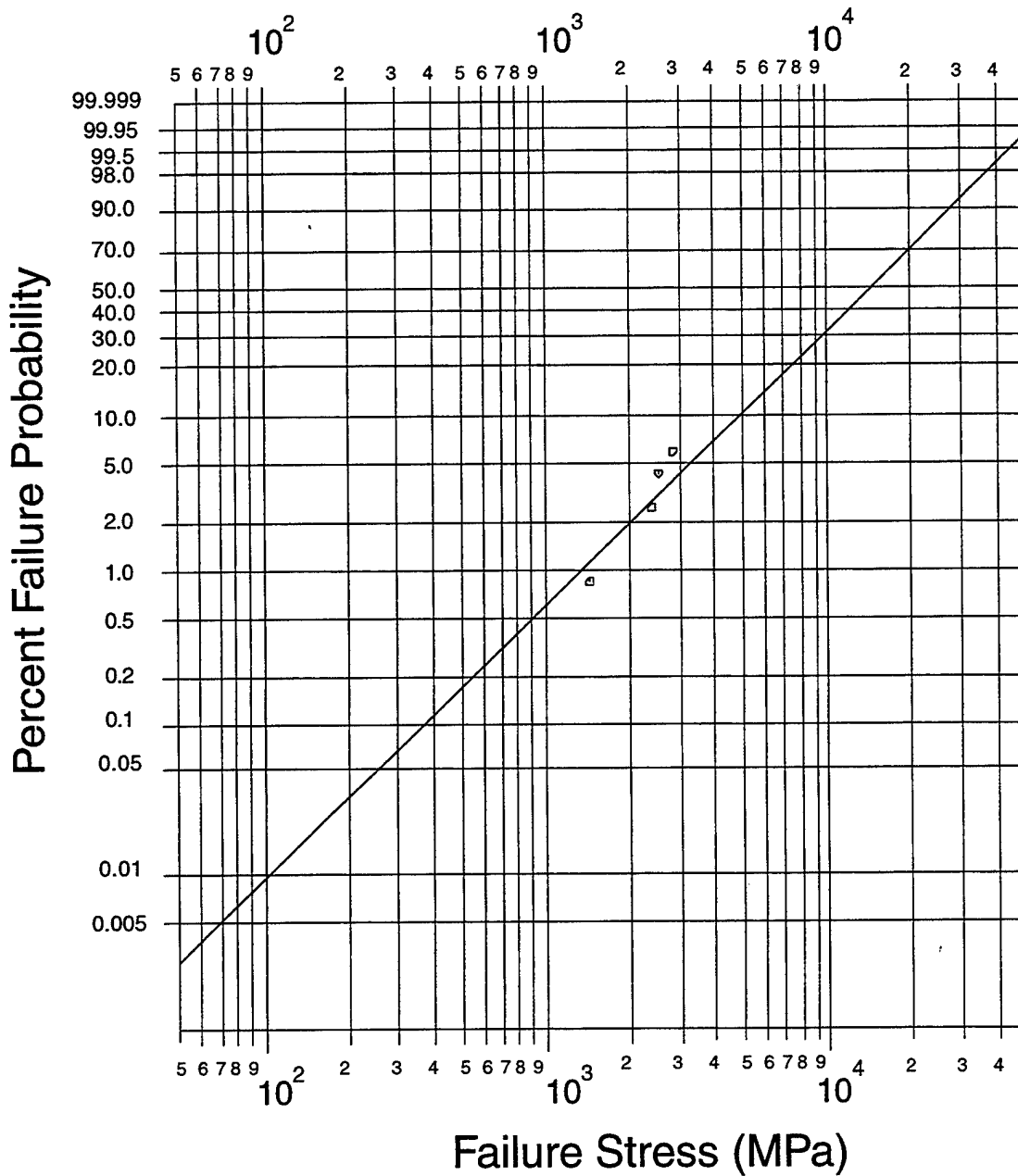
Figure 188. Censored data analysis for the low strength "composited" fibers. This data show a large scatter as indicated by its Weibull modulus.

221
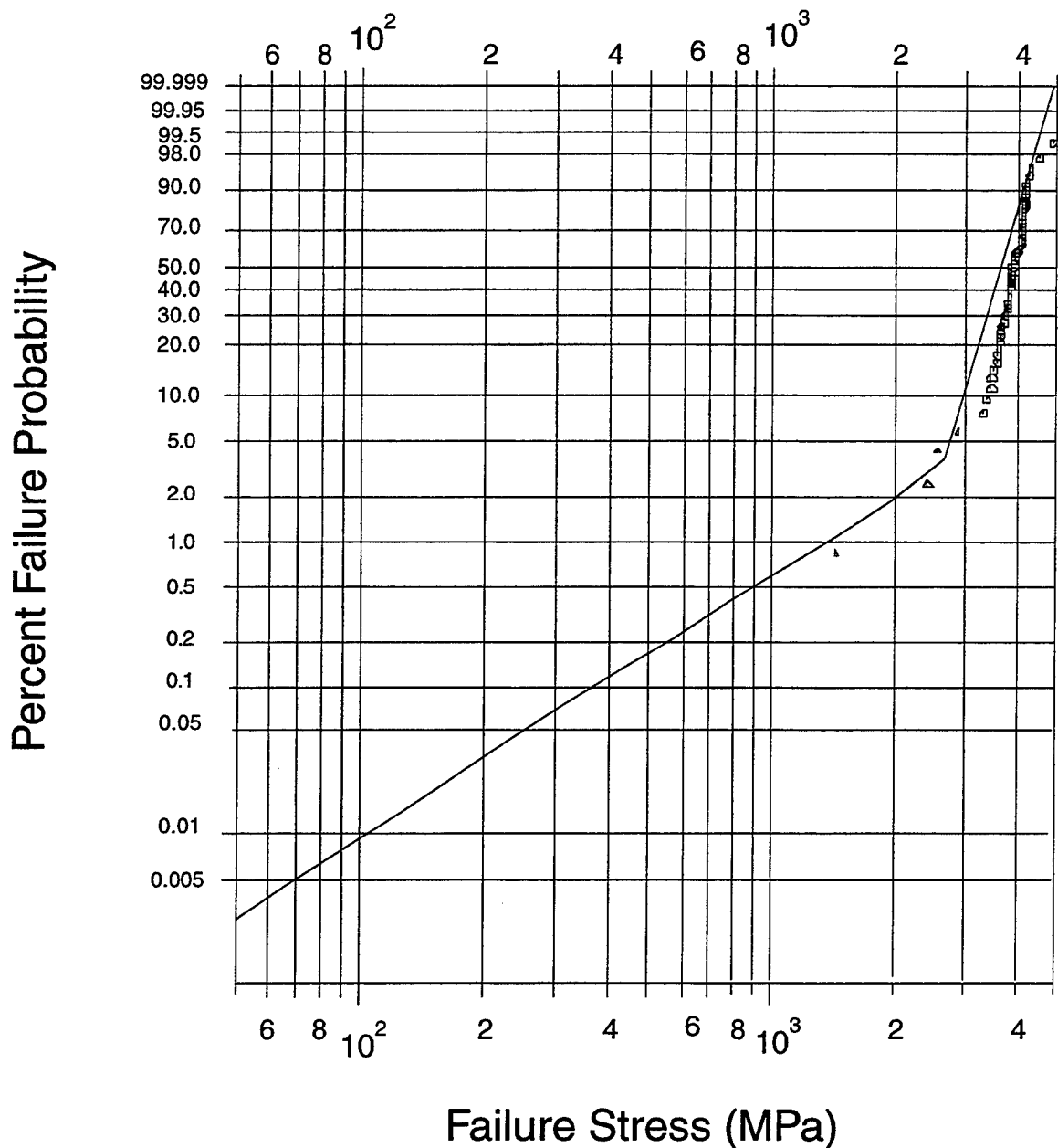
Figure 189. Combined Weibull plot for the "composited" censored data analysis.
The fit of the data show a reasonable fit for the combined, concurrent failure, data.

4.7.2.3 Strength of Fatigued Fibers

Specimen 2A/0C11 was tested in fatigue at a stress level of 689 MPa, the specimen failed at the grips after 1,181,692 cycles. The specimen was subsequently etched in the following order. Etching one removed a 31.75 mm (1.25 in) section of material starting from the fractured side; this was a section well below the main fatigue crack and included the grip section. Etching two removed a 76.2 mm (3.0 in) section which went just past the main fatigue crack. The third etching removed section about 114 mm (4.5 in) in length which went up to the remaining grip. Twenty-eight fibers from the ones remaining in the grip section were tested; these fibers show a predominant single failure mode with a small tendency for a second failure mode, as shown in Figure 190. The analysis shows a slight strength increase of the fatigue data relative to the composited data, 3995 MPa vs. 4240 MPa. Although statistically this difference is not very significant, the slight strength increase can be attributed to the breakage of fibers during the fatigue testing of the specimen, and consequently the effect of the low strength fibers was not included in the analysis. The summary of all of the fiber testing is shown in Table 19.

4.7.3 Fiber Fracture Failure Origins

Fractographic analysis of four failed fibers was performed to determine their failure origins. Two of the fibers had a low strength to failure while the other two had a high strength to failure. The four fibers were SEMed at a magnification of 400X and 1000X. The two low strength fibers clearly show, Figure 191a, that failure originated from surface defects. One of the fibers shows the failure originating from a bubble type defect; the second fiber shows the failure originating from the surface, but from no discernible feature, Figure 191b. The high strength fiber failure is internally originated. Figure 192a shows one of the internal failures originating from the interface with the carbon core which had a defect; the second fiber failure origin is not that easily identified, but it looks very similar to the internal failure of the previous fiber as shown in Figure 192b.

4.7.4 Composite Design Limits

The large variability in the strength of the fibers presents a problem. The problem this variability presents deals with specifying design limits for composite components. A popular approach is to use the nominal strength of the fibers in the calculation of the strength of the composite, but this approach would yield a nominal strength for the composite, a strength that would be inappropriate for design. The ultimate strength of composite panels can be observed in the tensile tests summarized in Table 14, the average of the four specimens tested at room temperature is 1515 MPa (220 ksi), equivalent to 3400 MPa (493 ksi) on the fibers assuming no residual stresses on the
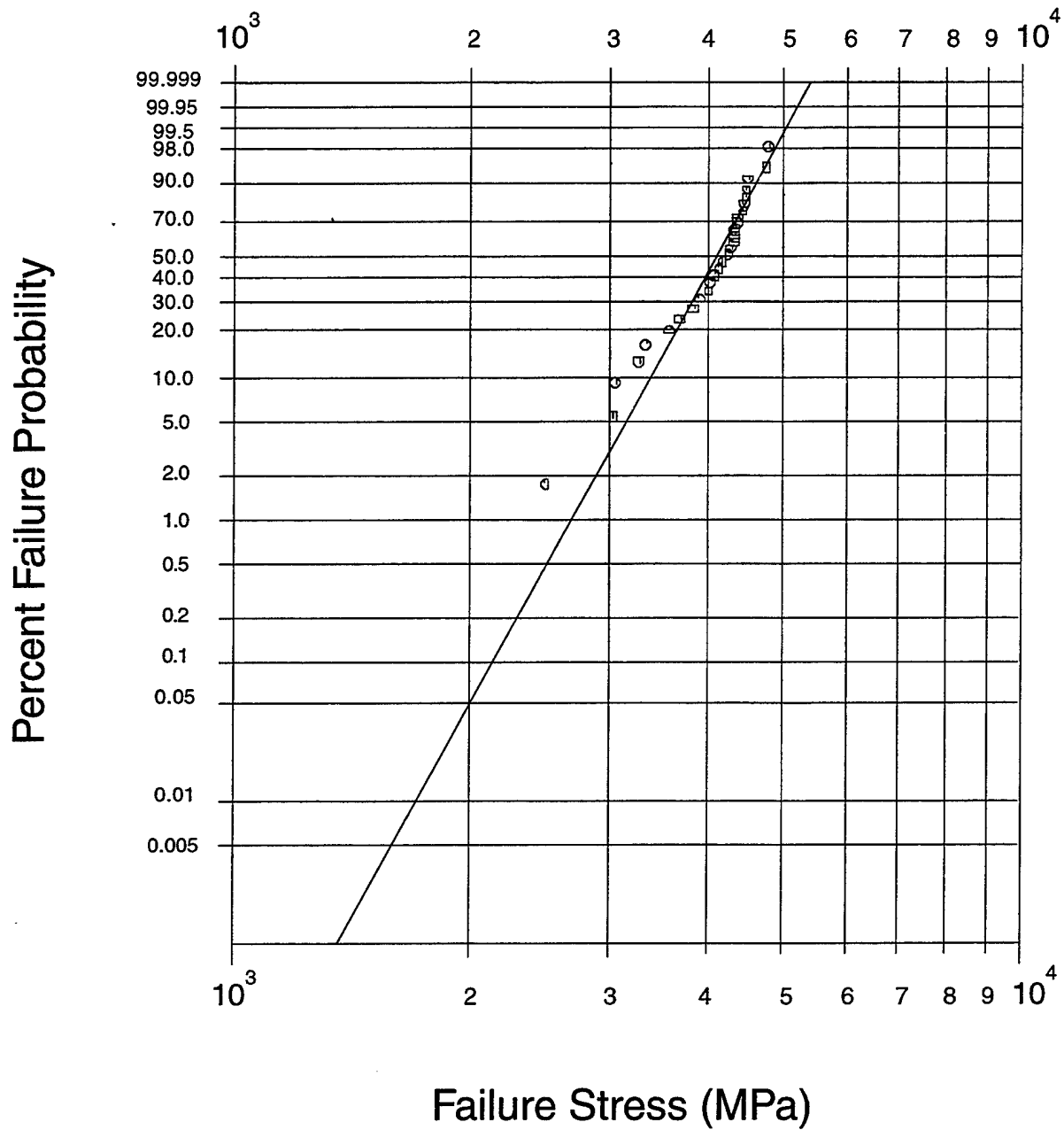
Figure 190. Fiber strength variability for "fatigued" fibers.
The strength of these fatigued fibers is very similar to the strength of the "composited" fibers. The data show a small tendency of a concurrent flaw population.

224
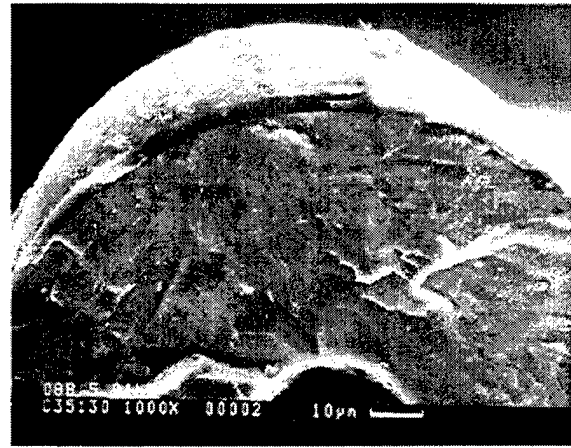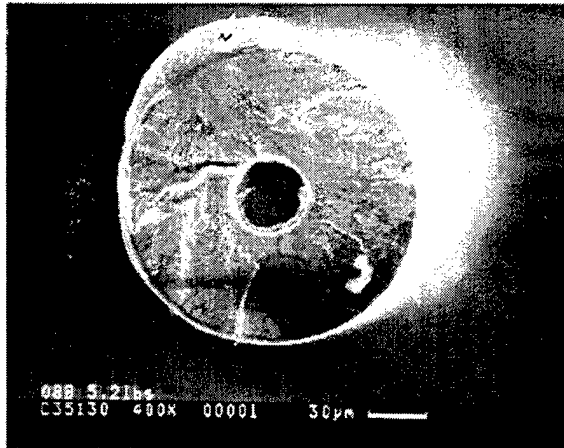
(a)
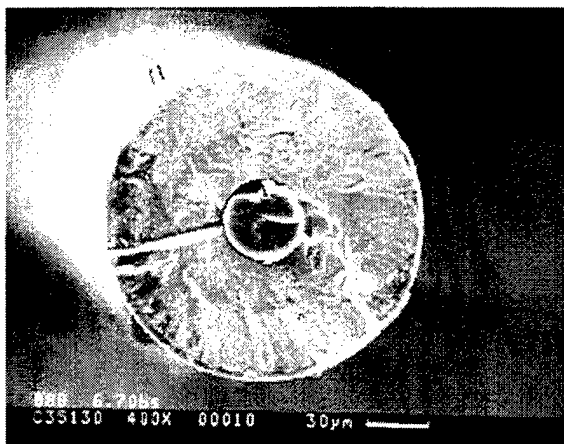
(b)

Figure 191.   **Surface failure initiation of low strength fibers.**
   a) Failure origin at bubble defect. b) Failure origin with no discernible surface defect.

225
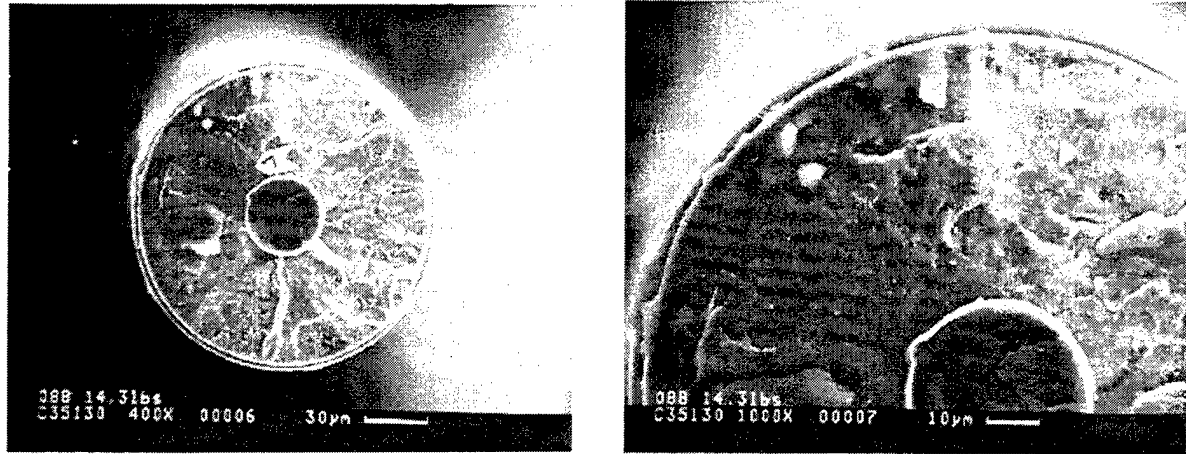
(a)
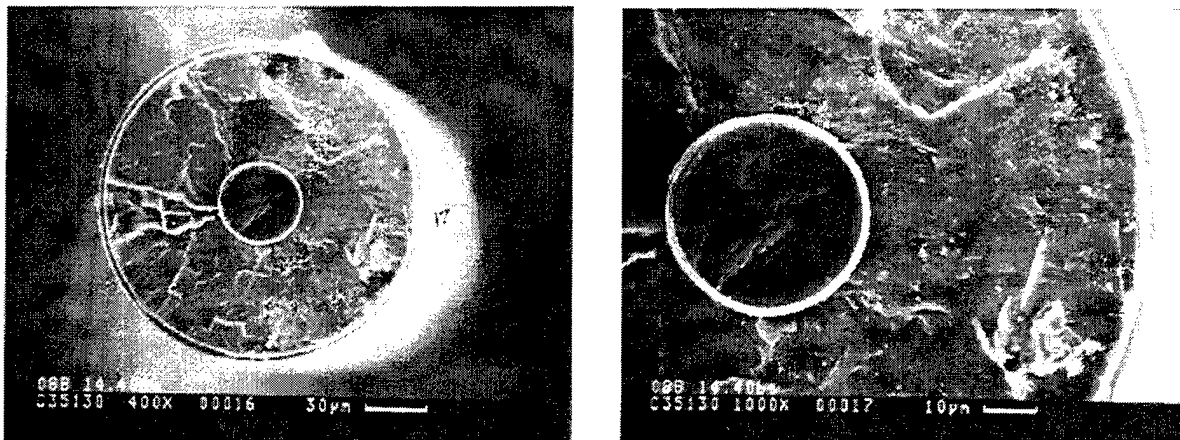
(b)

Figure 192. **Volume failure initiation for high strength fibers.**
a) Failure origin at interface with carbon core, at location of defect on core. b) Failure origin with no discernible internal defect.

226

constituents. When the residual stresses are taken into account the equivalent stress in the fibers goes up to 3750 MPa (544 ksi), consistent with the average composited fiber strength shown in Table 19. This rule of mixture approach satisfactorily predicts the ultimate strength of the composited specimen.

4.8 Coefficient of Thermal Expansion

4.8.1 Experimental Procedure

The coefficient of thermal expansion (CTE) of an MMC composite (Ti-24Al-11Nb/SCS6) and a consolidated titanium aluminide foil system were measured in the three orthogonal directions, as shown in Figure 193. The measurements were made using a Thermomechanical Analyzer (TMA) 2940 over a temperature range of room temperature to 760°C. Several heat cycles were used to determine the CTE; the cycle and test conditions are summarized in Table 20. The specimen dimensions are 6.35 mm length, 6.35 mm width with 1.9 mm thick for the composite specimens and 1.0 mm thick for the matrix only specimen. The sides of the specimens that were used to measure the CTE, the sides in contact with the probe and the stage, were machined parallel to each other.
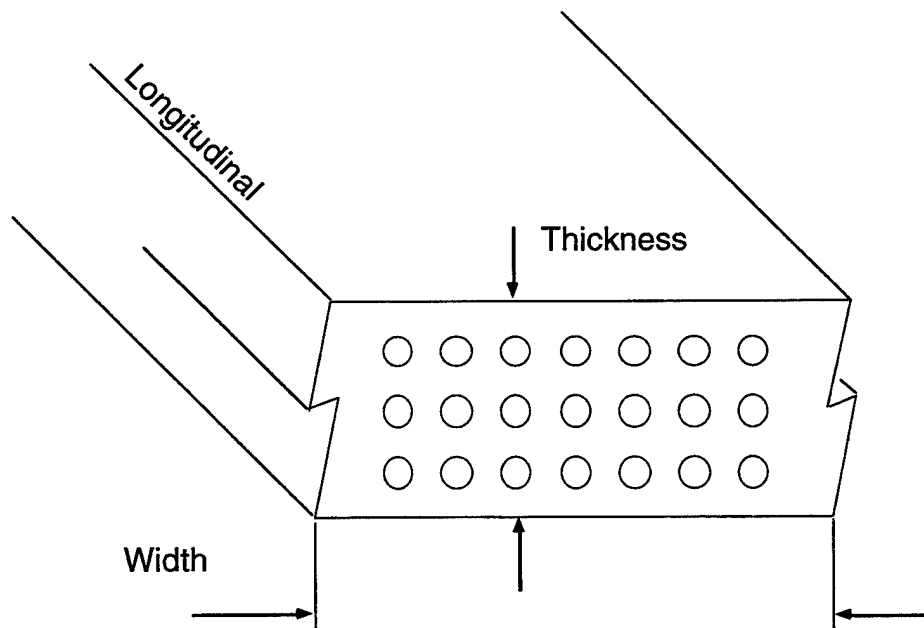
Figure 193. Direction of the measured coefficient of thermal expansion.

Table 20. Cycle used for measuring the coefficient of thermal expansion in the Thermomechanical Analyzer.

Load	0.05N
Ramp Rate	5 C/min
Purge	80 cc/min He
Sampling interval	3 sec/ data point

Method Segments:
First Heat
1) Ramp From 0C to 760C
2) Isothermal for 3 min.
3) Ramp from 760C to 0C
4) Isothermal for 3 min.
Subsequent Heat
1) Ramp From 0C to 760C
2) Isothermal for 3 min.
3) Ramp From 760C to 0C

The coefficient of thermal expansion was measured on a total of three specimen types in three orthogonal directions. Specimen one was a consolidated (unexposed) composite, specimen two was a consolidated composite (exposed), tensile tested to failure and subsequently cycled 100 times from room temperature to 650°C (1200°F) with a 1 hour hold time at 650°C (1200°F). Specimen three was a consolidated titanium aluminide foil system, it contained no fibers, it was processed using the same process for the composite specimens.

4.8.2 Matrix Alloy Results

The CTE for the matrix in the orthogonal directions is shown in Figure 194. The longitudinal and width directions give very similar results at the higher temperatures with reasonable discrepancies at the lower temperatures. This behavior can be interpreted as another indication of the matrix being isotropic in the plane of the foil, the first indication of this behavior was shown in the tensile test results as explained in Section 4.2.2.1.1. In the thickness direction, the CTE is reasonably higher than in the other directions.

The CTE results of the multiple heatings are shown in Figure 195 for the longitudinal and in Figure 196 in the thickness direction. The results in the longitudinal direction

228

Matrix Only Titanium Aluminide Coefficient Of Thermal Expansion
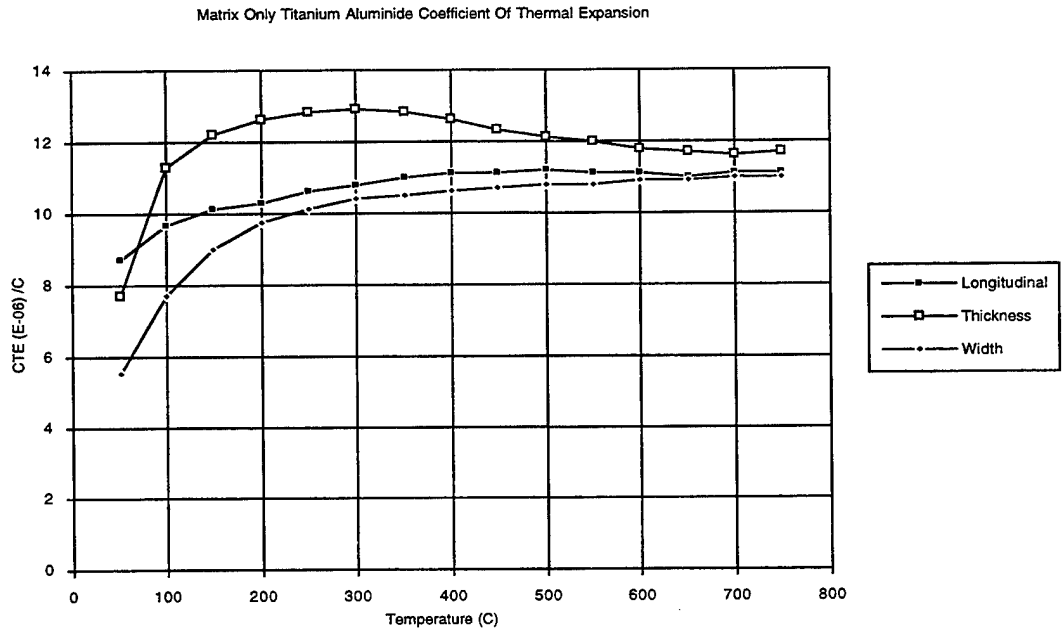
Figure 194.   Coefficient of thermal expansion for the Ti-24-11 matrix only specimen in the three
orthogonal directions.

Matrix Only CTE Variation With Heat Cycle, Longitudinal
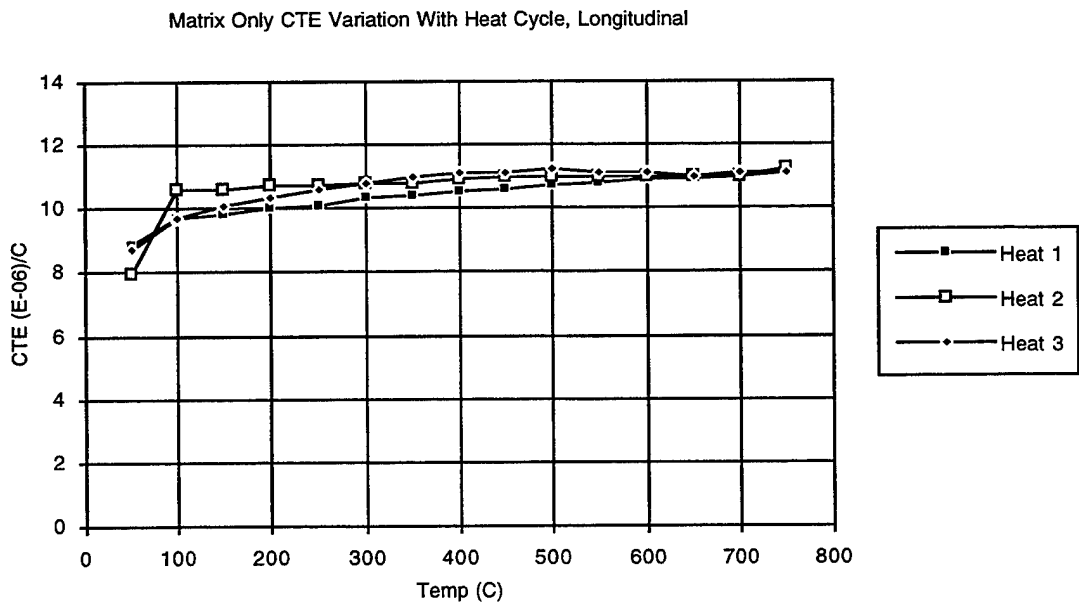
Figure 195.   Variation in the coefficient of thermal expansion for the Ti-24-11 matrix only
specimen in the longitudinal direction as a function of the heat cycle.

229

Matrix Only Ti Al Variation With Heat Cycle, Thickness
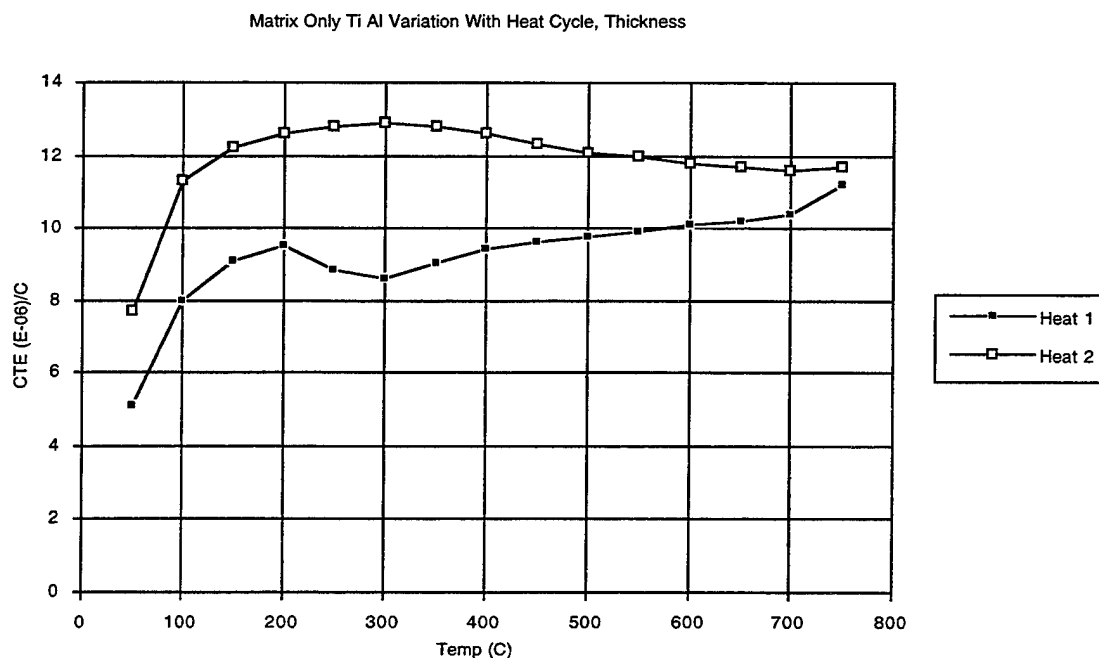
Figure 196. Variation in the coefficient of thermal expansion for the Ti-24-11 matrix only specimen in the thickness direction as a function of heat cycle.

are considered to be constant from heat to heat based on the small discrepancy. The results in the thickness direction are clearly in disagreement and upon review of the data, it was observed that the first heat was contaminated by an outside vibration source. In an attempt to salvage the results, the data were smoothed and the results were plotted. As a result of this problem, the second heat results were used.

4.8.3 MMC Unexposed Specimen Results

The unexposed MMC CTE results are shown in Figure 197. A comparison of the measured results against analytically predicted results was performed, the results show a reasonable agreement with the theory. Figure 198 and Figure 199 show the result of the multiple heatings, note the small tendency for the CTE to decrease with heating cycle number.

Equation 112 can be used in the calculation of the CTE in the longitudinal direction, while equation 113 was used for the calculation in the width and thickness direction. A value of $\zeta = 2$ (curve fitting parameter) provides reasonable agreement with experimental data.

230

$$\alpha_l = \frac{\alpha_f E_f V_f + \alpha_m E_m (1 - V_f)}{E_m (1 - V_f) + E_f V_f} \qquad [112]$$

$$\alpha_T = \frac{\alpha_m [\alpha_f + \zeta \alpha_m + \zeta V_f (\alpha_f - \alpha_m)]}{[\alpha_f + \zeta \alpha_m - V_f (\alpha_f - \alpha_m)]} \qquad [113]$$

4.8.4 MMC Exposed Specimen Results

The exposed MMC CTE results are shown in Figure 200. A comparison of the measured and analytical results were performed using the above equations and give reasonable agreement in the longitudinal and width direction. The agreement in the thickness direction is not very good at the higher temperatures. The variation of the CTE with heating cycles are shown in Figure 201 and Figure 202.

Note that there is not much difference in CTE between the unexposed and the exposed specimens, but that there was a tendency for the CTE for the exposed specimen to increase with heat, contrary to the observations made for the unexposed specimens. There was an increase in the thickness CTE of the exposed specimens relative to the unexposed specimens, this could be a sign of debonding of the layers of the composite, and it deserves to be investigated further.
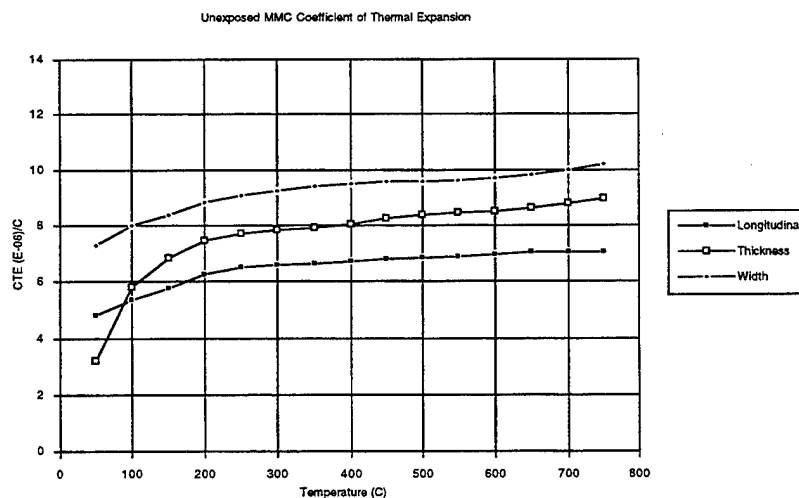
Figure 197. Coefficient of thermal expansion for the unexposed SCS6/Ti-24-11 system only specimen in the three orthogonal directions.

231
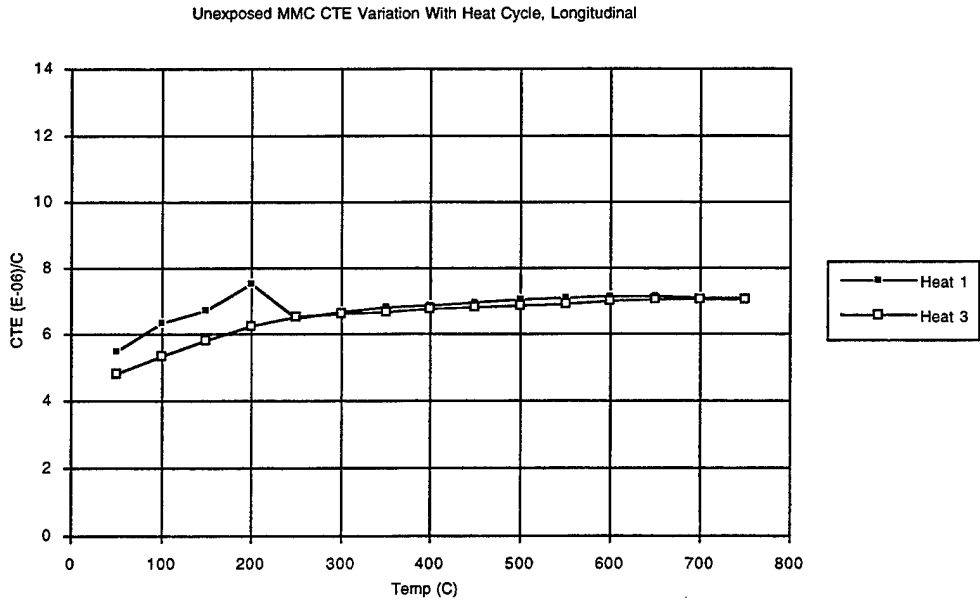
Figure 198.   Variation in the coefficient of thermal expansion for the unexposed SCS6/Ti-24-11 system only specimen in the longitudinal direction as a function of the heat cycle.
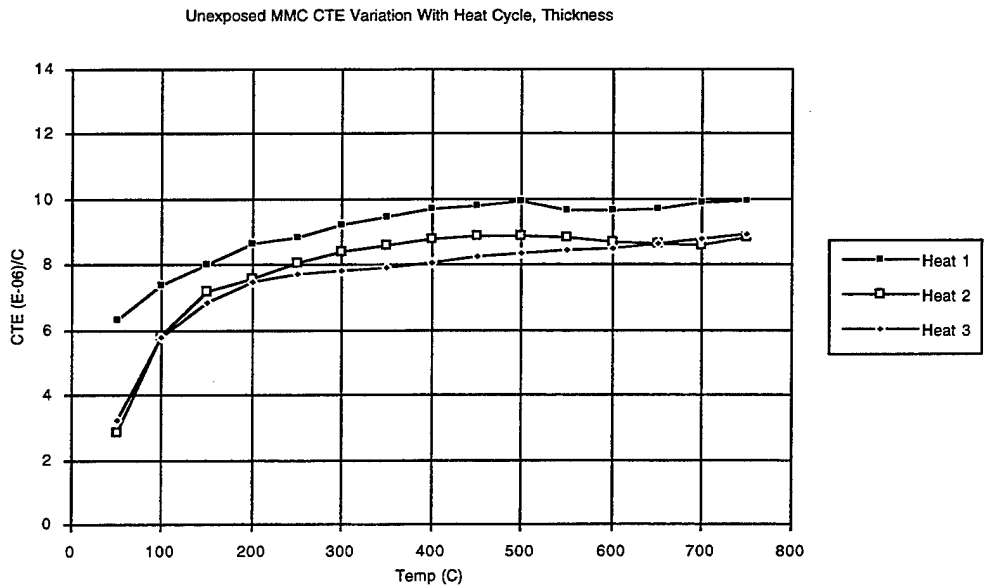
Figure 199.   Variation in the coefficient of thermal expansion for the unexposed SCS6/Ti-24-11 system only specimen in the thickness direction as a function of heat cycle.

232
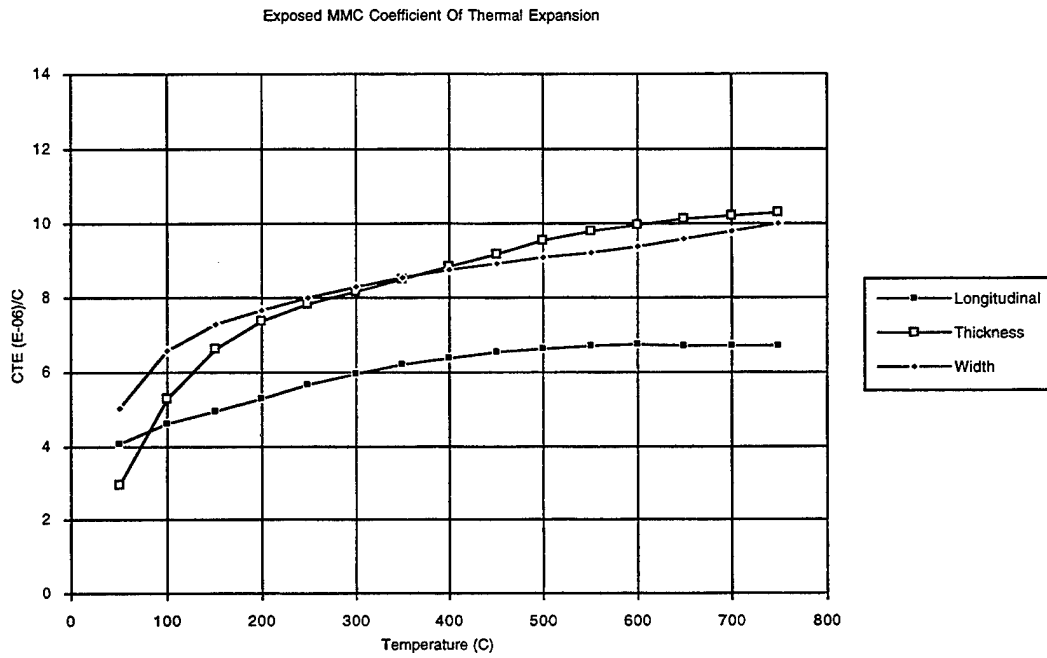
Figure 200.   Coefficient of thermal expansion for the exposed SCS6/Ti-24-11 system specimen in the orthogonal directions.
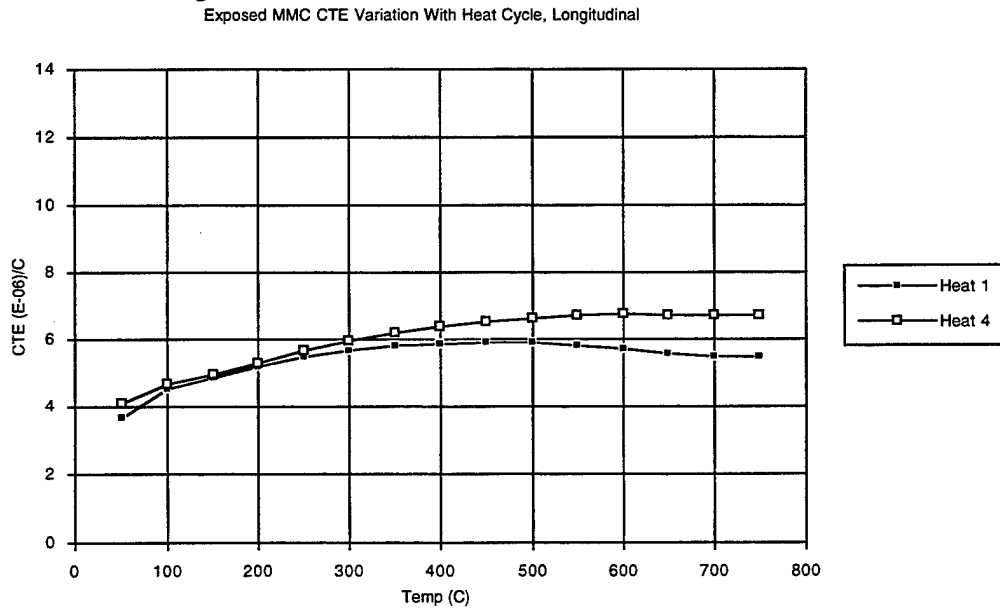
Figure 201.   Variation in the coefficient of thermal expansion for the exposed SCS6/Ti-24-11 system only specimen in the longitudinal direction as a function of the heat cycle.

233

Exposed MMC CTE Variation With Heat Cycle, Thickness
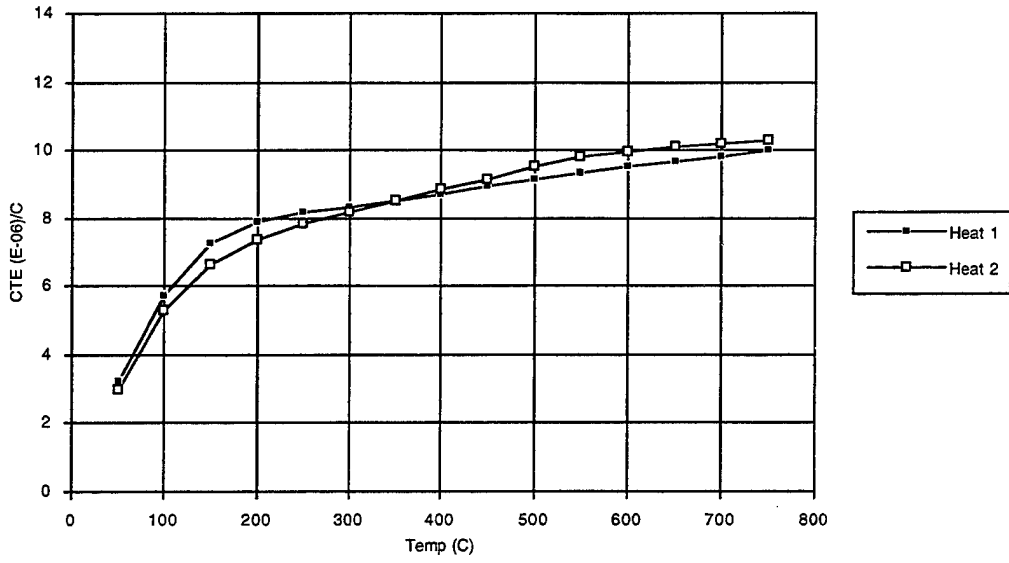
Figure 202. Variation in the coefficient of thermal expansion for the exposed SCS6/Ti-24-11 system only specimen in the thickness direction as a function of heat cycle.

4.9 Micromechanical Mechanisms of Fatigue Crack Growth

4.9.1 Room Temperature Crack Growth Micromechanics

4.9.1.1 Crack Bridging

One room temperature fatigue crack growth specimen (2A/0B13) with a far field stress of 1172 MPa (170 ksi) and R = 0.1 and a test frequency of 20 cpm, after a growth of 0.607 mm from the SEN specimen edge, broke in the grip due to grip induced damage. This specimen was then etched to remove the alloy matrix, leaving only the fibers. This etching was done in small increments of the specimen length by successive immersion in the acid mixture described in Section 4.7.2.2. The specimen was suspended, grip fracture end down, in the solution to a depth of about 32 mm and the fibers released were collected and assumed to represent fatigue damage arising far from the initial crack and perhaps due to grip related damage. Seven such fibers were released from a cross section expecting to contain over 400 fibers.

A second etching was done at a level of just above the main crack and, likewise, the released fibers were collected. At this point, only 7 fibers were released. This is compared to as many as 45 (8 layers x 0.607 mm crack length / 0.106 ifs) fibers in the cross section spanned by the crack and 6 to 8 fibers directly exposed to the machining operation on the edge of the specimen gage. Even including the edge exposed fibers which are expected to have suffered damage, 85% of the fibers encompassed by the crack remained intact, a clear evidence of fiber bridging at stresses as high as 1172 MPa (170 ksi).

4.9.1.2 Estimate of Residual Life from a Detectable Crack at Room Temperature

From Figure 115, one can calculate fatigue crack grow rates for 20 cpm tests at an R of 0.1. Using the relationship accompanying this figure, and an assumed detectable crack length of 0.70 mm (0.027") and critical crack sizes calculated from an apparent fracture toughness derived from Figure 68 (Specimen 2B/0B11), one can compute estimated residual fatigue crack growth life for various stresses.

From Table 21 it can be seen that, at interesting stresses of about 1103 MPa (160 ksi), the growth life of a crack beyond its detectable size is on the order of 13,000 cycles at room temperature.

Table 21.   Estimated room temperature residual life from 0.70 mm initial flaw

σ max, MPa	a$_c$, mm	da/dN, mm/cycle	N$_P$
689.5	3.00	4.58 x10^{-6}	502,000
827.4	2.08	1.53 x10^{-5}	90,000
1034.2	1.33	3.15 x10^{-5}	20,000
1103.2	1.17	3.68 x10^{-5}	13,000
1172.1	1.04	4.22 x10^{-5}	8,000

4.9.2   Crack Growth Micromechanics at 550°C

4.9.2.1   Crack Bridging

LCF specimens tested at 965.3 MPa (140 ksi) and 1103.2 MPa (160 ksi) maximum stress (specimens 1A/0A21 & 1A/0A22) were examined in detail for evidence of crack bridging. Both specimens exhibited multiple failure origins, failing with rather small surface crack lengths of 0.88 mm (0.035") and 0.44 mm (0.017") respectively. In both cases, there was evidence of fiber bridging of the crack prior to final separation. The most convincing being the observation that the fiber fracture is not on the same plane as the matrix fracture. No information about when, in the fracture, the fibers did break was obtained from these observations. So, the question is open as to whether or not the fibers failed in the wake of the growing crack is still open. The temperature of 550°C (1022°F) is too low to exhibit significant carbon core oxidation in the time periods of the tests.

Crack growth specimens tested at 827.4 MPa (120 ksi) and 1034 MPa (150 ksi) far field stress which failed in 23,807 and 2,863 cycles respectively were examined for evidence of crack bridging. In both cases, the fracture plane of the fiber and the matrix were not coincident. Neither specimen exhibited incipient cracks parallel to the main one, so evidence of when the bridging fibers failed is absent.

From the above discussion, it is clear that crack bridging does occur at 550°C (1022°F) at far field stresses as high as 1103.2 MPa (160 ksi) in SEN specimens with an initially bridged precrack. However, the extent of crack growth in either the LCF or the SEN specimens was quite limited at the high stress. Reference to Figure 121 implies failure at a K$_{max}$ of about 88 MPa(m)$^{0.5}$, if there is no prior damage due to lower stress cycling. This fracture toughness apparently declines significantly with such exposure. Combining this with the high applied stress necessary to make these mate-

rials attractive for engine disk materials presents the problem of having rather small critical cracks of about 1.60 mm (0.063") for the 1034 MPa (150 ksi) far field stress and about 1.40 mm (0.055") for 1103.4 MPa (160 ksi).

4.9.2.2 Estimate of Residual Life from a Detectable Crack at 550°C.

From Figure 119 it was seen that failure occurred at a crack length between 1.20 and 1.60 mm (0.047" to 0.063") for a test at 550°C (1022°F) with a 1034.2 MPa (150 ksi) far field stress in about 2,800 cycles. Assuming a reliable crack detection limit of 0.70 mm (0.027"), 1,800 cycles were taken to grow the crack to that size. Then we have 2,800 - 1,800 = 1,000 cycles of growth, N_p, (or 950 cycles if a_c = 1.20 mm) between a detectable crack and failure. Of course, reducing the stress will reduce crack growth. From Figure 117, it is seen that low stress fatigue cycling at the same temperature has reduced the apparent fracture toughness to about 44.6 MPa(m)$^{0.5}$ with an attendant critical crack length, when corrected for 1034.2 MPa (150 ksi) far field stress, of 0.455 mm (0.018"). This is below a reliable detection limit, so damage tolerant design is not feasible with this MMC, after a prior cyclic exposure to a lower stress and with no detectable crack growth. From Figure 117 it is seen that, even at the lower stress of 827.4 MPa (120 ksi), the critical crack is 0.711 mm (0.028"), which is at the detectable limit, so that even with this low stress pre-exposure, there is no cyclic life beyond that associated with a detectable crack. Viewing of the combined curves for the two stresses, Figure 121, leaves one with the impression that the growth characteristics of the pre-exposed and the unexposed samples tested at two different stresses belong to the same population, implying that the exposure has little effect on crack growth resistance. It is the apparent fracture toughness that seemed to have been most seriously degraded.

4.9.3 Crack Growth Micromechanics at 650°C

4.9.3.1 Crack Bridging

LCF specimens tested at 689.5 MPa (100 ksi), specimen and 965.3 MPa (140 ksi) were examined for evidence of crack bridging. The higher stress specimen did exhibit some secondary, parallel cracks, all with fibers bridging them. The main fracture did show considerable evidence of fiber bridging by the fracture planes of the fiber and matrix not being coincident. As in the 550°C (1022°F) tests, it is not clear as to when the bridged fibers did fracture. The smaller secondary cracks with bridging were too short to project whether or not the fibers would survive to much larger cracks. In an attempt to place the fracture of the fibers in space, relative to the passing of the matrix crack, the higher stress sample (specimen 1A/0C22) was examined for evidence of fiber core oxidation. None was found either on the fracture or on fibers at the specimen edge where the specimen machining had exposed the core. The total time at temperature of the

specimen was about 100 minutes and this is evidently not enough to oxidize the fiber's carbon core and there remains no evidence of when, in the test, the fibers did fracture in the high stress LCF tests.

Crack growth specimens with far field stress of 689.5 MPa (100 ksi) were also examined for evidence of bridging. Specimen 2A/0D22 which failed after 36,162 cycles at a 20 cpm test frequency or for a total of over 1,800 minutes exposure of the early part of the fatigue test, not only showed the same sort of bridging discussed above for the LCF test, but it was evident that the carbon core of the bridging fibers had not oxidized. However, SCS6 fibers on the specimen edge, for which the carbon core had been exposed by machining, had lost their carbon core to oxidation. This clearly indicates that the bridged fibers had broken late in the test because the cores had not been oxidized as had the fibers exposed from the beginning of the test. Therefore, at least for this relatively low stress at 650°C (1200°F), fatigue crack growth is accompanied by significant fiber bridging and the bridging persists in the wake of the propagating crack.

4.9.3.2 Estimate of Residual Life from a Detectable Crack at 650°C.

Using the a vs. N data from specimen 2A/0D22, Figure 128, and an assumed detectable flaw size of 0.70 mm (0.027") one can determine the number of cycles to reach a critical crack size of 2.76 mm (0.108") at a far field stress of 689.5 MPa (100 ksi). This effort is facilitated by recognizing the straight line segments of the plot and simply separating the integration into two steps. The result of such a computation is a growth life, N_p = 14,578 cycles of growth from a detectable flaw to one of critical size. A similar integration, using the data from fatigue crack growth specimen 2A/0A22 tested under the same conditions, gives a growth life, N_p = 21,143 cycles. From Figure 66 we can see an LCF life for this MMC to be about 81,000 cycles at 650°C (1200°F) which implies a life to a detectable crack on the order of 60,000 cycles. This interpretation is subject to question, however, because the LCF tests were conducted at a much higher frequency than were the crack growth tests. The latter showed clear frequency and hold time effects as discussed Section 4.5.3.3.3. The division of, $N_f = N_p + N_i$, remains an area worthy of examination.

Unfortunately, there are no data for higher far field stresses but it is clear that N_p will decrease by virtue of both the higher growth rate and the smaller critical crack length, a_c. A simple means of estimating a critical crack length assumes a relationship like:

$$K_{c, max} = Y\sigma \sqrt{a_c}. \tag{114}$$

Using such a relationship, a far field stress of 1034.2 MPa (150 ksi) yields a critical crack length, a_c = 0.78 mm (0.031") which is very close to the detectable crack length. This

presents serious challenges to the use of the program material in a damage tolerant application at stress levels sufficiently high to be attractive for disk design.

4.9.3.3   Local Crack Growth Between Fibers at 650°C

The ductile nature of Ti-24-11 at this temperature provides some evidence of local crack growth rate in the form of striations on the fracture surface. A quick study of Figure 122 and Figure 128 shows a rather consistent global growth rate of 2.1×10^{-5} to 2.25×10^{-5} mm/cycle up to near 35,000 cycles, where a more rapid rate began and continued until fracture.

This is compared with striation measurements on an LCF sample (1A/0B21) tested with the a far field stress of 689.5 MPa (100 ksi) and at 650°C (1200°F). Figure 203 is a summary fractograph display showing striations, near the origin, which translate to local crack growth in the matrix in the zone roughly equidistant from adjacent fibers, of near 5.1 to 7.1×10^{-4} mm/cycle. At a location near the end of crack growth and the onset of catastrophic fracture, the indicated growth rate was 6.4×10^{-4} mm/cycle. From these results, the growth rate appears to be nearly constant, despite the crack length.

After examining Figure 128, one would confirm that fatigue crack growth rate is relatively insensitive to crack length. The similarity ends here, however, as the growth rate of 2.25×10^{-5} mm/cycle on a macro scale from the figure is only about 3.75% of the local matrix growth rate from the fractographs of the LCF specimen, Figure 203. The conclusion drawn here is that the matrix crack grows at a nonuniform rate, on a microscale, and is apparently faster in the regions of the matrix farthest from the adjacent fibers and that this rate is not sensitive to crack length.

A direct observation of crack growth rate on a microscale was made on specimen 2A/0A22, the subject of Figure 122. Here, fractographic evidence depicts a growth rate of 3.5×10^{-4} to 6.1×10^{-4} mm/cycle as shown in the composite fractographic study of this specimen, seen in Figure 204. This is nearly 25 times more rapid than the global crack growth rate of 2.1×10^{-5} mm/cycle shown by Figure 122. This is verification that the nature of crack propagation in this MMC system at 650°C (1200°F) involves very rapid local growth over short distances and retardation as the crack encounters fibers. In this way, the average growth rate is different by a factor of about nearly 25. A graphical presentation of this information is seen in Figure 205 where the growth rate calculated from striation spacing is compared with the macro crack growth concluded from Figure 122.

Maintenance of the growth inhibiting mechanisms associated with the presence of reinforcing fibers, coupled with an intrinsically more fatigue crack growth resistant matrix alloy/microstructure, should enhance the MMC fatigue strength.

(a)

C40872 4000X 00041 3μm

(b)

C40872 2000X 00044 10μm
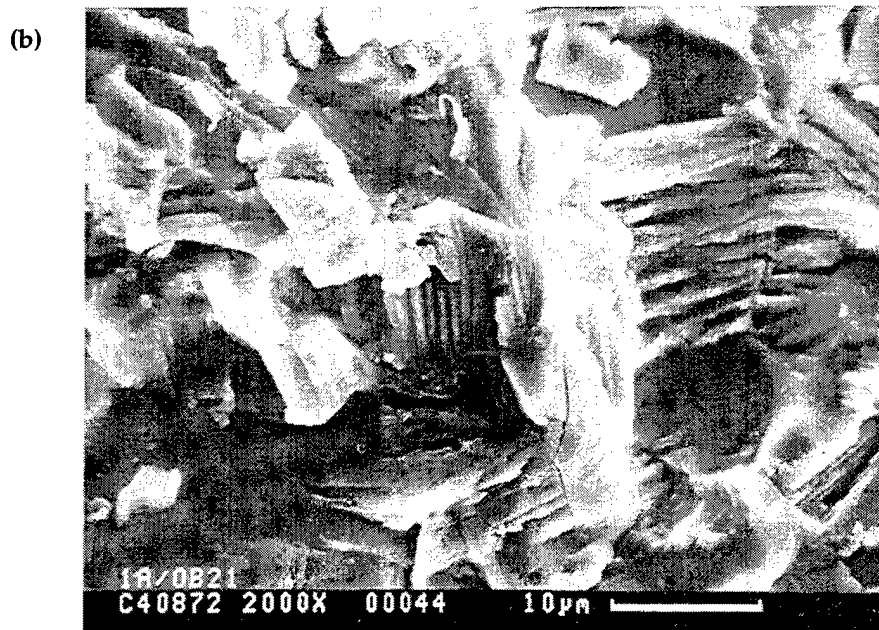
Figure 203.   Fractographic study of LCF specimen tested in air at 650°C, R = 0.1, f = 1 Hz, and a far field stress = 689.5 MPa.

(c)
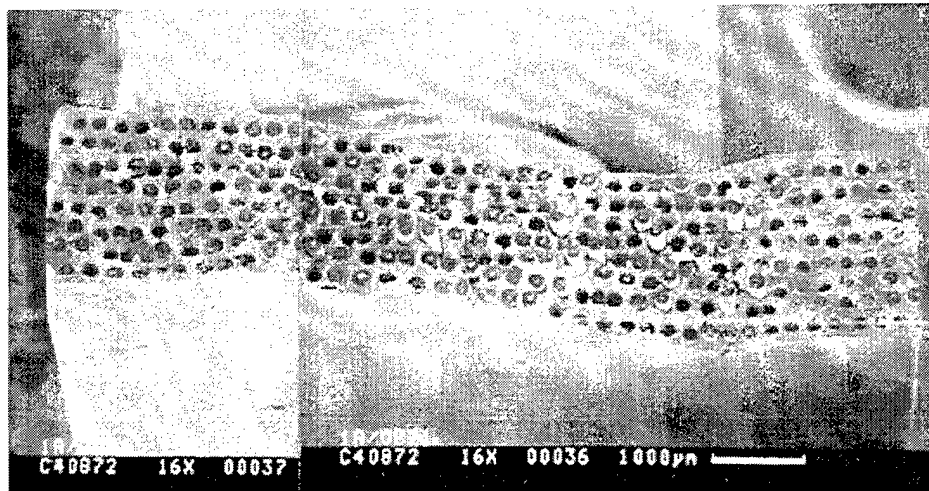
Figure 203 cont.   Fractographic study of LCF specimen tested in air at 650°C,
                         R = 0.1, f = 1 Hz, and a far field stress = 689.5 MPa.
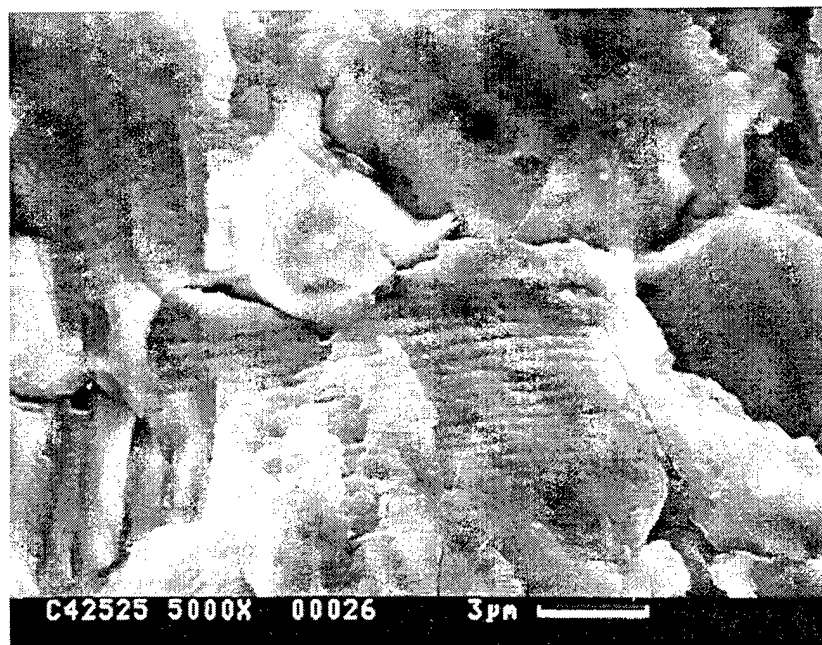
Figure 204.   Fractograph on the matrix in an MMC fatigue crack growth specimen at a crack
              length of 1.0 mm.
              Specimen was tested at 650°C with R = 0.1, f = 20 cpm and a far field stress of 689.5
              MPa. Striation spacing indicates that the growth rate is about 3.5×10^{-4} mm/cycle.

241

2A/0A22, Fatigue Crack Growth Specimen Fractographic Comparison
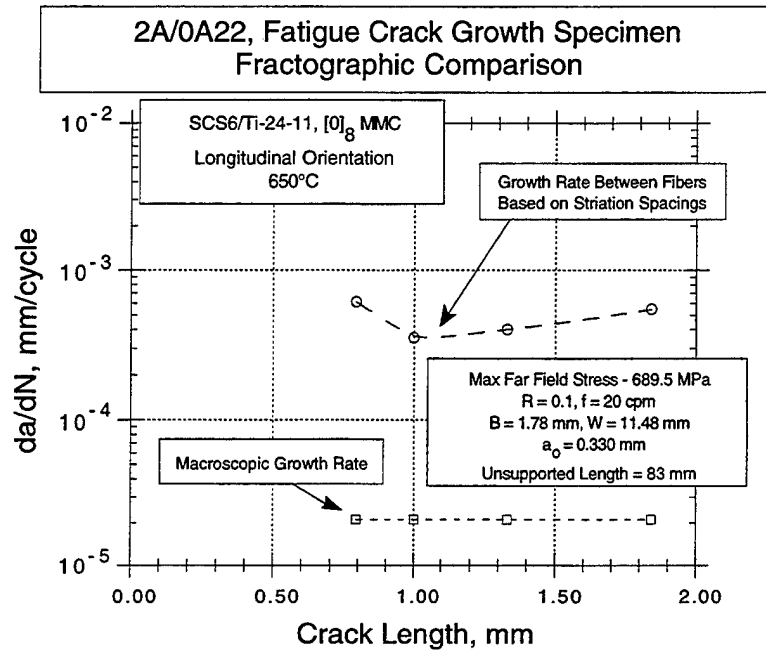
Figure 205. Comparison of global (macroscopic) crack growth rate with the growth rate determined from striation count at points nearly equi-distant from fiber centers on the same SEN fatigue crack growth specimen.
Test temperature = 650°C, R = 0.1, f = 20 cpm. Growth rate is not crack length dependent and the local rate is much higher than the macroscopic rate.

4.9.4 Summary of Critical Crack Size and Residual Life Estimates

Using the information discussed in the above paragraphs, one can estimate certain of the critical parameters related to ENSIP requirements, including critical crack size for catastrophic failure, a_c, and the number of growth cycles at a constant maximum cyclic load a specimen can endure after the detectable crack size is reached, N_p. Table 22 presents this information for three levels of stress at the three test temperatures used in this program. In some cases there was no supporting crack growth data to permit estimates of N_p.

242

Table 22. Estimates of critical crack sizes and residual life beyond detectable crack length, a_d = 0.70 mm

Temperature	Stress (MPa)	a_c (mm)	N_P beyond 0.70 mm
room temp	689.5	3.00	502,000
	827.4	2.08	90,000
	1034.2	1.33	20,000
550°C	689.5	2.70	no supporting data
	827.4	1.88	no supporting data
	1034.2	1.20	950
550°C damaged with applic. of Prior low stress fatigue	689.5	1.02	no supporting data
	827.4	0.71	0
	1034.2	0.46	0
650°C	689.5	1.76	14,578
	827.4	1.22	no supporting data
	1034.2	0.78	0

4.10 Micromechanic Analysis and Mechanical Behavior of the Composite

In this section the mechanical behavior of the composite is analyzed; the goal is to understand the residual stress state in the constituents, the stress-strain behavior and the ultimate strength of the composite. From analysis of the data it is observed that the fiber volume fraction of the specimens vary from about 34 percent to 39 percent with an average of 37 percent as compared to the 35 percent goal. It is also observed that the residual stresses can be correlated more closely to the analytically predicted values than to the measured stresses using x-ray diffraction. It is also observed that the rule of mixtures approach for predicting stress-strain behavior is only adequate for very low strains, and as a result a new approach is presented that predicts the stress-strain behavior of the composite very well up to the ultimate strength.

4.10.1 MMC Constituent Volume Fraction

The intent of this program was to produce MMC specimens with 35 percent fiber volume fraction. Due to manufacturing variability it is expected that the fiber volume fraction of each specimen would vary. In order to obtain a measure of this variability, five specimens were photographed and their photomicrographs were used to count the fibers in each specimen, the fiber count and the respective specimen dimensions provided the values summarized in Table 23a. A second measure of the fiber volume fraction was obtained by back calculating this quantity from the measured composite elastic modulus of the tensile test results, the results are shown in Table 23b. Results show

that specimen fiber volume fraction ranged from 34 to 39 percent and that the average specimen had a fiber volume fraction of 37 percent.

Table 23.   Summary of fiber volume fraction calculations, a) results from photomicrographs, b) results from stress-strain curves.

38.9
37.2
36.6
38.6
37.7

a)

34
37.6
36.1
35.6
37.6
38.5
35.5

b)

The back calculated results were obtained using a rule of mixtures approach for the elastic modulus, the equation used is as follows:

$$V_f = \frac{E_c - E_m}{E_f - E_m}$$ [115]

where

E_c is the composite elastic modulus

E_f is the fiber elastic modulus

E_m is the matrix elastic modulus

A fiber volume fraction of 35 percent is used in correlation of the stress-strain curves as presented in the following sections. Reasonable correlation is obtained, but it is observed that a much better correlation could have been obtained by using a fiber volume fraction value calculated from the elastic portion of the stress-strain curves.

4.10.2   Constituent Residual Stress Calculation

Knowledge of the residual stresses in the constituents of the composite material is important because they must be taken into account in the prediction of the stress-strain curve and the ultimate composite strength. In this section only the longitudinal residual stresses are of interest since they are the ones that control the longitudinal behavior of the composite. Although the residual transverse stresses in the matrix play a role in

the yield point of the matrix, they are considered to be of second order for this behavior. The longitudinal residual stresses for the fiber and matrix are given by the following equations, where the effective consolidation temperature is assumed to be the same as the consolidation temperature used for processing of the composite of 1010°C (1850°F).

$$\sigma_f = \frac{\left(1 - V_f\right) E_f E_m \left(\alpha_f - \alpha_m\right) \cdot \Delta T}{\left(1 - V_f\right) E_m + V_f E_f}$$ [116]

$$\sigma_m = \frac{V_f E_f E_m \left(\alpha_f - \alpha_m\right) \cdot \Delta T}{\left(1 - V_f\right) E_m + V_f E_f}$$ [117]

where:

V_f is the fiber volume fraction

α_f is the coefficient of thermal expansion of the fiber

α_m is the coefficient of thermal expansion of the matrix

ΔT is the difference of the consolidated temperature and the composite test temperature

The above equations yield residual stresses in the fiber and matrix as a function of fiber volume fraction as summarized in Table 24. It is observed that the residual stresses in the fiber is more sensitive than the stresses in the matrix with fiber volume fraction. The matrix residual stress at 35 percent volume fraction is 316 MPa as compared to 400 MPa measured from x-ray diffraction. The resulting fiber stress is 588 MPa, equivalent to 0.147 percent compressive residual strain in the fibers.

The above results indicate that the composite may be loaded to a strain of 0.147 percent before loading the fibers in tension; any greater strain will load the fibers in tension and breaking of the fibers is then possible. The matrix residual stresses are lower than its yield point, hence it can still carry some load before deforming plastically, assuming that the yield point of the matrix is 395 MPa (57 ksi), the average of the values shown in Table 13, the fiber can be loaded to a strain level of 0.14 percent from its residual state stress. This means that the matrix will begin yielding just before the fiber residual stresses are exceeded. Since the matrix behaves as an elastic-perfectly plastic material until 5 percent strain, the matrix is not able to carry any extra load after this point and the fibers take over. From there on the behavior of the composite is governed

245

by the behavior of the fibers until the matrix starts to strain harden. But since the strain to failure of the fibers is on the average 1.0 percent, this last portion of the behavior is not possible for this system.

Table 24.   Summary of the effect of fiber volume fraction on the residual stresses of the matrix and fibers.

Vol. Fraction (%)	Fiber Res. Stress (Mpa)	Matrix Res. Stress (Mpa)
34	-608	313
34.5	-598	315
35	-587	316
35.5	-577	318
36	-567	319
36.5	-557	321
37	-548	322
37.5	-539	323
38	-530	325
38.5	-521	326
39	-512	327

4.10.3   Load-Displacement Behavior of the MMC

As a result of the observations in Section 4.10.2, it was required to develop a new model to describe the mechanical behavior of the composite in the longitudinal direction. The model developed addresses the load-displacement behavior of the composite and attempts to predict the ultimate load of tensile MMC specimens. The approach uses micromechanical analyses and damage mechanics principles to derive the models.

The global behavior of composite materials in the longitudinal direction is most commonly approximated by the rule of mixtures. In this section we attempt to model the load-displacement/stress-strain behavior of the composite in the longitudinal direction by using a modified rule of mixtures approach. This new approach consists of the incorporation of the parallel bar model for the behavior of the fibers in the rule of mixture equations. The parallel bar model is commonly used in damage mechanics to predict the brittle response of materials (Krajcinovic, Reference 28.)

Using the rule of mixtures approach one can relate the stress in the matrix and the fibers to the far field applied stress by the following equation.

$$\sigma_c = V_f \sigma_f + (1 - V_f) \sigma_m \qquad [118]$$

where:

σ_c the smeared composite stress

σ_f the stress in the fiber

σ_m the stress in the matrix

The above equation can be transformed into a stress-strain relationship of the composite by substituting the corresponding stress-strain relationship for the fiber and the matrix. The stress-strain relationship of the matrix has already been presented in Chapter 4, the matrix exhibits a classical stress-strain curve with a pronounced yield point. The rule of mixtures approach yields:

$$\sigma_c = V_f E_f \varepsilon + (1 - V_f) E_m \varepsilon \qquad [119]$$

where

ε is the applied strain to the composite specimen

This equation is valid until the point when fibers start to be loaded in tension, which means that fibers may start breaking. From there on the behavior of the fiber bundle must be taken into account.

The stress-strain behavior of the individual fibers follow the classical brittle material type of stress-strain curve, which is linear until failure. But since more than one fiber are used in the composite specimen, one must derive the stress-strain relationship of the fiber system; the system in question is represented by a parallel bar model, as shown in Figure 206.

The stress-strain curve for the parallel bar model, for fibers with Weibull distributed strength, can be obtained by formulating the equations derived by Krajcinovic, Reference 28, in terms of stress-strain instead of load-displacement. It is observed in the following equation that the behavior of the fiber bundle is not linear anymore, and in fact, it has a bell shape response as shown in Figure 207.
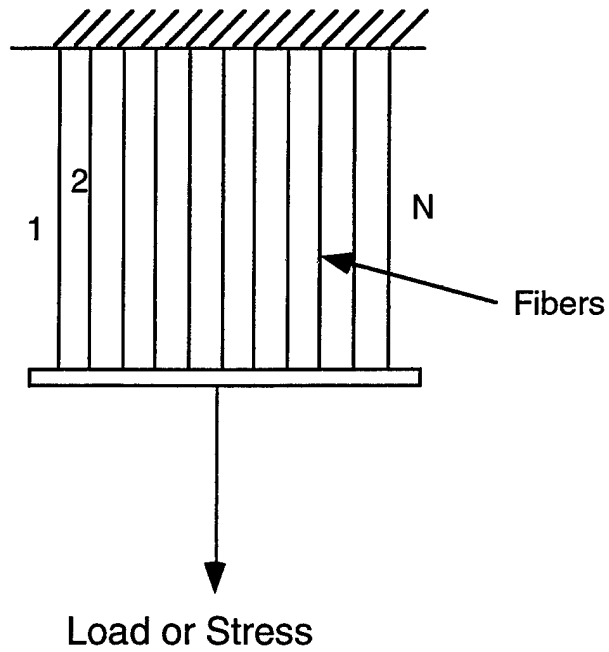
Figure 206.   **Parallel bar model. All fibers are assumed to see the same strain.**
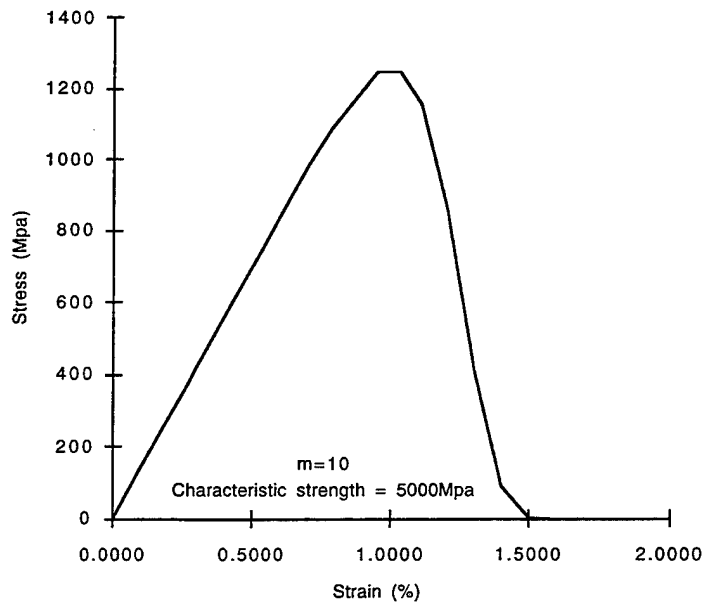
Figure 207.   **Stress-strain behavior of the parallel bar model.**

248

$$\sigma_f = E_f \varepsilon \exp\left[-\left(\frac{E_f \varepsilon}{\sigma_o}\right)^m\right] \qquad [120]$$

where:

σ_o is the fiber second Weibull parameter, or characteristic strength of the tested fibers

m is the first Weibull parameter, or Weibull slope

Three important results can be derived from this equation, the maximum load the fiber bundle can carry, the strain at failure and the level of damage in the composite at the time of failure. The maximum stress the fiber bundle can carry is given by

$$\sigma_{f,\max} = \sigma_o m^{-\left(\frac{1}{m}\right)} e^{-\left(\frac{1}{m}\right)} \qquad [121]$$

and the corresponding strain

$$\varepsilon = \frac{\sigma_o m^{-\left(\frac{1}{m}\right)}}{E_f} \qquad [122]$$

with the following damage level, D, at ultimate load

$$D = 1 - e^{-\left(\frac{1}{m}\right)} \qquad [123]$$

The damage level predicts the percentage of fibers that have been broken at ultimate load. The damage level at any other load or strain is given by

$$D = 1 - e^{-\left(\frac{E_f(\varepsilon - \varepsilon_{fR})}{\sigma_o}\right)^m} \qquad [124]$$

Analysis of the deformation using the newly derived stress-strain equations indicate that three distinct regions should be present in the curve. The first region would be a linear region that follows the rule of mixture approach. This region is the result of the compressive residual stresses in the fibers, and it continues until the point the applied stress level results in a zero load in the fibers or equivalently, when a strain equivalent to the residual fiber strain is applied to the composite. The second region is one where the composite follows the newly derived model with a rule of mixtures which incorporates the parallel bar model. This region continues until the point where the matrix begins to yield. The third region then starts at the point when the matrix starts yield-

ing and it continues until fracture. In this last region the nonlinear stress-strain behavior of the matrix must be used. The equations that represent these three regions can be represented by the following three equations:

Region I

$$\sigma_c(\varepsilon) = V_f E_f \varepsilon + (1 - V_f) E_m \varepsilon \qquad [125]$$

for $\varepsilon \leq \varepsilon_{fR}$

where ε_{fR} is the fiber residual strain.

Region II

$$\sigma_c(\varepsilon) = V_f E_f \varepsilon_{fR} + V_f E_f (\varepsilon - \varepsilon_{fR}) \exp\left[-\left(\frac{E_f(\varepsilon - \varepsilon_{fR})}{\sigma_o} \right)^m \right] + (1 - V_f) E_m \varepsilon \qquad [126]$$

for $\varepsilon_{fR} \leq \varepsilon \leq \varepsilon_{m,y}$

where

$\varepsilon_{m,y}$ is the strain required to reach the matrix yield strain. In this system is 0.147 percent composite strain at room temperature.

And Region III

$$\sigma_c(\varepsilon) = V_f E_f \varepsilon_{fR} + V_f E_f (\varepsilon - \varepsilon_{fR}) \exp\left[-\left(\frac{E_f(\varepsilon - \varepsilon_{fR})}{\sigma_o} \right)^m \right] + (1 - V_f) \sigma_m(\varepsilon) \qquad [127]$$

for $\varepsilon \geq \varepsilon_{m,y}$

This new approach was compared to the stress-strain curves obtained for the longitudinally tested specimens. Figure 208 through Figure 211 show the true stress-strain curve for the specimens and alongside the predictions with this new model. The first prediction used the nonlinear stress-strain curve for the matrix and a fiber characteristic strength of 4000 MPa (580 ksi) with Weibull modulus of 10, as obtained from the data presented in Section 4.8. At room temperature, Figure 208, the agreement between the model and the true behavior is good for the Region I and part of Region II, but it does not predict the ultimate load accurately. In order to match the ultimate load and the stress-strain curve, the characteristic stress of the fibers was changed to 5000 MPa (725 ksi), this increased strength matches the stress-strain curve very well as shown in

Specimen 1B/0A13 Tensile Behavior
(Room Temperature)
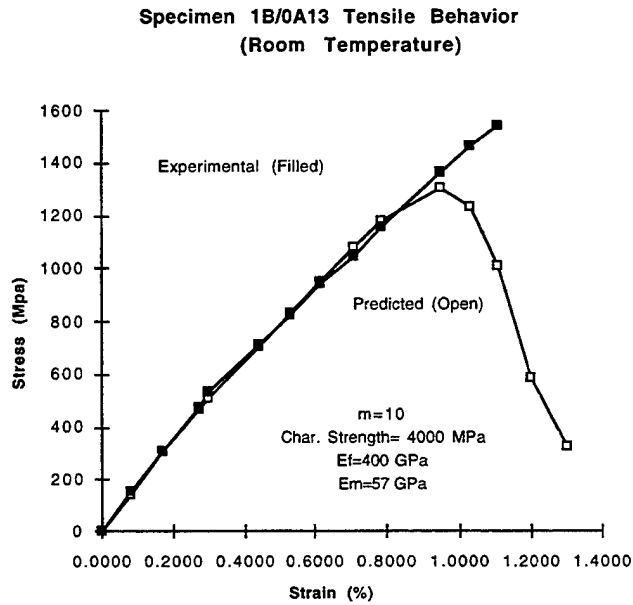
Figure 208. **Comparison of the modified rule of mixture stress-strain behavior with test data.**
First attempt at matching the models with a characteristic fiber strength of 4000 MPa, final fracture is not in agreement.

Specimen 1B/0A13 Tensile Behavior
(Room Temperature)
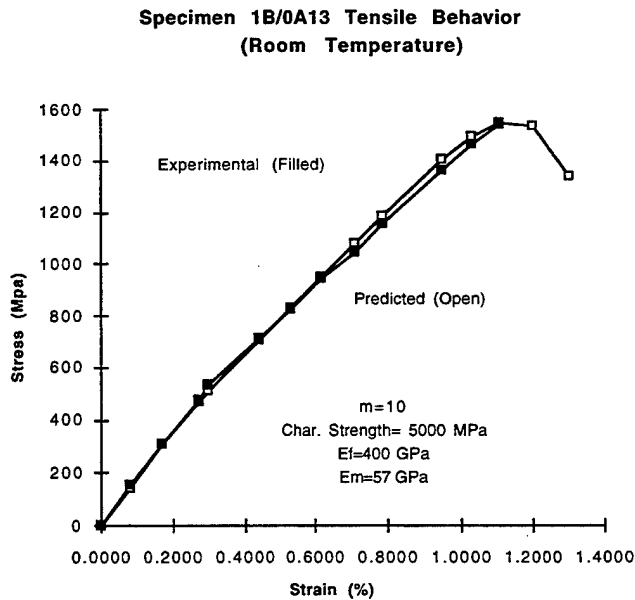
Figure 209. **Comparison of the modified rule of mixture approach with test data assuming a stronger fiber.**
A much better fit is obtained using a fiber characteristic strength of 5000 MPa.

251

Specimen 1B/0A24 Tensile Behavior (550C)
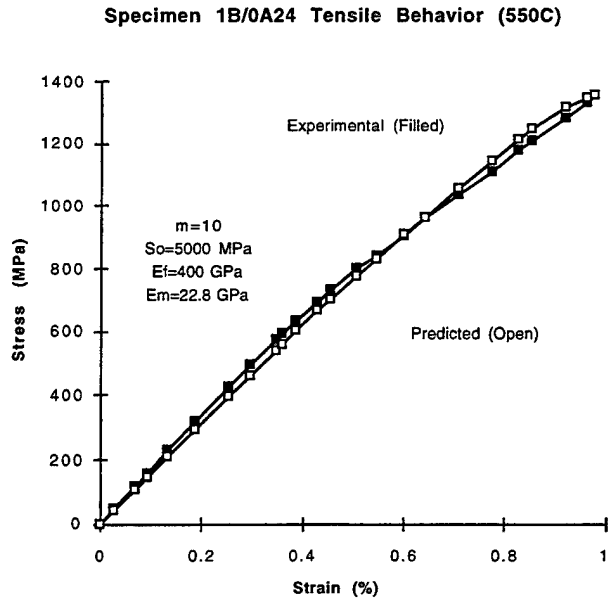
Figure 210. Comparison of the modified rule of mixture approach with elevated temperature , 550°C, data.

A good fit is obtained using a fiber characteristic strength of 5000 MPa, the same as for room temperature.

Specimen 1B/0A23 Tensile Behavior (650C)
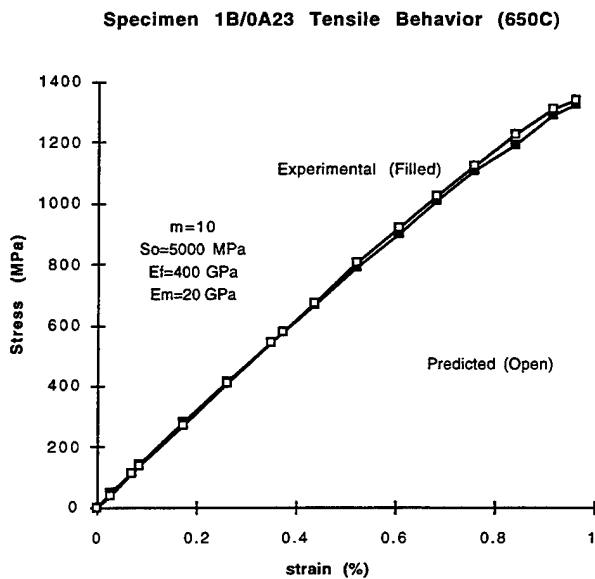
Figure 211. Comparison of the modified rule of mixture approach with elevated temperature, 650°C, data.

A good fit is obtained using a fiber characteristic strength of 5000 MPa, the same as for room temperature.

252

Figure 209. The seeming increase of fiber strength may be explained as being a size effect commonly observed in ceramic materials. At higher temperatures, the new equations also predict the stress strain curves reasonably well as shown in Figure 210 and Figure 211.

The damage calculated for a composite specimen at ultimate load is given by $D = 1 - e^{-\left(\frac{1}{m}\right)}$, as derived in this section. For a Weibull modulus of 10, the predicted damage level is 10 percent. This damage level for a composite with fibers with characteristic strength of 5000 MPa (725 ksi) corresponds to a stress level on the fibers at ultimate load of 3990 MPa (579 ksi), a value that matches very closely to the average stress on the fibers for the specimens tested in this program, hence the results calculated in this section matches with the results in Section 4.7.4.

The characteristic strength value required to match the stress-strain curve is 5000 MPa (725 ksi), equivalent to an effective fiber length of 2.72 mm (0.107 in), as given by the following equation

$$L_e = L_o \left(\frac{\sigma_o}{\sigma_R} \right)^m$$

[128]

where:

L_e the effective length of the fiber

L_o the gage length of the tested fibers, 25.4 mm (1 in)

σ_R the required characteristic strength to match the stress-strain curve

Curtin, Reference 29, has derived equations that determine the fiber effective length for ceramic matrix composites (CMCs). In his formulation Curtin concludes that the fiber effective length of the composite is a function of the fiber Weibull parameters, the fiber testing gage length, the interfacial shear stress between the fiber and the matrix and the radius of the fiber. From Curtin's results for CMCs one can conclude that the variables affecting the effective fiber length for metal matrix composites (MMCs) may be the same, although the functional relationship may be different. Derivation of the relationship for MMCs will not be attempted here.

At this point one must note that the shear stress at the fiber matrix interface is a function of the residual stresses and hence a function of temperature. One would expect to see a decrease in the strength of the fibers due to a decrease in interfacial shear stress. But it is observed that the characteristic strength has stayed constant with temperature for this material.

4.10.4 Matrix Shakedown Stress Prediction

Four longitudinal specimens were loaded under Low Cycle Fatigue with the purpose of understanding the behavior of the residual stresses in the matrix. Two were tested at room temperature and two at high temperature (650°C (1200°F)). It was observed, as discussed in Section 4.1.4 and results summarized in Table 10, that the residual stresses in the matrix relaxed after a small number of cycles. This section explains the reason why this behavior is observed in the matrix; the behavior is explained by using the modified rule of mixture approach discussed in the previous section.

The stress level applied to the specimens of 1035 MPa (150 ksi) is high enough to strain the composite to Region III in the stress-strain curve. This means that the matrix is plastically deforming. The strain at this load is predicted to be 0.68 percent as shown in Figure 212, the stresses in the constituents at this point are redistributed as follows. The matrix is loaded to its yield point of 395 MPa (57 ksi), 315 MPa (45.6 ksi) is the residual stress and 80 MPa (11.7 ksi) is the portion it carries of the applied load; the fiber carries the rest of the load, a total of 2810 MPa (407 ksi), 580 of these are in compression due to the residual stresses, hence the real fiber stress at the maximum load is 2230 MPa (323 ksi). Upon unloading the matrix behaves elastically and so does the fiber, this means that the unmodified rule of mixtures approach applies and the composite unloads as shown again in Figure 212. The relationship for the unloading behavior is as given by the following equation.

$$\sigma_c = \sigma_{max} - \left[\left(V_f E_f + \left(1 - V_f\right) E_m \right) \left(\varepsilon_{max} - \varepsilon \right) \right]$$ [129]

where

σ_{max} is the maximum applied stress

ε_{max} is the strain due to the maximum stress

The composite recovers only the elastic portion of the strain as predicted by the rule of mixtures, hence the residual strain in the composite is predicted to be 0.1 percent, a 0.58 percent stain recovery from the loaded condition. Since the matrix behaves elastically during the unloading, the matrix unloads a stress equivalent to the recovered strain for a total stress of 330 MPa; hence, the residual stress of the matrix is the difference between its yield point and the recovered stress, for a total residual stress of 65 MPa (9.4 ksi). For the composite to be in internal equilibrium, the fibers must carry a load to balance the matrix stresses and this is calculated to be 120 MPa (17.5 ksi), compression.

It is important to note here that the measured and the predicted residual stresses do not match for either of the residual stresses in the pristine specimen or for the unloaded

Predicted Load-Unload Behavior at Room Temperature for a Max Stress of 1035 MPa
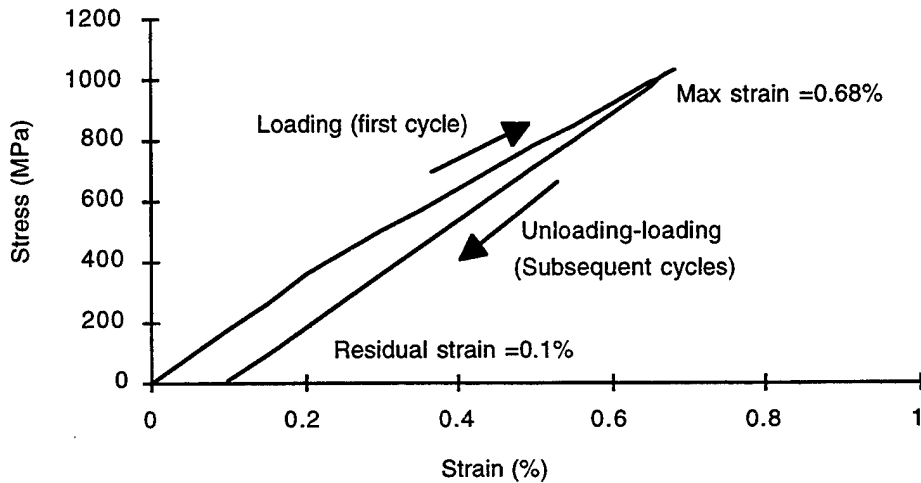
Figure 212. Load-unload behavior of the composite specimen at room temperature. Applied maximum stress of 1035 MPa results in a residual strain of 0.1 percent.

one. Of interest is that the discrepancy in the residual stresses is approximately 100 MPa (14.8 ksi) in each case. This could mean that either the matrix has a yield point that is 100 MPa (14.8 ksi) over the measured one or that there is some parasitic stress in the x-ray diffraction measurement.

Given the behavior of the composite upon loading, and the matrix in particular, one can rationalize that upon unloading the overall stresses in the composite must change not only the longitudinal residual stresses. The residual hoop stresses must also change. During the plastic deformation of the matrix it is likely that plastic strains occur not only in the longitudinal direction, but also in the hoop direction due to the residual compressive stresses. If this were the case, it could be anticipated that the hoop residual stresses would redistribute upon loading and further relax upon unloading. Upon unloading it is anticipated that the hoop stresses would relax at least by the elastic Poisson ratio effect, which in this case would be a 100 MPa (14.8 ksi) relaxation of the residual hoop stresses. This hoop effect relaxation would have a significant effect on the fiber effective strength. Relaxation of the hoop stress would reduce the interfacial shear stress, which in turn would increase the effective fiber length, resulting in lower fiber effective strength. See Section 4.5.3.4.4.

4.10.5 Load-Unload-Reload Behavior of the Composite

One of the MMC specimens was tested under a load-unload-reload sequence to study its stress-strain behavior after reload. It was observed in Figure 51, specimen 1B0B11, that the stress-strain curve tracks the original stress strain curve after the specimen is reloaded to the load from which it was unloaded. This behavior can satisfactorily be explained by the discussion in specimen unloading in Section 4.10.5 and the modified rule of mixture equations.

If we continue the discussion from the point where the specimen is unloaded, as discussed in the last section; upon reload, the specimen must backtrack the unloading until a stress is applied that either deforms the matrix plastically, breaks more fibers, or both. From the unload behavior one knows that the matrix will not yield again until it sees the same stress from which it unloaded, and one also knows that the fibers will not break again until they experience a stress level greater that the one they experienced during the first loading. This means that the composite will backtrack its unloading curve up to the point from which the composite was unloaded. From that point on the matrix will yield and the fibers are again likely to start breaking. At this point the composite is in the same stress state and damage level that it was before unloading, hence it must continue on its stress-strain curve as if no unloading had happened. A prediction, and comparison, for the behavior of specimen 1B0B11 is shown in Figure 213, this figure shows a good agreement between the predicted and the experimental behavior.
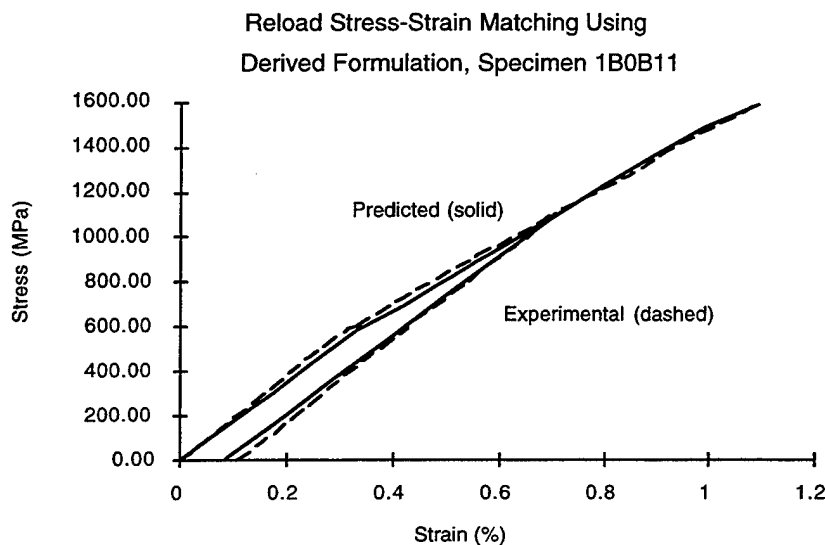
Figure 213. Load-unload-reload behavior of specimen 1B0B11 and the predicted behavior using the modified rule of mixture approach.

SECTION 5.0
MODEL VERIFICATION

Introduction

Phase V of this program provides for verification of the analytical models developed under Phase IV. Verification was performed through testing of specimens under stress and temperature conditions that simulate engine operating conditions. These tests were performed on specimens similar to the specimens tested under Phase IV, but they incorporate complications in an engine cycle; for example, hold times, major and minor cycles.

The intent of this section is also to evaluate the capabilities of the MMCLIFE V3.0 code. Through a review of realistic cycle requirements, analysis needs were identified; these should be incorporated into the MMCLIFE V3.0 code in subsequent developments. The execution of the Code to predict specimen life under simulated cycles should highlight improvements needed to the Code.

5.1   Test Conditions, Experimental and Analytical Procedures

The test conditions for the verification tests were based on a review of the engine operating cycles for the TFE731, the T800 and the F109 engines. The TFE731 engine is a commercial application, the T800 is a helicopter military application and the F109 is a fighter trainer military application. Observed in these cycles are the typical take-off condition, the climb, cruise and shutdown. The military cycles also include minor cycles which are an indication of the combat-type needs of military aircraft. The three engines cycles are shown in Figure 214 through Figure 216.

The stress and temperature conditions anticipated for these cycles and design conditions that take advantages of high strength metal matrix composite designs are described on Table 2 for different component locations and fiber orientation. The temperature conditions described in this table are within the test conditions of the data in Phase IV, but the stress levels are well above the test conditions from Phase IV.

The confirmatory specimen tests were performed under isothermal conditions using specimens with configurations shown in Figure 41 and Figure 42. The tests were performed using similar procedures as described in Section 4.

Commercial Fan Cycle

Speed Level (%)

Take Off

Cruise

Idle

Idle

T= 425°C

Time (No Scale)
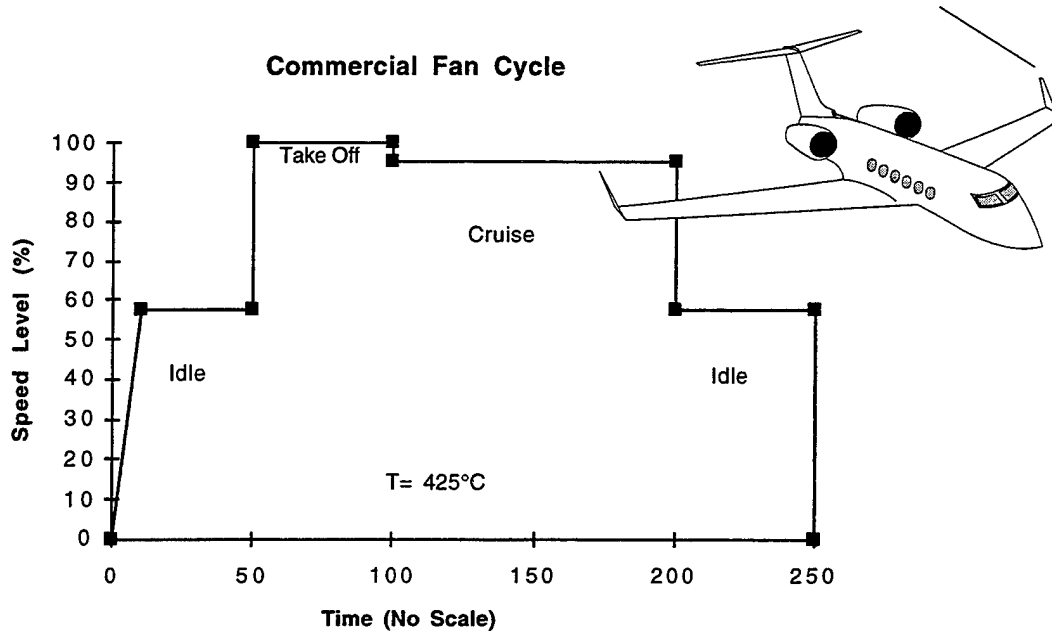
Figure 214.   Typical operation cycle for a commercial engine, this is the FAA cycle used for the design of the TFE731 engines.

T800 Military Cycle

Speed Level (%)

Max Power

Max Power

Idle

Idle

Idle

1 Major Cycle

1 Minor Cycle

T= 600°C

Time (No Scale)
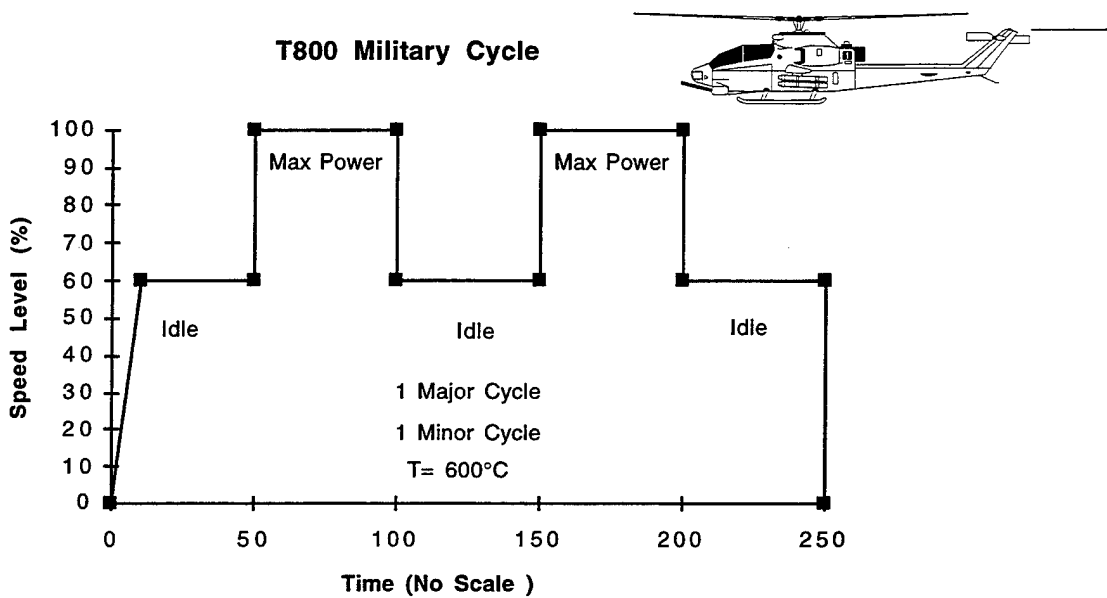
Figure 215.   Operation cycle used for the design of the T800 engine for use on the Apache Helicopter.
Note the second Max power condition.

258

F109 Military Cycle
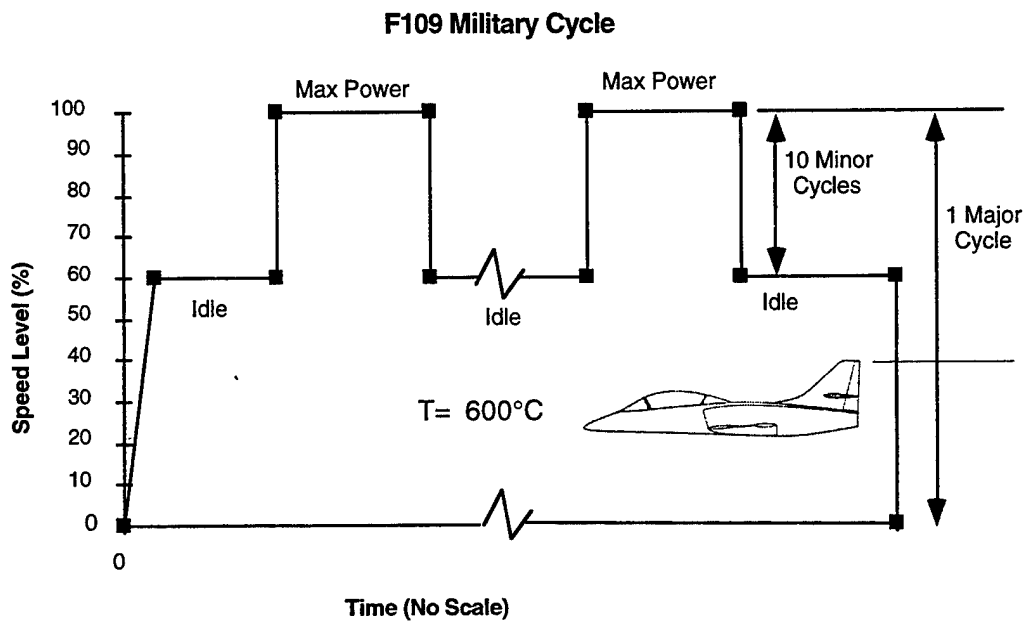
Figure 216. Operation cycle used for the design of the F109 engine for use in a trainer application.
Training consists of multiple idle to full power conditions

5.2 Phase V Test Matrix, Testing Considerations, Initial Predictions and Assumptions

A total of three longitudinal specimens remained after Phase IV. Based on the requirements to substantiate the MMCLIFE V3.0 code with a realistic engine cycle and the need to explore observations made during the review of the data generated in Phase IV, the test matrix shown in Table 25 was formulated. Figure 217 is the confirmatory cycle the longitudinal specimens were tested at. This table describes the intended test conditions and the specimen initial crack sizes.

A total of three transverse specimens remained after Phase IV testing. The confirmatory specimen cycle for the transverse specimens consists of only major and minor cycles as shown in Figure 218. The predicted specimens lives and specimen testing conditions are shown in Table 26.

259

Table 25.   Phase V test matrix for longitudinal specimens and initial specimen predictions.

Specimen	Temp (C)	Stress (Mpa)	Stress Ratio	Initial Crack Size (mm)	Initial Prediction (Cycles)
2A0A12*	RT	689.5	0.5	0.233	50640
		965	0.5	0.635	17360
2A0A13*	550 (C)	758	0.1	0.315	1140
		896	0.1	0.635	1820
2A0A23*	RT	827	0.5	0.216	15560
		586	0.5	1.27	no growth
S0B11	650 (C)	827	0.1	0.267	9930
S0B13	650 (C)	Confirmatory Cycle	0.1/0.5	0.229	2808
2A0E21	650 (C)	Confirmatory Cycle	0.1/0.5	0.234	7830
S0A15	650 (C)	Confirmatory Cycle	0.1/0.5	0.200	7920

* Specimens to be tested at two conditions to obtain more data

Longitudinal Specimen
Verification Cycle

2 min hold

R=0.5, 20 CPM
5 minor cycles

Major cycle with R=0.1

Stress (%)

Time (No Scale))
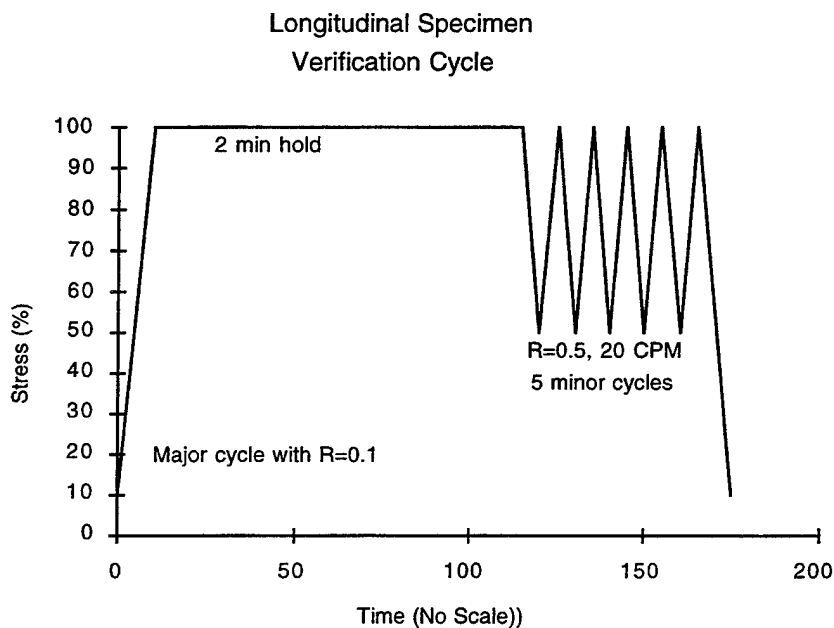
Figure 217.   Longitudinal confirmatory specimen cycle.
This cycle is based on the cycles described in Figure 214 through Figure 216.

Transverse Specimen Verification Cycle

I Major Cycle, R=0.1
5 Minor Cycles, R=0.5
20 CPM ramps
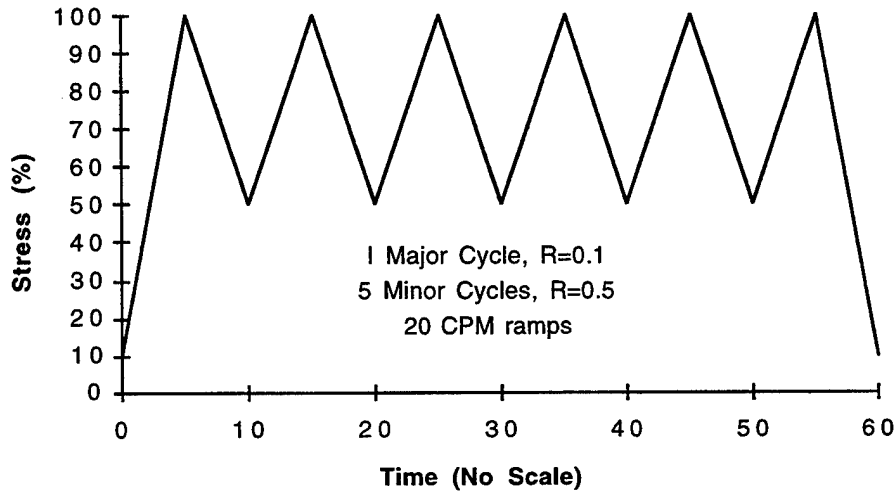
Figure 218. **Transverse confirmatory specimen cycle.**
This cycle is based on the cycles described in Figure 214
through Figure 216

Table 26. **Phase V test matrix for transverse specimens and specimen predictions.**

Specimen	Temp (C)	Stress (MPa)	Stress Ratio	Initial Crack Size (mm)	Initial Life Prediction (Cycles)
2A90E22	RT	96.5	0.1	1.27	3090
2A90D22	RT	145	0.5	1.27	860
2A90D12	RT	96.5	0.1	1.27	3090
2A90D11	550	145	0.5	1.27	26340
2A90A13	650	145	0.5	1.27	510
2A90D221	RT	75.8	0.1/0.5	0.635	21030
2A90B13	RT	75.8	0.1/0.5	2.54	394
2A90B23	650	41	0.1/0.5	2.54	423
2A90B22	650	41	0.1/0.5	2.54	423

5.3 Phase V Specimen Test Results

The intent of the specimens tested in Phase V was to confirm the life predictive capabilities of the MMCLIFE V3.0 code. The final results of the testing are summarized in Table 27 and Table 28. The testing consisted of a total of two longitudinal specimens and a total of three transverse specimens.

Table 27. Longitudinal specimen test matrix, final test conditions.

Specimen	Stress (MPa)	R-Ratio	Temp (°C)	Freq (CPM)	Comments
2A/0E21	825	0.1/0.5	650	20 w/2 min hold	853 Blocks to failure same as S/0A15
S/0B13	1100	0.1/0.5	650	20 w/2 min hold	Failed after 3 blocks
S/0A15	825	0.1/0.5	650	20 w/2 min hold	176 Blocks to failure. Test is invalid due to skewed crack

Table 28. Transverse specimen test matrix, final test conditions.

Specimen	Stress (MPa)	R-Ratio	Temp (°C)	Freq CPM	Comment
2A/90D12	41	0.1/0.5	650	20	1564 Cycles
2A/90B13	76	0.1 /0.5/ 5 MINOR CYCLES	RT (25)	20	60 cycles
2A/90B23	41	0.1 /0.5/ 5 MINOR CYCLES	650	20	751 cycles

5.3.1 Longitudinal Confirmatory Specimen Results

The testing of the longitudinal confirmatory specimens consisted of testing three specimens at 650°C (1200°F), one at 1100 MPa (160 ksi) and two at 825 MPa (120 ksi). The testing of the specimen at 1100 MPa (160 ksi) had limited success in that it failed after only 3 cycles, while the predicted life for this specimen was 2800 cycles. The predicted versus actual life indicates three orders of magnitude difference.

The testing of the specimens at 825 MPa (120 ksi) was more successful, the life of one specimen was 176 cycles and for the second was 853 cycles. The predicted lives for these specimens were 7900 and 7800 cycles respectively, this predicted life difference was the result of the different initial crack size of the specimens. The results of the testing of these specimens in shown in Figure 219. This figure shows the large variability in crack growth and life that may be expected in this type of material system.

5.3.2 Transverse specimen results

A total of three transverse specimens were tested: one at room temperature and a stress level of 76 MPa (11 ksi) and two at 650°C (1200°F) and 41 MPa (6 ksi) background stress. The results of this testing are shown in Figure 220 and Figure 221. These figures show the same crack growth trend at room temperature as well as at elevated temperature. The data at elevated temperature for specimen 2A90B23 were plotted as tested and then shifted by a number of cycles to match the crack size between both specimens. This allows us to make a direct comparison between the two specimens. The comparison shows that there is only a small disparity in the crack growth rate and on the critical crack size. There is also a minor variation in the total number of cycles to failure, but it is not as pronounced as for the longitudinal specimens. This small vari-
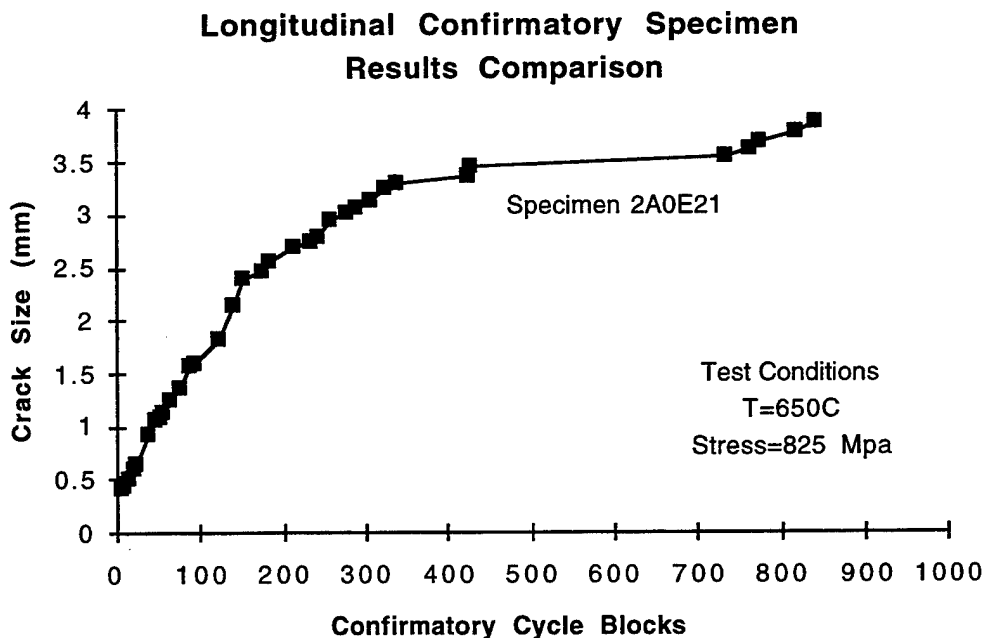
Figure 219. Large variability in crack growth, and life, can be observed in the two confirmatory specimens even though the initial crack size was almost identical and specimens had the same loading conditions.

Transverse Confirmatory Specimen

Crack Growth at Room temperature

Test Conditions
T=25°C
Stress=76 MPa
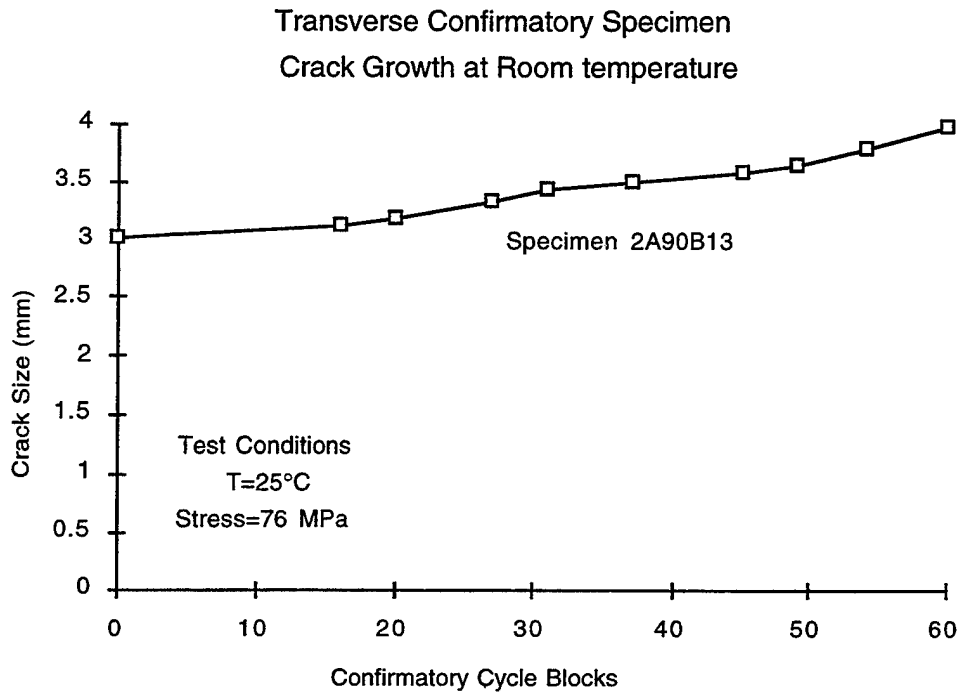
Specimen 2A90B13

Figure 220. Crack growth of transverse specimen at room temperature.

Transverse Confirmatory Specimen

Crack Growth at Elevated Temperature

Test Condition
T=650°C
Stress =41 MPa

Specimen 2A90D12
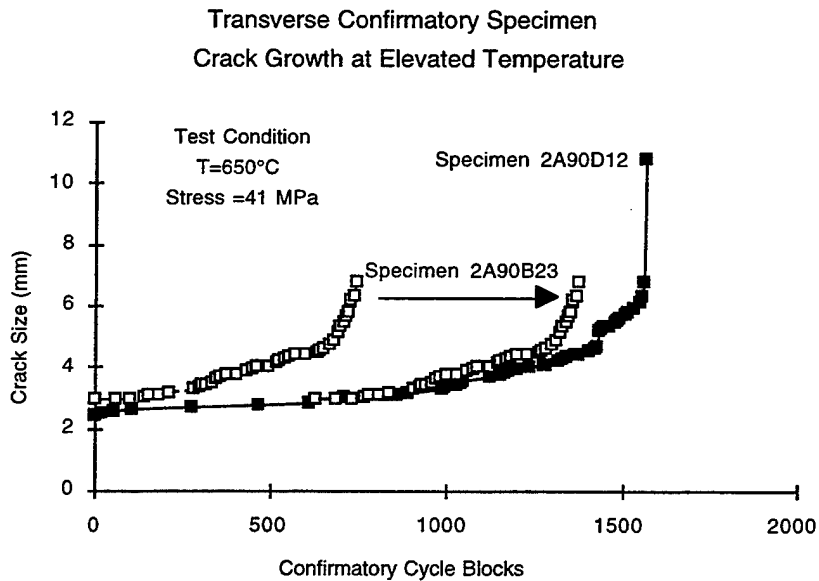
Specimen 2A90B23

Figure 221. Transverse specimen crack growth at elevated temperature, note the good crack growth agreement in these two identically loaded specimens.
Specimen 2A90B23 was shifted to make a direct comparison with crack size.

264

ability may be no greater than expected for crack growth testing of any monolithic material.

5.4 Discussion on Strength and Life Prediction Model Deficiencies in the MMCLIFE V3.0 Code

The intent of this program has been to develop an understanding of the damage tolerance capabilities and behavior of advanced metal matrix composites, in particular the SCS6/Ti24-11 system. In order to understand the crack growth behavior of the MMC, theories were incorporated into the MMCLIFE V3.0 code that predict the behavior of the composite under bridged crack growth, as discussed in Chapter 3. The accuracy of this model has been exercised by testing the confirmatory specimens that were presented in Section 5.3 and performing a priori predictions of the specimen's crack growth behavior. The success of this exercise was limited as to the prediction of the longitudinal tests but was successful in the transverse tests. The major discrepancy in the longitudinal prediction consisted of the lack of capability to predict the transient crack growth behavior observed at the beginning of crack growth and the inability to predict final fracture. The intent of this section is to postulate some possible reasons for such behavior.

5.4.1 Discussion of Longitudinal Specimen Test Results and Life Prediction with the MMCLIFE V3.0 Code

Figure 222 present the data obtained from the tested specimens and predictions performed with the MMCLIFE V3.0 code. As can be observed in these two figures of crack growth versus cycles, three crack growth regions exist in these specimens. The first is a region of transient crack growth which transitions into a slower steady crack growth region. The steady-state crack growth region then transitions into the typical accelerated crack growth portion which ensues final failure. The initial transient region is not usually observed in monolithic materials, but it was also observed in the baseline specimens of Phase IV, indicating that this behavior may be typical for bridged crack growth of this composite material, and is expected based on modeling of bridged crack growth behavior.

As shown by these figures, the first region of crack growth is characterized by a low interfacial shear stress which may be considered as an indication of unbridged crack growth. The interfacial shear stress in these two specimens is nearly identical at 0.07 MPa and 0.05 MPa respectively, which are near zero. One may ask about the behavior of the interfacial shear stress as the crack develops and how it evolves into its steady-state value. Understanding of this behavior may yield better life prediction models.
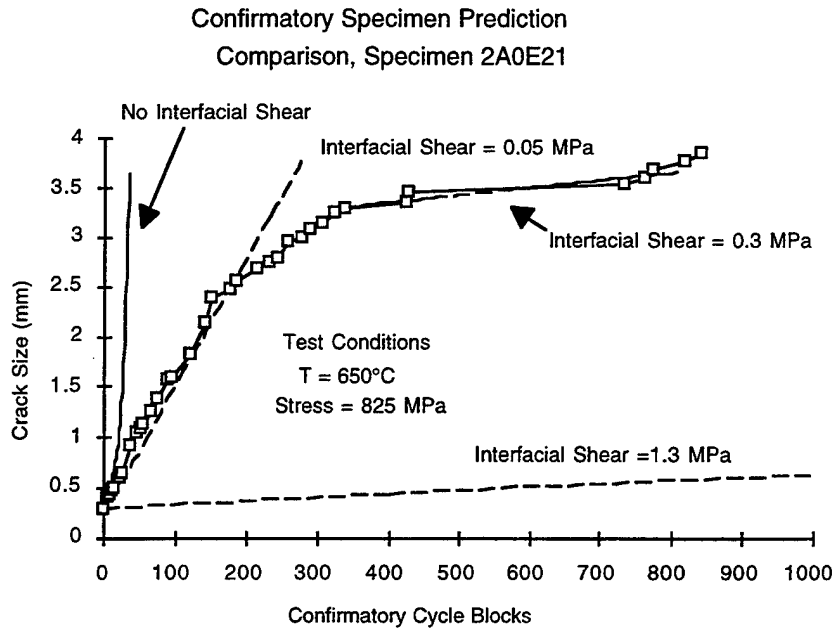
Figure 222. Confirmatory specimen longitudinal crack growth, crack growth prediction is accurate for steady-state growth region.

This specimen has a much longer transient life and hence a much longer total life.

Observations can be made about the first region of crack growth. One may hypothesize that the nature of this transition region may be influenced by the proximity of the first row of fibers to the edge of the specimen or the likelihood of breaking fibers on the first few rows of fibers. Broken fibers will not bridge, hence creating accelerated crack growth regions. Or is it purely an edge effect, which means that it takes some crack length before a fully bridged crack develops and hence the larger crack growth rate. The edge effect hypothesis can be related to the fact that the interfacial shear strength in the pristine specimens far away from the edges is nonexistent, due to the plane strain condition, and that it takes some minimum crack opening displacement to change the stress fields such that an interfacial shear stress develops.

The steady-state crack growth region is not well predicted by the average interfacial shear stress calculated from the baseline data (Figure 222). The region of accelerated crack growth is not predicted by MMCLIFE V3.0. Reasons for this may be associated with the inability of the code to deal with fiber strength distribution and the beginning of fiber failures prior to the maximum fiber stress reaching the unique fiber strength assigned by the user of MMCLIFE V3.0. In Section 4.10.3, the effect of fiber strength distribution was discussed relative to UTS of a longitudinally loaded MMC. It is suggested that if such a consideration were incorporated in MMCLIFE V3.0, crack acceleration may be predictable.

In order to add the above capabilities to the MMCLIFE V3.0 code, an improved understanding of this transient crack growth behavior needs to be developed. Also better methods need to be developed that relate the measured interfacial shear stress to the effective shear stress observed by the specimen during crack growth. As observed in the data, interfacial shear stress has a major effect on crack growth rate and hence in the life of the composite. And finally methods need to be developed that can predict accelerated crack growth rates for bridged cracks.

The final fracture prediction is an essential capability that is required to take advantage of the damage tolerance capabilities of MMCs. Analysis performed with the MMCLIFE V3.0 code predicts a stable crack growth mode for the specimens loaded in the longitudinal direction, when in fact the specimen behavior is to transition to an accelerated crack growth region which leads to final fracture. One must postulate then that crack bridging is not effective after some point. Reasons for this could be the effect of the residual stress redistribution as the crack grows, the stress redistribution will tend to increase the residual stresses in the matrix and the fibers. Also as the crack grows, the likelihood of failing fibers in the wake of the crack is increased, the resulting load increase in the fibers would increase the fraction of fibers that are broken and as a result ensue final fracture. Note that final fracture of the composite, as predicted in Section 4.10, required only 10 percent broken fibers for catastrophic failure. The inability of the code to account for other than 100 percent bridging may preclude the accurate prediction of the crack growth behavior.

The crack growth prediction of the composite must also take into account the following items. The residual stress state of the matrix and fibers, the statistical variability of the strength of the fibers, the capability of the program to predict the interfacial shear strength based on the consolidation temperature of the system and the operating temperature. The shear strength must be predicted from the consolidation temperature because otherwise it just becomes a fitting parameter.

With regards to the observed interfacial shear strength in the 650°C (1200°F) tests, it is interesting to note that the matrix average shakedown stresses shown in Table 17 in Section 4.4.2.1.4.1 correspond to a consolidation temperature of 650°C (1200°F). Hence one would expect that no interfacial shear strength would exist at this temperature, as observed in the crack growth data of Figure 222. But one has to remember that such shakedown stresses were for specimens loaded to 1035 MPa and the crack growth specimens were loaded to 825 MPa (120 ksi), hence the shakedown stress will be different. From analysis using the procedure in Section 4.10.5, it is calculated that no plastic strain is induced in the matrix at a specimen stress level of 825 MPa (120 ksi). This stress level is the threshold of plasticity for the matrix. The thermal longitudinal stress on the matrix is 80 MPa (11.7 ksi) at 650°C (1200°F). If some plasticity occurs due to the

825 MPa (120 ksi) load being at the threshold of plasticity, the residual thermal stress would go down and the interfacial shear strength at this temperature would be close to zero.

Because the prediction of crack growth behavior is very dependent upon the interfacial shear strength, the above discussions condense into a significant problem statement. It is necessary to accommodate a variable interfacial shear strength, τ, and predict this variability as it is influenced not only by the consolidation cycle, but also by the localized cumulative, thermal and strain history of the MMC as it is part of a larger component.

The incorporation of the true state of stress in the matrix is important because the crack growth rate depends indirectly on the applied far field stress and the stress ratio, but directly on the matrix local state of stress. The local state of stress in the matrix will depend on the residual stresses and on the applied stress. At room temperature, it was observed that the residual stress in the matrix was as high as its yield point, hence any further applied load would drive the matrix into the plastic region, the applied matrix stress intensity range will remain the same, but the stress ratio will vary and will likely be higher than the applied value, this would tend to increase the matrix crack growth rate.

The incorporation of the statistical fiber strength variability is believed to be of importance. As the crack grows and the fibers in the bridging region begin to take on the load relieved by the matrix due to the crack growth, the likelihood of breaking fibers increases, this would tend to change the effective fiber volume fraction of the composite. The increase of fiber volume fraction would indicate that a higher portion of the applied load is carried by the fiber which would further accelerate the fiber breakage and hence final fracture.

5.4.2   Discussion on Transverse Specimen Test Results and Life Prediction with the MMCLIFE V3.0 Code

The results of the transversely tested specimens are shown in Figure 223 through Figure 225; predicted life for these specimens are shown along with the experimental lives. As can be seen in these three figures, the MMCLIFE V3.0 does a very good job of predicting the behavior of these specimens. Specimen 2A90B13 was tested at room temperature, the predicted versus actual crack growth can be seen in Figure 224, this figure shows that crack growth rate is under predicted. The matrix stiffness ratio required to match the experimental crack growth is more than twice of what the data generated in Phase IV predicts. Note that, as shown in Table 3, the variability in the matrix stiffness ratio is rather large with values ranging from 0.6 to 4. An analytically calculated stiffness ratio was also used as shown in Figure 223 and denoted as "actual." The data

show that the experimental stiffness ratio is larger than unity hence producing the effect of a stress concentration, while the actual stiffness ratio is that of producing a stress shielding. It is reasonable to expect that the true behavior of the crack growth would be enhanced by the presence of the fibers, mostly because of the residual stress field and the stress concentration, hole type, that would develop as the crack grows through the composite in the transverse direction.

The predicted versus actual crack growth for the specimens tested at 650°C (1200°F) are shown in Figure 224 and Figure 225. The MMCLIFE V3.0 code does an excellent job in predicting the crack growth with only small deviation for the prediction of final fracture. The stiffness ratio that correlates this crack growth is very close to the average calculated of 1.5 from that of the specimens in Phase IV. Again, the same effect of the calculated stiffness ratio is observed for the high temperature specimens.

With regards to the improvements required for transverse life prediction by the MMCLIFE V3.0 Code, it would consist of an enhanced understanding of the effect of fibers on the accelerated crack growth of the transverse specimen.

The MMCLIFE V3.0 code provides the basic approach for calculating composite life prediction. For it to be useful, we need to better understand the micromechanics of crack growth which would then develop into analytical approaches that can be incorporated into this life prediction tool.

Confirmatory Specimen Prediction
Comparison, Specimen 2A90B13
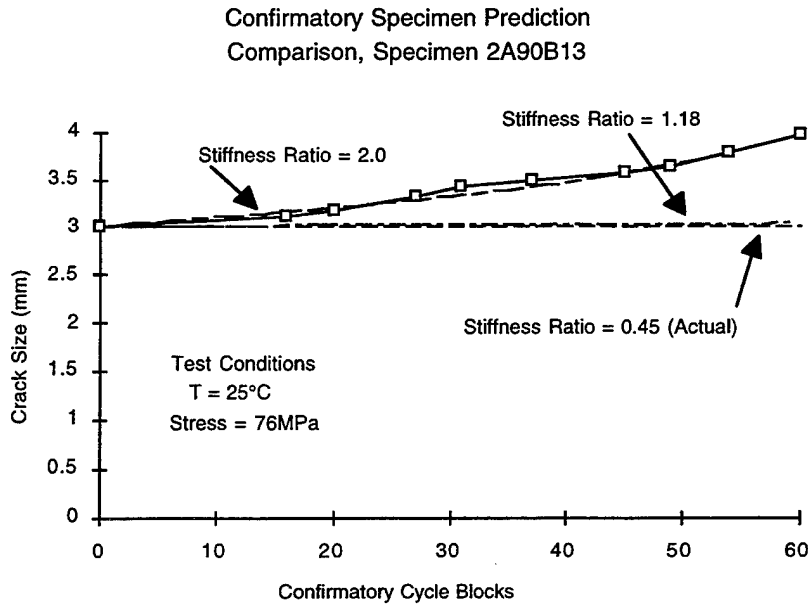
Figure 223. Confirmatory specimen transverse crack growth at room temperature.
A higher stiffness ratio is required to match growth, the MMCLIFE V3.0 code does a good job predicting life, if the stiffness ratio is adjusted to a higher value. Stiffness ratio, f, is defined by equation 85.

Confirmatory Specimen Prediction
Comparison, Specimen 2A90B23
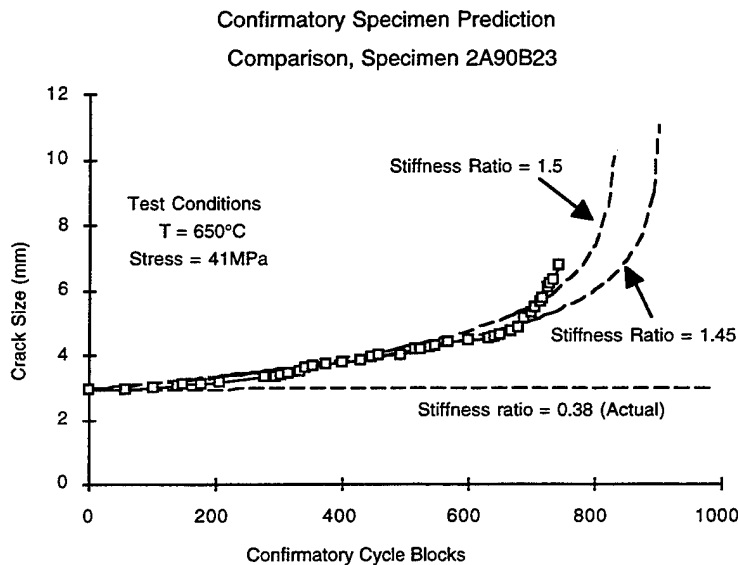
Figure 224. Confirmatory specimen transverse crack growth at 650°C (Specimen 2A90B23).
The MMCLIFE V3.0 code does a good job predicting life with only minor deviation from the average stiffness ratio. Success required adjustment of stiffness ratio to a higher value.

Confirmatory Specimen Prediction
Comparison, Specimen 2A90D12
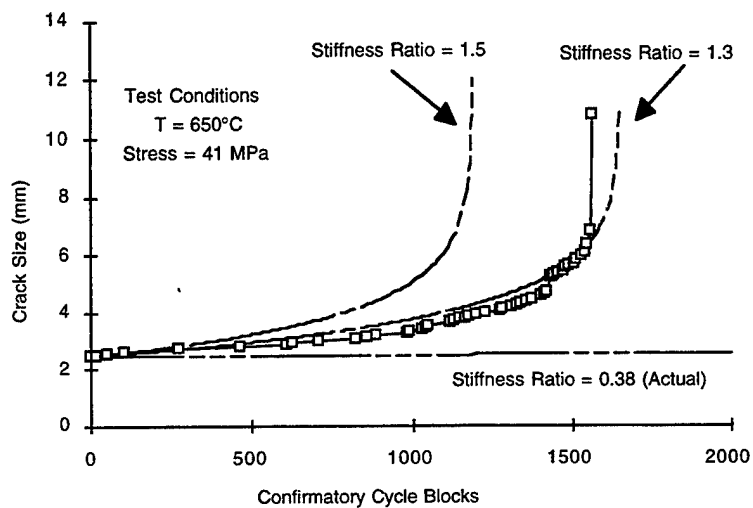
Figure 225. **Confirmatory specimen transverse crack growth at 650°C (Specimen 2A90D12).** The MMCLIFE V3.0 code does a good job predicting life with only minor deviation from the average stiffness ratio. Success required adjustment of stiffness ratio to a higher value.

5.5   Suggestions for Improvements in MMCLIFE V3.0

5.5.1   Residual Stress

The residual stresses in the matrix and fiber are computed from the CTE mismatch and the processing temperature for the MMC. There are two elements of this residual stress that are important.

- The longitudinal stress that serves to put the fiber into compression and the matrix into tension, and

- The tensile hoop stress in the matrix that serves to "clamp" the fiber affecting a load transfer mechanism and it is the origin of what we call the interfacial shear strength, τ.

This clamping stress is important because without it and any real chemical bond between the fiber and the matrix there would be no interfacial shear strength. This friction stress, which has elements from the "clamping" forces from the shrinking of the matrix about the fiber and from roughness at the interface from the outset as well as any cyclic roughening that may occur in the form of fiber coating damage or debris from the relative cyclic motion at the interface.

Experimental evidence in this program and a micro mechanical analysis of the matrix material indicates that the longitudinal residual stress is not stable and tends to reduce to some portion of the original value after the first longitudinal fatigue cycle. Experimental evidence also shows that the effective residual interfacial shear stress increases as cycles are accumulated which may be due to cyclic roughening that may occur due to fiber coating damage or debris from the cyclic motion of the interface. The MMCLIFE V3.0 code does not account for this behavior, it uses the computed value for residual stresses as fixed throughout the program, accounting only for the various temperature effects. It is apparent that such matters must be accounted for in the way stresses are distributed in the matrix and fibers because constituent behavior is an important ingredient in the model used.

It is unknown what happens to the hoop stresses that clamp the matrix around the fiber when longitudinal fatigue cycles are imposed on the sample but it is clear in all of the attempts to use MMCLIFE V3.0 to predict the a vs. N curves, a variation in τ must be used to fit the plot and the various values for τ that seem to create a best fit to the actual test data all start out with a low value of τ and increase until failure is imminent. If we attach an interpretation to these results that is associated with friction stress, one could say that as the relative cyclic motion between the fiber and the matrix proceeds, debris is created that increases the friction coefficient at the interface, thereby increasing the apparent τ. To further support this, specimens that start out with a long hold

time at maximum load (5 minutes) the apparent value for τ is near zero to cause a curve fit with the actual data. The rate of cyclic sliding, or the relative velocity will have just this observed effect on a friction related measurement. It is not clear what value of τ one must use in any case but it is obvious that its value is dependent on the number of cycles and the rate of cycling and must be part of the model for effective life prediction.

5.5.2   Criteria for Failure

Criteria for failure in the MMCLIFE V3.0 consists of three elements: 1) A composite K_{IC} calculated from specimen data, 2) a given crack length specified by the user and 3) fiber failure. It is suggested that a third criteria be added which would includes a tensile failure mode based on the combined residual strength of the remaining bridged fibers and uncracked ligament of MMC. This type of failure criteria would incorporate the micro mechanical analysis derived in Section 4.10.

5.5.3   Transverse Fatigue Crack Propagation Mechanisms

In the case of transverse loading, the MMCLIFE V3.0 assumes that the matrix is carrying a load proportional to V_m and the portion of a crack front residing on the fiber/matrix interface is assumed proportional to V_f. The observation is that the cracks follow a path that contains a much larger portion of interface area than assumed in the code and this being the weakest link forces a much lower crack growth resistance. Furthermore, the local crack growth mode in the matrix is largely mixed mode, with a large Mode III component for which the constituent data is not available nor is there provision for its input. To be effective, the code must be capable of incorporating more than Mode I and it must be capable of dealing with a crack's tendency to seek out a week surface to follow by diverting from Mode I.

5.6   Discussions Relative to Interfacial Shear Strength (Friction Stress)

5.6.1   Observations Regarding Computed Effect on Crack Tip Shielding

As can be observed in the confirmatory specimen prediction comparison with the actual test data, as shown in Figure 222, the interfacial shear stress greatly affects the crack growth rate of the specimen and hence the number of cycles to failure of the composite. The same effect was observed in the baseline data, Figure 26 through Figure 33 in Section 3, which was analyzed to determine the interfacial shear stress for this material. It was also observed that there was a large variability in the interfacial shear stress between specimens. This variability in interface shear stress makes the predic-

tion of the crack growth rate for a given specimen virtually impossible, indicating that only the statistics, i.e. averages and variances, should be compared. Also of interest is the crack growth behavior, it initially has a relatively fast crack growth rate which tends to decelerate to a constant and stable crack growth rate followed by a sudden crack growth rate acceleration leading to final failure. Perusal of the figures in Section 3 and Figure 222, shows that the model does not do a good job predicting the overall crack growth behavior, it is believed that the model overestimates crack tip shielding for very low ratios of a/w, crack size over the specimen width ratio, and c_o/w, initial unbridged notch size over the specimen width ratio.

Crack bridging models incorporated into the MMCLIFE V3.0 code are based on the canonical functions derived by Cox and Lo (Reference 13), the limits of applicability for these canonical functions for less than 2 percent error are for c_o/w ratios of 0.1 to 0.6. The error associated with extrapolations outside this range is not reported by Cox and Lo. The use of these canonical functions in the MMCLIFE V3.0 code has been to extrapolate to the whole range of possible cases, hence it extrapolates to ratios of c_o/w<0.1 and ratios of c_o/w>0.6. Extrapolation to c_o/w=0.0 is needed for the case of the SEN (single edge notch) specimen which is the specimen type used for all of the crack growth testing performed in this program. The extrapolation of the canonical functions to the SEN geometry shows a well behaved set of curves that follow the same shape as seen in the range of applicability, a cursory comparison, performed by McDonnell Douglas Aerospace, with the solution reported by Cox and Lo in their earlier paper (Reference 13) confirm this behavior, but no evaluations as to the amount of error incurred was calculated, it is expected this is within engineering error.

An explanation for the discrepancies in crack growth behavior for low a/w ratios can be found in an argument posed by Cox (Reference 30) in that a minimum crack size is necessary in order for bridging to develop its maximum effectiveness. Cox defines the bridging length scale, a_n, to be the crack length over which the bridging zone matures. The value of a_n can be calculated from the following equation.

$$a_n = \frac{\pi}{4}\left[\frac{3}{32} \frac{\rho^2 E^3 K_c^2}{V_f^4\left(1 - V_f\right)^2 \tau^2 E_f^2 E_m^2} \right]^{1/3}$$
[130]

which corresponds to a value of approximately 0.05 mm (0.002 in) for the SCS6/Ti-24-11 system used in this program. In order to match the crack size for which the bridging

zone matures for this system, an interfacial shear stress of the order of 0.15 Pascal (1 psi) would be required, an extremely low value.

A second model incorporated into the MMCLIFE V3.0 code is based on the canonical functions developed by Begley and McMeeking (Reference 18) this model calculates the stress on the bridging fibers. This model is used in the calculation of failure for a condition in which fiber failure is the limiting case. The limits of applicability for this model are described by Begley and McMeeking to be the range of $c_0/w > 0.001$ and $c_0/w < 0.7$, and also of their sigma normalization factor of $\Sigma > 0.005$ and $\Sigma < 0.25$. Although this failure mode was not exercised in this program for the confimatory specimen, the interfacial shear stress calculated using the fiber push-out tests would have indicated the tests would have been in the range of applicability, but the interfacial shear stress calculated from the figures in Section 3 indicates the value of $\Sigma = 0.75$, which is greater than 0.25 and therefore outside of the range of applicability.

5.6.2 Recommendations for Improved MMCLIFE V3.0 Code with Regards to Crack Tip Shielding

Based on the above observations, in order to improve the accuracy of the MMCLIFE V3.0 code, it is recommended that the canonical functions derived by Cox and Lo be evaluated outside of the recommended range of applicability and if found to be largely in error, that a new set of functions be derived in a subsequent program. These functions should then be incorporated into the MMCLIFE V3.0 code. Also, it is important to note that the bridging factor is very sensitive to the interfacial shear stress, hence it is important to properly characterize the interfacial shear stress of the composite. Proper characterization may include a statistically representative sample, with mean and standard deviations calculated. Last, it is important to understand the behavior observed in Figure 222 and Figure 26 through Figure 33, where it is observed that the crack growth is matched best using a low value of interfacial shear stress for small crack sizes, whereas a higher value of interfacial shear stress matches the crack growth best for larger crack sizes. Such behavior would suggest a bridging model which would incorporate the interfacial shear stress as a function of crack size or as a function of cycles.

5.6.3 Frequency Effects

It was also observed that the calculated interfacial shear stress varied, depending on the test frequency. This variability may relate to the strain hardening nature of the matrix. Consider the action at a fiber/matrix interface of an MMC being cyclically strained parallel to the fiber orientation. First, we have the decrease in the residual stress as described in Table 12. In addition to this we have the creation of damage that may involve a certain amount of plastic deformation in the matrix near the interface. High strain rate sensitivity of the matrix may come into play when the small asperities at the

fiber-matrix interface are plastically strained to accommodate the relative motion of the interface. At low frequencies, a low shear strain rate would ensue whereas at high frequencies high shear strain rates would ensue. In addition, consider the environmental effects such as may be the case in elevated temperature testing, more time is available for environmental degradation by oxygen diffusion along the open crack if the crack is open for a longer time period of each cycle. Oxidation of the carbon rich SCS layer may contribute to reduced friction stress at the crack tip and on any fibers bridging the crack in the crack's wake. While this may be partially true it cannot be entirely true because once the test frequency is increased during the test, there is an immediate reduction in crack growth rate. If the interface had been destroyed, on the bridging fibers in the crack's wake, their reduced effectiveness in crack retardation should remain once the frequency is increased and an immediate reduction in rate would not be expected. Furthermore, upon reducing the test frequency or adding a hold time, there is an immediate increase in crack growth rate. One is forced to the conclusion that the rate of loading or the hold at maximum load, or both, have effects on the effectiveness of the bridging mechanism and any environmental effect at the temperatures used in this program, is of lesser influence.

At room temperature, when just the frequency is reduced without a dwell at maximum load, there is an immediate increase in growth rate and the MMCLIFE V3.0 model indicates an immediate reduction in the value of τ is necessary to fit the data. After a short period of crack growth, the growth rate returns to a level more closely associated with the original higher test frequency. But, with a relatively long dwell at maximum load, this return does not occur. It may be associated with the plasticity of the matrix alloy and its strain rate sensitivity and, in the case of the dwell, an added factor associated with an elastic behavior or creep at room temperature may effectively reduce the local residual stress in the matrix. This reduces the clamping effect of the matrix on the fibers and will decrease the effective value for τ. If the test frequency were higher and there were no dwell at maximum load, this time dependent reduction of local residual stress would not be significant and we are then left with the loading rate effects if the matrix strain rate hardens.

In the confirmatory tests, each major cycle had a hold time and, according to the above discussion they would have lower effective vales of τ. This is confirmed by the results, (Figure 222) that required much lower values of τ to fit the data than did the simple tests run at 20 cpm (Figure 31 through Figure 33). It is also noticed that, while low, τ did increase with time or cycles at 650°C (1200°). If the oxidation mechanism of removing the interference fit material, carbon, at the interface were operating alone, one would expect τ to decrease. This leads to the conclusion that debris created during the relative slipping of the fiber and matrix, is created that roughen up the interface causing some increase in τ, despite the possible oxidation effect.

276

5.6.4 Summary Discussions about Interfacial Shear Strength, or Friction.

For the materials used in this program, there is no chemical bonding between the matrix and the SCS carbon rich layer on the fiber so the only strength of the interface is that imparted by the residual stresses. The interfacial normal strength is vanishingly small and the interfacial shear strength is derived from a friction term that comes from a combination of the clamping stress associated with differential thermal expansion between the fiber and matrix as they cool from the processing temperature and some asperities in the fiber surface created during fiber manufacturing and/or handling or during consolidation. From this it is clear that the value of τ will be very temperature sensitive and will vary some depending on the handling and consolidation conditions. The interfacial shear stress will virtually disappear at a temperature that approaches the effective zero stress temperature. This temperature will be lower than the processing temperature as creep and stress relief can, and does, occur while cooling.

The semistatic measurements of τ by a pull out test method results in values much higher than even those derived from a curve fitting of the crack growth data from simple tests. Even after fatigue cycling, which did reduce the pull out value, the measured value of τ was higher than was the value necessary to provide a fit to fatigue crack growth data at room temperature. Degradation of the friction stress due to fatigue cycling accompanies a reduction of average longitudinal residual stress in the matrix, implying a concomitant reduction in the clamping residual stress in the matrix. This phenomenon is seen whether the test is run at room temperature or at elevated temperature. All of this precedes the existence of a crack. In this program, all of the actual residual stress reduction and pull out measurements of τ were conducted on uncracked LCF specimens so the presence of a crack is not a necessary condition. In the presence of a crack, the bridging mechanisms all involve, in one way or another, the relative sliding of fiber and matrix and the degree to which this mechanism retards or slows crack growth is dependent upon energy being consumed in this sliding process that is not available, then, for advancing the crack. Higher values of the friction stress, τ will result in greater effectiveness in retarding crack growth. As cracks grow by fatigue, the effective value of τ quickly decreases due to the shakedown in residual stress but after the higher amplitude cycling at a crack tip, there is created damage at the interface that leaves the interface effectively roughened with a concurrent increase in τ. At elevated temperatures, oxidation of the carbon rich fiber coating also serves to reduce interface friction by removing the SCS layer.

The MMCLIFE V3.0 does not account for a cycle history effect on τ and is weak in this regard in cases, such as the program material, τ is so dependent. The problem is intensified by the fact that during elevated temperature service or testing a new, effective,

zero stress temperature is established. Furthermore, with biaxial loading the matrix is pulled away from the fiber and this will have its effect on reducing the ability of the matrix to transfer load to the fiber by reducing the effective interfacial shear strength or friction stress. To effectively incorporate crack bridging as a crack retardation mechanism, the life prediction codes must be capable of dealing with a variable value of τ. And the pathway to the variations is very temperature and strain cycle dependent and will be influenced by rate, dwell, strain during a component's life MMCLIFE V3.0 requires the user to introduce a single value for τ. This may not be adequate for life prediction. Only after a specimen is tested can we now go back and assign values of τ that must have been available to the process at various stages in the test.

Because the program materials, in the test configuration used, failed after very little crack growth when the stresses were high enough to be of interest for rotor design, there is no information about long, bridged, cracks but the conditions discussed above must be relevant.

SECTION 6

GUIDELINES FOR IMPROVED MATERIAL PROCESSING AND DURABILITY

6.1 Matrix Alloy

6.1.1 Matrix Strength and Ductility

While Ti-24Al-11Nb matrix tested in this program has plenty of in-plane ductility, it is weak from a tensile strength standpoint and the creep strength is poor. The in-plane ductility (uniform elongation) is associated with a rather high work hardening exponent and a noticeable lack of thickness direction strain and no noticeable local necking before tensile failure.

6.1.2 Microstructure

Grain size is small, leading to the higher ductility and, perhaps, to the low creep strength. The amount of beta phase is low by comparison to the normal Ti-24-11 microstructure and is probably a product of the extensive cold working and intermediate anneals as well as the HIP cycle used for bonding or debulking. The beta phase is retained in interconnected islands among the equiaxed primary α_2 grains. There is very little evidence of transformed beta microstructure wherein α_2 platelets would be evident. When this sort of feature dominates the regions of the microstructure which had been beta at the last elevated temperature exposure, favorable properties are expected. The retained beta in the microstructure of the program alloy is likely to be metallurgically unstable and transform slowly during service. An implication of this includes a possible relief of some of the residual stresses during this transformation. While this may be beneficial from the standpoint of enhancing resistance to fatigue crack initiation, it may also result in part distortion during service. All-in-all, a stable microstructure is better and foil manufacture and MMC consolidation processes should incorporate measures to avoid metallurgical instability.

6.1.3 Texture

In-plane isotropy is evident, but through-thickness strength is much higher as evidenced by the hardness impression study reported in Section 4.2.2.1.4 and the Poisson ratio study on NEAT foil, Section 4.2.4. As a result of this crystallographic texture hardening in the thickness direction, it is expected that the elastic and plastic properties are all anisotrophic. Furthermore one would expect that the behavior of cracks grown from

the MMC surface, normal to the fibers, will be different from those grown normal to the fibers but from a specimen edge. Unfortunately, the program scope does not include such studies, but it does offer a fruitful area of research. Behavior modeling is complicated considerably if the anisotropic behavior of the matrix is accounted for.

6.1.4 Matrix Alloy Selection

Alloys superior to Ti-24Al-11Nb do exist and there is a new generation under development (Reference 31, Air Force Contract F33615-91-C-5647). Goals for the alloy development part of the contract do include considerations of most of the issues discussed above.

6.2 MMC System

6.2.1 Residual Stresses

In the manufacture of a rotating component, frequent low temperature stress relief cycles during part manufacture may serve the purpose of stabilizing the microstructure. Of course these cycles will also effect properties, so the matrix design properties must be obtained using materials which have been suitably cycled in such a manner as to stabilize them and, at the same time, represent the entire manufacturing process. Similarly, damage tolerance modeling and supporting data must be taken with equivalent considerations.

Because the cycles of stress relief and/or matrix structure modification, discussed above, are very part specific (the part geometry will dictate the number of subelements that need to be manufactured and the number of bonding cycles necessary to incorporate them into a final part), one would conclude that data for design and damage tolerance modeling must come from specific parts or subelements manufactured in the same manner. An alternate notion would be to build the model up from constituent properties which can be measured in coupons having the same thermal and thermomechanical history and then include considerations of $\Delta\alpha$ and interdiffusion during the consolidation cycles, stress relief cycles and service cycles in the model to account for residual stresses and interface property modifications.

6.2.2 Property Characterization and Design Database

Without the above considerations, there would be little benefit in developing a property database for any MMC. It is especially important for MMCs exposed to elevated temperatures in service and for which damage tolerance is a design consideration. Simple elastic properties such as specific stiffness are much less sensi-

tive to the above considerations and stiffness critical applications should not be as complex as those involving strength.

6.2.3 Post Consolidation Thermal Treatments

As for the Ti-24-11 matrix, evidence to date indicates that a fine microstructure imparts significant in-plane ductility and therefore relative freedom from thermal fatigue cracking of the matrix in MMCs. However, this microstructure is not so good when strength considerations become important. Transverse creep properties, even at room temperature, are poor. If this is the only alloy of choice, a microstructure modification should be considered to improve strength. While the fine grain size enhances the ability to consolidate the MMC at lower temperatures in order to minimize interdiffusion with the reinforcement, it leaves the MMC with the above weaknesses. It is suggested that, after the consolidation is completed at as low a temperature as possible, a short time heating to a higher subtransus temperature will coarsen the microstructure. It would be best to incorporate this during the final HIP consolidation cycle. All subsequent thermal cycles ought to be in the stress relief range. Some simple experiments will aid in defining the appropriate cycle.

6.3 Microstructural Characteristics of Fatigue Crack Growth in MMCs

Effects of crack bridging, on samples with cracks growing normal to the fibers, at elevated temperature do not appear to provide the anticipated benefits of crack retardation. While the cracks are clearly bridged in fatigue crack growth testing at room temperature, 550°C (1022°F) and 650°C (1200°F), the crack growth does not arrest or even show signs of extended retardation. While the growth rate is clearly slower than the unreinforced matrix, at stresses of interest in gas turbine disk design, the damage tolerance is questionable. The failure conditions at these temperatures and stresses imply an apparent fracture toughness not a great deal higher than that shown by many of the common monolithic disk materials. The resultant short critical flaws present significant challenges to the NDE technology. Critical crack lengths on the order of less than 5 to 7 inter-fiber distances may be too short to clearly detect in service. Crack acceleration is not obvious until just before failure, leaving little time for detection.

6.3.1 Environmental Effects

While definitive experiments have not been conducted, evidence leads to the conclusion that, at elevated temperatures, once the fibers become exposed to the atmosphere, the damage rate becomes severe, and damage tolerance under these conditions is poor. This is likely due to environmental degradation of the interface properties, probably from oxidation. Solutions to this sort of deficiency include keeping the MMC bur-

ied but this fails to make the best use of the material. However, improved interface coatings between the fiber and the matrix, designed to resist environmental degradation are clearly necessary.

6.3.2 Interfacial Strength, Effect of Elevated Temperature

An additional factor comes from the fact that there is no real bonding between the fiber and the matrix. Load transfer is primarily dependent upon the clamping effect of the matrix on the fiber derived from the residual stresses. Of course, at higher temperatures, the residual stresses are relaxed and the clamping forces reduced. As a result, the effectiveness of the bridging diminishes by virtue of the reduced value of interfacial friction stress, τ, which can become vanishingly small as the effective consolidation temperature is approached. Because of the low creep strength of the program matrix material, it is quite possible that the effective consolidation temperature may be on the order of the test temperature. For the case of the program materials, the effective consolidation temperature (zero stress temperature) is on the order of 590°C (1100°F).

6.3.3 Alloy Effects

A more creep resistant matrix will clearly help retain a higher effective consolidation temperate. Improved creep strength is a feature of the program of Reference 31, Air Force Contract F33615-91-C-5647. An additional goal of the referenced program is to enhance the interfacial strength which should improve the effectiveness of crack bridging at elevated temperatures.

6.3.4 Characteristics of Room Temperature Fatigue Crack Growth, Longitudinal with Fully Bridged Precracks

Room temperature crack growth in longitudinally oriented samples appears to be completely bridged, with crack growth much slower than in the unreinforced matrix. The growth rates seem to be a linear function of stress and independent of crack length on the completely bridged cracks for the edge notch specimen used in this program. This linear crack growth rate as a function of stress indicates significant crack bridging effect and the resulting crack growth retardation.

6.3.4.1 Characteristics of Room Temperature Fatigue Crack Growth, Transverse Orientation

Room temperature fatigue crack growth parallel to the reinforcing fibers is very rapid, with the interface offering essentially no resistance to an advancing crack. The very severe effect of dwell at maximum load leads to the conclusion that room temperature, sustained load, crack growth is an active mechanism. The da/dN vs. ΔK plots in all

cases are nearly vertical, indicating a damage intolerant material when the cracks are running parallel to the reinforcement. The fiber/matrix interface is a dominant crack path, and it is not certain that increasing its strength will also increase resistance to crack growth. Hence it is suggested that not only should the interface be strengthened to accommodate the need for increased transverse strength but it should also be toughened by some mechanism that increases the energy necessary for the crack. An example might be a ductile, crack blunting, interface zone.

The matrix resistance to crack propagation can be improved by extrinsic means associated with microstructure modification. Because of need to consolidate the matrix at a relatively low temperature to avoid excessive reaction between the matrix and fiber coating, high temperature exposure of the foil before consolidation is not a likely route to matrix toughening. Post consolidation thermal treatments are the most likely route and are discussed in Section 6.2.3. Microstructures considered better for creep and for resistance to crack propagation are similar and contain significant amounts of acicular-like transformation product of the beta phase.

Decreasing fiber volume fraction will allow a greater participation of the matrix in the process of crack propagation parallel to the reinforcing fibers with the concomitant increased flexibility in developing crack resistant microstructures. A lower fiber fraction is made possible with higher strength fibers as well as increased interfacial normal strength.

6.3.5 Fiber Strength Effects

Clearly, use of higher strength fibers will permit a lower volume fraction of fibers for strengthening purposes, leaving a larger fraction of the transverse cross section as matrix to bear the transverse loads and through which an increased area fraction of the crack must propagate. Incidentally, the level of residual stresses from consolidation will be reduced with a lower fiber volume fraction. Higher strength fibers also imply a greater strain to fiber failure with a resultant greater MMC LCF strength.

6.3.6 Cyclic Degradation of Residual Stresses at Room Temperature

The MMCLIFE V3.0 code, performs a calculation of residual stress based on the input processing temperature and holds this value constant throughout all calculations. Such a case of invariant residual stress does not hold for the materials used in this program. In the course of this contract, it was verified that residual stresses clearly are not stable and while specimens are tested under isothermal conditions, even at room temperature, the residual stress level clearly decrease significantly and this occurs very quickly, at least when the maximum stress in the fatigue cycle is high enough to be useful for

rotor designs. The level to which the residual stress decays can be calculated by the micromechanical analysis developed in Section 4.10.

Dealing with residual stress in an MMC demand that an effective Damage Tolerant Life model must account for a fluctuating level of residual stress as it clearly affects the fiber and, therefore, the composite strain to failure by virtue of the effect on the fiber mean stress. The residual stress reductions observed during fatigue cycling were in the longitudinal direction, but one might expect that the hoop residual stresses around the fiber, which give rise to the interfacial shear stress (friction stress), τ, will also decay. If this is the case, as evidenced in the discussions surrounding Table 12 where pull-out tests revealed a degradation in τ with fatigue cycles, the ability to transfer load between fibers and matrix can be affected. Also affected will be the impact that bridging has on crack retarding.

It is clear that there needs to be developed a better understanding of the dynamics of residual stresses in MMCs as they encounter service cycles and, to the extent that residual stresses are used in the MMCLIFE V3.0 or other damage tolerance codes, the codes must be flexible enough to deal with this time and/or cycle dependent variation. Bookkeeping residual stresses as a function of stress cycle, temperature cycle, hold time and other effects is possible only when the service cycle is well known and it will also require high computing power. Perhaps, by understanding the phenomenon well enough to simplify the effects so that they can be dealt with in a truncated fashion, the codes may be appropriately modified.

The observed hold time effects and effects of low frequency testing, both of which result in accelerated fatigue crack growth rates, imply time dependent room temperature deformation or crack growth mechanisms that may be exacerbated by variable residual stresses. This effect is seen at room temperature which eliminates creep and/or environmental degradation as primary contributors

6.4 ENSIP Guidelines and Considerations for MMC Disk Design and Construction

6.4.1 Description of ENSIP

The Engine Structural Integrity Program, ENSIP, is described by MIL-STD-1783. Its purpose is to establish structural performance, design development and verification requirements that assure structural integrity for engine systems. It is an organized and disciplined approach to the structural design, analysis, qualification, production, and life management of gas turbine engines.

The specific objective of ENSIP is to ensure structural safety, durability, reduced life cycle costs and increased service readiness. Durability is a key component of the program and ENSIP defines this as the ability of engine components to resist cracking (including vibration, corrosion, and hydrogen induced cracking), corrosion, deterioration, thermal degradation, delamination, wear and the effects of foreign and domestic object damage for a specified period of time.

6.4.2 Role of the MMC Damage Tolerance Concepts Contract Program

Damage tolerance, the ability of the engine to resist failure due to the presence of flaws, cracks, or other damage for a specified period of unrepaired usage, is one focus of this contract, "Damage Tolerance Concepts in Ti-Aluminide Matrix Composites." The principal factor in this contract is the tolerance of cracks in the MMC structure through crack growth characterization and adoption of an existing MMC life prediction code developed by McDonnell Douglas, MMCLIFE, to engine disk conditions.

6.4.2.1 Material Selection and Control of Manufacturing

This is an obvious issue and the selection of materials and manufacturing will involve the expected damage tolerance they will deliver. In this program, the materials were selected with the anticipation that the lessons learned will be transferable to other MMC systems, assuming that MMCs are intrinsically damage tolerant. In Section 6.3, the lessons learned were discussed, relative to materials selection and better processing, in order to improve damage tolerance.

6.4.2.2 Use of Fracture Resistant Design Concepts

It was assumed, from the onset, that MMCs have inherent damage tolerance based on their fatigue crack growth resistance. It was shown, by work under this contract, that this is partially true, but disappointment arises from the material's relatively low ap-

parent fracture toughness and small critical flaw size under temperature and stress conditions useful for disk design.

6.4.2.3   Use of Reliable Inspection Methods

Inspection tools and the reliability of their flaw detection limits are key to successful application of ENSIP in that flaw size assessments permit rezeroing the fatigue crack growth life, after each inspection, to that associated with a flaw which is assumed present at the detectable size limit. Suitable allowance must be made for reliability shortfalls in the inspection process, in property variability and in the variable nature of flaw characteristics.

The inspection intervals are established by flaw growth rate under service conditions and the flaw size that will cause catastrophic failure. This is all tempered by the above uncertainties and it is further compounded by additional uncertainties associated with incomplete records of actual service conditions and environments as well as additional effects of undetected mechanical foreign object damage (FOD) damage.

All of this speaks for the need to have comfortable margins between projected life from a known or assumed flaw and the inspection intervals. Compressor disks of MMC, to be useful relative to their high cost, must operate at high stresses (combination of applied and residual stresses) and this forces entry into the da/dN curve at quite high levels of ΔK, even with small flaw sizes. Implications of this for the MMC system in the current study were introduced in Section 4.9 and those discussions will be reintroduced in this discussion of ENSIP.

6.4.2.4   Verification of the Damage Tolerance of the Program MMC

The program MMC, Ti-24Al-11Nb (atomic %) matrix, unidirectionally reinforced with 35 vol. % SCS6 silicon carbide fibers, was extensively tested in the form of 8–layer panels. Low cycle fatigue and fatigue crack growth at temperatures up to 650°C (1200°F) provided a database from which to adjust the modified MMCLIFE, life prediction code. Analysis of the test results indicate that, indeed, the crack growth rate in longitudinal MMC samples is much lower than in the monolithic material. On the other hand, transverse sample testing indicates very low tolerance for cracks, and the crack growth rate is high at very low stress intensities and is intolerant of hold times at all temperatures.

Further examination of the data in Section 4.9 suggests that, while the crack growth rate is low in longitudinal oriented specimens, the stress levels of interest in disks, combined with the apparent fracture toughness derived from the crack length at catastrophic

failure of the crack growth specimen, give a very short critical crack length. The question as to the inspection capability and the effective residual life after the generation of an inspectable crack must guide our considerations of ENSIP for this material in disk applications.

6.4.2.5 Life Prediction Model Development as it Relates to ENSIP

The major modifications to the McDonnell Douglas MMCLIFE code, MMCLIFE version 3.0, are those associated with naturally occurring cracks being fully bridged at the outset, with higher stresses than those for which the code was initially developed. The code was further modified to incorporate the latest understanding of the effects of crack bridging by the reinforcing fibers. Considering the symmetry of MMC reinforcement in disks, it was considered appropriate that the principle stresses are longitudinal (tangential in the disk) and transverse (radial in the disk) with the hoop reinforced disk having life limited by the growth of radial cracks (growing normal to the reinforcement fibers). Because disks with working loads such as airfoils will introduce radial stresses, the transverse life prediction is clearly important.

6.4.3 Application of ENSIP Concepts to Materials in this Study

The considered applications are assumed to be MMC inserts buried in a monolithic titanium material. Furthermore, the highest stresses are tangential stresses in a disk or impeller bore and cracks are most likely to originate in this monolithic envelope and propagate radially towards the MMC. The effective ΔK as the crack reaches the MMC is clearly related to the surface length of crack (2C) at that point as well as the thickness of the monolithic envelope (a). As a consequence, the inspection capabilities and limitations assumed for this program are justifiably those associated with monolithic alloys and this determines the initial flaw size estimate.

It is a considered assumption that the current state of art of Non Destructive Inspection will reliably detect surface connected cracks on the order of 0.70 mm (0.027") and it is based on this that applications of ENSIP are discussed.

6.4.3.1 Residual Life After Generation of Crack of an Inspectable Size

Table 22 is reproduced as Table 29. This table describes the residual life of a program MMC sample after an inspectable crack is obtained. It clearly shows that at higher temperatures (>550°C (1022°F)) and stresses (>827 MPa), there is little residual life, and an

287

ENSIP criteria cannot be applied, with this material system, to components stressed at levels of interest in MMC reinforced impeller designs.

Table 29. Estimates of critical crack sizes and residual life beyond detectable crack length, a_d = 0.70 mm

Temperature	Stress (MPa)	a_c (mm)	N_P beyond 0.70 mm
room temp	689.5	3.00	502,000
	827.4	2.08	90,000
	1034.2	1.33	20,000
550°C	689.5	2.70	no supporting data
	827.4	1.88	no supporting data
	1034.2	1.20	950
550°C damaged with applic. of Prior low stress fatigue	689.5	1.02	no supporting data
	827.4	0.71	0
	1034.2	0.46	0
650°C	689.5	1.76	14,578
	827.4	1.22	no supporting data
	1034.2	0.78	0

Furthermore, there appears a complicating factor of cumulative damage, not so much as it reflects crack growth, but in the apparent fracture toughness. While, in principle, a crack's progress can be followed by periodic inspections during a component's service life, it is quite another problem assessing cumulative reduction in a component's failure criteria.

6.4.3.2   Transversely Loaded MMCs and ENSIP

Because disks with working loads such as airfoils will introduce radial stresses, the transverse life prediction is clearly important. For the program material, at all temperatures, fatigue crack growth is rapid at low stress levels and the da/dN vs. ΔK plots are nearly vertical. In this case, there is virtually no damage tolerance, as a growing crack is very nearly catastrophic from the beginning of its existence.

6.4.4   Summary Comments Regarding ENSIP and MMC Reinforced Disks

From the above discussions, it becomes apparent that without major breakthroughs in both materials and NDE technology, ENSIP concepts are impractical for highly stressed MMC reinforced components used at elevated temperatures. At ambient temperatures, where attractive strength limiting MMC applications make sense and where large trans-

verse stresses are avoided, Table 29 implies feasibility of ENSIP. The same sort of conclusion would be drawn, no matter the matrix alloy, because of the lack of interfacial strength and the thermal expansion mismatch between the fiber and the matrix.

Under condition where off-axis stresses are significant, the program MMC material exhibits virtually no damage tolerance, would be described by a significant fatigue life between the formation of a detectable crack and the failure event so as to provide for in-service inspections or a comfortable and reliable warning of pending failure. The off axis stresses must be kept very low in order to use MMCs in rotor designs. If the matrix strength were to be increased along with significant increases in interfacial normal strength (between fiber and matrix constituents) transverse properties may be increased. This would be added to the more significant effects associated with use of higher strength fiber which enables use of lower fiber volume fractions to support the higher hoop stresses and will increase the volume fraction of matrix material to deal with the matrix dominated, off axis, stresses.

The program material, when fatigue tested at useful disk design stresses parallel to the fiber orientation, exhibits only a small difference between the ΔK associated with entry into the da/dN curve at a detectable crack length, and the ΔK associated with failure. This is a severe shortcoming for a material intended for use in an ENSIP design and will require very short, maybe impractical, inspection intervals. This situation is even worse at elevated temperatures.

It is true that MMCs bring an added dimension to rotor performance capability because of their higher strength but there is the above described concomitant reduction in damage tolerance. State-of-art monolithic materials do not permit such performance levels and would also have little damage tolerance under the same severe operating stresses. However, within the realm they are intended for use, they do have acceptable damage tolerance and have given good service for many years. Were the program MMCs used under conditions where their damage tolerance is acceptable, the payoff in performance would be minimal and probably not high enough to justify the added costs associated with these materials as they are made today.

SECTION 7.0

REFERENCES

Reference 1   Finefield, M. A., Harmon, D. M., Saff, C. R., and Harter, J. A., "Thermomechanical Load History Effects in Metal Matrix Composites–Final Report," WL-TR-94-3015, Wright-Patterson Air Force Base, OH, 1994.

Reference 2   Harmon, D. M., Saff, C. R., and Graves, D. L., "Durability of Continuous Fiber Reinforced Metal Matrix Composites–Final Report," AFWAL-TR-87-3060, Wright-Patterson Air Force Base, OH, 1987.

Reference 3   Lekhnitskii, S. G., *Anisotropic Plates*, Gordon and Breach Science Publishers, 1968.

Reference 4   Peterson, R. E., *Stress Concentration Design Factors*, Wiley & Sons, New York, 1953.

Reference 5   Seely, F. B. and Smith, J. O., *Advanced Mechanics of Materials*, Wiley & Sons, New York, 1952.

Reference 6   Harmon, D. M. and Saff, C. R., "Stress and Strength Analyses for Fiber Reinforced Metal Matrix Composites," In: Johnson, W. S. ed, *Metal Matrix Composites: Testing, Analysis, and Failure Modes*, ASTM STP 1032, Philadelphia: American Society for Testing and Materials, 237-250, 1989.

Reference 7   Jones, Robert M., *Mechanics of Composite Materials*, McGraw Hill Book Company, New York, 1975.

Reference 8   Piggot, M. R., *Load Bearing Fibre Composites*, Pergamon Press, Oxford, p. 205, 1980.

Reference 9   Smith, K. N., Watson, P., and Topper, T. H., "A Stress-Strain Function for the Fatigue of Metals," *Journal of Materials*, Vol. 5, No. 4, pp. 767-778, 1970.

Reference 10   Tada, H., Paris, P. C., and Irwin, G. R., *The Stress Analysis of Cracks Handbook*, 2nd Edition, pp. 17.3, 19.11, and 19.12, 1985.

Reference 11   Sih, G. C., *Handbook of Stress Intensity Factors*, Bethlehem, PA: Lehigh University, 1973.

Reference 12   Badaliance, R., "Application of Strain Energy Density Factor to Fatigue Crack Growth Analysis," *Engineering Fracture Mechanics*; 13(3)1980.

Reference 13   Cox, B. N. and Lo, C. S., "Simple Approximations for Bridged Cracks in Fibrous Composites," *Acta Metall. Mater.*, Vol. 40, No. 7, pp. 1487-1496, 1992.

Reference 14   McMeeking, R. M. and Evans, A. G., "Matrix Fatigue Cracking in Fiber Composites," *Mechanics of Materials*, Vol. 9, pp. 217-227, 1990.

Reference 15   Cox, B. N. and Lo, C. S., "Load Ratio, Notch, and Scale Effects for Bridged Cracks in Fibrous Composites," *Acta Metall. Mater.*, Vol. 40, No. 1, pp. 69-80, 1992.

Reference 16   Cox, B. N. and Marshall, D. B., "Stable and Unstable Solutions for Bridged Cracks in Various Specimens," *Acta Metall. Mater.*, Vol. 39, No. 4, pp. 579-589, 1991.

Reference 17   Cox, B. N. and Marshall, D. B., "The Mechanics of Matrix Cracking in Brittle-Matrix Fiber Composites," *Acta Metall. Mater.*, Vol. 33, No. 11, pp. 2013-2021, 1985.

Reference 18   Begley, M. R. and McMeeking, R. M., "Fatigue Crack Growth with Fiber Failure in Metal Matrix Composites," *Composites: Science and Technology*, 53, 365, 1995.

Reference 19   Hutchinson, J.W. and Jenson, H.M., "Models of Fiber Debonding and Pullout in Brittle Composites with Friction," *Mech. of Matls.*, 9, 139–163 (1990).

Reference 20   Revelos, W.C., Smith, P.R., "Effect of Environment on the Thermal Fatigue Response of an SCS6/Ti24Al/11Nb Composite," *Metallurgical Transactions*, 23A, 587, Feb. 1992.

Reference 21   Swanson, S.R., Messick, M., and Toombes, G.R.; "Comparison of Torsion and Iosipescu In-plane Shear Test Results for a Carbon Fiber-Reinforced Epoxy Composite," *Composites*, 16, No. 3, 220, July 1985.

Reference 22   Gambone, M.L., Fatigue and Fracture of Titanium Aluminides, *WRDC-TR-89-4145*, February 1990.

Reference 23   Johnson, H. H., "Calibrating the Electric Potential Method for Studying Slow Crack Growth," *Materials Research and Standards*, 5, No. 9, Sept. 1965, pp. 442-445.

Reference 24   Larsen, J.M., Moran, J.L., Jira, J.r., and Blatt D., "Effects of Fiber Matrix Interfacial Degradation on High Temperature Fatigue Crack Growth in SCS6/TiMetal 215," In Press, *Proceedings of the Eight World Conference on Titantium*, Birmingham, U.K., 1996.

Reference 25   John, R. Jira, J.R., Larsen, J.M., Ashbaugh, N.E., "Analysis of Bridged Fatigue Cracks in Unidirectional SCS6/Ti-24Al-11Nb Composites," *Procedings of Fatigue '93*, Ecole Polytechnique, Monteal, Canada, 3-7 May 1993.

Reference 26   Ditmars, M., Hall, J.A., and Keiser, R., *"Unpublished Research, "* AlliedSignal IR&D, Dec. 1988.

Reference 27   Weibull, W., "A Statistical Theory of the Strength of Materials," *Royal Swedish Academy of Engineering Sciences Proceedings*, Volume 151, pp 1–45, 1939.

Reference 28   Krajcinovic, D., "Damage Mechanics," *Mechanics of Materials*, Vol. 8, pp. 117-197, 1989.

Reference 29   Curtin, W.A., "Theory of Mechanical Properties of Ceramic-Matrix Composites," *Journal of the American Ceramic Society*, Vol. 74 [11], pp. 2837-45, 1991.

Reference 30   Cox, B.N., "Extrinsic Factors in the Mechanics of Bridged Cracks," *Acta Metallurgical Materiallia*, Vol. 39, No. 6, pp. 1189-1201, 1991.

Reference 31   *Air Force Contract F33615-91-C-5647*, "Advanced Ti-Based MMC System Development."

APPENDICES

Appendix A

"Residual Stress Measurement in Continuous Fiber Titanium Matrix Composites," James, M.R. et al., X–Ray Analysis, 36, 1993

Appendix B

"Analysis of Fiber Debonding and Sliding Experiments in Brittle Matrix Composites," Marshall, D.B., Acta Met., 40, No. 3, pp. 427-441, 1992.

Appendix C

"The Determination of Interfacial Properties from Fiber Sliding Experiments. The Roles of Misfit Anisotropy and Interfacial Roughness," Marshall, D.B., Shaw, D.C., Morris, W.L., submitted to Acta Metl, June 1994.

Appendix A

"Residual Stress Measurement in Continuous Fiber Titanium Matrix Composites,"
James, M.R. et al., X–Ray Analysis, 36, 1993.

RESIDUAL STRESS MEASUREMENTS IN CONTINUOUS FIBER TITANIUM MATRIX COMPOSITES

M. R. James
Rockwell International Science Center
Thousand Oaks, CA 91360

and

M. A. Bourke, J. A. Goldstone and A. C. Lawson
Los Alamos National Laboratory
Los Alamos, NM 87545

ABSTRACT

Metal matrix composites develop residual strains after consolidation due to the thermal expansion mismatch between the reinforcement fiber and the matrix. X-ray and neutron diffraction measured values for the longitudinal residual stress in the matrix of three titanium MMCs are reported. For thick composites (> 6 plies) the surface stress measured by x-ray diffraction matches that determined by neutron diffraction and therefore represents the stress in the bulk region consisting of the fibers and matrix. For thin sheet composites, the surface values are lower than that in the interior and increase as the outer rows of fibers are approached. While a rationale for this behavior has yet to be developed, accounting for composite thickness is important when using x-ray measured values to validate analytic and finite element calculations of the residual stress state.

INTRODUCTION

The design and application of new composite materials require the development of analytical methods capable of predicting the durability and damage tolerance of these materials when subjected to the mechanical and thermal loads typical of the intended application. This presents a daunting problem if the magnitudes of residual stresses present during loading are unknown. Differences in the coefficients of thermal expansion between the two (or more) constituent phases of a composite material generate thermal mismatch stresses on cooling from fabrication temperatures. Predictions of residual stress distributions by finite element calculations account for various mechanisms of relaxation. thermal mismatch. and transformation strains

during cooling. However, validation of the computed models requires experimental measurements of the residual strains that are not easily accomplished using conventional methods. X-ray diffraction has been used to measure the residual stress parallel to the fiber direction at the surface of the samples, but some ambiguity remains as to whether or not this value characterizes that of the fiber/matrix interior. X-ray and neutron diffraction measurements are compared here to validate the applicability of the surface x-ray measurement to determine the residual stress in continuous fiber composites.

STRAIN MEASUREMENT BY DIFFRACTION

Recent advances in triaxial stress analysis have made it possible to analyze the residual stress state in both the metal and reinforcement phase in continuous fiber and particulate reinforced composites.[1,2] For the latter composite system, the standard biaxial stress analysis procedure cannot be used because the reinforcement produces a normal stress within the penetration depth of the x-rays. For continuous fiber reinforced systems, however, ample matrix exists between the fiber and the surface so that the normal component induced by the fiber is zero near the surface, as shown in two titanium matrix systems reinforced with continuous 145 µm diameter SiC fibers.[3]

One recurring problem with the measurement of residual stress by x-ray diffraction in composites is verifying that surface measurements accurately portray the state of stress in the fiber/matrix region of the interior. We have tried to do this by making measurements as a function of depth into the composite.[3,4] To account for the effects of layer removal in determining the residual stress into the depth of a composite, we considered the continuous fiber metal matrix composites to be a three-layer system comprising two outer layers of homogeneous matrix and an inner core representing the region in which both fibers and matrix are present. The outer layers have a thickness on the order of 100 µm, but may be substantially thicker if extra matrix material is used, for instance to enable subsequent machining of the surface. Previous measurements in a SiC/Ti-25Al-10Nb-3V-1Mo [0]3 (where [0]3 implies three fiber layers in a unidirectional lay-up) system indicated that the axial residual stress increases from the surface to the core region. More recently, similar measurements on SiC/β21S [0]4 showed a gradient, but not on a SiC/Ti-24Al-11Nb [0]6 composite (Fig. 1).[4]

Neutrons can have wavelengths that permit diffraction from crystalline materials but are also neutral particles that penetrate into most materials more effectively than X-rays. Recently several studies have used neutrons to non-destructively measure the strain in metal matrix composites.[5-9] Neutrons enable strain measurements of the average state in the bulk of a material and avoid the uncertainty associated with unrepresentative surface conditions. The neutron studies were conducted at the Manuel Lujan Jr.

Neutron Scattering Center (LANSCE), a spallation neutron source located at Los Alamos National Laboratory. Spallation sources produce pulses of polychromatic neutrons at discrete intervals. The wavelength of a detected neutron can be determined by its time of flight to a detector so that all the neutrons in each pulse contribute to the diffracted spectrum. The recorded spectra include lattice reflections from all the phases present in the specimen. This makes the measurements less vulnerable to texture problems than when using a monochromatic diffractometer.
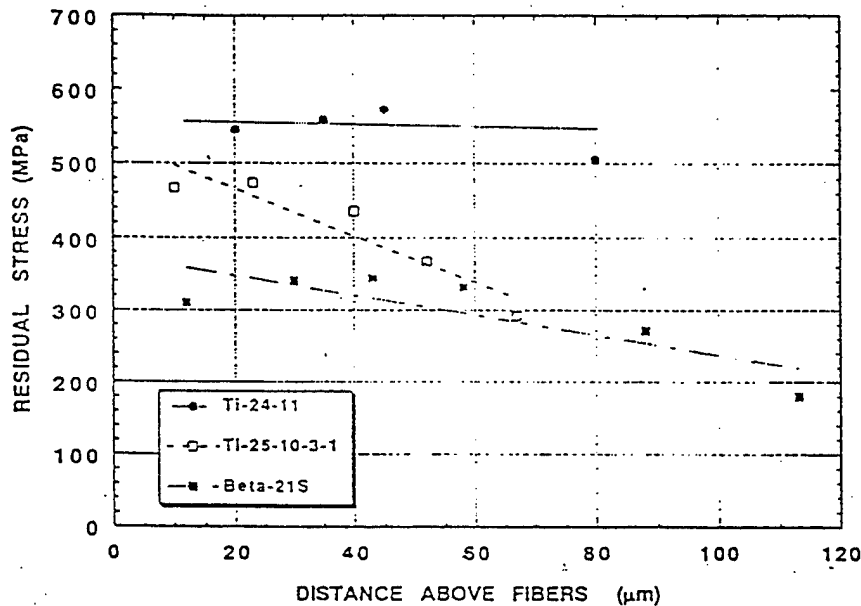
Fig. 1 Depth profile of axial residual stress in titanium matrix composites as measured by x-ray diffraction.

The strains induced in lattice spacings due to residual stress or grain interaction effects are usually in the range of 10^{-5} to 10^{-3}. Thus a diffractometer must have sufficient resolution to resolve changes of that order. At a pulsed source the resolution of an instrument is related to the distance a neutron must travel from the target to the detector (through the specimen). Long flight paths offer better resolution. The Neutron Powder Diffractometer (NPD) at LANSCE lies at the end of a 32 m flight path and can measure strains of $< 3 \times 10^{-5}$.

EXPERIMENTAL PROCEDURE

Measurements were made on four composite samples: SiC/Ti-6Al-4V [0]$_8$; two SiC/Ti-24Al-11Nb [0]$_8$ processed with different SiC mats; and SiC/Ti-25Al-10Nb-3V-1Mo [0]$_3$. The three intermetallic matrix composites had fiber volume fractions of ~ 0.35 while the Ti-6Al-4V composite

fiber volume fraction was only 0.24. All samples were made by the foil/fiber/foil technique with Textron SCS-6 SiC fibers. Equivalent monolithic samples (same composition but not the same thermal-mechanical history) were used to provide an unstrained reference. A small volume (<15 mm³) of SiC fibers was also examined to help identify reflections in the composites because textures of the composite matrices were significantly different from the monolithic materials.

Specimens were placed in the diffractometer with their fiber axes horizontal and at 45° to the neutron beam (Fig 2). Time-of-flight diffraction patterns were recorded in each of the 4 detector banks. The 90° detectors recorded the strain parallel and normal to the fiber axis as shown. The neutron beam was 50 mm high and 10 mm across. No attempt was made to collimate the incident or diffracted neutrons for the bulk measurement. The sampling volume was determined by the intersection of the neutron beam with the specimen. Care was taken to ensure that the center of each specimen was placed accurately at the same position; the concern was that introducing a change in the path length from the diffracting volume to the detectors would alter the time of flight which could be misinterpreted as a strain. Titanium is a relatively poor neutron scatterer and the best results were obtained for specimens with large sampling volumes that were examined for long periods of ~ 6 hours actual beam time.
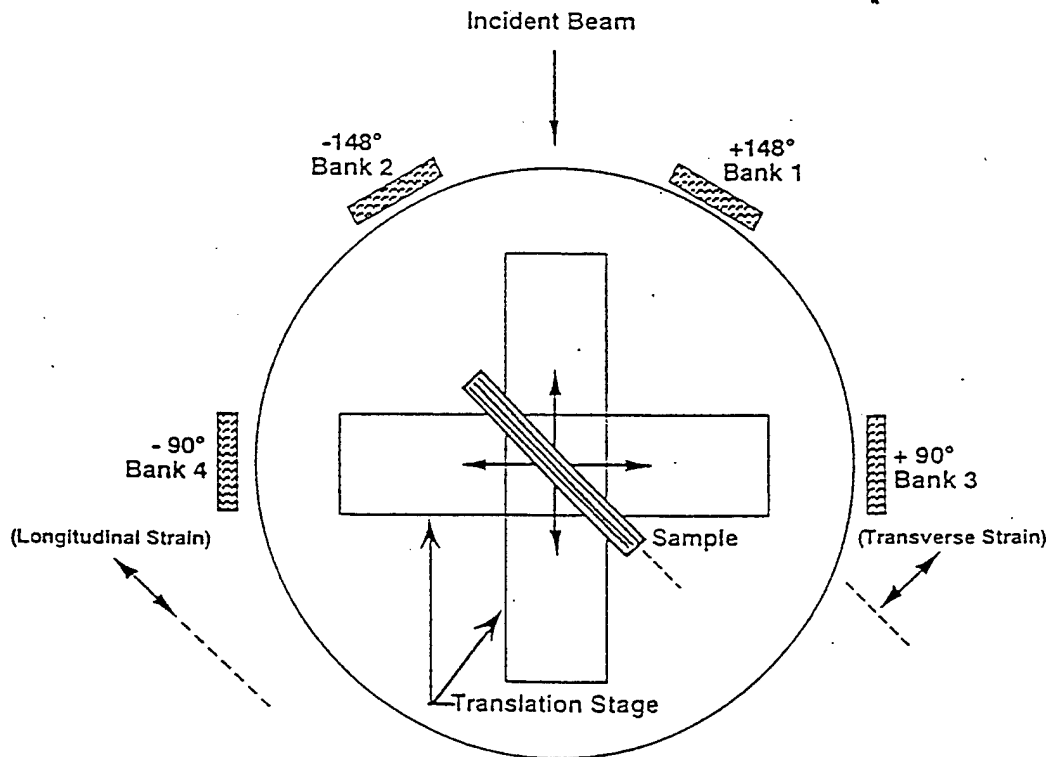
Fig. 2 Arrangement of specimen and detectors at NPD.

298

Bragg reflections were fitted individually and strains were calculated by comparing equivalent reflections between the composite matrix and monolithic alloy. Strong texture variations were noted between the composite specimens and their monolithics. In many cases corresponding reflections disappeared completely or became too weak to fit. In cases where the SiC reflections were close to or overlapped the titanium reflections the silicon carbide spectra were useful for identification purposes.

When using interplanar spacings to calculate strain, the single crystal elastic constants should be used to allow for the respective compliance of different directions. For the Ti-6Al-4V matrix, enough (identified) reflections were recorded to estimate the lattice parameters using a least squares fit (Fig. 3). This averages the strain measured for different reflections but is not rigorous because no attempt was made to control which reflections were used for the fit. However, aside from the (00.2) and (11.0) reflections, the variation is less than 10%.
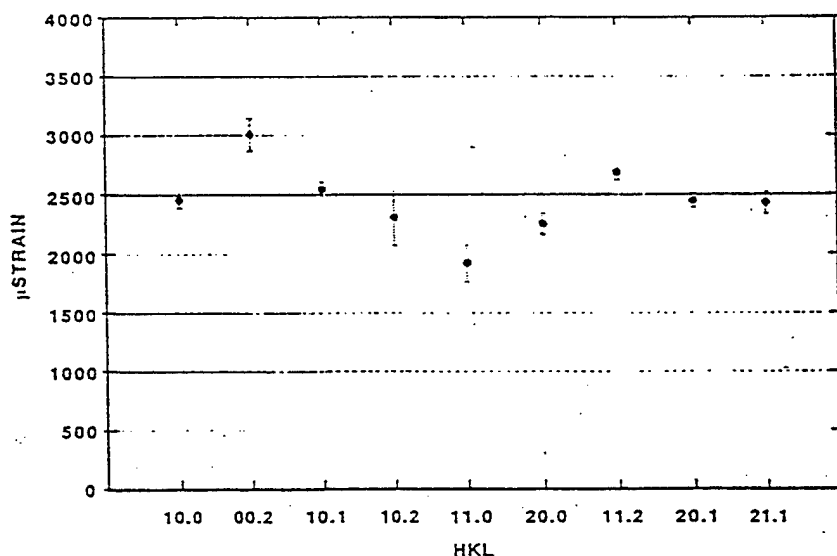
Fig. 3   Measured strain by hkl in the hexagonal α_2 phase of SiC/Ti-6Al-4V $[0]_8$

RESULTS

Neutron and x-ray diffraction results are given in Table 1. Only data parallel to the fibers are discussed since the strain in the axial direction is constant throughout the volume. The error in the neutron results for the SiC/Ti-6Al-4V sample is the standard deviation calculated for the 9 reflections matched between the monolithic strain free standard and the composite

(Fig. 3). For the other two composites, far fewer reflections were matched because of the severe texture. The quoted error for the x-ray strain measurements is that from the error in the linear least squares fit to d vs. $\sin^2\psi$.

Table 1 Comparison of x-ray and neutron measurements

	RESIDUAL STRAIN (x10⁻³)		RESIDUAL STRESS (MPa)	
	X-RAY	NEUTRON	X-RAY	NEUTRON
SiC/Ti-6-4	2.5 ± 0.1	2.5 ± 0.3	257	257
SiC/Ti-24-11	7.2 ± 0.3	5.7 ± 0.2	585	585
SiC/Ti-24-11	7.4 ± 0.3	5.4 ± 0.2	595	555
SiC/Ti-25-10-3-1	3.7 ± 0.4	4.6 ± 0.2	300	475

The x-ray diffraction measured value of the elastic modulus for the SiC/Ti-6Al-4V composite is 103 GPa, but only 81 GPa for the two intermetallic matrices.[3] The bulk elastic constant, more appropriate for the neutron data for which the strain is averaged over many planes, is 103 GPa. The appropriate elastic constants are used to convert the x-ray and neutron measured strains into stress as tabulated in Table 1. The calculated residual stresses are astonishingly close for the Ti-6Al-4V and Ti-24Al-11Nb matrices. Such exact agreement is fortuitous since a simple average of the strain over all hkl planes was used. More rigorous analysis requires the use of the compliance along each direction in calculating an effective residual stress. For the thin 3-ply SiC/Ti-25Al-10Nb-3V-1Mo composite, the neutron measurement of bulk residual stress is considerably higher than the surface measurement made by x-ray diffraction. As deduced from Fig. 1, the x-ray measured residual stress in the fiber/matrix core region (data points near zero distance above fiber) for the Ti-25Al-10Nb-3V-1Mo system agrees quite well with the magnitude of the bulk residual stress measured by neutron diffraction. For this sample, the surface measurement was not a good indicator of the internal matrix residual stress in the fiber direction.

DISCUSSION

Results on the thick (>6 ply) composites agree with previous neutron and x-ray results.[3, 9-11] The neutron data confirm that for thick composites, x-ray surface measurements of residual stress adequately describe the state of longitudinal stress. But for the thin 3 ply SiC/Ti-25Al-10Nb-3V-1Mo composite the longitudinal stress is not uniform through the thickness. This may be a result of the non-symmetric lay-up, or simply due to the very thin nature of the composite. Fortunately, most continuous fiber MMCs have symmetric lay-ups which equal or exceed six plies. Thus x-ray measurements are very useful for validating predictions of the residual stress state in MMCs.

One advantage of using a pulsed source in making these measurements resulted from the strong texture variations that were observed. Reactors provide a high intensity continuous flux of moderated thermal neutrons that are usually monochromated to a single wavelength. Using monochromatic neutrons, the specimen must be reoriented in order to maintain the scattering vector parallel to the fiber axis for different reflections. In view of the variation in texture between the monolithic and composite specimens, considerable manipulation could be required to match peaks of sufficient intensity in both samples. Using the NPD, the lattice spacings can be measured simultaneously on many diffraction peaks and choice of the best peaks from which to calculate strain can be done subsequent to the data collection.

A second advantage of examining the complete diffraction pattern lies in avoiding the risk of selecting a special case reflection. Bragg reflections arise from grains in a specific orientation within the sampling volume. By examining many Bragg reflections a more representative picture of the material deformation response is obtained than if a single family of grains were examined, corresponding to one Bragg reflection. In addition all the lattice reflections are recorded with the same resolution in each spectrum and multiphase materials are conveniently examined.

ACKNOWLEDGMENTS

REFERENCES

1. J.B. Cohen, *The Measurement of Residual Stresses in Composites*, Powder Diffraction, 1: 15-21 (1986).

2. James, M. R., *Residual Stresses in Metal Matrix Composites*, International Conference on Residual Stresses II, eds. G. Beck, S. Denis and A. Simon, Elsevier, pp. 429-35 (1989).

3. B.N. Cox, M. R. James, D.B. Marshall and R.C. Addison, *Determination of Residual Stresses in Thin Sheet Titanium Aluminide Composites*, Metal. Trans. A, 21A:2701-2707 (1990).

4. M.R. James, *Behavior of Residual Stresses During Fatigue of Metal Matrix Composites*, Residual Stresses-3, ed. H. Fujiwara, T. Abe and K. Tanaka, Elsevier, pp. 555-560 (1992). .

5. G.L. Povirk, M.G. Stout, M. Bourke, J.A. Goldstone, A.C. Lawson, M. Lovato, S.R. MacEwen, S.R. Nutt and A. Needlemann, *Mechanically Induced Residual Stresses in Al/SiC Composites*, Scripta Met., 25:1883-1888 (1991).

6. S. Majumdar, J.P. Singh, D. Kupperman and A.D. Krawitz, *Application of Neutron Diffraction to Measure Residual Strains in Various Engineering Composite Materials*, J. Eng. Mat. and Tech., 113:51-59 (1991).

7. D.S. Kupperman, S. Majumdar, J.P. Singh, *Residual Strain in Advanced Composites*, Neutrons News, 2:15-18 (1991).

8. A.J.Allen, M.A.M. Bourke, S. Dawes, M.T. Hutchings, and P. J. Withers, *The Analysis of Internal Strains Measured by Neutron Diffraction in Al-SiC Metal Matrix Composites*, Acta. Metall. & Mater., 40:2361-73 (1992).

9. A. Saigal, D.S. Kupperman, and S. Majumdar, *Residual Strains in Titanium-Matrix Composites*, Mater. Sci. and Engng., A150:59-66 (1992).

10. K.M. Brown, R. Hendricks. and W.D. Brewer, *X-Ray Diffraction Measurements of Residual Stresses in SiC Reinforced Titanium Composites*, in Fundamental Relationships Between Microstructure and Mechanical Properties of MMCs, ed. M.N. Gungor and P.K. Liaw, TMS, pp. 269-86 (1990).

11. N. Jayaraman and P. Rangaswamy, *Residual Stresses in Ti3Al-SCS6 Fiber Reinforced Metal Matrix Composites*, in Proceedings from Titanium Aluminide Composite Workshop, eds. P.R. Smith, S.J. Balsone and T. Nicholas, WL-TR-91-4020, Materials Behavior Branch, Wright Laboratory, WPAFB, pp. 522-31 (1991).

Appendix B

"Analysis of Fiber Debonding and Sliding Experiments in Brittle Matrix Composites,"
Marshall, D.B., Acta Met., 40, No. 3, pp. 427-441, 1992.

ANALYSIS OF FIBER DEBONDING AND SLIDING EXPERIMENTS IN BRITTLE MATRIX COMPOSITES

D. B. MARSHALL

Rockwell International Science Center, 1049 Camino Dos Rios, Thousand Oaks,
CA 91360, U.S.A.

Abstract—The use of a recent analysis of fiber debonding and sliding in brittle matrix composites to interpret the results of fiber pulling and pushing experiments is examined. The stress–displacement relations are expressed in normalized forms that are convenient for curve fitting to experimental measurements and the analysis is extended to provide stress–displacement relations for cyclic loading in addition to monotonic loading. The ranges of some of the important elastic parameters and their influence on the stress–displacement relations are examined. Differences between single and multiple fiber pulling and between pushing and pulling experiments are assessed.

Résumé—On examine l'usage d'une analyse récente de la décohésion et du glissement des fibres dans des composites à matrice fragile afin d'interpréter les résultats d'expériences de traction-compression sur les fibres. Les relations contrainte–déplacement sont exprimées sous des formes normalisées qui conviennent pour faire coïncider les courbes et les mesures expérimentales, et cette analyse est étendue pour obtenir des relations contrainte–déplacement dans le cas d'une charge cyclique ajoutée à la charge monotone. On étude le domaine de variation de quelques paramètres élastiques importants, et leur influence sur les relations contrainte–déplacement. On met en évidence des différences entre les expériences de traction sur une ou plusieurs fibres, et entre les expériences de compression et de traction.

Zusammenfassung—Es wird untersucht, inwieweit eine kürzlich entwickelte Analyse der Ablösung und des Gleitens von Fasern in Verbundwerkstoffen mit spröder Matrix auf Ergebnisse von Experimenten des Faserausziehens und -einstoßens angewendet werden kann. Die Spannungs–Dehnungsbeziehungen werden in normalisierter Form dargestellt, weil diese günstig für die Kurvenanpassung der experimentellen Messungen sind, Die Analyse wird erweitert, um zusätzlich zu den Spannungs–Dehnungsbeziehungen für monotone Belastung solche für zyklische Belastung zu erhalten. Der Bereich einiger wichtiger elastischer Parameter und deren Einfluß auf die Spannungs–Dehnungsbeziehungen werden untersucht. Die Unterschiede zwischen Einzelfaser- und Vielfashfaserausziehen und zwischen Zug- und Druckexperimenten werden behandelt.

1. INTRODUCTION

Techniques based on the pushing and pulling of fibers have been developed recently for measuring mechanical properties of interfaces in ceramic and intermetallic matrix composites [1–18]. A wide variety of specimen and loading configurations have been used, including single or multiple fibers and very thick or thin specimens. The most sensitive of these experiments provide continuous measurements of the applied force and the relative sliding displacements of the fiber and matrix, as debonding and sliding progress stably along the fiber [2–7]. Calculation of interfacial properties, such as debond energy and frictional sliding resistance, from these measurements relies on curve fitting with theoretical predictions derived from micromechanics modeling of the debonding and sliding process.

Most analyses of fiber sliding have been based on shear-lag models with various degrees of approximation. The simplest models assume that sliding along a debonded interface is resisted by a constant shear stress τ, an approximation that turns out to be remarkably good for many experiments [2–7]. This model has also been extended to account for the effects of Mode II fracture energy associated with the tip of the debond crack and axial residual stress in the fiber [6]. Other models have been suggested based on a Coulomb friction law governing the sliding resistance, but not accounting for the influence of axial residual stress in the fibers (which we shall show later has a dominant effect on the response) [19, 20]. Three recent analyses have accounted for both axial and radial residual stresses with a Coulomb friction law, one by Hutchinson ad Jensen [21] for mechanically loaded fibers, another by Cox [22] for thermally loaded fibers (i.e. sliding that occurs near a free surface during thermal cycling, as a result of a mismatch in thermal expansion coefficients of the fibers and matrix) and the third by Kerans and Parthasarathy [23] for the special case of a single isotropic, mechanically loaded fiber in an infinite matrix.

Exact numerical results, based on a full elasticity solution for the matrix, have been obtained recently by Freund [24] for the problem of complete sliding of

a finite, unbonded fiber along a cylindrical hole in an infinite matrix. Direct comparison of stress distributions in the fiber with those of the Lamé solution used by Hutchinson and Jensen [21] indicated good agreement over a wide range of relative elastic stiffness values. Numerical solutions and approximate analytical results have also been given by Sigl and Evans [25] for partial debonding and sliding. Another analytical approach, which is approximate and which also requires numerical solutions to obtain slip lengths and displacements, has been used by McCartney [26] to analyze a variety of fiber sliding problems. However, for comparison with fiber sliding experiments, the explicit analytical results of Hutchinson and Jensen [21] are especially convenient, as well as being more general than most prior work in the treatment of boundary conditions, debonding, and anisotropy.

The purpose of this paper is to examine the use of Hutchinson and Jensen's analysis to deduce interfacial properties from experimental measurements of fiber sliding. Their analysis provides explicit relations for the relative sliding displacements as a function of monotonically increasing applied load. The model will be extended to provide similar relations for displacements during an unload/reload cycle. Such measurements provide valuable additonal information for deducing interfacial properties, since the displacements are independent of the debond energy and the initial axial residual stress in the fibers.

Although the analysis of Hutchinson and Jensen provides concise and convenient expressions for stresses, strains, and debond energies, the displacement equations contain a large number of parameters which characterize the elastic properties of the fibers and matrix, residual misfit strains, anisotropy of the fibers, volume fraction of fibers, friction coefficient (or, in the case of constant sliding resistance, a frictional stress) and interfacial debond energy. The equations will be expressed in a normalized form that reduces the number of explicit parameters to three, in addition to load and displacement. One of these parameters is a combination of elastic constants; another, S_{R0}, characterizes the initial residual stresses; and the third parameter, Γ, characterizes the Mode II debond energy at the crack tip (S_{R0} and Γ are also dependent on elastic constants). The influence of each of these parameters on the load–displacement curves will be examined. The ranges of some of the important elastic parameters in typical composites will be explored, and differences between single fiber and multiple fiber pulling will be assessed.

2. REVIEW OF MODEL OF HUTCHINSON AND JENSEN

The concentric cylinder model depicted in Fig. 1(a) is taken to represent a composite reinforced with a volume fraction $f = R_f/R$ of aligned continuous fibers. The analysis is restricted to composites with a residual compressive stress acting across the fiber–matrix interface, as is usually the case with intermetallic matrix composites and sometimes the case with ceramic matrix composites. Pulling (or pushing) on the fiber at the end of the cylinder (which corresponds to a sectioned surface or a crack surface of the composite) causes a debond crack to grow along the fiber–matrix interface. The length of the debond is dictated by a Mode II fracture energy, G_C, at the crack tip and frictional sliding over the debonded surfaces. Two types of sliding resistance will be considered; (1) a constant frictional stress, τ_0, between the fibers and matrix over all regions where sliding occurs, and (2) Coulomb friction, with the frictional stress being proportional to the normal stress, σ_r, (which is negative) across the sliding interface

$$\tau = \mu\sigma_r \qquad (1)$$

where the friction coefficient, μ, is taken as constant.

The frictional sliding causes relative displacements of the fiber and matrix at the end of the cylinder ($z = l$). These displacements are measured in push/pull experiments and are related to the opening displacements of a bridged crack in the composite. The displacements are given by integrals of the axial strains in the fiber and matrix. The analysis of Hutchinson and Jensen [21] provides solutions for the axial strains in terms of frictional properties, debond energy and other relevant parameters. Most of the discussion here will refer explicitly to fiber pulling, although the analysis applies also to pushing, and specific relations for pushing will be presented in Section 6.

The notation of Hutchinson and Jensen [21] will be used as far as possible, although some new normalizing parameters will be defined in later sections. The matrix is taken as elastic and isotropic, with Young's modulus E_m and Poisson's ratio v_m. The fiber is taken to be transversely isotropic, with Young's moduli E_f and E_r, in the axial and transverse directions, and Poisson's ratios v_f and v_r governing transverse Poisson's strains due to axial and transverse loading respectively.[†] The properties v_r and E_r enter the analysis via the parameter $\zeta_f \equiv (1 - v_r)E_f/E_r$. Here we define $\xi_f \equiv \zeta_f/(1 - v_f)$, so that for isotropic fibers $\xi_f = 1$. To maintain analytical tractability, the analysis of unload/reload cycles will be restricted to cases with either $v_f = v_m$ or $f = 0$. The elastic misfit strains between the fiber and matrix are ϵ_r^T and ϵ_z^T in the radial and axial directions, characterized in Ref. [21] by $\epsilon^T \equiv \epsilon_r^T$ and $\lambda \equiv \epsilon_r^T/\epsilon_z^T$. As discussed in Ref. [21], the misfit could arise from mismatch of thermal

---

†For a transversely isotropic material loaded in the axial or transverse directions there are three Poisson's ratios, v_{zr}, v_{zr} and v_{rr}, where v_{ij} refers to strain in direction i due to stress in direction j. However, since v_{rz} and v_{zr} are related by $v_{zr} = v_{rz}E_r/E_r$, only two of the Poisson's ratios, $v_{rz} \equiv v_f$ and $v_{rr} \equiv v_r$, in addition to the Young's moduli E_f and E_r, are needed to specify the elastic response.

Fig. 1. (a) Composite cylinder model used for analysis. (b) Axial stresses in fiber during initial loading.

expansion coefficients, or from irregularities of the fiber surface. For the former, ϵ^T and λ are constant under isothermal conditions, whereas the misfit due to nonuniformity would be dependent upon the amount of sliding, and thus the applied load and position along the fiber. Preliminary analyses of misfit strains due to nonuniformity have been done recently by several authors [23, 27] and could possibly be incorporated in the present analysis. However, this is not attempted here. If the residual stresses cause yielding of the matrix during cooling from the fabrication temperature, both ϵ^T and λ may differ from values calculated for a purely elastic response during cooling.

Stresses and strains in any section transverse to the z axis were evaluated on the basis of the Lamé solution, an approximation that is valid if the axial stresses vary slowly over distances comparable to the fiber radius. This condition is satisfied if τ is small compared with the axial stress in the fiber, σ_f. Two types of boundary conditions on the outer cylindrical

surface were considered: Type I has zero normal and shear tractions, whereas Type II also has zero shear tractions, but has radial displacement, u_r, constrained to be the same as its value far ahead of the debond crack. Type I conditions are appropriate for single fiber pulling or pushing experiments and in general at positions well ahead of the debond crack. Type II conditions are appropriate over the debonded region of a composite in which all fibers are pulled equally (such as bridging fibers within a crack), provided the slip length is small compared with the specimen width. Type II conditions were also used by Cox [22] in analyzing sliding of fibers near a free surface during thermal cycling, whereas earlier analyses used only Type I boundary conditions. We will see later that large differences in load–displacement relations can result from these different boundary conditions.

The axial stresses, σ_f, in the fiber during initial loading are shown schematically in Fig. 1(b). Well ahead of the debonded region the stresses and strains

306

are constant and given by the Lamé problem with Type I boundary conditions, as well as the conditions that the axial strains ϵ_f and ϵ_m in the fiber and matrix be equal and the normal stresses and displacements at the fiber–matrix interface be continuous. With the superscript (+) denoting positions well ahead of the debond, the subscript r denoting radial stresses, strains and displacements at the interface, and the subscripts f and m denoting axial quantities in the fiber and matrix, the stresses and strains† are given by

$$\sigma_f^+ = a_1 f \sigma_a - a_2 E_m \epsilon^T \tag{2a}$$

$$\sigma_r^+ = a_3 f \sigma_a - a_4 E_m \epsilon^T \tag{2b}$$

$$\epsilon_f^+ = \epsilon_m^+ = a_5 f \sigma_a / E_m + a_6 \epsilon^T \tag{2c}$$

where the a's are nondimensional functions of f, E_f/E_m, ν_f, ν_f/ν_m, ξ_f, and λ, given in Ref. [21], and σ_a is the axial stress in the loaded end of the fiber (for convenience in later analysis of single fiber loading, corresponding to $f = 0$, this definition of loading parameter differs slightly from that in Ref. [21], where the average stress $\bar{\sigma} = f \sigma_a$ is used). Behind the debond crack tip the *changes* in stresses and strains relative to their values far ahead of the crack (i.e. $\Delta\sigma_f = \sigma_f - \sigma_f^+$, $\Delta\epsilon_f = \epsilon_f - \epsilon_f^+$, etc.) are given by the Lamé problem without mismatch strain and, since there is relative sliding, with $\Delta\epsilon_f \neq \Delta\epsilon_m$. With continuity of $\Delta\sigma_r$ and Δu_r across the interface, and the equilibrium requirement $f\Delta\sigma_f + (1 - f) \Delta\sigma_m = 0$, the stresses and strains may be written as

$$\Delta\sigma_m = \left(\frac{f}{1-f}\right)\Delta\sigma_f \tag{3a}$$

$$\Delta\sigma_r = b_1\Delta\sigma_f \tag{3b}$$

$$\Delta\epsilon_f = b_2\Delta\sigma_f/E_m \tag{3c}$$

$$\Delta\epsilon_m = -b_3\Delta\sigma_f/E_m \tag{3d}$$

where the b's are another set of nondimensional functions of the same parameters as the a's (with the exception of λ) given in Ref. [21]. There are two sets of b's corresponding to Type I and Type II boundary conditions.

There is a jump in the fiber stress from just behind to well ahead of the debond crack tip, which is dependent upon the Mode II fracture energy, G_c. This relation is given approximately by [21]

$$\gamma \equiv \sigma_f^- - \sigma_f^+ = \frac{(1-f)}{fc_1c_3}\left(\frac{E_m G_c}{R_f}\right)^{1/2} \tag{4}$$

where

$$c_1 = (1 - fa_1)(b_2 + b_3)^{1/2}/(2f) \tag{5a}$$

$$c_3 = (1 - f)/(1 - fa_1) \tag{5b}$$

and the superscript (−) denotes quantities just behind the crack tip. Comparison with full numer-

ical solutions in Ref. [21] shows that equation (4) is a good approximation if the sliding distance exceeds 2–3 times the fiber radius. The error is shown to be $\sim\tau/\sigma_f^-$, and thus becomes less significant as the applied load increases.

The axial stresses in the fiber over the debonded region are governed by the equilibrium condition

$$\frac{d\sigma_f}{dz} = \frac{-2\tau}{R_f} \tag{6}$$

and the boundary conditions at $z = 0$ and l. For constant frictional stress, σ_f increases linearly as shown in Fig. 1(b), whereas for Coulomb friction the increase is nonlinear. The curvature is determined by the parameter b_1 in equation (3), which relates changes in normal interfacial stress to changes in axial stress. Hutchinson and Jensen [21] pointed out that b_1 can be either positive or negative. For Type I boundary conditions b_1 is always positive, so that the compressive interfacial stress decreases in magnitude as σ_f increases, corresponding to the commonly perceived effect of Poisson's contraction, and leading to the curvature shown in Fig. 1(b). However, for Type II boundary conditions, b_1 can be negative for certain combinations of elastic properties. Physically this difference arises because under Type I conditions the relaxation of axial *tension* in the matrix during sliding causes transverse *expansion* of the outer boundary of the cylinder, so that in order to impose Type II conditions with $u_r = 0$ at the outer boundary, compressive normal tractions must be applied to the outer boundary. If the stress at the fiber–matrix interface due to the tractions exceeds the reduction in stress due to Poisson's contraction of the fiber, then b_1 is negative. In this case the curvature of the relation $\sigma_f(z)$ is opposite to that shown in Fig. 1(b) (i.e. increasing slope with increasing z).

To illustrate the range of composite properties for which b_1 is negative under Type II boundary conditions, the expression given by Hutchinson and Jensen [21] is plotted in Fig. 2 as a function of E_f/E_m for selected values of the other parameters (f, ν_f, ν_m/ν_f, and ξ_f; note that b_1 is independent of λ). It is clear that large values of f, E_f/E_m, ν_f, and ν_m/ν_f tend to make b_1 negative. Moreover, for most composites of practical interest, b_1 is in fact negative.

Two displacements are of interest in the following sections. The relative displacement of the fiber and matrix at $z = l$ (which corresponds to the measurements obtained in fiber pulling/pushing experiments) is given by

$$\delta = \int_0^l (\epsilon_f - \epsilon_m)\, dz = \frac{b_2 + b_3}{E_m}\int_0^l \Delta\sigma_f\, dz \tag{7}$$

and is, therefore, proportional to the shaded area in Fig. 1(b). The displacement that is used as the crack opening in continuum models of crack bridging is the

---

†Strains in both the fibers, ϵ_f^+, and matrix, ϵ_m^+ are measured relative to the unstressed state of the matrix.

additional fiber displacement due directly to debonding and sliding [28–30] given by

$$\Delta = \int_0^l (\epsilon_f - \epsilon_f^+) \, dz = \frac{b_2}{E_m} \int_0^l \Delta\sigma_f \, dz \ . \qquad (8a)$$

Therefore, the displacements δ and Δ are related simply by

$$\Delta = \left(\frac{b_2}{b_2 + b_3}\right)\delta. \qquad (8b)$$

Equation (8b) relates the displacements measured in a *multiple* fiber pulling experiment directly to the crack opening in bridging models for given fiber stress, σ_a. However, the relation is less direct for single fiber pulling experiments, because in that case, δ is evaluated using Type I boundary conditions whereas δ for the multiple fiber pulling (and crack opening) is evaluated with Type II boundary conditions over the debonded region.

3. DISPLACEMENTS DURING FIBER PULLING: COULOMB FRICTION

In this section the relative displacements, δ, of the fiber and matrix at $z = l$ are evaluated as the stress σ_a applied to the end of the fiber is increased continuously from zero to a peak value σ_p (initial loading), decreased to zero, and then increased again to σ_p. During initial loading, debonding and sliding progress stably along the fiber/matrix interface, whereas during unloading reverse sliding occurs. The unload/reload cycle exhibits hysteresis due to the frictional response of the interface. The fiber strength is assumed to be larger than σ_p so that failure of the fiber does not occur. The peak stress is also restricted to be smaller than the limiting value at which the normal interfacial stress decreases to zero; at this limit the debond extends along the entire fiber, with a constant length zone of contact behind the debond tip, as discussed by Hutchinson and Jensen [21].

3.1. Initial loading

The displacement, δ, during initial loading is obtained by integration of equation (7), after first evaluating the axial stresses in the fiber over the debonded region by integration of equation (6), with τ given by equations (1), (2b) and (3b), and the boundary conditions $\sigma_f = \sigma_r^-$ at $z = 0$ and $\sigma_f = \sigma_a$ at $z = l$. Details are given in the Appendix. The displacement and the corresponding debond length can be conveniently expressed as follows, in terms of dimensionless parameters normalized by the peak value of the applied stress, σ_p

$$\delta/\delta^* = -AS_{R0}\ln\left[\frac{S_{R0} - S_a}{S_{R0} - \Gamma'}\right] + \Gamma' - S_a \qquad (9)$$

and

$$l/R_f = \left(\frac{1}{2\mu}\right)\ln\left[\frac{S_{R0} - S_a}{S_{R0} - \Gamma'}\right] \qquad (10)$$

where

$$S_a = \sigma_a/\sigma_p \qquad (11a)$$

$$S_{R0} = -\frac{\sigma_{R0}}{(1 - a_1 f)\sigma_p} \qquad (11b)$$

$$\Gamma' = \frac{\Gamma}{(1 - a_1 f)\sigma_p}, \Gamma = \gamma + \sigma_{f0}^+ \qquad (11c)$$

$$\delta^* = \left[\frac{(b_2 + b_3)(1 - a_1 f)}{2b_1}\right]\left(\frac{\sigma_p R_f}{\mu E_m}\right) \qquad (11d)$$

$$A = \left(1 - \frac{a_2 b_1}{a_4}\right)^{-1} \qquad (11e)$$

$$\sigma_{R0} = \left(\frac{a_4}{a_2 b_1} - 1\right)\sigma_{f0}^+ = \sigma_{f0}^+/(A - 1) \qquad (11f)$$

$$\sigma_{f0}^+ = -a_2 E_m \epsilon^T. \qquad (11g)$$

Thus equation (9) provides a relation between displacement δ and applied load, S_a, with four other parameters which characterize the frictional properties of the interface (δ^*), the residual stresses (S_{R0}), the interfacial debond energy (Γ'), and the elastic properties and misfit strain anisotropy of the fiber and matrix (A). Equation (9) requires $(a_3 f/b_1) = 0$. This condition is satisfied for single fiber pulling experiments (i.e. $f = 0$), or for $v_f = v_m$ (for which $a_3 = 0$) with Type I boundary conditions (for which b_1 is always finite). However, for multiple fiber pulling with Type II boundary conditions, certain combinations of elastic properties give $b_1 = 0$ (see Fig. 2), for which $(a_3 f/b_1)$ is singular. This limit results in a constant frictional stress along the debonded interface (see Section 4). For values of v_f/v_m close to unity, the transition between very small values of $(a_1 f/b_1)$ and the singular values occurs over small ranges of the other elastic parameters. Therefore attention hereunder will be restricted to the case $(a_3 f/b_1) \approx 0$. The full expression for non-zero values of this parameter, given in equation (A7), is equivalent to equations (47) and (49) of Ref. [21]. For the special case $f = 0$ with an isotropic fiber and isotropic misfit strains, equation (9) is equivalent to the expression derived by Kerans and Parthasarathy [23].

The dependence of the parameter A on E_f/E_m for various values of λ, f, and v is shown in Fig. 3 for both multiple fiber pulling or pushing (Type II boundary conditions) and for single fiber experiments in which one fiber is pulled or pushed from a composite containing many fibers (in this case $f = 0$ for evaluation of b_1, but $f \neq 0$ for evaluation of a_2 and a_4). Since

$$\left|\frac{a_2 b_1}{a_4}\right| < 1$$

for all reasonable composite properties, positive values of b_1 give $A > 1$ and negative values of b_1 give $0 < A < 1$.

(a)

(b)

(c)

(d)
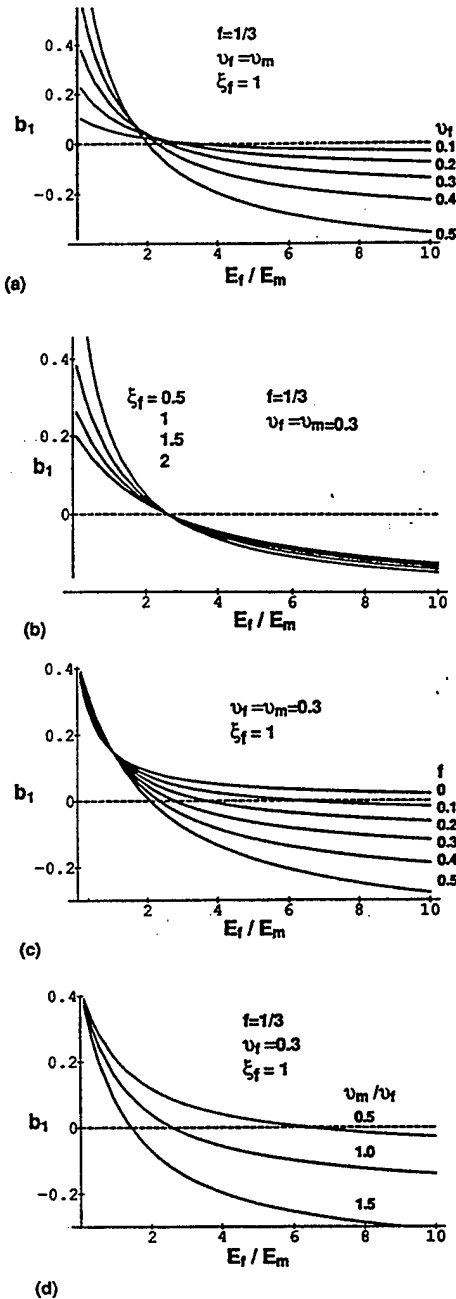
Fig. 2. Dependence of the parameter b_1 on properties of fiber and matrix, for Type II boundary conditions.

values being defined by the mismatch strain anisotropy, λ, through its influence on the parameter A. Then the dimensionless parameter S_{R0} represents the radial residual stress and $S_{f0} = (A - 1)S_{R0}$ represents the axial residual stress. The parameter Γ' relates directly to the applied stress required for initiation of debonding. To cause debonding, the applied stress must exceed the axial stress ahead of the debond, plus the stress jump at the debond tip, i.e. $\sigma_a > \sigma_f^+ + \gamma$, or with, equations (2a) and (11c), $\sigma_a(1 - a_1 f) > \Gamma$. Therefore, the condition for debonding becomes $S_a = \Gamma'$.

Spontaneous debonding and sliding (i.e. at $\sigma_a = 0$) can occur during formation of the free surface at $z = l$ if $\Gamma' \leqslant 0$. For the modeling of bridged cracks, the displacement due to this spontaneous debonding becomes part of the crack opening displacement and equation (9) is not affected. However, in fiber pulling and pushing experiments, the displacements are measured relative to the spontaneously debonded condition, whereupon the displacement is reduced by an amount $\delta(0)$ given by equation (9) at $\sigma_a = 0$. Therefore the measured

(a)

(b)

(c)
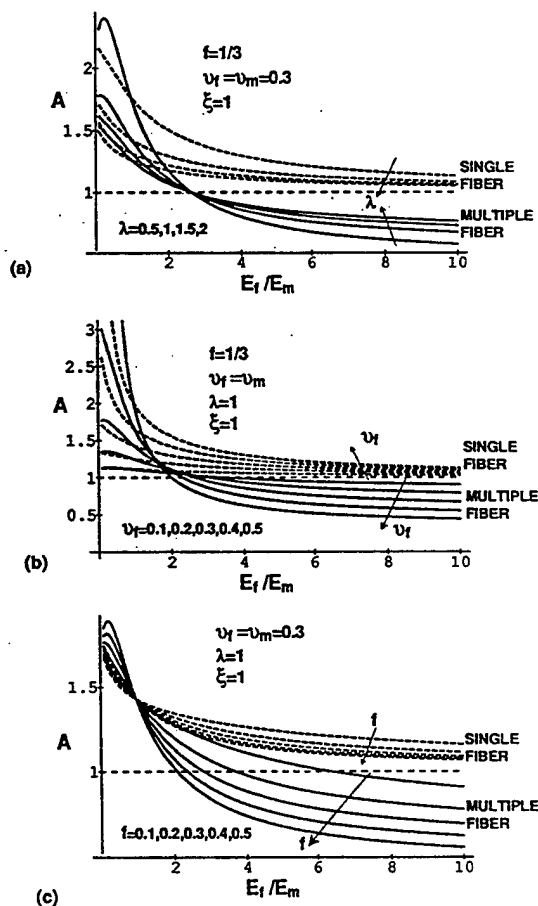
Fig. 3. Dependence of the parameter A on properties of fiber and matrix. Multiple fiber pulling or pushing corresponds to Type II boundary conditions on outer surface of cylinder. Single fiber results correspond to one fiber being pulled or pushed from a composite.

The other parameters may be interpreted physically as follows. The stress σ_{f0}^+ is the residual axial stress in the fiber in the absence of applied load and debonding, as indicated in Fig. 1(b). The residual stress parameter σ_{R0}, while related to σ_{f0}^+ by equation (11f), can also be written as $\sigma_{R0} = \sigma_{r0}/b_1$, where σ_{r0} is the normal interfacial stress when the axial stress in the fiber is zero. Note that, since σ_{r0} must be negative, σ_{R0} is positive for $b_1 < 0$ and negative for $b_1 > 0$. The axial and radial residual stresses could be treated as independent parameters, their relative

309

displacement is

$$\frac{\delta - \delta(0)}{\delta^*} = -A S_{R0} \ln\left[\frac{S_{R0} - S_a}{S_{R0}}\right] - S_a,$$

$$(\Gamma' < 0). \quad (12)$$

In this case there is no effect of the debond energy G_c on the stress–displacement measurements; conversely, under this condition such measurements cannot be used to evaluate G_c, although they do provide an upper bound for the debond energy, defined by the condition $\Gamma' < 0$, i.e. $\gamma < |\sigma_{f0}^+|$.

The range of applied loads for which the preceding relations hold is limited by the requirement that the normal interfacial stress be compressive. This condition is violated for tensile applied loads above a critical value when b_1 is positive, and for compressive loads above critical value for negative values of b_1. At these critical loads the debond extends along the entire length of the fiber with a constant limited zone of contact behind the debond tip [21, 26]. Equation (9) approaches this limit asymptotically at $S_a = S_{R0}$. For a given peak load, the interfacial stress is smallest at $z = l$, and can be written

$$\sigma_{rs} = b_1 \sigma_p (1 - a_1 f)(1 - S_{R0}). \quad (13)$$

If the product $(b_1 \sigma_p)$ is positive (i.e. fiber pulling with $b_1 > 0$ or fiber pushing with $b_1 < 0$), S_{R0} is positive (S_{R0} can be written as $S_{R0} = -\sigma_{r0}/[(1 - a_1 f)b_1 \sigma_p]$). Therefore, σ_{rs} is compressive only for $S_{R0} > 1$. For negative values of $(b_1 \sigma_p)$, S_{R0} is negative and σ_{rs} is always compressive.

For the purpose of curve fitting to experimental push/pull experiments, and for comparison with unload/reload cycles, it is convenient to refer the displacements to the peak load displacement, δ_p, given by equation (9) at $\sigma_a = \sigma_p$ (i.e. $S_a = 1$)

$$\frac{\delta_p - \delta}{\delta^*} = -A S_{R0} \ln\left[\frac{S_{R0} - 1}{S_{R0} - S_a}\right] + S_a - 1. \quad (14)$$

In this form a single curve can be plotted, as shown in Fig. 4, for all values of Γ' and given A, S_{R0} and δ^*, with Γ' simply affecting the position of the displacement origin, corresponding to debond initiation at $S_a = \Gamma'$. Moreover, with Γ' evaluated from the intercept at $\delta = 0$, S_{R0} can be determined from a single-parameter curve fit to the measured stresses and displacements, normalized to their maximum values, provided the value of A is known independently. An example of a set of curves for $\Gamma' \leqslant 0$ and $A = 1.14$ (corresponding to the properties of a Ti_3Al/SiC composite studied in Ref. [7]) and various values of S_{R0} is shown in Fig. 5.

3.2. Unload/reload cycle

The axial fiber stresses during unloading, after loading initially to a peak load σ_p, are shown schematically in Fig. 6(a). Reverse sliding occurs
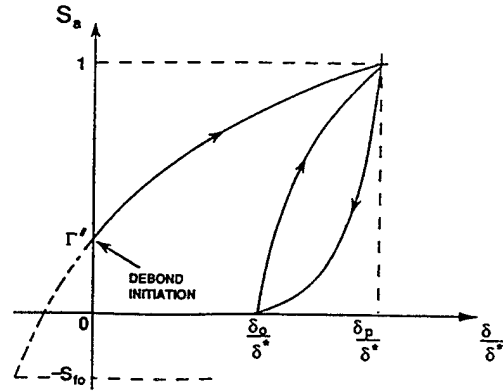
Fig. 4. Schematic representation of stress–displacement relation during initial loading, unloading and reloading.

within a distance s of the end of the cylinder and the *recovery* in displacement is given by

$$\delta_p - \delta = \frac{b_2 + b_3}{E_m} \int_{l-s}^{l} (\Delta\sigma_{fp} - \Delta\sigma_f)\,dz \quad (15)$$

where the subscript p is used to denote quantities evaluated at the maximum load of the initial loading segment.

Following an analysis similar to that of the initial loading (see Appendix), the displacement becomes

$$\frac{\delta_p - \delta}{\delta^*} = (S_{R0} - S_a)\left[1 - \sqrt{\frac{S_{R0} - 1}{S_{R0} - S_a}}\right]^2. \quad (16)$$

Equation (16) requires $(a_2 a_3 f / a_4) \ll 1$. This parameter is zero for either $v_f = v_m$ or $f = 0$, and is very small for all other likely composite properties (see Appendix). Also, equation (16) holds only for $s < l_p$. If Γ' is larger than a critical value defined in Fig. A1 (approximately $\Gamma' \geqslant 0.5$), the reverse slip region reaches the end of the debond before unloading is complete. The displacements under this condition are evaluated in the Appendix. However, this complication can be avoided in principle by the choice of a sufficiently large maximum load for the initial loading cycle.
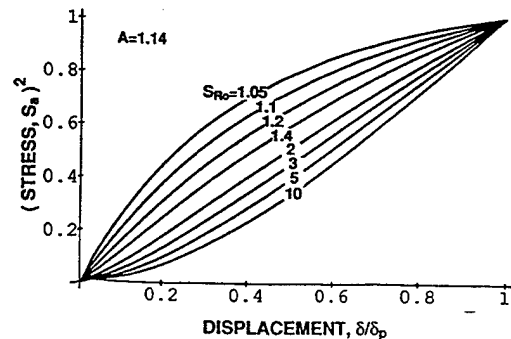
Fig. 5. Stress–displacement relation during initial loading, for $A = 1.14$ and various values of residual stress parameter S_{R0}. Coulomb friction model.

The axial fiber stresses during reloading back to $\sigma_a = \sigma_p$ are shown schematically in Fig. 6(b). The displacements are given by

$$\delta - \delta_0 = \frac{b_2 + b_3}{E_m} \int_{l-t}^{l} (\Delta\sigma_f - \Delta\sigma_{f0}) \, dz \qquad (17)$$

where the subscript 0 denotes quantities evaluated at the end of the previous unloading half cycle. The displacement, expressed relative to the peak load displacement, becomes (Appendix)

$$\frac{\delta_p - \delta}{\delta*} = \frac{\delta_p - \delta_0}{\delta*}$$

$$-(S_{R0} - S_a)\left[1 - \sqrt{\frac{S_{R0}}{S_{R0} - S_a}}\right]^2. \qquad (18)$$

These relations between the normalized displacements and stresses during unloading and reloading contain only one other parameter, S_{R0}, which, as mentioned earlier, characterizes the residual stress normal to the interface. Therefore the data from unload–reload cycles are useful supplements to the initial loading data for evaluating parameters. The
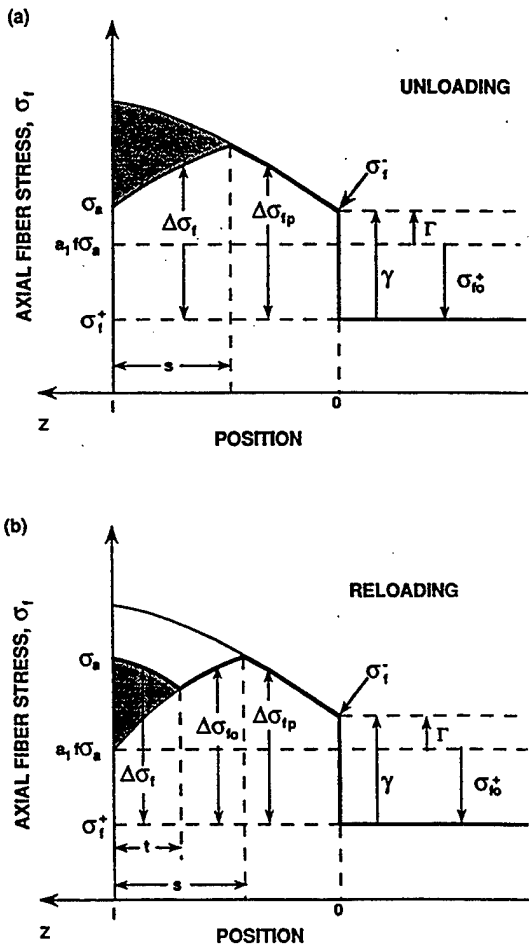
Fig. 7. Stress–displacement relation during an unload/reload cycle for $A = 1.14$ and various values of residual stress parameter, S_{R0}. Coulomb friction model.

unload–reload curves are plotted in Fig. 7 for various values of S_{R0}.

It is useful to identify two distinct effects of residual stresses on the *changes* in axial fiber stress during sliding and hence on the displacements. One enters via the normal interfacial stress, which determines the slope of $\Delta\sigma_f(z)$ (Figs 1 and 6). The other is the direct influence of the residual axial stress in the fiber, σ_{f0}^+, which adds a constant value to $\Delta\sigma_f(z)$ and affects the debond length, l, during initial sliding. During unloading and reloading, the changes in displacement are determined exclusively by the first of these effects, whereas the displacements during initial loading are affected most strongly by the influence of σ_{f0}^+. Consequently, the ratio of displacements δ_p and $(\delta_p - \delta_0)$ resulting from initial loading and complete unloading provides a sensitive measure of the magnitude of the residual stress parameter S_{R0}, as shown in Fig. 8. Moreover, the role of the *axial* component of residual stress can be seen from Fig. 8 by recognizing that the curve for $A = 1$ corresponds to zero axial residual stress [$a_2 = 0$ in equation (2a) and equation (11e)]. Since $(\delta_p - \delta_0)$ is independent of A, the curves for various values of A in Fig. 8 provide a direct comparison of the relative displacements during initial loading with and without axial residual stress. We note also that the result of Gao *et al.* [19] [their equation (2.28)], who analyzed initial fiber sliding with Type I boundary conditions and without axial residual stress

Fig. 6. Axial stresses in fiber during (a) unloading and (b) reloading, after loading initially to a peak stress σ_p. Change in displacement is proportional to area of shaded region. Coulomb friction model.
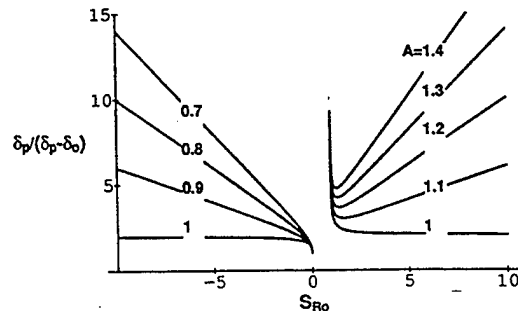
Fig. 8. Ratio of the displacement δ_p caused by initial loading to stress σ_p, to the displacement $(\delta_p - \delta_0)$ recovered during complete unloading. Coulomb friction model.

311

in the fiber, is equivalent, with $v_f = v_m$ or $f = 0$, to equation (9) with $A = 1$.

4. DISPLACEMENTS DURING FIBER PULLING: CONSTANT FRICTION

With the frictional stress taken as a constant, τ_0, the change in axial fiber stress, $\Delta\sigma_f(z)$, during initial monotonic loading increases linearly along the sliding region as shown in Fig. 1. The displacement, δ, from equation (7) can be written immediately [from inspection of the areas in Fig. 1, with equation (6)] as

$$\delta = \frac{(b_2 + b_3)R_f}{4\tau_0 E_m}[(\sigma_a - \sigma_f^+)^2 - \gamma^2] \qquad (19)$$

which is equivalent to equation (37) of Ref. [21]. Equation (19) is also obtained from the Coulomb friction result, equation (A7), in the limit $b_1 \to 0$, which corresponds to the normal interfacial stress being independent of changes in axial stress. With the definitions of equation (11), equation (19) can be written in terms of the same normalized parameters used for the Coulomb friction model

$$\delta/\delta' = S_a^2 + 2(A - 1)S_{R0}S_a - \Gamma'^2$$
$$- 2(A - 1)S_{R0}\Gamma' \qquad (20)$$

where

$$\delta' = \left[\frac{(b_2 + b_3)(1 - a_1 f)^2}{4}\right]\left[\frac{R_f\sigma_p^2}{\tau_0 E_m}\right]. \qquad (21)$$

The parameter δ' is related to the corresponding parameter, δ^*, that normalizes the displacements in the Coulomb friction model by

$$\delta'/\delta^* = \frac{\mu b_1(1 - a_1 f)\sigma_p}{2\tau_0}. \qquad (22)$$

As in the case of the Coulomb friction model, spontaneous debonding and sliding occur at a free surface if $\Gamma' \leq 0$. Then the displacement measured in a fiber pulling or pushing experiment becomes

$$\frac{\delta - \delta(0)}{\delta'} = S_a^2 + 2(A - 1)S_{R0}S_a. \qquad (23)$$

In this case the debond energy cannot be evaluated from the displacement measurements. The displacement measured relative to the peak load displacement, δ_p, is

$$\frac{\delta_p - \delta}{\delta'} = 1 + 2(A - 1)S_{R0} - S_a^2$$
$$- 2(A - 1)S_{R0}S_a. \qquad (24)$$

During unloading from a peak load σ_p, the recovery in displacement is given by equation (15), which becomes [see Fig. 9(a)]

$$\delta_p - \delta = \left[\frac{(b_2 + b_3)(1 - a_1 f)^2 R_f}{8\tau_0 E_m}\right][\sigma_p - \sigma_a]^2 \qquad (25)$$
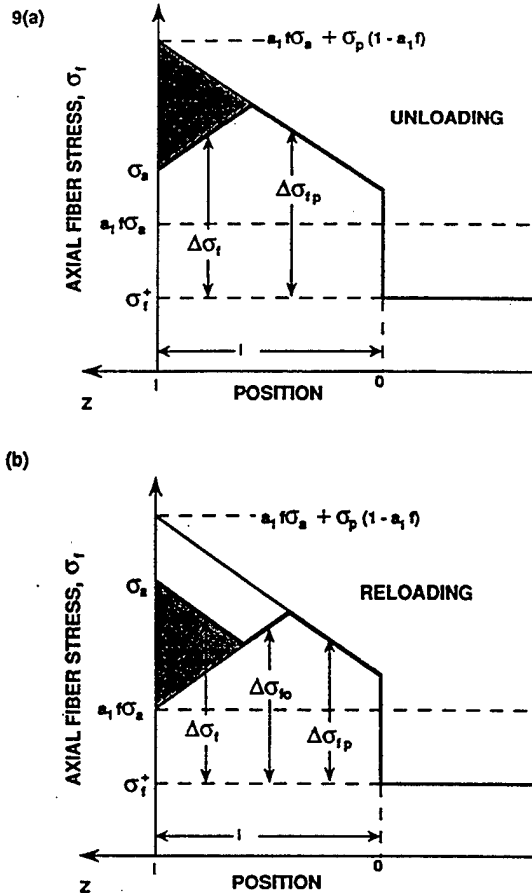
Fig. 9. Axial stresses in fiber during (a) unloading and (b) reloading after loading initially to peak stress σ_p. Change in displacement is proportional to area of the shaded region. Constant friction model.

or, in terms of the previously defined normalized parameters

$$\frac{\delta_p - \delta}{\delta'} = (1/2)[1 - S_a]^2. \qquad (26)$$

Equations (25) and (26) are restricted to situations where σ_p is sufficiently large that the region of reverse slip does not reach the end of the debond before unloading is complete, as discussed in the previous section. For the constant friction model this condition requires $(1 - a_1 f)\sigma_m \geq 2\Gamma$, i.e. $\Gamma' < 1/2$. The corresponding displacement equations for smaller values of σ_m can be derived straightforwardly following the above procedure.

The displacements during reloading [equations (17) and Fig. 9(b)] are given by

$$\delta - \delta_0 = \left[\frac{(b_2 + b_3)(1 - a_1 f)^2 R_f}{8\tau_0 E_m}\right]\sigma_a^2 \qquad (27)$$

where δ_0 is the displacement at the end of the previous unloading half-cycle. In terms of the normalized parameters, equation (27) becomes

$$\frac{\delta_p - \delta}{\delta'} = \frac{\delta_p - \delta_0}{\delta'} - S_a^2/2. \qquad (28)$$
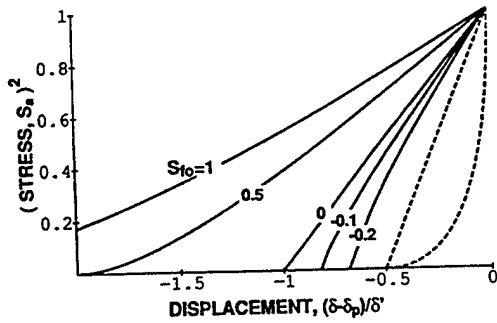
Fig. 10. Stress–displacement relation for constant friction model during load unload/reload cycle for various values of the residual stress parameter $S_{fo} = S_{R0} (A - 1)$. Full curves initial loading [equation (24)] broken curves unloading [equation (26)] and reloading [equation (28)].

The number of independent parameters in the normalized equations (20), (26) and (28) is one fewer than in their counterparts for Coulomb friction, since A and S_{R0} appear only in equation (20) in the combination $(A - 1)S_{R0}$, which is just the normalized axial residual stress, S_{fo}. These equations are plotted in Fig. 10 for several values of S_{fo}.

It is instructive to compare the results of this section with an approximate constant τ analysis [6], used previously to model single fiber pushing experiments. In that analysis, elastic interactions of the fiber and matrix via Poisson's effects were neglected, but effects of debonding and residual axial fiber stresses were included. In the notation of this paper, the initial loading equation from Ref. [6] for pulling a fiber with compressive residual axial stress (equivalent to pushing a fiber with residual tensile axial stress) becomes

$$\delta = \frac{R_f}{4\tau_0 E_f} [(\sigma_a - \sigma_{fo}^+)^2 - 4G_c E_f/R_f]. \qquad (29)$$

The corresponding result from equation (19) (with $f = 0$ for single fiber pulling) can be written

$$\delta = \frac{b_2 R}{4\tau_0 E_m} \left[(\sigma_a - \sigma_{fo}^+)^2 - \frac{4E_m G_c}{b_2 R_f} \right] \qquad (30)$$

where we have used equations (4) and (5) to substitute for γ, and the fact that $b_3 = 0$ for $f = 0$. These two relations differ only by the substitution of E_f for E_m/b_2. A similar correspondence is also obtained for the unloading and reloading equations and
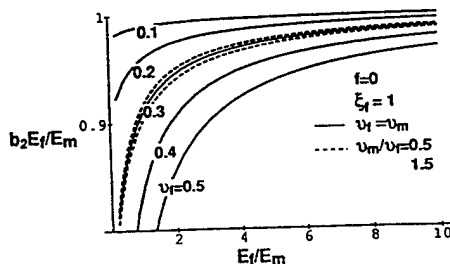
Fig. 11. Variation of $E_f/(E_m/b_2)$ at $f = 0$ with other matrix and fiber properties.

for residual stresses of opposite sign. The ratio $E_f/(E_m/b_2)$ with $f = 0$ is shown in Fig. 11 for various values of E_f/E_m, v_f/v_m, and v_f (b_2 is independent of λ). For values of these parameters typical of ceramic and intermetallic composites ($E_f/E_m > 2$ with v_f and $v_m < 0.3$), this ratio differs from unity by less than 5%. Therefore the analysis of Ref. [6] is a close approximation to the constant τ analysis for single fiber experiments in such materials.

5. RELATIONS BETWEEN CRACK OPENING DISPLACEMENTS AND SINGLE AND MULTIPLE FIBER DISPLACEMENTS

Crack bridging laws can be deduced directly from single fiber pushing or pulling experiments. Two steps are involved; one is to relate the crack opening used in continuum bridging models to the displacements measured in multiple fiber experiments [equation (8b)] and the other is to relate the displacements measured in single and multiple fiber experiments by evaluating these displacements under appropriate boundary conditions. For multiple fiber measurements, Type II boundary conditions are used to evaluate the b parameters in equation (3). For single fiber measurements, several test configurations are possible. If a single fiber within a composite is tested, the b parameters are evaluated using $f = 0$ (for which Type I and II boundary conditions are the same), whereas the a parameters of equation (2) are evaluated using the actual value of f for the composite. However, there is some uncertainty in the choice of matrix elastic properties for the evaluation of the b's in this case, since in the near field there is all matrix, whereas in the far field the average composite properties would be more appropriate. Since strain gradients are highest in the near-field region, the matrix properties E_m and v_m are used in the following calculations. For a model test specimen comprising a single fiber in a cylinder of matrix, a single value of f would be used for evaluation of all parameters, but this value may differ from that in a composite.

The displacements measured in single and multiple fiber experiments and the crack opening displacements can differ substantially. As an illustration, stress–displacement relations are plotted in Fig. 12 using the following properties typical of intermetallic composites [7]: $f = 0.36$, $E_f/E_m = 5.1$, $\lambda = 1$, $E_f = E_r$, and $v_f = v_r = v_m = 0.3$ (other relevant parameters calculated from these properties are listed in Table 1). The parameter S_{R0} depends on the ratio of the peak applied stress, σ_p, to the residual axial stress, σ_{fo}^+, in the fibers; for this example, the value $\sigma_p/\sigma_{fo}^+ = 3.0$ was chosen, as this corresponds to an experiment reported in Ref. [7]. The displacement scaling parameters δ^* and δ' for the Coulomb and constant friction models are defined in equations (11d) and (21); the values of the terms in square brackets in these equations

(a)

(b)
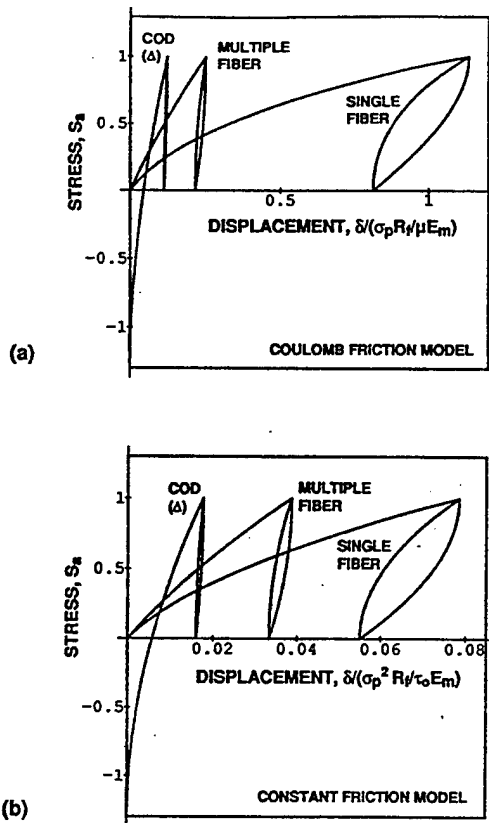
Fig. 12. Comparison of stress–displacement relations for crack bridging (COD) and for single and multiple fiber pulling experiments for a composite with properties given in Table 1.

are listed in Table 1. The displacements for single and multiple fiber pulling are plotted in Fig. 12 in the form $\delta/[(\sigma_p R_f)/(\mu E_m)]$ for the Coulomb friction model and $\delta/[(\sigma_p^2 R_f)/(\tau_0 E_m)]$ for the constant friction model. The crack opening displacements are expressed in terms of Δ, given for this composite by $\Delta = 0.31\delta$ [equation (8b)]. The curves for single and multiple

Table 1. Composite properties used for Fig. 12

	Single fiber pull	Multiple fiber pull
E_f/E_m	5.1	
$v_f = v_m = v_f$	0.3	
f	0.36	
λ	1	
$A = \left(1 - \dfrac{a_2 b_1}{a_4}\right)^{-1}$	1.14	0.768
$\dfrac{b_2}{b_2 + b_3}$		0.31
$\dfrac{(b_2 + b_3)(1 + a_1 f)}{2 b_1}$	2.33	−0.855
$(b_2 + b_3)(1 - a_1 f)^2/4$	0.047	0.011
$S_{R0} = \dfrac{\sigma_{f0}^+/\sigma_p}{(A - 1)(1 - a_1 f)}$	2.36[a]	−5.6[a]

[a]These values correspond to $\sigma_p/\sigma_{f0}^+ = 3.0$, corresponding the experiment in Ref. [7] with initial axial residual stress $\sigma_{f0}^+ = 800$ MPa and peak stress $\sigma_p = 2.4$ GPa.

fiber pulling hold for $\Gamma' < 0$, whereas the crack opening displacement curves apply only for $G_c = 0$ (i.e. $\Gamma' = -S_{R0}$). For other values of Γ', the curves shift along the displacement axes, as discussed in Sections 3 and 4. For given applied stress, the displacements in single fiber pulling are larger than in multiple fiber pulling. Moreover, the fraction of the initial displacement that is recovered during unloading is larger for single, than for multiple fibers.

The negative crack bridging stresses at small displacements in Fig. 12 represent crack-opening pressure, and reflect the fact that compressive applied load would be needed to keep a matrix crack fully closed in this composite [31] (because of residual tensile stress in the matrix). The displacements in this region correspond to the spontaneous debonding and sliding discussed with reference to fiber pulling experiments in Section 3.

6. DISPLACEMENTS DURING FIBER PUSHING EXPERIMENTS

The axial fiber stresses during initial monotonic compressive loading are shown schematically in Fig. 13(a). In this case, the direction of sliding over the debonded interface and the sign of the stress jump

(a)

(b)
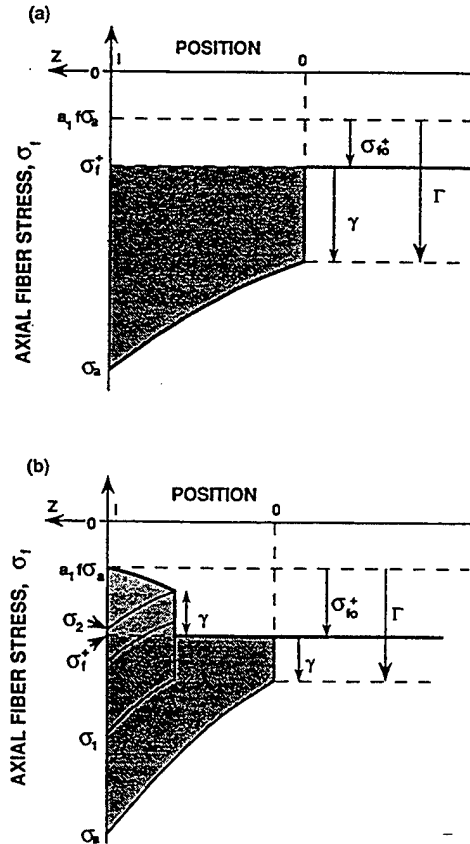
Fig. 13. Axial stresses in fiber during initial loading in fiber pushing test: (a) no spontaneous debonding; (b) with spontaneous debonding.

at the debond tip are reversed. With the change in sliding direction, the frictional stress, τ, becomes positive, a change which may be accomplished by defining the friction coefficient, μ, in equation (1) to be negative. The change in sign of the stress jump causes γ to become negative, and equation (4) to be redefined as

$$\gamma \equiv \sigma_f^- - \sigma_f^+ = \frac{-(1-f)}{fc_1 c_3}\left(\frac{E_m G_c}{R}\right)^{1/2}. \quad (31)$$

The equations of Sections 3 and 4 are unaltered provided spontaneous debonding does not occur, although σ_a is negative, leading to changes in sign of many of the other parameters, and negative displacements. In addition, with the sign change in the relation between γ and the debond energy, G_c, the parameters Γ and Γ', which are dependent on γ, take different values in fiber pushing experiments; in pulling experiments, Γ is equal to the *difference* between the magnitudes of γ and the residual axial fiber stress, σ_{f0}^+, [equation (11c)], whereas in pushing experiments, Γ is negative, with magnitude equal to the *sum* of the magnitudes of γ and σ_{f0}^+.

If spontaneous debonding occurs, the axial fiber stresses during initial loading are altered as shown in Fig. 13(b). For applied loads larger in magnitude than σ_1 in Fig. 13(b), the changes in displacement are still given by the expressions in Sections 3 and 4. However, for smaller applied loads the displacements are altered. For applied loads smaller than σ_2 in Fig. 13(b) the displacements are given by the expressions for reloading after unloading [the second term of equation (18) for Coulomb friction and equation (28) for constant friction], whereas for loads in the range σ_1 to σ_2 the displacements are equivalent to those occurring between σ_1 and σ_2 in Fig. A2(b) [equation (A16) with σ_p replaced by σ_1].

7. THE ONSET OF COMPLETE SLIDING IN A THIN SLICE OF COMPOSITE

Calculation of the load needed to cause complete sliding of a fiber within a specimen of finite thickness would require analysis of the interaction of the stress field ahead of the debond crack with the back surface of the specimen, as the debond approaches the back surface. Moreover, the boundary condition depicted in Fig. 1 far ahead of the debond tip must be disturbed in order to allow the back surface to be stress-free. The true boundary condition would become sensitive to details of the gripping arrangement. Nevertheless, some qualitative insight into the problem of the onset of complete sliding (and most likely on upper bound for the critical load) may be obtained by ignoring these effects and setting the debond length in the present analysis [equation (10)] equal to the specimen thickness.

In general, the critical loads needed to cause complete sliding in pulling and pushing experiments would be expected to differ. If we assume that the

effect of the back surface on the debond crack as it approaches the surface is similar in both experiments (i.e. that the debond breaks through when it approaches a critical distance from the surface [23]) and that the gripping arrangements are the same, the analysis of the previous sections can be used to compare the critical loads in pulling and pushing, by evaluating σ_a for both cases at a fixed value of l (without having to specify l). For the Coulomb friction model, this is done by evaluating equation (10) for pushing and pulling, using the results noted in Section 6. The axial stresses in the fiber are shown schematically in Fig. 14. Two effects contribute to the applied stresses in pulling, σ_a^t, and pushing, σ_a^c being different; one is the opposite signs of Poisson's strains in the two experiments, which causes the magnitude of $\Delta\sigma_a$ to be larger in pushing (for b_1 positive), and the other is the offset along the stress axis due to the fact that $\Delta\sigma_a$ is measured relative to the residual axial stress in the fiber (σ_{f0}^+). For the constant friction model, only the latter effect contributes. In this case, the applied stresses at a given slip length are related by

$$|\sigma_a^c| - |\sigma_a^t| = 2|\sigma_{f0}^+|. \quad (32)$$

When the debonds reach the ends of the fibers in the cases depicted in Fig. 14(a) (i.e.) with $\Gamma' > 0$, the
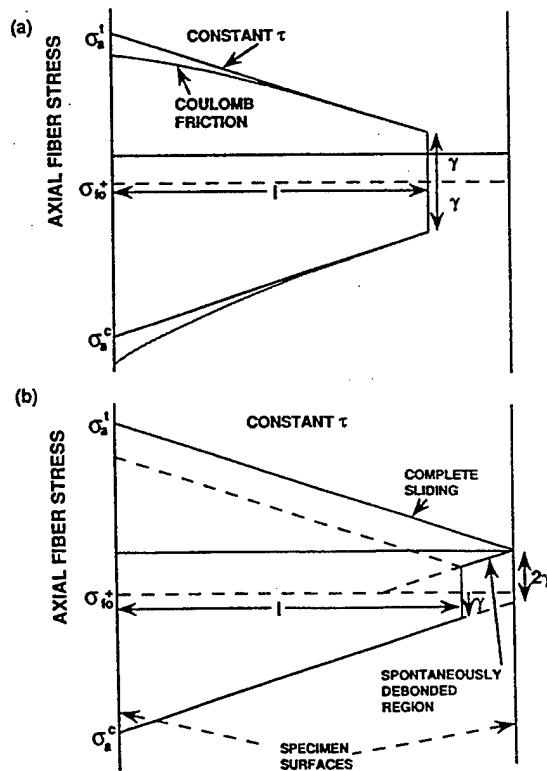
Fig. 14. (a) Comparisons of axial fiber stresses in pushing and pulling experiments for given debond length. (b) Axial fiber stresses for constant friction model with $|\gamma| < |\sigma_{f0}^+|$ as debond approaches back surface of a specimen of finite thickness.

applied loads for both pulling and pushing are larger than those which can be supported by frictional resistance, so that sudden load drops occur. Therefore, the *peak* loads are related by equation (32).

A different response is expected if $\Gamma' < 0$. In this case, spontaneous debonding occurs at the back surface before the push or pull test begins [Fig. 14(b)]. When the debond that is driven by pushing the fiber approaches the spontaneously debonded region near the back surface, a sudden load drop again occurs. However, when the debond that is driven by pulling the fiber reaches the same location, the applied load is smaller than that needed to cause complete sliding. The load must be further increased to reverse the direction of sliding over the spontaneously debonded region, as indicated in Fig. 14(b). Therefore, a sudden load drop does not occur. In this case, the *peak* loads in the pushing and pulling experiments are related by

$$|\sigma_a^c| - |\sigma_a^t| \approx 2|\gamma| \quad (\Gamma' < 0). \tag{33}$$

It is emphasized that these relations are approximate and may be strongly affected by different gripping arrangements in pulling and pushing tests.

REFERENCES

1. D. B. Marshall, *J. Am. Ceram. Soc.* **67**, C259 (1984).
2. D. B. Marshall and W. C. Oliver, *J. Am. Ceram. Soc.* **70**, 542 (1987).
3. T. P. Weihs and W. D. Nix, *Scripta metall.* **22**, 271 (1988).
4. T. P. Weihs and W. D. Nix, *J. Am. Ceram. Soc.* **74**, 524 (1991).
5. T. P. Weihs, C. M. Dick and W. D. Nix, in *MRS Symp. Proc. 120* (edited by E. D. Lemkey, S. G. Fishman, A. G. Evans and J. R. Striffe) (1988).
6. D. B. Marshall and W. C. Oliver, *J. Mater. Sci. Engng* **A126**, 95 (1990).
7. D. B. Marshall, M. C. Shaw and W. L. Morris, *Acta metall. mater.* **40**, 443 (1992).
8. J. D. Bright, D. K. Shetty, C. W. Griffin and S. Y. Limaye, *J. Am. Ceram. Soc.* **72**, 1891 (1989).
9. P. D. Jero and R. J. Kerans, *Scripta metall.* **24**, 2315 (1990).
10. M. K. Brun and R. N. Singh, *Adv. Ceram. Mater.* **3**, 506 (1988).
11. J. W. Laughner and R. T. Bhatt, *J. Am. Ceram. Soc.* **72**, 2017 (1989).
12. G. Morsher, P. Pirouz and A. H. Heuer, *J. Am. Ceram. Soc.* **73**, 713 (1990).
13. R. J. Kerans, R. S. Hay, N. J. Pagano and T. A. Parthasarathy, *Am. Ceram. Bull.* **68**, 429 (1989).
14. J. I. Eldridge and P. K. Brindley, *J. Mater. Sci. Lett.* **8**, 1451 (1989).
15. C. J. Yang, S. M. Jeng and J-M. Yang, *Scripta metall.* **24**, 469 (1990).
16. K. Kendall, *J. Mater. Sci.* **10**, 1011 (1975).
17. E. P. Butler, E. R. Fuller Jr and H. Chan, *MRS Symp. Proc. Tailored Interfaces in Composites Materials.* V 170 (1990).
18. E. P. Butler, E. R. Fuller Jr, T. R. Palamides and H. M. Chan, *Proc. Int. Symp. on Advances in Processing of Ceramic and Metal Matrix Composites* (edited by H. Mostaghacci). Pergamon Press, Oxford (1990).
19. Y-C. Gao, Y-M Mai and B. Cottrell, *J. appl. Math. Phys.* **39**, 550 (1988).
20. D. K. Shetty, *J. Am. Ceram. Soc.* **71**, C107 (1988).
21. J. W. Hutchinson and H. M. Jensen, *Mech. Mater.* **9**, 139 (1990).
22. B. N. Cox, *Acta metall. mater.* **38**, 2411 (1990).
23. R. J. Kerans and T. A. Parthasarathy, *J. Am. Ceram. Soc.* **74**, 1585 (1991).
24. L. B. Freund, *Eur. J. Mech.* In press.
25. L. S. Sigl and A. G. Evans, *Mech. Mater.* **8**, 1 (1989).
26. L. N. McCartney, *Proc. R. Soc.* **A425**, 215 (1989).
27. E. R. Fuller Jr, E. P. Butler and W. C. Carter, in *Proc. Nato Advanced Research Workshop on Toughening Mechanisms in Quasi Brittle Materials*, Northwestern University (1990).
28. L. N. McCartney, *Proc. R. Soc.* **A409**, 329 (1987).
29. B. Budiansky and J. C. Amazigo, *J. Mech. Phys. Solids* **37**, 93 (1989).
30. D. B. Marshall and B. N. Cox, *Mech. Mater.* **7**, 127 (1988).
31. D. B. Marshall and A. G. Evans, *Materials Forum* **11**, 304 (1988).

APPENDIX A

Initial Loading

The axial fiber stresses during initial monotonic loading are obtained by integration of equation (6), with τ given by equations (1), (2b) and (3b), and the condition $\sigma_f = \sigma_f^-$ at $z = 0$. The result can be expressed as

$$\Delta\sigma_f = \gamma - \alpha(1 - e^{-\eta z}) \tag{A1}$$

where

$$\eta = 2\mu b_1 / R_f \tag{A2}$$

$$\alpha = \sigma_r^- / b_1 \tag{A3}$$

and γ is defined in equation (4). Equation (A1) is equivalent to equation (44) of Ref. [21]. The length, l, over which debonding and sliding occur is given by setting $\sigma_f = \sigma_a$ at $z = l$

$$\eta l = -\ln\left[\frac{\sigma_a - \sigma_f^+ + \alpha - \gamma}{\alpha}\right]. \tag{A4}$$

The displacement δ, obtained from equations (7), (A1) and (A4) is

$$\delta = \frac{b_2 + b_3}{\eta E_m}\left[(\alpha - \gamma)\ln\left(\frac{\sigma_a - \sigma_f^+ + \alpha - \gamma}{\alpha}\right) + \gamma - (\sigma_a - \sigma_f^+)\right] \tag{A5}$$

which can be shown to be equivalent to equations (47) and (49) in Ref. [21].

It is convenient at this stage to expand the terms within the square bracket of equation (A5) and regroup them into parameters that characterize the applied loading, the residual stresses, and the debond energy. After some manipulation with equations (2)–(4) and (A3), these terms can be expressed as

$$\alpha - \gamma = \left(\frac{a_3 f}{b_1}\right)\sigma_a + A\sigma_{R0} \tag{A6a}$$

$$\alpha - \gamma - \sigma_f^+ + \sigma_a = \left(1 - a_1 f + \frac{a_3 f}{b_1}\right)\sigma_a + \sigma_{R0} \tag{A6b}$$

$$\gamma - (\sigma_a - \sigma_f^+) = -(1 - a_1 f)\sigma_a + \Gamma \tag{A6c}$$

$$\alpha = \left(\frac{a_3 f}{b_1}\right)\sigma_a + \sigma_{R0} + \Gamma \tag{A6d}$$

where the parameters A, σ_{R0}, Γ, and σ_{f0}^+ are defined in equation 11(c) to (g) of the text. With these relations, equation (A5) becomes

$$\delta = \frac{b_2 + b_3}{\eta E_m} \left\{ \left(\left(\frac{a_3 f}{b_1} \right) \sigma_a + A\sigma_{R0} \right) \right.$$

$$\times \ln \left[\frac{\left(1 - a_1 f + \frac{a_3 f}{b_1} \right) \sigma_a + \sigma_{R0}}{\left(\frac{a_3 f}{b_1} \right) \sigma_a + \Gamma + \sigma_{R0}} \right]$$

$$\left. - (1 - a_1 f)\sigma_a + \Gamma \right\}. \tag{A7}$$

Further simplification of equation (A7), for $(a_3 f/b_1) = 0$, can be achieved by normalizing the parameters by the peak value of applied stress, σ_p, to give equation (9) in the text. Similarly, equation (10) of the text follows from equation (A4).

Unload Reload

Using the same procedure as for the initial loading, $\Delta\sigma_f$ during unloading can be evaluated as

$$\Delta\sigma_f = -(\alpha - \gamma) + (\alpha - \gamma + \sigma_a - \sigma_f^+)e^{-\eta(l_p - z)} \tag{A8}$$

where l_p is given by equation (A4) at $\sigma_a = \sigma_p$. The reverse slip length, s, is obtained by setting $\Delta\sigma_f$ equal to $\Delta\sigma_{fp}$ at $z = l - s$

$$2\eta s = \ln \left[\frac{\alpha - \gamma + \sigma_a - \sigma_f^+}{\alpha - \gamma + \sigma_p - \sigma_{fp}^+} \right]. \tag{A9}$$

Equation (A9) requires that α be independent of σ_a. With some manipulation of equations (A6), (11f) and (11c), this condition becomes $(a_2 a_3 f/a_4) \ll 1$. This parameter is zero for either $f = 0$ or $v_f = v_m$, and is very small for all other likely composite properties; $(a_2 a_3 f/a_4) < 0.06$ for all values of E_m/E_f and ξ_f with $0.5 < (v_m/v_f) < 1.5$, $v_f < 0.5$, $f < 0.5$, and $\lambda < 2$. Therefore, since the exact expression for s with nonzero values of $(a_2 a_3 f/a_4)$ is very lengthy, it is not pursued here. The displacement evaluated from equations (15), (A8), and (A9) in terms of the normalized parameters defined previously is given in equation (16) of the text.

The fiber stress $\Delta\sigma_f$ during reloading can be evaluated as

$$\Delta\sigma_f = -(\alpha - \gamma) + (\alpha - \gamma + \sigma_a - \sigma_f^+)e^{-\eta(z - l_t)}. \tag{A10}$$

The new slip length, t, is obtained by setting $\Delta\sigma_f$ equal to $\Delta\sigma_{f0}$ at $z = l - t$

$$2\eta t = \ln \left[\frac{\alpha - \gamma - \sigma_{f0}^+}{\alpha - \gamma + \sigma_a - \sigma_f^+} \right]. \tag{A11}$$

As with the corresponding expression for unloading, this expression requires $(a_2 a_3 f/a_4) \ll 1$. The displacement evaluated from equations (17), (A10) and (A11), expressed relative to the peak load displacement and in terms of the normalized parameters defined previously, is given in equation (18) of the text.

Unload/Reload Relations for Small Loads

If the peak stress during the initial loading is smaller than a critical value, reverse slip during unloading can reach the end of the debonded region before unloading is complete. The condition to avoid this is $s < l$ at complete unload, with l given by equation (A4) at $\sigma_a = \sigma_p$, and s given by equation (A9) at $\sigma_a = 0$. In terms of the normalized parameters
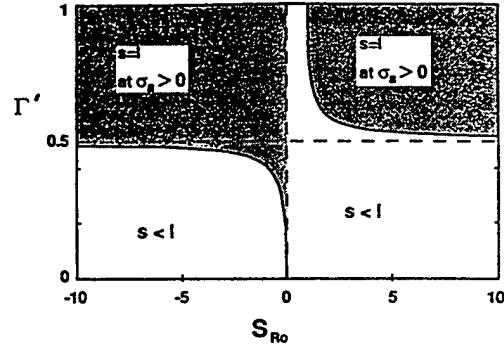
Fig. A1. Condition for region of reverse slip (length, s) to reach end of initial debond (length, l) before complete unloading. Coulomb friction model.

defined in equations (11) this condition can be written as

$$\Gamma'^2 - 2S_{R0}\Gamma' + S_{R0} > 0. \tag{A12}$$

Equation (A12) is plotted in Fig. A1. For $|S_{R0}| \geqslant 2$, the condition $s < l$ is satisfied for $\Gamma' \lesssim 0.5$.

For larger values of Γ' the axial fiber stresses at several stages of unloading are shown schematically in Fig. A2(a). For the first part of the unloading (i.e. for $\sigma_3 < \sigma_a < \sigma_p$), s is smaller than l_p, so the displacements are given by
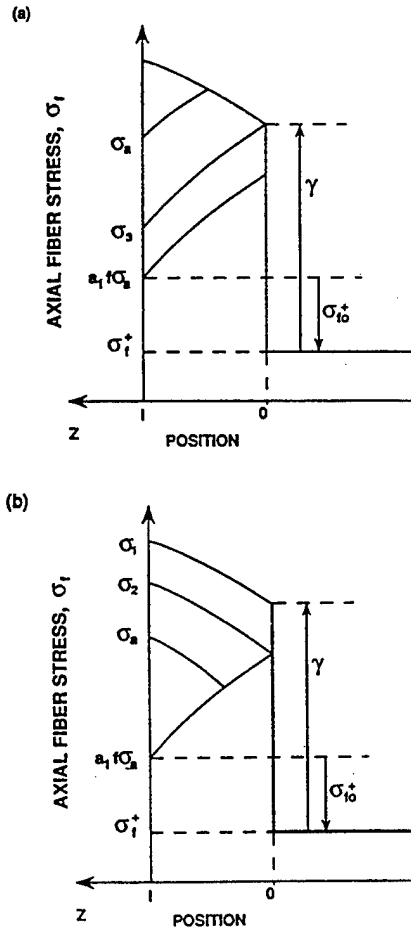
Fig. A2. Axial fiber stresses at several stages during unloading (a) and reloading (b) under conditions where reverse slip reaches the end of the initial debond before unloading is complete.

equation (16). The stress, σ_3, at which $s = l_p$ is given by equations (A4) and (A9), with $\sigma_a = \sigma_p$ in equation (A4) and $\sigma_a = \sigma_3$ in equation (A9). In terms of the normalized parameters, the result is

$$S_3 = S_{R0} - (S_{R0} - \Gamma')^2/(S_{R0} - 1). \qquad \text{(A13)}$$

For continued unloading below S_3, the sliding distance is fixed at $s = l_p$, and the lower limit of integration for equation (15) becomes zero. The displacement in this load range becomes

$$\frac{\delta_p - \delta}{\delta^*} = \frac{(1 - \Gamma')(\Gamma' - S_a)}{(S_{R0} - \Gamma')} \quad (S_a < S_3). \qquad \text{(A14)}$$

The axial stresses during reloading are shown schematically in Fig. A2(b). For $\sigma_a < \sigma_2$ the displacements are given by equation (18), but with $(\delta_p - \delta_0)/\delta^*$ given by equation (A14) at $S_a = 0$. The stress, σ_2, at which the new slip length, t, equals l_p is given by equations (A4) and (A11)

$$S_2 = S_{R0} - (S_{R0} - 1)^2 S_{R0}/(S_{R0} - \Gamma')^2. \qquad \text{(A15)}$$

For $\sigma_a > \sigma_2$, the slip length is fixed at $t = l_p$ and the lower limit of integration for equation (17) becomes zero. In this case the displacement becomes

$$\frac{\delta - \delta_0}{\delta^*} = (1 - \Gamma')\left[\frac{S_{R0}}{S_{R0} - \Gamma'} - \left(\frac{S_{R0} - S_a}{S_{R0} - 1}\right)\right]$$
$$(S_a > S_2). \qquad \text{(A16)}$$

APPENDIX B

Nomenclature

$a_i, b_i = $ dimensionless functions of elastic properties, f, and λ defined in Ref. [21]

$$A = \left[1 - \frac{a_2 b_1}{a_4}\right]^{-1}$$

$E = $ Young's modulus
$f = $ volume fraction of fibers
$G_C = $ Mode II fracture energy at debond tip
$R_f = $ fiber radius
$v = $ Poisson's ratio
$\zeta_f = (1 - v_r)E_f/(1 - \hat{v}_f)E_r$
$\epsilon^T = $ misfit strain
$\lambda = \epsilon_r^T/\epsilon_z^T$, anisotropy of misfit strain
$\sigma_a = $ stress applied to end of fiber
$\sigma_f = $ axial stress in fiber
$\delta, \Delta = $ displacements [equations (7) and (8)]
$l = $ debond length
$\tau = $ frictional stress
$\mu = $ coefficient of friction
$\gamma = $ normalized debond energy [equation (4)]
$S_a = $ normalized applied stress, σ_a/σ_p
$S_{R0} = $ normalized residual stress [equation (11b)]
$\Gamma = $ normalized debond energy [equation (11c)]
$\delta^*, \delta' = $ normalizing parameters for displacement [equations (11d) and (21)]
$\sigma_{R0} = $ residual stress parameter [equation (11f)]
$\sigma_{f0}^+ = $ residual axial stress in fiber [equation (11g)]

Subscripts

r = radial
f = fiber, axial
m = matrix, axial
p = peak load
o = unload

Superscripts

+ = position well ahead of debond
− = position just behind debond tip

Appendix C

"The Determination of Interfacial Properties from Fiber Sliding Experiments. The Roles of Misfit Anisotropy and Interfacial Roughness," Marshall, D.B., Shaw, D.C., Morris, W.L., Acta Met., No. 43, pp 2041, 1995.

THE DETERMINATION OF INTERFACIAL PROPERTIES FROM FIBER SLIDING EXPERIMENTS: THE ROLES OF MISFIT ANISTROPY AND INTERFACIAL ROUGHNESS

D. B. MARSHALL, M. C. SHAW and W. L. MORRIS

Rockwell International Science Center, 1049 Camino Dos Rios, Thousand Oaks, CA 91360, U.S.A.

Abstract—Models of fiber sliding in composite materials are assessed to determine the requirements for unambiguous evaluation of interfacial properties from fiber pulling experiments. If independent measurements of residual axial and radial strains are available, then curve fitting of calculated stress–displacement relations to fiber sliding data can provide unique values for the friction coefficient, the interfacial debond energy, and a parameter characterizing interfacial roughness. However, in the absence of residual strain measurements, unique determination of these parameters is not possible, because interfacial roughness and anistropy in residual misfit strain between fibers and matrix have very similar influences on the stress–displacement relation. The analysis is applied to fiber pulling data from a Ti_3Al matrix composite to evaluate changes in interfacial properties after cyclic loading at both room temperature and 650°C.

1. INTRODUCTION

Various fiber pushing or pulling experiments have been devised recently to allow measurement of the mechanical properties of fiber–matrix interfaces in ceramic [1–24] and intermetallic [25–31] matrix composites. The most sensitive of these supply continuous measurements of force, p, and displacement, u, as the end of a single fiber is loaded and a debond crack progresses stably along the interface [2, 11, 16, 17, 24, 29]. The relation $p(u)$ is affected by the debond energy of the interface, frictional sliding that occurs over the debonded region of interface, residual stresses, and the elastic properties of the fiber and matrix [2, 11, 32–34].

Quantitative determination of these properties from measured force–displacement relations requires modeling of the physical processes occurring at the interface and curve fitting of the resulting relation $p(u)$ to the data. As such, it is an inverse problem which suffers from uncertainty in the uniqueness of its solutions. The purpose of this paper is to examine the results of some simple models of interfacial sliding and thereby define requirements for experimental data to be able to distinguish various models.

One of the properties to be examined is the effect of interfacial roughness on frictional sliding. Measured force–displacement relations in several composite systems have shown clear deviations from the response expected from a smooth interface with sliding resistance defined by the Coulomb friction law [29]. This deviation has been attributed to the effect of roughness: in the constrained geometry of

fiber sliding, roughness causes an increase in the average normal interfacial stress, which tends to negate the Poisson's contraction when the fiber is pulled, and add to the Poisson's expansion when it is pushed. In some fiber pulling experiments, these effects appear to have cancelled exactly, giving a response that is consistent with a constant friction along the debonded interface [29]. Independent evidence has also been obtained of the importance of interfacial roughness: photoelastic measurements [18] and measurements of reseating during cyclic pushout and pullout experiments [13, 22, 23]. In response to these observations, several detailed models of roughness effects have appeared [35–37]. In this paper, several simple models will be examined to determine the extent to which details of such models might be determined from experimental data. The analysis is applied to fiber pulling data from a Ti_3Al matrix composite to evaluate changes in interfacial properties and residual stresses caused by thermomechanical fatigue.

2. BASIS OF EXPERIMENTAL DATA AND MODELS

The experiments of interest here involve pulling or pushing a single fiber in a composite and measuring the applied force and the relative displacement of the fiber and matrix [Fig. 1(a)]. If the fiber–matrix interface is sufficiently weak, debonding and sliding occur. Attention will be restricted to composites with compressive residual stresses in the fibers and to test pieces with thickness large compared with
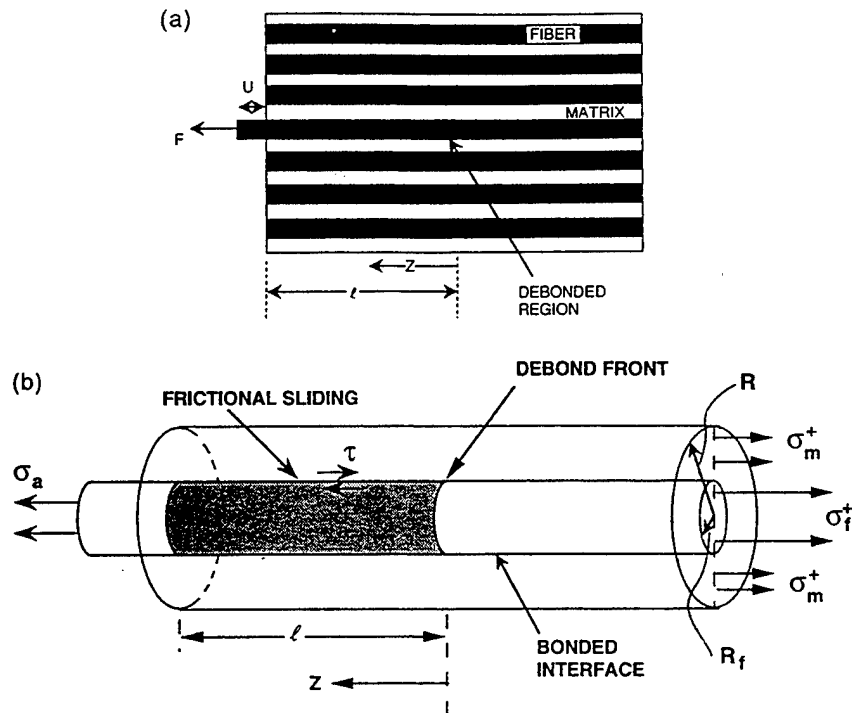
Fig. 1. (a) Schematic of fiber sliding experiment. (b) Concentric cylinder model used for fiber sliding analysis.

the length of fiber over which debonding and sliding occur. Under these conditions, the debonded region extends stably along the fiber with increasing load, the length of debonding being determined by a Mode II fracture energy at the crack tip, the residual stresses, and frictional stresses acting over the debonded region.

Two equivalent approaches have been used to analyze the resulting force–displacement relations. One approach views Fig. 1 as a miniature fracture mechanics experiment; a Mode II strain energy release rate is related to a crack resistance curve evaluated by treating the frictional forces acting over the debonded surface as crack bridging tractions [14]. In this analysis, the crack resistance curve is an increasing function of the debond length as long as frictional forces act over the entire debonded surface. If the crack surfaces separate (e.g. due to Poisson's contraction), a steady-state bridging zone is realized and unstable growth of the debond ensues. The other approach, which is adopted here, involves direct calculation of the strains in the fiber and matrix and integration to obtain the relevant displacement [32–35].

2.1. Experimental measurements

Since the displacement measurements required are accumulated changes in elastic strains over the debonded region of interface, their magnitudes are usually small. Typical displacement ranges of interest are $\sim 10\,\mu$m for ceramic and intermetallic

matrix composites containing large CVD fibers [29] (~ 100–$140\,\mu$m diameter) and $\sim 1\,\mu$m for ceramic matrix composites with smaller polymer-derived fibers [2] (~ 10–$20\,\mu$m diameter). Displacement resolutions at least two orders of magnitude smaller than these values are needed for the experiments under consideration here. This has been achieved in several different experiments. In ceramic matrix composites with the smaller fibers, a nano indenter, with displacement resolution of ~ 0.2 nm, has been used to push fibers [2, 4, 16]. In ceramic matrix composites with larger fibers, pushing experiments have been done with flat punches using mechanical test machines, with the required displacements being obtained by subtracting a calibrated compliance from the measured crosshead displacement [8]. Fiber pulling experiments have been done by tensile loading of single fiber, glass matrix test specimens containing a precrack [24]. In intermetallic matrix composites with larger fibers, fiber pulling experiments have been done with relative displacements of the fibers and matrix being obtained by analysis of high resolution optical images obtained from the region where the fiber enters the matrix [29]. This technique, which relies on differential displacement analysis, is capable of providing displacement resolution of $\sim 0.01\,\mu$m from optical micrographs [38].

Typical results from a fiber pulling experiment in a Ti_3Al/SiC composite are shown in Fig. 2. Included in this figure are data from several unload–reload cycles. In principle, the unload–reload data can be

included in the curve fitting to evaluate interfacial properties. However, the curve fitting here will be restricted to the initial loading data, with the unload–reload data being left for comparison with predicted curves as an independent check of the models.

2.2. Underlying assumptions of analysis

The concentric cylinder model will be taken to represent a composite reinforced with a volume fraction $f = (R_f/R)^2$ of aligned continuous fibers [Fig. 1(b)]. Hutchinson and Jensen [34] have shown that a shear lag analysis based on the Lamé solution for the concentric cylinder is adequate for calculating the axial stresses and strains, provided the debond length is sufficiently large ($\ell/R_f \geqslant 2$). For the experiments described in the previous section, the debond lengths, ℓ, over the entire data range, satisfy this requirement.

The parameters that enter this analysis may be grouped as follows: (1) the fiber radius, the volume fraction of fibers, and the elastic properties of the fibers and matrix; (2) the Mode II interfacial debond energy G_c; (3) the residual stresses, characterized by a misfit strain with components ϵ_z^T and ϵ_r^T in the axial and radial directions; (4) the frictional properties of the interface, characterized for the case of the Coulomb friction law by a friction coefficient, μ; and (5) additional parameters to characterize roughness if present. For the purpose of curve fitting, we will assume that the properties of the constituents of the composite collected into the first group are known, since they can be measured independently. The other parameters are assumed to be unknown.

Residual stresses are commonly calculated using known fabrication temperatures and known (or assumed) thermal expansion coefficients. However, such calculations can be substantially in error because of the difficulty in accounting rigorously for creep effects at high temperatures during cooling, plasticity at low temperatures, the temperature variations of thermal expansion coefficients, and anisotropy in thermal expansions. For example, very few measurements of transverse thermal expansion coefficients of reinforcing fibers exist. In one case where such measurements have been made, the longitudinal and transverse expansion coefficients differ significantly [9].

In many composites, direct measurements can be made of the axial residual stresses or strains. X-ray methods have been used to measure residual strains in the matrix, whereas residual strains in the fibers of intermetallic matrix composites have been obtained by direct measurement of fiber relaxation after removing the matrix by etching [39]. The latter experiments provide especially sensitive measurements of residual strains and will be used here to reduce the number of unknown parameters in the curve fitting by one.

3. MODELS OF INTERFACIAL SLIDING

3.1. Smooth interface with Coulomb friction law

The relative displacements, u, of the fiber and matrix at $z = \ell$ in the concentric cylinder model of Fig. 1 have been calculated for a smooth interface with sliding resistance, τ, defined by the Coulomb friction law

$$\tau = \mu \sigma_n \tag{1}$$

where μ is the friction coefficient and σ_n is the normal stress at the interface. The results can be conveniently expressed in the normalized form [32]

$$u/u^* = -AS_{Ro} \ln \left[\frac{S_{Ro} - S_a}{S_{Ro} - \Gamma'} \right] + \Gamma' - S_a \tag{2}$$

where S_a is equal to the applied stress, σ_a, normalized by the peak applied stress, σ_p, used for the experiment. The other parameters are defined as follows.

(i) A is a dimensionless parameter defined in Ref. [32] and in the Appendix [equation (A4)], which is a function of the elastic properties of the composite and its constituents (Young's moduli, Poisson's ratios and volume fraction, f, of fibers, represented collectively here by the symbol $\epsilon\ell$), as well as the ratio, λ, of the radial and axial thermal misfit strains ($\lambda = \epsilon_r^T/\epsilon_z^T$) that give rise to residual stresses, i.e.

$$A = A(\epsilon\ell, \lambda). \tag{3}$$

(ii) S_{Ro} is a parameter that depends on the residual stress and is given, for single fiber loading, by

$$S_{Ro} = \frac{-\sigma_{fo}^+}{(A-1)\sigma_p} \tag{4}$$

where σ_{fo}^+ is the residual axial stress in the fibers. Since σ_{fo}^+ is a function of the misfit strains ϵ_z^T and ϵ_r^T (or, equivalently ϵ_z^T and λ), as well as f and the elastic properties, S_{Ro} can be written

$$S_{Ro} = S_{Ro}(\epsilon\ell, \lambda, \epsilon_z^T). \tag{5}$$

(iii) Γ is a parameter that depends on the interfacial debond energy and the residual stress

$$\Gamma = \frac{\gamma + \sigma_{fo}^+}{\sigma_p} \tag{6a}$$

where

$$\gamma = 2(E_b G_c/R_f)^{1/2} \tag{6b}$$

with E_b being an elastic constant defined in Refs [32] and [34] and in the Appendix [eq. (A9)].

(iv) The normalizing displacement u^* is related to the friction coefficient, μ

$$u^* = \frac{R_f \sigma_p}{\mu E'} \tag{7}$$

where E' is another elastic constant [32] {Appendix, equation (A10)]. Therefore, the normalized displacements of equation (2) are a function of the
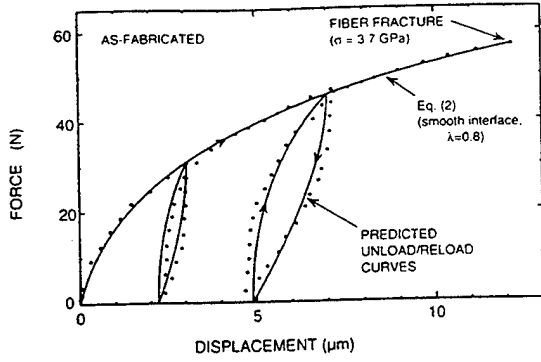
Fig. 2. Stress–displacement data for fiber pulling experiment from as-fabricated Ti$_3$Al/SiC composite. Experimental measurement errors are approximately equal to the size of the plotted data points. Initial loading curve [equation (2)] is fitted to data. Unload–reload curves are predicted using fitted parameters from initial loading curve.

following parameters

$$u/u^* = f_1(S_a, \epsilon\ell, G_c, \lambda, \epsilon_-^{\mathsf{T}}). \qquad (8)$$

The separation of the parameters characterizing the debond energy, the frictional response, and the residual stresses into the normalized parameters of equation (2) makes curve fitting relatively straightforward and more constrained than a general curve fit with this many adjustable parameters. The friction coefficient μ enters only in the scaling parameter u^* for the displacements and is effectively evaluated by scaling the displacements to one data point, say the peak displacement. The debond energy enters only through the parameter Γ', which from equation (2) is equal to S_a at $u = 0$, i.e. the intercept on the stress axis for a plot of S_a vs u/u^*. Thus, with μ and G_c evaluated from these two points, the only remaining unknown parameters (assuming the properties $\epsilon\ell$ are known) are the residual stress parameters ϵ_-^{T} and λ, which enter through A and S_{Ro}, and which can be evaluated by fitting the shape of the curve $S_a(u)$.

The number of degrees of freedom in this curve fit can be further reduced to one by obtaining an independent measurement of a residual stress. (This is usually necessary because use of data with finite measurement errors for fitting the shape of a curve such as the initial loading curve of Fig. 2 with two adjustable parameters does not provide unique values.) For the fiber relaxation measurement mentioned in Section 2.2, the relaxation strain, ϵ^*, is a function of the following variables [Appendix, equation (A2)]

$$\epsilon^* = \epsilon^*(\epsilon\ell, \lambda, \epsilon_-^{\mathsf{T}}). \qquad (9)$$

Therefore, equation (8) can be written

$$u/u^* = f_2(S_a, \epsilon\ell, G_c, \epsilon^*, \lambda) \qquad (10)$$

and a single parameter curve fit yields the parameter λ.

3.2. Constant friction model

If the Coulomb friction stress is replaced by a constant sliding resistance τ_o over the debonded region, the displacements are given by [32]

$$u/u' = S_a^2 + 2(A - 1)S_{Ro}S_a$$
$$- \Gamma'^2 - 2(A - 1)S_{Ro}\Gamma' \qquad (11)$$

where

$$u' = -\frac{R_f \sigma_p^2}{4\tau_o E_b} \qquad (12)$$

(the sign of τ_o is taken to be negative, consistent with the definition of τ in equation (1) for the Coulomb friction model). All of the comments concerning curve fitting for the Coulomb friction model apply also in this case.

To compare the responses of the Coulomb friction and constant friction models, it is convenient to normalize the stresses by the residual stress. Thus, with

$$S_a' = S_a/S_{Ro} \equiv -(A - 1)\sigma_a/\sigma_{fo}^+, \qquad (13a)$$

$$\Gamma'' = \Gamma'/S_{Ro} \equiv -(A - 1)[\gamma/\sigma_{fo}^+ + 1] \qquad (13b)$$

and

$$u_n = u^* S_{Ro} \equiv \frac{-R_f \sigma_{fo}^+}{\mu E'(A - 1)} \qquad (13c)$$

equations (2) and (11) become

$$u/u_n = -A \ln\left[\frac{1 - S_a'}{1 - \Gamma''}\right] + \Gamma'' - S_a' \qquad (14)$$

and

$$u/u_n = \left(\frac{\mu\sigma_{ro}}{\tau_o}\right)\left[(A - 1)S_a' + \frac{1}{2}S_a'^2 - (A - 1)\Gamma'' - \frac{1}{2}\Gamma''^2\right] \qquad (15)$$

where σ_{ro} is the normal stress across the debonded fiber–matrix interface when the axial stress in the fiber is zero. [Equation (15) follows from the preceding equations and the equations in the Appendix.] These stress–displacement relations are plotted in Fig. 3 for the case $\Gamma'' = 0$. When normalized in this way, the Coulomb friction law gives a single universal curve which approaches an asymptote
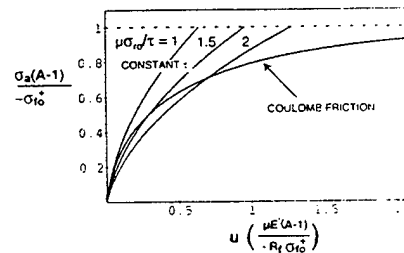

Fig. 3. Comparison of stress-displacement relations for constant interfacial frictional sliding stress and frictional stress defined by Coulomb friction law.

at $S'_a = 1$, corresponding to the stress at which interfacial separation due to Poisson's contraction of the fiber occurs. The constant friction stress model gives a set of curves for different values of the parameter

$$\chi = \tau_o/\mu\sigma_{ro}, \tag{16}$$

which is a measure of the relative magnitudes of the frictional stresses in the two models. For $\chi = 1$, the two models give almost identical results for $S'_a \leqslant 0.3$, i.e. the difference between the models is not distinguishable at low loads. Physically, this means that at low loads, the Poisson's contraction is negligible compared with the residual compressive strains normal to the interface. To distinguish the two models from such experiments, data are required at loads above about half of the load needed for interfacial separation (S'_a 0.5).

3.3. Coulomb friction law with roughness at fiber–matrix interface

Debonded interfaces invariably have roughness at some scale. The response during sliding is dependent on the dimensions of the asperities. At small asperities, local contact stresses are very high and sliding causes deformation and fracture without forcing the bodies either side of the interface to move apart. The micromechanics of such processes underlie the macroscopic friction response; for example, the Coulomb friction law. At larger scale asperities, the surfaces are forced to move apart without deforming plastically. In the constrained cylindrical configuration of fiber sliding, this causes an increase in the average normal stress and thence an increase in the frictional sliding resistance. It is this increased sliding resistance associated with constrained sliding that is referred to here as the roughness effect.

The average (local) radial stress at any position z within the debonded region of interface during fiber pulling can be written as the sum of three components, the radial stress far ahead of the debond tip (σ_r^+), the increase in stress due to the roughness-induced mismatch strain (ϵ_θ), and the change in stress due to the change in Poisson's contraction or expansion of the fiber (which is proportional to the change in axial stress in the fiber) [35]

$$\sigma_r = \sigma_r^+ + BE_m\epsilon_\theta + b_1\Delta\sigma_f \tag{17}$$

where $\Delta\sigma_f$ is the difference between the axial stresses at the location of interest and far ahead of the debond tip, and b_1 and B are dimensionless elastic constants defined in the Appendix [equations (A3b) and (A7)]. If the local sliding displacements, u, are larger than the average half-width of the roughness (and if the

roughness is not periodic), then ϵ_θ is a constant, independent of u. However, for smaller values of u, the mismatch strain ϵ_θ is dependent upon the local sliding displacements.† Two approximate limiting analyses will be considered here: one with ϵ_θ constant, corresponding to large sliding displacements, and the other with ϵ_θ proportional to $\Delta\sigma_f$, corresponding to small displacements.

3.3.1. Large displacements. If the roughness-induced mismatch strain is constant and if the frictional stress is given by the Coulomb friction law [equation (1)] with $\sigma_n = \sigma_r$, as given by equation (17), then the frictional stress can be written as

$$\tau = \tau_o + \mu\sigma_n^o \tag{18}$$

where σ_n^o is the normal stress that would be present for a smooth interface, and τ_o is a constant given by

$$\tau_o = \mu BE_m\epsilon_\theta. \tag{19}$$

Therefore, the effect of roughness in this case is equivalent to imposing the modified friction law defined by equation (18).

When the analysis leading to equation (2) is repeated using this modified friction law, a very simple result emerges: the displacements are given by an expression with the same form as equation (2), but with the parameters A and S_{Ro} replaced by A' and S'_{Ro}, where

$$A' = \frac{A + \chi}{\chi + 1} \tag{20}$$

$$S'_{Ro} = S_{Ro}(1 + \chi) \tag{21}$$

and χ is the same parameter defined in equation (16), although with τ_o defined by equation (19). With this definition of τ_o, the roughness parameter χ is also equal to the ratio of the radial mismatch strains due to the roughness and the thermal expansion mismatch

$$\chi = \epsilon_\theta/\lambda\epsilon_z^T \tag{22}$$

Curve fitting to experimental data proceeds in the same manner as described in Section 3.1, although in this case, there is an additional parameter, χ, to be obtained from the curve fit, i.e. equation (10) becomes

$$u/u^* = f_3(S_a, \epsilon\ell, G_c, \epsilon^*, \lambda, \chi). \tag{23}$$

3.3.2. Small displacements. If the sliding displacements are smaller than the average half-period of the roughness, so that the asperities do not slide over their nearest neighbors, the roughness-induced mismatch strain increases as the sliding displacement increases. The sliding displacements are zero at the tip of the debond crack and increase with distance z along the debonded region [Fig. 1(b)], at a rate that is dependent upon the distribution of misfit strains. Self-consistent solutions to this problem have been found for roughness with a sawtooth shape

---

†In the small displacement domain, there is also a net axial component of the local contact force which adds to the sliding resistance. This has been evaluated in detail elsewhere [35], but is not addressed here.

[35]. Here, we adopt an approximation that crudely models the increasing misfit strain with increasing z, while giving a very simple result. The misfit is taken to be proportional to the axial fiber stress difference $\Delta\sigma_f$

$$\epsilon_\theta = \beta \Delta\sigma_f / E_m \qquad (24)$$

where β is a dimensionless constant. With this misfit strain, the radial stress from equation (17) becomes

$$\sigma_r = \sigma_r^+ + b_1(1 - Y)\Delta\sigma_f \qquad (25)$$

where

$$Y = -\beta B / b_1. \qquad (26)$$

Equation (25) is equivalent to the result for a smooth interface [i.e. equation (17) with $\epsilon_\theta = 0$] with b_1 replaced by $b_1' = b_1(1 - Y)$. Since this equation is the only point at which the parameter b_f enters the displacement analysis for the smooth interface, the displacements for the roughness defined by equation (24) are given by equation (2) with b_1 replaced by b_1'. Both A and S_{Ro} in equation (2) are dependent on b_1 and thus become functions of Y, as well as the other parameters mentioned in Section 3.1.

Curve fitting to experimental data again follows the procedure described in Section 3.1 with the additional parameter Y to be evaluated from the curve fit, i.e. equation (10) becomes

$$u/u^* = f_4(S_a, \epsilon\ell, G_c, \epsilon^*, \lambda, Y). \qquad (27)$$

3.4. Uniqueness of solutions

Using the curve fitting procedure discussed in Section 3.1 for the smooth interface governed by Coulomb friction, with the additional measurement of axial relaxation ϵ^*, unique solutions are obtained for the fitted parameters μ, Γ, and λ. Moreover, once λ is known, the misfit strain ϵ_z^T and hence all of the residual stress components can be evaluated.

Both of the roughness models introduce an additional unknown parameter, so that curve fitting to the shape of the initial loading curve involves two adjustable parameters: λ and χ for one model, or λ and Y for the other. One way to assess whether unique solutions for these parameters can be obtained by curve fitting is to determine the possible sets of solutions for the two parameters, A' and S_{Ro}', that appear explicitly in the displacement equations. Thus, A' and S_{Ro}' are plotted for various values of λ and χ in Fig. 4(a) and for various values of λ and Y in Fig. 4(b). In both cases, the allowed values of A' and S_{Ro}' fall within a narrow band close to the values obtained for the smooth interface with varying values of λ. This indicates that many different combinations of λ and χ, or λ and Y, can give approximately the same values of A' and S_{Ro}' and hence, similar load–displacement curves. In other words, interfacial roughness and increasing anisotropy in the thermal misfit strain have very similar effects on the
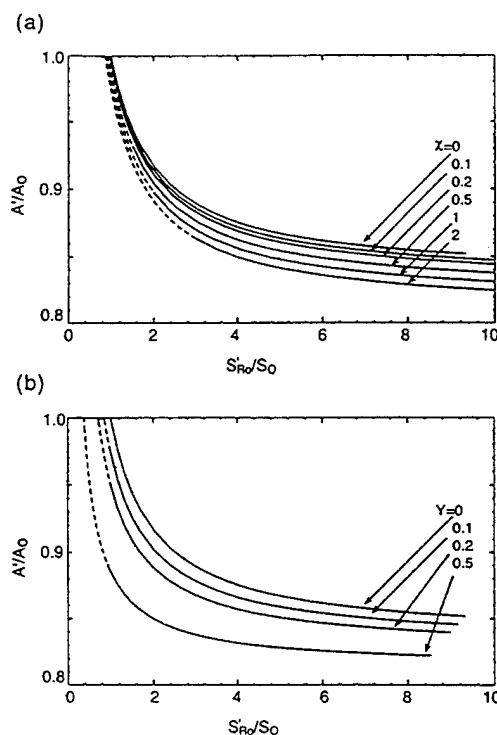
Fig. 4. Solutions of modified parameters S_{Ro}' and A' for two limiting roughness models. Both parameters are normalized by their values S_0 and A_0 for a smooth interface ($\chi = 0$, $Y = 0$) and isotropic misfit strain ($\lambda = 1$). Each curve for a given value of χ or Y represents the solutions for S_{Ro}' and A' for various values of λ: increasing λ shifts the solution (S_{Ro}', A') to the right along the curve, with $\lambda > 1$ over the solid portion of the curve and $\lambda < 1$ over the broken portion.

load–deflection curve and, therefore, are not easily distinguished by curve fitting.

4. EXPERIMENTAL DATA: THE INFLUENCE OF THERMOMECHANICAL FATIGUE ON INTERFACIAL SLIDING

4.1. Experiments

To investigate possible effects of thermomechanical fatigue on interfacial properties of titanium aluminide composites, fiber pulling experiments, as described in Section 2.1, were done on specimens cut from the central gauge sections of several uncracked tensile test specimens that had been subjected to cyclic loading. The composite contained four rows of SiC fibers (SCS-6, Textron Specialty Materials) in a matrix of Ti–24Al–11Nb. It was fabricated by the foil–fiber–foil method (by Textron). Specimens in three conditions were tested: (1) as-fabricated; (2) after cyclic loading at room temperature (500 cycles at 0–300 MPa); and (3) after cyclic loading at 650°C (500 cycles at 0–300 MPa).

From each gauge section, four rectangular bars (40 × 3 × 0.7 mm) were cut. One of these was used for measurement of fiber relaxation, while the others were used for single fiber pulling experiments. In the relaxation measurement, the matrix was etched from

Table 1. Properties of composites

Property	Composite		
	As-received	Cyclically loaded RT	Cyclically loaded 650°C
f	0.34	0.39	0.35
ϵ^*	0.0015	0.00039	0.00062
E_f (GPa)	415	415	415
E_m (GPa)	62	62	62
$v_f (= v_m)$	0.3	0.3	0.3

the central region of the beam, with the ends being masked. The increased separation of the ends was measured from optical micrographs taken against a fixed reference gauge before and after etching [39]. These measurements yielded the values of ϵ^* listed in Table 1. The single fiber pulling experiments were done as described in detail in Ref. [29]. From a small region near the center of each beam, all of the matrix and all except one of the fibers were removed by a combination of etching and mechanical cutting. Pullout of the remaining fiber from the matrix was then effected by loading the ends of the beam using a fixture on the stage of an optical microscope. The relative sliding displacements of the fiber and matrix were obtained by differential image analysis of *in situ* micrographs.

4.2. Analysis of results

Results of the fiber pulling experiments are shown in Figs 2, 5 and 6, along with curves fitted to the data

according to the models of Section 3. The fitted curves for the two roughness models are almost identical: therefore, to avoid repetition, only the plots for the large displacement model are shown in Figs 5 and 6. Various parameters evaluated from the fitted curves are listed in Table 2.

The curve fitting followed the procedure outlined in Section 3.1: with the end points at zero and maximum displacement being fixed to give calibrated values of Γ' and u^*, the intermediate data were used for fitting the parameters λ and χ or λ and Y. The other parameters in Table 2 were then evaluated using these fitted parameters and equations given in Section 3, the Appendix or Refs [32] and [34]. The errors indicated for λ, χ and Y in Table 2 are estimates of the uncertainties from the curve fitting.
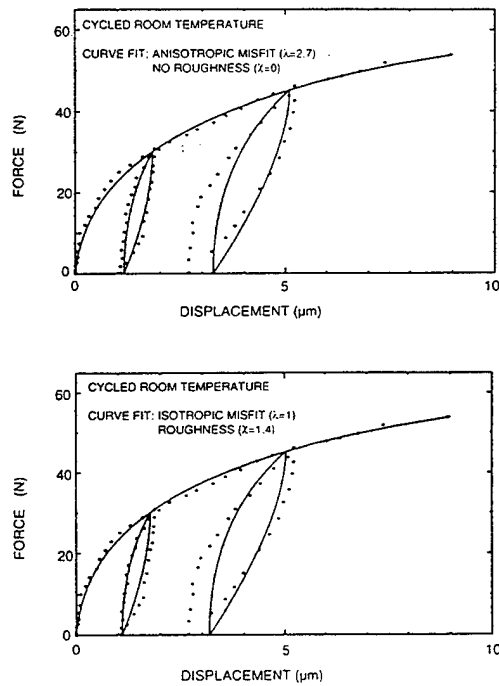
Fig. 5. Comparison of fiber sliding data and fitted curves, for Ti$_3$Al/SiC composite after cyclic loading at room temperature: (a) smooth interface, anisotropic residual misfit strain; and (b) rough interface, isotropic misfit strain.
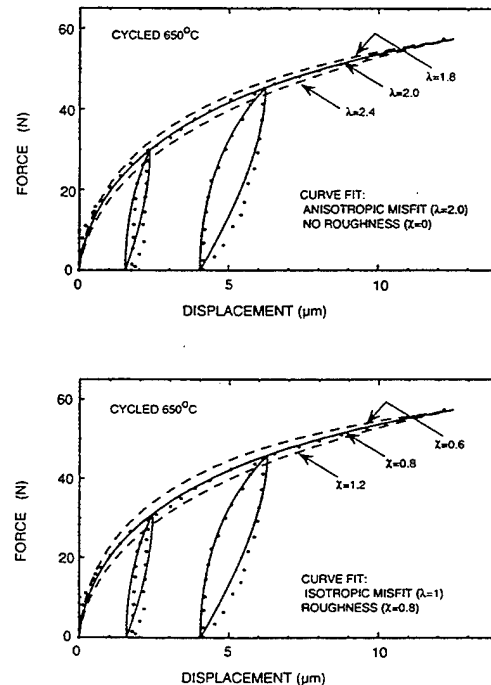
Fig. 6. Comparison of fiber sliding data and fitted curves for Ti$_3$Al/SiC composite after cyclic loading at 650°C: (a) smooth interface, anisotropic misfit strain; and (b) rough interface, isotropic misfit strain. Dark curves are the best fit for initial loading (and predicted for unload/reload cycles) The lighter curves corresponding to different values of λ and χ are included to give an indication of the sensitivity of the curves to these parameters.

Table 2. Parameters inferred from fiber sliding measurements†

| Model	Parameter	As-received	Cyclically loaded RT	Cyclically loaded 650°C
Smooth interface	λ	0.8 ± 0.1	2.7 ± 0.1	2.0 ± 0.1
($\chi = Y = 0$)	σ_{fo}^{+} (MPa)	-730	-252	-355 ± 5
$\tau = \mu\sigma_r$	σ_{ro}^{+} (MPa)	-170	-143	-159 ± 7
Anisotropic misfit	μ	0.75	1.1	0.78 ± 0.1
	τ_{max} (MPa)	128	155	124 ± 10
	τ_{min} (MPa)	38	32	30 ± 2
	G_c (J/m²)	$\leqslant 22$	<2.6	$<5.3 \pm 0.2$
Rough interface (large displacements)	χ		1.4 ± 0.1	0.8 ± 0.1
$\tau = \tau_o + \mu\sigma_r$	σ_{fo}^{+} (MPa)		-201	-311 ± 0
With isotropic misfit ($\lambda = 1$)	σ_{ro}^{+} (MPa)		-59	-86 ± 0
	μ		1.1	0.82 ± 0.1
	τ_{max} (MPa)		155	127 ± 10
	τ_{min} (MPa)		31	28 ± 3
	G_c (J/m²)		<1.7	$<4.0 \pm 0$
Rough interface (small displacements)	Y		0.55 ± 0.02	0.42 ± 0.02
with isotropic misfit ($\lambda = 1$)	σ_{fo}^{+} (MPa)		-201	-311 ± 0
	σ_{ro}^{+} (MPa)		-62	-90 ± 0
	μ		2.5	1.4 ± 0.1
	τ_{max} (MPa)		160	126 ± 8
	τ_{min} (MPa)		30	28 ± 2
	G_c (J/m²)		<1.7	$<4.0 \pm 0$

†Errors indicated for λ, χ and Y are estimated uncertainties from curve fitting. Errors shown for other parameters are the errors that result from the uncertainties in λ, χ and Y (thus, zero errors are indicated for parameters that are independent of χ and Y). These arrors are shown for only one specimen; they are similar for the others.

The errors indicated for the other parameters are the errors due to these uncertainties in λ, χ and Y.

The fiber pulling data from the as–fabricated composite can be fit reasonably well by the Coulomb friction law with a smooth interface and $\lambda = 1$ (isotropic misfit strain), although slightly better fit is obtained with $\lambda = 0.8$ (Fig. 2). The data from both specimens that had been subjected to fatigue loading [Figs 5(a) and 6(a)] were also consistent with the smooth-interface/Coulomb-friction model, but with significantly larger values of λ ($\lambda = 2.7 \pm 0.1$ and 2.0 ± 0.1) corresponding to the radial misfit strain being larger than the axial misfit. The significance of this anisotropy is confirmed by comparing the measured loads with the predicted response for an isotropic mismatch. For $\lambda = 1$, the maximum load that could be applied to the fiber (i.e. when the normal interfacial stress at $z = \ell$ decreases to zero) would be 25 N. This is less than half of the measured peak loads.

Alternatively, the load–displacement data for the fatigue specimens could be fit as well using either of the roughness models described in Section 3 with an isotropic mismatch strain. The fitted curves for the large sliding model ($\chi = 1.4 \pm 0.1$ for the specimen cycled at room temperature and $\chi = 0.8 \pm 0.1$ for the specimen cycled at 650°C) are shown in Figs 5(b) and 6(b), while the parameters evaluated from these curves and similar curves for the small–sliding roughness model are listed in Table 2. These results confirm that the effect of roughness on fiber sliding is similar to that of increasing λ.

The unload–reload curves shown in Figs 2, 5 and 6 are *predicted* using the equations given in Ref. [32] with the parameters obtained from curve fitting to the initial loading data. Again, the results of the three models are all very similar and agree well with the measurements.

4.3. Implications of results

The results indicate that tension–tension cyclic loading at both room temperature and high temperature caused significant relaxation of the residual axial stresses in the composite. Before loading, the measured axial stress in the fiber was ~730 MPa (compressive). The corresponding tensile axial stress in the matrix calculated using the measured volume fractions and the requirement for force balance is ~375 MPa. After cyclic loading at room temperature, these stresses were reduced to 200–250 MPa for the fiber stress and 130–160 MPa for the matrix stress (the ranges represent the values obtained from the different sliding models in Table 2). After loading at 650°C, the axial stresses were 300–350 MPa in the fibers and 160–190 MPa in the matrix. These conclusions are consistent with X-ray measurements of residual axial stresses in the matrix of the same specimens: 400 ± 30 MPa before loading; 159 ± 30 MPa after room temperature cyclic loading; and 131 ± 30 MPa after cyclic loading at 650°C [40].

The results also indicate that either: (1) the residual stress normal to the interface had not changed much after cyclic loading, so that the ratio of misfit strains in the radial and axial directions increased; or (2) if the radial stress had relaxed in concert with the axial stress, this relaxation was accompanied by damage to the interface, which caused an increased resistance to sliding consistent with a roughness induced effect. For the reasons discussed in Section 3, it is not possible to distinguish these possibilities from fiber sliding and axial relaxation data such as presented in this study. Additional data such as

measurement of radial mismatch strain would be required.

The parameters listed in Table 2 correspond to the extremes of these possibilities; on the one hand, no damage to the interface and very little relaxation of residual radial misfit strains, which would require misfit anisotropies of $\lambda = 2.7$ and $\lambda = 2.0$ after cyclic loading (the misfit was approximately isotropic before cyclic loading), or on the other hand, equal relaxations of radial and axial strains (i.e. misfit strain remains isotropic) accompanied by increased roughness. Although the physical implications of these models differ, the magnitudes of the interfacial sliding stresses are not sensitive to the models, as expected, since the measured fiber displacements relate directly to the distribution of interfacial sliding stresses (the values τ_{max} and τ_{min} listed in Table 2 are the frictional stresses at either end of the debonded region of the interface at the peak loads indicated in Figs 2, 5 and 6). The magnitudes of the sliding stresses are consistent with values reported in similar composite systems.

The data for all specimens are consistent with stress–displacement relations that pass through the origin. Therefore, the parameter Γ' was set to zero for the curve fitting. However, for $\Gamma' = 0$, equation (6) gives only an upper bound for γ; for smaller values of γ (i.e. $\gamma < \sigma_{fo}^+$), the residual axial stresses cause spontaneous debonding of the interface near the free surface of the matrix that is exposed by etching (i.e. where the fiber exits the matrix). In this case, the stress–displacement relation for fiber pulling is not affected by the magnitude of γ and is given by equation (2) with $\Gamma' = 0$ [32]. Therefore, the fiber pulling experiments can only provide the upper bound $\gamma = \sigma_{fo}^+$. The corresponding values of G_c are listed in Table 2. The decreases in these upper bounds after cyclic loading reflect the decreases in residual axial stresses. Data from fiber pushing experiments could, in principle, be used to determine actual values of G_c, since the displacements in that case are not independent of γ.

5. CONCLUSIONS

Analysis of several fiber sliding models has set some bounds on the types of data needed for unambiguous determination of interfacial properties from fiber sliding experiments. In addition to the elastic properties and dimensions of the constituents (assumed known), there are in general at least five parameters that affect sliding. These parameters define the interfacial debond energy, the interfacial sliding resistance, residual stresses (two parameters) and interfacial roughness. If the residual stresses (both radial and axial) are measured independently, the other parameters can be determined from sufficiently sensitive fiber sliding data, although whether different models of friction and roughness can be distinguished may depend on the range of data

accessible. For example, Coulomb friction and constant friction models can only be distinguished if data are available at sufficiently high loads. If residual stress measurements are not available, the effects of roughness and anisotropic residual stresses cannot be distinguished, for they both have similar effects on the fiber sliding characteristics.

The analysis was applied to data from a fiber reinforced titanium aluminide composite that had been subjected to cyclic loading: both fiber sliding measurements and measurements of residual axial stresses were available. The results indicated that cyclic loading at both room temperature and high temperature caused large relaxation in the residual axial stress and *either* a corresponding reduction in radial residual stress with damage to the interface and consequent roughness effects in fiber sliding, or very little reduction in residual radial stress and no damage to the interface. To distinguish these two possibilities, independent measurements of residual radial stress would be needed.

REFERENCES

1. D. B. Marshall. *J. Am. Ceram. Soc.* **67**, C259 (1984).
2. D. B. Marshall and W. C. Oliver, *J. Am. Ceram. Soc.* **70**, 542 (1987).
3. M. K. Brun and R. N. Singh, *Adv. Ceram. Mater.* **3**, 506 (1988).
4. T. P. Weihs and W. D. Nix, *Scripta. metall.* **22**, 271 (1988).
5. U. V. Deshmukh and T. W. Coyle, *Ceram. Engng Sci. Proc.* **9**, 627 (1988).
6. N. Shatry and D. G. Brandon, Interfacial friction and debond strength of aligned ceramic matrix composites. Proc. CIMTEC Meeting, Italy (1988).
7. J. W. Laughner and R. T. Bhatt, *J. Am. Ceram. Soc.* **72**, 2017 (1989).
8. P. D. Jero, T. A. Parthasarathy and R. J. Kerans, in *High Temperatue Ceramic Matrix Composites* (edited by R. Naslain, J. Lamon and D. Doumeingts), pp. 401–412. Goodhead, Cambridge (1993).
9. R. W. Goettler and K. T. Faber, *Comp. Sci. Technol.* **37**, 129 (1989).
10. J. D. Bright, D. K. Shetty, C. W. Griffin and S. Y. Limaye, *J. Am. Ceram. Soc.* **72**, 1891 (1989).
11. D. B. Marshall and W. C. Oliver, *Mater. Sci. Engng* **A126**, 95 (1990).
12. G. Morsher, P. Pirouz and A. H. Heuer, *J. Am. Ceram. Soc.* **73**, 713 (1990).
13. P. D. Jero and R. J. Kerans, *Scripta metall. mater.* **24**, 2315 (1990).
14. E. P. Butler, E. R. Fuller and H. Chan, *MRS Symp. Proc.* **170**, 17 (1990).
15. E. P. Butler, E. R. Fuller Jr, T. R. Palamides and H. M. Chan, in *Proc. Int. Symp. Advances in Processing of Ceramic and Matrix Composites* (edited by H. Mostaghacci). Pergamon Press, Oxford (1990).
16. T. P. Weihs and W. D. Nix, *J. Am. Ceram. Soc.* **74**, 524 (1991).

17. T. A. Parthasarathy, P. D. Jero and R. J. Kerans, *Scripta metall. mater.* **25**, 2457 (1991).
18. P. D. Jero, R. J. Kerans and T. A. Parthasarthy, *J. Am. Ceram. Soc.* **74**, 2793 (1991).
19. E. R. Fuller, E. P. Butler and W. C. Carter, in *Proc. NATO Conf. Toughening Mechanisms in Quasi Brittle Materials* (edited by S. P. Shah), pp. 385–403. Academic Press, Kluwer (1991).
20. P. D. Warren, T. J. Makin and A. G. Evans, *Acta metall. mater.* **40**, 1243 (1992).
21. C. H. Hsueh, M. K. Ferber and P. F. Becher, *J. Mater. Res.* **4**, 1529 (1989).
22. T. J. Makin, P. D. Warren and A. G. Evans, *Acta metall. mater.* **40**, 1251 (1992).
23. T. J. Makin, J. Y. Yang, C. G. Levi and A. G. Evans, *Mater. Sci. Engng* **A161**, 285 (1993).
24. D. Mumm and K. T. Faber, *Acta metall. mater.* **43**, 1259 (1995).
25. J. I. Eldridge and P. K. Brindley, *J. Mater. Sci. Lett.* **8**, 1451 (1989).
26. C. J. Yang, S. M. Jeng and J.-M. Yang, *Scripta metall. mater.* **24**, 469 (1990).
27. J. I. Eldridge, R. T. Bhatt and J. D. Kiser, *Ceram. Engng Sci. Proc.* **12**, 1152 (1991).
28. P. Kantzos, J. Eldridge, D. A. Koss and L. J. Gosn, *MRS Symp. Proc.* **273**, 135 (1992).
29. D. B. Marshall, M. C. Shaw and W. L. Morris, *Acta metall. mater.* **40**, 443 (1992).
30. M. C. Watson and T. W. Clyne, *Acta metall. mater.* **40**, 141 (1992).
31. J. I. Eldridge, *MRS Symp. Proc.* **273**, 325 (1992).
32. D. B. Marshall, *Acta metall. mater.* **40**, 427 (1992).
33. R. J. Kerans and T. A. Parthasarathy, *J. Am. Ceram. Soc.* **74**, 1585 (1991).
34. J. W. Hutchinson and H. M. Jensen, *Mech. Mater.* **9**, 139 (1990).
35. T. A. Parthasarathy, D. B. Marshall and R. J. Kerans, *Acta metall. mater.* **42**, 3773 (1994).
36. C. K. Bhihe and A. G. Evans, *Ceramic Engineering and Science Proceedings.* 17th Annual Conference on Composites and Advanced Ceramics (1993).
37. W. C. Carter, E. P. Butler and E. R. Fuller, *Scripta metall. mater.* **25**, 579 (1991).
38. M. R. James, W. L. Morris and B. N. Cox, *Exp. Mech.* **30**, 60 (1990).
39. B. N. Cox, M. R. James, D. B. Marshall and R. C. Addison, *Metall. Trans.* **21A**, 2701 (1990).
40. M. R. James, Damage tolerance concepts for titanium aluminide composites. 7th Interim Report, Wright Patterson Air Force Base Contract No. 33615-89-C-5621.

APPENDIX

The analysis leading to equation (2) is based on the Lamé solution for the stresses and strains in sections normal to the z axis [32, 34, 35]. With the superscript ($+$) denoting positions well ahead of the debond crack, the subscript (r) denoting radial stresses, strains and displacements at the interface, and the subscripts (f) and (m) denoting axial quantities in the fiber and matrix, the stresses and strains† well ahead of the debonded region in the absence of roughness effects are given by

$$\sigma_f^+ = a_1 f \sigma_a - a_2 E_m \epsilon_z^T \qquad \text{(A1a)}$$

$$\sigma_r^+ = a_3 f \sigma_a - a_4 E_m \epsilon_z^T \qquad \text{(A1b)}$$

$$\epsilon_f^+ = \epsilon_m^+ = a_5 f \sigma_a / E_m + a_6 \epsilon_z^T \qquad \text{(A1c)}$$

where the as are nondimensional functions of f, E_f/E_m, v_f,

---

†Strains in both the fibers, ϵ_f^+, and matrix ϵ_m^+ are measured relative to the unstressed state of the matrix.

v_f/v_m, ξ_f, and λ, given in Ref. [34], and σ_a is the axial stress in the loaded end of the fiber. (E_f and E_m are the Young's moduli of the fiber and matrix, v_f and v_m are the Poissons ratios and ξ_f is a parameter defining the elastic anistropy of a transversely isotropic fiber.) The residual stresses in the fibers in the absence of debonding and sliding, given by equation (A1) with $\sigma_a = 0$, will be denoted σ_{f0}^+ and σ_{r0}^+. The axial relaxation strain, ϵ^*, of the fibers measured when the matrix is removed by etching is given by

$$\epsilon^* = \epsilon_z^T (1 - a_6). \qquad \text{(A2)}$$

Behind the debond crack tip the *changes* in stresses and strains relative to their values far ahead of the crack (i.e. $\Delta\sigma_f = \sigma_f - \sigma_f^+$, $\Delta\epsilon_f = \epsilon_f - \epsilon_f^+$, etc.) are given for a smooth interface by

$$\Delta\sigma_m = \left(\frac{f}{1-f}\right)\Delta\sigma_f \qquad \text{(A3a)}$$

$$\Delta\sigma_r = b_1 \Delta\sigma_f \qquad \text{(A3b)}$$

$$\Delta\epsilon_f = b_2 \Delta\sigma_f / E_m \qquad \text{(A3c)}$$

$$\Delta\epsilon_m = -b_3 \Delta\sigma_f / E_m \qquad \text{(A3d)}$$

where the bs are another set of nondimensional functions of the same parameters as the as (with the exception of λ) given in Ref. [34]. The parameter A in equation (2) is defined as [32]

$$A = \left(1 - \frac{a_2 b_1}{a_4}\right)^{-1}. \qquad \text{(A4)}$$

The radial stresses behind the crack tip, σ_r, and well ahead of the crack tip, σ_r^+, are related by

$$\sigma_r = \sigma_r^+ + b_1 \Delta\sigma_f. \qquad \text{(A5)}$$

If the debonded interface is rough, sliding causes an additional radial misfit strain ϵ_0, which results in superposition of the radial stress

$$\sigma_r^\theta = B E_m \epsilon_0 \qquad \text{(A6)}$$

where

$$B = (b_1 a_2 - a_4)/\lambda. \qquad \text{(A7)}$$

The dimensionless elastic parameter B is negative and independent of λ.

The relative displacement of the fiber and matrix at $z = \ell$ in Fig. 1(b) (which corresponds to the measurements obtained in fiber pulling–pushing experiments) is given by

$$\delta = \int_0^\ell (\epsilon_f - \epsilon_m)\,dz = \frac{1}{E_b}\int_0^\ell \Delta\sigma_f\,dz \qquad \text{(A8)}$$

where

$$E_b = E_m/(b_2 + b_3). \qquad \text{(A9)}$$

The elastic constant E' that appears in the normalizing displacement u^* [equation (7)] is given by

$$E' = 2b_1 E_b \qquad \text{(A10)}$$

The constants a_i and b_i, which determine the elastic constants appearing in the body of this paper, can be evaluated from expressions given in Hutchinson and Jensen [34] or are available on a computer file from the authors. For the special case of a single fiber in a finite matrix with isotropic mismatch strain ($\lambda = 1$), isotropic fibers, and equal Poisson's ratios in fibers and matrix, the following

expressions are obtained

$$b_1 = \frac{E_c v}{[(1+v)E_f + (1-v)E_c]}$$ (A11)

$$B = -\frac{E_f(1-f)}{[(1+v)E_f + (1-v)E_c]}$$ (A12)

$$A = \frac{(1+v)E_f + (1-v)E_c}{E_f + (1-2v)E_c}$$ (A13)

$$E_b = \frac{E_f E_m(1-f)}{E_c(1+v)} A$$ (A14)

$$a_6 = fE_f/E_c$$ (A15)

where E_c is the rule-of-mixtures modulus ($E_c = fE_f + (1-f)E_m$).

For the analysis of the experimental data in this paper, which involved pulling a single fiber within a composite containing many fibers, the constants a_i were evaluated using the value of f corresponding to the composite (as well as anisotropic misfit strain, $\lambda \neq 1$), whereas the constants b_i were evaluated using $f = 0$. For the pushing or pulling of multiple fibers, all of the constants a_i and b_i would be evaluated using the value of f for the composite, with b_i evaluated using type II boundary conditions (see Refs [32] and [34]).